

Editors

Assoc Prof. Enes YİĞİT, Ph.D
Assist Prof. Umut ÖZKAYA Ph.D

**PIONEER AND
CONTEMPORARY STUDIES
IN ENGINEERING**

PIONEER AND CONTEMPORARY STUDIES IN ENGINEERING

Editors:

Assoc. Prof. Enes YİĞİT,

Ph.D - Assist Prof. Umut ÖZKAYA Ph.D



Pioneer and Contemporary Studies in Engineering

Editors: Assoc Prof. Enes YİĞİT, Ph.D - Assist Prof. Umut ÖZKAYA Ph.D

Editor in chief: Berkan Balpetek

Cover and Page Design: Duvar Design

Printing : JUNE-2023

Publisher Certificate No: 49837

ISBN: 978-625-6945-90-6

© Duvar Publishing

853 Sokak No:13 P.10 Kemeraltı-Konak/Izmir/ Turkey

Phone: 0 232 484 88 68

www.duvar yayinlari.com

duvarkitabevi@gmail.com

Chapter 1	7
Determination of Optimum Machining Parameters of Incoloy 901 Super Alloy with Cemented Carbide Tools by the Taguchi Method <i>Abdullah ALTIN , Muhammed Cihat ALTIN</i>	
Chapter 2	21
Water Penetration Effects on Concrete Strength and Prevention Approaches <i>Muhammed MARAŞLI, Serkan SUBAŞI, , Doğu RAMAZANOĞLU, Volkan ÖZDAL, Yasemin HATİPOĞLU</i>	
Chapter 3	45
The Critical Role of GDL Properties in Enhancing Proton Exchange Membrane Fuel Cell Performance <i>Hüseyin KAHRAMAN, İdris CESUR</i>	
Chapter 4	59
Design of Multilayer Radar Absorber Using Grey Wolf Optimization Algorithm <i>Şeyma ATICI, Enes YİĞİT, Umut ÖZKAYA</i>	
Chapter 5	75
The Effect of Changes in Consumption Habits on the Ecological Footprint During Covid-19 Pandemic <i>Cemre Belit ÇOBANOĞLU KAYIKCI, Nazlıcan YEŞİLOVA, Emine ELMASLAR ÖZBAŞ, Atakan ÖNGEN, Hüseyin Kurtuluş ÖZCAN, Serdar AYDIN, Sinan GÜNEYSU</i>	
Chapter 6	99
A Review on Machinability of Inconel 718 <i>Abdullah ALTIN, Muhammed Cihat ALTIN</i>	
Chapter 7	115
Cone Crusher Structural Analysis Requirement <i>Ali Kemal ÇAKIR</i>	

Chapter 8	127
Large Language Models and Their Current Use Cases	
<i>Akın ÖZÇİFT</i>	
Chapter 9	141
Evaluation of Production Mechanism of	
Polyester Composites: Determination of Physical and Chemical Properties	
<i>Ercan AYDOĞMUŞ, Ahmet Beyzade DEMİRPOLAT</i>	
Chapter 10	155
Wind Speed Estimation by using	
Geographic Information System (GIS) and Machine Learning (ANN):	
A case study of Kastamonu Region in Turkey	
<i>Mehmet GÜRDAL</i>	
Chapter 11	187
Evaluation of Suitability of Antalya (Turkey) Karst Travertine Plateau	
for Underground Dam	
<i>Mehmet OZCELIK</i>	
Chapter 12	205
Investigation of Turkey's Thermal Water Resources	
<i>Melike YALILI KILIÇ</i>	
Chapter 13	219
Comparison of Incentives and Supports Applied in	
Utilizing Solar Energy in Turkey and Germany	
<i>Murat BATAN</i>	
Chapter 14	241
Forward Dynamic Structural Modification of Rotor Systems Using	
Frequency Response Functions with Sherman-Morrison-Woodbury Formula	
<i>Murat ŞEN, Orhan ÇAKAR</i>	
Chapter 15	259
Design of Fractional Order PD Controller Based on	
PSO Algorithm for Fractional Order Systems	
<i>Münevver Mine ÖZYETKİN, Hasan BİRDANE</i>	

Chapter 16	293
Cost-Based Optimization of Raw Materials in Production of High Carbon Ferrochrome <i>Sinan KAPAN, Ünal ÇAMDALI, Nevin ÇELİK, Osman YİĞİD</i>	
Chapter 17	305
Rule-based Explainable Artificial Intelligence <i>Sinem AKYOL</i>	
Chapter 18	327
A Study on Meta-Heuristic Algorithms Used for Problem Solving in Recent Years <i>Ahmet AKKAYA, Cemil KÖZKURT, Rafet DURGUT</i>	
Chapter 19	353
Treatment of Textile Industry Wastewater Containing Reactive Black 5 and Reactive Orange 16 Dyes By UV/H ₂ O ₂ Oxidation <i>Ayşe Elif ATEŞ, Sinan ATEŞ</i>	
Chapter 20	367
Valorisation of Tropical Fruit Waste for Sustainable Biofuel Production through the Biorefinery Approach <i>Mukaddes KILIÇ BAYRAKTAR, Ernestine Fabiola DJOUCHE</i>	
Chapter 21	383
Mathematical Modelings for the Thin-Layer Drying of Red Pepper Slices <i>Murat ERDEM, Muhammet AYDIN, Filiz ÖZGEN</i>	
Chapter 22	409
An Overview of the Empirical Investigations into the Classification of Power Quality Disturbances <i>Sıtkı AKKAYA</i>	
Chapter 23	431
A Novel Method for the Analysis of Multiscale Fracture Problems with Energy Density Concepts <i>Murat SARIBAY</i>	

Chapter 24

453

A Review of the Experimental Studies on Analysis of
Power Quality Disturbances

Sıtkı AKKAYA

Chapter 25

479

Current Approach in Sourdough Fermentation

Çisem BULUT ALBAYRAK, Lütfiye ÇETİN, Eren GÜVENDİ

Chapter 1

Determination of Optimum Machining Parameters of Incoloy 901 Super Alloy with Cemented Carbide Tools by the Taguchi Method

Abdullah ALTIN¹

Muhammed Cihat ALTIN²

1 Prof. Dr.; Yuzuncu Yıl University, Van Vocational of Higher School, Mechanical and Metal Technology Department. Van/Turkey,
aaltin@yyu.edu.tr ORCID No:0000-0003-4372-8272

2 Öğr. Gör. Muhammed Cihat ALTIN, Yuzuncu Yıl University, Van Vocational of Higher School, Electric and Energy Department. Van/Turkey,
caltin@yyu.edu.tr ORCID No:0000-0002-5224-8978.

ABSTRACT

In this research work, was made a study on the effects of turning conditions on incoloy 901 nickel-based superalloy and performed a precision analyzes using the Taguchi L27 orthogonal array. Using the results of variance analysis (ANOVA) and signal-to-noise (S / N) ratio and taking into account the "smaller is better" approach were statistically investigated to establish a correlation amongst the speed of cutting, feed rate and cutting tool with respect to surface quality and cutting forces. KCU10, K313 and KCU25 cemented carbide cutting tool were used in experimental study. The experimental results have revealed the most important factor influencing the cutting force and surface quality was the type of the cutting tool and it's had a serious effect on both, KCU10 and followed by KCU25 was found better than the other cutting tool. Optimum parameters for the cutting forces was found 0,150 mm/rev., 90 m/min. with KCU10 cutting tool The found findings can help for revealed the optimization of machining parameters and surface characteristics of Incoloy 901 during high speed turning.

Keywords: Taguchi, optimization, Incoloy 901, Surface roughness, Cutting force.

INTRODUCTION

Nickel-based superalloys have attracted a great deal of interest from aircraft and nuclear industry with the heat treatment industry because of its resistance to heat, excellent mechanical properties, resistance to corrosion and high temperature operation (Chouldhury, 1997:195). These alloys are used extensively in the chemical industry to produce heaters, condensers for the treatment of fatty acids, evaporator pipes for the production of sodium sulphate, pipe mirrors and other equipment. Nickel-based superalloys are among the materials that are known to be the most difficult to process in obtaining a quality surface (Ezugwu et al, 1998:1)

Superalloys are grouped into forging, casting and powder metallurgy alloys. Inconel 901 is the most widely used material among commercial superalloys in the aerospace industry (Field, 1968:151). In the machining of nickel-based superalloys, the short tool life and the frequent deterioration of the surface quality of the workpiece are seen as an issue that needs to be investigated. Residual stresses formed on the surface of the part may adversely affect the mechanical stress and corrosion properties of the machined material during the chip removal process (Warbuton, 1967:151).

The amount of super alloys used in the engine, due to its ability to operate at high temperatures, reached 60% of the total aircraft engine weight in the 1990s and is constantly increasing (Bartlay, 1988:178). The high oxidation resistance of these alloys at temperatures exceeding 650 °C and the tensile strength at the phase boundaries are excellent. 45% of the produced superalloy is forged and 25% is cast nickel-based superalloy (Chouldhury, 1996:23). Nickel-based superalloys contain at least 50% nickel (Sims, 1972:25). Nickel is the main compositional element. Due to its low thermal conductivity and high cutting strength, however, due to the intense heat generated at the cutting edge, processing is still very difficult (Loria, 1992:33). Hard abrasive carbides (eg MC, M₂₃C₆) present in the microstructure of nickel-base superalloys provide abrasive wear that causes tool wear. In parallel with the developing technology, manufacturing and material technology is also in a rapid development process, and "quality and economy in production" are at the forefront. For this reason, in industrial applications, it is possible to reach the goal by using all possible options in manufacturing and all kinds of materials that are production tools (Ezugwu, 2003:233). Considering the metallurgical and mechanical properties, the diversity of the material used requires the use of different processing methods. However, a processing technique for each material or the determination of the material to be used in production according to the existing processing possibilities negatively affects the quality in production (White,

1956:12). Structural deterioration in the processed surface and surrounding areas depending on the processing method is another factor affecting the production quality and processing economy. For this reason, the material constituting the whole and the manufacturing method used in its processing have been and will continue to be the main subject of current research (Chouldhury, 1995:125).

It is a new machining method that has been started to be used in companies that process parts on CNC machines in high speed machining, aerospace industry, automotive and mold making. In general, this method is the cutting process using small tools with low cutting passes at high speeds and advances. This process has started to be replaced by a slow and more cutting process with a small number of passes and large tools. Although the amount of chip removed in high-speed machining technology is low, the machining time of the part is 30% less on the general average, and in some cases, the part that comes out of the CNC machine becomes ready for use without the need for polishing (Brandt. 1990:273). In high speed machining, cutting tools will wear out faster than in normal cutting operations. Due to the negative effects of this type of wear on the measurement accuracy, when choosing cutting tools in high-speed machining, TiN (titanium-nitride) and TiCN (titanium-carbon-nitride) for materials below 40 RC and TiAlN (titanium-aluminum-nitride) for materials with hardness above 40 RC) coated cutting tools are recommended (Richards, 1989:575). Incoloy 901 can be machined at low cutting speeds (30-50 m/min.) with cheaper cemented carbide tools, while at higher cutting speeds (150-250 m/min.) it can be machined with more expensive whisker-reinforced aluminum oxide ceramic tipped tools. For this reason, researchers tried to determine the most suitable cutting conditions by experimenting with different cutting tool materials and different cutting parameters (Govindan et al. 2014:89).

However, there are very few studies on Incoloy 901 material on this subject in our country. As a result of the literature research, the studies on this subject, the methods followed and the results obtained are examined in detail in this work.

Materials and Method

Experimental studies were carried out under dry cutting conditions at a power of 10 kW and a speed of 50-3500 rpm. JOHNFORD T35 is an industrial CNC lathe. (F_x , F_y , F_z) were measured using a three-piece piezo electric Kistler brand 9257 B type dynamometer. The device is mounted on a stand with a suitable load lifter. The device visually displays a direct and continuous graph record of each of the three forces. Depth of cut (1 mm) and feed rate (0.10-

0.125 and 0.15 mm/rev.) were selected and fixed considering the ISO 3685 standard and manufacturer's recommendations. Surtrasonic 3-P measuring device and 40° approach angle PCLNR 2525 M12 type tool holder were used for measurement.

Analysis of Variance

ANOVA is used to statistically determine the importance of process factors that affect performance characteristics (Adinarayana et al. 2014:20). Response Surface Methodology (RSM) is used to obtain an empirical correlation between control factors and responses. A total of 27 experiments were performed based on the L27 orthogonal experiment design. The L27 orthogonal design consists of 27 columns (26 degrees of freedom) corresponding to 9 columns and 3 levels of turning experiments (Sujit et al. 2014:236). The S/N ratio is a statistical measure of the performance characteristics of the Taguchi method and is a logarithmic function of the desired response (Hweju, 2020:691). ANOVA results for main cutting force and average surface roughness are given in Table 1 and Table 3. The result of cutting forces and surface roughness measurements and the S/N ratio are shown in Table 2.

Experimental Work and Measurement

Design of experiments

In this study, the materials prepared in Ø2x40 " (inch) dimensions were processed by subjecting to chip removal processes in CNC turning experiments. Turning experiments were designed using the Taguchi method. Taguchi's L27 experimental matrix was used to evaluate the responses. Three cutting parameter levels are selected, namely cutting speed (V), feedrate (f), and cutting tool type (C).

Results

Analysis of the S/N ratios

The results of experiments and S/N ratios determined by

$$x_i(k) = -10 \log\left(\frac{1}{y_i^2(k)}\right) \quad \text{For "larger is better" response} \quad (1)$$

$$x_i(k) = -10 \log(y_i^2(k)) \quad \text{For "smaller is better" response} \quad (2)$$

$$x_i(k) = -10 \log([y_i(k) - y_0]^2) \quad \text{For "nominal is better" response} \quad (3)$$

Where y_i is the response of the process. The smaller values of both responses are the optimal, for instance. [18]. In order to compare the influence of factors on different responses, the average S/N ratios of responses related to the levels are calculated and given in Table 2. In this work, the optimum machining conditions that give either smallest roughness or cutting force values are determined by selecting the largest S/N ratio for each cutting condition. From the Figure 1, it is apparent that optimum combination of the parameters for a single response of Fz is A1B3C1. The results of this study also indicates that the optimal conditions of machining parameters for surface roughness Ra is A2B1C3. From this analysis, different optimum combinations are determined for Fz and Ra.

Table 1: ANOVA results for cutting force (Fz) at Inconel 901

Source	DF	Adj SS	Adj MS	F-Value	P-Value	Contribution
C	A 2	3,84	0.1,919	0,80	0.555	%14
V	B 2	1504,2	752,1	314,1	0,003	%58,54
f	C 2	1056,4	528,2	220,6	0.005	%41,1
Error	2	4,79	2,394			%0,18
Total	8	2569,2				100.00

Table 2: S/N ratios for Ra and Fz in Inconel 901 with cemented carbide cutting tools.

Feed rate	Cutting speed	Cutting tool	Main cutting force Fz (N)	S/N ratio For Fz	Average of surface roughness (Ra)	S/N ratio For Ra
0.100	60	KCU10	360,92	-51,148	1,033	-0,28201
0.100	60	K313	420,82	-52,48	1,253	-1,95902
0.100	60	KCU25	483,96	-53,696	2,920	-9,30766
0.100	75	KCU10	344,11	-50,733	0,729	2,74545
0.100	75	K313	402,28	-52,090	1,732	-4,77096
0.100	75	KCU25	442,87	-52,925	2,820	-9,00498
0.100	90	KCU10	333,89	-50,472	1,299	-2,27218
0.100	90	K313	401,25	-52,068	2,041	-6,19686
0.100	90	KCU25	452,66	-53,115	2,820	-9,00498
0.125	60	KCU10	374,45	-51,467	0,712	2,95040
0.125	60	K313	449,95	-53,063	1,213	-1,67722
0.125	60	KCU25	513,42	-54,209	1,604	-4,10409
0.125	75	KCU10	358,84	-51,098	0,846	1,45259
0.125	75	K313	424,46	-62,556	0,939	0,54669
0.125	75	KCU25	477,01	-52,556	1,283	-2,16453

0.125	90	KCU10	360,38	-51,135	0,835	1,56627
0.125	90	K313	409,18	-52,238	0,932	0,61168
0.125	90	KCU25	478,09	-53,590	1,380	-2,79758
0.150	60	KCU10	358,63	-51,092	0,898	0,93447
0.150	60	K313	422,34	-52,513	1,069	-0,57955
0.150	60	KCU25	487,11	-53,752	1,721	-4,71562
0.150	75	KCU10	344,09	-50,733	0,765	2,32677
0.150	75	K313	397,12	-51,978	2,110	-6,48565
0.150	75	KCU25	450,22	-53,068	2,352	-7,42875
0.150	90	KCU10	316,95	-50,019	1,398	-2,91014
0.150	90	K313	395,05	-51,933	1,438	-3,15518
0.150	90	KCU25	463,80	-53,326	2,059	-6,27313

Table 3: ANOVA results for surface roughness (Ra) at inconel 901

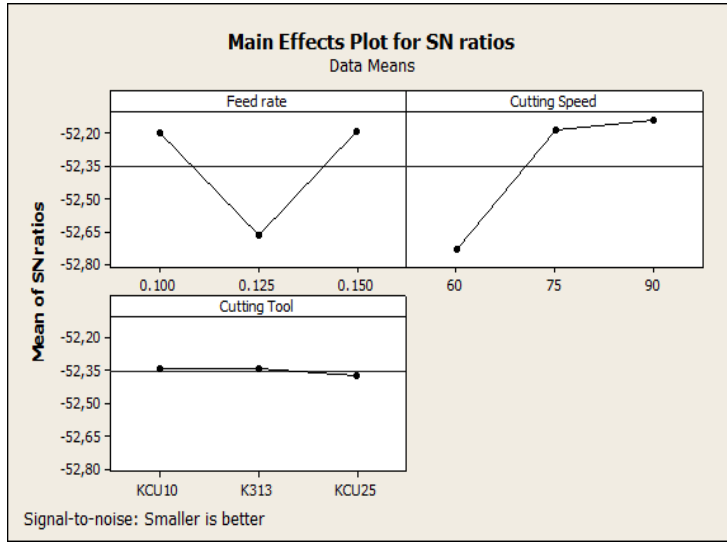
Source	DF	Adj SS	Adj MS	F-Value	P-Value	Contribution
C	2	0.0,0133	0,0066	0,09	0.917	%1,19
V	2	0.0603	0.0301	0,41	0.710	%5,4
F	2	0.8916	0,4458	6,03	0.142	%80,09
Error	2	0.1479	0.0739			%13,28
Total	8	1,1132				%100

Table 4: The optimum result and verification test (Ra (μm) for surface roughness (Ra) at Inconel 901.

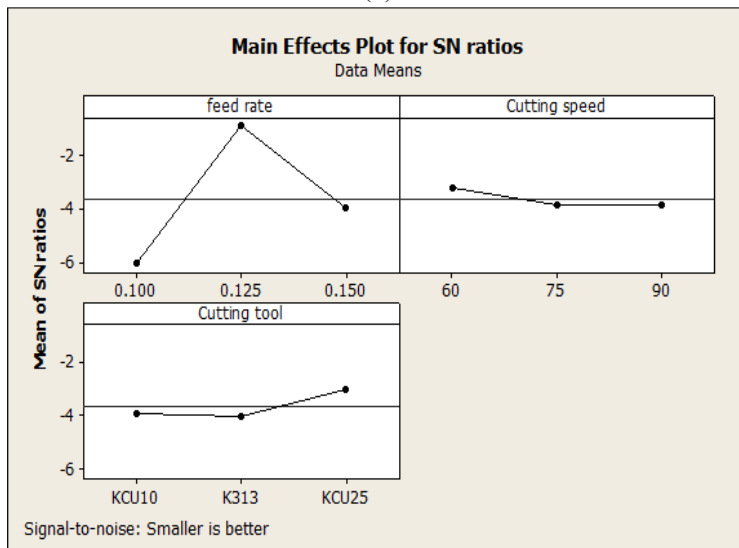
	Initial cutParameters	Optimum cutting parameters	
		Predicted Verification	Verification experiment
Level	0,150-75-KCU 10	0,125-60-KCU 25	0,125-60-KCU 25
Surface roughness	2,820	1,069	1,055
S / N ratio (dB)	-9,004	-0,579	-0,465
S / N ratio	8,539		
Error (dB)	8,425		

DISCUSSION

From the Figure 1, it is apparent that optimum combination of the parameters for a single response of Fz is A1B3C1. The results of this study also indicates that the optimal conditions of machining parameters for surface roughness Ra is A2B1C3. From this analysis, different optimum combinations are determined for Fz and Ra. cutting speed increases as cutting forces decrease. The surface roughness changes as the cutting speed increases.

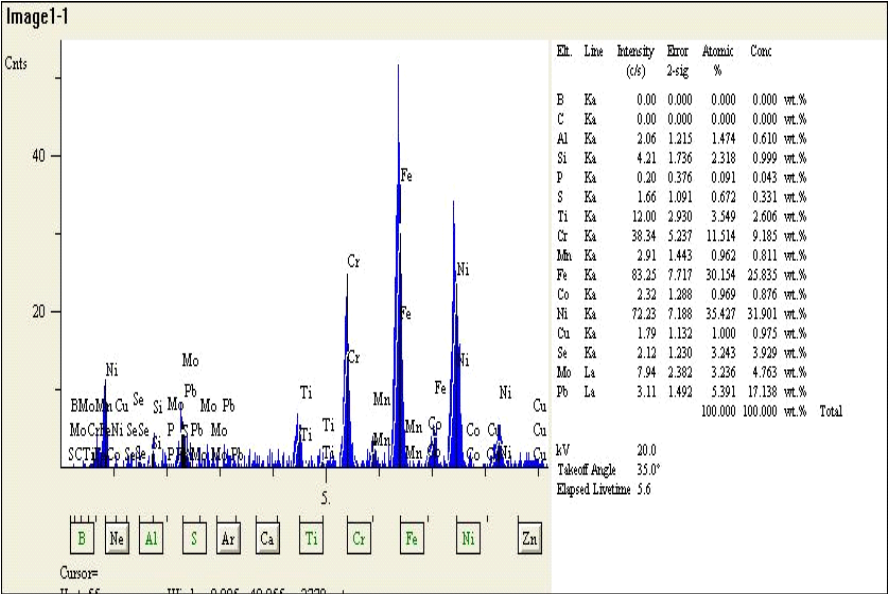


(a)

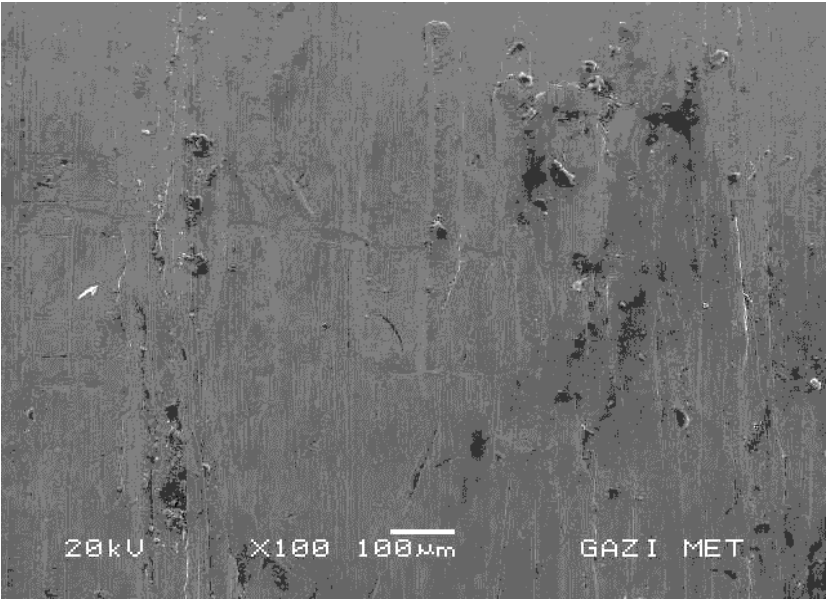


(b)

Figure 1: Average response graphs of (a) cutting forces (b) surface roughness according to feed rate, cutting speed and cutting tool at Inconel 901.



(a)



(b)

Figure 2: (a) SEM secondary electron photo micrograph of the base material as-received condition of Incoloy 901 superalloy and EDS spectrums (b) M6C carbide particles shown in the inset.

CONCLUSION

In this study, Incoloy 901 is tested and the Taguchi orthogonal array set is thought to be suitable for analyzing the cutting force and average surface roughness described in this study. It was observed that the cutting speed and feed rate had a higher effect on the cutting force while the feed rate and cutting speed had a higher effect on the average surface roughness. It was observed that the cutting speed and feed rate had a higher effect on the cutting force while the feed rate and cutting speed had a higher effect on the average surface roughness. Optimum parameters for the cutting forces was found 0,150 mm/rev., 90 m/min. with KCU10 cutting tool. For the surface roughness 0,125 mm/rev. 60 m/min and KCU25 cutting tool was found better parameters. The most effective factor on the cutting force by ANOVA is found to be cutting speed (58.54%), followed by feed rate (41.10%) and for the surface roughness the most effective factor is feed rate (80,09%), followed by cutting speed (5,4%) for machining Incoloy 901. For the surface roughness 0,125 mm/rev. 60 m/min and KCU 25 cutting tool was found better parameters. The most effective factor on the cutting force by ANOVA is found to be cutting speed (58.54%), followed by feed rate (41.10%) and for the surface roughness the most effective factor is feed rate (80,09%), followed by cutting speed (5,4%) for machining Incoloy 901.

Acknowledgment

This work is supported by the University of Yuzuncu Yıl under Grants No. BAP 2015VMYO-B093 project

References

- Adinarayana M, Prasanthi G, and Krishnaiah G, "Optimization for Surface Roughness, MRR, Power Consumption Turning of En24 Alloy Steel Using Genetic Algorithm ," International Vol. 3, No. 1, pp. 20-26, January 2014. *Journal of Mechanical Engineering and Robotics Research*.
- Bartlay, E., "Super Alloys a Technical Guide", p178 (1988).
- Brandt, G., Gerendas, A., Mikus, M.W., "Car mechanics of ceramic cutting tools when machining ferrous and non-ferrous alloys", *J. European Ceramic Soc.*, 6 (5), 273-290 (1990).
- Chouldhury, I. A, El-Baradie, M. A., Machinability assessment of nickel based alloys: tool life in turning Inconel 718, In *Proceedings of the Sixth Cairo University International MDP Conference*, 233-240, Cairo, Egypt (1996).
- Chouldhury, I. A., "Machinability studies of high strength materials and the development of a data base system", PhD thesis, Dublin City University p125 (1995).
- Chouldhury, I. A., El-Baradie, M. A., "Machining nickel base superalloys: inconel 718", *Proc Instn Mech Engrs*, Vol 212, Part B, 195-205 (1997). Chouldhury, I. A., El-Baradie, M. A., "Machining nickel base superalloys: inconel 718", *Proc Instn Mech Engrs*, Vol 212, Part B, 195-205 (1997).
- Ezugwu, E. O., Bonney, J., Yamane, Y., "An overview of the machinability of aeroengine alloys", *Journal of Materials Processing Technology*, 134, 233-253 (2003).
- Ezugwu, E. O., Wanga, Z. M., Machadop A. R., "The machinability of nickel-based alloys: a review", *Journal of materials Processing Technology*, Volume 86, Issues 1-3, 1-16 (1998).
- Field, M., "Machining aerospace alloys", Iron and Steel Institute, Special Report 94, 151-160 (1968). Warbuton, P., "Problems of Machining Nickel-Based Alloys", Iron and Steel Institute, Special Report 94, 151-160 (1967).
- Govindan P and Vipindas M P, "Surface Quality Optimization in Turning Operations Using Taguchi Method-A Review," *International Journal of Mechanical Engineering and Robotics Research*, Vol. 3, No. 1, pp. 89-118, January 2014.
- Hweju, H "Effect of Machine-Tool Rigidity on Geometric Error Formation in Turning Operation," *International Journal of Mechanical Engineering and Robotics Research*, Vol. 9, No. 5, pp. 691-695, May 2020. DOI: 10.18178/ijmerr

- Loria, E. A., “Recent development in the progress of super alloy 718”, J. Maler, Sci, 44 (6), 33-36 (1992).
- Philip, T.V. and Mccaffrey, T.J. ,“Metals Handbook, 10th edition”, ASM international, USA p 56 (1990). Wireless LAN Medium Access Control (MAC) and Physical Layer (PHY) Specification, IEEE Std. 802.11, 1997.
- Richards, N., Aspinwall, D., “Use of ceramic tools for machining nickel- based alloys”, Int. J. Mach. tools Manuf., 294, 575-588 (1989).
- Sims, C.T., Hagel, W.C., The Superalloys Wiley, New York p 25 (1972).
- Sujit Kumar Jha, "Optimization of Process Parameters for Optimal MRR during Turning Steel Bar Using Taguchi Method and Anova," International Journal of Mechanical Engineering and Robotics Research, Vol. 3, No. 3, pp. 231-243, July 2014.
- White, C. H., “Nickel Base Alloys”, Wiggins Alloy.p 12 (1986)

Chapter 2

Water Penetration Effects on Concrete Strength and Prevention Approaches

Muhammed MARAŞLI¹

Serkan SUBAŞI²

Doğu RAMAZANOĞLU³

Volkan ÖZDAL⁴

Yasemin HATİPOĞLU⁵

1 Fibrobeton Building Elements San. Ins. Tic. A.S, R&D department.
muhammed@fibrobeton.com.tr ORCID No: 0000-0003-2684-1003

2 Prof. Dr., Duzce University, Faculty of Engineering, Department of Civil Engineering,
serkansubasi@duzce.edu.tr ORCID No: 0000-0001-7826-1348

3 Fibrobeton Building Elements San. Ins. Tic. A.S, R&D department.
doguramazanoglu@duzce.edu.tr ORCID No: 0000-0002-6356-5792

4 Fibrobeton Building Elements San. Ins. Tic. A.S, R&D department.
volkan.ozdal@fibrobeton.com.tr ORCID No: 0000-0003-0033-0563

5 Fibrobeton Building Elements San. Ins. Tic. A.S, R&D department.
yasemin.hatipoglu@fibrobeton.com.tr ORCID No: 0000-0003-1045-9264

ABSTRACT

Concrete is an enduring and versatile building material that has been utilized for centuries. Its composition comprises cement, water, and aggregates, and can be strengthened with steel to resist high loads and stresses. Nonetheless, the permeability of concrete to water remains a significant challenge in its usage. Water ingress can occur through multiple sources, such as rainfall, ground moisture, and capillary action, leading to a range of issues such as reduced strength, cracking, and corrosion of steel reinforcement.

This book section aims to investigate the effects of water penetration on concrete strength and present an overview of the prevention methods that can be employed to mitigate these effects. The upcoming chapters will initially examine the causes and forms of water penetration in concrete and their consequences on its strength. Subsequently, different prevention strategies will be discussed, including mixed design techniques, curing practices, surface treatments, and structural approaches. Furthermore, the section will delve into the testing and evaluation methods for water penetration in concrete and provide real-life case studies and examples of the prevention methods in action.

The ultimate objective of this book section is to provide readers with an all-inclusive comprehension of the impacts of water penetration on concrete strength and the approaches that can be implemented to prevent and address these concerns. By the section's conclusion, readers will have an enhanced understanding of the intricate interplay between water and concrete and the importance of appropriate design, construction, and maintenance practices to guarantee the durability and longevity of concrete structures.

Keywords: Concrete, Water Penetration, Strength, Prevention Methods, Durability.

INTRODUCTION

Concrete is a popular construction material due to its strength, durability, and versatility. However, its susceptibility to water penetration has been a major concern for construction professionals for decades. Water can enter concrete through various sources such as rainfall, ground moisture, and capillary action, leading to a range of problems, including reduced strength, cracking, and corrosion of steel reinforcement.

To address this issue, engineers and scientists have been developing prevention strategies and testing methods to determine the extent of water penetration in concrete structures. This book section titled "Water Penetration Effects on Concrete Strength and Prevention Approaches" will provide an in-depth exploration of the effects of water penetration on concrete strength and the prevention strategies that can be used to mitigate these effects.

The book section will begin with an overview of the causes and types of water penetration in concrete, as well as their impact on its strength. The authors will examine the various prevention approaches, including mix design strategies, curing techniques, surface treatments, and structural approaches. The book section will also cover methods for testing and evaluating water penetration in concrete, such as the use of non-destructive testing methods.

In addition to discussing prevention strategies, the book section will provide real-world case studies and examples of successful prevention approaches in action. This will help readers to understand how to apply these approaches in practice, and how to adapt them to their specific project needs.

The goal of this book section is to equip readers with the knowledge and tools necessary to design and construct durable, long-lasting concrete structures that can withstand the effects of water penetration. By the end of this section, readers will have a deeper understanding of the complex interplay between concrete and water, and the importance of proper design, construction, and maintenance practices.

Purpose And Scope of The Section

The purpose of this book section is to provide a comprehensive understanding of the effects of water penetration on concrete strength and the prevention approaches that can be used to mitigate these effects. This section aims to explore the various causes and types of water penetration in concrete and their impact on its strength. Additionally, the section will discuss the prevention approaches that can be taken to mitigate water penetration, including mixed design strategies, curing techniques, surface treatments, and structural approaches.

The scope of this book section is broad, covering a range of topics related to water penetration in concrete. The section will start with an overview of the causes and types of water penetration and their impact on concrete strength. Then, it will delve into the various prevention approaches that can be used to mitigate these effects, including mix design strategies, curing techniques, surface treatments, and structural approaches. The section will also cover methods for testing and evaluating water penetration in concrete and provide real-world case studies and examples of prevention approaches in action.

Overall, the purpose and scope of this book section are to equip readers with a comprehensive understanding of the effects of water penetration on concrete strength, and the prevention approaches that can be used to address these issues. By the end of this section, readers should have a deeper appreciation for the importance of proper design, construction, and maintenance practices to ensure the longevity and durability of concrete structures in the face of water ingress.

Overview Of the Contents

Introduction:

This section provides background and context for the topic, describes the purpose and scope of the section, and provides an overview of the contents of the section.

Understanding Water Penetration in Concrete:

This part delves into the role of water in concrete's composition and strength, the various causes and sources of water penetration in concrete, and the different types of water penetration and their effects on concrete strength.

Prevention Approaches:

This section provides an overview of the main prevention approaches to water penetration in concrete, including concrete mix design strategies, proper curing techniques, surface treatments and coatings, and structural approaches.

Testing and Evaluation of Water Penetration:

This part discusses methods for testing water penetration in concrete, interpreting test results, and strategies for addressing identified water penetration issues.

Case Studies and Examples:

This section presents real-world examples of the effects of water penetration on concrete strength, case studies of prevention approaches in action, and lessons learned and best practices.

Conclusion and Future Directions:

This final part summarizes the key takeaways and contents of the section and provides recommendations for future research and development in this area.

UNDERSTANDING WATER PENETRATION IN CONCRETE

The Role of Water In Concrete's Composition And Strength:

Water plays a critical role in the creation of concrete, as it activates the cement and allows it to harden and bind with the aggregates. However, excessive water in the mix can lead to weakened concrete with reduced strength, as it can cause segregation and compromise the structural integrity of the material (Qu et al., 2023). Moreover, water penetration can have a significant impact on concrete strength over time, particularly in cold climates where freeze-thaw cycles can cause cracking and spalling. To mitigate these negative effects, builders carefully manage the amount and distribution of water in the mix and use various techniques such as adding admixtures and protective coatings to ensure the creation of strong and durable concrete (Shi et al 2022). In order to understand the effects of water penetration on concrete strength, it's important to first understand the role of water in concrete's composition and strength.

Causes and sources of water penetration in concrete:

Water penetration is a common issue in concrete structures that can lead to a range of problems, such as reduced strength, cracking, and spalling. The sources of water penetration in concrete can vary, but some of the most common ones include rainfall, ground moisture, and capillary action (Shen et al., 2021). Rainfall can enter concrete structures from above, while ground moisture can seep in from below. Capillary action happens when moisture is drawn up through the concrete from the ground due to the material's porous nature (Saberian et al., 2017). Other sources of water penetration in concrete can include leaks, plumbing issues, and improper drainage. To prevent water penetration, builders can use various techniques, such as adding waterproofing agents to the mix and applying protective coatings to the surface of the concrete (Saberian et al., 2017). Proper drainage and site grading can also help prevent water from pooling and penetrating the concrete structure.

The effects of water penetration on concrete strength:

The effects of water penetration on concrete strength can be severe and long-lasting. Water can weaken the bond between the cement and the aggregates, leading to reduced strength and durability of the material (He et al., 2023). It can also cause the formation of cracks, which can allow water to penetrate deeper into the concrete and exacerbate the problem. In addition, water penetration can cause corrosion of steel reinforcement, which can weaken the structure and ultimately lead to structural failure if left untreated. This is particularly problematic in coastal areas where saltwater can accelerate the corrosion process. To prevent

these issues, builders must take steps to prevent water penetration, such as using waterproofing agents and coatings, properly sealing joints and cracks, and ensuring proper drainage (Hassani et al., 2017). By doing so, they can help ensure the long-term durability and safety of concrete structures.

The different types of water penetration in concrete:

In addition to the sources of water penetration, there are also different types of water penetration in concrete that builders should be aware of. Surface water is water that sits on top of the concrete surface and can cause damage over time, particularly if it is left to sit for prolonged periods. Subsurface water, on the other hand, penetrates the concrete pores and travels through the material, which can lead to reduced strength and durability. Vapor diffusion is another type of water penetration, which occurs when water vapor moves through the concrete. This can lead to moisture buildup within the material and can contribute to mold growth and other problems (Amran et al., 2020). Finally, freeze-thaw cycles occur when water freezes and expands within the concrete, causing damage and weakening the structure over time. Understanding these different types of water penetration is crucial for developing effective prevention strategies. Builders can take steps such as using waterproofing agents, properly sealing joints and cracks, and ensuring proper drainage to prevent water penetration and preserve the durability of concrete structures (Juhart et al., 2019).

PREVENTION APPROACHES

Preventing water penetration into concrete is crucial to ensure the durability and longevity of concrete structures (Ramezani pour et al., 2011; Coppola et al., 2022).

The following approaches can help prevent water penetration:

Proper mix design:

The right mix design of concrete is critical to ensuring its durability and resistance to water penetration. The mix should be designed to have a low water-cement ratio, adequate cement content, and appropriate chemical admixtures (Kamal et al., 2020).

Curing:

Proper curing of concrete is essential to prevent water penetration. Curing should start as soon as possible after placement, and the concrete should be kept moist for a specified period to allow it to reach its full strength and prevent cracking (Shimabukuro and Hashimoto, 2009).

Surface treatments:

Applying a surface treatment, such as a sealant or coating, can help prevent water penetration into concrete. These treatments can fill small cracks and pores in the concrete surface and create a barrier against water penetration (Dai et al., 2010).

Waterproofing additives:

Waterproofing additives can be added to the concrete mix to improve its resistance to water penetration. These additives can improve the concrete's ability to resist water penetration by filling the pores and capillaries in the concrete (Gojević et al., 2021).

Proper drainage:

Adequate drainage around the concrete structure is essential to prevent water from accumulating around it. Proper drainage can be achieved by installing a proper slope, using drainpipes, and ensuring that gutters and downspouts direct water away from the structure (Todd, 2015).

Maintenance:

Regular maintenance is essential to prevent water penetration into concrete structures. This includes inspecting the structure for cracks, repairing any damage, and ensuring that the drainage systems are functioning correctly (Bróanaco et al., 2017).

By implementing these approaches, water penetration and the resulting concrete deterioration, including freeze-thaw damage, chemical attack, and corrosion of steel reinforcement, can be prevented.

Overview of the main prevention approaches

Concrete is a widely used construction material due to its durability, strength, and cost-effectiveness. However, concrete is prone to water penetration, which can cause various types of concrete deterioration, such as freeze-thaw damage, chemical attack, and corrosion of steel reinforcement. Therefore, it is essential to design a concrete mix that can resist water penetration and ensure the long-term durability of concrete structures.

The following are some concrete mix design strategies that can improve water resistance:

Low Water-Cement Ratio:

The water-cement ratio (W/C) is a critical factor in concrete mix design as it affects the strength, durability, and workability of concrete. The W/C ratio determines the amount of water needed to hydrate the cement in the mix. A low W/C ratio can improve the concrete's resistance to waterpenetration by reducing the capillary pore size and limiting the amount of water available to penetrate the concrete (Kim et al., 2014).

Increased Cement Content:

The amount of cement in the concrete mix is another critical factor in improving water resistance. Increasing the cement content can reduce the size of capillary pores and increase the strength of the concrete, making it less permeable to water. However, increasing the cement content also increases the cost of the concrete mix (Kolias and Georgiou, 2005).

Chemical Admixtures:

The use of chemical admixtures is an effective way to improve water resistance in concrete. Admixtures such as water-reducing agents, air-entraining agents, and pozzolanic materials can improve the workability, strength, and durability of concrete. These admixtures can also improve the concrete's resistance to water penetration by reducing capillary porosity, creating an air-void system, and filling pores and voids in the concrete (Cano-Barrita et al., 2016).

Use of Supplementary Cementitious Materials (SCMs):

SCMs such as fly ash, slag, and silica fume can improve the water-resistance of concrete by reducing the size and number of capillary pores in the concrete. These materials react with the cement in the mix to form additional calcium silicate hydrate (C-S-H) gel, which fills the capillary pores and makes the concrete less permeable to water (Li et al., 2022).

Surface Treatments:

Applying surface treatments such as sealers and coatings can also improve the water-resistance of concrete. These treatments can fill small cracks and pores in the concrete surface, create a barrier against water penetration, and protect the concrete from freeze-thaw damage, chemical attack, and corrosion of steel reinforcement (Safiuddin, 2017).

In conclusion, designing a concrete mix that can resist water penetration is crucial to ensure the long-term durability and performance of concrete structures. Concrete mix design strategies such as low W/C ratio, increased cement content, chemical admixtures, use of SCMs, and surface treatments can improve the water-resistance of concrete and make it more durable and resistant to damage caused by water. Therefore, it is essential to consider these strategies when designing a concrete mix for construction projects.

Concrete Mix Design Strategies to Improve Water Resistance

Concrete is a widely used construction material known for its durability and robustness. To enhance the water resistance of concrete, several mixed design strategies can be applied.

One of the most important factors to consider when improving water resistance is the water-cement ratio. High water-cement ratios can lead to excessive water content, causing shrinkage and cracking. Therefore, reducing the

water-cement ratio results in denser concrete that resists water penetration effectively (Chan et al., 2018).

The cement content in the mix is another important factor in enhancing water resistance. Increasing the cement content improves the density of concrete and enhances its ability to resist.

water penetration. However, adding too much cement can increase the risk of cracking, so it is crucial to balance the water-cement ratio and cement content (Matar and Barhoun, 2020).

Using admixtures is another approach to improve water resistance. Admixtures are substances added to the concrete mix to enhance its properties and resistance to water penetration. Water-reducing agents, plasticizers, and waterproofing agents are examples of admixtures that can be used to improve water resistance without affecting workability (Chan et al., 2018).

Proper curing techniques are also essential in enhancing the water resistance of concrete. Curing involves maintaining proper moisture and temperature conditions to ensure optimal hydration and strength development (Ibrahim, 2013). The concrete should be kept moist for a specified period to prevent cracking and improve its resistance to water penetration

Researchers have also explored using nanomaterials to improve concrete's water resistance. Nanomaterials like nanoparticles, nanotubes, and nanofibers can be added to the mix to enhance the concrete's strength and durability (Nazari and Riahi, 2011). They can also reduce porosity and improve water resistance.

In conclusion, improving the water resistance of concrete is critical to ensuring its longevity and durability. Mix design strategies like adjusting the water-cement ratio and cement content, using admixtures, and proper curing techniques can all help improve water resistance. The use of nanomaterials is also an emerging area of research that holds promise for enhancing the water resistance of concrete.

Proper Curing Techniques to Prevent Water Penetration

Effective curing methods play a crucial role in preventing water from infiltrating concrete structures. Curing is a procedure that maintains the moisture level of the concrete surface after placement to enable it to solidify and strengthen correctly. The process significantly affects the durability and waterproofing capability of the concrete.

Water can penetrate concrete and weaken, damage, or cause it to collapse. Therefore, implementing proper curing techniques is essential in preventing water from infiltrating the concrete, making it strong and long-lasting. Below are some techniques that can be utilized to ensure proper curing and prevent water penetration in concrete:

Start curing immediately after placement:

Commence the curing process immediately after the concrete has been placed to minimize moisture loss and guarantee that the concrete reaches its full potential strength (Zeyad, 2022).

Keep the concrete surface moist:

Maintain the concrete surface's moisture to prevent it from drying out and causing cracks to form. This can be achieved by using a curing compound, wet burlap, or plastic sheeting to cover the surface (Zeyad, 2022).

Regulate the concrete temperature:

The temperature of the concrete should be controlled within specific limits during the curing process. Fluctuations in temperature can cause the concrete to crack and weaken, which can lead to water infiltration (Yanjie et al., 2022).

Extend the curing time:

It is necessary to prolong the curing period to ensure that the concrete attains its full strength and resistance to water infiltration. The duration of the curing period can differ depending on factors such as the type of concrete mix, climate conditions, and the thickness of the structure (Zhao et al., 2012).

Avoid excessive water exposure:

Shield the concrete from excessive water exposure, such as rain or pooling, during curing. Prolonged exposure to water can weaken the concrete surface, leading to cracks and water infiltration (Safiuddin, 2017).

Adopting proper curing techniques is critical to prevent water penetration into concrete structures. These methods can aid in creating durable and robust concrete structures that can withstand water infiltration. It is essential to follow proper curing procedures to prevent problems resulting from water damage, such as chemical attacks, corrosion of steel reinforcement, and freeze-thaw damage.

Surface Treatments and Coatings for Water Resistance

To protect concrete surfaces from water penetration and improve their durability, surface treatments and coatings can be applied. These options are suitable for both new and existing surfaces to prevent water from entering the concrete's pores and capillaries, which can lead to damage over time.

There are different types of surface treatments and coatings available, each with its unique properties and benefits. Sealers are a cost-effective option that penetrates the concrete's surface to create a protective barrier. They are made from materials like acrylics, epoxies, and silanes and can be clear or colored. Coatings, on the other hand, create a physical barrier by forming a film on the concrete surface. They are thicker than sealers and can be made from materials

like acrylics, epoxies, and urethanes, among others. Coatings can also be applied in various colors and finishes (Pan et al., 2017).

While membrane systems are a more expensive option, they provide long-lasting protection against water penetration. These systems consist of a waterproof membrane layer applied to the concrete surface and can be made from materials like rubber, PVC, and asphalt.

When choosing a surface treatment or coating for water resistance, several factors should be considered, including the concrete structure's location and use, the level of water exposure, and the desired aesthetic effect. It is crucial to prepare the concrete surface adequately before applying any surface treatment or coating, which includes cleaning the surface of debris and contaminants and removing any existing coatings or sealers (Weiss, 2001).

In summary, surface treatments and coatings are necessary for protecting concrete from water penetration and improving its durability. Sealers, coatings, and membrane systems are all effective options, and the appropriate choice depends on various factors that should be carefully considered before application.

Structural Approaches to Prevent Water Penetration

In addition, to mix design, curing, and surface treatments, there are several structural approaches that can be taken to prevent water penetration in concrete structures.

Waterproof membranes:

One way to prevent water penetration is to apply a waterproof membrane on the concrete surface. Waterproof membranes can be made of various materials, including bitumen, asphalt, and synthetic polymers. These membranes are placed over the concrete surface before backfilling or applying a protective layer. Waterproof membranes can also be used in conjunction with surface coatings to provide additional protection (Haynes et al., 2021).

Drainage systems:

Another way to prevent water penetration is to design an effective drainage system around the concrete structure. This system can include surface drains, gutters, downspouts, and underdrains to divert water away from the structure. The drainage system should be designed to accommodate expected water volumes and be regularly inspected and maintained (Erdağ and Öztürk Kardoğan 2022).

Structural reinforcement:

Proper structural reinforcement can also help prevent water penetration. Reinforcing steel should be placed in such a way that it is adequately covered by concrete and does not become exposed due to cracking or spalling (Trejo et al.,

2000). Corrosion-resistant reinforcement, such as epoxy-coated or stainless steel, can also be used to prevent corrosion and further deterioration.

Joint sealing:

Joints in concrete structures can be a source of water penetration. Proper sealing of joints with a flexible sealant can prevent water from entering. Joint sealing can also prevent debris and other contaminants from entering the joint and causing further damage (Kim et al., 2022).

Sloping:

The slope of the surrounding terrain can also play a role in preventing water penetration. Proper grading and sloping of the land around the concrete structure can help prevent water from pooling or collecting near the structure.

In conclusion, structural approaches can be effective in preventing water penetration in concrete structures. Waterproof membranes, drainage systems, structural reinforcement, joint sealing, and proper sloping can all be effective methods to prevent water from entering the concrete. These methods should be considered in addition to proper mix design, curing, and surface treatments to ensure the durability and longevity of concrete structures.

TESTING AND EVALUATION OF WATER PENETRATION

Methods For Testing Water Penetration in Concrete

Testing and evaluation of water penetration in concrete structures is a critical aspect of ensuring their durability and longevity. Water penetration can cause various types of deterioration in concrete, including freeze-thaw damage, chemical attack, and corrosion of steel reinforcement, among others. Therefore, it is essential to test and evaluate the water resistance of concrete structures to ensure their performance and prevent premature failure.

There are various methods of testing and evaluating the water penetration resistance of concrete structures, including:

Water penetration testing:

This involves applying water under pressure to the concrete surface and observing whether it penetrates through the concrete. There are different methods of water penetration testing, including the standard test methods such as ASTM C1202, ASTM C1585, and ASTM D4585 (Obla et al., 2016).

Water absorption testing:

This involves measuring the amount of water absorbed by the concrete surface over a specified period. The water absorption rate can be used as an indicator of the concrete's water resistance (Wang, 2014).

Chloride ion penetration testing:

Chloride ions are one of the primary causes of concrete deterioration. Chloride ion penetration testing involves measuring the depth of penetration of chloride ions into the concrete using various test methods, such as ASTM C1202, ASTM C1556, and ASTM G109 (Obla et al., 2016)..

Electrical resistance testing:

This involves measuring the electrical resistance of the concrete surface, which can be used to determine its water penetration resistance (Tomlinson et al., 2017).

Infrared thermography:

This involves using thermal imaging to detect areas of water penetration or moisture within the concrete structure. This method can be particularly useful for identifying water penetration issues in large concrete structures.

In addition to testing and evaluation, it is also important to periodically inspect concrete structures for signs of water penetration and deterioration. Regular maintenance, repair of cracks and damage, and the use of appropriate surface treatments and coatings can help prevent water penetration and prolong the life of concrete structures (Tomita and Chew, 2022).

Concrete structures require regular testing and evaluation to ensure they are resistant to water penetration, which can affect their durability and longevity. To determine the water resistance of concrete, different methods are available, including water absorption testing, chloride ion penetration testing, electrical resistance testing, infrared thermography, and water penetration testing. Moreover, regular inspections and maintenance can help prevent water penetration and extend the lifespan of concrete structures. Hence, conducting frequent testing and maintenance is crucial to ensure the durability and longevity of concrete structures.

Interpretation of Test Results

The evaluation of water penetration in concrete structures is an important process that involves interpreting test results to gain valuable insights into the condition of the structure and potential risks. Qualitative and quantitative results are the two main types of tests used for this purpose. Qualitative results involve visual inspection to determine the condition of the concrete surface by examining its color, texture, and surface finish for signs of discoloration, spalling, or cracking, which indicate water penetration and possible damage to the structure. Quantitative results provide a more precise measure of water penetration, and several types of tests can be used, including water absorption tests, electrical resistance tests, and chloride ion penetration tests. Interpreting test results

requires a thorough understanding of the test method and its limitations and comparing the results to established standards and guidelines to determine the level of risk associated with water penetration and the need for remedial action. Overall, accurate interpretation of test results is crucial for evaluating water penetration in concrete structures (Brandt et al., 2012).

Strategies For Addressing Identified Water Penetration Issues

Water infiltration into concrete structures can cause severe damage, making it crucial to promptly address any identified issues. To mitigate water infiltration problems, the following strategies can be employed:

Repair any damage:

If there are cracks, holes, or other types of damage to the concrete structure, the first step is to repair them to address water infiltration issues. Depending on the damage's extent, repairs may involve filling cracks with a sealant or replacing a portion of the concrete (Issa and Debs, 2007).

Apply surface treatments:

Surface treatments or coatings can help prevent water infiltration into the concrete by filling in small cracks and pores on the surface, creating a barrier against water penetration (Pigino et al., 2012).

Waterproofing:

Applying a waterproofing layer to the concrete surface can help prevent water infiltration. There are various waterproofing products available, such as coatings, sealants, and membranes, that should be chosen based on the type of concrete, location, and severity of the problem (Haynes et al., 2021).

Improve drainage:

Enhancing the drainage around the concrete structure can prevent water accumulation and infiltration. Adequate drainage can be achieved by installing a proper slope, using drainpipes, and ensuring that gutters and downspouts direct water away from the structure (Tyagi, 2017).

Consider re-design:

If water infiltration is severe and cannot be fixed through repair or surface treatment, re-designing the structure may be necessary. This may involve changing the slope or elevation of the structure, adding more drainage systems, or using different materials (Chang et al., 2021).

Regular maintenance:

Regular maintenance is vital to prevent water infiltration problems from arising. This involves inspecting the structure for cracks and other types of damage, ensuring drainage systems work correctly, and promptly addressing any issues.

In conclusion, addressing water infiltration issues in concrete structures requires a combination of repair, surface treatment, waterproofing, drainage improvement, and maintenance. It is critical to identify and address water infiltration issues as soon as possible to prevent further damage and ensure the structure's long-term durability.

CASE STUDIES AND EXAMPLES

Real-World Examples of Water Penetration Effects on Concrete Strength

Water penetration can have severe impacts on the strength and durability of concrete structures, leading to costly repairs and potentially compromising the safety of the structure. Here are some real-world examples of water penetration effects on concrete strength:

Freeze-thaw damage:

In cold climates, water can penetrate concrete and freeze, causing the water to expand and create internal pressure, which can lead to cracking and spalling (Théréné et al., 2020). The Grand Coulee Dam in Washington State experienced significant freeze-thaw damage due to water penetration, requiring extensive repairs and reinforcement (University of Washington, 1949).

Chemical attack:

Exposure to chemicals, such as acids or alkalis, can cause concrete to deteriorate, leading to weakened structural integrity. The wastewater treatment plant in Portland, Oregon, experienced a chemical attack due to water penetration, resulting in significant concrete corrosion and the need for extensive repairs (Woyciechowski et al., 2019).

Corrosion of steel reinforcement:

When water penetrates concrete and reaches the steel reinforcement, it can cause corrosion, leading to structural weakness and potential failure. The seawall in San Francisco experienced corrosion of its steel reinforcement due to water penetration, requiring extensive repairs and reinforcement (Fuhaid and Niaz, 2022).

Alkali-silica reaction:

Water can also trigger a chemical reaction between the alkali in cement and reactive silica minerals in the aggregate, leading to expansion and cracking. The Hoover Dam in Nevada experienced an alkali-silica reaction due to water penetration, requiring significant repairs and monitoring (Adamo et al., 2020).

In conclusion, water penetration can have severe consequences on the strength and durability of concrete structures. Real-world examples of freeze-thaw damage, chemical attack, corrosion of steel reinforcement, and alkali-silica

reaction highlight the importance of addressing water penetration issues in concrete structures and implementing effective prevention and repair strategies.

Case Studies of Prevention Approach in Action For GRC

Glass fiber reinforced concrete (GFRC) is a composite material made of cement, sand, water, and glass fibers. GFRC has become increasingly popular in construction due to its high strength, durability, and aesthetic appeal. However, GFRC can also be prone to certain risks and vulnerabilities, making prevention approaches essential. Here are a few examples of case studies of prevention approaches in action for GFRC:

Preventing cracking:

GFRC is susceptible to cracking, particularly in areas with high-temperature fluctuations (Amed and Kabay (2019). To prevent cracking, one approach is to use a mixed design with a low water-to-cement ratio and a high fiber content. The studies demonstrate the effectiveness of this approach by testing two GFRC panels, one with a high water-to-cement ratio and a low fiber content, and one with a low water-to-cement ratio and a high fiber content (Yuan and Jia, 2022). The panel with the low water-to-cement ratio and high fiber content showed significantly less cracking under thermal cycling tests.

Preventing corrosion:

Corrosion of the glass fibers in GFRC can compromise the material's strength and durability. To prevent corrosion, one approach is to use alkali-resistant glass fibers.

(ARG). A case study from the University of Colorado Boulder tested the effectiveness of ARG in preventing corrosion. The study compared two GFRC panels, one with ARG and one with non-ARG fibers, exposed to a highly alkaline environment. The panel with ARG fibers showed significantly less degradation due to corrosion (Kwan et al., 2018).

Preventing impact damage:

GFRC can also be susceptible to impact damage, particularly in areas with high traffic or potential for impact. To prevent impact damage, one approach is to use a high-performance sealer (Safiuddin, 2017). The impact resistance of two GFRC panels, one sealed with a high-performance sealer and one without. The panel with the high-performance sealer showed significantly less damage under impact tests.

In conclusion, prevention approaches are essential to ensure the strength, durability, and safety of GFRC. Case studies such as these provide valuable insights into the effectiveness of various prevention approaches in action.

CONCLUSION AND FUTURE DIRECTIONS

Lessons learned and best practices on GRC:

Here are some lessons learned and best practices for GRC:

Quality control is crucial for ensuring the quality and consistency of GRC. Regular testing of materials, proper mixing, and maintaining consistent production processes are essential to ensure the final product meets the desired specifications.

- Design considerations are essential for ensuring the durability and performance of GRC. Designers should consider the right thickness and reinforce the structure where necessary to prevent cracking and damage.
- Manufacturing techniques play a vital role in ensuring the strength and quality of GRC. Using a low water-to-cement ratio to prevent cracking, using alkali-resistant glass fibers to prevent corrosion, and using high-performance sealers to prevent impact damage are some best practices.
- Proper installation is essential for the durability and performance of GRC. Following proper installation procedures, including proper preparation of the installation surface, proper sealing, and proper handling of the GRC panels to prevent damage, are some best practices.
- Regular maintenance and repair are essential for ensuring the longevity and performance of GRC. Regular inspections, prompt repairs of any damage, and cleaning to prevent buildup of dirt and other contaminants are some best practices.
- Education and awareness are crucial for preventing damage to GRC. Educating stakeholders and the public about potential risks and best practices for handling and maintaining GRC can help to prevent damage and ensure its longevity.

By implementing these lessons learned and best practices, stakeholders can work together to ensure the quality and longevity of GRC products, minimizing potential risks and increasing their effectiveness.

REFERENCE

- Adamo, N., Al-Ansari, N., Sissakian, V., Laue, J., & Knutsson, S. (2020). Dam Safety: Use of Instrumentation in Dams. *Journal of Earth Sciences and Geotechnical Engineering*, 145–202. Clockss. <https://doi.org/10.47260/jesge/1115>
- Amed B., Kabay N. (2019). Glass Fibre Reinforced Precast Concrete Containing High Content Pozzolan Materials. *Sigma Journal of Engineering and Natural Sciences*. 37(2): 675-686.
- Amran, Y. H.M., Alyousef, R., Alabduljabbar, H., Alaskar, A., & Alrshoudi, F. (2020). Properties and water penetration of structural concrete wrapped with CFRP. *Results in Engineering*, 5, 100094.
- ASTM C1202-12, 2012, “Standard Test Method for Electrical Indication of Concrete’s Ability to Resist Chloride Ion Penetration,” ASTM International, West Conshohocken, PA, 7 pp.
- ASTM C1585-13, 2013, “Standard Test Method for Measurement of Rate of Absorption of Water by Hydraulic-Cement Concretes,” ASTM International, West Conshohocken, PA, 6 pp.
- ASTM D4585/D4585M-13 2013, “Standard Practice For Testing Water Resistance Of Coatings Using Controlled Condensation”’ASTM International, West Conshohocken, PA, 6 pp.
- Branco, J. M., Descamps, T., & Tsakanika, E. (2017). Repair and Strengthening of Traditional Timber Roof and Floor Structures. *Building Pathology and Rehabilitation*, 113–138.
- Brandt, A. M., & Jóźwiak-Niedźwiedzka, D. (2012). Diagnosis of Concrete Quality by Structural Analysis. *Advances in Civil Engineering Materials*, 1(1), 20120004.
- Cano-Barrita, P. F. de J., & León-Martínez, F. M. (2016). Biopolymers with viscosity-enhancing properties for concrete. *Biopolymers and Biotech Admixtures for Eco-Efficient Construction Materials*, 221–252.
- Carlos A.L. Chernicharo, Thiago Bressani-Ribeiro, Livia C.S. (2019). LobatoConstruction of UASB reactors for sewage treatment. *Anaerobic Reactors for Sewage Treatment: Design, Construction and Operation*, 112–125. https://doi.org/10.2166/9781780409238_0112
- Chan, N., Young-Rojanschi, C., & Li, S. (2018). Effect of water-to-cement ratio and curing method on the strength, shrinkage and slump of the biosand filter concrete body. *Water Science and Technology*, 77(6), 1744–1750.
- Chang, H.-K., Tan, Y.-C., Lai, J.-S., Pan, T.-Y., Liu, T.-M., & Tung, C.-P. (2013). Improvement of a drainage system for flood management with assessment of the potential effects of climate change. *Hydrological*

Sciences Journal, 58(8), 1581–1597.

<https://doi.org/10.1080/02626667.2013.836276>

Collections <https://digitalcollections.lib.washington.edu/digital/collection/grandcoulee/id/161>. Accessed: 2023-04-07

Concrete being repaired on face of Grand Coulee Dam, March 1949 - Grand Coulee Dam Construction, 1933-1942 - University of Washington Digital

Coppola, L., Beretta, S., Bignozzi, M. C., Bolzoni, F., Brenna, A., Cabrini, M., Candamano, S., Caputo, D., Carsana, M., Cioffi, R., Coffetti, D., Colangelo, F., Crea, F., De Gisi, S., Diamanti,

Dai, J.-G., Akira, Y., Wittmann, F. H., Yokota, H., & Zhang, P. (2010). Water repellent surface impregnation for extension of service life of reinforced concrete structures in marine environments: The role of cracks. *Cement and Concrete Composites*, 32(2), 101–109.

Erdağ, A., & Öztürk Kardoğan, P. (2022). The Effect of Horizontal Drainage Lengths on the Stability of a Homogeneous Earth-Fill Dam Under Seepage Conditions. *Gazi Üniversitesi Fen Bilimleri Dergisi Part C: Tasarım ve Teknoloji*.

Fuhaid, A.F.A. and Niaz, A. (2022). Carbonation and Corrosion Problems in Reinforced Concrete Structures. *Buildings* 12, 586. <https://doi.org/10.3390/buildings12050586>

Gojević, A., Ducman, V., Netinger Grubeša, I., Baričević, A., & Banjad Pečur, I. (2021). The Effect of Crystalline Waterproofing Admixtures on the Self-Healing and Permeability of Concrete. *Materials*, 14(8), 1860.

Hassani, M., Vessalas, K., Sirivivatnanon, V., & Baweja, D. (2017). Influence of permeability- reducing admixtures on water penetration in concrete. *ACI Mater. J*, 114, 911-922.

Haynes, M. A., Coleri, E., & Obaid, I. (2021). Performance of Waterproofing Membranes to Protect Concrete Bridge Decks. *Transportation Research Record: Journal of the Transportation Research Board*, 2675(9), 1693–1706.

Haynes, M.A., Coleri, E., & Obaid, I. (2021). Performance of Waterproofing Membranes to Protect Concrete Bridge Decks. *Transportation Research Record: Journal of the Transportation Research Board*, 2675(9), 1693–1706.

He, S., Huang, R., Xiao, L., Xiao, L., & Mei, G. (2023). Investigation of the reverse-seepage technique to enhance the chloride ion invasion resistance of rectangular section concrete: Experiments and numerical analysis. *Construction and Building Materials*, 363, 129743.

- Ibrahim, M., Shameem, M., Al-Mehthel, M., & Maslehuddin, M. (2013). Effect of curing methods on strength and durability of concrete under hot weather conditions. *Cement and Concrete Composites*, 41, 60–69.
- Issa, C. A., & Debs, P. (2007). Experimental study of epoxy repairing of cracks in concrete. *Construction and Building Materials*, 21(1), 157–163.
- Juhart, J., Bregar, R., David, G. A., & Krüger, M. (2019). Air permeability, water penetration and water absorption to specify durability of eco-efficient concrete. *RILEM Technical Letters*, 4, 67–73.
- Kamal, M. R., Rumman, R., Manzur, T., Noor, M. A., & Bari, M. S. (2020). A Novel Durability Based Concrete Mix Design Using Supplementary Cementitious Materials and Modified Aggregate Band Gradation. *International Journal of Civil Engineering*, 19(1), 39–50
- Kim, J., Zollinger, D., & Cho, W. (2022). Experimental Study of the Effects of Moisture on the Performance of Concrete Pavement Joint Sealants. *Transportation Research Record*, 2676(7), 585–596.
- Kim, Y.-Y., Lee, K.-M., Bang, J.-W., & Kwon, S.-J. (2014). Effect of W/C Ratio on Durability and Porosity in Cement Mortar with Constant Cement Amount. *Advances in Materials Science and Engineering*, 2014, 1–11.
- Kolias, S., & Georgiou, C. (2005). The effect of paste volume and of water content on the strength and water absorption of concrete. *Cement and Concrete Composites*, 27(2), 211–216.
- Kwan, W. H., Cheah, C. B., Ramli, M., & Chang, K. Y. (2018). Alkali-resistant glass fiber reinforced high strength concrete in simulated aggressive environment. *Materiales de Construcción*, 68(329), 147. <https://doi.org/10.3989/mc.2018.13216>
- Li, G.; Zhou, C.; Ahmad, W.; Usanova, K.I.; Karelina, M.; Mohamed, A.M.; Khallaf, R. (2022). Fly Ash Application as Supplementary Cementitious Material: A Review. *Materials*, 15, 2664.
- M. V., Ferone, C., Frontera, P., Gastaldi, M. M., Labianca, C., ... Todaro, F. (2022). The Improvement of Durability of Reinforced Concretes for Sustainable Structures: A Review on Different Approaches. *Materials*, 15(8), 2728.
- Matar, P., & Barhoun, J. (2020). Effects of waterproofing admixture on the compressive strength and permeability of recycled aggregate concrete. *Journal of Building Engineering*, 32, 101521.
- Nazari, A., & Riahi, S. (2011). Computer-aided design of the effects of Fe2O3 nanoparticles on split tensile strength and water permeability of high strength concrete. *Materials & Design*, 32(7), 3966–3979.

- Obla, Karthik & Lobo, Colin & Kim, Haejin. (2016). Tests and Criteria for Concrete Resistant to Chloride Ion Penetration. *ACI Materials Journal*, 113. 10.14359/51689107.
- Pan, X., Shi, Z., Shi, C., Ling, T.-C., & Li, N. (2017). A review on concrete surface treatment Part I: Types and mechanisms. *Construction and Building Materials*, 132, 578–590.
- Pigino, B., Leemann, A., Franzoni, E., & Lura, P. (2012). Ethyl silicate for surface treatment of concrete – Part II: Characteristics and performance. *Cement and Concrete Composites*, 34(3), 313–321.
- Qu, L., Song, W., Wang, Q., Xu, S., & Hou, C. (2023). Effects of hydrophobic modified fly ash on resistance of chloride corrosion and water penetration of cement mortar in the early hydration stage. *Journal of Building Engineering*, 64, 105573.
- Ramezaniyanpour, A. A., Pilvar, A., Mahdikhani, M., & Moodi, F. (2011). Practical evaluation of relationship between concrete resistivity, water penetration, rapid chloride penetration and compressive strength. *Construction and Building Materials*, 25(5), 2472–2479.
- Saberian, M., Jahandari, S., Li, J., & Zivari, F. (2017). Effect of curing, capillary action, and groundwater level increment on geotechnical properties of lime concrete: Experimental and prediction studies. *Journal of Rock Mechanics and Geotechnical Engineering*, 9(4), 638–647.
- Safiuddin, M. (2017). Concrete Damage in Field Conditions and Protective Sealer and Coating Systems. *Coatings*, 7, 90. <https://doi.org/10.3390/coatings7070090>
- Shen, L., Lo Monte, F., Di Luzio, G., Cusatis, G., Li, W., Felicetti, R., Lombardi, F., Lualdi, M., Cao, M., & Ren, Q. (2021). On the moisture migration of concrete subject to high temperature with different heating rates. *Cement and Concrete Research*, 146, 106492.
- Shi, Z., Wang, Q., Li, X., Lei, L., Qu, L., Mao, J., & Zhang, H. (2022). Utilization of super- hydrophobic steel slag in mortar to improve water repellency and corrosion resistance. *Journal of Cleaner Production*, 341, 130783.
- Shimabukuro, A., & Hashimoto, K. (2009). Effect Of Curing Method And Curing Period On Characteristic Of Compressive Strength For Ca Concrete. *Cement Science and Concrete Technology*, 63(1), 274–280.
- Théréné, F., Keita, E., Naël-Redolfi, J., Boustingorry, P., Bonafous, L., & Roussel, N. (2020). Water absorption of recycled aggregates: Measurements, influence of temperature and practical consequences. *Cement and Concrete Research*, 137, 106196. <https://doi.org/10.1016/j.cemconres.2020.106196>

- Todd, A. (2015). Moisture control: surface and subsurface drainage. *Highways*, 277–303.
- Tomita, K., & Chew, M. Y. L. (2022). A Review of Infrared Thermography for Delamination Detection on Infrastructures and Buildings. *Sensors*, 22(2), 423.
- Tomlinson, D., Moradi, F., Hajiloo, H., Ghods, P., Alizadeh, A., & Green, M. (2017). Early age electrical resistivity behaviour of various concrete mixtures subject to low temperature cycling. *Cement and Concrete Composites*, 83, 323–334.
- Trejo, David & Monteiro, P. & Jr, B.C. & Thomas, G.. (2000). Microstructural design of concrete reinforcing bars for improved corrosion performance. *ACI Structural Journal*. 97. 78- 83.
- Tyagi, A. C. (2017). Drainage and Environmental Sustainability. *Irrigation and Drainage*, 66(3), 451–452. Portico.
- Wang, L. (2014). Experimental Study on Water Absorption by Concrete Damaged by Uniaxial Loading. *Proceedings of the 4th International Conference on the Durability of Concrete Structures*.
- Weiss, R. J. (2001). Six things you should know about XML.
- Woyciechowski, P., Adamczewski, G., & Łukowski, P. (2019). Chemical corrosion of concrete tank in sewage treatment plant as the cause of failure. *MATEC Web of Conferences*, 284, 07007. <https://doi.org/10.1051/matecconf/201928407007>
- Yanjie, B., Hui, S., Bai, Y., & Cai, Y. (2022). Mechanical properties and damage mechanisms of concrete under four temperature gradients combined with acoustic emission method. *Journal of Building Engineering*, 57, 104906.
- Yuan Z, Jia Y. (2022). Experimental Study on the Mechanical Properties, Water Absorption, and Fiber Degradation of Naturally Aged Glass Fiber and Polypropylene Fiber-Reinforced Concrete. *Materials*. 15(11):3760. <https://doi.org/10.3390/ma15113760>
- Zeyad, A. M., Tayeh, B. A., Adesina, A., de Azevedo, A. R. G., Amin, M., Hadzima-Nyarko, M., & Saad Agwa, I. (2022). Review on effect of steam curing on behavior of concrete. *Cleaner Materials*, 3, 100042.
- Zhao, H., Sun, W., Wu, X., & Gao, B. (2012). Effect of initial water-curing period and curing condition on the properties of self-compacting concrete. *Materials & Design*, 35, 194–200.

Chapter 3

The Critical Role of GDL Properties in Enhancing Proton Exchange Membrane Fuel Cell Performance

Hüseyin KAHRAMAN¹

İdris CESUR²

¹ Asst. Prof. Dr. ; Sakarya Uygulamalı Bilimler Üniversitesi Teknoloji Fakültesi Makina Mühendisliği Bölümü.
huseyink@subu.edu.tr ORCID No: 0000-0003-3322-9904

² Assoc. Prof. Dr.; Sakarya Uygulamalı Bilimler Üniversitesi Teknoloji Fakültesi Makina Mühendisliği
Bölümü. icesur@subu.edu.tr ORCID No: 0000-0001-7487-5676

The world's increasing energy demand is a critical issue in today's society. The reliance on fossil fuels has contributed to environmental problems, including global warming, prompting the need for alternative energy sources. Hydrogen energy and fuel cells offer an attractive solution to this problem, and specifically, proton exchange membrane (PEM) fuel cells have shown promising performance in energy production. However, the performance of PEM fuel cells is heavily dependent on the properties of the gas diffusion layer (GDL), a critical component that facilitates the transport of reactants and products in the fuel cell. This article reviews the effect of various GDL properties, such as porosity, permeability, compressive strength, and compression pressure, on the performance of PEM fuel cells. In particular, we investigate the relationship between GDL porosity and its effect on compression force, permeability, and compressive strength. The analysis reveals that optimizing GDL properties can significantly enhance PEM fuel cell performance, and further research is needed to explore the full potential of hydrogen energy and fuel cells in meeting the world's energy demand.

Keywords: Fuel cell, PEMFC, GDL, Conductivity, Porosity.

INTRODUCTION

The world's energy demand has been increasing steadily in recent years, with a significant rise in population, urbanization, and industrialization. The energy sector is the largest source of greenhouse gas emissions, primarily caused by the combustion of fossil fuels (Kahraman et al. 2016). The increase in energy demand has resulted in heavy dependence on non-renewable energy sources, leading to several challenges, including geopolitical tensions, price volatility, and environmental concerns (Kahraman and Coban 2020).

Fossil fuels have been the primary energy source for decades, but their use has significant drawbacks. The combustion of fossil fuels releases carbon dioxide and other greenhouse gases into the atmosphere, contributing to global warming and climate change. The effects of global warming are visible, including melting glaciers, rising sea levels, and extreme weather events. The exploitation of fossil fuels also has geopolitical implications, as some countries rely heavily on them, leading to tensions and conflicts (Kahraman and Orhan 2017).

To address the environmental and economic concerns related to fossil fuels, alternative energy sources have emerged. These sources include renewable energy such as solar, wind, hydroelectric, and geothermal energy. They offer a promising alternative to non-renewable sources, which reduces greenhouse gas emissions and addresses climate change. Additionally, energy efficiency and conservation measures are also essential to reduce energy consumption (Orhan, Saka, and Kahraman 2020).

Hydrogen energy has gained significant attention in recent years as a potential solution to the energy crisis. Hydrogen can be produced from renewable energy sources and used in fuel cells to generate electricity. Fuel cells convert the chemical energy of hydrogen and oxygen into electricity, emitting only water as a byproduct. They offer several advantages over traditional combustion engines, including higher efficiency, lower emissions, and quieter operation (Rahimirad and Sadabadi 2023).

Proton Exchange Membrane Fuel Cells (PEMFCs) are one of the most promising types of fuel cells, mainly due to their high-power density and fast start-up. PEMFCs have several components, including Gas Diffusion Layers (GDLs), which play a crucial role in their performance. GDLs facilitate the transfer of reactants and products between the electrodes and the reactant gases, and they also provide mechanical support to the electrodes. The properties of GDLs significantly affect PEMFC performance, including parameters such as compression pressure, porosity, permeability, and compressive strength (Zhang et al. 2023).

The optimization of GDL properties is crucial for the effective operation of PEMFCs. The compression pressure applied to GDLs affects their porosity, permeability, and compressive strength, ultimately impacting the fuel cell performance. The porosity of GDLs affects their ability to transport reactants and products and their compressive strength. Higher porosity GDLs can lead to higher performance in PEMFCs. Additionally, the permeability of GDLs affects their ability to transport reactants and products and can impact the fuel cell performance. Therefore, the optimization of GDL properties is necessary to improve PEMFC performance and enhance the commercial viability of fuel cell technology (Zhang et al. 2023).

MATERIALS AND METHOD

Porosity and permeability are important properties of the gas diffusion layer (GDL) in a proton exchange membrane (PEM) fuel cell. The GDL is a porous material that serves as the interface between the catalytic layer and the gas flow channels in the fuel cell. It plays a key role in facilitating the transport of gases (such as hydrogen and oxygen) and water within the fuel cell (Fu et al. 2022).

In general, the porosity of the GDL refers to the fraction of the volume that is occupied by void space, or pores, within the material. A high porosity allows for a greater surface area for gas exchange and facilitates the transport of gases and water within the fuel cell. However, a high porosity can also lead to reduced mechanical strength and increased gas leakage.

Permeability, on the other hand, refers to the ease with which gases and liquids can pass through the pores in the material. A high permeability allows for efficient gas exchange, but a low permeability can help to reduce gas leakage. The permeability of the GDL is influenced by factors such as the size and shape of the pores, as well as the tortuosity (or winding path) of the pores (Mukherjee, Bonnet, and Lapique 2020).

In general, it is desirable to have a GDL with a high porosity and high permeability, as this allows for efficient gas exchange and water transport within the fuel cell while minimizing gas leakage. However, it is important to balance these properties to achieve optimal performance, as high porosity can lead to reduced mechanical strength and high permeability can lead to increased gas leakage (Holzer et al. 2017).

The internal resistance of a proton exchange membrane (PEM) fuel cell is a measure of the resistance to the flow of electrons and ions within the fuel cell. It is influenced by various factors, including the thickness and conductivity of the membrane, the efficiency of the catalysts, and the resistance of the gas diffusion layers (GDLs).

The internal resistance of a PEM fuel cell can be affected by the compression force applied to the cell. Applying a high compression force can help to improve the contact between the various layers in the fuel cell, leading to a reduction in the internal resistance. This can improve the overall performance of the fuel cell by increasing the efficiency of electron and ion transport (Huo et al. 2023).

On the other hand, applying too much compression force can lead to damage to the fuel cell, such as delamination of the layers or cracking of the membrane. It is therefore important to carefully optimize the compression force to achieve the desired level of performance while avoiding damage to the fuel cell.

To study the relationship between compression force and internal resistance in a PEM fuel cell, a testing setup could use to apply different levels of compression force to the fuel cell and measure the corresponding internal resistance. This data could then be plotted to visualize the relationship between these two variables.

The porosity of the gas diffusion layer (GDL) in a proton exchange membrane (PEM) fuel cell is an important factor that can affect the performance of the fuel cell. The GDL is a porous material that serves as the interface between the catalytic layer and the gas flow channels in the fuel cell, and its porosity plays a key role in facilitating the transport of gases and water within the fuel cell.

In general, GDL materials with a high porosity may be more prone to changes in porosity with changes in compression force, as the pores in the material can collapse or become distorted under high levels of compression. GDL materials with a low porosity may be less sensitive to changes in compression force, as they have fewer pores to collapse or distort.

To study the relationship between GDL porosity and compression force, you could use a testing setup to apply different levels of compression force to a sample of the GDL material and measure the corresponding porosity. This data could then be plotted to visualize the relationship between these two variables. It is important to carefully control the testing conditions, such as the type and size of the sample, the rate of compression, and the temperature and humidity, to ensure the results are accurate and meaningful (Wang et al. 2023).

The hydraulic conductivity of a material is a measure of its ability to transmit fluids (such as water) through its pores. It is typically expressed in units of length per time (such as meters per second or centimeters per day).

The porosity of a material is a measure of the fraction of its volume that is occupied by void space, or pores. Porosity and hydraulic conductivity are often correlated, with materials having a higher porosity tending to have a higher

hydraulic conductivity. This is because a higher porosity means there are more pores available for fluid transport, which can increase the overall rate of fluid flow through the material.

The hydraulic conductivity of the gas diffusion layer (GDL) in a proton exchange membrane (PEM) fuel cell is an important factor that can affect the performance of the fuel cell. The GDL is a porous material that serves as the interface between the catalytic layer and the gas flow channels in the fuel cell, and its hydraulic conductivity plays a key role in facilitating the transport of gases and water within the fuel cell.

The hydraulic conductivity of the GDL is influenced by factors such as the size and shape of the pores, the tortuosity (or winding path) of the pores, and the presence of other materials (such as catalysts) within the pores. A high hydraulic conductivity allows for efficient transport of gases and water within the fuel cell, but a low hydraulic conductivity can help to reduce gas leakage.

In general, it is desirable to have a GDL with a high hydraulic conductivity, as this allows for efficient gas exchange and water transport within the fuel cell while minimizing gas leakage. However, it is important to balance the hydraulic conductivity with other properties, such as porosity and mechanical strength, to achieve optimal performance (Leonard et al. 2023).

RESULTS

In the case of the gas diffusion layer (GDL) in a proton exchange membrane (PEM) fuel cell, the relationship between GDL porosity and hydraulic conductivity can be complex, as the hydraulic conductivity can be influenced by factors such as the size and shape of the pores, the tortuosity (or winding path) of the pores, and the presence of other materials (such as catalysts) within the pores.

To study the relationship between GDL porosity and hydraulic conductivity, you could use a testing setup to measure the hydraulic conductivity of a sample of the GDL material at different levels of porosity. This data could then be plotted to visualize the relationship between these two variables. It is important to carefully control the testing conditions, such as the type and size of the sample, the fluid being used, and the temperature and humidity, to ensure the results are accurate and meaningful.

Hydraulic conductivity is a measure of the ability of a material to transmit fluids (such as water) through its pores. It is typically expressed in units of length per time (such as meters per second or centimeters per day).

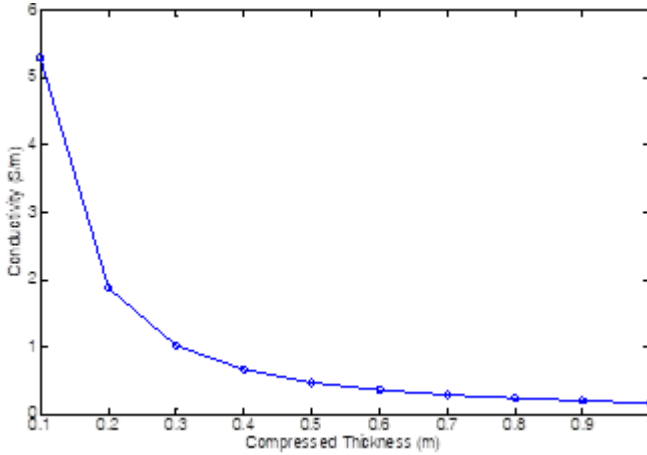


Figure 1: Conductivity as a Function of GDL Compressed Thickness

The following statements can be deduced from Fig.1;

- The graph shows that as GDL compression thickness increases, conductivity generally decreases. This suggests that there may be an inverse relationship between GDL compression thickness and conductivity.
- The graph appears to exhibit non-linear behavior, where the rate of change in conductivity with respect to GDL compression thickness may not be constant. This could indicate that there might be a threshold or optimum compression thickness for achieving the highest conductivity.
- The graph suggests that compression of the GDL has an impact on its conductivity. As the GDL is compressed to thinner thicknesses, the resulting increase in contact between the GDL and adjacent layers could potentially improve the conductivity. However, beyond a certain compression thickness, the conductivity may start to decrease due to increased resistance or reduced pore space for gas diffusion.
- The graph may also indicate that the GDL material properties, such as porosity, tortuosity, and electrical conductivity, could play a significant role in determining the overall conductivity as a function of compression thickness. Different GDL materials may exhibit varying behavior in terms of their conductivity response to compression thickness.
- The graph does not provide information about the specific compression thickness that yields the highest conductivity. Further analysis or experimentation may be needed to determine the optimum compression thickness for the particular GDL material or application under consideration.

- The graph's findings may have practical implications for designing and optimizing fuel cells or other electrochemical devices that utilize GDLs. It suggests that careful control of GDL compression thickness may be necessary to achieve the desired level of conductivity and overall performance.

In the Fig.2, four different variables have been investigated. Temperature distribution: The graph shows the distribution of temperature along the x direction of the GDL surface. It is important to analyse the temperature distribution as it affects various electrochemical and transport processes in the fuel cell. Temperature gradients may arise due to thermal losses or variations in reactant flow rates, and can impact the overall performance and durability of the fuel cell.

Oxygen concentration distribution: The graph displays the distribution of oxygen concentration along the x direction of the GDL surface. This information is critical as it affects the oxygen diffusion and transport to the catalyst layer, which is essential for the oxygen reduction reaction (ORR) at the cathode. Variations in oxygen concentration may impact the performance and efficiency of the fuel cell.

Water vapor concentration distribution: The graph illustrates the distribution of water vapor concentration along the x direction of the GDL surface. Water management is crucial in PEM fuel cells as it affects membrane conductivity, reactant transport, and catalyst performance. Understanding the distribution of water vapor concentration helps in assessing the effectiveness of the fuel cell's water management system.

Saturation distribution: The graph shows the distribution of saturation along the x direction of the GDL surface. Saturation refers to the amount of water vapor present in the GDL relative to its maximum capacity at a given temperature and pressure. Saturation impacts the GDL's ability to store and transport water, which can affect its performance, particularly in terms of water flooding or drying out of the GDL.

Trends and gradients: The graph may reveal trends, gradients, or variations in the distributions of temperature, oxygen concentration, water vapor concentration, and saturation along the x direction of the GDL surface. These trends and gradients provide insights into the behaviour of the fuel cell and can help identify potential issues or areas for optimization.

The graph may also show the relationship between temperature, oxygen concentration, water vapor concentration, saturation, and their distribution along the x direction of the GDL surface. Understanding how these variables interact

with each other can provide valuable information for optimizing the fuel cell's performance and improving its efficiency.

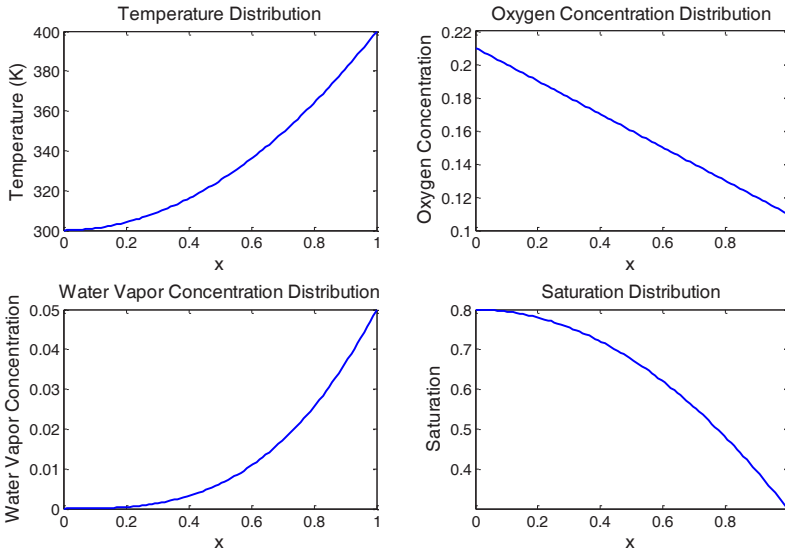


Figure 2: Distributions of temperature, oxygen concentration, water vapor concentration and saturation through the x direction.

DISCUSSION

The optimization of GDL properties, such as porosity, permeability, and compressive strength, is essential for the effective operation of PEMFCs. High porosity GDLs allow for efficient gas and water transport within the fuel cell, leading to higher performance. Similarly, high permeability GDLs enable efficient gas exchange, but it is crucial to balance these properties to avoid reduced mechanical strength and increased gas leakage. The compression force applied to GDLs also affects the internal resistance of PEMFCs, which is a measure of the resistance to the flow of electrons and ions within the fuel cell. To study the relationship between compression force and internal resistance in a PEM fuel cell, a testing setup could be used to apply different levels of compression force to the fuel cell and measure the corresponding internal resistance. This data could then be plotted to visualize the relationship between these variables and optimize the compression force for optimal fuel cell performance.

The world's increasing energy demand and the environmental concerns associated with fossil fuels have led to the emergence of alternative energy sources such as renewable energy and hydrogen energy. Optimizing the

properties of gas diffusion layers in fuel cells, such as PEMFCs, is crucial for improving their performance and enhancing the commercial viability of fuel cell technology. Further research and development in this area can contribute to the transition towards a more sustainable and clean energy future, addressing the challenges posed by increasing energy demand, climate change, and geopolitical tensions associated with fossil fuels.

COCLUSION

The increasing energy demand in the world has led to heavy dependence on non-renewable energy sources, primarily fossil fuels, resulting in significant environmental and economic challenges. Alternative energy sources, such as renewable energy and hydrogen energy, offer promising solutions to address these challenges. The optimization of gas diffusion layer (GDL) properties, including porosity, permeability, and compression pressure, is crucial for the effective operation of proton exchange membrane fuel cells (PEMFCs). Further research and development in this area can contribute to enhancing the performance and commercial viability of fuel cell technology, leading to a more sustainable and efficient energy future.

REFERENCE

- Fu, X., Wen, Q., Han, J., Wei, J., Li, Y., Ning, F., & Zhou, X. (2022). One-step to prepare high-performance gas diffusion layer (GDL) with three different functional layers for proton exchange membrane fuel cells (PEMFCs). *International Journal of Hydrogen Energy*, 47(61), 25769–25779.
- Holzer, L., Pecho, O., Schumacher, J., Marmet, Ph., Büchi, F. N., Lamibrac, A., & Münch, B. (2017). Microstructure-property relationships in a gas diffusion layer (GDL) for Polymer Electrolyte Fuel Cells, Part II: Pressure-induced water injection and liquid permeability. *Electrochimica Acta*, 241, 414–432.
- Huo, W., Wu, P., Xie, B., Du, Q., Liang, J., Qin, Z., Zhang, G., Sarani, I., Xu, W., Liu, B., Wang, B., Yin, Y., Lin, J., & Jiao, K. (2023). Elucidating non-uniform assembling effect in large-scale PEM fuel cell by coupling mechanics and performance models. *Energy Conversion and Management*, 277, 116668.
- Kahraman, H., Cevik, I., Dündar, F., & Ficici, F. (2016). The Corrosion Resistance Behaviors of Metallic Bipolar Plates for PEMFC Coated with Physical Vapor Deposition (PVD): An Experimental Study. *Arabian Journal for Science and Engineering*, 41(5), 1961–1968.
- Kahraman, H., & Coban, A. (2020). Performance improvement of a single pem fuel cell using an innovative flow field design methodology. *Arabian Journal for Science and Engineering*, 45(7), 5143–5152.
- Kahraman, H., & Orhan, M. F. (2017). Flow field bipolar plates in a proton exchange membrane fuel cell: Analysis & modeling. *Energy Conversion and Management*, 133, 363–384.
- Leonard, D. P., Komini Babu, S., Baxter, J. S., Meyer III, H. M., Cullen, D. A., & Borup, R. L. (2023). Natural fiber-derived gas diffusion layers for high performance, lower cost PEM fuel cells. *Journal of Power Sources*, 564, 232619.
- Mukherjee, M., Bonnet, C., & Lapicque, F. (2020). Estimation of through-plane and in-plane gas permeability across gas diffusion layers (GDLs): Comparison with equivalent permeability in bipolar plates and relation to fuel cell performance. *International Journal of Hydrogen Energy*, 45(24), 13428–13440.
- Orhan, M. F., Saka, K., & Kahraman, H. (2020). Analysis and modeling of a membrane electrode assembly in a proton exchange membrane fuel cell. *Journal of Renewable and Sustainable Energy*, 12(4), 044302.

- Rahimirad, Z., & Sadabadi, A. A. (2023). Green hydrogen technology development and usage policymaking in Iran using SWOT analysis and MCDM methods. *International Journal of Hydrogen Energy*.
- Wang, J., Jiang, H., Chen, G., Wang, H., Lu, L., Liu, J., & Xing, L. (2023). Integration of multi-physics and machine learning-based surrogate modelling approaches for multi-objective optimization of deformed GDL of PEM fuel cells. *Energy and AI*, 100261.
- Zhang, M., Yu, M., Liu, Z., Tu, Z., & Liu, W. (2023). Moisture migration in the cathode GDL of PEMFC under variable physical parameters based on a modified two-fluid model. *International Journal of Hydrogen Energy*.

Chapter 4

Design of Multilayer Radar Absorber Using Grey Wolf Optimization Algorithm

Şeyma ATICI¹

Enes YİĞİT²

Umut ÖZKAYA³

¹ Bursa Uludag University Engineering Faculty Optic and Photonics Engineering;
seymaatici4@gmail.com; ORCID No: 0009-0009-9020-7593

² Assoc. Dr.; Bursa Uludag University Engineering Faculty Electrical and Electronics Engineering Department;
enesyigit@uludag.edu.tr; ORCID No: 0000-0002-0960-5335

³ Dr. Lecturer; Konya Technical University Faculty of Engineering and Natural Sciences Department of
Electrical and Electronics Engineering; uozkaya@ktun.edu.tr ;

ABSTRACT

In multilayer radar absorber (MRA) design, the ability to reasonably define the electrical and geometrical variables of the material presents challenging and complex optimization problems. In this study, optimum MRA designs were carried out in different frequency bands with various thickness and number of layers with the grey wolf optimization (GWO) algorithm, which is one of the most up-to-date optimization algorithms. The created MRAs are designed to operate at normal angle of incidence and in frequency bands 1-20, 2-8 and 8-12 GHz. In the optimization, a set of materials with predefined electrical variables was used. Aiming to have the minimum reflection coefficient and minimum thickness of the total material; the electrical variables and thickness of each layer, as well as the number of layers and order of the material to be formed, are optimized. The model of objective function was created with the impedance equation model formulation. Many MRA material designs with thin and low reflection coefficient have been achieved with the GWO algorithm.

Keywords: Radar absorber material (RAM), Multilayer radar absorber (MRA), Optimization, Grey wolf optimization (GWO) algorithm, Electromagnetic scattering

INTRODUCTION

Protecting against EM waves is crucial not only for health, information security, and the proper functioning of electronic devices, but also for military purposes in order to hide from radar waves (Chen, et al., 2023). Just as it is important to camouflage optically in the field in defense strategies, it is equally essential to be able to hide military vehicles and ammunition from radar and to prevent their location from being detected.

In the last quarter century, research on radar absorbing materials (RAM) has gained momentum in order to hide from EM waves. A typical RAM aims to minimize the reflectivity of the EM wave on the material by absorbing the radar wave as much as possible. While doing this, it should work independently of the incident angle and polarization at wideband frequency and the material design should be as light and thin as. (Yigit & Duysak, 2021) Various approaches based on the use of single-layer, multi-layer, and/or resistive plates on a perfect electric conductor (PEC) have emerged for the development of radar absorbers. However, multi-layered radar absorber (MRA) structures have recently gained prominence due to their superior absorption capabilities (Yigit & Duysak, 2019). Michielssen et al., (1993:1024) synthesized an MRA using genetic algorithm(GA) in the frequency range of 0.2-2 GHz and 2-8 GHz with 16 virtual materials that defined the frequency-dependent permittivities and permeabilities of these materials (Table 1). This dataset was used as a reference for objective evaluations in ongoing MRA designs (Weile, Michielssen, & Goldberg, 1996) (Yao, Yang, Li, Xu, & Bi, 2023) (Asi & Dib, 2010) (Dib, Asi, & Sabbah, 2010) (Chamaani, Mirtaheri, & Shooredeli, 2008)

In order to produce a MRA with low reflectivity and thickness, the sequence and thicknesses of the materials used in the layers must be optimally defined. The inverse relationship between thickness and reflection coefficient in RAM design necessitates the use of optimization algorithms without sacrificing both parameters (Yigit & Duysak, 2021). For this purpose optimization algorithms such as artificial bee colony (ABC) (Toktas, Ustun, Yigit, Sabanci, & Tekbas, 2018) central force optimization (CFO) (Asi & Dib, 2010), particle swarm optimization (PSO) (Chamaani, Mirtaheri, & Shooredeli, 2008) (Roy, Roy, Tewary, Mahanti, & Mahanti, 2015) and genetic algorithm (GA) (Yao, Yang, Li, Xu, & Bi, 2023) (Weile, Michielssen, & Goldberg, 1996) have been used successfully to produce MRA material designs operating at different frequency ranges. However, there is no recent literature on any RAM study that has been performed using the grey wolf optimization (GWO) (Mirjalili, Mirjalili, & Lewis, 2014) algorithm, which has advantages over other optimization algorithms. This study was conducted to utilize the superior aspects of GWO in challenging RAM

design problems and to achieve a compromise between minimum reflection coefficient and minimum thickness at different frequency ranges. The materials were obtained from pre-defined materials database and optimum RAM design was realized using the GWO algorithm at normal incidence angle and various frequency bands.

FORMULATION AND PHYSICAL MODEL OF MRA DESIGN

The top layer of the MRA structure, consisting of n stacked plates, is in contact with free space while the bottom layer is combined with PEC, as shown in Figure 1. Each layer in the structure has a thickness of d_i and permittivity and permeability of ϵ_i and μ_i , respectively. It is assumed that the EM wave falls on the interface of the first layer with a normal incident angle from free space. Further studies will be conducted for different incident angles. The proposed approach for formulating the MRA design is the impedance equalization model (Hock, 2003). The internal impedance of each layer is denoted as Z_{0i} ;

$$Z_{0i} = \sqrt{\frac{\mu_i}{\epsilon_i}} \quad (1)$$

The complex permittivity and permeability values expressed here are calculated as $\epsilon = \epsilon' - j\epsilon''$ and $\mu = \mu' - j\mu''$ respectively. The impedance created in each layer of the propagation direction of the EM wave is determined as follows:

$$(Z_{in})_i = Z_{0i} \frac{(Z_{in})_{i+1} + Z_{0i} \tanh(\gamma_i d_i)}{Z_{0i} + (Z_{in})_{i+1} \tanh(\gamma_i d_i)} \quad (2)$$

In Equation 2, γ_i represents the propagation constant for each layer with an index of $i = 1, 2, 3, \dots, n$ and it is calculated as follows:

$$\gamma_i = j\omega\sqrt{\mu_i\epsilon_i} \quad (3)$$

In order to indicate the frequency f , the angular frequency $\omega = 2\pi f$ is defined in Equation 3. As understood from Equation 2, the input impedance at each interface between two layers depends on the sequential input impedances of the layers. That is, to measure the input impedance of the final layer, which is the (n) th layer, the input impedance of the $(n + 1)$ th layer, which is the PEC and acts as a short circuit, must be known, and since its impedance is zero, it is easy to

calculate. When the input impedances of the layers are calculated in sequence, the final input impedance $(Z_{in})_1$ is obtained, and the equivalent impedance value of the total MRA is calculated using this formula.

According to the reflection equation in Equation 4, impedance matching should be ensured between the impedance of the free space Z_{00} and the input impedance $(Z_{in})_1$ of the first layer at the free space interface. The reflection equation at the free space interface is given as follows:

$$\Gamma = \frac{(Z_{in})_1 - Z_{00}}{(Z_{in})_1 + Z_{00}} \quad (4)$$

In order to obtain an optimal MRA design, permittivity and permeability values $(\epsilon_i$ and $\mu_i)$ of each layer will be defined in the GWO algorithm and the geometric variables (d_i) that will create the minimum reflection coefficient and minimum thickness will be generated with GWO.

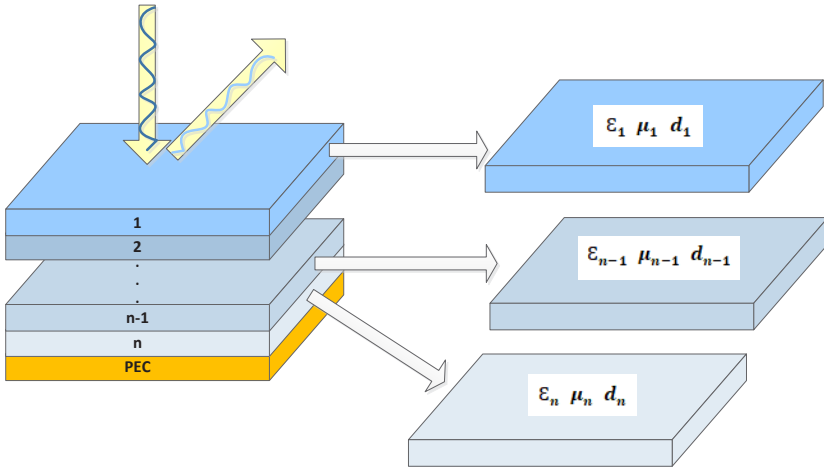


Figure 1: Proposed MRA Model

Table 1: Pre-defined material dataset

Lossless dielectric materials ($\mu' = 1, \mu'' = 0$)				
Material	ε'			
1	10			
2	50			
Lossy magnetic materials ($\varepsilon' = 15, \varepsilon'' = 0$)				
$\mu = \mu' - j\mu'' \quad \dots \mu'(f) = \frac{\mu'(1 \text{ GHz})}{f^a} \quad \mu''(f) = \frac{\mu''(1 \text{ GHz})}{f^\beta}$				
Material	$\mu'(1 \text{ GHz}) = 1$	a	$\mu''(1 \text{ GHz}) = 1$	β
3	5	0.974	10	0.961
4	3	1.000	15	0.957
5	3	1.000	12	1.000
Lossy dielectric materials ($\mu' = 1, \mu'' = 0$)				
$\varepsilon = \varepsilon' - j\varepsilon'' \quad \dots \varepsilon'(f) = \frac{\varepsilon'(1 \text{ GHz})}{f^a} \quad \dots \varepsilon''(f) = \frac{\varepsilon''(1 \text{ GHz})}{f^\beta}$				
Material	$\varepsilon' (1 \text{ GHz})$	α	$\varepsilon'' (1 \text{ GHz})$	β
6	5	0.861	8	0.569
7	8	0.778	10	0.682
8	10	0.778	6	0.861
Relaxation-type magnetic materials ($\varepsilon' = 15, \varepsilon'' = 0$)				
$\mu = \mu' - j\mu'' \quad \dots \mu'(f) = \frac{\mu_m f_m^2}{f^2 + f_m^2} \quad \dots \mu''(f) = \frac{\mu_m f_m f}{f^2 + f_m^2} \quad f \text{ and } f_m \text{ in GHz}$				
Material	μ_m		f_m	
9	35		0.8	
10	35		0.5	
11	30		1.0	

12	18	0.5
13	20	1.5
14	30	2.5
15	30	2.0
16	25	3.5

Source: (Michielssen, Sajer, Ranjithan, & Mittra, 1993)

GREY WOLF OPTIMIZATION (GWO) ALGORITHM

GWO is a recently developed nature-inspired optimization method that mimics the social behaviour and hunting mechanism of grey wolves (Salgotra, Singh, & Sharma, 2020). The herd consists of 5-12 individuals with a social-dominant hierarchy (Figure 2). At the top of the hierarchy, the α wolves make decisions on basic activities such as hunting, resting place, and waking time etc. and the decisions of α are imposed on the herd. β is a subdominant wolf that assists α in decision-making and other herd activities. β takes orders from α and gives orders to other wolves. ω is the lowest-ranking wolf and must submit to other dominant wolves in the herd. If a wolf is not α , β , or ω , it is a δ wolf. δ wolves obey α and β and rule over ω (Mirjalili, Mirjalili, & Lewis, 2014)

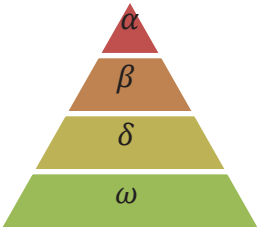


Figure 2: Grey Wolf Hierarchy

The social hierarchy and hunting strategy of grey wolves have been mathematically modelled in the GWO algorithm. In GWO, when the fitness values of the randomly generated population are sorted according to the objective function; the best, second best and third best solutions are assigned to α , β and δ , respectively. The remaining wolves (ω), which are the candidate solutions in the algorithm, use these three best solutions as references to reach the optimum solution. The positions of other candidates are updated based on these three best solutions.

The wolves' hunting behavior, where they surround their prey, is modeled as follows:

$$D = |C \cdot X_p(t) - X(t)| \quad (5)$$

$$X(t+1) = X_p(t) - A \cdot D \quad (6)$$

Here, t represents the current iteration, while A and C are coefficient vectors. X represents a wolf's position and X_p represents the prey's position vector.

$$A = 2 \cdot a \cdot r_1 - a \quad (7)$$

$$C = 2 \cdot r_2 \quad (8)$$

In equation 7, the value of a linearly decreases from 2 to 0 throughout the iteration. r_1 and r_2 are random values between 0 and 1.

$$D_\alpha = |C_1 \cdot X_\alpha - X|, \quad D_\beta = |C_2 \cdot X_\beta - X|, \quad D_\delta = |C_3 \cdot X_\delta - X| \quad (9)$$

$$X_1 = X_\alpha - A_1 \cdot (D_\alpha), \quad X_2 = X_\beta - A_2 \cdot (D_\beta), \quad X_3 = X_\delta - A_3 \cdot (D_\delta) \quad (10)$$

$$X(t+1) = \frac{X_1 + X_2 + X_3}{3} \quad (11)$$

To model the approach towards the prey mathematically, the value of a in equation 7 is linearly reduced from 2 to 0 in each iteration. The condition $|A| < 1$ forces the wolf to attack the prey. If a random value was assigned to a , the wolf could end up in any position instead of approaching the prey. Grey wolves move away from each other to search for prey and unite to attack it when found. Random values of A are used to model this approach and allows the GWO algorithm to search globally. Random values of $|A| < 1$ are generated for approach behavior and $|A| > 1$ for exploration behavior; forces the wolf to explore for new prey. Another component that supports the exploration of the GWO algorithm is C (equation 8). C is generated randomly between 0 and 2, which helps to exhibit more random behavior during optimization and prevents getting stuck in local minima. This component is especially useful in the last iterations when the algorithm may face local optimum stagnation. (Mirjalili, Mirjalili, & Lewis, 2014)

REALIZATION OF MRA DESIGN WITH GWO

The calculation and physical parameters for the algorithm in GWO and MRA design were obtained from the electrical properties of materials dataset (Michielssen,

Sajer, Ranjithan, & Mittra, 1993). The designs were implemented in three different frequency bands. The parameters to be optimized were defined as an n-layer number in a matrix of size 2n. The layer thickness limits of the layers were defined between 0-10 mm, with a maximum layer number of 6. For MRA design, optimization was performed with the objective function (OF) and 0.5 GHz frequency steps. The goal of the OF was to achieve MRA parameters with minimum thickness and minimum reflection, i.e., maximum absorption rate (Equation 12).

$$\text{minimum OF} = \gamma_1 \sum_{t=f_s}^{f_e} 20 \log_{10}(\max(|\Gamma|)) + \gamma_2 \sum_{i=1}^M d_i \quad (12)$$

Here, γ_1 and γ_2 are coefficients for reflection and thickness, respectively. f_s is the start frequency and f_e is the end frequency. M is the number of layers and d_i represents the thickness of each layer. The calculation (control) parameters for optimization include a population size of 50 and a maximum iteration of 2000.

THE PROPOSED MRA DESIGNS

In this section, three optimal MRA materials were designed using the GWO algorithm for three separate frequency bands: 2-8, 8-12, and 1-20 GHz. The number of layers, total thickness, and maximum, minimum, average values of reflection coefficients of the generated designs were provided. The designs with different numbers of layers (3, 4, 5, and 6) had a minimum thickness of 3.1316 mm and a maximum thickness of 4.8124 mm.

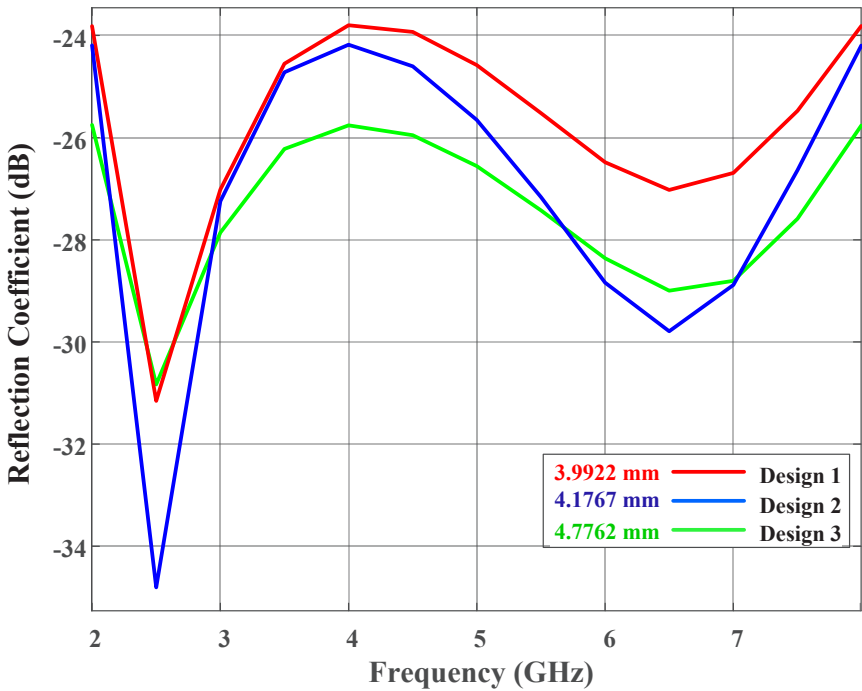
The designs were created with the number of layers 3, 4, 5, and 6 and the thickest design was 4.8124 mm while the thinnest was 3.1316 mm.

MRA Designs in the 2-8 GHz Frequency Band

Optimized MRA designs with 3, 4 and 5 layers were created in the 2-8 GHz frequency band. Reflection coefficient graphs of the optimized designs are presented in Figure 3, while the MRA parameters are listed in Table 2. As seen in Table 2, the thinnest design is Design 1 and the thickest design is Design 3. Here, the maximum reflection coefficient decreases proportionally, as the structure gets thicker.

Table 2: MRA Models at 2-8 GHz (thickness unit: mm)

MRA	Design 1		Design 2		Design 3	
Layer	Mat.	Thick.	Mat.	Thick.	Mat.	Thick.
1	16	0.46252	16	0.46619	16	0.3791
2	6	1.6992	6	1.9022	6	2.968
3	5	0.90301	5	1.1444	15	1.4291
4	9	0.6141	15	0.66389	-	-
5	14	0.31332	-	-	-	-
Total Thickness	3.9922		4.1767		4.7762	
Max/Min	-23.8014	-31.155	-24.1803	-34.8039	-25.7511	-30.8324
Avr. Reflection	-25.6815		-26.9926		-27.3744	

**Figure 3:** 2-8 GHz Reflection Coefficient of MRA Designs

MRA Designs in the 8-12 GHz Frequency Band

In this section, 3, 4, and 5-layered MRA designs were created in the 8-12 GHz frequency band. The reflection coefficient graphs of the optimized designs are presented in Figure 4, while the MRA parameters are given in Table 3. As can be seen in Table 3, the thinnest structure is Design 4, while the thickest structure is Design 5. While the maximum reflection coefficient usually decreases proportionally with increasing structure thickness, the situation here is the opposite of what is known. Design 4 obtained in this frequency band has been

found to be more performant than the other two designs (Design 5 and Design 6) in terms of both thickness and maximum reflection coefficient.

Table 3: MRA Models at 8-12 GHz (thickness unit: mm)

MRA	Design 4		Design 5		Design 6	
Layer	Mat.	Thick.	Mat.	Thick.	Mat.	Thick.
1	16	0.16491	16	0.23758	16	0.15168
2	16	0.00544	6	2.5811	8	2.7518
3	8	1.3689	3	0.021664	16	0.36077
4	6	1.1524	14	0.52153	-	-
5	16	0.43995	-	-	-	-
Total Thickness	3.1316		3.3619		3.2642	
Max/Min	-	-34.1665	-28.2676	-33.4653	-	-
Avr. Reflection	-32.6046		-31.0414		-31.7186	

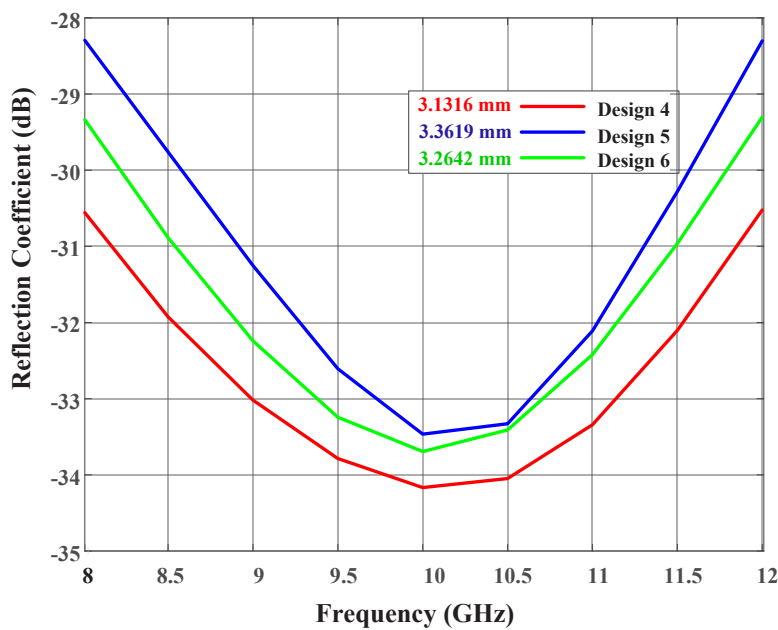


Figure 4: 8-12 GHz Reflection Coefficients of MRA Designs

MRA Designs in the 1-20 GHz Frequency Band

As depicted in figure 5, MRA with 4, 5, and 6 layers have been designed in the frequency band of 1-20 GHz, for wideband applications. Based on the data in Table 4, in wideband MRA designs, the number of layers increases and accordingly, the total thickness of the MRA also increases. However, despite

this, successful structures have been obtained without exceeding the total thickness limit of 5 mm.

Table 4: MRA Models at 1-20 GHz (thickness unit: mm)

MRA	Design 7		Design 8		Design 9	
Layer	Mat.	Thick.	Mat.	Thick.	Mat.	Thick.
1	16	0.20665	6	0.21006	16	0.21069
2	6	1.7313	6	1.5968	6	1.6797
3	16	0.51422	16	0.4402	16	0.47994
4	10	1.3187	9	0.82959	9	1.9837
5	11	0.29124	9	1.1853	-	-
6	4	0.75025	-	-	-	-
Total Thickness	4.8124		4.2619		4.3541	
Max/Min	-18.1091	-21.0131	-17.3703	-	-17.5785	-45.6337
Avr. Reflection	-18.7829		-18.825		-18.95	

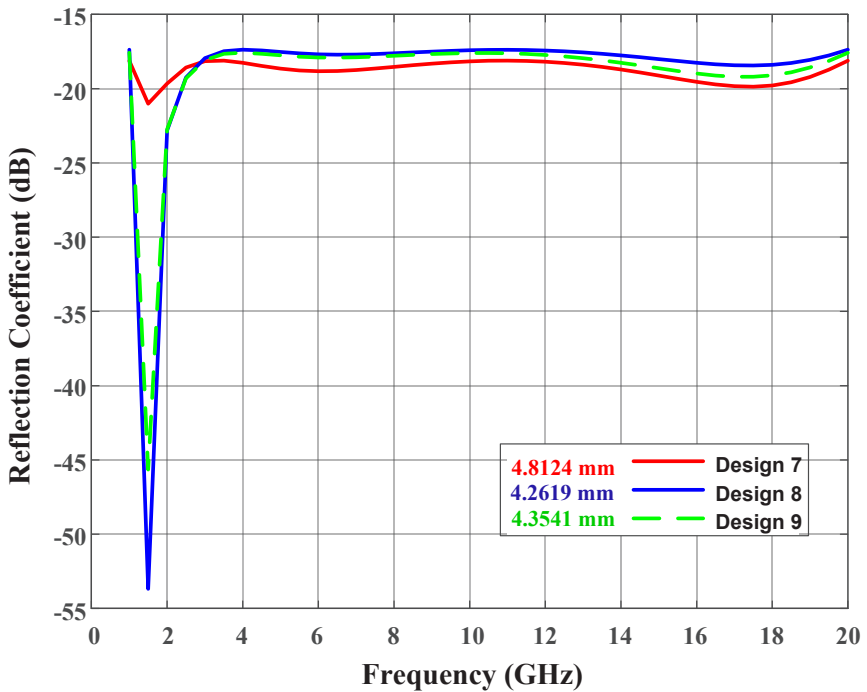


Figure 5: 1-20 GHz Reflection Coefficients of MRA Designs

CONCLUSION

This study presents the design process of the optimal MRA material using the GWO algorithm. The calculation of the reflection coefficient and optimization were carried out using the formulation of the objective function. The critical point in the design is to define the layer sequence for the minimum reflection coefficient and the minimum thickness of the MRA by optimally selecting the electrical parameters of the materials used in the layers. Three MRA material designs were created for three frequency bands: 2-8, 8-12, and 1-20 GHz. The optimization performed with the GWO algorithm is to select the materials from the pre-defined material database with complex permittivity and permeability values at the optimal layer number and define the thickness of each layer optimally. The designs are realized for normal incidence angles and the cases for oblique incidence angles will be performed in future studies. The created designs are quite thin and within reasonable limits of reflectivity. These pioneering results in the design of MRA with GWO algorithm show that GWO offers promise for future studies in the design of MRA materials.

REFERENCE

- Asi, M. J., & Dib, N. (2010). Design of multilayer microwave broadband absorbers using central force optimization. *Progress In Electromagnetics Research B*, Vol. 26, 101–113.
- Chamaani, S., Mirtaheri, S. A., & Shooredeli, M. A. (2008). Design of very thin wide band absorbers using modified local best particle swarm optimization. *AEU - International Journal of Electronics and Communications*, 549-556.
- Chen, Z., Zhang, Y., Wang, Z., Wu, Y., Zhao, Y., Liu, L., & Ji, G. (2023). Bioinspired moth-eye multi-mechanism composite ultra-wideband. *Carbon*, 542-548.
- Dib, N., Asi, M., & Sabbah, A. (2010). On the optimal design of multilayer microwave absorbers. *Progress In Electromagnetics Research C*, Vol. 13,, 171-185.
- Hock, K. (2003). Impedance matching for the multilayer medium - toward a design methodology. *IEEE Transactions on Microwave Theory and Techniques* , 908 - 914.
- Michielssen, E., Sajer, J. -M., Ranjithan, S., & Mittra, R. (1993). Design of lightweight, broad-band microwave absorbers using genetic algorithms. *IEEE Transactions on Microwave Theory and Techniques*, 1024-1031. doi:10.1109/22.238519
- Mirjalili, S., Mirjalili, S. M., & Lewis, A. (2014). Grey Wolf Optimizer. *Advances in Engineering Software*, 46-61.
- Roy, S., Roy, S. D., Tewary, J., Mahanti, A., & Mahanti, G. K. (2015). Particle Swarm Optimization for Optimal Design of Broadband Multilayer Microwave Absorber for Wide Angle of Incidence. *Progress In Electromagnetics Research B*, Vol. 62, 121–135.
- Salgotra, R., Singh, U., & Sharma, S. (2020). On the improvement in grey wolf optimization. *Neural Computing and Applications*, 3709–3748.
- Toktas, A., Ustun, D., Yigit, E., Sabanci, K., & Tekbas, M. (2018). Optimally Synthesizing Multilayer Radar Absorbing Material (RAM) Using Artificial Bee Colony Algorithm. *2018 XXIIIrd International Seminar/Workshop on Direct and Inverse Problems of Electromagnetic and Acoustic Wave Theory (DIPED)*, 237-241. doi:10.1109/DIPED.2018.8543261.
- Weile, D., Michielssen, E., & Goldberg, D. E. (1996). Genetic algorithm design of Pareto optimal broadband microwave absorbers. *IEEE Transactions on Electromagnetic Compatibility*, 518-525. doi:10.1109/15.536085

- Yao, H., Yang, J., Li, H., Xu, J., & Bi, K. (2023). Optimal design of multilayer radar absorbing materials:a simulation-optimization approach. *Advanced Composites and Hybrid Materials (2023)* , 6-43.
- Yigit, E., & Duysak, H. (2019). Determination of Optimal Layer Sequence and Thickness for Broadband Multilayer Absorber Design Using Double-Stage Artificial Bee Colony Algorithm. *IEEE TRANSACTIONS ON MICROWAVE THEORY AND TECHNIQUES*, 67.
- Yigit, E., & Duysak, H. (2021). Fully optimized multilayer radar absorber design using multi-objective abc algorithm. *International Journal of Engineering and Geosciences*, 136-145.

Chapter 5

The Effect of Changes in Consumption Habits on the Ecological Footprint During Covid-19 Pandemic

**Cemre Belit ÇOBANOĞLU KAYIKCI¹,
Nazlıcan YEŞİLOVA², Emine ELMASLAR ÖZBAŞ³,
Atakan ÖNGEN⁴, Hüseyin Kurtuluş ÖZCAN⁵
Serdar AYDIN⁶, Sinan GÜNEYSU⁷**

1 Istanbul University-Cerrahpaşa, Department of Environmental Engineering.
ccobanoglu@ogr.iu.edu.tr ORCID No: 0000-0002-2068-4791

2 Istanbul University-Cerrahpaşa, Department of Environmental Engineering.
nzlcnrkg@gmail.com ORCID No: 0000-0001-6276-3597

3 Assoc. Prof.; Istanbul University-Cerrahpaşa, Department of Environmental Engineering, Istanbul University-Cerrahpaşa, Environmental and Earth Sciences Application and Research Center.
elmaslar@iuc.edu.tr ORCID No: 0000-0001-9065-6684

4 Assoc. Prof.; Istanbul University-Cerrahpaşa, Department of Environmental Engineering, Istanbul University-Cerrahpaşa, Environmental and Earth Sciences Application and Research Center.
aongen@iuc.edu.tr ORCID No: 0000-0002-9043-7382

5 Prof. Dr.; Istanbul University-Cerrahpaşa, Department of Environmental Engineering, Istanbul University-Cerrahpaşa, Environmental and Earth Sciences Application and Research Center.
hkozcان@iuc.edu.tr ORCID No: 0000-0002-9810-3985

6 Prof. Dr.; Istanbul University-Cerrahpaşa, Department of Environmental Engineering, Istanbul University-Cerrahpaşa, Environmental and Earth Sciences Application and Research Center.
saydin@istanbul.edu.tr ORCID No: 0000-0002-0626-5224

7 Dr.; Istanbul University-Cerrahpaşa, Department of Environmental Engineering.
guneyisu@iuc.edu.tr ORCID No: 0000-0002-4875-101X

ABSTRACT

Ecological footprint is an important concept as being a tool which reveals impacts of human beings on natural systems coming out from all types of vital activities such as their own life, production and services, as based on concrete data. In this study, research was made about how Covid-19 pandemic affecting the whole world and causing various changes in our daily lives, influenced part of people's consumption habits and ecological footprint values in accordance. For this aim, a consumption habits change survey constituted of 30 questions has been prepared, and the study group was comprised of 500 people from different age groups, education levels and income levels. As the outcome of research, the highest and lowest ecological footprint values of individuals before the Covid-19 pandemic were determined as 11.9 global hectares and 6.3 global hectares, respectively, whereas during the Covid-19 pandemic, these values were determined as 11.4 global hectares and 4.0 global hectares, respectively. While the average ecological footprint values of the participants before the Covid-19 pandemic were 8.4 global hectares, it was found out that this value was 8.1 global hectares during the Covid-19 pandemic. During the Covid-19 pandemic period, while the ecological footprint of 50.83% of individuals on a global hectare basis increased, 27.50% of them decreased and 21.67% of them had no change.

Keywords: Consumption habits, Covid-19, Ecological footprint, Pandemic.

INTRODUCTION

On 11th of March, first Covid-19 pandemic case has been observed in Turkey and on the same date, World Health Organization announced that this newly developing virus was a pandemic. Education became interrupted, distance education and remote working system were started, curfews and bans were introduced to reduce the proliferative course of the epidemic (Budak and Korkmaz, 2020:62). Even though the restrictions were lifted from time to time (especially in the summer period), the restrictions were gradually brought up again, depending on the number of cases.

Impacts of human beings against nature, occurring during production and consumption and not being often noticed, constitute the ecological footprint. Concept of ecological footprint, that is introduced in the 1990s by Dr. Mathis Wackernagel and Prof. Dr. by William Rees was defined as an ecologically productive area (irrigable land, woodland, grassland, sea) within certain borders, whereas resources needed by individuals with a certain quality of life and consumption habits are produced and the wastes that emerge are transformed into harmless ones and the area where carbon dioxide is absorbed (Wackernagel and Rees, 1998). Ecological footprint is a methodology that is developed in order to measure the effect of human activities on the ecosystems. As the ecological footprint reveals the relationships between natural resource supply and demand, it provides a scientific basis for recognizing imbalances and for finding solutions. This is the reason why the 'trend towards ecological footprint reduction' is becoming significantly important (Günel et al., 2018). Ecological footprint calculations provide a broader perspective on the causes of environmental problems by revealing which activities, by whom, and to what extent natural resources are used, and determine ecological risks. Due to this reason, concept of ecological footprint, being one of the indicators of a sustainable life, contributes to our capacity to change our attitudes and behaviors towards the environment in a positive way by controlling the negative effects we leave on the world numerically (Galli et al., 2012:100; Çelik Coşkun and Sarıkaya, 2014:1761; Günel et al., 2018).

In the last few decades, environmental deterioration has come out as a major concern among researchers and policymakers across the world. The particulars that are apparent in this growing comprehension are constituted of the alarming rate of carbon dioxide (CO₂) emissions, a key driver of greenhouse gases (GHG) and its consequential impacts on global warming, climate change, biodiversity, air quality, and natural resources (Cowan et al., 2014:359; Rudolph and Figge, 2017:348). Together with the growing human consumption, this concern does not just increase the vulnerability of communities but also

intensifies the scarcity of ecological resources on earth (Nathaniel, 2020:1; Rahman, 2020). In this respect, ecological footprint captures the different resources required to sustain the human population (Ahmed et al., 2020a; Ahmed et al., 2020b; Langnel and Babington, 2020). An ecological footprint is the area of biologically productive land and water being required by an individual, community or activity in order to produce the resources it consumes and to dispose of the waste it creates. Ecological footprint is expressed in “global hectares” (kha). This includes infrastructure and areas for vegetation that will absorb waste carbon dioxide (CO₂). Global Hectares (kha) represent the productive capacity of 1 hectare of land over the world's average productivity. Hence, total amount of resources obtained from different types of land within a certain period and the demand had for these resources are expressed with a numerical value that is reduced to a common unit (URL1).

Personal footprint is correlated with personal consumption and particulars used by individuals such as food, transportation, goods and services, which depend on their lifestyles and preferences. When ecological footprint is classified according to consumption categories such as food, housing, transportation, products, services, the impact of consumption style on personal footprint can be calculated. For example, the share of food in the ecological footprint of personal consumption is 52%. Footprint consists of 21% products, 15% personal transportation, 6% services and 6% housing expenditures (URL1).

There are studies available in the literature about how these changes affect the ecological footprint values during the Covid-19 pandemic, which influences the whole world and causes many changes in our habits. According to recent study, COVID-19 pandemic has been found to cause a sharp decline in the global ecological footprint in 2020. In year 2017, the ecological footprint per capita was calculated as 3.5 kha for Turkey. This value is 5.4 kha for Russia, it is 8.1 kha for Canada, it is 8.1 kha for the United States, 3.7 kha for China, and it is 4.7 kha for Germany (URL2). However, after the COVID-19 pandemic, global ecological footprint data reveals that footprint related with forest products decreased by 8.4%, the footprint associated with food remained stable, and the carbon footprint decreased significantly by 14.5% (URL3). According to data obtained from the international sustainability organization “Global Footprint Network” and York University in Toronto, restrictions and quarantines related with the coronavirus have caused for global ecological footprint to be reduced by almost 10% (URL4). Murányi and Varga (2021) have analyzed the relationship between the pandemic and ecological, economic and social aspects. It was proven that these countries, whose Ecological Footprint is

calculated, are developed countries in general and that their ecological features are especially important. In their research, Yang and Usman (2021:893) evaluated the period between years of 1995-2018 and they examined the effects of the process of industrialization, economic growth and globalization in the ten countries having highest health expenditures (Australia, Austria, Denmark, Germany, Luxembourg, Netherlands, Norway, Sweden, Switzerland, USA) on the ecological footprint. Results showed that health expenditures, economic growth and industrialization process accelerated environmental pollution significantly, whereas globalization and urbanization processes reduced it. Solarin and Bello (2018:35) analyzed the data of 128 developed countries for the period between years of 1961-2013 and they found out that the ecological footprint is not stable and that the subsidies for cleaner energy and carbon taxes will have permanent effects on the countries. Özcan et al. (2019:130) classified countries as per income and they analyzed economies with different levels of income for the period between years of 1961–2013. The results reveal that the ecological footprint is not stable for low-middle income countries and that environmental policies are effective in low-income countries but that they are not effective in high-income countries.

Briefly speaking, “ecological footprint” is an important concept as a tool that reveals the effects of human beings on natural systems arising from all kinds of vital activities such as their own life, production and services, based on concrete data. To understand the relationship of consumers' lifestyles and consumption habits with natural resources is very important both in causing awareness of the importance of personal preferences in daily life and in developing national policies for sustainable consumption. In this study, research was made on how the Covid-19 pandemic, influencing the whole world and causing many changes in our daily lives, affected some of the consumption habits of people and, accordingly, ecological footprint values.

MATERIAL AND METHOD

A descriptive (screening) research model has been used in the study, by examining how the Covid-19 pandemic influences some of the consumption habits of people and ecological footprint values in accordance. Research group is constituted of 500 people from different age groups, education levels and income levels. In order to calculate the ecological footprint values, support was obtained from a website (URL2) that calculates the ecological footprint and the calculation categories in the ecological footprint calculation questionnaire on this site were taken as basis. In addition to the questions on this website, a new questionnaire was created by adding questions such as gender, age, city of

residence, education level, income level. This questionnaire being created was distributed to the participants online through Google. The questions asked in the questionnaire are presented in Table 1.

Table 1: Questions that are directed to the participants in the study for calculating the EF values of the individuals.

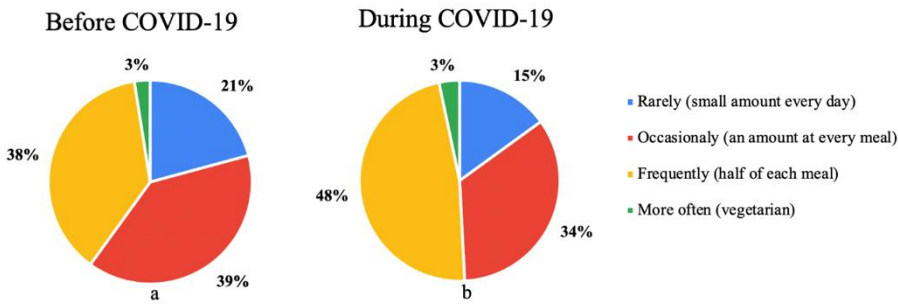
Number	Questions
1	Your gender
2	Your age
3	The city where you live
4	Your education level
5	Your income level
6	How often do you consume plant foods (grains, fruits, vegetables)?
7	How often do you consume chicken meat?
8	How often do you consume red meat?
9	How often do you consume fish meat?
10	How often do you consume milk, dairy products and eggs?
11	How much money do you spend monthly on decorating and maintaining your home?
12	How much money do you spend monthly on clothing?
13	How much money do you spend monthly on artistic and cultural activities?
14	How many people live in your house?
15	What kind of fuel do you use for heating?
16	How much of the energy you use consists of renewable energy sources?
17	What is the size of the house you live in?
18	What kind of vehicle are you using?
19	How many kilometers do you drive per week?
20	How many kilometers do you travel in a year by public transport?
21	How many hours do you travel in a year by plane?
22	How much is your monthly electricity bill?
23	How much is your monthly water bill?
24	How much is your monthly gas bill?
25	How much is your weekly kitchen expense?
26	Monthly cargo (online shopping etc.) usage amount?
27	The amount of packaging waste you create monthly?
28	Monthly drug use and preference (vitamin, immune system booster, etc.) amount?
29	Monthly cologne and disinfectant usage amount?
30	Monthly cleaning material (bleach etc.) usage amount?

Furthermore, arrangements were made to calculate the ecological footprint values for each individual before and during the Covid-19 pandemic separately. Ecological footprint values were calculated by entering the answers to the questions given in Table 1 into the ecological footprint calculation module specified in URL2. At the same time, with some of the questions in Table 1, it is aimed to understand the participant profile and to understand the change in some consumption habits of the participants in the Covid-19 period compared to the period before Covid-19 pandemic. This study was conducted between dates of December 2020 and March 2021. The results obtained from the questionnaire were assessed statistically by using SPSS program.

RESULTS

In this study, it was investigated how the Covid-19 pandemic, which affected the whole world and caused many changes in our daily lives, influenced some of the consumption habits of people and ecological footprint values in accordance. The change in some consumption habits during Covid-19 pandemic compared to the period before Covid-19 pandemic was also statistically evaluated.

Figure 1: Frequency of consumption of vegetative foods (grains, fruits, vegetables) (a- before the Covid-19 pandemic b- During the Covid-19 pandemic).



It was observed that proportion of those who consume plant foods (grains, fruits, vegetables) to make up half of each meal increased during the Covid-19 pandemic (Figure 1). While this rate was 38% before the Covid-19 pandemic, it increased to 48% during the Covid-19 pandemic. It is observed that the rate of those who stated that they rarely and sometimes consume vegetative food decreased during the epidemic (Figure 1 a,b).

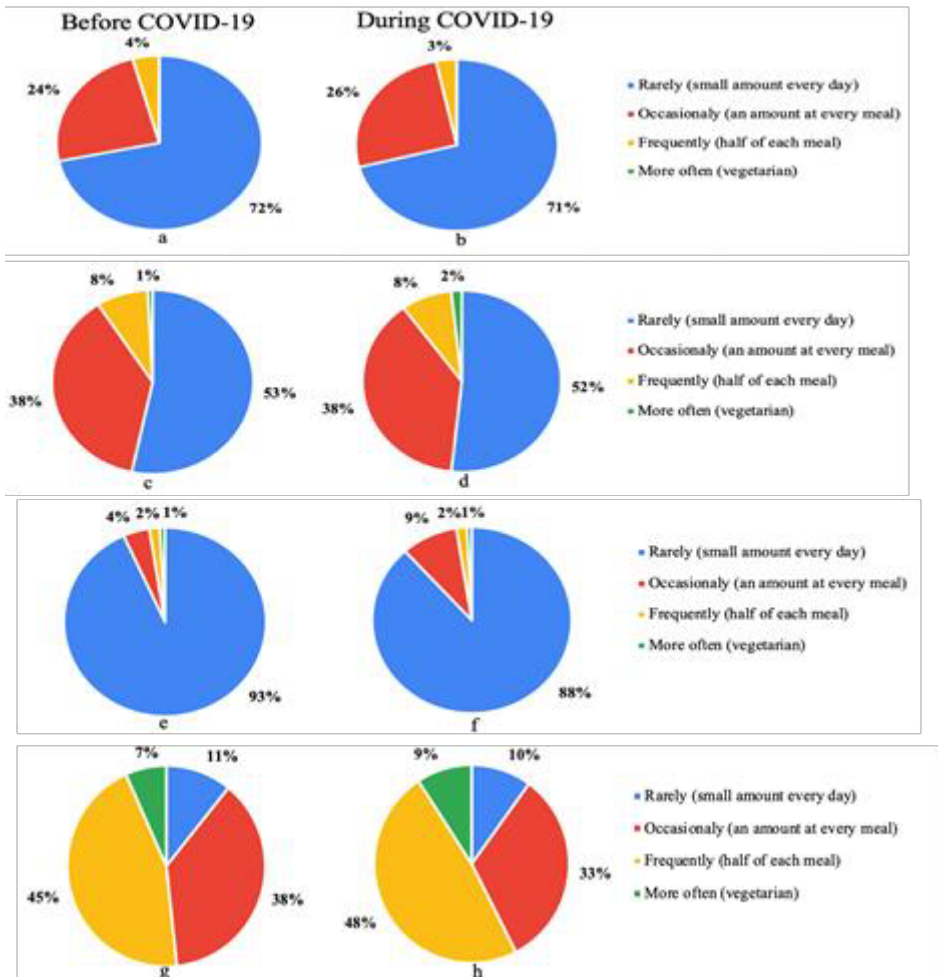


Figure 2: Consumption of animal food products (Chicken meat consumption frequency a-Before the Covid-19 pandemic b-During the Covid-19 pandemic; Frequency of red meat consumption (c- Before the Covid-19 pandemic d- During the Covid-19 pandemic; Frequency of fish meat consumption (e) – (Before the Covid-19 pandemic, during the f-Covid-19 pandemic); Frequency of consumption of milk, dairy products and eggs (g- Before the Covid-19 pandemic; h- During the Covid-19 pandemic).

It was observed that the consumption of chicken meat did not change much during the pandemic when compared to the pre-pandemic period (Figure 2 a, b). In a similar way, there was no significant change in the frequency of red meat consumption (Figure 2 c, d). When the frequency of fish meat consumption was considered, it was seen that the rate of those who rarely (once a week) consumed fish meat during the

pandemic decreased by 5%, and this decrease of 5% was reflected as a drop in those who sometimes (almost daily) consume fish meat (Figure 2 e, f). When the change in the frequency of consumption of milk, dairy products and eggs was examined, it was seen that the majority of the participants chose frequently (once or twice a day) (45%) and sometimes (almost daily) (38%) options before the Covid-19 pandemic. During the Covid-19 pandemic, it was observed that the percentage of those who frequently consume milk, dairy products and eggs increased even more (48%), and sometimes 3% of those who consume started to consume frequently (Figure 2 g, h). It is thought that the increase in consumption of plant foods, fish, milk, dairy products and eggs is due to the importance of healthy nutrition during the pandemic period and the fact that many people take time to prepare food for themselves due to their working from home during the pandemic period.

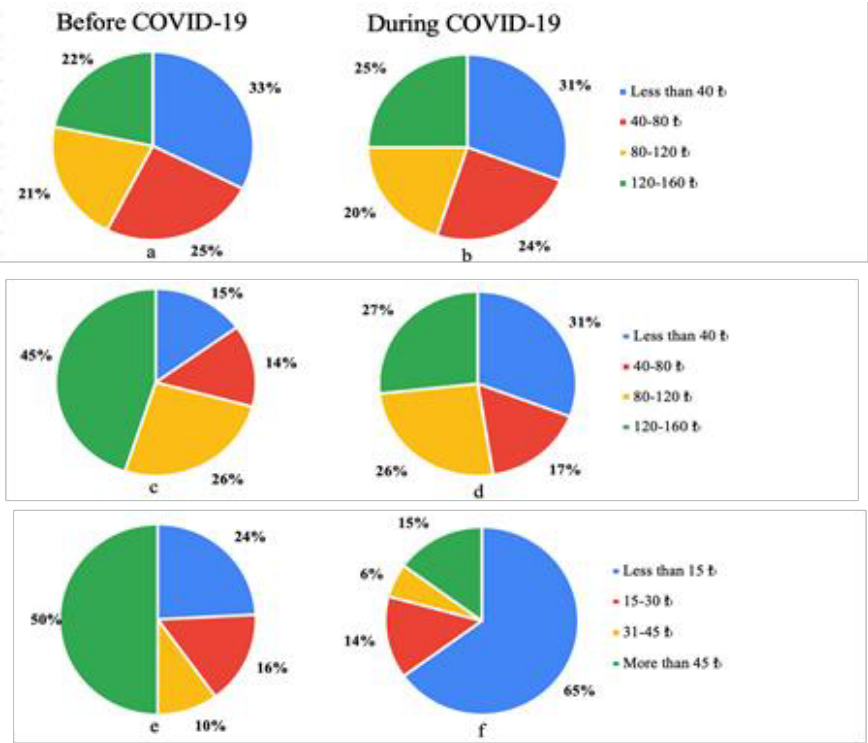


Figure 3: Expenditure on home decoration, clothing, artistic and cultural activities (Monthly expenditure on decoration and maintenance of the house a- Before the Covid-19 pandemic; b- During the Covid-19 pandemic; Monthly expenditure on clothing c- Before the Covid-19 pandemic; d- During the Covid-19 pandemic; monthly expenditure for artistic and cultural activities e- Before the pandemic of Covid-19; f- During pandemic of Covid-19).

It was found out that monthly expenditure on home decoration and maintenance has increased slightly during the Covid-19 pandemic compared to before the Covid-19 pandemic period (Figure 3 a,b). It was seen that monthly expenditure on clothing decreased during the pandemic when compared to the expenditure made before the pandemic period (Figure 3 c,d). It is seen that monthly expenditures for artistic and cultural activities decreased in a significant way during the Covid-19 pandemic time when compared to the period before the pandemic and 65% of the participants spent less than 15 TL per month for artistic and cultural activities during the pandemic period (Figure 3 e,f).

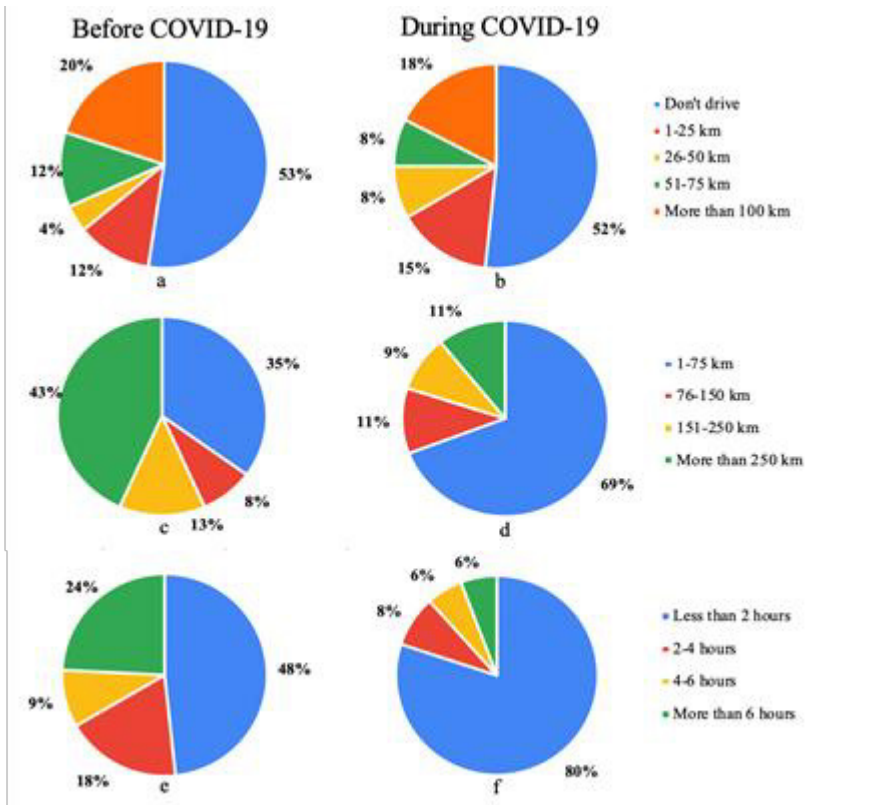


Figure 4: Change in transportation preferences (kilometers traveled in a week by car a- Before the Covid-19 pandemic b- During the Covid-19 pandemic; kilometers traveled by public transport in a year c- Before the Covid-19 pandemic d- During the Covid-19 pandemic; kilometers traveled by plane in a year e- During the f-Covid-19 pandemic before the Covid-19 pandemic).

When the answers given to the question about kilometers driven per week by car were examined, it was seen that the number of kilometers traveled by private vehicle in a week decreased when compared to the period before the pandemic but that approximately 1% of those who did not prefer to use private vehicles before the pandemic started using private vehicles during the pandemic period (Figure 4 a,b). It was observed that the use of public transport during the pandemic has also decreased significantly when compared to the pre-pandemic period (Figure 4 c,d). Similarly, the duration of travel by plane in a year has decreased significantly during the pandemic when compared to the pre-pandemic period (Figure 4 e,f).

It is considered that the increase in expenditures for home decoration and maintenance, the decrease in expenditure on clothing, artistic and cultural activities, and the decrease in vehicle usage and public transportation use are due to the fact that people spend longer time at home than the time they spent before the pandemic due to restrictions imposed during the pandemic. It is thought that people prefer to use their private vehicles for transportation instead of public transportation for the purpose of having protection against the disease due to the pandemic conditions.

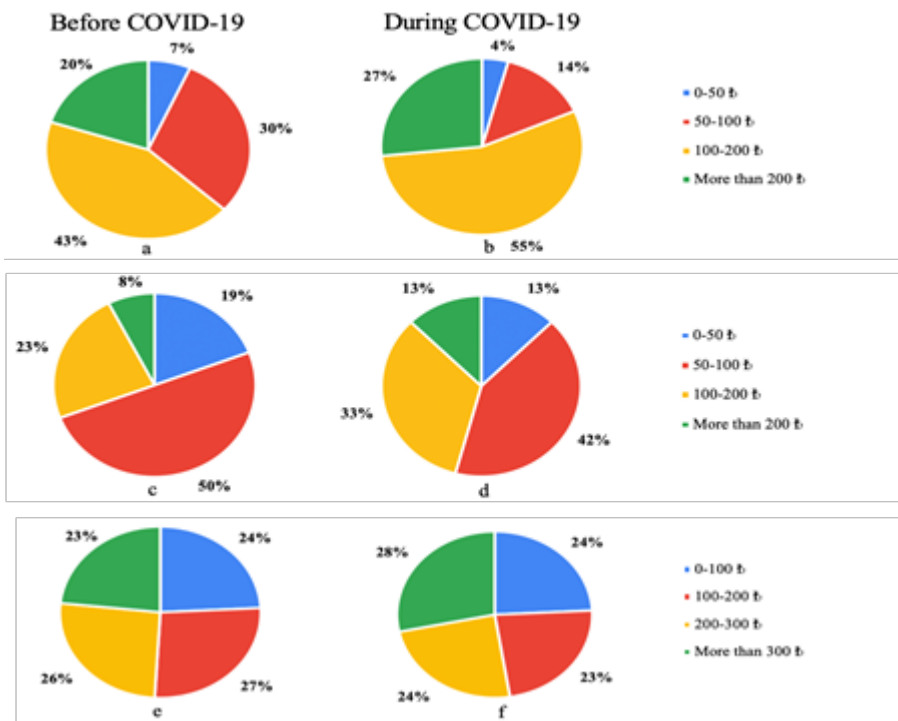


Figure 5: Change in monthly electricity, water and natural gas consumption (Change in monthly electricity consumption: a- Before the Covid-19 pandemic b- During the Covid-19 pandemic; Change in monthly water consumption: c- Before the Covid-19 pandemic d- During the Covid-19 pandemic; Change in monthly natural gas consumption: e- Covid-19 before the pandemic; during the f-Covid-19 pandemic).

During the Covid-19 pandemic, it was determined that the electricity and water consumption of individuals generally increased when compared to the pre-pandemic period. It is seen that there are no significant changes in natural gas expenditure (Figure 5 e,f). The reason for the increase in electricity and water consumption can be due to the use of more water for hygiene purposes and the use of electrical appliances for longer periods of time at home, since more time is spent at home.

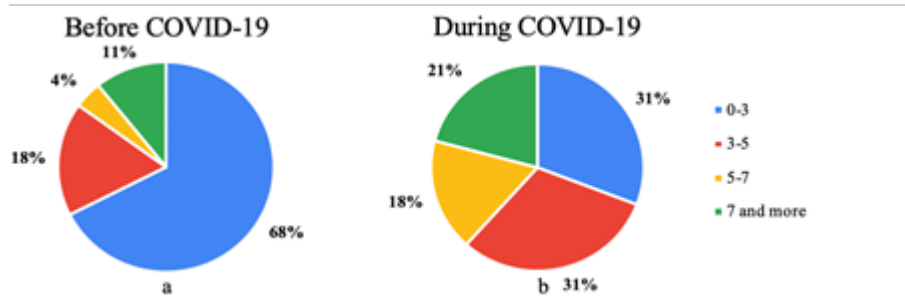


Figure 6: Number of monthly cargo (online shopping and similar) usage (a- before the Covid-19 pandemic b- During the Covid-19 pandemic).

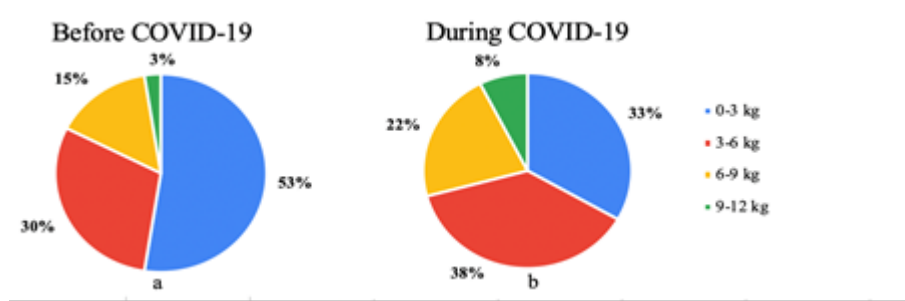


Figure 7: The amount of packaging waste generated monthly (a- before the Covid-19 pandemic b- During the Covid-19 pandemic).

When the number of monthly cargo usage is considered, it was determined that the cargo usage during the pandemic has increased apparently when compared to the pre-pandemic period (Figure 6 a,b). When the amount of packaging waste caused monthly is examined, it is seen that individuals produce more packaging waste during the pandemic than they produced before the pandemic (Figure 7 a,b). It is considered that this situation is because people do not want to be in a crowded environment due to the pandemic, and they do their shopping online. In addition, it can be said that as another reason for the increase in the amount of packaging waste, people may have turned to the consumption of packaged products with the thought of being hygienic.

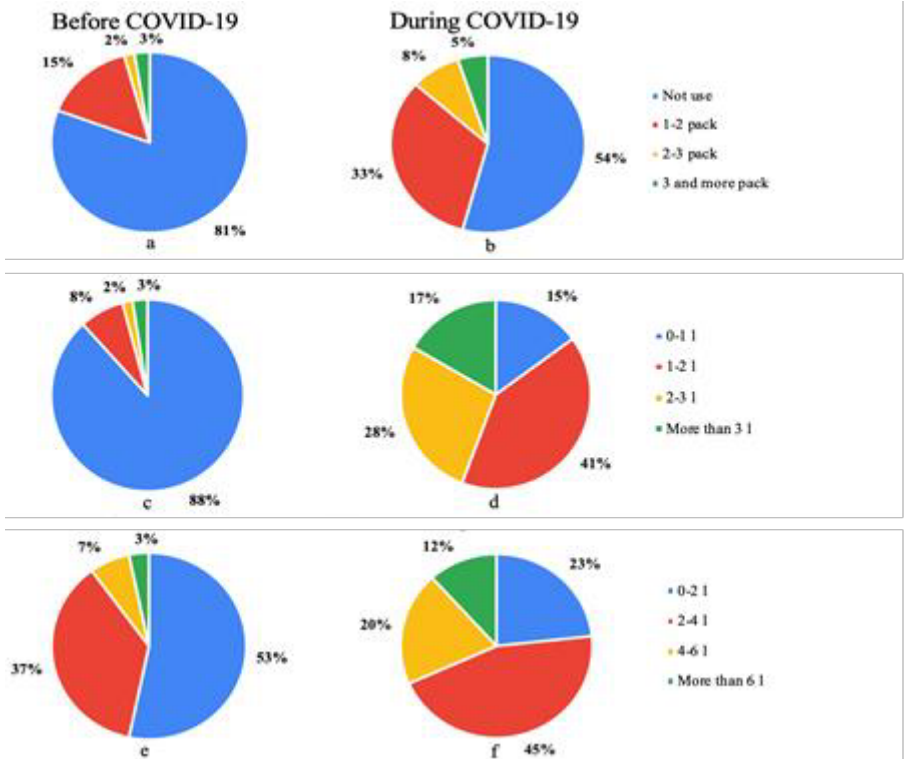


Figure 8: Drug use, cologne and disinfectant use, use of cleaning agents (Monthly amount of drug use (vitamin, immune system booster, etc.) a- Before the Covid-19 pandemic b- During the Covid-19 pandemic; Monthly amount of cologne and disinfectant use c- Before Covid-19 pandemic; d- During the Covid-19 pandemic; Monthly cleaning agent (bleach etc.) usage amount e- Before the Covid-19 pandemic; During the f-Covid-19 pandemic).

When the amount of monthly drug use (vitamins, immune system boosters, etc.) is examined, it is seen that the rate of those who said that they did not use such drugs before the pandemic was approximately 81%, whereas this rate decreased to 54% during the pandemic period. It has been observed that the use of vitamins or immune system boosters has increased because of the pandemic (Figure 8 a,b). While the percentage of those who say that they use 1 liter or less of cologne and disinfectant per month was 88% in pre-pandemic period, it is seen that it decreased to 15% during the pandemic, and the consumption of cologne and disinfectant increased significantly (Figure 8 c,d). In a similar way, the amount of monthly cleaning agent (bleach and similar) usage has increased considerably during the Covid-19 pandemic when compared to the period before the Covid-19 pandemic (Figure 8 e,f).

Statistical Assessment

According to the Kolmogorov-Smirnova Normality Test applied, since *Before Cov19 EF globalhectare* data is $p=0.196>0.05$ and *During Cov19 EF globalhectare* data is $p=0.200>0.05$ and the skewness and kurtosis values of these data sets are between -1.5 and +1.5, it shows normal distribution (Tabachnick and Fidell, 2019). Based on this result, parametric tests were applied to the data sets.

73.33% of the participants are women and 26.67% are men. As a result of the T test, the ecological footprint values before the covid-19 pandemic ($0.429>0.05$) and during the pandemic ($0.867>0.05$) do not show a significant difference as per the gender of the individuals.

Table 2: Statistical results according to the gender of the participants.

	Gender	Participant (%)	Mean (globalhectare)	<i>p</i>
Before Covid-19 EF	Female	73.33	8.359	0.429
	Male	26.67	8.547	
During Covid-19 EF	Female	73.33	8.124	0.867
	Male	26.67	8.084	

As a result of the T test, the ecological footprint values before the covid-19 pandemic ($0.429>0.05$) and during the pandemic ($0.867>0.05$) do not show a significant difference as per the gender of the individuals. While the average ecological footprint value of women before Covid-19 was 2.19% lower than men, the average ecological footprint value of women during Covid-19 was 0.49% higher than men. Generally, the average ecological footprint values of both women and men showed a decreasing trend during Covid-19 pandemic when compared to the period before Covid-19 pandemic. It was found out that this decrease was 2.81% in women and 5.41% in men (Table 2).

Table 3: Statistical results according to the age of the participants.

	Age	Participant (%)	Mean (globalhectare)	<i>p</i>
Before Covid-19 EF	11-20	10.83	8.746	0.310
	21-30	51.67	8.511	
	31-40	20.00	8.125	
	41-50	11.67	8.414	
	51-60	5.83	7.843	
During Covid-19 EF	11-20	10.83	8.338	0.927
	21-30	51.67	8.134	
	31-40	20.00	8.025	
	41-50	11.67	7.971	
	51-60	5.83	8.100	

10.83% of the participants are between the ages of 11-20, 51.67% of them are between the ages of 21-30, 20% are between the ages of 31-40, 11.67% are between the ages of 41-50 and 5.83% are between the ages of 51-60. As a result of the ANOVA test, the ecological footprint values before the Covid-19 pandemic ($0.310 > 0.05$) and during the pandemic ($0.927 > 0.05$) do not reveal a significant difference according to the age of the individuals. While the highest average ecological footprint values before Covid-19 pandemic belong to the participants aged 11-20 with 8,746 global hectares, the lowest average ecological footprint values belong to the individuals between the ages of 51-60 with 7,843 global hectares. While the highest average ecological footprint values in the Covid-19 period belong to individuals aged 11-20 with 8,338 global hectares, the lowest average ecological footprints belong to the participants between the ages of 41-50 with 7,971 global hectares (Table 3).

Table 4: Statistical results according to the education level of the participants.

	Education Level	Participant (%)	Mean (globalhectare)	<i>p</i>
Before Covid-19 EF	University	86.67	8.473	0.181
	High School	10.83	8.146	
	Secondary School	1.67	7.850	
	Primary School	0.83	6.300	
During Covid-19 EF	University	86.67	8.154	0.393
	High School	10.83	7.969	
	Secondary School	1.67	7.850	
	Primary School	0.83	6.300	

86.67% of the participants have university education, 10.83% of them have high school education, 1.67% of them have secondary education and 0.83% of them have primary education levels. As a result of the ANOVA test, the ecological footprint values before the Covid-19 pandemic ($0.181 > 0.05$) and during the pandemic ($0.393 > 0.05$) do not show a significant difference as per the education level of the individuals. While the highest average ecological footprint values before Covid-19 pandemic were observed in participants having university education with 8,473 global hectares, the lowest average ecological footprint values were observed in participants with primary education with 6,300 global hectares. During Covid-19 pandemic, the highest average ecological footprint values were observed with 8,154 global hectares in participants with university education level, while the lowest average ecological footprint values were observed in participants with primary education level with 6,300 global hectares (Table 4).

Table 5: Statistical results according to the income level of the participants.

	Income Level	Participant (%)	Mean (globalhectare)	<i>p</i>
Before Covid-19 EF	Upper than Minimum Salary	50.83	8.282	0.639
	Minimum Salary	5.83	8.586	
	Less than Minimum Salary	9.17	8.409	
	No Income	34.17	8.568	
During Covid-19 EF	Upper than Minimum Salary	50.83	8.123	0.868
	Minimum Salary	5.83	8.143	
	Less than Minimum Salary	9.17	8.355	
	No Income	34.17	8.029	

While 50.83% of the participants have an income level above the minimum wage, 5.83% have a minimum income, and 9.17% have an income level below the minimum wage, 34.17% have no income.

As a result of the ANOVA test, the ecological footprint values before the Covid-19 pandemic ($0.639 > 0.05$) and during the pandemic ($0.868 > 0.05$) do not show a significant difference according to the income levels of the individuals. While the highest average ecological footprint values before Covid-19 pandemic were observed in participants having minimum wage with 8,586 global hectares, the lowest average ecological footprint values were observed in participants having income above the minimum wage with 8,282 global hectares. During Covid-19 pandemic, the highest average ecological footprint values were observed with 8,355 global hectares in the participants with an income below the minimum wage, while the lowest average ecological footprint values were observed in the participants having no income with 8,029 global hectares (Table 5).

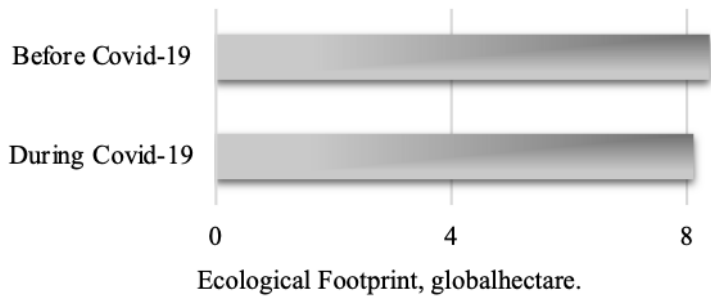


Figure 9: Comparison of the average ecological footprint values of individuals in globalhectare before and during Covid-19 pandemic.

Before the Covid-19 pandemic, the highest and lowest ecological footprint values of individuals were found out as 11.9 global hectares and 6.3 global hectares, respectively, and during the Covid-19 pandemic, these values were found out as 11.4 global hectares and 4.0 global hectares, respectively. While the average ecological footprint of the participants was 8.4 global hectares before the Covid-19 pandemic, it was determined that this value was 8.1 global hectares during the Covid-19 pandemic (Figure 9).

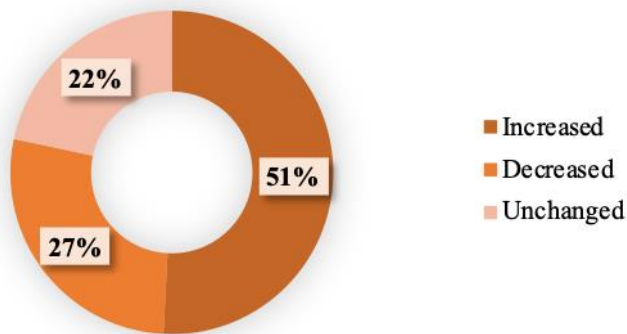


Figure 10: Change of ecological footprint values of individuals during the Covid-19 pandemic compared to the period before the Covid-19 pandemic.

During the Covid-19 pandemic, it was determined with this study that 51% of individuals have increased ecological footprints on a global hectare basis, while 27% have decreased ecological footprints and that there was a segment of 22% whose ecological footprints have not changed (Figure 10).

When the literature is reviewed, it is seen that as per the Global Footprint Network (GFN) data of ecological footprint values before the pandemic, the ecological footprint of consumption in the world in year 2014 was 20 billion global hectares (kha) and 2.84 kha per person. In Turkey, the ecological footprint of consumption in year 2014 is 249 million kha and the ecological footprint of per capita consumption is 3.21 kha. In year 2017, the ecological footprint per capita increased to 3.5 kha (URL1; URL2). In the study which they conducted before Covid-19 pandemic, Elmaslar Özbaş et al. (2019:179) found out that the ecological footprint for the 16-20 age range was 3.07 (the number of planet Earth), the ecological footprint for the 21-35 age range was 2716 (the number of planet Earth), the ecological footprint for the 36-50 age range was 3034 (number of planet Earth). When the ecological footprint of individuals being aged 16-20 based on their income rates is examined, it was seen that the ecological footprint value increases as the income rates increase. It has been determined that the high rate of purchasing technological equipment has an increasing impact on the ecological footprint, mainly for the participants in their 30s. When the ecological footprints of men and women between the ages of 21-35 and 36-50 years were compared as per their financial status, it was seen that the ecological footprint value increased with the increase in income. With regards to the total ecological footprint assessment, Turkey ranks as 13th in the list of countries with the largest total ecological footprint (according to the assessment made in year 2017) with a value of 2830×105 GH (global hectares). It is observed that the ecological footprint values have increased rapidly when compared with the biological capacity both globally and for Turkey, and that an ecological deficit has come out (URL2).

CONCLUSION

As a result of the study, it was found out that there were changes in the daily consumption habits of people before the Covid-19 pandemic and during the Covid-19 pandemic. It was observed that activities such as clothing shopping, artistic and cultural activities, travel have decreased, whereas electricity and water consumption, packaging waste amounts, disinfectant and cleaning materials consumption have increased because of the fact that people spent more time at home due to both restrictions and changes in people's preferences for being protection against pandemic.

In this study, it was found out that while the ecological footprint values of 51% of individuals increased on a global hectare basis during the Covid-19 pandemic, the ecological footprint values of 27% of individuals decreased and the ecological footprint values of 22% of individuals did not change. To be able

to reduce the ecological footprint, which is important in understanding the relationship of consumers' lifestyles and consumption habits with natural resources and raising awareness, during the pandemic, composting food scraps, promoting the work from home system, reducing airplane and car travel, preferring cycling and walking, properly disposing of disposable masks and gloves, reducing consumption, using reusable products and recycling them, placing bulk virtual ordering to reduce packaging and shipping are required. To be able to ensure a sustainable future, the expression of ecological openness must be reduced, meaning that the amount of ecological footprint should be reduced or the amount of biocapacity should be increased. Reducing the Ecological Footprint expression bears significant importance, as it is quite unlikely that the amount of biocapacity will be increased in a short time period.

REFERENCE

- Ahmed, Z., Asghar, M. M., Malik, M. N., & Nawaz, K. (2020). Moving towards a sustainable environment: The dynamic linkage between natural resources, human capital, urbanization, economic growth, and ecological footprint in China. *Resources Policy*, 67, Article 101677.
- Ahmed, Z., Zafar, M. W., & Ali, S. (2020). Linking urbanization, human capital, and the ecological footprint in G7 countries: An empirical analysis. *Sustainable Cities and Society*, 55, Article 102064.
- Budak, F. & Korkmaz, Ş. (2020), An overall evaluation for the Covid-19 pandemic process: The case of Turkey. *Journal of Social Research and Management*, 1, 62-79.
- Cowan, W. N., Chang, T., Inglesi-Lotz, R., & Gupta, R. (2014). The nexus of electricity consumption, economic growth and CO2 emissions in the BRICS countries. *Energy Policy*, 66, 359–368.
- Çelik Coşkun, I. & Sarıkaya, R. (2014). Sınıf öğretmeni adaylarının ekolojik ayak izi farkındalık düzeylerinin belirlenmesi, *Turkish Studies - International Periodical For The Languages, Literature and History of Turkish or Turkic* , 9/5 Spring, p. 1761-1787.
- Galli, A., Wiedmann, T., Ercin, E., Knoblauch, D., Ewing, B., & Giljum, S. (2012). Integrating ecological, carbon and water footprint into a “footprint family” of indicators: definition and role in tracking human pressure on the planet. *Ecological Indicators*, 16, 100-112.
- Gunal, N. (2018). Evaluation of university students' trends in reducing ecological footprint (Doctoral dissertation, Master's Thesis). Gazi University Graduate School of Natural and Applied Sciences, Ankara.
- Langnel, Z. & Babington, G. (2020) Globalization, electricity consumption and ecological footprint: An autoregressive distributive lag (ARDL) approach, *Sustainable Cities and Society*, 63, 102482.
- Murányi, A., & Varga, B. (2021). Relationship between the Covid-19 pandemic and ecological, economic, and social conditions. *Frontiers in Public Health*, 9.
- Nathaniel, S. P. (2020). Ecological footprint, energy use, trade, and urbanization linkage in Indonesia. *Mar Geo Journal*, 1–14.
- Özbaş, E. E., Hunce, S. Y., Özcan, H. K., & Öngen, A. (2019). Ecological footprint calculation. In *Recycling and Reuse Approaches for Better Sustainability* (pp. 179-186). Springer, Cham.
- Özcan, B., Ulucak, R., & Dogan, E. (2019). Analyzing long lasting effects of environmental policies: Evidence from low, middle and high income economies. *Sustainable Cities and Society*, 44, 130-143.

- Rahman, M. M. (2020). Environmental degradation: The role of electricity consumption, economic growth and globalisation. *Journal of Environmental Management*, 253, Article 109742.
- Rudolph, A., & Figge, L. (2017). Determinants of Ecological Footprints: What is the role of globalization? *Ecological Indicators*, 81, 348–361.
- Solarin, S. A., & Bello, M. O. (2018). Persistence of policy shocks to an environmental degradation index: the case of ecological footprint in 128 developed and developing countries. *Ecological Indicators*, 89, 35-44.
- Tabachnick, B. G., Fidell, L. S., & Ullman, J. B. (2019). *Using multivariate statistics* (Seventh).
- URL1: WWF, Turkey's Ecological Footprint Report, 2012, <https://www.wwf.org.tr/>, Date of Access: 28.04.2022, 02:33.
- URL2: <https://data.footprintnetwork.org/#/> , Date of Access: 28.04.2022, 02:33.
- URL3: <https://www.footprintnetwork.org/>, Date of Access: 28.04.2022, 02:33.
- URL4: <https://www.globalagriculture.org/whats-new/news/en/34095.html> , Date of Access: 28.04.2022, 02:33.
- Wackernagel, M. & Rees, W. (1998). *Our Ecological Footprint: Reducing Human Impact on the Earth*. 9. New Society Publishers.
- Yang, B., & Usman, M. (2021). Do industrialization, economic growth and globalization processes influence the ecological footprint and healthcare expenditures? Fresh insights based on the STIRPAT model for countries with the highest healthcare expenditures. *Sustainable Production and Consumption*, 28, 893-910.

Chapter 6

A Review on Machinability of Inconel 718

Abdullah ALTIN¹

Muhammed Cihat ALTIN²

1 Prof. Dr.; Yuzuncu Yıl University, Van Vocational of Higher School, Mechanical and Metal Technology Department. Van/Turkey,
aaltin@yyu.edu.tr ORCID No:0000-0003-4372-8272

2 Öğr. Gör. Muhammed Cihat ALTIN, Yuzuncu Yıl University, Van Vocational of Higher School, Electric and Energy Department. Van/Turkey,
caltin@yyu.edu.tr ORCID No:0000-0002-5224-8978.

ABSTRACT

With this study, a general summary of the work done by many scientists on the machining of Inconel 718 was given and the optimum machining conditions were tried to be determined.

When machining Inconel 718 with cemented carbide cutting tools, round shaped tools should be preferred, but square shaped ceramic cutting tools should be preferred in order to obtain a quality surface in machining with ceramic cutting tools, and round shaped ceramic cutting tools should be preferred for rough turning.

While determining the cutting conditions, the cutting parameters applied with the guidance of TS 10329 were heavy for Inconel 718 in many cutting operations and the cutting tools were not suitable for these conditions. With a lower depth of cut, a lower feed rate should be preferred. In particular, reducing the depth of cut from 2 mm to 1.5 mm and the feed rate from 0.20 mm/rev. to 0.12 mm/rev. will increase the cutting performance of the cutting tool and ensure a longer life.

In the machining of Inconel 718 with ceramic tipped tools on CNC lathe, cutting speeds above 250 m/min. cutting speeds and $f=0.20$ mm/rev. and parameter values above $d=2$ mm should not be overtested in terms of tool life. Because cutting tools are extremely sensitive to breakage while machining Inconel 718. These precision and expensive tools quickly wear out or break at higher cutting speeds.

Keywords: Machining, optimization, Inconel 718, Surface roughness, Cutting force.

1. Introduction

There are many scientific studies in the world on nickel-based super alloy Inconel 718 and it has known It is one of the most difficult metal to machining in the metal industry,. It is used in many space vehicles and aircraft engines due to its resistance to severe mechanical stresses at high temperatures. It is also frequently used in different areas of the industry. In this study, a compilation was made with the results of some of the studies that we consider important.

2. Studies on Machinability of Inconel 718 and Results

In the study conducted by N. Richards and D. Aspinwall (1989) (1), many cutting tests were carried out using whisker reinforced aluminum oxide ceramic tool and nickel-based super alloys Inconel 718 and Incoloy 901 materials. As a result of their studies, tool life and wear values were evaluated. As a result, it has been observed that a cutting speed of 750 m/min can be achieved with whisker-reinforced silicon carbide tool for Inconel 718. . Chip control is poor at these cutting speeds and continuous chips with saw teeth are obtained. The combination of high heat, high workpiece hardness, and abrasive chips created notches in the depth of cut. The machining of superalloys including titanium and aluminum has been particularly difficult. These alloys were hardened by precipitation of the Ni₃(Ti,Al) type γ' phase. Titanium and aluminum are interactive (mutually exchangeable) elements. In general, the γ' phase was expressed as increasing the amount of titanium and aluminum, and in this case, tool wear accelerated. Referring to Baker in his studies, "The notch formed at 230 m/min. cutting speeds of Incoloy 901 is 70% less in silicon nitride-based ceramics than in mixed aluminum oxide ceramics, and $V=150$ m/min. of cutting speed and $f=0.125$ mm/rev. It has been reported that Inconel 718 is not suitable for machining mixed oxide ceramics at speeds above the feed rate. Recommended parameters for Incoloy 901 (Kennametal KYON 2000), cutting speed 120-145 m/min., feed rate 0.2 mm/rev. and the depth of cut is 2 mm". However, at a cutting speed of $V=210$ m/min. and $f=0.25$ mm/rev. for the Inconel 718, feed rates above 0.30 mm/rev. are possible for sialon (Kennametal KYON 2000) tools. It has been reported that the notch formed is less than the notch formed at $f=0.175$ mm/rev. In their statements, it has been reported that carbide tools deteriorate due to thermal softening in the cobalt phase at speeds above 30 m/min. cutting speeds, and the heat generated at the tip develops differently according to the cutting tip geometry. Another noteworthy statement is that while the temperature at the cutting tip was 320 oC in the machining of cast iron under the same conditions at a cutting speed of $V=10$ m/min, this situation increased to 820 oC for Nimonic 75. Some of the

current whisker reinforced cutting tool materials recommended for use in machining Inconel 718.

In 1993, with the study conducted by A. Gatto and Liuliano (2), the wear patterns and amounts obtained when machining Inconel 718 material with 20% silicon reinforced Al₂O₃ tool CrN and (Ti,Al)N PVD coated tool and the same material with uncoated tool (SEM).) were examined under a scanning electron microscope.

In their studies, CrN and (Ti, Al) N coating on 20% SiCw (Al₂O₃) in terms of tool life and wear amount minimizes the heat effects compared to the uncoated tip, it is more than one coat compared to the same tools with Ti(C,N) and TiN coating. It was observed that they obtained longer tool life (2).

In their studies, it has been observed that CrN and TiN coated ceramic tools have similar friction coefficients and these tools have lower friction coefficients than (Ti,Al)N coated ceramic tools.

In conventional machining, cutting speed and feed rate are closely related to the type of tool material when machining a refractory material. Even expensive whisker tools with high cutting speed have short tool life. The machining parameters used during the machining of nickel-based superalloys are directly related to the high heat generated. These high temperatures are the main reasons affecting the brittleness of the SiCw whisker reinforced Al₂O₃ composite material. Again, in the previous studies of the same authors, notch wear and snapping occurred when machining a 0.4% carbon steel with a cutting speed of 1000 m/min with a SiCw (Al₂O₃) tool, similar wear with Inconel 718 material processed with the same tool at low cutting speeds. has been shown.

In another study conducted by A. Gatto and L. Iuliano (3) in 1993, the situations that cause tool breakage during machining of Inconel 718 super alloy were investigated and safer cutting parameters were determined. In another study, the effects of the heat generated during cutting on the amount of wear were investigated. The material used in the experiments is Inconel 718. The tool used is the 20% SiCw whisker-reinforced ceramic square shaped tool (4), which is placed in such a way that the side edge makes a 45° angle with the workpiece during cutting. The rake angle is -6°, the rake angle is 0°. The cutting speed during machining is between V=300 and 530 m/min. and feed f=0.08 to 0.22 mm/rev. and the depth of cut was kept constant (d=1.5mm). While serious cracking occurs at the lowest cutting speed and medium feed (V=300 m/min., f=0.12 mm/rev.) speeds, the same cutting speed and high feed (V=300 m/min., f=0.22 mm/rev.) no cracking was observed. At higher cutting speeds (V=400 m/min., f=0.22 mm/rev.), it was observed that the cracks formed destroyed the cutting edge.

While no suggestions were made for ideal parameters in their studies, the evaluation of different experimental situations was made as follows.

As a result of their studies, it has been found that different wear mechanisms occur in the tool along the tool-chip contact point as a result of the changing deformation energy, and the whisker capillaries are detached from the cutting tool material at high temperatures as a result of high cutting speeds (5). In experimental studies, no study has been done on cutting forces (3).

In the study (6) by Liao and Shiue in 1996, the wear mechanisms that occur during turning of Inconel 718 with two different cemented carbide (K20 and P20) tools were analyzed. With their work ($f=0.1$ mm/rev. feed, $d=1.5$ mm depth of cut and cutting speed $V=35$ m/min.) on the wearing surface of the cemented carbide tool, an adhered BUE layer very close to the cutting edge and on the cutting edge cracks were observed. A similar situation was encountered when the same cutting conditions were applied to the P20 quality carbide tool. As a result of the comparison between the two cutting tools, the wear of the P20 quality cutting tool is more uneven, the side edge wear length is larger and the crater is deeper. Using the electron microanalysis EPMA (electron probe micro analyzer) device, the elements in the layer formed on the chip surface of the cutting tool were analyzed and no difference was observed in the tool elements at the cutting speed of 35 m/min. But from the work material, nickel and iron were diffused on both cutting tool surfaces by diffusion. The reason for this was thought to be the heat generated at the tip of the cutting tool above 1000 °C.

In 1997 Rahman et al. (7), using different tool geometry and cutting parameters with different values, Inconel 718 material was subjected to machining tests in an uncooled lathe. Parameters used are cutting speeds of 30, 40, and 50 m/min, 0.2, 0.3 and 0.4 mm/rev. feed and a constant depth of cut of 2 mm. The flank wear of the cutting tool, the surface roughness of the workpiece and the cutting force elements were seen as performance determinants for tool life. In the experiments, the effects of the side edge cutting angle were studied by using two different quality cutting tools (K type PVD TIN coated carbide and multi-layered Al_2O_3 CVD coated cemented carbide). It was observed that the tool life increased by increasing the side edge cutting angle from -50 to 450 for both cutting tools. For example, with the enlargement of the side edge cutting angle, the heat generated at the tool-chip interface and effective in shaping the chip thickness decreased, and moreover, it allowed the heat generated on the larger side edge cutting angle to be distributed over a wider area. This helped heat away from the cutting edge during cutting. The large flank cutting angle also allowed the cutting forces to be distributed over the wider cutting edge, while at the same time reducing the notch, it was seen that it contributed positively to the

tool life. During the experiments, PVD TiN coated carbide tool showed excellent wear resistance at 150 and 450 approach angles. The same cutting tool, even at cutting speeds above 50 m/min., 0.4 mm/rev. It showed satisfactory performance at the forward and approach angle of 450. Both cutting tools, 30 m/min. at cutting speed, 0.2 mm/rev. They showed the best performance with an approach angle of 450 in progress. In the machining tests, as a result of the testing of the Al₂O₃ CVD coated cemented carbide tool, severe notch was observed and it was not found suitable for Inconel 718 in machining operations at all approach angles. The tools used in their work are two different coated carbide tools. One of them is EH20-Z-UP (TiN PVD coated cemented carbide tool) and the other is AC25 (TiN CVD coated cemented carbide tool) tool. As a result of the machining experiments, using different cutting parameters, different surfaces and different wear patterns were investigated in different cutting situations. Their results are:

1) A significant increase in tool life has been observed by increasing the approach angle of the cutting tool from -50 to 150 and then to 450. EH20-Z-UP, one of these cutting tool materials, showed a 64.3% reduction in tool life when the approach angle was reduced from 450 to -50.

2) For Inconel 718 material, the allowable cutting speed and feed values were found to be quite low compared to other materials. It has been accepted that the tool life decreases as the cutting speed value is increased, and this situation is caused by the low thermal conductivity, abrasiveness and work hardness of the material as a result of the high cutting forces.

The tool life of the EH20-Z-UP cutting tool was determined by more flank wear, whereas the depth of cut was more decisive for the tool life in the AC 25 cutting tool. It was determined that the EH20-Z-UP cutting tool showed excellent resistance to notch wear at the approach angles of 150 and 450 at the depth of cut, and as a result, the AC 25 cutting tool was not suitable for Inconel 718.

In the study conducted by A. Choudhury and M. A. El-Baradie in 1998 (8), the effects of cutting variables (cutting speed, cutting force and depth of cut) on cutting forces and tool life were defined when cutting Inconel 718 with coated and uncoated carbide tools. (9). The shape of the carbide tools they use is 800 rhombic and without chip breaker. These cutters were used for different cutting situations and the machining parameters were optimized by measuring the cutting forces. The flank wear was accepted as a criterion for tool life, and a comparison was made by considering the cutting speed, feed rate and depth of cut, which are among the coated and uncoated tool life elements. It turned out that the life of coated carbide tools is not better than that of uncoated carbide tools. With their work, machining tests were carried out to observe many of the following reasons.

- 1) Determination of optimum cutting conditions by measuring cutting forces,
- 2) Determining the effect of cutting variables on tool life and comparing coated and uncoated tools,
- 3) Determining the elements of the extended Taylor tool life equation and tool life constants.

As a result of their studies, excessive flank wear was detected during machining of Inconel 718 with cemented carbide tools at recommended cutting speeds (10).

Fully heat treated 55 mm in work. in diameter and 1 m. A stack of 2 different Inconel 718 materials with the same properties in length was used (8). The materials were subjected to a solution treatment at 980 oC for 2 hours for heat treatment, and then rested at 720 oC for 8 h for degreasing. It was then subjected to air cooling and then a treatment was carried out by keeping it at the furnace temperature at 620 degrees Celsius for 8 hours. The cutting tools used for turning experiments are coated and uncoated cemented tungsten carbide tools. These tools are CNMA 12 04 04 ISO defined uncoated tools (66) with 80o rhombic shape and H 13 A quality by Sandvik koromat company. For coated tools, GC 30 15 class tools were used. The bar used is ISO defined PCLNR 25 25 M12. Tool and bar combination provides 95o approach angle. The angles of the cutting edge are: The rake angle is -6o, the side edge angle is -6o and the clearance angle is 0o. GC 30 15 quality is coated and there is a thick aluminum oxide layer on top of the titanium carbide layer and the coating thickness is 10 micrometers in total. For the measurement of cutting forces, the lathe is equipped with 3 piezo-electric dynamometers, which are connected to the load amplifier. The cutting forces were obtained by a digital-analog converter and a computer. The results obtained from the computer were compared by recording the force signals with an ultraviolet recorder. The features and details of the lathe and the force measuring system are as follows (8).

1- Lathe type and name: Colchester M 1600, maximum rotation speed at 10 horsepower 1600 rev./min. Advancement area 0.06-1.0 mm/rev. between.

2- 3-element cysts dynamometer, type 92 625 A1, calibration area $F_f = 0 - 15000$ N (Newton), $F_p = 0 - 15000$ N and $F_c = 30000$ N with 3 cysts load amplifier type 5000 11 and one ultraviolet recorder, type M12 150 A

3- Microscope for measuring tool wear (mitutoyo TM 300 tool microscope).

The following results were obtained as a result of the experiments.

1) It has been observed that uncoated cemented carbide cutting tool materials perform better than coated carbide tools in terms of different cutting speed and different feed.

There was no significant difference in tool life for both coated and uncoated cemented carbide tools at cutting speeds of 26-48 m/min. It was observed that at higher cutting speeds, cutting forces increased at $V=50$ m/min and $f=0.30$ mm/rev feed due to high shear stress.

2) The usefulness of coated tools has only been demonstrated when the depth of cut exceeds 1 mm. As a result of these studies, it has been seen that the depth of cut element in Taylor's tool life equation, coated tools are more effective than uncoated tools.

3) It has been observed that the effect of cutting speed on tool life in coated tools draws more attention than feed and depth of cut. In uncoated tools, the effect of this in terms of tool wear was seen as cutting speed first, depth of cut and feed.

4) In the experiments they have done, it has been observed that in cases where tool wear exceeds 0.30 mm in terms of tool life, coated tools give shorter tool life than uncoated tools.

5) Recommended machining condition for machining Inconel 718 with cemented carbide inserts, cutting speed 20-25 m/min., feed 0.15 mm/rev. and the depth of cut should be selected at values above 1 mm.

Notch wear is also reported as a problem that shortens tool life during machining of nickel-based superalloys (11). Some researchers report that the temperature of the cutting edge becomes too high when machining Inconel 718 at low cutting speeds. With the advent of ceramic tipped tools, Inconel 718 can be machined by removing high chip volume at high cutting speeds. The machining values received are between 120 and 300 m/min cutting speeds. In this way, a 10-fold machining capacity was achieved on cemented carbide tools (12). Whisker reinforced aluminum oxide ceramic cutting tools, cutting speed range 200 to 700 m/min. and the feed rate is 0.37 mm/rev. Depending on the hardness of the work material, this situation changes) (1). However, this is the case for whisker-reinforced aluminum oxide-based ceramic tipped tools produced by SANDVIK. Sialon materials, which are still widely used in the United States and produced by KENAMETAL, are used as the main cutter in the machining of Inconel 718. KENAMETAL company serves in USA markets with many types of sialon.

In another study by A. Couldhury and M. A EI-Baradie (13) in 1998, chip removal tests were carried out with Inconel 718 material with different cutting

tools and tool wear patterns were evaluated. TiC-coated ceramic tipped tools were found to be most suitable for Inconel 718 material for machining above 400 m/min. cutting speed or at high feeds (14). However, at medium cutting speeds and low feeds (between 100 and 400 m/min.), whisker reinforced aluminum ceramic tipped tools showed better performance and tool life than uncoated carbide tools.

According to Lee et al. (15), high strength in nickel-based superalloys causes high temperatures and stresses during machining. The tool separates the chip interface and mostly the chip edge from the workpiece by tearing it. Fatigue on the tool, the work hardness layer and the adhesion of the workpiece contribute to notch wear. The notch is also attributed to the diffusion-friction wear mechanism.

However, the cutting forces during machining with these cutters were not measured. In the machining of Inconel 718 with ceramic tipped tools, notch wear was observed at the depth of cut as a result of the adhesion wear transferred from the workpiece to the tool and showing its effect. Notch wear resistance was equal for both sialone and whisker-reinforced silicon carbide tools. Again, flank wear showed itself as a diffusion wear in whisker reinforced tools and sialon tools.

In the study conducted by Arunachalan, R. Mannan, M. A. in 1998 (16), research was conducted on the progress and machining difficulties of cutting tools used in the machining of Inconel 718 material in the last 15 years. In this study, machining with high cutting speed was seen as promising in increasing productivity, and it was also determined that the correct selection of cutter geometry was important on machining efficiency.

In the study of E. O. Ezugwua, Z. M. Wanga and A. R. Machadob in 1999 (17), general and detailed information about the development of alloying elements added to nickel-based superalloys to gain some commercial properties and the use of superalloys is presented. The common problem in nickel-based superalloys, tool wear that shortens tool life, and machining mechanisms that lead to tool failure are compared and discussed in this study. Tool life and surface quality are the most important factors in machinability. In the machining of nickel-based superalloys, many conditions that adversely affect the tool such as notch formation in the cutting tool at the depth of cut, flank wear, cracking, fracture or alone or combined diffusion, crater, abrasion wear, thermal and mechanical fatigue cracks, rich oxygen environment or It has been observed that it can be minimized in the coolant environment. The use of high-pressure cooling and the rich nitrogen and argon environment tended to accelerate wear, which resulted in reduced tool life despite the ease of chip flow and ease of machining. In order to increase the performance in the tool, it was stated that as a result of increasing the power of the cutting edge by increasing the nose angle of the

cutting tool, it is necessary to expand the tool-chip contact area and reduce the approach angle. It has been pointed out that the whisker-reinforced ceramic tipped tools, which have been developed recently, outperform traditional carbide tools with cyalon ceramics and multi-layered cemented carbides, and provide superior machining performance at high cutting speeds (18).

In 1999, Jindal et al. (19), the effects of PVD TiN, TiCN and TiAlN coated carbide tools in cemented carbide tools when Inconel 718 is turned in coolant medium at cutting speeds of 46 and 76 m/min, keeping the feed rate and depth of cut constant. examined. It was observed that TiAlN and TiCN coated carbide tools performed better than TiN coated carbide tools at both cutting speeds. During the experiments, the side edge and nose wears, which are effective on the tool life of all three tools, were measured until the end of the tool life. As a result of the experiments, excellent performance was recorded with the TiAlN coated carbide tool at a cutting speed of 46 m/min. The maximum flank wear after 5 minutes of cutting was approximately 0.15 mm. In addition, TiAlN coated carbide cutting tools were found to exhibit lower nose and crater wear than TiCN and TiN coated carbide tools. Although the substrate material is the same for all coated tools, the different wear conditions that occur are attributed to the type of coating material. According to the result, the coating layer increased the wear resistance and reduced the cutting forces. TiAlN coating has higher hardness than other coating types. In the machining tests carried out above 750 0C on TiCN and TiN ' coated carbide tools, an increase in resistance to abrasive wear resistance was observed and at the same time chemical stability at high temperatures was observed. This high temperature stability is due to the protection of the TiAlN coating by the Al₂O₃ layer and the presence of a layer containing titanium, aluminum, oxygen and nitrogen during machining. As a result, the thermal conductivity of the TiAlN coating was the lowest among the three coatings tested. This is also due to the type of tool that retains low heat along with the heat carried by the chip. As a result, it has been observed that the TiAlN coating provides excellent crater resistance.

In 1999 Itakura et al. In the study conducted by (20), the wear mechanisms formed by turning the Inconel 718 material with P20 TiN/TiC coated carbide insert in an uncooled environment were investigated. Continuous and intermittent chip removal tests at constant depth of cut ($d=0.25$ mm), constant feed ($f=0.2$ mm/rev.) and cutting speeds of 30, 100 and 150 m/min. The temperature was measured with a thermocouple. However, with this method, only the heat generated at the contact point could be measured. During the continuous chip removal process, a stable BUE layer was formed on the tool chip surface. The resulting wear was seen on the side edge rather than the chip surface. The flank

wear was caused by the abrasive particles in Inconel 718, in addition, it was observed that the workpiece material penetrated the chip surface of the tool. The heat generated during chip removal is 30 m/min. at 713 0C at 100 m/min. at 1047 0C. At this temperature, the BUE adhesion was not stable and flank wear, rapidly developing wear, progressed both on the rake face and on the side edge cutting surface. This was seen as a result of the high temperature occurring at high shear rates causing surface oxidation and diffusion.

In the intermittent cutting process, it was determined that the BUE adhered to the chip surface formed as a thin film layer and this layer was repeatedly removed.

Prengel et al. In a study presented in 2001 (21), confirming the results of Jinde et al., he also processed Inconel 718 with different PVD cutting carbide tools in a coolant medium with multi-layer coatings. They stated that they observed plastic deformation and notching together with abrasive wear at cutting speeds higher than 61 and 76 m/min.

Ducros et al. In 2003, cutting speed 40 m/min., feed 0.2 mm/rev. and depth of cut 1.5 mm. He carried out experiments by machining with a lathe in a coolant medium (22). Comparing the two-layer coated carbide tools, abrasive wear on the cutting edge and snapping were seen as the main problems on the cutting edge. The depth of cut notch was found to be affected by the uncut part during machining, and this failure mode was mainly due to the hardening of the work material during machining, which occurred in both uncoated carbide and TiN/AlTiN coated carbide inserts. According to the author, abrasive wear was the main result of the hard carbide particles in Inconel 718. The hardness of the TiN /AlTiN double layer coating was 3900 Vickers hardness, which provided the best abrasive wear resistance in conventional multilayer and single layer coatings, in addition, the TiN / AlTiN double layer coating showed the best abrasion resistance to boiling. High temperature resistance was better in AlTiN coating compared to CrN and TiN coating, and resistance to BUE was better.

In the study conducted by Kramer and Hartung (23) in 1980, it was observed that the crater wear mechanism affects the tool life when machining Inconel 718 material.

1983 S. K. Bhattachoryya, A. Lawaid. In the study conducted by M. H. Lewis L. Walbanle (24), the wear mechanisms and their causes and cutting parameters that cause undesired machining were determined by machining the nickel-based superalloy Incoloy 901 material at different cutting parameters using a sialone ceramic tool. In their study, it was found that tool life is determined by side edge and notch wear. In their studies, high cutting speed and feed fracture were observed, notch wear was dominant at low cutting speeds, and flank wear was dominant at high cutting speeds. From the analysis of wear mechanisms, crater

wear, diffusion and plastic deformation determine the tool life, at lower cutting speeds, crater wear occurs, whereas at high cutting speeds, diffusion occurs after plastic deformation, and crater wear is either by the detachment of grainy sialon particles from the part or by their separation in bulk. has been found to occur. However, it has been observed that this wear occurs with the atomic displacement of the transition elements titanium and chromium by diffusion. (24).

Focke et al. In the experiment performed by (25) various tool materials on Inconel 718, it was observed that the crater wear occurred just behind the cutting tool tip, but there was no wear on the rake surface of the tool.

In the study conducted by Wright and Chow (26), it was observed that the fractures in the cutting edge of the carbide tool were caused by the heat generated in the 1st deformation zone. In machining nickel-based superalloys, the formation of a notch or a <v> shaped groove at the cutting line depth of the cemented carbide tool has been considered a common problem. Shaw et al. (27), it was observed that the temperature at the edge of the chip was 25% higher than the center of the chip. According to Whitney and Vaidyanathan, ceramic cutting tool materials are classified as follows (28).

- 1) Pure ceramic cutting tool materials ($Al_2O_3 + ZrO_2$)
- 2) Mixed ceramics ($Al_2O_3 + TiC$)
- 3) Sialon type ceramics ($Si_3N_4 + (Al_2O_3 . Y_2O_3)$)
- 4) Whisker reinforced silicon carbide ceramics ($Al_2O_3 + SiC$)

3. Discussion and Conclusion

In terms of tool life and surface quality, uncoated carbide SECO 883, V BB =0.08 mm, Fc =1149 N, Ra =0.45 μ m, in four different cemented carbide cutting tools, at V=45 m/min. with Tc =15.24 minutes metal removal time and 273 cm³ metal removal volume, it was found to be the most suitable for machining inconel 718. Among four different cemented carbide cutting tools, the lowest mean side edge wear area width, VBB=0.08 mm at V=45 m/min, the lowest roughness value, at V=45 m/min., Ra=0.45 mm, lowest actual cutting force achieved with 345 N uncoated carbide SECO 883 at V=75 m/min. While SECO 883 was found to be more suitable for machining based on surface quality, SECO 560 showed better performance in machining inconel 718 at speed of V=60 m/min.

With the machining of Inconel 718, in coated carbides, flank wear and cracking in uncoated carbides were more prevalent. All four carbide cutting tools showed resistance to wear at V= 15 m/min. At cutting speed V=30 m/min, 3 carbide tools, except the coated carbide KC 935, performed well. Coated carbide SECO 560 and SECO 883 at 45 m/min were found to be wear resistant, but the other two cutting tools fell short. At 60 m/min, only the SECO 560 was able to

withstand wear, while the other three cutting tools were deemed insufficient. At 75 m/min, it has been observed that all four cutting tools wear rapidly.

Surface roughness was between $R_a=0.45-0.98$ mm in round shaped carbide tools and $R_a=1.23-1.98$ mm in square shaped carbide tools. Coated carbide (SECO 560) performed close to uncoated carbide (SECO 883) in terms of surface quality at cutting speeds other than $V=30$ m/min. Coated carbide KC 9225 and KC 935 showed poorer performance with poor surface qualities. With uncoated carbide (SECO 883), low surface roughness was seen only at 45 m/min, but increased at other cutting speeds. Among the four different cutting tools, SECO 883 was found to be more suitable with the lowest surface roughness at $V=45$ m/min.

In terms of tool life and surface roughness, (KYON 4300 SNGN), $V=150$ m/min cutting speed $V_{BB}=0.13$ mm, $R_a=1.22$ μm and $F_c=852$, 52 N, $T_c = 4.57$ minutes cutting time and 273 cm³ metal removal volume was found to be the most suitable among the four ceramic tools. Silicon nitride based ceramic tool KYON 2100 SNGN, second with $R_a=1.42$ μm at $V=150$ m/min, ($\text{Al}_2\text{O}_3+\text{SiC}_w$) ceramic tool KYON 4300 RNGN third, silicon nitride based ceramic tool KYON 2000 RNGN ranked fourth. Square shaped ceramic tipped tools showed better performance in terms of surface quality than round shaped ceramic tipped tools. As the cutting speed increased, the surface roughness of all four cutting tools increased. The highest R_a value was $R_a=2.1$ μm at $V=300$ m/min with KYON 4300 SNGN. The average roughness value R_a was between 1.22-2.1 μm in square shaped ceramic tools, while R_a was between 1.65-1.96 μm in round shaped ceramic tools.

Side edge, crater, notch and plastic deformation wears have generally occurred in ceramic tipped tools. In RNGN round tools, notch is more dominant in the depth of cut, while in SNGN square tools, more side edge and crater wear is dominant. In terms of average flank wear, only square shaped ceramic tools were found to be durable at 150 m/min, while all four cutting tools performed well at 200 m/min. Except for the KYON 4300 SNGN, the other three ceramic tools performed well at the ($V=250$ m/min.) with the wear criterion under $V_{BB}=0.3$ mm. All of the tools were found not to be resistant to wear at the of $V=300$ m/min.

4. References

- Richards, N., Aspinwall, D., "Use of ceramic tools for machining nickel-based alloys", *Int. J. Mach. tools Manuf.*, 294, 575-588 (1989).
- Gatto, A., Iuliano, L., "High Speed machining of nickel- base superalloys, tool wear pattern and chip features", *Report to CIRP STC 'C'* (1993).
- Felloni, L., Gatto, A., Lppolito, R., Iuliano , L., "Wear mechanisms of a SiCw whiskers reinforced ceramic tool in high speed machining of Inconel 718 and C 40 steel", *1 st AITEM Congress*, Ancona, p 21(1993).
- Coromant Turning Tools 93/94, *AB Sandvik Coromant*, Catalog. p 45
- Gatto, A., Iuliano, L., "Performances of coated ceramic tools for high speed machining of nickel base super-alloys", *Report to CIRP STC 'C'* (1994).
- Liao, Y. S., Shiue, R. H., "Carbide tool wear mechanism in turning of Inconel 718 superalloy 718", *Journal of Materials Processing Technology* 55, 321-330 (1995).
- Rahman, M., Seah, W. K. H., Teo, T. T. , "The Machinability of Inconel 718", *Journal of Materials Processing Technology*, Volume 63 Issues 1-3, 199-204 (1997).
- Chouldhury, I. A., El-Baradie, M. A., "Machining nickel base superalloys: inconel 718", *Proc Instn Mech Engrs*, Vol 212, Part B, 195-205 (1997).
- Choudhury, I. A., El-Baradie, M. A., "Journal of Materials Processing Technology, 95, 30-39, turning research by response surface methodology", *Int. J. Prod. Res.* 13(4) (1975) 265-290 (1999).
- Chouldhury, I. A., El-Baradie, M. A., "Machinability of nickel-base super alloys : a general review", *Journal of materials Processing Technology*, Volume 77, Issues 1-3, 278-284 (1998).
- Recht, R. F., "A dynamic analysis of high speed machining", *Journal of engineering For Industry*, Vol.107, 309-315 (1985).
- Chouldhury, I. A., El- Baradie, M. A., "Machinability assessment of Inconel 718 by factorial design of experiment coupled with response surface methodology", *Journal of materials Processing Technology*, Volume 95, Issues 1-3, 30-39 (1999).
- Choudhury, I. A., El-Baradie, M. A., "Machinability of nickel base super alloys: a general review", *Proc. Advances in Materials and Processing Technologies AMPT'95*, Dublin, Ireland, vol. III, 1405-1413 (1995).
- Lee, M., Horne, J. G., Tabor, D., "The mechanism of notch formation at dept of cut line of ceramic tools machining nickel-base superalloys", *Proc. 2nd Int Conf*, Wear Materials Dearborn, MI, 460-464 (1979).
- Arunachalam, R., Mannan, M. A., "Machinability of nickel-based high temperature alloys", *Machining Science and Technology*, Vol. 4, Issue 1, 127-168 (2000).

- Ezugwu, E. O., Wanga, Z. M., Machadop A. R., “The machinability of nickel- based alloys: a review”, ***Journal of materials Processing Technology***, Volume 86, Issues 1-3, 1-16 (1998).
- Wardany, T.I.El., Mohammed, E., Elbestawi, M. A., “Cutting temperature and wear of ceramic tools in high speed machining of difficult-to-cut materials”, ***International Journal of Machine Tools and Manufacture***, Volume 36, Issues 5, 611-634 (1996).
- Jindal, P. C., Santhanam, A. T., Schleinkofer, U., Shuster, A. F., “Performance of PVD TiN, TiCN, and TiAlN coated cemented carbide tools in turning”, ***International Journal of Refractory Metals & Hard Materials***, 17, 163-170 (1999).
- Itakura, M., Kuroda, H., Omokawa, H., Itani, K., Yamamoto,Y., Ariura, “Wear mechanism of coated cemented carbide tool in coated in cutting of Inconel 718 super heat resisting alloy”, ***International Journal of Japanese Society for Precision Engineering*** 334, 326-333 (December 1999).
- Prenzel, H. G., Jindal., P. C., Wendt, K. H., Santhanam, A. T., Hedge, P. L., Penich, R.M., “A new class of high performance PVD coatings for carbide cutting tools”. ***Surface and Coatings Technology*** 139, 25-34 (2001).
- Ducros, C., Benevent, V., Sanchette, F., “Deposition, characterization and machining performance of multi layer PVD coatings on cemented carbide cutting tools”. ***Surface and Coatings Technology*** 163-164, 681-688 (2003).
- Kramer, B. M., Hartung, P. D., ***Proc. Int. Conf. Of Cutting Tool Mat***, Fort Mitchell, K,Y, 57-74 (1980).
- Bhattacharya, S. K., Jawid, A., Lewis, M. H., “Behaviour of sialon ceramic tools when machining cast iron”, ***Proc. 12th North A.m Manuf. res. Conf***, 265-270 (1984).
- Focke, A. E., Westermann, F. E., Eemi, A., Yavelak, J., Hoch, M., “Failure mechanism of superhard materials when cutting superalloys”, ***Proc. 4th Int.-Am.Conf.***, China, A 268-296 (April 1991).
- Wright, P. K., Chow, J. G., “Deformation charectereistics of nickel alloys during machining”. ***Trans. ASME, J. Engng. Mater. Technol.***, 104, 85-93 (1982).
- Shaw, M. C., “Metal Cutting Principles”, ***Oxford University Press***, New York pp 45(1986).
- Whitney, E. D., Vaidyanathan, P. N., “Engineered ceramics for high speed machining”, ***Proc. of Advances in Tool Material for in High Speed Machining, Scottsdale***, 77-82 (1987).

Chapter 7

Cone Crusher Structural Analysis Requirement

Ali Kemal ÇAKIR¹

¹ Asst. Prof. Dr.; Adnan Menderes University Department of Machinery and Metal Technologies, Aydın Vocational School, ali.kemal.cakir@adu.edu.tr ORCID No

ABSTRACT

Industrial machinery and equipment such as cone crushers are used to crush hard and abrasive rocks. These machines and equipment have been used for a long time to break rocks and similar materials.

The machinery and equipment used in the stone crushing process are exposed to heavy loads due to the long duration. For this reason, structural design analysis of cone crushers is required. For this reason, it is necessary to examine the design parameters of cone crushers and to investigate the efficiency of cone crushers. In this sense, it is important to calculate the force analysis of cone crushers. So, it is necessary to calculate the forces acting on the cone crusher. The stress values of the crusher material can be calculated by calculating the forces acting on the cone crusher. It contributes to the crusher efficiency with the force analysis. In addition, it helps the manufacturer to choose the material to be used correctly.

In this study, it will be reviewed some of the recent research on cone crusher structural design and optimization and discuss the main factors that affect the productivity and product quality of the cone crusher.

Keywords: Cone crusher, structural analysis, efficiency.

INTRODUCTION

Industrial machinery and equipment are used to break hard and abrasive rocks. These machines and equipment are used for a long time to break rocks and similar materials. In the stone crushing process, the machinery and equipment used are exposed to heavy loads due to the long durations. For this reason, structural design analysis of cone crushers is required. Therefore, it is necessary to examine the design parameters of cone crushers and to investigate the efficiency of cone crushers.

A cone crusher is a type of crusher that is used for crushing bulk materials by applying compressive forces. The cone crusher consists of a concave, a mantle, and an eccentric shaft that rotates around an axis. The chamber geometry, the crusher working parameters, and the rock characteristics determine the performance of the cone crusher.

In this article, we will review some of the recent research on cone crusher structural design and optimization and discuss the main factors that affect the productivity and product quality of the cone crusher.

Chamber Optimization

One of the key aspects of cone crusher structural design is the optimization of the crushing chamber. The crushing chamber is the space between the concave and the mantle, where the bulk material is subjected to compressive stress and broken into smaller fragments.

The shape and size of the crushing chamber affect the amount of material that can be processed in a given time, the degree of reduction that can be achieved, and the shape and size distribution of the product.

One of the recent studies on chamber optimization was conducted by Wu et al. [1], who analyzed the impact of key structural parameters such as the bottom angle of the mantle, the length of the parallel zone, and the eccentric angle on the productivity and product quality of the cone crusher.

The bottom angle of the mantle is the angle between the horizontal plane and the tangent line of the mantle at its lowest point. The length of the parallel zone is the distance between the two points where the mantle and concave are parallel to each other. The eccentric angle is the angle between the vertical axis and the axis of rotation of the eccentric shaft.

Wu et al. [1] used a mathematical model to calculate the amount of ore in the blockage layer, which is the layer of material that accumulates at the bottom of the crushing chamber and prevents further material from entering. They also considered the amount of ore uplift, which is the amount of material that is lifted up by the mantle during its rotation.

They revised the traditional mathematical model of crusher productivity by incorporating these factors and established a mathematical model for dual-objective optimization of productivity and product quality.

They applied their model to an existing C900 cone crusher and obtained the optimal values of the key structural parameters. They also simulated the dynamic characteristics of the cone crusher using the discrete element method (DEM) and verified their numerical results with the simulation results.

The main findings of their study are:

- The bottom angle of the mantle and the length of the parallel zone are within the range of 50° – 60° and 140 mm–190 mm, respectively. The productivity shows a positive correlation with the bottom angle and a negative correlation with the length of the parallel zone. But the dependence of product quality on the angle and the length is just the opposite.
- The eccentric angle is within the range of 1.4° – 2° and its decrease has a negative effect on the productivity and product quality.
- The optimal structural parameters of the C900 crusher chamber are: the swing speed of the mantle, 285 r/min; the length of the parallel zone, 150 mm; the bottom angle of the mantle, 55° ; the eccentric angle, 2° ; the eccentricity, 44.8 mm; and the engagement angle, 23° .

Multi-Objective Planning

Another approach to cone crusher structural design is to use multi-objective planning, which is a method that considers multiple objectives or criteria simultaneously and seeks to find a solution that satisfies all or most of them.

One of the studies that used multi-objective planning for cone crusher structural design was conducted by Huang et al. [2], who established a multi-objective planning model of the cone crusher chamber geometry, output and size reduction based on previous work [3].

The output and size reduction are two important performance indicators of the cone crusher. The output is the amount of material that is processed by the crusher per unit time, and it depends on factors such as chamber geometry, crusher working parameters, and rock characteristics. The size reduction is the degree of reduction in size that is achieved by the crusher, and it depends on factors such as chamber geometry, rock characteristics, and breakage mechanism.

Huang et al. [2] used a new chamber geometry design model based on the population balance model and the kinematic character of the rock in the chamber. They also used a cone crusher output optimization model based on equations of motion, and a size reduction model based on matrix theory.

They applied their model to optimize the cone crusher chamber geometry, output and size reduction, and obtained a set of optimal solutions that satisfy different objectives or preferences.

The main findings of their study are:

- The output and size reduction show a trade-off relationship, that is, increasing one objective will decrease the other. Therefore, a compromise solution that balances both objectives is needed.
- The output and size reduction are affected by the chamber geometry parameters, such as the base angle of cone, the length of parallel strip, the eccentricity, the eccentric angle, and the engagement angle. The optimal values of these parameters depend on the desired output and size reduction.
- The output and size reduction are also affected by the crusher working parameters, such as the speed of eccentric main shaft and the discharge setting. The optimal values of these parameters depend on the chamber geometry and the rock characteristics.

Setkaya, S. and Gemalmayan, N. [4] studied design changes and material selections in some critical parts of a cone crusher named TKL3000SE manufactured by a company. In their study, they determined the maximum crushing force on the mantle, which they determined in the cone crusher, to be used in the finite element analysis. Finite element analysis of mantle, concave, socket and main shaft was carried out with reference to this force. In their analysis, they determined that the most critical parts of cone crushers are the mantle and concave parts, where the breaking process takes place. In their study, they determined that as a result of the maximum force applied locally on the mantle, stresses of 200 Mpa on the mantle and 155 Mpa on the concave. Thus, considering the yield limit of the material, they determined that it is almost twice as safe.

Working Principle of Cone Crusher

The mantle in the crusher moves periodically. The mantle works by making an opening and closing movement according to the fixed concave. The intervening rock material is subjected to the compression force during the closing. The material moves down from the crusher chamber (Fig. 1) in the during opening. Pieces move under the influence of gravity. As the parts pass through the crusher, they are subjected to repeated compression several times due to circular oscillation. During each compression, the material is partially broken.

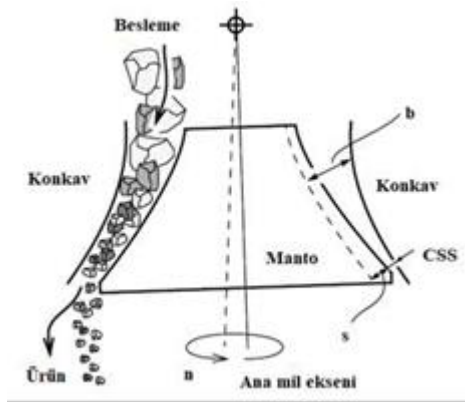


Figure 1. Working Principle of Cone Crusher [4]

Cone Crusher Types

Another aspect of cone crusher structural design is the type of cone crusher. There are mainly four types of cone crushers: spring cone crusher, hydraulic cone crusher, compound cone crusher, and gyratory cone crusher. Each type has its own advantages and disadvantages, and is suitable for different applications.

The spring cone crusher is one of the oldest and most widely used cone crushers on the market. It has a simple structure and reliable performance. It can crush various ores and rocks with medium hardness and above. It has a spring safety system that can protect the crusher from overload [5].

The hydraulic cone crusher is a modern and advanced version of the spring cone crusher. It has a hydraulic system that can adjust the discharge opening and clear the crushing chamber automatically. It can crush various ores and rocks with high hardness and above. It has a high efficiency and large capacity [5].

The compound cone crusher is a combination of the spring cone crusher and hydraulic cone crusher. It has both the advantages of spring safety system and hydraulic adjustment system. It can crush various ores and rocks with medium hardness and above. It has a unique cavity design and good product shape [5].

The gyratory cone crusher is a type of crusher that is similar to the gyratory crusher but has a cone-shaped crushing head instead of a flat one. It has a larger feed opening and a steeper cone angle that can produce finer products. It can crush various ores and rocks with high hardness and above. It has a spider-bearing support system that can control the crushing pressure [6] [7].

The following table summarizes some of the main features and differences of these four types of cone crushers.

Table 1. Types of cone crushers

Type	Structure	Advantages	Disadvantages
Spring cone crusher	Simple structure with spring safety system	Reliable performance, low cost, easy maintenance	Low efficiency, low capacity, poor product shape
Hydraulic cone crusher	Advanced structure with hydraulic system	High efficiency, high capacity, automatic adjustment and clearing, good product shape	High cost, complex maintenance, sensitive to oil temperature and pressure
Compound cone crusher	Combination of spring and hydraulic systems	Spring safety system, hydraulic adjustment system, unique cavity design, good product shape	High cost, complex maintenance, sensitive to oil temperature and pressure
Gyratory cone crusher	Similar to gyratory crusher but with cone-shaped head	Large feed opening, steep cone angle, fine product size, spider-bearing support system	High cost, complex maintenance, high power consumption

Force Analysis of Cone Crushers

Software support should be obtained for force analysis of Cone Crushers. As software, ANYS software and RockyDEM software can be used for force analysis calculations. DEM and FEM analyzes of the cone crusher should be done at the first stage. In order to perform the analysis, technical drawings of the breaker should be made and the sections where the force analysis will be made should be determined.

Fig. 2 shows the design and cross-section view of a cone crusher to be analyzed.

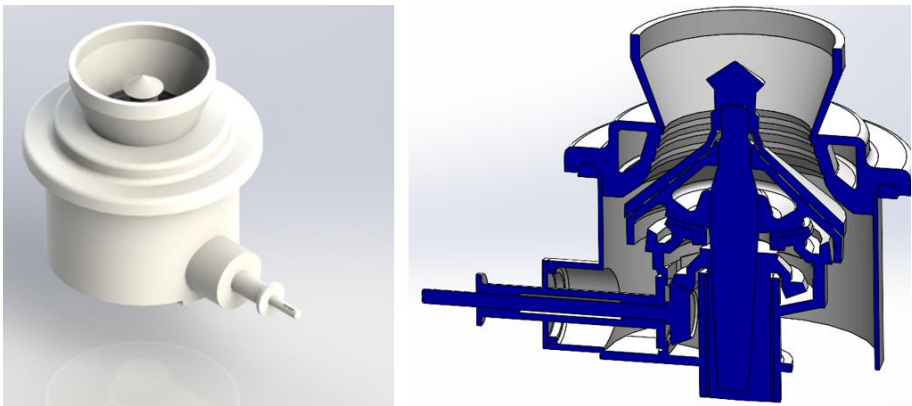


Fig. 2. CAD Geometry of Cone Crusher [8]

The cone crusher design is also influenced by the size and shape of the material being crushed. The size and shape of the material will affect the amount of force required to crush it. Therefore, the design of the crusher must take into consideration the material properties, including its compressive strength, hardness, and abrasiveness.

Force analysis is an essential aspect of cone crusher design. It involves the calculation of the forces acting on the moving parts of the crusher, including the mantle, the concave, and the eccentric shaft. The force analysis is necessary to ensure that the crusher can handle the required load without failure.

The force analysis involves the use of mathematical models and computer simulations to calculate the forces acting on the crusher's moving parts. The models take into account the material properties and the geometry of the crusher. The analysis includes the calculation of the stresses, strains, and deformations of the various components of the crusher.

The force analysis also helps in the optimization of the crusher design. It enables the engineers to identify the areas of the crusher that are subjected to high stresses and strains. This information can then be used to modify the design of the crusher to reduce the stresses and strains on these areas.

In order to define the cone crusher movement, the point called the pivot point is defined as the point where the movement axis and the shaft axis intersect. It can be seen in Fig. 3.

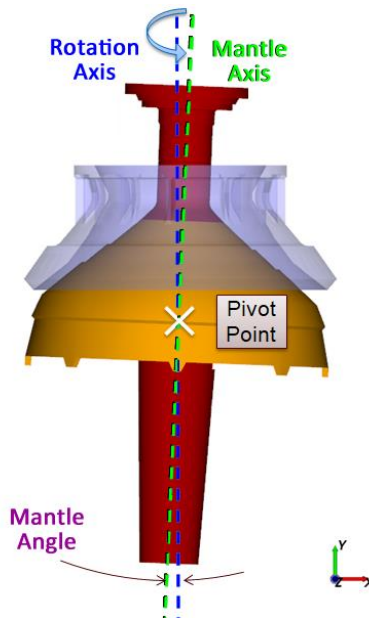


Fig. 3. Cone crusher motion and analysis identification [8]

Along with this definition, it is necessary to determine the axis of the movement. The Y axis is the axis of motion. The rotational speed must be defined. After all these processes, the force analysis can be calculated by creating the DEM model. Thus, stress values on the concave can be measured. Stress values should be below the yield stress values. Thus, concave material selection can be made.

CONCLUSION

In this article, it has reviewed some of the recent research on cone crusher structural design and optimization, and discussed the main factors that affect the productivity and product quality of the cone crusher. I have also introduced the four types of cone crushers and their features and differences. It is given some useful information and insights on cone crusher structural design in this study.

Cone Crusher design parameters change depending on the force change on the critical parts. Therefore, these variables must be taken into account in the manufacturing processes.

In addition, there is very little work in the literature on cone crusher design and its structural variables. In this study, this deficiency has been tried to be eliminated.

REFERENCES

- [1] Wu et al., "Chamber Optimization for Comprehensive Improvement of Cone Crusher Productivity and Product Quality", *Mathematical Problems in Engineering*, 2021.
- [2] Huang et al., "Multi-objective planning of cone crusher chamber, output and size reduction", *Minerals Engineering*, 2007.
- [3] Evertsson, C. "Cone Crusher Performance", PhD Thesis, Chalmers University of Technology, 2000.
- [4] Setkaya, S. ve Gemalmayan, N., "Konik Kırıcı Tasarımı ve Sonlu Elemanlar Yöntemi ile Doğrulanması", *Gazi Mühendislik Bilimleri Dergisi*, 2019, 5 (1): 65-76, <https://dx.doi.org/10.30855/gmbd.2019.01.07> (In Turkish).
- [5] Anonymous-a, Crusher Types and Features, <https://crushing-machine.com/crushing-equipment/cone-crusher-types-and-features/>, (Last accessed, 24.05.2023).
- [6] Anonymous-b, "Cone Crusher, <https://www.sciencedirect.com/topics/engineering/cone-crusher>, (Last accessed, 28.05.2023).
- [7] Anonymous-c, "Cone Crusher Technical Features", https://www.flsmidth.com/-/media/brochures/brochures-products/crushing-and-sizing/2021/raptor-cone-crusher_brochure.pdf, (Last accessed, 28.05.2023).
- [8] Investigation of Cone Crusher Structural Design Parameters, Investigation of Efficiency Values, BAP Project, BAP Project No: AYMYO-22001, Adnan Menderes University BAP Unit, May, 2023.

Chapter 8

Large Language Models and Their Current Use Cases

Akın ÖZÇİFT¹

¹ Prof. Dr. ; Manisa Celal Bayar Üniversitesi, Hasan Ferdi Turgutlu Teknoloji Fakültesi Yazılım Mühendisliği Bölümü. akin.ozcift@mcbu.edu.tr ORCID No: 0000-0002-5317-5678

ABSTRACT

Large language models, powered by advancements in artificial intelligence and deep learning, have emerged as powerful tools for natural language processing tasks. These models, exemplified by OpenAI's GPT-3, possess the ability to generate coherent and contextually relevant text, rendering them invaluable across a wide range of applications. This paper provides an overview of large language models and their current use cases across various domains. The introduction elucidates the concept of large language models, elucidating their architectures, training methodologies, and capabilities. From an application standpoint, these models find utility in tasks such as sentiment analysis, question answering, language generation, and translation.

Finally, the chapter concludes by identifying future directions for the development and application of large language models. It emphasizes the significance of ongoing research in areas including model interpretability, multi-modal learning, and domain adaptation, with the aim of further enhancing the capabilities and versatility of these models.

Keywords: large language models, natural language processing, deep learning, transformer, use cases.

INTRODUCTION

Large language models have emerged as powerful tools in the field of natural language processing (NLP), revolutionizing the way we interact with and process textual information. These models, built on advanced deep learning architectures, have demonstrated remarkable capabilities in understanding, generating, and manipulating human-like text. With their ability to learn from vast amounts of training data, large language models have found a wide range of applications across different industries. In this study, we provide a comprehensive overview of large language models and explore their current use cases.

One of the primary use cases of large language models is in the development of conversational agents, such as chatbots and virtual assistants. These models can engage in natural language conversations with users, answering questions, providing information, and simulating human-like interactions. The combination of deep learning algorithms and massive pre-training has significantly improved the conversational abilities of these systems, enabling more seamless and contextually relevant interactions (Radford et al., 2019).

Another prominent application of large language models is in machine translation. By leveraging their contextual understanding of language, these models can generate high-quality translations between different languages. They have the ability to capture subtle nuances, idiomatic expressions, and context-specific meanings, resulting in more accurate and fluent translations compared to traditional rule-based or statistical approaches (Gu et al., 2020).

Large language models have also shown exceptional performance in content generation tasks. They can generate coherent and contextually appropriate text, making them valuable tools for automated content creation. Whether it's generating articles, stories, or even code snippets, these models excel at producing human-like text based on a given prompt or a set of predefined rules (Lewis et al., 2020). However, it is important to address concerns related to the potential biases and ethical implications associated with content generation by large language models (Bender et al., 2021).

Furthermore, large language models have been successfully applied to information retrieval tasks, including question answering. By processing vast amounts of text data, these models can effectively retrieve relevant information from various sources and provide accurate answers to user queries. They can understand the context of the questions and retrieve the most appropriate information, showcasing their capability to comprehend and reason over complex textual data (Roberts et al., 2020).

In addition to the aforementioned use cases, large language models have found applications in sentiment analysis, text summarization, sentiment generation, and more. Their versatility and adaptability make them valuable tools in a wide range of NLP tasks.

In the following subsections, we will delve into each of these use cases, examining the underlying techniques and methodologies employed by large language models.

Large Language Models in Chatbots and Virtual Assistants Development

Chatbots and virtual assistants have become increasingly prevalent in various domains, ranging from customer support to personal assistants. The development of conversational agents has been significantly enhanced by the utilization of large language models. These models leverage deep learning algorithms and massive pre-training to understand and generate human-like text, enabling more engaging and contextually relevant conversations. More practically the use of LLMs in chatbots and virtual assistants' development based on the following points:

Pre-training and Fine-tuning: Large language models, such as OpenAI's GPT-3, are typically pre-trained on vast amounts of text data from the internet, allowing them to learn the underlying patterns and structures of language. This pre-training phase equips the models with a broad understanding of grammar, syntax, and semantic relationships. Following pre-training, fine-tuning is conducted on specific chatbot or virtual assistant tasks, enabling the models to adapt to domain-specific requirements and optimize their conversational abilities (Radford et al., 2019).

Contextual Understanding and Generation: Large language models excel in capturing the contextual cues and nuances of human language, allowing them to generate coherent and contextually appropriate responses. By considering the preceding context of the conversation, these models can provide more accurate and context-aware replies, leading to more interactive and engaging conversations with users. They are capable of handling diverse conversational flows, understanding ambiguous queries, and generating relevant and informative responses (Wolf et al., 2020).

Multimodal and Emotion-aware Interactions: Advancements in large language models have facilitated the development of chatbots and virtual assistants that can engage in multimodal interactions. These models can process and generate text in conjunction with other modalities, such as images or audio, enhancing the richness and effectiveness of the conversation. Furthermore, large language models are increasingly incorporating emotion-aware capabilities,

enabling chatbots and virtual assistants to recognize and respond to users' emotional states, fostering more empathetic and personalized interactions (Rasooli et al., 2020).

Ethical Considerations and Bias Mitigation: The deployment of large language models in chatbots and virtual assistants raises important ethical considerations. Bias in language models, inherited from the training data, can manifest in the responses generated by chatbots. Researchers and developers are actively working on mitigating bias through various techniques, including fine-tuning on carefully curated datasets and incorporating fairness-aware training approaches. Ensuring responsible and unbiased behavior of chatbots and virtual assistants is crucial to maintain user trust and fairness in their interactions (Bender et al., 2021).

Large Language Models in Machine Translation.

Large language models have emerged as powerful tools in the field of machine translation, revolutionizing the way we approach language translation tasks. These models, powered by deep learning algorithms and massive pre-training, have demonstrated remarkable capabilities in capturing the contextual nuances and complexities of different languages. In this section, we explore the application of large language models in machine translation and discuss their impact on improving translation quality and efficiency.

Contextual Understanding and Generation: Large language models, such as transformer-based architectures, excel in capturing the contextual information present in source sentences, enabling them to generate more accurate and fluent translations. By considering the entire input sentence and its context, these models can effectively handle complex sentence structures, idiomatic expressions, and domain-specific terminology. This contextual understanding allows large language models to produce translations that better preserve the original meaning and linguistic nuances (Vaswani et al., 2017).

Improved Translation Quality: The application of large language models in machine translation has led to significant improvements in translation quality. By leveraging their vast pre-training data and the ability to model long-range dependencies, these models can generate more coherent and contextually appropriate translations. They can better capture the semantics and pragmatics of the source language, resulting in translations that are more accurate and natural-sounding to human readers. The use of large language models has particularly benefitted low-resource languages, where traditional statistical machine translation approaches often face data scarcity issues (Gu et al., 2020).

Multilingual Translation: Large language models have the advantage of being able to handle multiple languages within a single framework. Multilingual models can leverage the shared representations across languages to improve translation quality even for language pairs with limited parallel training data. The ability of large language models to transfer knowledge across languages has opened up new possibilities for low-resource language translation and has shown promising results in multilingual translation scenarios (Aharoni et al., 2019).

Domain Adaptation: Large language models can be fine-tuned on specific domains or specialized translation tasks, enabling better adaptation to domain-specific terminology and improving translation accuracy. By fine-tuning the models on domain-specific parallel corpora or using domain-adaptive techniques, the models can generate translations that align with the specialized vocabulary and terminology of specific domains, such as medical or legal translation. This domain adaptation capability enhances the usability and applicability of large language models in real-world translation scenarios (Liu et al., 2021).

Post-Editing and Productivity: The use of large language models in machine translation has also improved post-editing workflows and increased productivity for human translators. By generating initial translations that are of higher quality and closer to the desired output, large language models reduce the amount of editing required, thereby speeding up the post-editing process. This improves the efficiency of human translators, allowing them to focus on fine-tuning and ensuring the naturalness and accuracy of the translations (Sennrich et al., 2016).

Large Language Models in Intelligent Content Generation

Large language models have revolutionized content generation tasks, enabling the automated creation of diverse types of textual content, such as articles, stories, and code snippets. These models, built on advanced deep learning architectures, have shown remarkable capabilities in generating human-like and contextually relevant text. In this section, we explore the application of large language models in content generation tasks and discuss their impact on various domains.

Text Generation: Large language models are capable of generating coherent and contextually appropriate text based on a given prompt or a set of predefined rules. By leveraging their vast pre-training data, these models can produce text that closely resembles human writing, capturing the syntax, grammar, and semantic structures of the target language. The generated text can be used for

various purposes, such as producing blog posts, news articles, or social media content (Lewis et al., 2020).

Storytelling: Large language models have been employed in storytelling applications, where they generate narratives, dialogues, and plotlines. By leveraging their ability to understand and mimic human-like language patterns, these models can create engaging and immersive stories. They can generate characters, dialogues, and plot twists, opening up new possibilities for interactive storytelling experiences and creative content generation (Fan et al., 2018).

Code Generation: Large language models have demonstrated promising results in generating code snippets and assisting with software development tasks. By understanding the structure and syntax of programming languages, these models can generate code segments based on specific requirements or user prompts. This has the potential to accelerate the development process, assist developers in finding code solutions, and automate repetitive coding tasks (Yin et al., 2021).

Personalized Content: Large language models can be fine-tuned on specific user data or preferences to generate personalized content. By incorporating user-specific information, such as demographics, browsing history, or previous interactions, these models can tailor the generated content to individual users. This enables the creation of personalized product recommendations, targeted marketing campaigns, or customized content for user-facing applications (Gao et al., 2021).

Creative Writing Assistance: Writers and creatives can benefit from large language models as creative writing assistants. These models can provide suggestions, help overcome writer's block, and enhance the creative process by generating alternative phrases, sentence structures, or plot ideas. They can serve as valuable tools for brainstorming, inspiration, and improving the overall quality of creative writing (Chiang et al., 2021). While large language models offer remarkable capabilities in content generation, ethical considerations should be taken into account. The potential for biased or inappropriate content generated by these models necessitates responsible usage and content moderation measures (Bender et al., 2021).

Large Language Models in Information Retrieval and Question Answering

Large language models have revolutionized the field of information retrieval and question answering, enabling more accurate and contextually relevant responses to user queries. These models, powered by deep learning techniques

and massive pre-training, have demonstrated remarkable capabilities in understanding and generating human-like text, thereby enhancing the effectiveness of information retrieval and question answering systems. In this section, we explore the application of large language models in information retrieval and question answering tasks and discuss their impact on improving search accuracy and user experience.

Information Retrieval: Large language models have significantly improved information retrieval systems by enhancing the understanding of user queries and the relevance of search results. These models can comprehend the semantic meaning of queries and capture the context of the information being sought. By leveraging their pre-training on vast amounts of text data, they can better interpret user intent and provide more accurate and contextually appropriate search results. Large language models have been successfully integrated into search engines, enabling more efficient and accurate retrieval of relevant information (Devlin et al., 2019).

Passage Ranking and Document Summarization: Large language models have been employed in passage ranking tasks, where the goal is to identify the most relevant passages within a document to answer a specific query. By considering the query and the content of the document, these models can effectively rank and select the most informative passages. Additionally, large language models have been utilized in document summarization, generating concise summaries that capture the key information from longer documents. This aids in extracting the most relevant information and improving the efficiency of question answering systems (Khattab and Zaharia, 2020).

Question Answering: Large language models have revolutionized question answering systems, enabling more accurate and comprehensive responses to user questions. These models can understand the nuances and context of questions, allowing them to provide relevant and precise answers. By leveraging their pre-training and fine-tuning on question answering datasets, large language models have achieved state-of-the-art performance on various question answering benchmarks. They can handle complex questions, perform inference, and generate detailed explanations, enhancing the overall user experience (Brown et al., 2020).

Conversational Question Answering: Large language models have also been employed in conversational question answering, where the system engages in a back-and-forth dialogue to provide information and answer user queries. These models can maintain context across multiple turns of conversation, enabling more coherent and natural interactions. By leveraging their ability to generate human-like responses, large language models enhance the conversational

experience and facilitate more interactive and dynamic question answering systems (Chen et al., 2021).

Multimodal Question Answering: Advancements in large language models have facilitated the integration of multimodal information in question answering systems. These models can process and generate text in conjunction with other modalities, such as images or videos, improving the richness and effectiveness of question answering. They can answer questions based on visual content or provide descriptive responses supported by multimodal information, enhancing the overall user experience (Zellers et al., 2020).

In conclusion, large language models have significantly advanced information retrieval and question answering tasks by improving search accuracy, enabling more comprehensive answers, and enhancing user experiences. Their ability to understand and generate human-like text has revolutionized the field, opening up new possibilities for intelligent information access. Further research and development in large language models hold the potential to continue pushing the boundaries of information retrieval and question answering systems.

CONCLUSION

As final words, large language models have emerged as powerful and versatile tools with a wide range of current use cases. These models, based on advanced deep learning architectures and extensive pre-training on vast amounts of text data, have revolutionized various fields and applications. They have demonstrated remarkable capabilities in understanding and generating human-like text, enabling advancements in natural language understanding, content generation, information retrieval, and question answering.

Large language models have proven to be instrumental in natural language understanding tasks, such as sentiment analysis, named entity recognition, and text classification. Their ability to capture contextual information and model complex language patterns has significantly improved the accuracy and efficiency of these tasks, opening up new possibilities in fields such as customer support, social media analysis, and content moderation.

In the realm of content generation, large language models have demonstrated their prowess in generating diverse types of textual content, including articles, stories, and code snippets. Their contextual understanding and creative capabilities have expanded the possibilities for automated content creation, creative writing assistance, and personalized content generation, empowering industries such as journalism, marketing, and software development.

Moreover, large language models have made a significant impact on information retrieval and question answering. By enhancing the relevance and accuracy of search results, they have improved information retrieval systems, enabling more efficient access to relevant information. Additionally, these models have revolutionized question answering systems, providing comprehensive and contextually appropriate responses to user queries. They have excelled in tasks such as passage ranking, document summarization, conversational question answering, and multimodal question answering, enhancing the overall user experience and facilitating intelligent information access.

While large language models have demonstrated tremendous potential and achieved remarkable results, ethical considerations and responsible usage are of utmost importance. Addressing concerns such as bias, fairness, and privacy is crucial to ensure that these models are deployed in an ethical and beneficial manner. Ongoing research and collaboration across academia, industry, and regulatory bodies are essential to further explore the capabilities, limitations, and ethical implications of large language models.

In summary, large language models represent a significant breakthrough in natural language processing and artificial intelligence. Their current use cases span various domains, including natural language understanding, content generation, information retrieval, and question answering. As advancements continue to be made, large language models hold the potential to further transform industries, enhance user experiences, and drive innovation in the field of natural language processing and AI.

REFERENCES

- Aharoni, R., et al. (2019). Massively Multilingual Sentence Embeddings for Zero-Shot Cross-Lingual Transfer and Beyond. In Proceedings of the 2019 Conference on Empirical Methods in Natural Language Processing and the 9th International Joint Conference on Natural Language Processing (pp. 4303-4314).
- Bender, E. M., et al. (2021). On the Dangers of Stochastic Parrots: Can Language Models Be Too Big? arXiv preprint arXiv:2104.04439.
- Brown, T. B., et al. (2020). Language Models are Few-Shot Learners. In Advances in Neural Information Processing Systems (pp. 18741-18755).
- Chen, Z., et al. (2021). Microsoft Research NLP (MSR-NLP) Systems at WOCHAT 2021: Large Language Models for Conversational Question Answering. In Proceedings of the 2021 Workshop on Open-domain Question Answering (pp. 138-143).
- Chiang, C. W., et al. (2021). Interactive Writing Assistant with Generative Language Models. arXiv preprint arXiv:2102.01404.
- Devlin, J., et al. (2019). BERT: Pre-training of Deep Bidirectional Transformers for Language Understanding. In Proceedings of the 2019 Conference of the North American Chapter of the Association for Computational Linguistics (pp. 4171-4186).
- Fan, A., et al. (2018). Hierarchical Neural Story Generation. In Proceedings of the 56th Annual Meeting of the Association for Computational Linguistics (Volume 1: Long Papers) (pp. 889-898).
- Gao, T., et al. (2021). Personalized Content Generation with Long-term Memory. In Proceedings of the 2021 Conference on Empirical Methods in Natural Language Processing (pp. 5565-5575).
- Gu, J., et al. (2020). Improved Training of Transformer-Based Machine Translation Models with Distribution Correction. arXiv preprint arXiv:2004.04849.
- Khattab, O., & Zaharia, M. (2020). ColBERT: Efficient and Effective Passage Search via Contextualized Late Interaction over BERT. arXiv preprint arXiv:2004.12832.
- Lewis, M., et al. (2020). CTRL: A Conditional Transformer Language Model for Controllable Generation. arXiv preprint arXiv:1909.05858.
- Liu, L., et al. (2021). Fine-Tuning Methods and Pretrained Language Models for Domain Adaptation in Neural Machine Translation. In Proceedings of the 2021 Conference of the Association for Machine Translation in the Americas (pp. 189-200).

- Radford, A., et al. (2019). Language Models are Unsupervised Multitask Learners. arXiv preprint arXiv:1910.10045.
- Rasooli, M. S., et al. (2020). Towards Emotion-Aware Conversational Agents. In Proceedings of the 58th Annual Meeting of the Association for Computational Linguistics: System Demonstrations (pp. 245-253).
- Roberts, A., et al. (2020). How Can We Know What Language Models Know? arXiv preprint arXiv:2103.00020.
- Sennrich, R., et al. (2016). Neural Machine Translation of Rare Words with Subword Units. In Proceedings of the 54th Annual Meeting of the Association for Computational Linguistics (Volume 1: Long Papers) (pp. 1715-1725).
- Vaswani, A., et al. (2017). Attention is All You Need. In Advances in Neural Information Processing Systems (pp. 5998-6008).
- Wolf, T., et al. (2020). Transformers: State-of-the-Art Natural Language Processing. In Proceedings of the 2020 Conference on Empirical Methods in Natural Language Processing: System Demonstrations (pp. 38-45).
- Yin, P., et al. (2021). Meta-Learning to Learn Fast for Code Search and Code Generation. In Proceedings of the 2021 Conference on Empirical Methods in Natural Language Processing (pp. 6942-6953).
- Zellers, R., et al. (2020). HellaSwag: Can a Machine Really Finish Your Sentence? arXiv preprint arXiv:1911.00359.

Chapter 9

Evaluation of Production Mechanism of Polyester Composites: Determination of Physical and Chemical Properties

Ercan AYDOĞMUŞ¹

Ahmet Beyzade DEMİRPOLAT²

¹ Assoc. Prof. Dr.,Firat University, Engineering Faculty, Department of Chemical Engineering.
E-mail: ercanaydogmus@firat.edu.tr, ORCID No: 0000-0002-1643-2487

² Assoc. Prof. Dr., Malatya Turgut Özal University, Arapgir Vocational School, Department of Electronics and Automation. E-mail: ahmetb.demirpolat@ozal.edu.tr ORCID No: 0000-0003-2533-3381

ABSTRACT

INTRODUCTION

Today, polyester materials have many application areas. Especially polyester composites can be developed according to the purpose of use. Cost-effective fillers are used to reinforce polyester resin matrix composites. Its mechanical performance, dynamic mechanical properties, impact resistance, and water absorbency are evaluated according to the properties of the filler (Gharbi et al., 2014:62). For example, it has been determined that the tensile strength, tensile modulus, flexural strength, and flexural modulus of glass fiber reinforced polyester composites are improved (Islam, 2019:24).

Glass fiber reinforced polyester composites are preferred in marine vehicles. It provides both mechanical strength in ships and protection against water or moisture (Baley et al., 2006:13). Besides, thermally stable and non-flammable composites are developed by reinforcing melamine and phosphate compounds into polyester resin. Thermophysical properties of polyester composites with flame retardant properties are also improved (Kandola et al., 2002:33).

In the research in the literature, natural fiber reinforcement is made from polyester composite materials. Natural fibers have recently become more attractive to researchers, engineers, and scientists as an alternative reinforcement for fiber-reinforced polymer composites. Due to its low cost, low density, stiffness, very good mechanical properties, high specific strength, non-corrosive, environmentally friendly, and biodegradable properties, it is used as a substitute for traditional fibers such as glass, aramid, and carbon. The tensile properties of natural fiber reinforced polymers are mainly affected by the interfacial adhesion between the matrix and the fibers. For example, polyester composites reinforced with natural fibers (such as sisal, hemp, etc.) are produced and improvements are observed in their mechanical properties. It has been determined that the mechanical properties of sisal and hemp reinforced polyester composites have increased. It has been observed that especially hemp and sisal combination composites show the best mechanical performance (Reddy et al., 2013:2).

In another research, ground wastes of carbon fiber reinforced polymer laminates are used as filler for polyester resin. Technological, mechanical, and frictional properties of the produced polyester composites have been evaluated. It has been understood that the mechanical strength of the composites improved compared to the pure polyester resin. Both a decrease in dynamic friction coefficient and a decrease in wear occurred in polyester composites. In terms of friction applications, polyester composites have been investigated and optimization studies are carried out (Smoleń et al., 2021:55).

In a study on polyester composites, fabric, and newspaper are reinforced into the resin matrix. Fabric and unbroken waste newspapers have been prepared to produce

fiber-containing hybrid composites. The tensile and flexural properties of the hybrid composite are found to be higher than the pure paper-based composite, but lower than the pure woven jute composite (Das, 2017:172).

In this study, studies on polyester composites have been investigated. Articles on the chemical reaction mechanism of polyester polymers have been searched. Evaluations are made about the production, physical and chemical processes of polyester composite materials.

Materials and Methods

In the literature, polymer composite materials have been developed using unsaturated polyester resin (UP), filler, methyl ethyl ketone peroxide (MEKP), and cobalt octoate (Co Oc). The type of filler used can be selected from inorganic or organic materials. The type and amount of catalysts affect the rate of the chemical reaction and the curing time of the polymer (Aydoğmuş et al., 2022). The amount of filler to be used in the production of polyester composite material and its homogenization with the mixture are very important (Aydoğmuş et al., 2022:139). UP, MEKP, and Co Oc give an exothermic chemical reaction. It is recommended not to mix the mixture for more than 2 minutes during the final stage of production (Yanen et al., 2021:10). In studies, low-density fillers should be used at a maximum of 10 wt.% and high-density fillers at a maximum of 25 wt.% (Yanen et al., 2022:36). In Figure 1, polyester composite production is shown schematically as an example. Approximately 95 wt.% UP, 1.5 wt.% MEKP, 0.5 wt.% Co Oc and 3 wt.% filler material are used in the production.

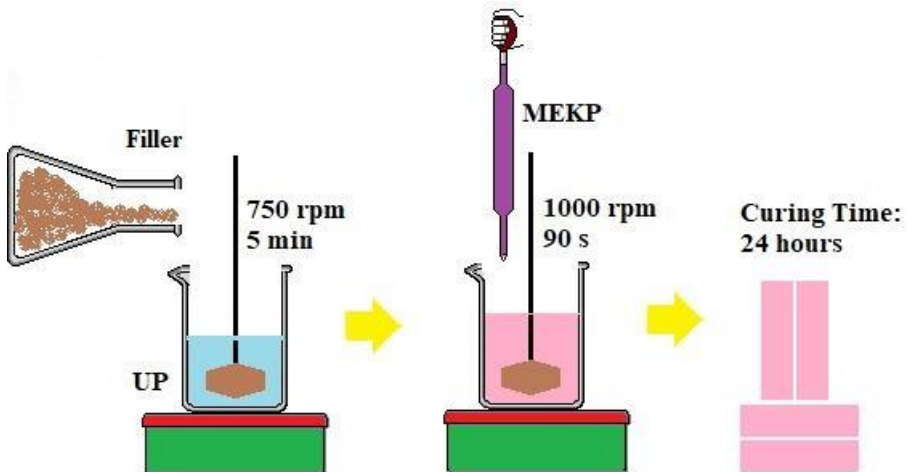


Figure 1: Chemical reaction mechanism of polyester polymer

Chemical Reaction of Polyester Polymers

The chemical production mechanism of polyester polymers is shown in Figure 2 as an example. It is seen that the reactive groups form chemical bonds with the styrene molecule (Miskolczi, 2013).

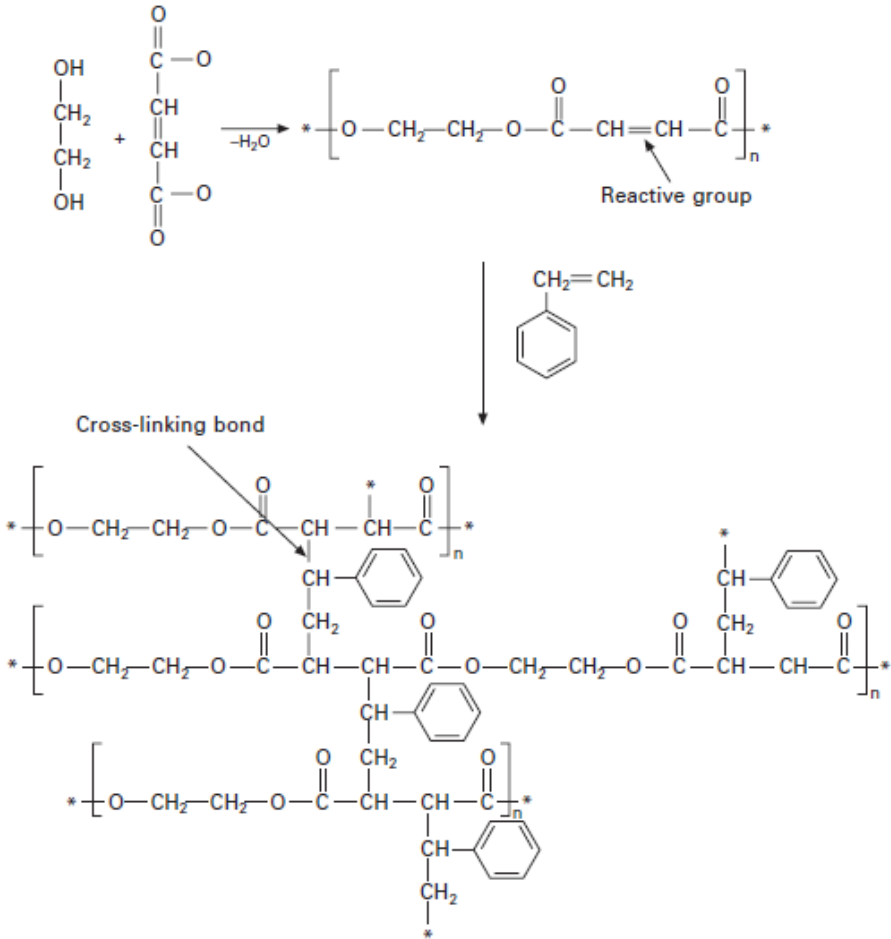


Figure 2: Chemical reaction mechanism of polyester polymer

In Figure 3, it is seen that maleic anhydride, phthalic anhydride, and modified palm oil react chemically under appropriate conditions. Then, the chemical reaction is completed with the help of styrene molecule, methyl ethyl ketone peroxide, and cobalt octoate compounds. The structure of the cured polyester polymer has been expressed in the figure (Aydoğmuş et al., 2021:44).

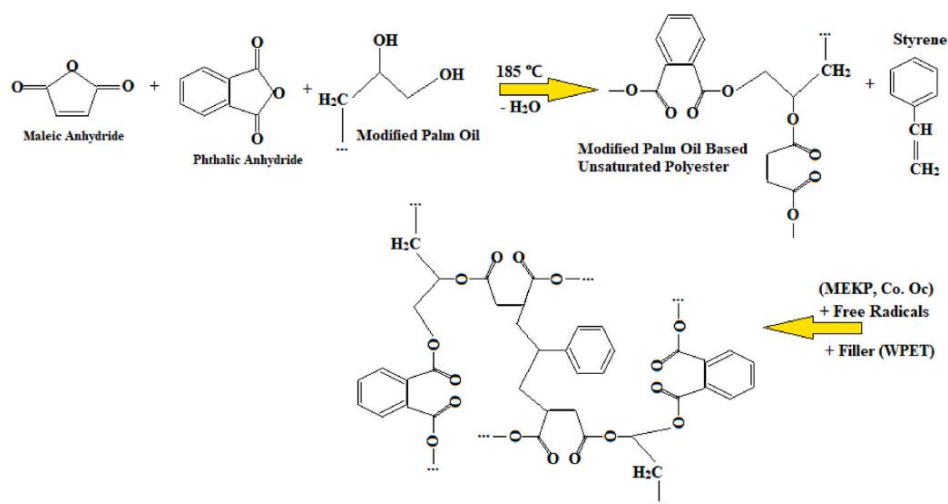


Figure 3: Chemical reaction mechanism of polyester polymer

As seen in Figure 4, 1,2-propanediol, maleic anhydride, phthalic anhydride, and unsaturated polyester resin give chemical reactions. Inappropriate working conditions, styrene molecule, methyl ethyl ketone peroxide, and cobalt octoate are added to the mixture. After a certain period after the chemical reaction occurs, the cured polyester polymer is formed (Orhan et al., 2021:42).

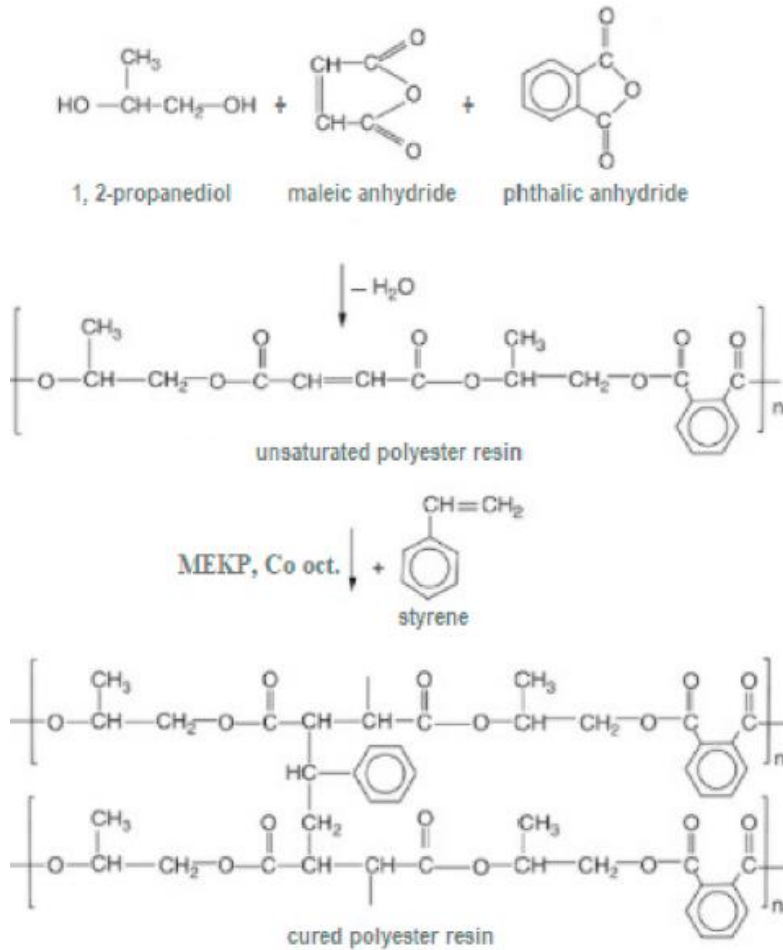


Figure 4: Chemical reaction mechanism of polyester polymer

Similarly, in Figure 5, the chemical reaction of maleic anhydride, phthalic anhydride, and modified castor (MCO) oil is shown. Each ingredient is added to the mixture at the appropriate temperature, pressure, and time. Besides, some properties of the polyester composite have been improved by adding organic and inorganic fillers to the system (Aydoğmuş et al., 2022:139).

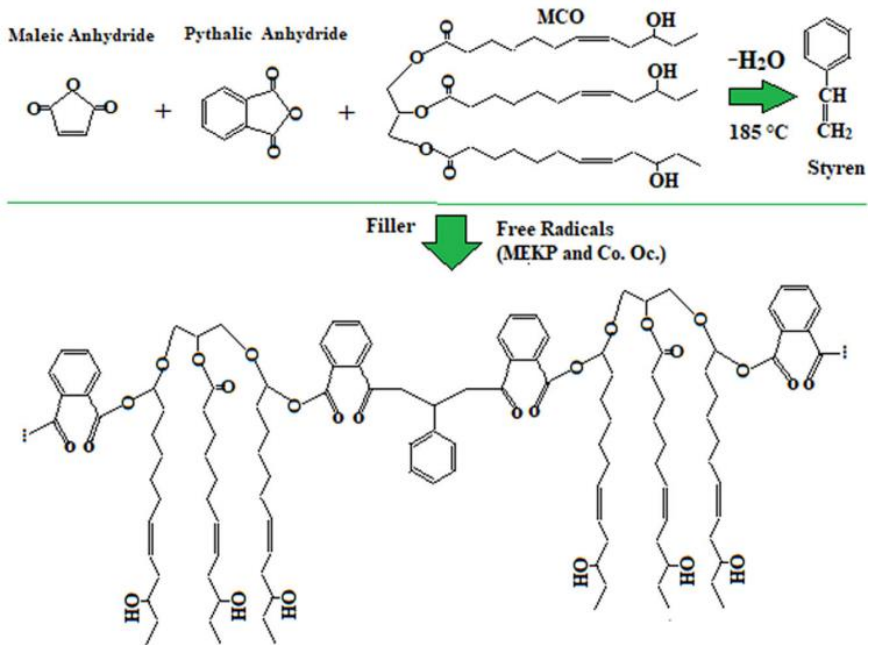


Figure 5: Chemical reaction mechanism of polyester polymer

In Table 1, some properties of polyester composites are expressed approximately. The values in the table are written approximately by finding the studies in the literature (Das, 2017:172, Aydoğmuş and Arslanoğlu, 2021:39, Aydoğmuş et al., 2021:44, Buran et al., 2023:2, Karataş and Aydoğmuş, 2023:7).

Table 1: Some thermophysical properties of polyester composites

Properties Polyester	Approximate range of properties
Density	1.15-1.40 g/cm ³
Shore D hardness	70 - 85
Thermal Conductivity	0.05 – 0.15 W/m·K
Tensile strength	20 -120 MPa
Elastic modulus	0.5 - 3.5 GPa
Compressive strength	30 – 100 MPa
Melting point	250 – 270 °C

CONCLUSION

The components and conditions required to produce polyester composites at the desired standards according to the intended use have been concluded below.

- ✚ Low-density fillers should be used for the production of lightweight polyester composites.
- ✚ High-density fillers should be preferred to increase the density of polyester composites.
- ✚ Organic biomass wastes can be preferred to reduce the hardness of the composites and increase their workability.
- ✚ Nanoparticles and fibrous biomass fillers can be used to improve the mechanical properties of polyester composites.
- ✚ If fillers with high thermal conductivity coefficients are reinforced into polyester, the thermal conductivity of the composite can increase.
- ✚ To improve the insulating properties of composites, either a hollow polymer matrix or fillers with a low thermal conductivity coefficient should be used.
- ✚ Inorganic fillers can be used to improve the thermal stability of polyester composites.
- ✚ To provide the composite with flame-retardant properties, fillers that cut off the contact of the polymer surface with air can be recommended.
- ✚ The catalyst (MEKP, Co Oc, etc.) ratios used to raise the chemical reaction rate of polyester composites can be increased in certain amounts.
- ✚ The use of high levels of filler in polyester composite production negatively affects the surface morphology of the material.
- ✚ Sufficient time curing (24 hours) is required to produce polyester composite under optimum conditions.

REFERENCES

- Aydoğmuş, E. (2022). Biohybrid nanocomposite production and characterization by RSM investigation of thermal decomposition kinetics with ANN. *Biomass Conversion and Biorefinery*, 12(10), 4799-4816.
- Aydoğmuş, E., and Arslanoğlu, H. (2021). Kinetics of thermal decomposition of the polyester nanocomposites. *Petroleum Science and Technology*, 39(13-14), 484-500.
- Aydoğmuş, E., Arslanoğlu, H., and Dağ, M. (2021). Production of waste polyethylene terephthalate reinforced biocomposite with RSM design and evaluation of thermophysical properties by ANN. *Journal of Building Engineering*, 44, 103337.
- Aydoğmuş, E., Aydın, M., and Arslanoğlu, H. (2022). Production and characterization of microsphere reinforced polyester composite: Modeling of thermal decomposition with ANN and optimization studies by RSM. *Petroleum Science and Technology*, 1-17.
- Aydoğmuş, E., Dağ, M., Yalçın, Z. G., and Arslanoğlu, H. (2022). Synthesis and characterization of waste polyethylene reinforced modified castor oil-based polyester biocomposite. *Journal of Applied Polymer Science*, 139(27), e52526.
- Baley, C., Perrot, Y., Davies, P., Bourmaud, A., and Grohens, Y. (2006). Mechanical Properties of Composites Based on Low Styrene Emission Polyester Resins for Marine Applications. *Applied Composite Materials*, 13, 1-22.
- Buran, A., Durğun, M. E., Aydoğmuş, E., and Arslanoğlu, H. (2023). Determination of thermophysical properties of *Ficus elastica* leaves reinforced epoxy composite. *Firat University Journal of Experimental and Computational Engineering*, 2(1), 12-22.
- Das, S. (2017). Mechanical properties of waste paper/jute fabric reinforced polyester resin matrix hybrid composites. *Carbohydrate Polymers*, 172, 60-67.
- Demirel, M. H., and Aydoğmuş, E. (2022). Waste Polyurethane Reinforced Polyester Composite, Production, and Characterization. *Journal of the Turkish Chemical Society Section A: Chemistry*, 9(2), 443-452.
- Demirel, M.H., and Aydoğmuş, E. (2022). Production and characterization of waste mask reinforced polyester composite. *Journal of Inonu University Health Services Vocational School*, 10(1), 41-49.
- Gharbi, A., Hassen, R.B., and Boufi, S. (2014). Composite materials from unsaturated polyester resin and olive nuts residue: The effect of silane treatment. *Industrial Crops and Products*, 62, 491-498.

- Islam, MN, Ar-Rashid, H., Islam, F., Karmaker, N., Koly, FA, Mahmud, J. et al. (2019). Fabrication and Characterization of E-Glass Fiber Reinforced Unsaturated Polyester Resin Based Composite Materials. *Nano Hybrids and Composites*, 24, 1-7.
- Kandola, B.K., Horrocks, A.R., Myler, P., and Blair, D. (2002). The effect of intumescent on the burning behaviour of polyester-resin-containing composites. *Composites Part A: Applied Science and Manufacturing*, 33(6), 805-817.
- Karataş, M., and Aydoğmuş, E. (2023). Obtaining Pectin Reinforced Polyester Composite and Investigation of Thermophysical Properties. *European Journal of Science and Technology*, 48, 64-66.
- Karataş, M., and Aydoğmuş, E. (2023). Physical and Chemical Properties of Organic Waste Reinforced Polyester Composites. *International Journal of Advanced Natural Sciences and Engineering Researches*, 7(4), 16-19.
- Karataş, M., and Aydoğmuş, E. (2023). Use of Inorganic Wastes as Fillers in Production of Polyester Composites and Evaluation of Properties of Obtained Composite. *International Journal of Advanced Natural Sciences and Engineering Researches*, 7(4), 20-24.
- Miskolczi, N. (2013). Polyester resins as a matrix material in advanced fibre-reinforced polymer (FRP) composites. In *Advanced fibre-reinforced polymer (FRP) composites for structural applications*, Woodhead Publishing, 44-68.
- Orhan, R., & Aydoğmuş, E. (2022). Investigation of some thermophysical properties of *Asphodelus aestivus* reinforced polyester composite. *Firat University Journal of Experimental and Computational Engineering*, 1(3), 103-109.
- Orhan, R., and Aydoğmuş, E. (2022). Production and characterization of waste corncob reinforced polyester composite. *European Journal of Science and Technology*, (42), 176-179.
- Orhan, R., Aydoğmuş, E., Topuz, S., and Arslanoğlu, H. (2021). Investigation of thermo-mechanical characteristics of borax reinforced polyester composites. *Journal of Building Engineering*, 42, 103051.
- Pekdemir, M.E., Aydoğmuş, E., and Arslanoğlu, H. (2023). Thermal decomposition kinetics of synthesized poly (N-isopropylacrylamide) and Fe₃O₄ coated nanocomposite: Evaluation of calculated activation energy by RSM. *Petroleum Science and Technology*, 1-18.
- Reddy, S.S.K., and Hussain, S.A. (2013). Development and testing of natural fiber reinforced composites with polyester resin. *International Journal of Engineering Sciences & Research Technology*, 2(10), 2701-2706.

- Şahal, H., and Aydoğmuş, E. (2022). Investigation of thermophysical properties of polyester composites produced with synthesized MSG and nano-alumina. *European Journal of Science and Technology*, (34), 95-99.
- Şahal, H., and Aydoğmuş, E. (2023). Use of Sunflower Seed Shells as Filler in Polyester Resin and Characterization of Obtained Composite. *2nd International Conference on Engineering, Natural and Social Sciences*, 1, 233-236.
- Şahal, H., Aydoğmuş, E., & Arslanoğlu, H. (2022). Investigation of thermophysical properties of synthesized SA and nano-alumina reinforced polyester composites. *Petroleum Science and Technology*, 1-17.
- Smoleń, J., Godzierz, M., Olesik, P., Pawlik, T., and Koziół, M. (2021). Utilization of CFRP waste as a filler in polyester resin-based composites. *Journal of Composite Materials*, 55(19), 2693-2701.
- Yanen, C., and Aydoğmuş, E. (2021). Characterization of thermo-physical properties of nanoparticle reinforced the polyester nanocomposite. *Dicle University Journal of the Institute of Natural and Applied Science*, 10(2), 121-132.
- Yanen, C., Dağ, M., and Aydoğmuş, E. (2022). Investigation of thermophysical properties of colemanite, ulexite, and tincal reinforced polyester composites. *European Journal of Science and Technology*, (36), 155-159.
- Yilmaz, E., Aydoğmuş, E., and Demir, A. Life Cycle Assessment and Characterization of Tincal Ore Reinforced Polyester and Vinylester Composites. *Journal of the Turkish Chemical Society Section B: Chemical Engineering*, 5(2), 183-194.

Chapter 10

Wind Speed Estimation by using Geographic Information System (GIS) and Machine Learning (ANN): A case study of Kastamonu Region in Turkey

Mehmet GÜRDAL¹

¹ Dr. Öğr. Üyesi; Kastamonu Üniversitesi Mühendislik ve Mimarlık Fakültesi Makine Mühendisliği Bölümü.
mgurdal@kastamonu.edu.tr ORCID No: 0000-0003-2209-3394

ABSTRACT

INTRODUCTION

Wind speed estimation is a critical task in various fields, including renewable energy, aviation, and weather forecasting. Accurate estimation of wind speed is essential for the optimal operation of wind turbines, the safety of aircraft, and the prediction of severe weather events. The estimation of wind speed is crucial for evaluating the wind energy potential of a specific location. Researchers have developed wind speed estimation models using artificial neural networks (ANNs) for different regions of Turkey. For instance, Çam et al. (Çam et al., 2005) employed ANNs to estimate wind speed and power values for seven regions using 50 years of wind data. The inputs included latitude, longitude, altitude, and measurement height, while the outputs were wind velocities and powers. The model predicted output values with mean error levels ranging between 3% and 6%. Öztopal (Öztopal, 2006) applied the ANN method to estimate the wind velocity of a target station using daily wind speed data from the nearest measurement stations in the northwestern region of Turkey. The results showed that the ANN method could avoid under and over estimation issues associated with objective analysis. Bilgili and Sahin (Bilgili and Sahin, 2010) compared the ANN approach with regression methods for wind speed prediction using meteorological variables of measuring stations in the eastern Mediterranean region of Turkey. Their study indicated that the ANN method outperformed both linear and nonlinear regression models. Bilgili and Sahin (Bilgili and Sahin, 2013) demonstrated the success of the ANN method in predicting wind speeds of a target station by using data from surrounding reference stations in the Aegean and Marmara regions. Similarly, Ulkat and Günay (Ulkat and Günay, 2018) used a neural network trained with geographical and atmospheric data from neighboring stations to accurately model wind speeds in the Aegean region, with geographical data having a greater influence than atmospheric variables. Işık et al. (IŞIK et al., 2019) achieved a 99% accuracy in predicting wind blowing durations for stations in the northeast region using the ANN method. Kılıç (Kılıç, 2019) estimated wind speeds for the southwestern part of Turkey with high accuracy ($R^2=0.99974$) through the ANN method. While previous studies have shown the accuracy of ANN prediction models for wind speeds, no comprehensive study has been conducted utilizing all available measurement stations to estimate wind speeds in Sivas Province.

Wind energy is a highly valued renewable energy source due to its abundance, reliability, and environmental benefits. However, accurate forecasting of both the amount and prices of electricity is crucial for suppliers, especially in intraday markets, to avoid generating more or less electricity than

required. Thus, Agbulut (Ağbulut, 2022) in his study, the wind speed data of Çesme district in Izmir, Turkey, was tested using four different models for 30-minute, 1-hour, and 3-hour time horizons. The results were compared using four statistical benchmarks, including MAD, MSE, MAPE, and RMSE. The proposed VSES model exhibited very satisfactory MAD, MSE, MAPE, and RMSE values of 0.318 m/s, 0.183 m/s, 14.60%, and 0.427 m/s, respectively, for the 30-minute horizon and 0.382 m/s, 0.258 m/s, 16.29%, and 0.506 m/s, respectively, for the 1-hour horizon. Therefore, the study concludes that the VSES model can be successfully applied for determining wind energy potential and used effectively for very short-term wind speed forecasting, particularly in intraday markets. However, Purlu et al. (Purlu et al., 2022) aimed to conduct short-term load forecasting for the Gebze region in Turkey using different Machine Learning-based prediction algorithms, including Artificial Neural Networks, Decision Tree, Support Vector Regression, and K-Nearest Neighbor. The input variables for the forecast models were load demand and weather variables such as temperature, humidity, pressure, and wind speed. The performance of the proposed algorithms and models was evaluated using error metrics such as Mean Absolute Error, Mean Squared Error, Mean Absolute Percentage Error, and R-squared. The study found that all proposed algorithms produced reliable and acceptable predictions, with the Support Vector Regression algorithm demonstrating the best performance with an error of 1.1%.

Over the years, researchers have developed various methods for wind speed estimation, ranging from physical models based on numerical weather prediction (NWP) to data-driven approaches using machine learning (ML) algorithms (Giebel and Kariniotakis, 2017). Numerical weather prediction models use mathematical equations to simulate atmospheric behavior and predict wind speeds at various locations. However, these models require extensive data inputs and are computationally expensive. Recent studies have explored the use of machine learning algorithms to estimate wind speeds, which have shown promising results. Machine learning algorithms use historical wind data to train models that can predict future wind speeds based on various factors such as geographic location, time of day, and weather conditions. Remote sensing technologies, such as lidar and radar, have also been used to estimate wind speeds. These technologies use the principles of laser and radio wave reflection to measure wind speeds at different altitudes and distances. Empirical models that relate wind speed to other meteorological variables, such as temperature, pressure, and humidity, have also been developed. These models can be simpler to implement than NWP or ML models and may be useful in

situations where data is limited. Despite these advances, there is still room for improvement in wind speed estimation. Some challenges in wind speed estimation include data quality issues, the lack of standardized measurement protocols, and the high variability of wind speeds across different locations and time scales. Addressing these challenges will require further research and innovation in wind speed estimation techniques.

In this study, we propose a novel approach to wind speed estimation that combines machine learning algorithms with feed forward. Our approach leverages historical wind data to train a model that can predict wind speeds with high accuracy. It has been evaluated the performance of our model using real-world data and compare it to other wind speed estimation methods. Our results demonstrate the potential of our approach for improving wind speed estimation in various applications. On the other hand, average and maximum wind speeds were visualised with Geographic Information Systems (GIS) through speed distribution contours.

Work zone

Kastamonu is located between 41 degrees 21' north latitude and 33 degrees 46' east longitude in the Western Black Sea region. Kastamonu consists of 20 districts together with the centre. Its height above sea level is 775 meters. Its surface area is 13,108 km². This constitutes 1.7% of the country's territory. Kastamonu Province consists mostly of hilly terrain. Kastamonu's surface area is 74.6% mountainous and forested, 21.6% plateau and 3.8% plain. Considering the change between 2000 and 2021, the average temperature for the provincial centre is between -0.5 and 20.8 °C. Geometric position of the Kastamonu city is shown in Fig. 1.



Fig. 1 Station of the indication centers
(Benefited from Google Earth and NASA maps)

Table 1: Statistical data of the measured regions

Province	Latitude	Longitude	Altitude (m)	Indication height (m)
Cide	41° 52'	32° 56'	36	10
Devrekani	41° 35'	33° 50'	1050	10
İnebolu	41° 58'	33° 45'	64	10
Kastamonu CC	41° 22'	33° 46'	800	10
Tosya	41° 0'	34° 2'	870	10

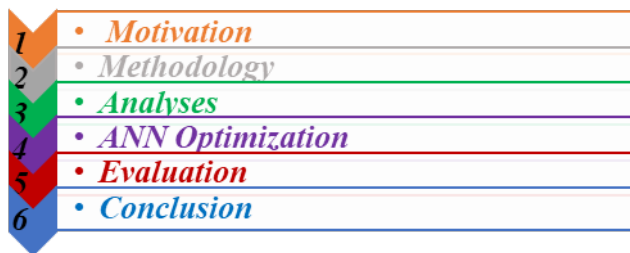
It has been shown highest and average wind speeds along Twenty-two years according to the measurement locations in Table 2. Besides, it has been considered basic motivation and steps in this study as seen as Fig. 2.

Table 2. Wind speed data of the measurement centres (2000-2021)

Table 2 :Wind speed data of the measurement centres (2000-2021)

Province	Highest WS (m/s)	Average WS (m/s)
Cide	31.82	2.48
Devrekani	22.17	1.82
İnebolu	31.11	3.95
Kastamonu CC	18.23	1.42
Tosya	37.13	2.11

It has been focused on wind speed estimation of Cide, Devrekani, İnebolu, Kastamonu City Center (CC), and Tosya location in this study as seen as Fig. 1. Geographic coordinates on world of this provinces have been given Table 1. These data were obtained from Kastamonu Meteorological Regional Directorate.

**Fig. 2:** Base steps of the study

Geographic information system (GIS)

The 1/200000 scale topographic maps gained from the General Directorate of Mapping (GDM) in Turkey have been coordinated using the ArcGIS 10.8 software and the Kastamonu and its four district boundary was drawn with the

D_WGS_1984 (European Datum 1984) projection system. The artificial neural network (ANN) approach has been implemented to the database of the average and highest WS data predicted for during 2000-2021 years (total twenty-two years) and the coordinates of 5 measurement locations. By applying the process in Fig. 3 respectively, average and maximum velocity distributions within the provincial borders could be obtained via ArcGIS system.

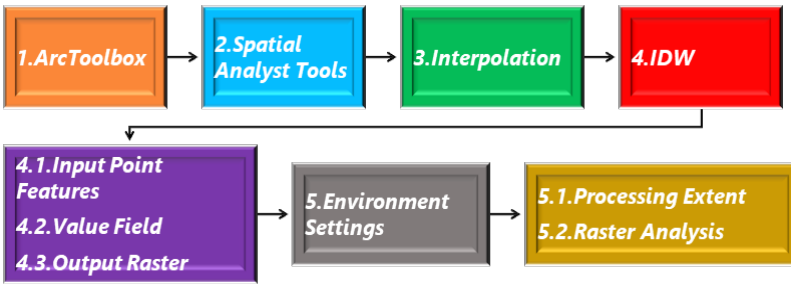


Fig. 3.: Flow chart of process on GIS

IDW (Inverse Distance Weighted) interpolation method is frequently used by researchers due to its advantages over other interpolation methods. These are Simplicity: IDW is an easy to implement and simple to understand method. Therefore, it can be easily applied in many situations for users. Speed: IDW interpolation can produce faster results than some other interpolation methods. This can be an advantage when large datasets need to be processed. Flexibility: IDW is not as rigid as other interpolation methods. For example, while methods such as kriging rely on a predetermined model assumption, IDW can work without any model assumption. Convergence properties: IDW uses an approach where points that are closer to the data points have a higher impact. This can help to improve convergence properties (Assouline et al., 2019; Bajjali, 2018). Basic equations (Díaz and Guedes Soares, 2020; Li and Heap, 2011) utilized in IDW is as seen as Eq.(1), Eq.(2), Eq.(3), and Eq. (4), respectively;

$$Z(x) = (\sum w_i Z_i) / (\sum w_i) \quad (1)$$

inhere: $Z(x)$ is the estimated value of the unknown location x , Z_i is the known value at a point i , w_i is the weight assigned to point i , calculated as the inverse distance between x and i raised to a power p :

$$w_i = 1 / (d_i^p) \quad (2)$$

where: d_i is the distance between x and i

The value of p determines the influence of distant points on the estimated value. A large value of p results in a sharp decrease in the weight of distant points, while a small value of p gives more weight to distant points. A modified version of the basic IDW equation, called the "adjusted IDW" or "shepard's method", is sometimes used to reduce the impact of extreme values:

$$Z(x) = (\sum w_i Z_i) / (\sum w_i) \quad (3)$$

where: w_i is calculated as:

$$w_i = 1 / (d_i^p + \epsilon) \quad (4)$$

where: ϵ is a small positive constant added to the denominator to avoid division by zero and reduce the effect of very small distances. These equations can be applied to any number of dimensions, and can be used to interpolate both continuous and categorical data.

Artificial neural network (ANN)

Estimating forced heat convection using Artificial Neural Networks (ANN) is one of the approaches used by researchers to model complex heat transfer systems (Berber and Gürdal, 2023; Gürdal, 2023). ANNs are machine learning algorithms that can be trained to recognize patterns in data, and can therefore be used to predict the behavior of heat transfer systems (Calisir et al., 2023; Colak et al., 2022). In order to utilise from ANN method in heat transfer prediction, a data set containing the heat transfer coefficient obtained as well as input parameters such as fluid velocity, fluid temperature and geometry of the system is required (Gao et al., 2022). This data can be used to train the ANN to recognize the relationships between the input variables and the target. Once the ANN is trained, it can be used to predict the heat transfer coefficient for new input conditions that it has not seen before. This is a valuable tool for designing and optimising heat transfer systems as it can save time and resources compared to traditional experimental methods (Rezaei Miandoab et al., 2022). However, ANN models only need to be as accurate as the data used to train them. Therefore, the input data should represent all operating conditions that the system may encounter. It has been presented ANN application procedure in Fig. 4. This application consists of base data set, their normalization, optimization, training, testing, and verification steps. Firstly, the dataset was normalized, and 70% of it was used for training the ANN model, while the remaining data was

used for verification and testing. MATLAB program was used to determine the best ANN architecture. The 'nftool' command was used to carry out the ANN modeling settings. The Neural Fitting module was used to obtain the MSE performance and regression analysis of the selected data, and to create and train the network. Besides, ANN topology of this present study including all layer for input, hidden, and output has been Fig. 5.

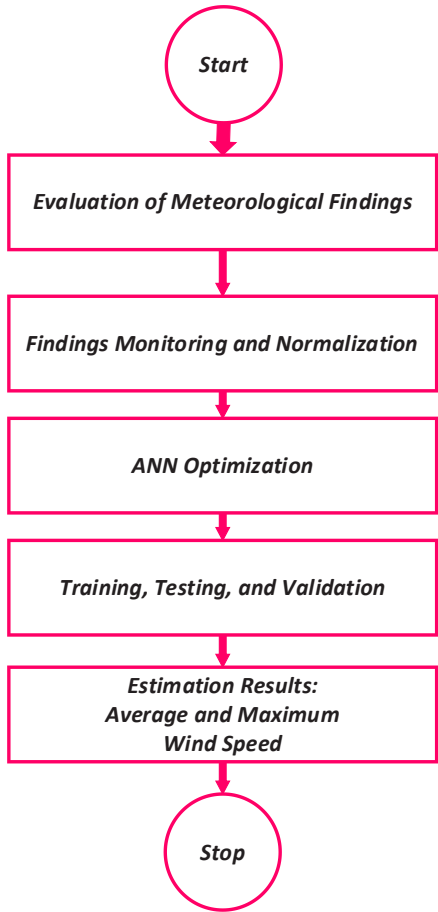


Fig. 4: Estimation steps with ANN of WS.

The ANN was constructed using a total of 240 data points obtained from measured findings for all province. To investigate the impact of input variables on prediction performance, other input variables were used in the ANN model. One of the challenges in developing ANN structures is deciding on the number of neurons in the hidden layer, as there is no certain number for the hidden layer (Çolak, 2021). It has been used the trial and error method to determine the best

performing hidden layer structure, and ultimately selected an ANN with 10 neurons in the hidden layer for further analysis. The authors surveyed literature to determine the best training algorithm and ultimately decided to use the Scaled Conjugate Gradient (SCG) algorithm, which has been shown to have superior performance in multilayer perceptron networks. The Learngdm and Tansig transfer functions were used in the hidden and output layers of the perceptron network. The efficiency of the ANN models was analyzed in three phases: the training phase, where the ANN model was trained; the validation phase, where the accuracy of the training was verified by computing MSE variables and examining error histograms; and the performance analysis phase, where the estimated values from the ANN model were compared with the target values to determine suitability. The last phase involved investigating the performance variables used to assess the performance analysis.

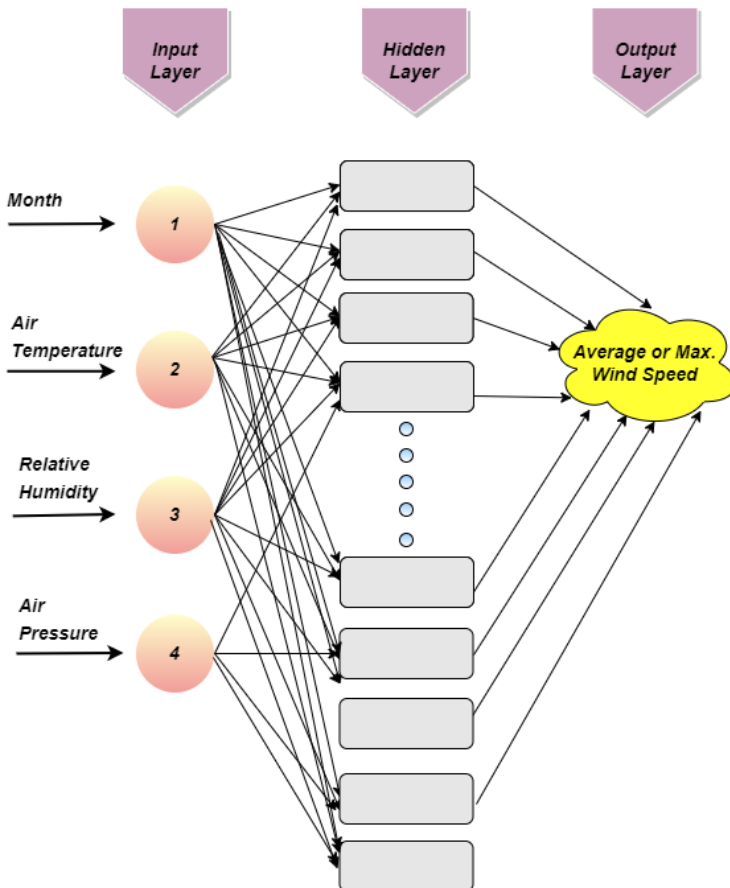


Fig. 5: Basic topology of the ANN study

To evaluate the prediction performance of the ANN structure, the authors examined the mean absolute error (MAE), correlation coefficient (R2) and average relative deviation (ARD%) values. Table 2 demonstrates the balances used to compute the performance variables (Çolak et al., 2020; Ocal et al., 2021). Additionally, the authors used mean squared error (MSE) to examine the best validation performance in their search for an optimal network construction, as shown in Fig. 6 (a). Lower worths of MSE were gained by employing SCG compare to Bayesian Regularization and Levenberg-Marquardt training algorithm for 4–10-1 model of ANN as it is seen in Fig. 6 (b).

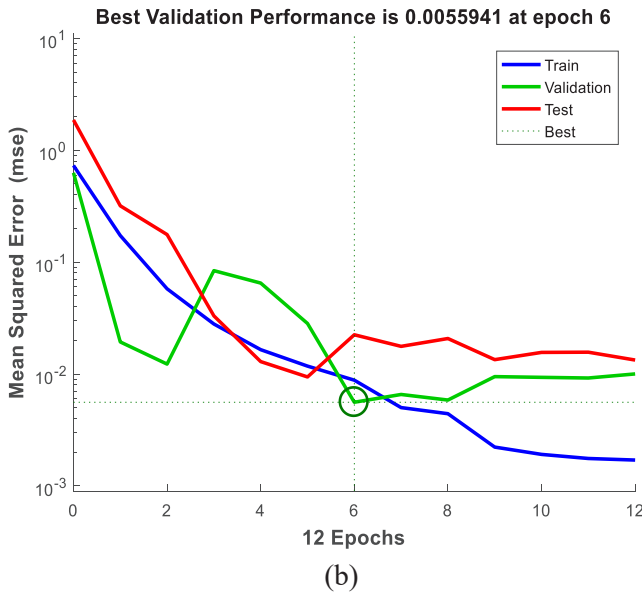
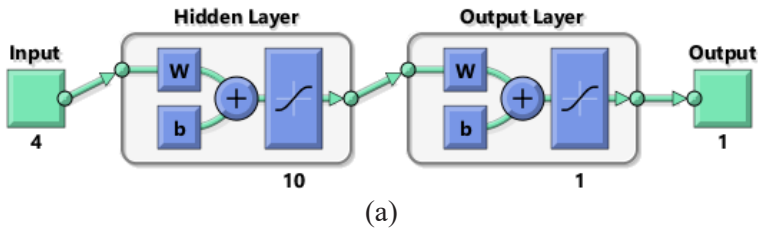


Fig. 6:(a), ANN structure of configuration, (b) Changing of MSE with epoch for the optimal network structure.

Inhere has been monitored the varying values of MSE as the training operation progresses for the best network with 10 neurons. The authors found that the optimal verification performance was achieved with an MSE value of 0.0055941 at epoch 6,

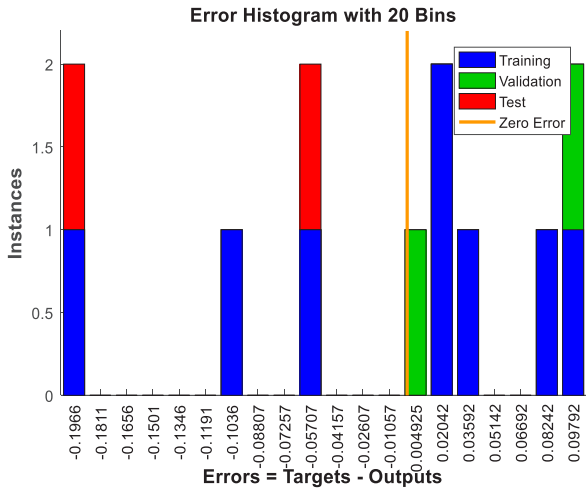
as presented in Fig. 6 (b). Deviations between training, validation, and test values as a results of training process has been shown with error histogram as seen as in Fig. 7 (a). The best results can be accepted as in case mininum of difference in between target and output findings. Fig. 7 (b) presents scatter plots for the training, validation, testing, and optimal model, where the horizontal axis gives the target values and the vertical axis represents the model outputs. An acceptable level of agreement between the two is achieved when the gradient of the line approaches 1 and the perpendicular intersection approaches 0. To assess the quality of the fit, three variables were examined: the R-value, the slope, and the y-intercept. Upon examining the scatter plots in Fig. 7 (b), it can be observed that the R-value is close to 1 for all graphs, indicating a good fit between the predicted and actual values. More information on the performance of the model can be found in Table 3.

Table 3: Base variables and equations benefited in determination of ANN model performance

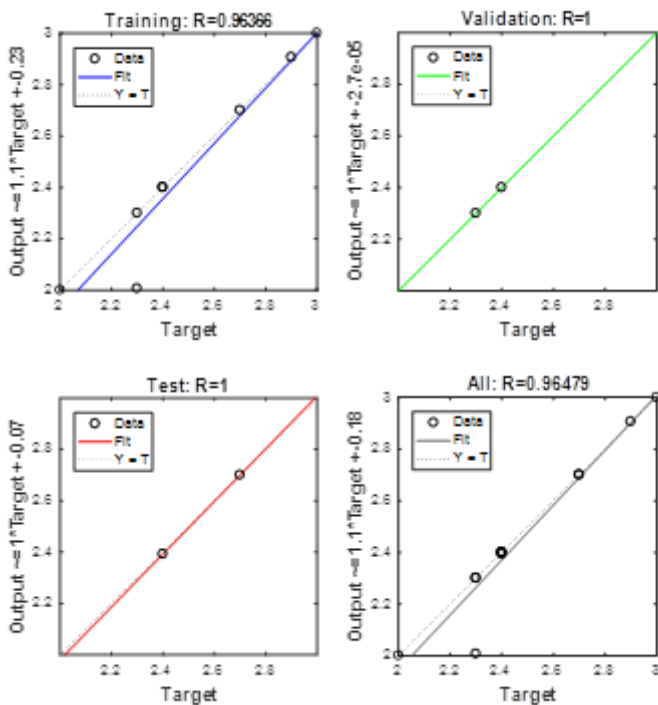
Parameter	Equation	Eq. Num	Reference
Mean absolute error (-)	$MAE = \frac{1}{n} \sum (WS_{meas} - WS_{pred})$	(1)	[1]
Mean square error (-)	$MSE = \frac{1}{n} \sum_{1-i}^n (WS_{meas} - WS_{pred})^2$	(2)	[2]
Average relative deviation (-)	$ARD(\%) = \frac{1}{n} \sum_{1-i}^n \left(\frac{WS_{meas} - WS_{pred}}{WS_{meas}} \right) \times 100$	(3)	[3]
Correlation coefficient (-)	$R^2 = 1 - \frac{\sum_{1-i}^n (WS_{meas} - WS_{pred})^2}{\sum_{1-i}^n (WS_{meas})^2}$	(4)	[4]

Table 4: Average statical variables of ANN performance along all month

Province	MAE	ARD (%)	MSE	R ²
Cide	-0.497	3.679	0.0721	0.9879
Devrekani	-0.125	0.077	0.0215	0.9942
İnebolu	-0.292	2.017	0.1030	0.9921
Kastamonu CC	0.1089	-5.520	0.0184	0.9905
Tosya	0.5487	-18.333	0.1676	0.9514



(a)



(b)

Fig. 7 : (a) Error histogram, (b) MSE variation with epoch

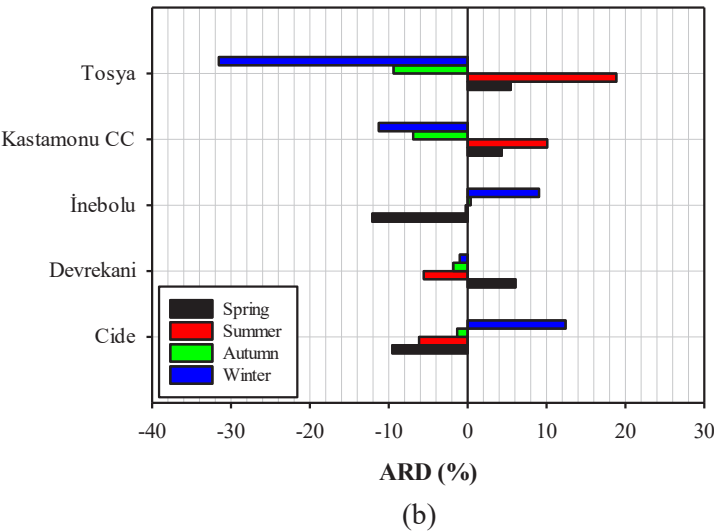
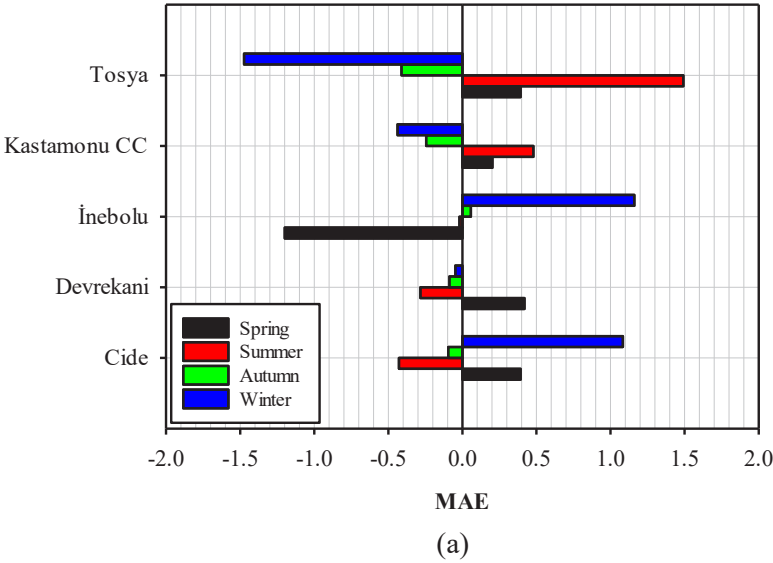
RESULTS AND DISCUSSION

Kastamonu province is one of the cities with high wind speed potential according to the Turkish Ministry of Energy and Natural Resources data ("T.R. Ministry of Energy and Natural Resources,"). Thus, it is possible to utilise wind energy and convert it into other types of energy. In this study, the average and maximum wind speed data of five settlement centres located within the borders of Kastamonu province for the long term (for the years 2000-2021) are estimated by using machine learning method and geographical information system in this study.

Estimation of wind speed with artificial neural network (ANN)

The most effective parameters on ANN performance were given in Table 3. The changes of MAE, ARD, MSE, and R2 parameters according to measurement stations and seasons are shown in Fig. 8(a), Fig. 8(b), Fig. 8(c), and Fig. 8(d) respectively. MAE, which is used to evaluate the performance of a machine learning model, expresses the average absolute difference between the predicted and measured values in a dataset as in Fig. 8(a). A lower MAE means that the model makes smaller errors in its predictions, indicating that the model is performing better. Therefore, when this figure is analysed, it is understood that the predictions are on average quite close to the actual values. In particular, the maximum deviation of 0.4 for all locations in autumn season and 1.48 in winter season was obtained for Tosya district. In a similar study, Ayodele et al. (Ayodele and Ogunjuyigbe, 2015) observed that MAE performance values ranged between 0.46 and 2.5. Thus, it can be stated that the MAE values obtained in this study (ranging between 0.1 and 1.5) are in agreement with the findings of Ayodele et al. ARD (%), another metric used to evaluate the accuracy of the forecasting model, shows the deviation value in percentage as shown in Fig. 8(b). A lowest ARD (%) indicates best performance of the model, as it means that the model has made smallest percentage errors in its predictions. Thus, while the best performances of the model were obtained in autumn in all measurement centres, the best prediction was made in Inebolu district with 0.24% in summer. On the other hand, in the study by Ayodele et al. (Ayodele and Ogunjuyigbe, 2015) the ARD % values were between 6.71% and 44.8%. In this study, ARD % values were in the range of 0.24 to 31.54% and were consistent with the literature. On the other hand, Lawan et al. (Lawan et al., 2020) tried to predict the wind speed in Sibul (a state in Malaysia) with ANN. In line with the results obtained from three different stations in Sibul region, they obtained the annual average ARD% performance between 5.51% and 6.29%. In this study, as shown in Fig. 8(b), the annual average ARD% performance at the measurement stations is between 3.60% and 16.31%. The consistency of the findings with the literature is proved again in this way. Bagci et al. (Bagci et al.,

2021) obtained MSE values between 0.0038 and 2.1432 under different training algorithms in their wind speed prediction study for Lake Van region in Turkey. In this study, as shown in Fig. 8(c), the annual average MSE values were calculated as 0.0721, 0.0215, 0.1030, 0.0184, 0.1676 for Cide, Devrekani, İnebolu, Kastamonu CC and Tosya, respectively. As it is understood from the results, MSE performances are within the minimum and maximum value range of Bagci et al [31] .



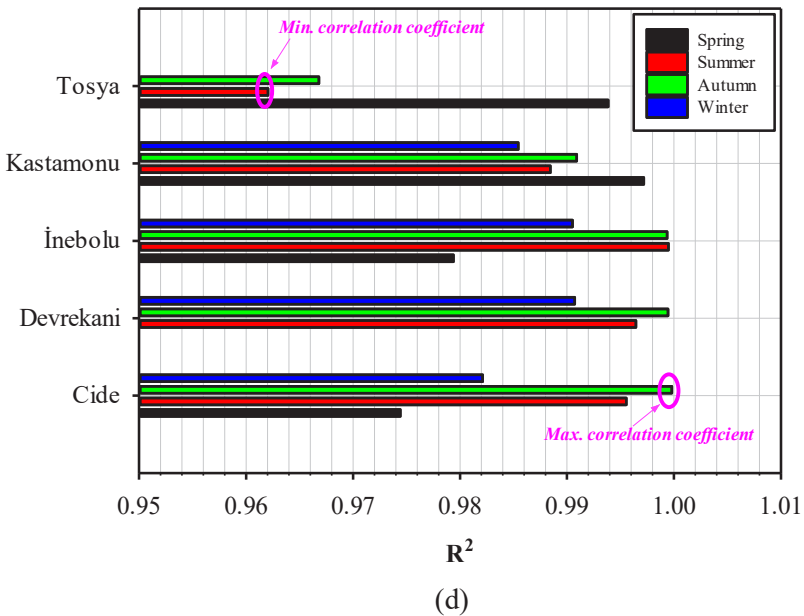
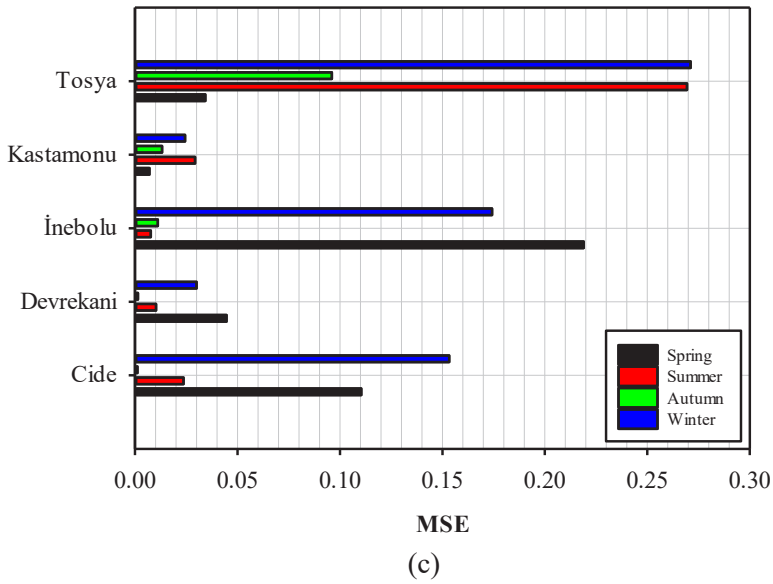
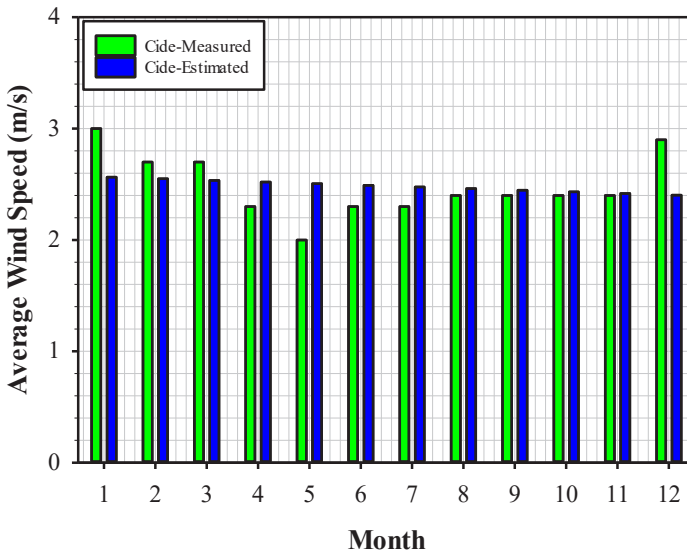
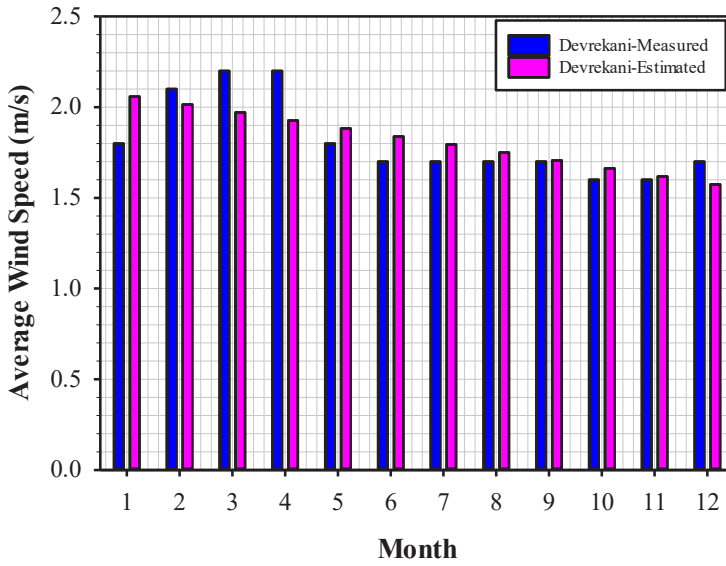


Fig. 8: (a) Variation of MAE, (b) ARD (%), (c) MSE, (d) R^2 according to the station and season

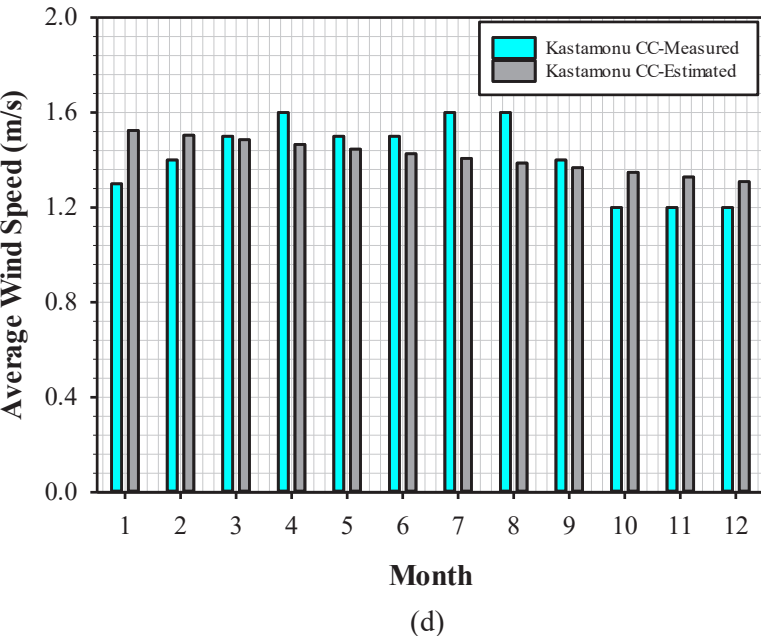
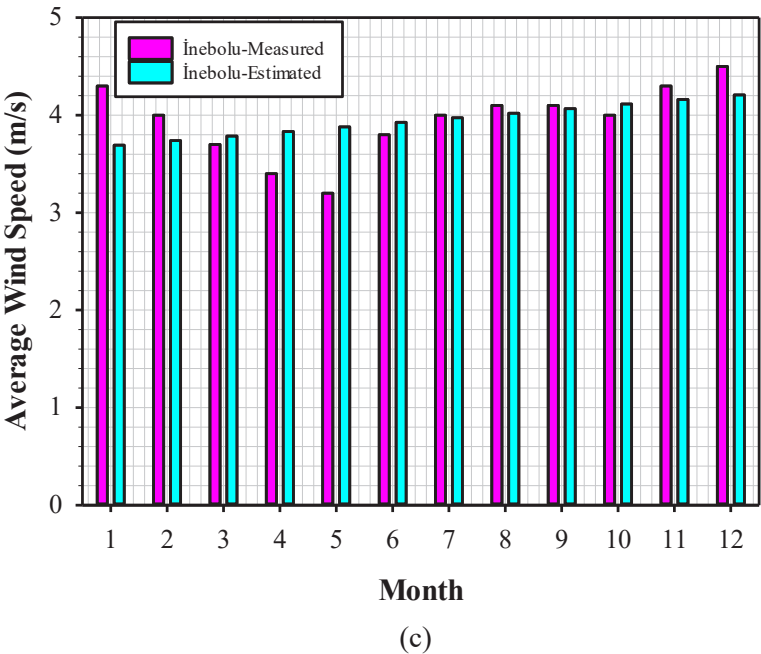
The R^2 value expresses the ratio of the variation of the predicted variables to the variation of the actual variables. In ANNs, the R^2 value is important to measure the performance of the model and to help improve the model. The variation of R^2 value for the ANN performance of this study according to the measurement centre and seasons is given in Fig. 8(d). When this figure is examined, the minimum R^2 value was obtained as 0.8831 for Tosya in summer and the maximum R^2 value was obtained as 0.9997 for Cide in autumn. These findings indicate that the predicted and measured wind speed magnitudes are quite close. In the study by Gürlek et al. (Gurlek et al., 2021) in the literature, R^2 values were calculated as 0.936, 0.860, 0.945 and 0.966 for Gemerek, Kangal, Sivas CC, and Suşehri districts, respectively. As it is understood, the convergence of the R^2 values and their agreement with the literature are within acceptable limits. It has been given measured and estimated average wind speed in measurement province according to month in Fig. 9. When it was detailed examined in figure, the measured average WS values along the years for Cide, Devrekani, İnebolu, Kastamonu CC, and Tosya district are observed by 2.48, 1.81, 3.95, 1.41, and 2.10 m/s, while estimated average WS has a more balanced change compared to the months. The average WS estimated with ANN according to spring, summer, autumn, winter season for Cide has been obtained as 2.52, 2.47, 2.43, 2.50 m/s as seen as in Fig. 9(a). The average WS of Devrekani district is examined in Fig. 9(b), it has been observed that the nearest predictions is in autumn season. Besides, maximum deviation is determined in march and april month. Among of the all measurement province, the highest average WS reached in İnebolu district according to all month as seen as Fig. 9(c). Although annual average WS is about 3.95 m/s inhere, the highest WS reach to 4.5 m/s in december month. The closest forecasts with ANN method was carried out in summer and autumn seasons. Measured average WS is 1.41 and 2.10 during years in Kastamonu CC and Tosya district, respectively as in Fig. 9(d) and Fig. 9(e). The best prediction was realised with average difference 0.203 in spring season for Kastamonu CC, while in same season with 0.393 in Tosya.

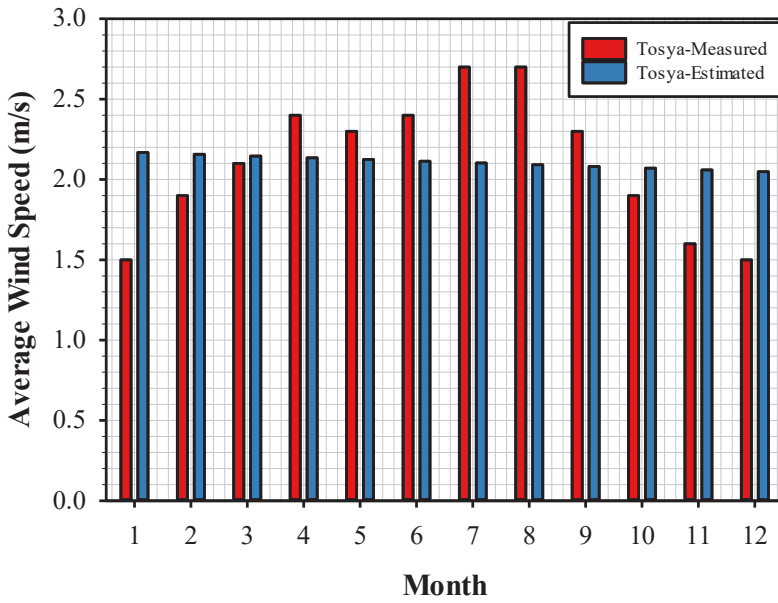


(a)



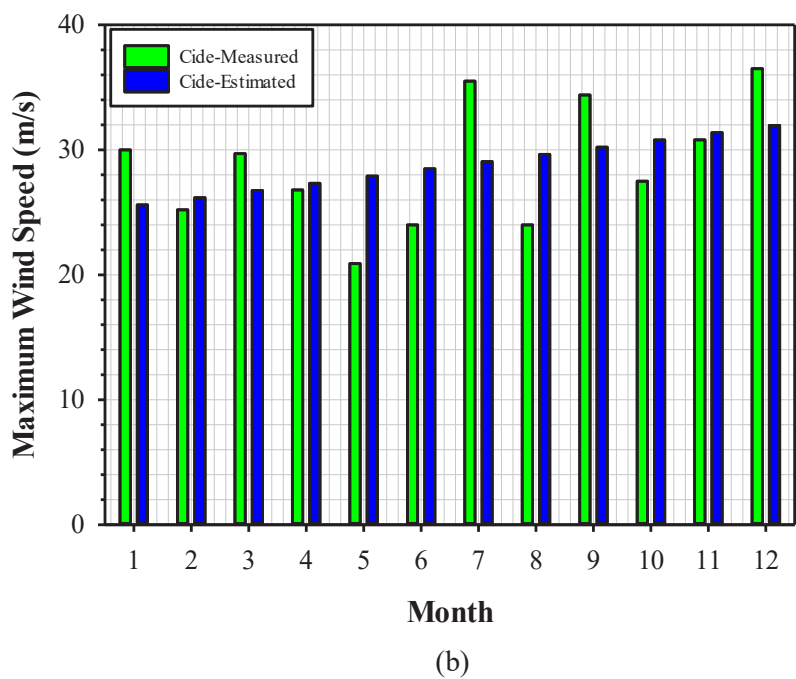
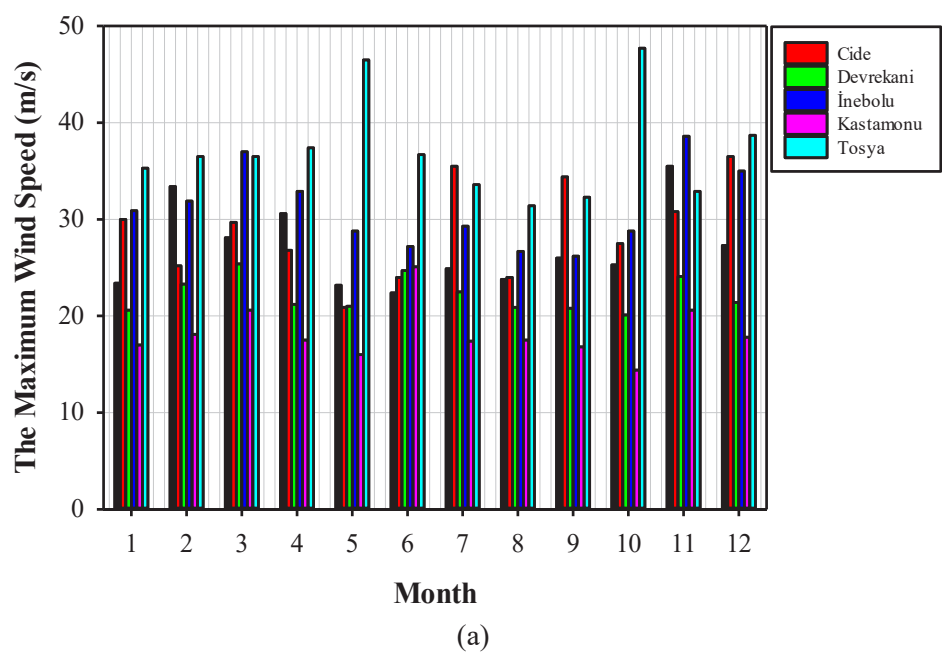
(b)

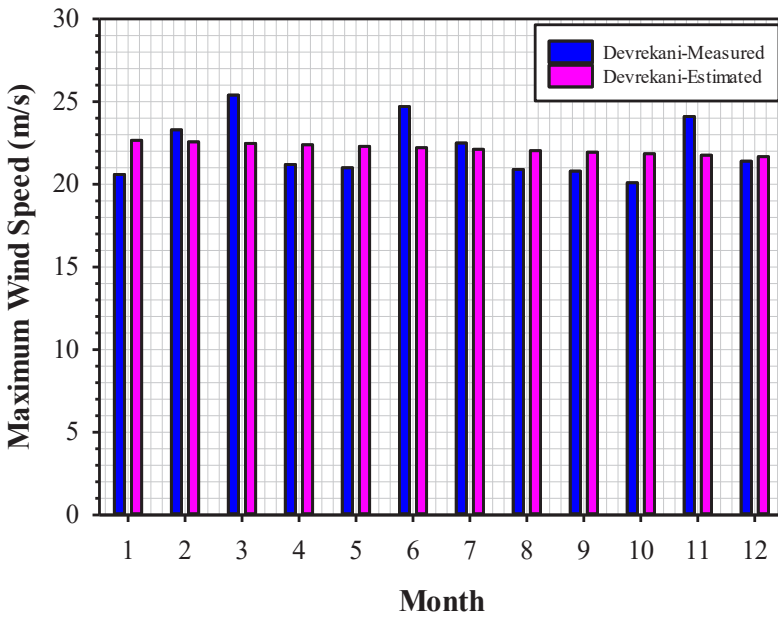




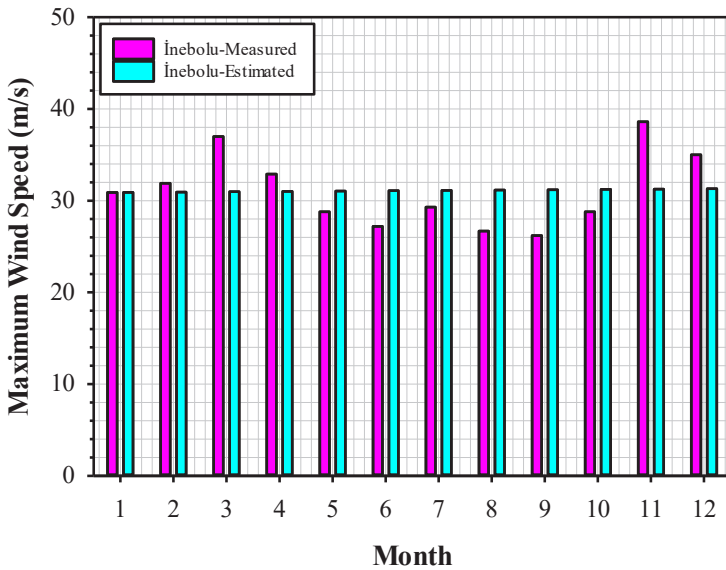
(e)

Fig. 9: Variation of the average wind speed according to (a) Cide, (b) Devrekani, (c) İnebolu, (d) Kastamonu CC, (e) Tosya province and month





(c)



(d)

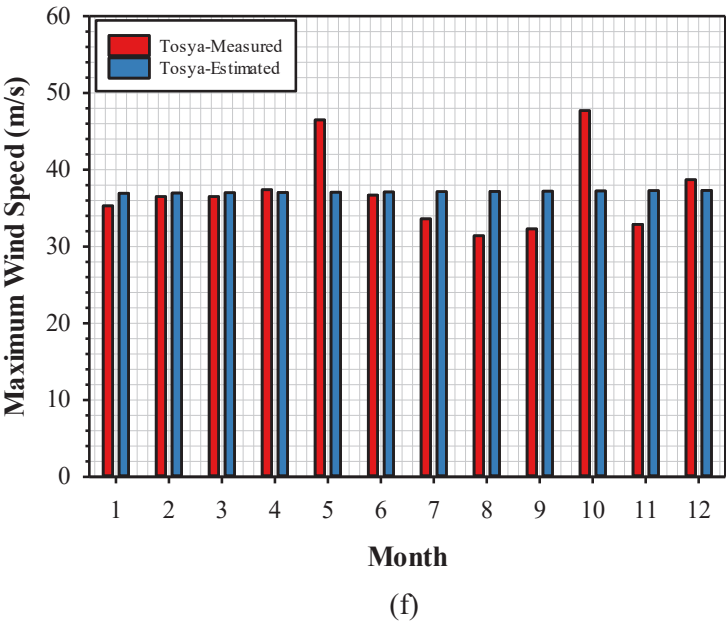
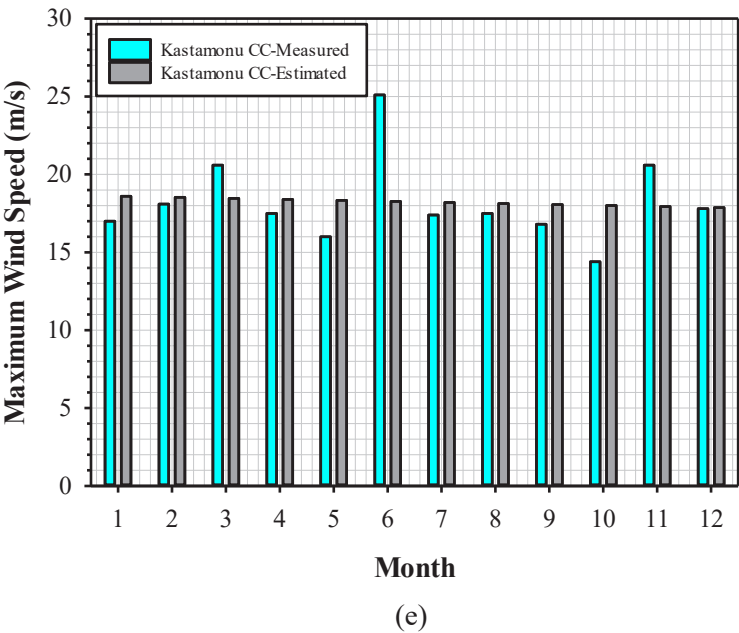
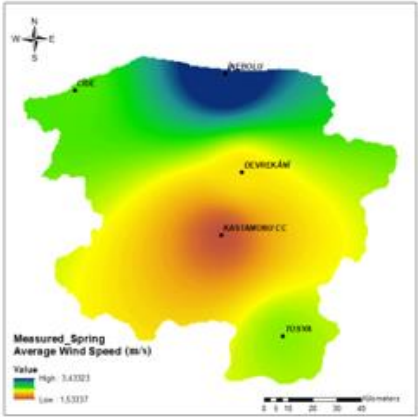


Fig. 10 Variation of the maximum wind speed according to (a) All province, (b) Cide, (c) Devrekani, (d) İnebolu, (e) Kastamonu CC, (f) Tosya province and month

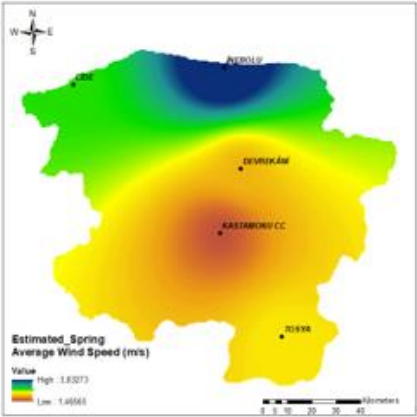
Similarly, reached maximum WS values according to month and measurement locations has been demonstrated in Fig. 10. The highest WS value in among the all province was seen as 47.7 m/s for Tosya in october month. However, the highest annual average wind speed was measured as 37.25 m/s in Tosya district. When the maximum WS values obtained are analysed as in Fig. 10(a), Fig. 10(b), Fig. 10(c), Fig. 10(d), Fig. 10(e), and Fig. 10(f), it is seen that 36.5 m/s in winter in Cide, 25.4 m/s in spring in Devrekani, 37 m/s in spring in İnebolu and 25.1 m/s in summer in Kastamonu CC. When the predicted WS values are compared, the average velocities throughout the year are similarly ranked as Tosya, İnebolu, Cide, Devrekani, Kastamonu CC.

Estimation of wind speed with geographic information system (GIS)

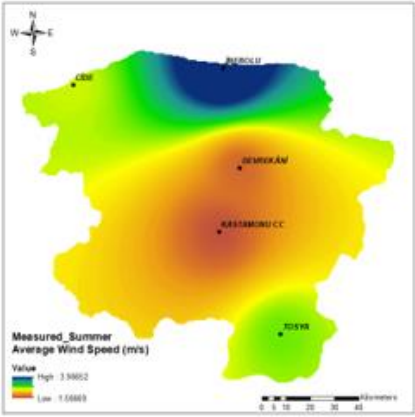
The interpolated average and maximum WS maps have been generated by using the ArcGIS 10.8 software considering the monthly tracked month, air temperature, relative humidity, and air pressure data. Fig. 11 and Fig. 12 display the interpolated maps of average and maximum WS period all season in twenty-two years. It is distinct from the figures that the map constituted with measured findings and the map producted with ANN design values are pretty suitable with one another. The maps are presented together for comparison of measured and predicted values for spring, summer, autumn and winter seasons respectively. Velocity distributions can be distinguished by colour contours. In the maps created by considering the seasonal averages, blue represents the highest wind speed while orange colour represents the lowest speed. It is observed that the velocity distributions obtained for different measurement centres in Fig. 11 and Fig. 12 are consistent with the results in Fig. 9 and Fig. 10 presented previously. For all seasons in Fig. 11, the average WS was obtained highest in İnebolu and the lowest in Kastamonu CC. CC towards the coastline. It displayed similar distribution estimated and measured WS values for the each station.



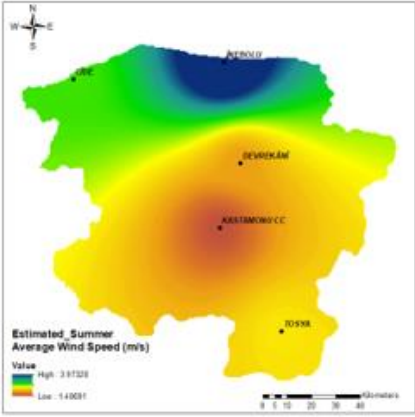
(a)



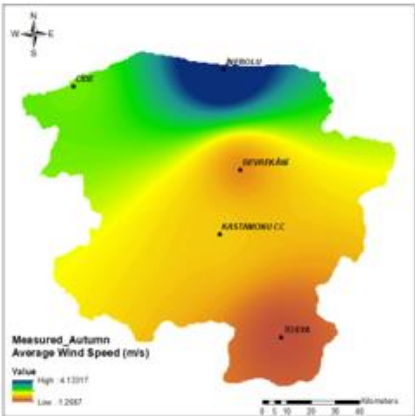
(b)



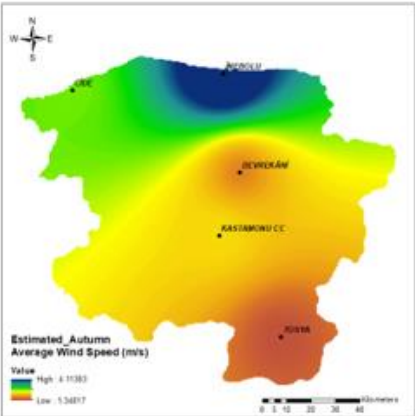
(c)



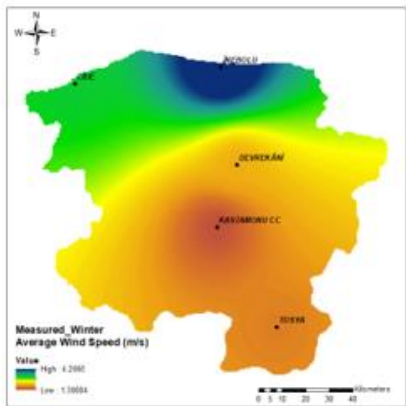
(d)



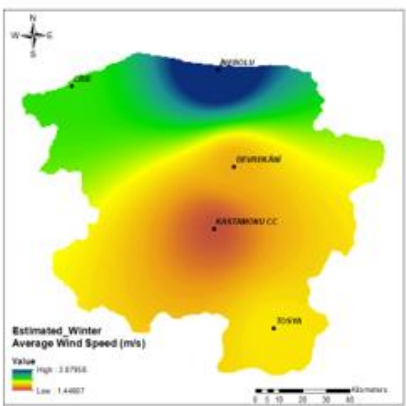
(e)



(f)

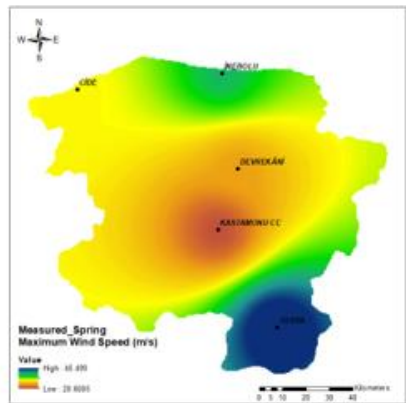


(g)

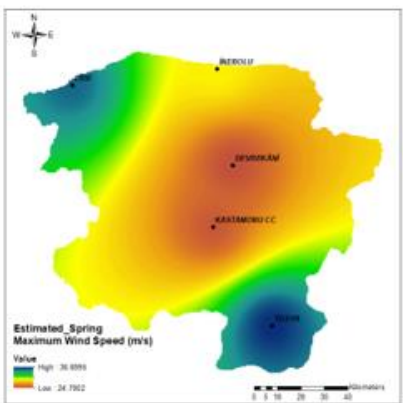


(h)

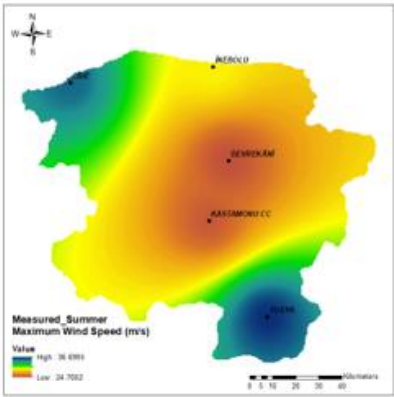
Fig. 11: Average WS (a) Measured for spring, (b) Estimated for spring, (c) Measured for summer, (d) Estimated for summer, (e) Measured for autumn, (f) Estimated for autumn, (g) Measured for winter, (h) Estimated for winter



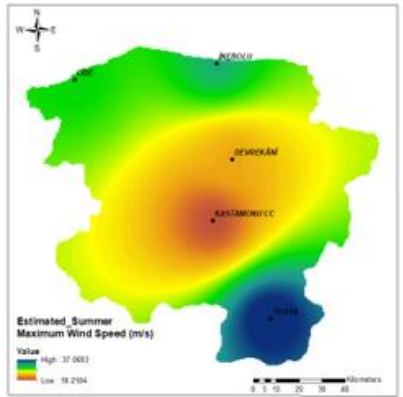
(a)



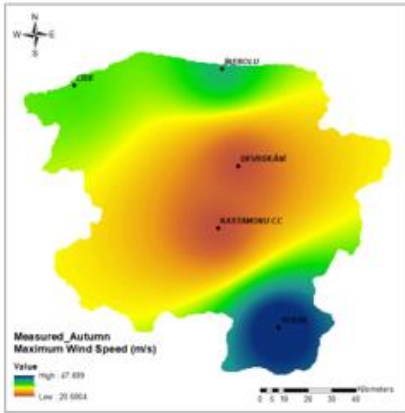
(b)



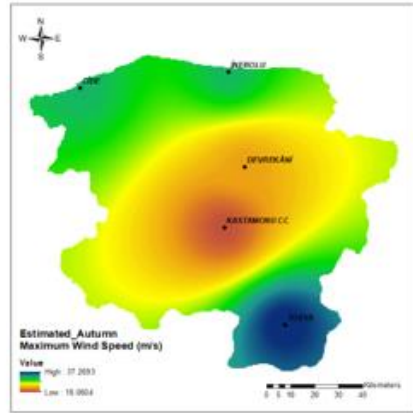
(c)



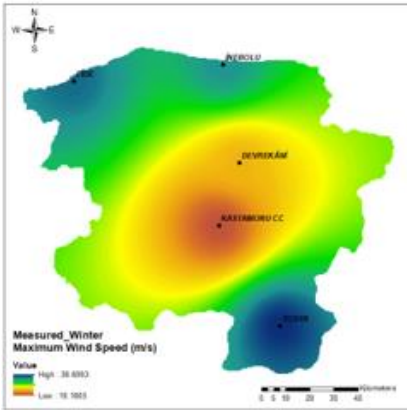
(d)



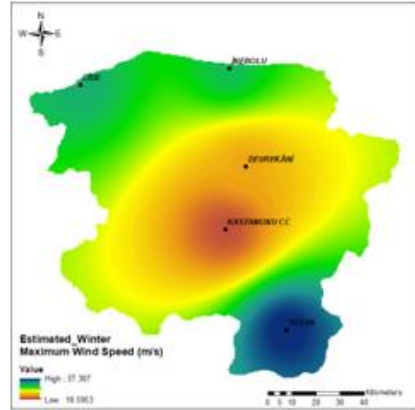
(e)



(f)



(g)



(h)

Fig. 12: Maximum WS (a) Measured for spring, (b) Estimated for spring, (c) Measured for summer, (d) Estimated for summer, (e) Measured for autumn, (f) Estimated for autumn, (g) Measured for winter, (h) Estimated for winter

CONCLUSION

The average and maximum wind speed values in twenty-two years of Kastamonu district in Turkey were predicted to appertain the month, air temperature, relative humidity, air pressure data by utilizing ANN with feed forward network. So, researchers will be conducted sensible methodology to predicted of the wind speed datas in afterwards of Kastamonu district. The MAE, ARD, MSE, and R^2 values of ANN performance along all month for the average wind speed datas of Kastamonu CC district, which the lowest wind speeds among all province are 0.497, 3.679%, 0.0721, and 0.9879, respectively. Throughout the years, the average wind speeds reached the highest values for İnebolu, which is located on the coastal strip. Similarly, ANN with feed

forward performance for İnebolu is 0.292, 2.017%, 0.1030, 0.9921 respectively. As understand from velocity distribution maps with Geographic Information System (GIS), ranking of wind speeds according to district are Cide, Tosya, Devrekani and Kastamonu CC, respectively. Besides, during the 22-year period, it was determined that the maximum wind speeds reached 47.7 m/s for Tosya. These ANN and GIS findings are quite fulfilling. As a result of the study, specially, it has been defined that the wind energy potential of the İnebolu district is quite good. It is considered that the wind energy potential of Kastamonu province can be used in various practices like the illumination applications, watering of farm land. It is considered that this potential could also be promoted in the future due to the improvement of the industry and the decrease in wind turbine expenses.

Acknowledgement

I would like to thank the Turkish State Meteorological Service for providing the meteorological data from Kastamonu meteorological stations.

REFERENCES

- Ağbulut, Ü. (2022). A novel stochastic model for very short-term wind speed forecasting in the determination of wind energy potential of a region: A case study from Turkey. *Sustainable Energy Technologies and Assessments*, 51, 101853.
- Assouline, D., Mohajeri, N., Mauree, D., Scartezzini, J.L. (2019). Machine learning and geographic information systems for large-scale wind energy potential estimation in rural areas. *Journal of Physics: Conference Series*. 1343, 012036.
- Ayodele, T.R., Ogunjuyigbe, A.S.O. (2015). Prediction of wind speed for the estimation of wind turbine power output from site climatological data using artificial neural network. *International Journal of Ambient Energy*, 38, 29–36.
- Bagci, K., Arslan, T., Celik, H.E. (2021). Inverted Kumarswamy distribution for modeling the wind speed data: Lake Van, Turkey. *Renewable and Sustainable Energy Reviews*, 135, 110110.
- Bajjali, W. (2018). Introduction to GIS. *ArcGIS for Environmental and Water Issues*, 1–10.
- Berber, A., Gürdal, M. (2023). Estimation of forced heat convection in a rectangular channel with curved-winglet vortex generator: A machine learning approach. *Thermal Science and Engineering Progress*, 37, 101563.
- Bilgili, M., Ozbek, A., Yildirim, A., Simsek, E. (2023). Artificial neural network approach for monthly air temperature estimations and maps. *Journal of Atmospheric and Solar-Terrestrial Physics*, 242, 106000.
- Bilgili, M., Sahin, B. (2013). Wind Speed Prediction of Target Station from Reference Stations Data. *Energy Sources, Part A: Recovery, Utilization, and Environmental Effects*, 35(5), 455-466.
- Bilgili, M., Sahin, B. (2010). Comparative analysis of regression and artificial neural network models for wind speed prediction. *Meteorology and Atmospheric Physics*, 109, 61–72.
- Calisir, T., Çolak, A.B., Aydin, D., Dalkilic, A.S., Baskaya, S. (2023). Artificial neural network approach for investigating the impact of convector design parameters on the heat transfer and total weight of panel radiators. *International Journal of Thermal Sciences*, 183, 107845.
- Çam, E., Arcaklioğlu, E., Çavuşoğlu, A., Akbiyik, B. (2005). A classification mechanism for determining average wind speed and power in several regions of Turkey using artificial neural networks. *Renewable Energy*, 30, 227–239.

- Çolak, A.B. (2021). A novel comparative investigation of the effect of the number of neurons on the predictive performance of the artificial neural network: An experimental study on the thermal conductivity of ZrO_2 nanofluid. *International Journal of Energy Research*, 45, 18944–18956.
- Colak, A.B., Karakoyun, Y., Acikgoz, O., Yumurtaci, Z., Dalkilic, A.S. (2022). A Numerical Study Aimed At Finding Optimal Artificial Neural Network Model Covering Experimentally Obtained Heat Transfer Characteristics Of Hydronic Underfloor Radiant Heating Systems Running Various Nanofluids. *Heat Transfer Research*, 53, 51–71.
- Çolak, A.B., Yıldız, O., Bayrak, M., Tezekici, B.S. (2020). Experimental study for predicting the specific heat of water based $\text{Cu-Al}_2\text{O}_3$ hybrid nanofluid using artificial neural network and proposing new correlation. *International Journal of Energy Research*, 44, 7198–7215.
- Díaz, H., Guedes Soares, C. (2020). An integrated GIS approach for site selection of floating offshore wind farms in the Atlantic continental European coastline. *Renewable and Sustainable Energy Reviews*, 134, 110328.
- Gao, J., Hu, Z., Yang, Q., Liang, X., Wu, H. (2022). Fluid flow and heat transfer in microchannel heat sinks: Modelling review and recent progress. *Thermal Science and Engineering Progress*, 29, 101203.
- Giebel, G., Kariniotakis, G. (2017). Wind power forecasting—a review of the state of the art. *Renewable Energy Forecasting: From Models to Applications*, (pp. 59–109). Sawston: Woodhead Publishing.
- Gürdal, M. (2023). Artificial intelligence approach for energy and entropy analyses of $\text{NiFe}_2\text{O}_4/\text{H}_2\text{O}$ nanofluid flow in a tube with vortex generator. *Engineering Analysis with Boundary Elements*, 152, 277–292.
- Gurlek, C., Sahin, M., Akkoyun, S. (2021). Estimation of the wind speed in Sivas province by using the artificial neural networks. *Wind and Structures*, 32, 161–167.
- Işık, A.H., Örgen, F.K.D., Şirin, C., Tuncer, A.D., Güngör, A. (2019). Prediction of wind blowing durations of Eastern Turkey with machine learning for integration of renewable energy and organic farmingstock raising. *Scientific Journal of Mehmet Akif Ersoy University*, 2, 47–53.
- Kılıç, B. (2019). Determination of wind dissipation maps and wind energy potential in Burdur province of Turkey using geographic information system (GIS). *Sustainable Energy Technologies and Assessments*, 36, 100555.
- Lawan, S.M., Abidin, W.A.W.Z., Masri, T. (2020). Implementation of a topographic artificial neural network wind speed prediction model for

- assessing onshore wind power potential in Sibu, Sarawak. *Egyptian Journal of Remote Sensing and Space Science*, 23, 21–34.
- Li, J., Heap, A.D. (2011). A review of comparative studies of spatial interpolation methods in environmental sciences: Performance and impact factors. *Ecological Informatics*, 6, 228–241.
- Maduabuchi, C., Nsude, C., Eneh, C., Eke, E., Okoli, K., Okpara, E., Idogho, C., Waya, B., Harsito, C. (2023). Renewable Energy Potential Estimation Using Climatic-Weather-Forecasting Machine Learning Algorithms. *Energies*, 16(4), 1603.
- Ocal, S., Gokcek, M., Colak, A.B., Korkanc, M. (2021). A Comprehensive And Comparative Experimental Analysis On Thermal Conductivity Of $\text{TiO}_2\text{-CaCO}_3$ /Water Hybrid Nanofluid: Proposing New Correlation And Artificial Neural Network Optimization. *Heat Transfer Research*, 52, 55–79.
- Öztopal, A. (2006). Artificial neural network approach to spatial estimation of wind velocity data. *Energy Conversion and Management*, 47, 395–406.
- Purlu, M., Andic, C., Turkay, B.E., Nobari, A.G. (2022). Short Term Load Forecasting Using Machine Learning Algorithms: A Case Study in Turkey. *IEEE Glob. Energy Conf. GEC, Batman, Turkey*, 13–18.
- Rezaei Miandoab, A., Bagherzadeh, S.A., Meghdadi Isfahani, A.H. (2022). Numerical study of the effects of twisted-tape inserts on heat transfer parameters and pressure drop across a tube carrying Graphene Oxide nanofluid: An optimization by implementation of Artificial Neural Network and Genetic Algorithm. *Engineering Analysis with Boundary Elements*, 140, 1–11.
- Rüzgar- T.R. Ministry of Energy and Natural Resources. (2021) <https://enerji.gov.tr/bilgi-merkezi-enerji-ruzgar> (accessed 4.29.23).
- Shboul, B., AL-Arfi, I., Michailos, S., Ingham, D., Ma, L., Hughes, K.J., Pourkashanian, M. (2021). A new ANN model for hourly solar radiation and wind speed prediction: A case study over the north & south of the Arabian Peninsula. *Sustainable Energy Technologies and Assessments*, 46, 101248.
- Ulkat, D., Günay, M.E. (2018). Prediction of mean monthly wind speed and optimization of wind power by artificial neural networks using geographical and atmospheric variables: case of Aegean Region of Turkey. *Neural Computing and Applications*, 30, 3037–3048.

Chapter 11

Evaluation Of Suitability Of Antalya (Turkey) Karst Travertine Plateau For Underground Dam

Mehmet OZCELIK¹

¹ Doç. Dr.; Süleyman Demirel University, Engineering Faculty, Geological Engineering, Isparta, Turkey.
Orcid ID: 0000-0003-4511-1946; E-mail: ozcelikmehmet@sdu.edu.tr

ABSTRACT

INTRODUCTION

Aquifers on the coastal karst are common around the Mediterranean. They represent current or future groundwater resources belonging to aquifers with potentially important storage capacity. In the short term, water demand is expected to increase significantly as a result of the increasing population and agricultural initiatives in Antalya. Alternative water sources are therefore required. Antalya has a wide variety of water sources, such as surface water, groundwater and spring water, to meet the city's needs. Since the karst structures in Antalya travertine plateau are rich in groundwater and the channel network of karst hydrosystem has been developed, it is suitable for the underground dam. An underground dam is a structure that holds freshwater in the reservoirs of the broad solution and enables productive freshwater use. These dams have other benefits that surface dams do not have, e.g. land is not submerged to store water and natural or manmade disasters have no chance of failure. Moreover, the surface area before and after the underground dam building may be used in the same way. Because of these advantages, many underground dams are located in different geological systems around the world. The suitability of the karst travertine plateau for underground dam construction was assessed in this study using 3D modelling and GIS-based analysis.

Water resource management has become more important as a result of global warming. Underground dams in arid and semi-arid climates can be an ideal solution for storing flood or temporary river water. Many such structures, in particular, have already been completed in North and East Africa, as well as the Middle East. However, feasibility studies for ground surveys suitable for underground dam construction are required. Karst is characterized by a large number of closed and few open surface depressions, a well-developed underground drainage network, and a strong relationship between surface water and groundwater circulation (Bonacci, 2004; Ford and Williams, 2007). In the near future, karst carbonate aquifers can be considered as possible water supplies (Doerfliger et al., 2008). This can be viewed in two different ways. The first is a network of fractures that form within deposits of carbonate rock masses. The karst aquifer networks are highly heterogeneous and anisotropic compared to other aquifers. The second is karst hydrosystem conductive network (Turk et al., 2014). Thus, in karst hydrosystems, there are various pore sizes, from capillary fractures to large fractures, and underground rivers. An underground dam is an engineering structure which stores freshwater for sustainable use in the geological environment (Onder and Yilmaz, 2005; Jamali et al., 2018; Ebrahimi et al., 2021). Using available technology, such as the mix-in-place construction process, underground dams that store a few hundred to several million m³ of groundwater

have been installed previously and put to practical use in karst regions. The idea of an underground dam has recently spread, and a lot of underground dams have been installed in karst areas. Large numbers of underground infrastructure systems were developed in the karst area of SW China to allow better use of the groundwater resources (Daoxian, 1991). Underground dams are formed by clogging underground caves, karst canals and rivers. They have very little storage capacity and almost all water is collected in canals and caves (Lin Hua, 1989). The Minafuku underground dam in the Miyakojima Islands in Japan was designed and constructed in the 1972. Underground dam HEPP Ombla was installed about 200 m behind the natural spring outflow in Croatia's karst structure (Roje-Bonacci and Bonacci, 2013). Stevanovic (2015) explains the small underground dams in Indonesia (Bribin Cave) and Iraq (Gali Basera). Dams on the subsurface flows can be categorized into two types: a dam covering the whole cross-section of the underground river (full-section dam) and a dam covering half of the cross-section of the underground river (partial cross-section dam). However, they can be further categorized in three forms, based on their position on subterranean streams: dam site near source (fore dam), dam site near karst window (window dam) and dam site near a swallow hole and transforming karst depression into reservoir (back dam) (Daoxian, 1992). Despite Antalya's rising population, it has been chosen as an area of study due to the increasing daily need for water (Figure 1).

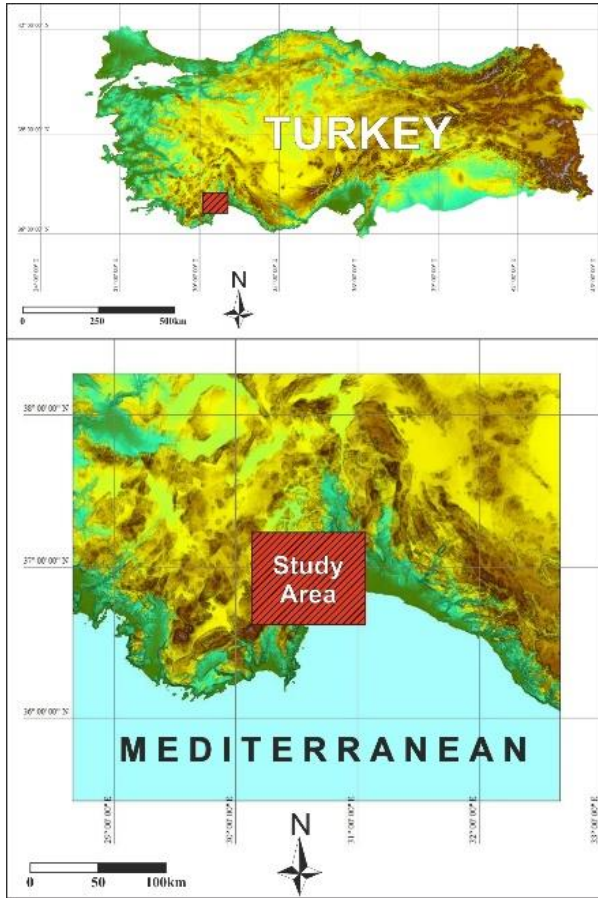


Figure 1: Location map of Antalya

Antalya travertine maximum deposit thickness is 300 m. Antalya region is predominantly formed by active karst aquifer consisting of travertine. Travertine has distinctive karstic features such as hydraulic conduits, dolines, springs and caves where the main source of agricultural and drinking water is the groundwater from travertine aquifers. GIS is a suitable solution for the precise position of regions in compliance with available requirements and guidelines to this end. This article presents the suitability of the Antalya travertine plateau for the construction of the underground dam by combining the geographic information system (GIS) based analysis with by 3D modelling. This article suggests using GIS techniques to underground dams to be installed in karstic areas as an alternative or potential alternative water supply.

METHODOLOGY

Karst morphology and hydrogeology

Antalya travertine plateau, located in Turkey's Mediterranean region. It is the travertine bed formed by the world's largest fresh water resource, covering more than 630 km². The gradual travertine plateau consists of 3 levels. The Upper plateau extends to the masses of carbonate rock in Beydağları. Düden and Kırkgözüler spring waters flow from karst aquifers with very large groundwater reservoirs from carbonate platforms, notably the Beydağları. The city of Antalya was situated on the Middle plateau (40 ± 150 m asl.). The Middle Plateau enters the Mediterranean and ends with cliffs of travertine. The Lower Plateau starts under the cliffs and extends under the Mediterranean. Its scale is unknown. There is an uncertain relation between the travertine plateau and the underlying carbonate rocks (Günay et al. 1995). Travertine has substantial primary porosity, and often very well defined karst structures. The karst network is distinguished by the interconnected hydraulic conduits, multiple sinkholes, springs and dolines. Kırkgözüler spring (15 m³ / s) is known as the carbonate source for travertine precipitation hydrologically connected between Beydağları and Upper Plateau on an area of approximately 1 km² (SHW 1985; Burger 1990; Günay et al. 1995). Kırkgözüler spring drain the mountains of Beydağları an accumulation of carbonates greater than 1000 m. The degassing of CO₂ at the outlet results in accumulation of travertine as the spring water is normally supersaturated with respect to calcite (Burger, 1990; Günay et al., 1995; Kosun et al., 2019). Karstification thus occurred well before the deposition of travertine. Before the current spring phase, paleo-spring caverns located in carbonates above the Kırkgözüler spring orifices are thought to suggest past discharge points. It is believed that the continuous karst system, which extends to deeper regions of the carbonate complex, is covered by the present sea level and encourages the lateral regeneration of the travertine aquifer (SHW, 1985). As a result, the Kırkgözüler spring network is regarded as the outflow of the hydraulic conduits, discharging the groundwater laterally through the travertine from the carbonate rocks (Ozcelik and Sarp, 2018). The travertine recharge zone is not limited to the plateau but stretches to the Kırkgözüler spring catchment area, measured at 4300 km² (Tezcan, 1993). Large amounts of groundwater runoff from the concentrated mountains of Beydağları flow through and across the travertine plateau into the Mediterranean. Groundwater flows through the Düden spring travertine discharges (18 m³/s) on the Upper Plateau, at the border of the Upper and Middle plateau. The water starts to flow into the Mediterranean from the spring up the Düden River (Figure 2). Other water discharges are known to flow through interconnected hydraulic conduits which are discharged directly into the

Mediterranean through a series of unnamed groundwater springs on the Lower Plateau near Antalya Bay. In addition to the field studies, geological classifications made using the Landsat 8 tape dates from 1985 satellite data made an important contribution to the accuracy of the study (Figure 3).



Figure 2: General view of the Düden River



Figure 3: Landsat 8 Enhanced Thematic Mapper + image with a fusion of bands 4, 5, 7 and 8 showing the location of the Antalya region (<https://earth.esa.int>)

Subsurface flows and key springs

Karstic aquifers have a rather dynamic nature and are heterogeneous. In these types of aquifers, the groundwater flow is dominated by the second and third forms of porosity, including the fractures and large hydraulic conduits, respectively (Labat et al., 2000; Kalantari and Rouhi 2018). Large hydraulic conduits allow rapid movement of the water, discharging groundwater in recent times. The smaller hydraulic conduits that are less connected hold the water for a longer period of time and thus discharge older groundwater (Weymer et al., 2020). The variable mixing of these various groundwater components at any point in the aquifer for sampling or calculation requires the utmost caution in evaluating important aquifer management variables, such as recharge levels or groundwater velocity (Nativ et al., 1999). Owing to karstic formation the Antalya's water supplies are very complicated. Kirkgözler aquifers at an altitude of about 305 m above sea level form the most significant water supplies of this part of the study area. The aquifers are 30 km away from Antalya and come to the surface at the foot of the Beydağları Mountains as springs in around 70 ha of land. From here the water flows in east direction for about 2 km and disappeared in the sinkhole of Biyikli. Approximately 14.5 km southeast of the sinkhole the water emerges in a sedimentary region of 200 by 100 meters, disappears again and comes 3.5 km farther on to the surface. Kirkgözler and Düden karst springs are important water resources in Antalya which play an important role in this region's economy and population. These spring waters, especially the Beydağları (Kosun, 2012), are discharged from carbonate platform karst aquifers with very large groundwater reservoirs. Groundwater and springs are Antalya's primary source of water supply.

Suitability of karstic areas for underground dam

Karst describes the slow water-enriched dissolution role of carbon dioxide on soluble rocks including carbonates, evaporates, and halite (White 1988; Ford and Williams 2007). A number of different landforms reflect morphological effects at the surface, the most common being dolines and sinkholes. Below the surface, fracture networks of different sizes are created by dissolving the soluble rocks, leading to a network of voids, the sections of which are known as caves, wide enough to be explored by humans (Roje-Bonacci and Bonacci 2013). Populated karst ecosystems can be found worldwide, but in terms of sustainable water supply, their natural boundary conditions often lead to distinct challenges. This situation is exacerbating, particularly in developing and emerging countries, because suitable technologies and water management principles are rarely available (Oberle et al. 2016).

Such dams have the advantage of being able to hold more water than detritic aquifers in this area and of being less vulnerable to evaporative losses as the water is stored underground and there is no chance of destruction due to natural or man-made disasters. In addition, the surface area may be used in the same way before and after the construction of the underground dam (Apaydın 2009; Shirani et al. 2017; Kharazi et al. 2019). The underground dam enables the production of water supplies in regions where, due to geological conditions, the construction of surface dams is difficult and groundwater cannot be used in its current state (karst areas, etc.). Underground dams consist of a wall which blocks the groundwater flow and prevents the intrusion of seawater, as well as structures (wells, intake pipes and pumps) containing the groundwater (Ishida et al., 2011). Because pumping is needed in an underground dam for the use of stored groundwater, the maintenance costs can be higher than those of a surface dam (Costall et al., 2020).

Underground dam for water supply

Karst aquifers are the primary source of drinking water in many areas around the world, capable of storing and distributing significant volumes of water (Parise et al., 2018; Kalhor et al., 2019). Antalya region lies on a wide plateau where karstic travertine platform and other sedimentary rocks dominate the bedrock. In the western side of the travertine plateau, the carbonate rocks are massive and micro-crystalline. This unit's fracturing structures are perpendicular to one another, and the dissolution voids are parallel with the dip (Ozcelik, 2014; 2015). The karst properties are correlated with unit carbonate content and matrix porosity. The use of geographic information system (GIS) and remote sensing (RS) techniques have been accepted as valuable tools due to their cost- and time-efficiency by means of identifying, sustaining, and managing groundwater sources (Jha et al., 2010; Jasrotia et al., 2016; Agarwal and Garg, 2016). The application of these techniques helps to improve the accuracy of results in the identification of groundwater potential zone (Rao and Jugran, 2003; Ozcelik and Sarp, 2018). These analyses allow GIS tools to support efficient management of spatial data and extract information, and use of digital models in the water resources management. The successful variables are chosen for this purpose in order to determine the karst conduit section in which the underground dam will use digital models; including elevation (Figure 4a), lithology (Figure 4b), slope direction (Figure 4c), slope (Figure 4d), rivers (Figure 4e) and drainage map layers (Figure 4f). The hydrological conditions are closely related to certain defined parameters and thus have a direct effect on water accumulation in the reservoir. Combining GIS based analysis with numerical modelling, the

suitability of Antalya travertine plateau for underground dam construction has been demonstrated by 3D modelling (Fig. 5).

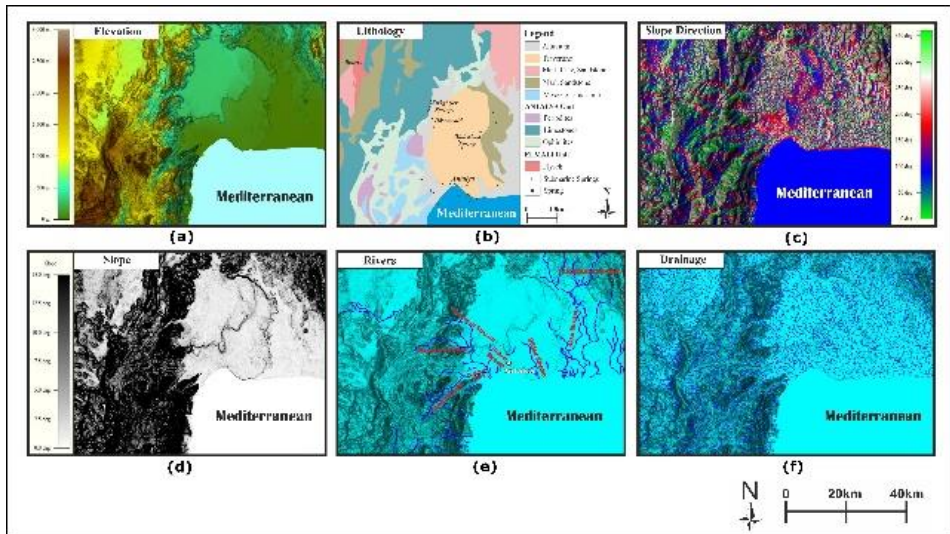


Figure 4: Map layers used to 3D modelling: (a) Elevation, (b) lithology, (c) slope direction, (d) slope, (e) rivers and (f) drainage map

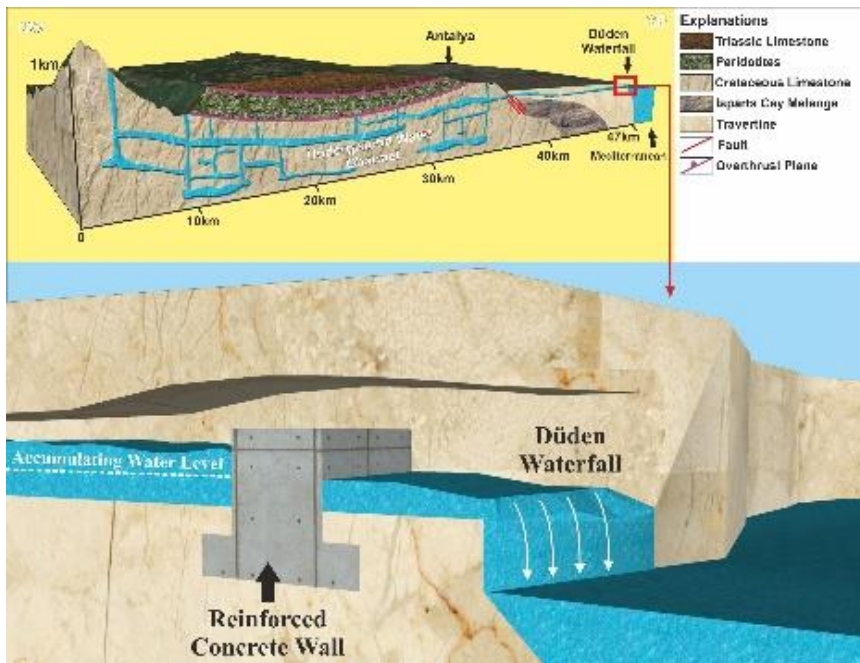


Figure 5: 3D modelling of Antalya travertine plateau

The carbonate rocks in the region have karst aquifer systems. Surface and groundwater from the surrounding lithological units of the region are deposited in karst aquifer systems and alluvium deposits (Elhatip, 1997). Surface drainage is negligible because of fast percolation of precipitation into well-developed karst aquifer systems with mostly bare outcrops. The primary groundwater resource in the study region is the springs situated at the local contact between the carbonates and the impermeable Eocene-Miocene units. It was proposed for this reason that the construction of underground dams should be built as vertical walls in the direction of underground storage of hydraulic conduits (underground rivers). In this situation, the groundwater flow through the karstic conduits would be blocked which allows the water to be deposited through karstic structures and to collect in the groundwater reservoir.

DISCUSSIONS

The suitability of the chosen region for the underground dam was investigated within the scope of this study. At this stage; The karstic structure of the proposed study area, the formation of water resources, and the climate of the region were all evaluated. The karst underground environment is distinguished by its morphological structures. Due to the solubility of the rocks, a karst underground environment can form. The quality water beneath the karst surface provides many important ecosystem services, such as the treatment of leaked water and the storage of large amounts of water over long periods of time. It provides underground animals with essential habitats. Karst terrain provides a variety of habitats and niches for obligate subterranean species. Furthermore, the position of the sinkholes on the Antalya travertine plateau should be monitored during the proposed study. Antalya's climate is warm and temperate. The winter months in Antalya are much rainier than the summer months. This climate is classified as Csa by Köppen and Geiger. Antalya's average annual temperature is 18.6 °C (65.5 °F). Annual precipitation totals 1009 mm (39.7 inches). Karst floods must be closely monitored.

CONCLUSIONS

Despite the rising population of Antalya, it was chosen as a study area due to the increasing daily need for water. Antalya city became the fastest-growing city in Turkey with population growth and as a result the region was dominated by unregulated urbanisation. Antalya's demand for irrigation and drinking water is mainly supplied from groundwater, springs and surface water. Water in karstic rocks appears to travel more easily through joints, cracks, and hydraulic conduits than through the rock material's interstitial porosity itself. Some of the water

resources in the karstic travertine plateau are used for the city's water supply, and most of them flow from underground karstic rivers and streams into the sea. However, karst resources contain large quantities of karst water, which is promising for future water supply. This is why it demonstrates that the best choice for Antalya's permanent water supply is to use the underground dam construction and the karst aquifer system. Combining geographic information system (GIS) based analysis with numerical modelling, the suitability of Antalya travertine plateau for underground dam construction has been demonstrated by 3D modelling. This method showed that it is possible to locate the location of the considered objective by applying different information layers according to their order of importance. In this analysis, the key factors in locating underground dam were lithology, slope, stream flow, drainage depth, slope direction, elevation and hydrogeology. Kırkgözüler and Düden karst systems in particular have hydraulic conduits which are ideal for underground dams. The present study evaluated alternative and potential alternatives to water supply for urban Antalya city. Water supply from construction of underground dams was evaluated as an alternative water option for urban area. At the end of the evaluation it was proposed that the karst travertine plateau would be suitable for underground dam construction to meet the rising water needs in Antalya.

REFERENCES

- Agarwal, R., and Garg, P. K. (2016). Remote sensing and GIS based groundwater potential and recharge zones mapping using multi criteria decision making technique. *Water Resources Management*, 30(1), 243-260.
- Apaydin, A. (2009). Malibogazi groundwater dam: an alternative model for semi-arid regions of Turkey to store and save groundwater. *Environmental Earth Science*, 59, 339-345.
- Bonacci, O. (2004). Hazards caused by natural and anthropogenic changes of catchment area in karst. *Natural Hazards and Earth System Science*, 4, 655-661. <https://doi.org/10.5194/nhess-4-655-2004>
- Burger, D. (1990) The travertine complex of Antalya, Southwest Turkey. *Geomorphology*, 77, 25-46.
- Costall, A., Harris, B., Theo, B., Schaa, R., Wagner, F., and Pigois, J. (2020). Groundwater through flow and seawater intrusion in high quality coastal aquifers. *Scientific Reports*, 10(1). <https://doi.org/10.1038/s41598-020-66516-6>.
- Daoxian, Y. (1992). Hydrological and environmental problems in karst area. (www.karst.edu.cn/en/ndex.php?c=artcle&a=vew&d=19)
- Doerfliger, N., Fleury, P., and Ladouche, B. (2008) Inverse modelling approach to allogenic karst system characterization. *Groundwater*, 47, 414-426.
- Ebrahimi, J., Moradi, H. R., and Chezgi, J. (2021). Prioritizing suitable locations for underground dam construction in south-east of Bushehr Province. *Environmental Earth Science*, 80, 680. <https://doi.org/10.1007/s12665-021-09978-9>
- Elhatip, H. (1997). The influence of karst features on environmental studies in Turkey. *Environmental Geology*, 31(1/2), 27-33
- Ford, D., and Williams, P. (2007). *Karst hydrology and geomorphology*. Wiley, Chichester, p 563
- Fujino, K., Doyama, K., and Tagawa, S. (2005). Sub-surface dam in coastal area. Res Rep. *Yatsushiro National College of Technology*, 27, 43-47.
- Goldscheider, N., and Drew, D. (2007). *Methods in karst hydrogeology. International contributions to hydrogeology*. Taylor & Francis, London
- Günay, G., Tezcan, L., Ekmekci, M., and Atilla, O. (1995). *Present state and future trends of karst groundwater pollution in Antalya travertine plateau - Turkey*. National report of Turkey. Karst groundwater protection. Final report. COST Action-65. European Commission. Report EUR 16547 EN. Luxembourg, Belgium, pp. 305-324.
- <https://earth.esa.int/web/earth-watching/image-of-the-week/content/-/article/antalya-turkey> (accessed date 10.04.2021)

- Ishida, S., Tsuchihara, T., Yoshimoto, S., and Masayuki, I. (2011). Sustainable use of groundwater with underground dams. *JARQ: Japan Agricultural Research Quarterly*, 45, 51-61. <https://doi.org/10.6090/jarq.45.51>.
- Jamali, A. A., Randhir, T. O., and Nosrati, J. (2018). Site suitability analysis for subsurface dams using boolean and fuzzy logic in arid watersheds. *Journal of Water Resources Planning and Management*, 144(8), 04018047.
- Jasrotia, A. S., Kumar, A., and Singh, R. (2016). Integrated remote sensing and GIS approach for delineation of groundwater potential zones using aquifer parameters in Devak and Rui watershed of Jammu and Kashmir, India. *Arabian Journal of Geosciences*, 9(4), 1-15.
- JGRC (Japan Green Resources Corporation) (2001). *Subsurface dams for agricultural use in subtropical regions*. Japan Green Resources Agency pp. 6.
- JGRC (Japan Green Resources Corporation) (2004). *Technical reference for effective groundwater development*. Japan Green Resources Agency pp. 325.
- Jha, M. K., Chowdary, V. M., Chowdhury, A. (2010). Groundwater assessment in Salboni Block, West Bengal (India) using remote sensing, geographical information system and multi-criteria decision analysis techniques. *Hydrogeology Journal*, 18(7), 1713-1728.
- Kalantari, N., and Rouhi, H. (2018). Discharge hydraulic behaviour comparison of two karstic springs in Kuhe-Safid anticline, Khuzestan, Iran. *Carbonates and Evaporites*, 34, 1343–1351. <https://doi.org/10.1007/s13146-018-0427-0>
- Kalhor, K., Ghasemizadeh, R., Rajic, L., and Alshawabkeh, A. (2019). Assessment of groundwater quality and remediation in karst aquifers: A review. *Groundwater for Sustainable Development*, 8, 104-121. <https://doi.org/10.1016/j.gsd.2018.10.004>.
- Kharazi, P., Yazdani, M. R., and Khazealpour, P. (2019). Suitable identification of underground dam locations, using decision-making methods in a semi-arid region of Iranian Semnan Plain. *Groundwater for Sustainable Development*, 9, 100240. <https://doi.org/10.1016/j.gsd.2019.100240>
- Kosun, E. (2012) Facies characteristics and depositional environments of Quaternary tufa deposits, Antalya, SW Turkey. *Carbonates Evaporites*, 27, 269-289.
- Kosun, E., Varol, B., and Taşkıran, H. (2019). *The Antalya tufas: landscapes, morphologies, age, formation processes and early human activities*. C. Kuzucuoğlu et al. (eds.), *Landsc and Landf of Turkey*, World

- Geomorphological Landscapes. https://doi.org/10.1007/978-3-030-03515-0_7
- Labat, D., Ababou, R., and Mangin, A. (2000). Rainfall-runoff relations for karstic springs. Part I: convolution and spectral analysis. *Journal of Hydrology*, 238(3-4), 123-148.
- Lin Hua, S. (1989). *Subsurface reservoirs and karst geomorphology*. Proceedings of the third multidisciplinary conference on sinkholes, Balkema, Rotterdam, 369-376.
- Nativ, R., Günay, G., Hötzl, H., Reichert, B., Solomon, D. K., and Tezcan, L. (1999). Separation of groundwater flow components in a karstified aquifer using environmental tracers. *Applied Geochemistry*, 14, 1001-1014.
- Oberle, P., Ikhwan, M., Stoffel, D., and Nestmann, F. (2016). Adapted hydropower-driven water supply system: assessment of an underground application in an Indonesian karst area. *Applied Water Science*, 6, 259-278. <https://doi.org/10.1007/s13201-016-0425-0>
- Onder, H., and Yilmaz, M. (2005). Underground dams, a tools of sustainable development and management of ground water resources. *European Water*, 11(12), 35-45.
- Ozcelik, M. (2014). Effect of wastewater on building foundation in karst travertine areas in Antalya, Turkey. *Bulletin of Engineering Geology and the Environment*, 74(4), 1213-1224. <https://doi.org/10.1007/s10064-014-0695-4>
- Ozcelik, M. (2015). Foundation investigations and design in a karst terrain for the Antalya Aquarium complex, Turkey. *Quarterly Journal of Engineering Geology and Hydrogeology*, 48, 204-211. <https://doi.org/10.1144/qjegh2014-044>
- Ozcelik, M., and Sarp, G. (2018). Evaluation of sustainable water supply alternatives in karstified rock masses using GIS and AHP methodology for Antalya (Turkey) urban area. *Environmental Earth Sciences*, 77, 696. <https://doi.org/10.1007/s12665-018-7881-9>
- Parise, M., Gabrovsek, F., Kaufmann, G., and Ravbar, N. (2018). Advances in Karst Research: Theory, Fieldwork and Applications. *Geological Society, London, Special Publication*, 466, 1-24. <https://doi.org/10.1144/SP466.26>
- Rao, Y. S., and Jugran, D. K. (2003). Delineation of groundwater potential zones and zones of groundwater quality suitable for domestic purposes using remote sensing and GIS. *Hydrological Sciences Journal*, 48(5), 821-833.
- Roje-Bonacci, T., and Bonacci, O. (2013). The possible negative consequences of underground dam and reservoir construction and operation in coastal karst areas: an example of the hydro-electric power plant (HEPP) Ombla

- near Dubrovnik (Croatia). *Natural Hazards and Earth System Sciences*, 13, 2041-2052. <https://doi.org/10.5194/nhess-13-2041-2013>
- Shirani, K., Shafiey, Dastjerdi, A., and Rahnamarad, J. (2017). Integration of multi-criteria decision matrix and geographical information system to site selection for an underground dam. *Electronic Journal of Geotechnical Engineering*, 22, 3669-3686
- SHW (General Directorate of State Hydraulic Works) (1985). *Antalya Kirkgoz kaynakları ve traverten platosu karst hidrojeolojik etud raporu (Hydrogeological investigation report of Antalya travertine plateau and water sources)*. Jeoteknik Hizmetler ve Yeraltısuyu Dairesi Başkanlığı, Ankara (in Turkish)
- Stevanovic, Z. (2015). *Karst Aquifers - Characterization and Engineering: Cham*, Switzerland, Springer, 692 p. <https://doi.org/10.1007/978-3-319-12850-4>
- Tezcan, L. (1993). *Mathematical model of karst aquifer systems using tridium isotope*. PhD thesis, Hacettepe University, 125 pp (in Turkish)
- Turk, J., Malard, A., Jeannin, P-Y., Petric, M., Gabrovsek, F., Ravbar, N., Vouillamoz, J., Slabe, T., and Sordet, V. (2014). Hydrogeological characterization of groundwater storage and drainage in an alpine karst aquifer (the Kanin massif, Julian Alps). *Hydrological Processes (wileyonlinelibrary.com)*. <https://doi.org/10.1002/hyp.10313>
- Weymer, B. A., Wernette, P. A., Everett, M. E., Pondthai, P., Jegen, M., and Micallef, A. (2020). Multi-Layered high permeability conduits connecting onshore and offshore coastal aquifers. *Frontiers in Marine Science*, 7, 531293. <https://doi.org/10.3389/fmars.2020.531293>
- White, W. B. (1988). *Geomorphology and hydrogeology of karst terrains*, Oxford University Press, Oxford

Chapter 12

Investigation of Turkey's Thermal Water Resources

Melike YALILI KILIÇ¹

¹ Prof. Dr.; Bursa Uludag University, Faculty of Engineering, Department of Environmental Engineering, myalili@uludag.edu.tr ORCID No: 0000-0001-7050-6742

ABSTRACT

Thermal waters are waters that are beneficial for human health due to the fact that they contain elements such as potassium, magnesium, sodium, iron, chloride, calcium, selenium, lithium, manganese, and that their temperature increases when leaving the ground. People who want to benefit from the healing properties of hot water want to take a holiday in the regions where thermal waters are available in almost every season. While resting providing supportive treatment of various diseases at the same time, causes an increase in the interest in thermal regions. Turkey is a country rich in thermal water resources and is among the top five in the world. In this study, in which general information about thermal waters is given, examples from thermal water resources in Turkey are given.

Keywords: Health tourism, hot spring, termal waters, Turkey

1. INTRODUCTION

The waters collected in the hollow layers underground by filtering from the ground to form the geothermal reservoirs by heating. These waters rise to the surface under pressure and form geothermal water resources at different temperatures. Since geothermal waters come into contact with the minerals, salts, and elements in the rocks, they carry them with heat energy as they rise to the surface (Özbek ve Özbek, 2011:104).

Thermal waters are very beneficial for human health due to the minerals they contain. Many people benefit from thermal waters in order to find solutions to rheumatism, gall bladder, kidney, urinary tract, muscle, skin, stomach, intestinal diseases, hernia, calcification, and stress-related problems (Zengin and Eker, 2016:167). Apart from the treatment of diseases, thermal waters are also preferred by people to relax, renew, store energy, and gain beauty (Boyras and Çetin, 2019:86). As a result of the combination of the thermal hot waters, the source of healing, with the climate, air, and natural beauties of the region, positive improvements are seen in people. To relieve the tiredness of the year, to be alone with nature, and to benefit from the healing properties of hot water, people want to spend time in the regions where thermal waters are available every season. In addition, environmental problems that have arisen due to global warming and climate change experienced in the world in recent years have also led to people's desire to protect their health more. In this context, as in the rest of the world, people in our country, on the one hand, prefer to take a vacation and rest; on the other hand, they prefer to provide supportive treatment of various diseases at the same time. At this point, the concept of thermal tourism began to become clear.

Thermal tourism, known as health tourism, is tourism with the aim of having fun, resting, and having a good time with methods such as water-mud baths, inhalation, and applications that emerge by combining treatments such as physical therapy, exercise, psychotherapy, and diet. Places where thermal tourism is made, are generally known as "spring centers". Thermal tourism aims to provide a suitable environment for people to benefit from the healing waters, receive supportive treatments under the control of a doctor, and have a good time by resting and having fun (Erdoğan and Aklanoğlu, 2008:84).

In this study, information about thermal water is given and various examples from thermal water resources in Turkey are presented.

2. THERMAL WATERS

Thermal waters are waters that come from underground to the surface, are very beneficial for human health, and have a temperature of at least 20 °C. The difference between thermal waters from other spring waters is the high-temperature level. As the thermal waters come into contact with many different minerals and elements, they carry these minerals in their bodies, as well as the increase in temperature. Elements such as potassium, magnesium, sodium, iron, chloride, calcium, selenium, lithium, and manganese are among the main elements found in thermal waters. Since the amounts of underground elements and minerals vary from region to region, the content of thermal waters also differs from region to region. Therefore, some thermal waters are acidic and some are basic (URL-1, 2023).

Thermal waters, which are very beneficial for human health, can be used for cardiovascular diseases, skin, skin, digestive system, rheumatism, gynecological diseases, physiotherapy, etc. It is known to be good for many problems. Although people generally prefer thermal regions to find some healing and relaxation for such ailments, it should not be expected to give the same positive effect for every ailment in everybody (URL-2, 2023).

3. EXAMPLES FROM TURKEY'S THERMAL REGIONS

Türkiye is a very rich country in terms of thermal water resources (Figure 1). There are more than 1300 thermal springs in our country, and it is stated that more than 600 of them have temperatures above 20 °C. Compared to the world, Turkey is the first in Europe in terms of thermal water resources and is among the top five in the world (Özşahin and Kaymaz, 2013:25).

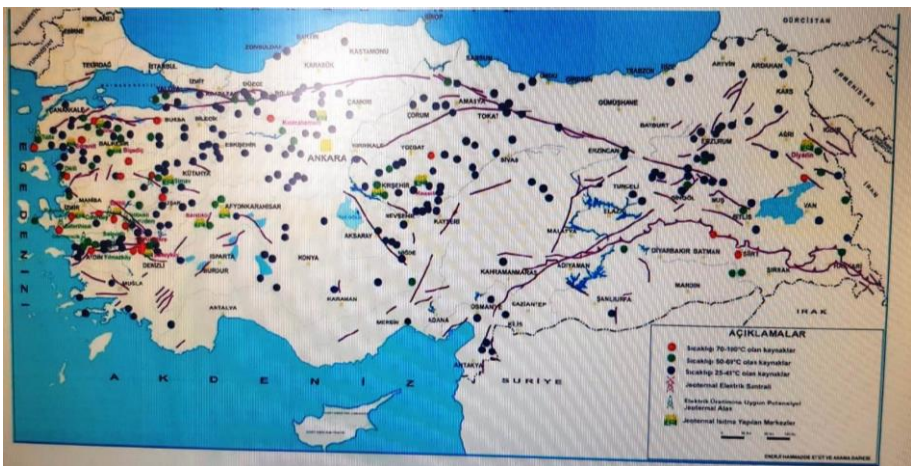


Figure 1: Thermal Regions of Turkey (URL-3, 2023)

3.1. Afyonkarahisar

Afyonkarahisar, which is one of the important centers of Turkey in terms of thermal tourism, is a very preferred place due to its ease of transportation and a large number of accommodation facilities. While there were eight thermal facilities in the province in the 2000s, the number of facilities reached 37 in 2010 (URL-3, 2023). The thermal springs in the province were declared as Tourism Centers with the decision of the Council of Ministers published in the Official Gazette dated 17.10.1993 and numbered 21700 (Erdoğan and Akınoğlu, 2008:88).

3.1.1. Gecek Spring: The waters of the spring, located 18 km from Afyonkarahisar in the direction of Kütahya, contain sodium chloride and bicarbonate, and the water temperature is 56 °C. The hot waters of the spring, which are recommended by a doctor to support rheumatism and physical therapy, are also used for geothermal heating purposes (Ekiz and Yazıcı, 2016:70).

3.1.2. Ömer Spring: Although there are 8 spring outlets in Ömer Spring, located on the Kütahya road, only one of them is used as a thermal water source. The temperature of the water is 54 °C and it is used in diseases such as joint, rheumatism, and polio (Taş, 2012:143).

3.1.3. Hüdai Spring: It is a tourism center located in the district of Sandıklı and known for its mud baths. Combining the alluvial floor of Sandıklı Plain with thermal springs, a mud with high therapeutic properties emerged. The temperature of the water in the spring is around 68°C and it is stated that it arises from a geological crack that continues for 500 m. The pH value of the water is 6.6-7 and the radioactivity value is 13-25 emans. As a result of mixing the soil with this healing hot water, mud at a temperature of 45 °C is formed (URL-3, 2023; URL-4, 2023).

3.1.4. Gazlıgöl Spring: Located in Gazlıgöl town in İhsaniye district, this hot spring is an important source known since the Phrygians. The temperature of the water in Gazlıgöl spring is 64°C, pH value is 6.9, radioactivity value is between 0.2-1.29 eman. Gazlıgöl waters are very useful against rheumatism, skin, heart, liver, urinary tract diseases (URL-5, 2023).

3.1.5. Heybeli Kaplıcası: The history of Heybeli Thermal Spring, located in Bolvadin district, dates back to the Roman and Byzantine periods. The

temperature of the waters, which is stated to come out with high pressure from the fractures formed as a result of faulting, is 46°C. Its pH value is 6.8-7 and its radioactivity value is 6.9-12.1 eman. It is stated that the hot spring waters, which are known to be good for skin diseases due to their sulfur content, are also beneficial for joint, muscle, rheumatism disorders and stress disorders (URL-5, 2023; URL-6, 2023).

3.2. Bursa

The thermal water resources in Bursa are located in a large area in the northern part of Uludağ. Thermal waters are around 46-82 °C and discharge to Çekirge and Kükürtlü regions (URL-7, 2023). The main thermal springs in the city are Kükürtlü, Tümbüldek, Oylat, Çekirge, Horhor, Zeyni Nine and Gemlik (Terme) Thermal Springs (URL-3, 2023). Due to the rich minerals in Bursa thermal spring waters, it is used as a complementary treatment in the treatment of many diseases, such as rheumatic, nervous, skin, urinary tract, and gynecological diseases, with the advice of a doctor (Alkan, 2020:53). Information about the main thermal springs in Bursa is summarized below:

3.2.1. Kükürtlü Thermal Springs: The Kükürtlü Thermal Springs, located in the city center, is divided into two parts Small Kükürtlü for women and Büyük Kükürtlü for men. These sulfurous waters are at a temperature of 87 °C and are known to be suitable for peripheral vascular and inflammatory diseases (URL-8, 2023).

3.2.2. Tümbüldek Thermal Waters: The temperature of the water of the spring, located in the village of Akarca within the borders of Mustafakemalpaşa district, is 51°C. It is known that these waters with sodium-calcium bicarbonate are good for cardiovascular, stomach, intestine, liver, and gall bladder diseases (URL-9, 2023; URL-10, 2023).

3.2.3. Oylat Thermal Waters: These thermal springs, which are 27 km away from İnegöl district, are the first healing waters that come to mind in the Marmara Region. Located in an area surrounded by trees in the southeast of Uludağ, this spring is at an altitude of 840 m from the sea. Various properties of Oylat thermal water, which is acrotothermal water, are given in Table 1 (URL-3, 2023).

Table 1: Various Properties of Oylat Thermal Water

Resources	Temperature (°C)	pH	Mineral Content
Oylat Bath	40	7,26	Sulfate, bicarbonate, calcium
Sızı Water	30,5	7,18	Sulfate, bicarbonate, calcium
Göz Water	10	3,04	Sulfate, hydrogen ion, iron

3.2.4. Çekirge Thermal Waters: The hot springs connected to the Vakıfbahçe spring are located in Çekirge and all the hotels in this district are connected to these hot springs. Various properties of Çekirge thermal water are given in Table 2 (URL-3, 2023).

Table 2: Various Properties of Çekirge Thermal Water

Resources	Temperature (°C)	pH	Properties	Mineral Content
Vakıfbahçe	47	6,98	Hyperthermal, hypotonic, oligomitalic and radioactive	Bicarbonate, sulfate, calcium, magnesium
Karamustafa	58	6,6	Hyperthermal, hypotonic, radioactive	Bicarbonate, sulfate, calcium, magnesium
Kaynarca and Yenikaplıca	77	6,78	Hyperthermal, hypotonic	Bicarbonate, sulfate, calcium, sodium
Kükürtlü	78	6,44	Hyperthermal, hypotonic	Bicarbonate, sulfate, calcium, sodium, carbon dioxide, sulfur

3.2.5. Horhor Thermal Waters: These thermal waters in the city center are 40 °C acrothermal water and many facilities benefit from this source. It is stated that these thermal waters, which are known to be very beneficial for low back pain, nerves, joints, and tissues, are recommended as supportive treatment (Alkan, 2020:55).

3.2.6. Zeyni Nine Thermal Waters: The waters of Yıldız Termal and other accommodation facilities on the way to Uludağ are fed from this source, and there are 8 touristic facilities, 15 municipal licensed facilities, and 2 baths in this region (Alkan, 2020:54).

3.2.7. Gemlik (Terme) Springs: It is stated that this hot spring, located on the road to Umurbey village in the Gemlik district, is good for rheumatic diseases, mental fatigue, and heart diseases (URL-11, 2023).

3.3. Yalova

The thermal springs, located 12 km from the city center, are among the important thermal springs of our country and are known as Yalova-Thermal and Armutlu Springs (URL-12, 2023). For many years, people have been coming to find healing from the hot springs, where transportation to the region is very easy. In general, the diseases that Yalova thermal waters are good for are rheumatism, sciatica, digestive system, kidney, female, gall bladder, urinary tract, liver, and skin diseases (URL-4, 2023).

There are four different springs in the hot spring area, which is 100 meters above the sea. The characteristics of these sources also differ from each other.

3.3.1. Yalova Main Source: Water temperature is 57 °C, pH value is 7.66, radioactivity value is 2.89 eman.

3.3.2. Valide Hanım Kurna Head: The water temperature is 56 °C and the pH value is 7.46.

3.3.3. Valide Hanım Spring: Water temperature is 64 °C, pH value is 7.48, radioactivity value is 0.57 eman.

3.3.4. Yalova Eye Water: Water temperature is 55 °C, pH value is 6.88, radioactivity value is 4.2 (URL-5, 2023)

3.4. Denizli

Due to its geographical location, being in a central place that connects many places and having thermal water resources, Denizli has become a center of attraction with its historical and cultural values. The fact that Pamukkale, which is world-renowned, is located within the borders of the province, has become one of the places frequented by tourists (URL-5, 2023). Denizli is a very rich province in terms of thermal water resources. Sarayköy, Akköy Gölemezli, Buldan Tripolis, Çardak Beylerbeyi, and Pamukkale are among the main thermal centers known within the provincial borders.

3.4.1. Sarayköy Thermal Center: Sarayköy district, located on the Denizli-Aydın-İzmir highway, is very rich in terms of geothermal resources. One of the

most important of these resources is the 4 facilities located in the geothermal area in Hamamaltı near Karataş Village. The temperature of the thermal water, which is good for rheumatism, skin, gynecological diseases, and urinary tract diseases, is 80 °C (URL-13, 2023).

3.4.2. Akköy Gölemezli Thermal Center: Akköy Gölemezli Thermal Tourism Center is close to Pamukkale Special Environmental Protection Area. In addition to thermal tourism, geothermal resources in the district are also used in terms of geothermal greenhouse cultivation. The temperature of the thermal water changes around 35-60 °C, and it is good for diseases such as skin, hemorrhoids, calcification, and rheumatism (Aksu and Aktuğ, 2011:17).

3.4.3. Buldan Tripolis Thermal Center: The temperature of the thermal water in the Çizmeli (Yenice) Thermal Springs, which is 16 km away from the town of Buldan, is 56 °C, and it is suitable for rheumatism, atherosclerosis, liver failure, skin, stomach, and kidney ailments (Aksu and Aktuğ, 2011:17).

3.4.4. Çardak Beylerbeyi Thermal Center: This thermal center, which is 20 km from the town and 78 km from the center, is 3 km from the center of Beylerli (URL-6, 2023).

3.4.5. Pamukkale Thermal Waters: Pamukkale was included in the UNESCO world heritage list in 1988 and has become an important tourism center located near the ruins of the archaeological city of Hierapolis (Unesco, 2018). Pamukkale is a structure consisting of white-colored travertines precipitated by the lime solution in its structure, evaporation, and the decomposition of carbon dioxide in the water (Boyraz and Çetin, 2019:87). The temperature of the thermal water is 35 °C and it is recommended by the doctor that it will be useful in rheumatism, cardiovascular, paralysis, nervous system, skin, and eye disorders (URL-3, 2023).

4. RESULTS

Due to its geographical location, Turkey acts as a bridge connecting the East and the West. Tourists who know the benefits of thermal waters come to our country, which has a favorable climate and rich geothermal resources. In the thermal facilities, which are preferred to support the healing of ailments with the advice of a doctor, people are healed on the one hand and have fun and rest on the other. However, the opportunities for thermal water resources could not be utilized at the desired international level. For more people to benefit from the

regions where thermal water resources are located in our country, initiatives should be initiated to increase the number of existing facilities and to ensure that the facilities are operated in all months of the year. Unfortunately, although many people know the benefits of thermal water, they cannot benefit from it because they cannot allocate a budget for this area. For this purpose, increasing the number of thermal facilities with government support and an environmentalist approach will encourage competitive tourism. In order to attract tourists from abroad to thermal waters and to increase their utilization rates, it is necessary to properly introduce the thermal water resources in different provinces of our country and to offer advantageous holiday opportunities. In this context, increasing the promotion of thermal water resources is very important both for tourists and for the economy of our country.

REFERENCES

- Aksu, C., ve Aktuğ, E. (2011). Güney ege bölgesi termal turizm araştırması. Güney Ege Kalkınma Ajansı, 1-43.
- Alkan, F. (2020). Bursa'nın şifalı kaplıcaları ve bursa müzelerinde sergilenmeleri. Afyon Ve İstanbul Uluslararası Türk-İslam Tıp Tarihi ve Etiği Kongreleri (2018-2019), 51-60, Konya.
- Boyras, M., ve Çetin, A. (2019). Termal otel işletmelerinde jeotermal kaynak kullanımının yönetici bakış açısıyla değerlendirilmesi: denizli ili örneği. Süleyman Demirel Üniversitesi Vizyoner Dergisi, 10(23), 84-98.
- Ekiz, E., ve Yazıcı, H. (2016). Termal turizmde farklı bir destinasyon: jeoturizm (afyonkarahisar örneği). ZfWT, 9(1), 67-81.
- Erdoğan, E., ve Aklanoğlu, F. (2008). Termal turizm ve afyon-gazlıgöl örneği. Natural and Applied Sciences, 3(1), 83-92.
- Özbek, D., ve Özbek, T. (2011). Jeotermal kaynakların sağlık ve termal turizmde değerlendirilmesi. Haber Bülteni, 99-113.
- Özşahin, E., ve Kaymaz, Ç.K. (2013). Türkiye'nin termal su kaynaklarının coğrafi açıdan değerlendirilmesi. Atatürk Üniversitesi Edebiyat Fakültesi Sosyal Bilimler Dergisi, 50, 25-38.
- Taş, B. (2012). Afyonkarahisar ilinde termal turizmin gelişimi. SDÜ Fen Edebiyat Fakültesi Sosyal Bilimler Dergisi, 26, 139-152.
- Unesco, (2018). World Heritage List, Hierapolis-Pamukkale.<http://whc.unesco.org/en/list/485> Access: 21.03.2023
- URL-1, 2023 <https://www.enuygun.com/bilgi/turkiye-nin-termal-haritasi/> Access: 15.03.2023
- URL-2, 2023. <https://serapool.com/termal-su-nedir> Access: 15.03.2023
- URL-3, 2023. <https://shgmturizmdb.saglik.gov.tr/Eklenti/10949/0/07pdf.pdf> Access: 16.03.2023
- URL-4, 2023. <http://www.kaplicalar.org> Access: 16.03.2023
- URL-5, 2023. <https://termalrehber.com/kaplicalar> Access: 16.03.2023
- URL-6, 2023. <https://www.kulturportali.gov.tr/turkiye/afyonkarahisar/TurizmAktiviteleri/heybeli-kaplicasi> Access: 16.03.2023
- URL-7, 2023. Bursa İli 2020 Yılı Çevre Durum Raporu Access: 17.03.2023
- URL-8, 2023. <https://www.gotobursa.com.tr/tr/mezan/kukurtlu-kaplicasi-401/> Access: 17.03.2023
- URL-9, 2023. <https://www.mustafakemalpasa.bel.tr/ilcemiz/tumbuldek-kaplicalari.html> Access: 18.03.2023
- URL-10, 2023. <https://www.bursa.com.tr/tr/mezan/tumbuldek-kaplicalari-ve-icmeleri-406/> Access: 20.03.2023

- URL-11, 2023. <https://www.kulturportali.gov.tr/turkiye/bursa/turizmaktiviteleri/gemlik-terme-kaplicalari> Access: 20.03.2023
- URL-12, 2023. <https://www.yalova.bel.tr/sayfa/kaplicalar> Access: 21.03.2023
- URL-13, 2023. <https://www.yatirimadestek.gov.tr> Access: 21.03.2023
- Zengin, B., ve Eker, N. (2016). Sakarya ili termal turizm potansiyelinin değerlendirilmesi. Kastamonu Üniversitesi İktisadi ve İdari Bilimler Fakültesi Dergisi, Temmuz, 13.

Chapter 13

Comparison of Incentives and Supports Applied in Utilizing Solar Energy in Turkey and Germany

Murat BATAN¹

¹ Asst. Prof; Batman Üniversitesi, Mühendislik-Mimarlık Fakültesi, İnşaat Mühendisliği Bölümü, muratbatan@yahoo.com, ORCID No: 0000-0002-9207-4730.

ABSTRACT

Greenhouse gases cause global warming as well as their polluting effect. Many countries have focused to RES (renewable energy sources) to reduce their greenhouse gas emissions. In this study, Turkey which has a high solar energy potential, and Germany one of the leading countries in benefiting from solar energy were compared. Despite the low solar energy potential of Germany, the reasons of how it obtained this success were investigated. For this purpose, incentives and supports given to solar energy in Turkey and Germany and the targets of both countries in this field were examined. In the examinations, it was determined that Germany stood out with a few important incentives. The most important of these is the purchase at a fixed price for 20 years of electricity produced from RES. In addition, reducing of the power plant costs thanks to Germany's advanced technology, the purchasing from higher price of electricity generated from solar energy and its strong and stable economic structure have also increased investments. Giving comprehensive incentives for solar energy for only 16 provinces within the scope of the 6th region in Turkey have effected partially negative the investments. In addition, the purchasing from a lower price of electricity produced from solar energy in Turkey, purchase period for 10 years, the instability, fluctuations in exchange rates have adversely affected investments. It is expected that this study will be a guide for Turkey and other countries that want to invest in renewable energy resources to ensure that they can use their potential in the best way.

Keywords: Solar energy, incentives, Turkey, Germany, European Union

1.INTRODUCTION

Today, there are many negativities that are thought to be caused by climate change. These negativities are the increase in natural disasters such as overheating, drought, storms, floods and forest fires. The increase in natural disasters causes destructions and decrease in agricultural production in many regions. As a result, very serious financial losses and loss of life are experienced (Batan, 2014).

Therefore, after the 1990s, governments, scientists, non-governmental organizations in many countries work on reducing the negative effects of climate change and organize meetings and congresses. As a result of these efforts, it was agreed that a very important part of global warming is caused by human influence (IPCC, 2021). The idea that greenhouse gases such as CO₂, CO, SO₂, N₂O, CH₄, HFCs, which are released by human beings as a result of various processes trigger warming has now been proven as a result of scientific studies. Greenhouse gases are caused by fossil fuels such as coal, oil and natural gas which are used to generate energy (Ozcan, 2018).

Two-thirds of greenhouse gases emitted in the world originate from energy production (Ozcan, 2018). For this reason, many countries are now in search of clean and continuous energy sources. For this reason, there has been a trend towards energy sources such as solar energy, wind energy, hydraulic energy, biomass energy, geothermal energy which are defined as renewable energy sources. Solar energy which has the greatest potential and can be utilized in many countries in the world, comes to the fore among these energy sources.

The sun emits 174 peta-watts energy. The amount of the solar energy absorbed by the lands and oceans is 89 PW. This amount is 2850 times more than the energy demand in the World (Park and Eissel, 2010). Solar energy potential that can be used in the world is 120,000 TWh. Wind energy potential, Hydraulic energy potential, geothermal energy potential and energy potential that can be produced from oceans including tides are 2-4 TWh, 0.5 TWh, 12 TWh, 2 TWh respectively (Enerji ve Çevre, 2017). The energy coming from the sun is equal to 50 times of the coal reserves and 800 times of the oil reserves (Dinçer, 2011). These numbers show clearly the potential of solar energy.

In practice, the usage amount of solar energy in energy production is ahead of other renewable energy sources. The total renewable energy capacity excluding hydraulic energy in the world is 1179 GW in 2018. Solar energy capacity is 480 GW in 2018. This corresponds to around 41% of the total renewable energy capacity (Celik and Ozgur, 2020). 127 GW of the 325 GW electricity generation plants in 2020 consists of solar power plants (Solar AVM, 2022). The installed solar power capacity in the world is expected to increase by

1 TW by 2030 (Chen and et all., 2018). Thanks to the increase in the support given to R&D(research and development) investments and the developing technology, the first investment cost of renewable energy power plants is decreasing day by day. Together with the incentives given today, it has come to a position to compete with fossil fuels (Saygin and Godron, 2018).

There are also some reasons that make it necessary to transition to RES.The polluting effect of fossil energy sources and the fact that they will be depleted in the near future are some of these reasons. In addition, some countries need to transition to renewable energy sources in order to get rid of foreign dependency in energy (Park and Eissel, 2010).

The regions with high solar energy potential in the world are shown on the map given in Figure 1 below. According to the map, most of the continent of Africa and Australia, Saudi Arabia, the southwestern parts of the America, the northeastern parts of South America, and most of Iran are regions with high solar energy potential (Alshahrani and et all., 2019).

In this study, in section 1, the solar energy potential in the world, the regions with high solar energy potential, the reasons for the transition to renewable energy sources were explained. In section 2, historical development in utilizing solar energy, usage areas of solar energy and leading countries in benefiting from solar energy were given. In section 3 were examined incentives and supports given to solar energy in Germany one of the leading countries in solar energy technology and investments in the world and in Turkey which is one of the countries with the largest solar energy potential in Europe. Since Germany is a member of the EU and Turkey is in the EU accession process, incentives and supports given to RES in the EU and EU's targets and achievements in this field were given first in section 3. In section 4, The reasons why Germany is one of the leading countries in solar energy were discussed in order to guide to Turkey in using its high potential. In section 5, the conclusions drawn from the discussions in section 4 were given. Suggestions were presented to increase solar energy investments in Turkey. In addition, the reasons why RES investments should be increased in both countries were explained in section 5.

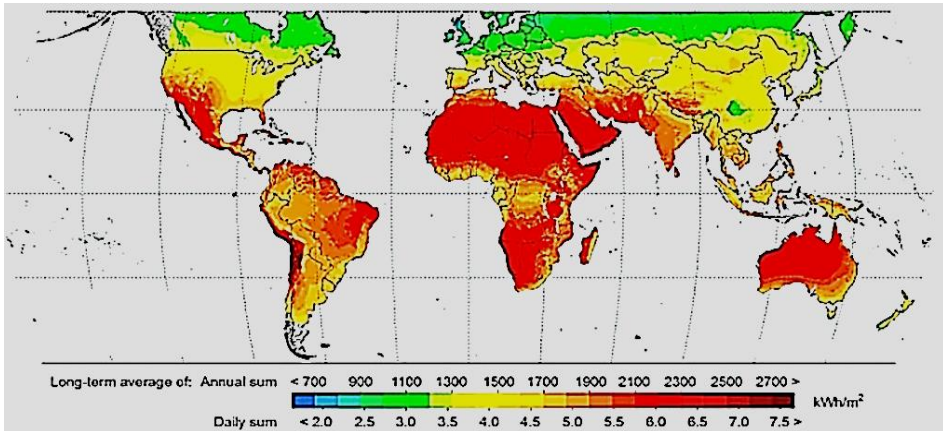


Figure 1. Regions with high solar energy potential in the world
(Alshahrani and et al., 2019).

2.HISTORICAL DEVELOPMENT OF SOLAR ENERGY USE, USAGE AREAS OF SOLAR ENERGY AND LEADING COUNTRIES IN SOLAR ENERGY USE

2.1.Historical development in utilizing solar energy

In order to see the progress in the use of solar energy, it is necessary to look at its historical development. The first application of solar energy was made in 215 BC by Archimedes, who reflected and burned the sunlight on the ships besieging Syracuse (Kaplukan, 2014).

Solar energy utilization increased in the 17th century with using of the lens by Galileo (Kaplukan, 2014). The first solar collector was made by the Swiss scientist Horace de Saussure in 1767. French physicist Alexandre-Edmund Becquerel discovered the photovoltaic effect by inventing a device that can measure light intensity in 1839. In this device, solar energy is absorbed and electrons are separated from atoms. An electrical effect is created with this way (Girgin, 2011), (DEK-TMK, 2009).

British scientist Willoughby Smith discovered that selenium is a photoconductor in 1873. American explorer Charles Fritts made the world's first working solar cell by coating selenium with a very thin layer of gold in 1884. Later, French engineer Charles Tellier designed the first non-condensing and non-reflective solar machine (DEK-TMK, 2009).

The first commercial applications in solar energy were made in America. American Aubrey Eneas conducted solar machine experiments and founded "The Solar Motor Corporation", the world's first solar power company in 1892. Albert Einstein won the 1921 Nobel Prize in Physics for her article on the Photoelectric Effect in 1905. Following the work of Russell Ohl in 1946 Gerald

Pearson, Calvin Fuller and Daryl Chapin built the first silicon solar cell with 6% efficiency in 1954 (Girgin, 2011), (DEK-TMK, 2009). PV(photovoltaic) power systems were used in space studies since the early 1960s (Girgin, 2011).

The first industrial type plant was established in the United States with 384 MW parabolic mirror system in 1984. Solar tower systems began to be established in the 1990s. Investments in solar energy increased in the 2000s and there were great developments especially in PV industry production (DEK-TMK, 2009).

2.2.Usage areas of solar energy

Solar energy is generally used for two purposes. One of them is electricity generation and the other is heat generation. Apart from these two purposes, there are also different uses of solar energy albeit limited. Different technologies are used to benefit from solar energy and the efficiency of these technologies is increasing day by day and their costs are decreasing (Girgin, 2011).

Planar and vacuum solar collectors are used to obtain heat from solar energy at home, in industry and in swimming pools. Black painted solar pools are used to collect and store heat. Trompe wall is generally used for heating in barns. Solar chimneys working on the principle of movement of heated air are used to generate electricity. PV systems and concentrated systems are also from active methods using to produce electricity directly from solar energy (Kateroğlu, 2022), (Girgin, 2011).

In addition, It is used in water purification obtaining clean water by distilling the steam obtained by evaporating water with solar energy. Solar energy is used for heating, cooling and lighting the housings with the changes made in the structure and design of the housings. The solar pan is generally used for cooking with solar energy in villages or in underdeveloped countries where there is no electricity (Kateroğlu, 2022), (Girgin, 2011).

2.3.Leadng countries in benefiting from solar energy

The leading countries in energy produced from renewable energy plants including hydraulic energy in the world according to 2022 data are China, the United States, Brazil, Germany and Japan respectively (IRENA, 2023). The ranking in per capita RES capacity in the world are Denmark, Germany, Sweden, Spain and Portugal respectively (Kateroğlu, 2022).

The ranking differs slightly when only solar energy is considered. The leading countries in energy produced from SPPs(solar power plants) in the world according to 2022 data are China, the United States, Japan, Germany,

Italy. The Asian continent is first in the world with 597 GW installed solar power capacity according to 2022 data. China has 393 GW installed capacity, Japan has 78 GW installed capacity. Europe continent excluding Turkey with 227 GW installed capacity is second in the world. Germany has 66 GW installed capacity. American continent has 162 GW installed capacity. Only the United States has 113 GW installed capacity (Celik, and Ozgur, 2020), (IRENA, 2023).

The ranking is the same in the use of solar energy in PV systems. PV system capacity ranking is China, United States, Japan, Germany, Italy according to 2022 data. Concentrated SPPs are still very limited in the world. The concentrated solar energy capacity ranking with existing plants is Spain, The United States, South Africa, Morocco, India according to 2022 data (IRENA, 2023).

The ranking of the leading countries in obtaining heat from solar energy in the world are China, the United States, Germany and Turkey respectively (Kocakuşak, 2018).

As can be seen, although Germany is in almost all rankings, Turkey has only been able to enter the rankings in obtaining heat with solar collectors.

3.INCENTIVES AND SUPPORTS TO SOLAR ENERGY IN TURKEY AND GERMANY

3.1.Supports given to RES in the European Union and EU's targets and achievements in this field

In this section, It will be appropriate to give information about renewable energy policies and renewable energy targets in the EU before Germany and Turkey. Germany is a member of the EU, and Turkey is a candidate for EU membership. Because of this, Germany and Turkey look to the EU's renewable energy policies and targets as a model.

Spain, Turkey, Italy and Greece are ranked as the countries with the highest solar energy potential in Europe (Erkoç, 2018). Spain in concentrated solar energy capacity is first in the world. As can be seen, Germany is not among the countries with high solar energy potential. However, Germany has become one of the most important countries in benefiting from solar energy and other renewable energy sources in Europe and in the world thanks to its incentive policies and technology. Germany is second in PV system capacity in the world (Kocakuşak, 2018), (Kateroğlu, 2022). EU countries provide production incentives or financial incentives such as taxes and grants to increase the use of RES. In this way, the EU has become a pioneer in the world in this field. EU member countries support research and development programs and exemplary

projects in RES field. One of the most important incentives in EU is the purchase guarantee with an fixed price for a certain period of electricity produced from RES power plants. EU countries provide subsidies for initial RES investment. In addition, incentives and supports such as tax exemption or tax deduction, lower VAT rates, low-interest loans, swappable green certificates, tender calls for renewable energy projects by governments have been implemented in EU countries (Celik, and Ozgur, 2020), (Dinçer, 2011).

Thanks to these incentives and supports, the EU provided 80% of its electricity generation capacity from RES in 2022. The EU has reached a power generation capacity of approximately 570 GW from RES in 2022 (IRENA, 2023).

EU imports more than half of the energy it uses. Most of the imported energy consists of fossil fuels (EURONEWS, 2020). The EU aimed to increase the use of RES in order to reduce this dependence on energy and to eliminate the polluting effect of fossil fuels and their contribution to heating. In this scope, the EU aims to reduce to 20% below of 1990 levels the greenhouse gas emissions by 2030. In the longer term, it has aimed to completely end greenhouse gas emissions by 2050. Member states are free to set targets higher than these (Telli, Erat and Demir, 2021).

EU member states revised their renewable energy directive in 2018. According to this directive, the EU has aimed to meet from RES 32% of the total amount of energy they use until 2030. As it is known, the transportation sector has a great impact on greenhouse gas emissions. For this reason, the EU has set a separate target for the transportation sector. EU has aimed to meet from RES 10% of the energy used in the transportation sector (Telli, Erat and Demir, 2021).

Incentives and supports implemented for RES including solar energy in the EU, the EU's targets and achievements in this field are given in Table 1 below.

Table 1. Incentives and supports implemented for RES including solar energy in the EU, EU’s targets and achievements in this field

Incentives and supports implemented for RES including solar energy in the EU	Supporting research and development programs and exemplary projects in RES areas
	Guarantee of purchasing with fixed price for a certain period of the electricity produced from RES power plants
	Subsidizing some of the initial RES investments
	Tax exemption or tax deduction for RES investments
	Lower VAT rates and low-interest loans for RES investment
	Swappable green certificates
	Tender calls for renewable energy projects
EU's targets in this field	Reducing to 20% below of 1990 levels the greenhouse gas emissions by 2030
	Completely end greenhouse gas emissions by 2050
	Providing 32% of the used total energy from renewable sources by 2030
	Meeting 10% of the energy used in the transportation sector from RES
EU's achievements in this field	EU provided 80% of its electricity generation capacity from RES in 2022
	EU has reached a power generation capacity of approximately 570 GW from RES in 2022
	EU produced about 200 GW of energy from the sun in 2022 year.

Sources: (Celik, and Ozgur, 2020), (Dinçer, 2011), (Telli, Erat and Demir, 2021), (IRENA, 2023).

3.2.Incentives and supports given to solar energy in Germany and Germany’s targets and achievements in this field

Germany is substantially dependent on foreign energy. According to 2020 year, Germany's dependence on foreign energy is 64%. Most of the imported energy consists of fossil resources (EURONEWS, 2020). Energy use is responsible for 80% of Germany's greenhouse gas emissions. In order to get rid of foreign dependency in energy and to reduce greenhouse gas emissions, Germany has turned to RES and set some targets.

Germany published an “energy concept report” in 2010. Right after that, in 2011, Germany declared "Energiewende", which means energy transition in german. In the same year, he prepared a "special action plan" (Telli, Erat and Demir, 2021). With these processes, the transition to RES accelerated and the use of fossil fuels began to decrease.

Germany has set a target of reducing greenhouse gas emissions by 40% below of 1990 levels by 2030. In the long term, it has set a target of about 90%

below 1990 levels by 2050 (Telli, Erat and Demir, 2021). In line with this target, Germany targets to consume 20% less fossil fuels by 2050 (Renn, and Marshall, 2016).

Germany aims to reduce from 41 GW to 17 GW its installed coal plants by 2030. In this way, it has been calculated that Germany can reduce greenhouse gas emissions by 60% in the energy sector (Telli, Erat and Demir, 2021). Along with fossil fuels, Germany wants to phase out nuclear power 2050 (Renn, and Marshall, 2016). Germany decided to close 8 old nuclear power plants after the Fukushima nuclear power plant disaster in 2011. In addition, Germany focused on energy efficiency with *Energiewende* (Inderberg, Tews, and Turner, 2018).

These efforts of Germany yielded results and in 2018, the share of RES with 40% in electricity production exceeded coal which remained 39%. Germany is the country with the largest share in electricity production and consumption from wind, solar and biomass energy among EU countries (Telli, Erat and Demir, 2021). Germany produced approximately 148 GW of energy from RES in 2022 (IRENA, 2023). In Germany's energy mix, RES now account for 14.7% of the total. Between 2000 and 2018, Germany's net energy imports decreased by 12% (Telli, Erat and Demir, 2021). Germany has not reached this success only because of its renewable energy potential. Investments in its innovative technologies and advanced industry have played a major role in this success.

One of the countries with the least sunlight in the world is Germany. Despite this, Germany has achieved significant advances, particularly in the field of solar energy (Telli, Erat and Demir, 2021). Germany produced about 66 GW of energy from the sun in 2022. Germany generated electricity from the sun around 7 times more electricity than Turkey which has significant solar energy potential in 2022 (IRENA, 2023).

Germany is home to six of the world's top producers of solar panels. This shows that how much solar technology has advanced in Germany (Dunford, and et al., 2013). Germany's PV system capacity is fourth in the globe (IRENA, 2023). It has risen to the first place in the world in per capita PV system capacity (Kateroğlu, 2022). PV systems now account for 8.4% of Germany's electricity generation (Raghoebarsing, and et al., 2022).

Incentives and supports applied to RES including solar energy in Germany, Germany's targets and achievements in this field are summarized in Table 2 below.

Table 2. The incentives given to RES including solar energy, in Germany, the targets and achievements of Germany in this field.

Incentives and supports implemented for RES including solar energy in Germany	-Long-term loans with low interest rates
	-Grant funding to cover a portion of the initial installation expenses for new RES plants
	-20 year fixed price purchase guarantee with a feed-in tariff (FIT) for electricity generated from RES
	-Adjusting energy purchase costs in accordance with market circumstances
	-Establishing different purchase prices for various renewable energy types
	-Raising tariff prices for electricity produced from RES
	-Creating guides and booklets that outline the advantages of RES and the steps involved in installing a power plant
Germany's targets in this field	-Giving extra incentives for small scale rooftop solar power plants between 1 kWp and 10 kWp
	-Germany targets to lower 40% its greenhouse gas emissions compared to 1990 levels by 2030.
	-Germany targets to lower about 90% its greenhouse gas emissions compared to 1990 levels by 2050.
	-Germany targets to cut the installed coal capacity of its power plants from 41 GW to 17 GW by 2030.
	-Germany targets to boost to 65% the proportion of electricity produced from RES by 2030.
	- In accordance with EU targets, Germany wants to phase out fossil fuels. In this scope, Germany has set a target to consume 20% less fossil fuels by 2050.
	-Germany plans to gradually end nuclear power plants.
Germany's achievements in this field	-Germany targets to raise energy efficiency within the scope of Energiewende.
	-49% of the electricity was generated with RES in 2022 year. With this ratio, electricity generation from RES has surpassed electricity generation from coal which is Germany's largest energy source.
	-The proportion of RES in the energy mix in Germany was climbed to 14.7%.
	-Between 2000 and 2018, Germany's net energy imports fell by 12% as a result of a rise in the use of renewable energy.
	-Germany reached 66 GW solar power generation capacity in 2022 year.
	-Regarding PV system capacity, Germany is fourth in the globe. It has risen to the first place in the world in per capita PV system capacity.
	-The percentage of PV in the generation of power rose to 8.4%.
	-Germany has started to the production of electric vehicles that reduce greenhouse gas emissions in the transportation sector.

Sources: (Park and Eissel, 2010), (Telli, Erat and Demir, 2021), (Kateroğlu, 2022), (Erkoç, 2018), (Renn, and Marshall, 2016), (Inderberg, Tews, and Turner, 2018), (Raghoebarsing, and et all., 2022), (IRENA, 2023).

3.3.Incentives and supports given to solar energy in Turkey and Turkey's targets achievements in this field

Turkey is substantially dependent on foreign energy like Germany. Turkey imports about 70% of the energy it needs. This rate will decrease a little with the natural gas reserves found in the Black Sea. However, natural gas is also a fossil energy source. Turkey's emissions of greenhouse gases must drop by 21% by 2030 year with the Paris climate agreement signed in 2015. For this reason, Turkey invests to energy production from renewable clean energy sources (Telli, Erat and Demir, 2021).

Turkey aims to end its greenhouse gas emissions by 2050 in line with EU targets. In the past ten years, Turkey has tripled its capacity to produce power using RES (Telli, Erat and Demir, 2021). Turkey's installed electricity generation capacity is 103,809 MW in 2022 year (ETKB, 2022). The amount of energy produced with RES in Turkey has climbed to about 56 GW in 2022 thanks to incentives and legal regulations (IRENA, 2023). Turkey now produces more than half of its electricity from RES. Turkey has accomplished this as a result of its more renewable, more domestic approach (Telli, Erat and Demir, 2021).

In addition, Turkey has joined the Paris Climate Agreement, thus the World Bank and some other organizations have given Turkey a loan of 3 billion 150 million dollars to cut its greenhouse gas emissions (Anadolu Ajansı, 2021). This means that Turkey will increase its RES investments in the coming period.

Turkey is one of the countries with a great potential for solar energy. Electricity generation from solar energy in Turkey has shown great development in recent years. Electricity generation capacity from the sun in Turkey has reached approximately 10 GW in 2022 (IRENA, 2023). PV systems account for 6% of Turkey's electricity production (Raghoebarsing, and et all., 2022).

Turkey produced the first domestic electric car TOGG in 2023 in order to reduce greenhouse gas emissions in the transportation sector and to close the foreign trade deficit (Telli, Erat and Demir, 2021).

Incentives and supports given to solar energy in the Turkey, Turkey's targets and achievements in this field are summarized in Table 3 below. In the table, incentives and supports within the scope of the 6th region in Turkey were given. Significant incentives are also provided for the provinces in the 4th and 5th regions in solar energy. However, the incentives given for the 16 provinces in the 6th region generally covering the eastern provinces are more comprehensive than the incentives in all other regions (Ulusal Müşavirlik, 2022).

Table 3. Incentives and supports given to solar energy in Turkey, Turkey's targets and achievements in this field

6th region incentives and supports applied in solar energy in Turkey	-Guaranteed fixed-price purchases for 10 years with feed in tariff(FIT) incentive for the electricity generated from RES.
	-Establishing different purchase prices for various renewable energy types
	-Allotment of land
	-Obligation for retail power providers to buy the electricity generated by RES.
	-Exemption from the requirement to get a license the renewable energy facilities up to 5 MW
	-Discount on the license charge for plants that need a license
	-Additional fee contribution up to 5 years when domestic equipment is utilized
	-VAT exemption for procurement of machinery and equipment purchased for SPP
	-Exemption from customs taxes while purchasing machinery and equipment for SPP from abroad
	-50% reduction in income taxes
	-10 years of insurance premium exemption
	-5 years of property tax exemption
Turkey's targets in this field	-Exemption from the municipality's building permit fees
	-According to the Paris Agreement, Turkey targets to cut its greenhouse gas emissions by 21% by 2030.
	-Turkey targets to end its greenhouse gas emissions by 2050 in line with EU targets.
	-Turkey targets to boost to 63 GW the amount of energy generated from RES by 2024.
	-Turkey aims to increase above 38% the share of renewable energy in 2023.
	-Turkey aims to reduce by 14% the primary energy consumption rate by 2023.
	-Turkey aims to use 14.8 billion tons of domestic lignite and hard coal resources by 2023 year.
Turkey's achievements in this field	-Turkey aims to use all of its hydraulic potential until 2023 year.
	-Energy production from RES of Turkey has increased to approximately 56 GW in 2022 year.
	- In the past ten years, Turkey has tripled its capacity to produce power using RES.
	-Electricity generation capacity from the sun in Turkey has reached approximately 10 GW in 2022 year.
	-PV systems account for 6% of Turkey's electricity production.
	-Turkey started to invest to solar energy more than Germany in 2017.
	-The World Bank and some other organizations have given to Turkey a loan of 3 billion 150 million dollars to cut its greenhouse gas emissions.
	-Turkey started to produce electric vehicle that reduce greenhouse gas emissions.

Sources: (Telli, Erat and Demir, 2021), (Ozcan, 2018), (Dinçer, 2011), (KUZKA, 2016), (Raghoebarsing, and et all., 2022), (ETKB, 2014), (Ulusal Müşavirlik, 2022), (Sirin, and Yilmaz, 2021), (Atmaca, 2019), (Arnoğlu Akan, and et all., 2015), (Anadolu Ajansı, 2021), (IRENA, 2023).

4.EVALUATION AND DISCUSSION

Turkey gets 60% more sunlight than Germany. Germany ranks among the places with the least amount of sunlight worldwide (Telli, Erat and Demir, 2021). This is clearly seen in the map given in Figure 2 below. While more than half of Germany is shown in green on the map most places in Turkey are shown in red. The rest of Germany is shown in yellow on the map. As can be seen from the scale on the map, the solar energy potential decreases from red to blue. While Turkey has an annual solar energy technical potential of 189 GWh, Germany's annual solar energy technical potential is 71 GWh (Karagöl, ve Kavaz, 2017).

Turkey is in the second rank after Spain in Europe in solar energy potential (Telli, Erat and Demir, 2021), (Erkoç, 2018). However, Turkey was unable to fully utilize its potential. According to data from 2022 year, Germany which has a far lower potential than Turkey generated electricity from the sun around 7 times more from Turkey (IRENA, 2023). In this study, the reasons of this success of Germany were investigated. For this, incentives and supports given to solar power plants in both countries were examined. In addition, the incentives in both countries were compared with the incentives given in the EU.

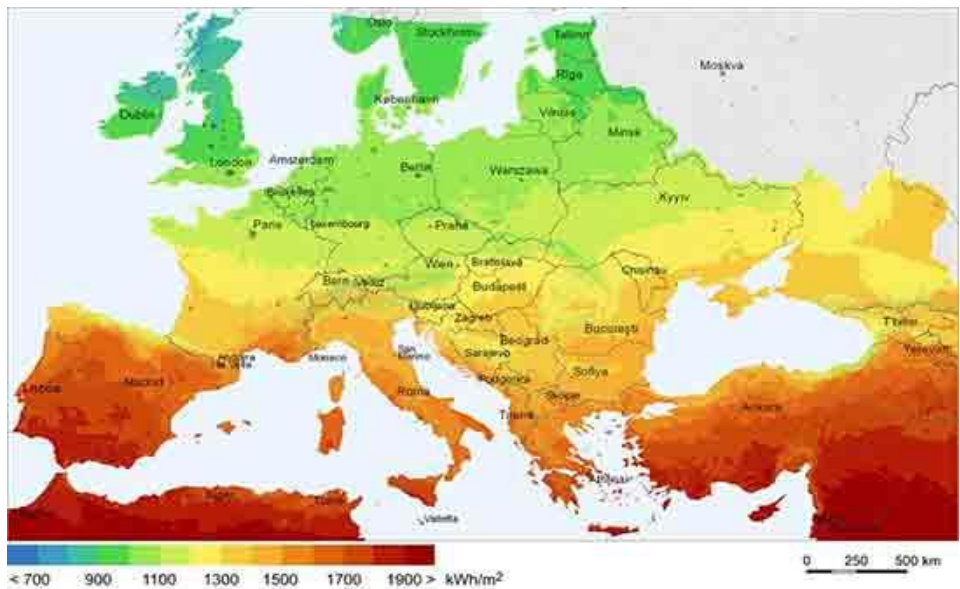


Figure 2. Regions with high solar energy potential in Europe
(ENERJİ.GEN, 2023).

In the comparisons made, it was determined that EU, Germany and Turkey are giving important incentives such as fix price purchase assurance to the

power generated by SPP for a certain period, tax exemption, grants and low-interest loans.

However, Germany differs positively from Türkiye and EU in some incentives. The most significant of these is that Germany buys electricity generated by solar power projects for 20 years at a fixed price (Park and Eissel, 2010). This period is 10 years in Turkey (Telli, Erat and Demir, 2021), (Ulusal Müşavirlik, 2022). In addition, Germany updates its purchase prices according to market conditions (Erkoç, 2018). It has been determined that government purchase prices in Turkey lag behind market conditions (EPİAŞ, 2023). Germany reflects on the bills of consumers under the name of “renewable energy contribution” the incentives and grants it gives to renewable energy plants (Norm Enerji, 2012). In this way, these supports given to renewable energy power plants are shared by all citizens. In this way, the government can contribute more to RES. Thus, Germany has kept higher the purchase price of electricity produced from RES and longer the purchase period at a fixed price. Investments to RES are increasing with such regulations.

It has been determined that Germany supports small-scale rooftop solar power systems with a capacity of 1 kWp to 10 kWp in order to satisfy consumer demand (Park and Eissel, 2010), (Telli, Erat and Demir, 2021). Germany provides support for the initial installation cost of rooftop power plants. Since the consumers use themselves most or all of the energy they produces, the government hasn't to purchase the electricity produced from the rooftop power plant at a fixed price for 20 years. This will not bring a burden on both the state and to the citizen which is reflected its bill. In addition, since the electricity produced is not given to the grid, transmission line investments are decrease.

For increaeasing RES investments, Germany creates guidelines and booklets outlining the advantages of RES and what needs to be done for power plant installation. In this way, Germany encourages the public and large investors to invest in this area by raising awareness. The intense demand of the people for small rooftop power plants in Germany also shows the importance of this awareness and incentives (Park and Eissel, 2010).

Turkey and Germany produce almost all of the electricity generation from the sun with PV systems (IRENA, 2023). Germany is home to six of the world's top producers in PV panels (Dunford, and et all., 2013). Germany's progress in PV technology reduces also the initial investment costs of SPP. In addition, Germany's developed industry and strong economic structure are also attractive to investors.

As mentioned above, some important incentives are given to RES in Turkey. In addition to these, incentives such as land allocation, license exemption,

property tax exemption, insurance premium exemption, customs tax exemption are also given in Turkey. SPP investments are increasing rapidly thanks to these incentives. However, Turkey was late in RES investments compared to Germany. Turkey has started to give serious incentives to RES investments in the last 10 years. In the past ten years, Turkey has tripled its capacity to produce electricity using RES. Turkey invested more than Germany to solar energy in 2017 (Telli, Erat and Demir, 2021).

Despite this progress, considering Turkey's potential in solar energy, it is known that, Turkey does not fully use its potential in this area. Turkey must increase to 20 years the fixed price purchase guarantee period of electricity produced from RES in order to increase investments. However, although the state obliges retail electricity companies to purchase electricity produced from RES, this burden indirectly affects the state (Ulusal Müşavirlik, 2022), (Sirin, and Yilmaz, 2021). Because, electricity companies will have to give price by taking this situation into account in the tenders. For this reason, since the incentives and supports given in Turkey are not reflected to consumer bill, the purchase price of electricity and the purchase guarantee period from the fixed price are lower. When some legal regulations in Turkey and Germany are examined, consumers are encouraged to produce electricity as much as they need. This is thought to be one of the reasons why electricity purchase prices have not been raised sufficiently.

However, more support should be given to this area in Turkey due to the higher initial investment cost of small-scale rooftop solar power plants. In addition, the number of domestic manufacturers in Turkey should be increased in order to reduce the initial investment costs. More resources should be allocated to R&D research in order to increase the efficiency and reduce the cost of high-tech products such as panels and inverters in Turkey.

The biggest contradiction in Turkey is to support lignite and coal from fossil energy sources besides supporting RES investments (Ozcan, 2018). Since Turkey is a developing country, annual electricity consumption has increased by approximately 7% in recent years (Arioğlu Akan, and et al., 2015). Turkey gives incentives for the extraction of 14.8 billion tons of domestic lignite and hard coal in order to meet this need (Ozcan, 2018), (Arioğlu Akan, and et al., 2015). This reduces the competitiveness of RES investments which already have high initial investment costs with fossil energy investments. In addition, this situation makes it difficult for Turkey to fulfill its greenhouse gas emission obligations according to the Paris agreement (Ozcan, 2018).

5.CONCLUSIONS AND SUGGESTIONS

When the incentives and supports in two countries and the EU are examined, it is seen that Turkey does not have a very important deficiency in solar energy except a few incentives. The main problem in Turkey is the delay in RES investments compared to Germany. However, Turkey has provided good progress in this field compared to many other countries. It should not be forgotten that Germany is one of the leading countries in the world in this field. In terms of renewable energy, it is anticipated that Turkey would rank as the fifth-largest nation in Europe and the eleventh-largest nation in the globe by 2024 (Telli, Erat and Demir, 2021).

It is importance to increase the guarantee purchase period and the purchase price at a fixed price, especially for electricity produced from RES in Turkey. It is necessary to create conditions that will allow to produce the electricity they need to the electricity consumers in Turkey. In addition, it is necessary to shorten the time until the SPP installation stage and to simplify the legal procedures in Turkey (Kocakuşak, 2018). Incentives should not be given to the extraction of domestic lignite and hard coal which is one of the biggest obstacles for Turkey to increase RES investments. Lignite and hard coal are our domestic energy sources. However, it is known that about half of the lignite with high reserves in our country is of lower quality and lower calorific value than imported lignite (MTA, 2023). In addition, greenhouse gas emissions increase and harm the environment as a result of the use of poor quality coal and lignite. For this reason, our domestic lignite and hard coal resources should be extracted by the state without incentives and exported to countries that do not have a greenhouse gas emission commitment. This will also contribute to closing Turkey's foreign trade deficit.

Economic instability and serious exchange rate fluctuations affect investments negatively in Turkey. Giving for only 16 provinces in the 6th region of he comprehensive supports to RES investments in Turkey prevents enough investments. For this reason, the use of imported products should be abandoned by focusing on domestic production in order to achieve economic stability and not to be affected by exchange rate fluctuations in Turkey. Turkey has made progress in this regard in recent years thanks to its more renewable, more domestic policy (Telli, Erat and Demir, 2021). The level of domestic output is still insufficient, though.

Germany and Turkey are both foreign dependent for energy. Both countries have signed the Paris climate agreement. Imports of energy account for 65% of Turkey's deficit in international trade (Ozcan, 2018). Energy use is responsible for 80% of Germany's greenhouse gas emissions (Telli, Erat and Demir, 2021).

Turkey's self-sufficiency in total energy production has decreased. It decreased to 25% in 2014 while the percentage of Turkey's self-sufficiency was 54.42% in 1980. In this decline, increasing energy demand, increasing imports of natural gas and coal and renewable energy plants that did not increase at a level to meet the increasing energy demand have played a role (Ozcan, 2018). Since Germany imports most of the energy it uses, the rate of self-sufficiency in energy is low (EURONEWS, 2020). In addition, Germany plans to phase out nuclear power plants (Renn, and Marshall, 2016).

This will further reduce Germany's self-sufficiency rate in energy. For this reason, both countries need to increase their RES investments in the future in order to get rid of foreign dependency, reduce greenhouse gas emissions and increase self-sufficiency rates in energy.

Reducing by 50%-90% of the initial investment cost of RES power plants in the last 10 years has led to an increase in investments in this field all over the World (Saygin, and Godron, 2018). With R&D studies in the future, it is expected that, the initial investment costs of RES power plants will be further reduced and their efficiency will be increased. If this happens, it will be inevitable to transition to RES in the whole world.

REFERENCES

- Alshahrani A., and et all., (2019), The technical challenges facing the integration of small-scale and large-scale PV systems in to the grid: A critical review, *Electronics*, 8, 1443.
- Anadolu Ajansı(AA), (2021), <https://www.aa.com.tr/tr>, adresinden 20 Mart 2023 tarihinde alınmıştır.
- Arıoğlu Akan, and et all.,(2015)., A comparative analysis of renewable energy use and policies: Global and Turkish perspectives, *Sustainability*, 7(12), 16379-16407.
- Atmaca, S., (2019), 2208 kWp Arazi tipi güneş enerji santrali ön fizibilite ve ön fiyat teklifi, *Vira Solar&Sega Solar*.
- Batan M., (2014), *Küresel İklim Değişikliği ve Beklenen Sonuçları*, Doktora Tezi, Dicle Üniversitesi, Fen Bilimleri Enstitüsü, Diyarbakır, Türkiye.
- Chen Y, and et all., (2018), From laboratory to production: learning models of efficiency and manufacturing cost of industrial crystalline silicon and thin-film photovoltaic technologies, *IEEE journal of Photovoltaics*, 8(6),1531-1538.
- Celik A.N., and Ozgur E.,(2020), Review of Turkey's photovoltaic energy status: Legal structure, existing installed power and comparative analysis, *Renewable and Sustainable Energy Reviews*, 134, 110344.
- DEK-TMK, (2009), *Dünya'da ve Türkiye'de güneş enerjisi*, Dünya Enerji Konseyi Türk Milli Komitesi, EKC Form Ofset, Yayın no:001, Ankara.
- Dinçer, F., (2011), Türkiye'de güneş enerjisinden elektrik üretimi potansiyeli-Ekonomik analizi ve AB ülkeleri ile karşılaştırmalı değerlendirme, *KSU Mühendislik Dergisi*, 14(1).
- Dunford, M., and et all., (2013), Geographical interdependence, international trade and economic dynamics: The Chinese and German solar energy industries, *European Urban and Regional Studies*, 20(1), 14-36.
- ENERJİ.GEN, (2023), *Dünya'da güneş enerjisi*, <https://www.enerji.gen.tr/dunyada-gunes-enerjisi.html>, adresinden 07 Nisan 2023 tarihinde alınmıştır.
- Enerji ve Çevre, (2017), *Dünya'nın elektrik ihtiyacını güneş karşılayacak*, <https://www.enerji-dunyasi.com/yayin/262>, adresinden 8 Nisan 2023 tarihinde alınmıştır.
- Erkoç R., (2018), *Güneş enerji santrallerinin modellenmesi, ekonomik analizi ve değerlendirme: Almanya ve Türkiye uygulamaları*, Yüksek Lisans Tezi, Ordu Üniversitesi, Yenilenebilir Enerji Enstitüsü, Ordu, Türkiye.

- EPIAŞ, (2023), *Güneş enerjisine dayalı üretim tesisi 2023 yılı fiyatı*, <https://www.epias.com.tr/tum-duyurular>, adresinden 06 Şubat 2023 tarihinde alınmıştır.
- ETKB, (2014), *Ulusal yenilenebilir eylem planı*, Enerji ve Tabii Kaynaklar Bakanlığı, Ankara, Türkiye.
- ETKB, (2022), *Türkiye elektrik enerjisi talep projeksiyonu raporu*, <https://enerji.gov.tr/bilgi-merkezi-enerji-elektrik>, adresinden 10 Mart 2023 tarihinde alınmıştır.
- EURONEWS, (2020), Avrupa ülkeleri enerjide dışa ne kadar bağımlı, doğalgazı hangi ülkelerden alıyor? <https://tr.euronews.com>, adresinden 15 Nisan 2023 tarihinde alınmıştır.
- Girgin, M.H., (2011), *Bir fotovoltaik güneş enerjisi santralinin fizibilitesi, Karaman bölgesinde 5 MW'lık güneş enerjisi santrali için enerji üretim değerlendirmesi ve ekonomik analizi*, Yüksek Lisans Tezi, İstanbul Teknik Üninersitesi, Enerji Enstitüsü, İstanbul, Türkiye.
- Inderberg, T. H. J., Tews, K., and Turner, B., (2018)., Is there a prosumer pathway? Exploring household solar energy development in Germany, Norway, and the United Kingdom, *Energy Research & Social Science*, 42, 258-269.
- IPCC, (2021), 6th Assessment Report, <https://www.ipcc.ch/report/ar6>, adresinden 03 Nisan 2023 tarihinde alınmıştır.
- IRENA, (2023), *Renewable capacity statistics 2023*, International Renewable Energy Agency, Abu Dhabi.
- Kapluhan, E., (2014). Enerji coğrafyası açısından bir inceleme: güneş enerjisinin Dünya'daki ve Türkiye'deki kullanım durumu. *Coğrafya Dergisi*, (29), 70-98.
- Karagöl, T., E., ve Kavaz, İ., (2017), Dünyada ve Türkiye'de Yenilenebilir Enerji, SETA, *Analiz Dergisi*, 4(197), 5-32.
- Kateroğlu, E., (2022), *Endüstri 4.0 ve enerji dönüşümü: Türkiye'de güneş enerjisi teknolojilerinden elektrik üretimi potansiyelinin değerlendirilmesi*, Yüksek Lisans Tezi, Hacı Bayram Veli Üniversitesi, Lisansüstü Eğitim Enstitüsü, Ankara, Türkiye.
- Kocakuşak, R.,(2018), *Yenilenebilir enerji kaynaklarından güneş enerjisinin, Türkiye'deki önemi ve GES kurulum araştırması*, Yüksek Lisans Tezi, Maltepe Üniversitesi, Sosyal Bilimler Enstitüsü, İstanbul, Türkiye.
- KUZKA, (2016), *Güneş enerji santrali (GES) ön fizibilite raporu*, Kuzey Anadolu Kalkınma Ajansı, <https://www.kalkinmakutuphanesi.gov.tr> adresinden 10 Aralık 2022 tarihinde alınmıştır.

- MTA, (2023), *Kömür*, Maden Tetkik Arama, mta.gov.tr, adresinden 12 Nisan.2023 tarihinde alınmıştır.
- Norm Enerji, (2012), *Almanya’da güneş enerji teşvikleri*, http://www.normenerji.com.tr/menu_detay.asp?id=9881, adresinden 10 Mart 2023 tarihinde alınmıştır.
- Ozcan, M., (2018), The role of renewables in increasing Turkey’s self-sufficiency in electrical energy, *Renewable and Sustainable Energy Reviews*, 82, 2629-2639.
- Park, SC., and Eissel, D., (2010), Alternative energy policies in Germany with particular reference to solar energy, *Journal of Contemporary European Studies*, 18(3), 323-339.
- Raghoebarsing, A., and et all., (2022)., The status of implementation of photovoltaic systems and its influencing factors in European countries, *Progress in Photovoltaics: Research and Applications*. DOI:10.1002/pip.3613.
- Renn, O., and Marshall, J. P. (2016)., Coal, nuclear and renewable energy policies in Germany: From the 1950s to the “Energiewende. *Energy Policy*, 99, 224-232.
- Saygın D., and Godron P., (2018), Lessons from global experiences for accelerating energy transition in Turkey through solar and wind power, *Sabancı University and Agora Energiewende*, Istanbul.
- Sirin, S. M., and Yilmaz, B. N., (2021), The impact of variable renewable energy technologies on electricity markets: An analysis of the Turkish balancing market, *Energy Policy*, 151, 112093.
- Solar AVM, (2022), *Enerji kaynağı olarak güneş ve potansiyeli*, <https://solaravm.com/enerji-kaynagi-olarak-gunes-ve-potansiyeli>, adresinden 10 Mart 2023 tarihinde alınmıştır.
- Telli, A., Erat, S., and Demir B., (2021), Comparison of energy transition of Turkey and Germany: energy policy, strengths/weaknesses and targets, *Clean Technologies and Environmental Policy*, 23, 413-427.
- Ulusal Müşavirlik, (2022), *Güneş enerjisi ve rüzgar enerjisi yatırım teşvikleri*, <https://ulusalmusavirlik.com/ges-ve-res-yatirim-tesvikleri.htm>, adresinden 02 Nisan 2023 tarihinde alınmıştır.

Chapter 14

Forward Dynamic Structural Modification of Rotor Systems Using Frequency Response Functions with Sherman-Morrison- Woodbury Formula

Murat ŞEN¹

Orhan ÇAKAR²

¹ Dr. Res. Asst.; Firat University, Department of Mechanical Engineering, Elazig, Türkiye, msen@firat.edu.tr ORCID No: 0000-0002-3063-5635

² Prof. Dr.; Firat University, Department of Mechanical Engineering, Elazig, Türkiye, cakaro@firat.edu.tr ORCID No: 0000-0001-6947-3875

ABSTRACT

In many model updating studies on rotor systems, it is very common to make mass, spring or disk-like modifications on the rotors at many points. It is necessary to know how the dynamic properties of the rotor system will change as a result of these modifications. This can be possible with dynamic structural modification methods.

The dynamic structural modification method based on the SMW formula is adapted to rotor systems and presented. The presented method is very practical for real engineering applications due to it uses the FRFs (frequency response function) of mechanical systems directly. The presented method is verified with simulation studies on created FE rotor model and very effective results are obtained.

Keywords: Structural modification, frequency response function, SMW formula, rotor system

INTRODUCTION

During the design phase of the rotors, the static and dynamic loads they will carry, as well as the operating frequencies, are issues that need to be carefully considered. However, some operations such as a repair or product development or model update on any rotor system cause the dynamic properties of these systems to change. Therefore, it is necessary to know in advance how the changes in the dynamic properties of these structures will occur. One of the most suitable methods for this is undoubtedly structural modification applications. The subject of structural modification has become widespread rapidly with the developments in computer and software technology after the 1970s. One of the first studies in this field is the matrix mixing method presented by Rayleigh (Rayleigh, 1945). With this method, the modal properties of a modified system were tried to be determined. Later, this approach was used and continued to be developed by many researchers and analytical methods began to be developed in structural modification studies (Hee, 2001; To, 1989). In the first studies in this field, system models composed of simple masses and springs were used to avoid dealing with rotational coordinates. In this context, Weissenberger (Wiesenberger, 1966; Wiesenberger, 1968) conducted research on how the dynamic properties of undamped systems consisting of masses and springs change with the expansion. These studies have inspired many researchers and it has been started to investigate how dynamic behaviors are affected by system models on which viscous damping elements are added (Pomazal, 1969).

One of the most important problems frequently encountered in structural dynamics is the difficulties in determining the dynamic behavior of complex mechanical systems. Analysis of complex structures composed of many subcomponents can be quite difficult. In addition, when a new additional system is added to an engineering system as part of a design update or product improvement, the dynamic behavior of the new system must be determined again. In this context, the dynamic properties of each subsystem can be determined separately and the dynamic behavior of the system created by using structural coupling techniques can be determined. Similarly, complex systems can also be divided into subsystems and analyzed (Mottershead & Friswell, 1993; Imregun, 1987; Frey, 1998; Hu & Chen 2008). These techniques are frequently used by researchers working in the field of structural dynamics (Klerk et al., 2008; Wang & Zheng, 2012; Tao & Jimin, 1999; Şen & Çakar, 2023).

In the field of structural modification, one of the most effective methods is using FRFs (Frequency Response Function) directly belonging to the system,

which does not require a mathematical or modal model of the system (Özgüven, 1990; Yee & Tsuei, 1991; Kyprianou et al., 2005; Park & Park, 2000). FRFs used in these methods can be obtained numerically or experimentally. In the analysis of some very complex mechanical structures, obtaining FRFs numerically can be very laborious and time-consuming. The use of experimental methods to obtain FRFs of such structures provides great convenience. In this context, structural modification methods based on SM (Sherman & Morrison, 1950) and SMW (Woodbury, 1950) formulas using FRFs have also been developed. These formulas are often used as a tool to calculate the inverse of a matrix with some elements modified using the inverse of the original matrix and the modifications. In this context, Hong and Kim (Hong & Kim, 1996) developed a new method for the analysis of vibration and noise problems using the SM formula on a one-dimensional system and verified the solutions they obtained using the method they developed with real solutions. Çakar and Şanlıtürk (Çakar & Sanlitürk, 2005) studied the elimination of accelerometer mass loading effects present in experimentally measured FRFs using the structural modification method based on the SM formula. Ozer and Royston (Özer & Royston, 2005) tried to determine the damping parameters of a multi-degree-of-freedom damped system using the SM formula and demonstrated the validity of the method with their numerical verification studies.

When the studies carried out in the field of structural dynamics from the past to the present are examined, it is seen that the use of structural modification in rotors is quite limited. However, rotors are widely used in many areas of engineering applications (Şen, 2022; Şen et al., 2022; Şen et al., 2022; Şen & Çakar, 2021). Looking at the previous studies in this field, it can be said that it has gained momentum with the developments in the field of structural dynamics. Within the scope of the first structural dynamics studies in rotor dynamics, it is seen that many studies have been carried out to reduce helicopter vibrations. In one of these, Hylton et al. (Hylton et al., 2016) tried to solve the problems in determining the dynamic properties of these structures with dynamic flexibility models due to the change in the connection boundary conditions in rotor blades, and they succeeded in increasing the accuracy of the rotor blade frequencies determination significantly. In other studies, anti-resonance frequencies have been used to reduce helicopter vibrations (Desjardins & Hooper, 1978; Rita et al., 1978; Bartlet & Flannelly, 1974). Similarly, Wang et al. (Wang et al., 1979) carried out studies to reduce helicopter vibrations by placing regional attachments on the helicopter fuselage. In addition, they tried to generate anti-resonance frequencies on the system by

changing the stiffness values and tried to verify the proposed method on a simple numerical model they created for the helicopter fuselage. Trisovic N. (Trisovic, 2007) tried to improve the dynamic structure of a motor shaft by increasing the lowest natural frequency by using sensitivity analysis methods. Birchfield (Birchfield, 2013) investigated the effects of rotor connections on rotor dynamics. He tried to show how the dynamic behavior of the rotor system, which is formed by bringing together different elements such as rotor, disc, motor, flexible bearing and a platform carrying them, whose dynamic properties are known, can be determined by using the dynamic properties of each element. For this, he determined the dynamic properties of the new system, which is obtained by combining two separate subsystems consisting of many mass, spring and damping elements with known dynamic properties. He used the classical structural coupling technique, using one or more coupling points with spring and damping elements. By associating the numerical model he created with the experimental data he obtained, he tried to increase the rotor performance by making spring modifications on the flexible bearing element that he positioned at certain points on the rotor. Liu et al. (Liu et al., 2016) carried out a study within the scope of inverse structural modification in which FRFs for torsional vibration were used to reduce torsional vibrations in rotor systems. They tried to determine the necessary modification parameters with an optimization algorithm they created. Tsai et al. (Tsai et al., 2018) applied a structural modification technique known from the literature to an experimental system consisting of coupled gears and two shafts and bearings carrying them. In the study, it has been tried to ensure that the system has natural frequencies at the desired values by making mass modifications. In this technique, the FRFs of the modified system are expressed with a ratio depending on the system matrices and the modifications, and the required mass modifications are calculated by minimizing the numerator and denominator separately. In the experimental application, discs with holes around which mass can be added were placed on one of the shafts and the calculated mass modifications were provided by bolt and nut connections attached to the holes on these discs.

SMW FORMULA BASED FORWARD DYNAMIC STRUCTURAL MODIFICATION

The SMW formula is a mathematical formula based on matrix theory, developed for inverse operations in mathematics. This formula can be used in structural modification studies for modification and model updating studies based on FRFs. The SMW formula can be effectively used in multi-rank

modification applications. If the change in dynamic stiffness of a structurally modified system is rewritten as:

$$[\Delta Z] = [U][V]^T \quad (1)$$

where, $[\Delta Z]$ represents the dynamic stiffness change matrix, $[U]$ and $[V]$ are the modification matrices and $(^T)$ represents the matrix transpose. Here, the dynamic stiffness change represents the total mass $[\Delta M]$, stiffness $[\Delta K]$ and damping $[\Delta C]$ changes, and the dynamic stiffness of the new system formed after the modification can be expressed as follows.

$$Z^* = [Z + \Delta Z] = ([K] + [\Delta K]) - \omega^2 ([M] + [\Delta M]) + j\omega([C] + [\Delta C]) \quad (2)$$

Where, Z^* represents the dynamic stiffness matrix of the modified system, ω is the frequency (r/s) and $j = \sqrt{-1}$. The dynamic stiffness change matrices given by Equation 1 can be written as follows for n coordinates.

$$\begin{aligned} U_1 &= [1 \quad 0 \quad \dots \quad 0]_{nx1}^T & V_1 &= [\Delta k_1 - \omega^2 \Delta m_1 + j\omega \Delta c_1 \quad 0 \quad \dots \quad 0]_{nx1}^T \\ U_2 &= [0 \quad 1 \quad \dots \quad 0]_{nx1}^T & V_2 &= [0 \quad \Delta k_2 - \omega^2 \Delta m_2 + j\omega \Delta c_2 \quad \dots \quad 0]_{nx1}^T \\ &\dots\dots\dots & &\dots\dots\dots \\ U_n &= [0 \quad 0 \quad \dots \quad 1]_{nx1}^T & V_n &= [0 \quad 0 \quad \dots \quad \Delta k_n - \omega^2 \Delta m_n + j\omega \Delta c_n]_{nx1}^T \end{aligned} \quad (3)$$

The dynamic stiffness of the new system obtained after the modifications can be expressed as follows, together with the dynamic stiffness of the original system and the modifications using SMW formula.

$$[Z^*]^{-1} = [Z]^{-1} - [Z]^{-1} [U] ([I] + [V]^T [Z]^{-1} [U])^{-1} [V]^T [Z]^{-1} \quad (4)$$

With the relationship between dynamic stiffness and dynamic flexibility ($[Z]^{-1} = [\alpha]$), this equation can be rearranged as follows.

$$[\alpha^*] = [\alpha] - [\alpha][U]([I] + [V]^T [\alpha][U])^{-1} [V]^T [\alpha] \quad (5)$$

Where, $[\alpha^*]$ is the modified dynamic flexibility type FRF matrix of the system with the dimension of the coordinates of the determined system. The equation obtained here can be expressed as follows for the FRFs (response, excitation and modification coordinates) belonging only to the active coordinates illustrated with subscript (a).

$$[\alpha^*]_a = [\alpha]_a - [\alpha]_a [U]([I] + [V]^T [\alpha]_a [U])[V]^T [\alpha]_a \quad (6)$$

The modification matrices given by Equation 3 can be arranged as follows for n coordinates.

$$[U] = [U_1 \ U_2 \ \dots \ U_n] = \begin{bmatrix} 1 & 0 & 0 & 0 \\ 0 & 1 & 0 & 0 \\ 0 & 0 & \ddots & 0 \\ 0 & 0 & 0 & 1 \end{bmatrix} \quad (7)$$

$$[V] = [V_1 \ V_2 \ \dots \ V_n] \quad (8)$$

$$[V] = \begin{bmatrix} \Delta k_1 - \omega^2 \Delta m_1 + j\omega \Delta c_1 & 0 & 0 & 0 \\ 0 & \Delta k_2 - \omega^2 \Delta m_2 + j\omega \Delta c_2 & 0 & 0 \\ 0 & 0 & \ddots & 0 \\ 0 & 0 & 0 & \Delta k_n - \omega^2 \Delta m_n + j\omega \Delta c_n \end{bmatrix} \quad (9)$$

USING THE FORWARD DYNAMIC STRUCTURAL MODIFICATION METHOD BASED ON THE SMW FORMULA ON ROTORS

As mentioned in the previous section, this method is a method that provides a solution for multi-rank modifications and obtains the FRFs of the modified system by using the FRFs of original system and the modification matrices. In this section, it is explained how to use the SMW formula for structural modification studies on rotors. For this purpose, a simple rotor system with

some mass, spring and disc modifications is created by using and given with Figure 1.

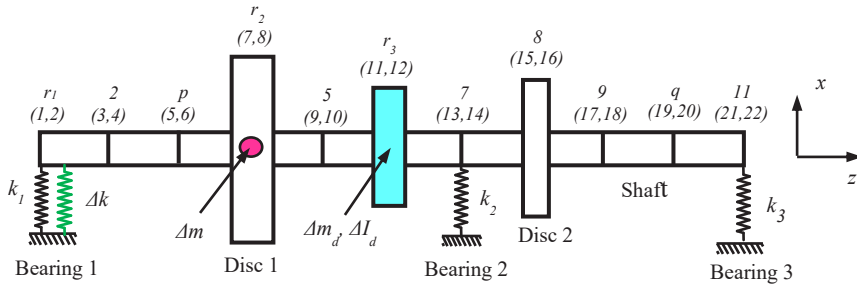


Figure 1: Mass, stiffness and disc modifications on the rotor system

In Figure 1, bending vibrations in the x - z plane of a rotor system for stationary condition is taken into account and the FE model is created by portioning the shaft of the rotor system into 10 equal parts with obtaining 11 nodal points on the shaft. The shaft is modeled by using Euler-Bernoulli beam approach. Here, each node has two coordinates one belongs the translational and the other belongs to the rotational coordinate with totally 22 coordinates on the shaft. The bearings of the rotor system are modeled with springs k_1 , k_2 and k_3 on the nodes 1, 7 and 11 for only translational coordinates of the nodes they are connected. Discs are placed on the shaft on the nodes 4 and 8. Stiffness modifications (Δk) are applied to the bearings in the translational coordinate. Disc modifications are applied for two coordinates on the nodes where the modification disc is connected for the translational coordinate, the mass of the disk (Δm_d) and the rotational coordinate, the diametric mass moment of inertia of the disc (ΔI_d). The lumped mass modification (Δm) is applied to the translational coordinate of the point on which the disc is connected assuming this modification will be applied on the disc of the rotor system.

For the rotor system given in Figure 1, let us assume that a change of spring (Δk) at point r_1 , lumped mass (Δm) at point r_2 and a disk (Δm_d , ΔI_d) at point r_3 , respectively. In this case, the FRFs of the active coordinates of the original system and the resulting system after the modifications, including the response $p(5)$ and the excitation coordinates $q(19)$, and the modification coordinates $r_1(1)$, $r_2(7)$, $r_3(11)$ and $r_3(12)$ can be written as follows.

$$[\alpha]_a = \begin{bmatrix} \alpha_{p(5)p(5)} & \alpha_{p(5)r_1(1)} & \alpha_{p(5)r_2(7)} & \alpha_{p(5)r_3(11)} & \alpha_{p(5)r_3(12)} & \alpha_{p(5)q(19)} \\ \alpha_{r_1(1)p(5)} & \alpha_{r_1(1)r_1(1)} & \alpha_{r_1(1)r_2(7)} & \alpha_{r_1(1)r_3(11)} & \alpha_{r_1(1)r_3(12)} & \alpha_{r_1(1)q(19)} \\ \alpha_{r_2(7)p(5)} & \alpha_{r_2(7)r_1(1)} & \alpha_{r_2(7)r_2(7)} & \alpha_{r_2(7)r_3(11)} & \alpha_{r_2(7)r_3(12)} & \alpha_{r_2(7)q(19)} \\ \alpha_{r_3(11)p(5)} & \alpha_{r_3(11)r_1(1)} & \alpha_{r_3(11)r_2(7)} & \alpha_{r_3(11)r_3(11)} & \alpha_{r_3(11)r_3(12)} & \alpha_{r_3(11)q(19)} \\ \alpha_{r_3(12)p(5)} & \alpha_{r_3(12)r_1(1)} & \alpha_{r_3(12)r_2(7)} & \alpha_{r_3(12)r_3(11)} & \alpha_{r_3(12)r_3(12)} & \alpha_{r_3(12)q(19)} \\ \alpha_{q(19)p(5)} & \alpha_{q(19)r_1(1)} & \alpha_{q(19)r_2(7)} & \alpha_{q(19)r_3(11)} & \alpha_{q(19)r_3(12)} & \alpha_{q(19)q(19)} \end{bmatrix} \quad (10)$$

$$[\alpha^*]_a = \begin{bmatrix} \alpha_{p(5)p(5)}^* & \alpha_{p(5)r_1(1)}^* & \alpha_{p(5)r_2(7)}^* & \alpha_{p(5)r_3(11)}^* & \alpha_{p(5)r_3(12)}^* & \alpha_{p(5)q(19)}^* \\ \alpha_{r_1(1)p(5)}^* & \alpha_{r_1(1)r_1(1)}^* & \alpha_{r_1(1)r_2(7)}^* & \alpha_{r_1(1)r_3(11)}^* & \alpha_{r_1(1)r_3(12)}^* & \alpha_{r_1(1)q(19)}^* \\ \alpha_{r_2(7)p(5)}^* & \alpha_{r_2(7)r_1(1)}^* & \alpha_{r_2(7)r_2(7)}^* & \alpha_{r_2(7)r_3(11)}^* & \alpha_{r_2(7)r_3(12)}^* & \alpha_{r_2(7)q(19)}^* \\ \alpha_{r_3(11)p(5)}^* & \alpha_{r_3(11)r_1(1)}^* & \alpha_{r_3(11)r_2(7)}^* & \alpha_{r_3(11)r_3(11)}^* & \alpha_{r_3(11)r_3(12)}^* & \alpha_{r_3(11)q(19)}^* \\ \alpha_{r_3(12)p(5)}^* & \alpha_{r_3(12)r_1(1)}^* & \alpha_{r_3(12)r_2(7)}^* & \alpha_{r_3(12)r_3(11)}^* & \alpha_{r_3(12)r_3(12)}^* & \alpha_{r_3(12)q(19)}^* \\ \alpha_{q(19)p(5)}^* & \alpha_{q(19)r_1(1)}^* & \alpha_{q(19)r_2(7)}^* & \alpha_{q(19)r_3(11)}^* & \alpha_{q(19)r_3(12)}^* & \alpha_{q(19)q(19)}^* \end{bmatrix} \quad (11)$$

Modification matrices for these changes can be created as follows.

$$[U] = \begin{bmatrix} 1 & 0 & 0 & 0 & 0 & 0 \\ 0 & 1 & 0 & 0 & 0 & 0 \\ 0 & 0 & 1 & 0 & 0 & 0 \\ 0 & 0 & 0 & 1 & 0 & 0 \\ 0 & 0 & 0 & 0 & 1 & 0 \\ 0 & 0 & 0 & 0 & 0 & 1 \end{bmatrix} \quad [V] = \begin{bmatrix} 0 & 0 & 0 & 0 & 0 & 0 \\ 0 & \Delta k & 0 & 0 & 0 & 0 \\ 0 & 0 & -\omega^2 \Delta m & 0 & 0 & 0 \\ 0 & 0 & 0 & -\omega^2 \Delta m_d & 0 & 0 \\ 0 & 0 & 0 & 0 & -\omega^2 \Delta I_d & 0 \\ 0 & 0 & 0 & 0 & 0 & 0 \end{bmatrix} \quad (12)$$

The FRFs of the active coordinates of the modified system can be calculated by using Equation 9-11 in Equation 6. The rows and columns consisting of zeros in the modification matrix given in Equation 11 belong to the response and excitation coordinates and it is thought that there will be no modification in these coordinates.

NUMERICAL SIMULATIONS

In this section, the validity of the method is demonstrated by some numerical simulation studies on the rotor system for which the FE model is created and given in Figure 1. The rotor system discussed here consists of 3 bearings, a shaft and 2 discs placed on the shaft. In this rotor system different simulation studies were carried out by making stiffness modifications on the bearings (Δk), lumped mass modifications on the discs (Δm) and the disc modifications in the

coordinates determined on the shaft (Δm_d , ΔI_d) The physical and the mechanical properties of the rotor system are given in Table 1.

Table 1: Physical and mechanical properties of the rotor FE rotor model created for simulation studies

Parameter	Value
Shaft diameter (mm)	20
Shaft length (mm)	1000
Shaft density (kg/m ³)	7800
Shaft Modulus of Elasticity (GPa)	210
Disc1-2 diameter (mm)	230-170
Disc1-2 thickness (mm)	23-17
Disc1-2 density (kg/m ³)	7850-7850
Bearing 1-2-3 stiffness (kN/m)	250-220-220

In Table 2, some numerical simulation results are given. In the table Modification Type represents which modification (mass (m)-stiffness (k), mass (m)-disc (D), stiffness (k)-disc (D) or mass (m)-stiffness (k)-disc (D)) is made for relevant modification application. Modification Coordinate column represents the nodal points and the related coordinates of the modifications. Resonance frequencies are obtained for the first 5 modes of bending vibrations in Hz. Modification Values are in g, N/m and mm for the mass, stiffness and disc modifications respectively. The negative value means the removal modification from the system while the positive value means additional modification value.

D and t are the diameter and the thickness of the modification disc respectively. Firstly, the resonance frequencies are obtained for the first five modes of the original rotor system and for each modification applications, the resonance frequencies are obtained again and tabulated with that of the frequencies calculated with the presented method comparatively. As seen in Table 2, the resonance frequencies of the modified systems for each application can be obtained with the presented method directly (without error).

Table 2: Mass, spring and disc modification applications on the given rotor system

Modification Type (<i>m, k, D</i>)	Modification Coordinate (<i>r</i>)	Modification Value (<i>g, N/m, mm</i>)	Resonance Frequency (Hz)					
			Mod Number	1	2	3	4	5
			Original	24.3	52.3	125.6	192.2	279.2
<i>m</i> <i>k</i>	4(7)	750	Modified	20.3	49.1	125.1	191.2	279.0
	7(13)	-100000	Calculated	20.3	49.1	125.1	191.2	279.0
<i>m</i> <i>D</i>	8(15)	350	Modified	22.4	49.0	111.4	183.9	258.9
	6(11,12)	<i>D</i> =150, <i>t</i> =15	Calculated	22.4	49.0	111.4	183.9	258.9
<i>k</i> <i>D</i>	1(1)	75000	Modified	23.2	52.8	122.2	193.1	287.5
	5(9,10)	<i>D</i> =130, <i>t</i> =13	Calculated	23.2	52.8	122.2	193.1	287.5
<i>m</i> <i>k</i> <i>D</i>	4(7)	400	Modified	25.0	50.3	122.6	184.7	278.9
	7(13)	60000	Calculated	25.0	50.3	122.6	184.7	278.9
	9(17,18)	<i>D</i> =100, <i>t</i> =10						

One of the FRFs of obtained for each modification applications belong to the original (black dashed line) and modified (red straight line) rotor systems with calculated (blue circle shaped line) ones are illustrated in Magnitude (m/N)-Frequency (Hz) graphs in Figure 2-Figure 5 below. The validity of the presented method can be seen clearly with these FRF graphs. The FRFs of the modified rotor systems and the calculated ones are in very good agreement.

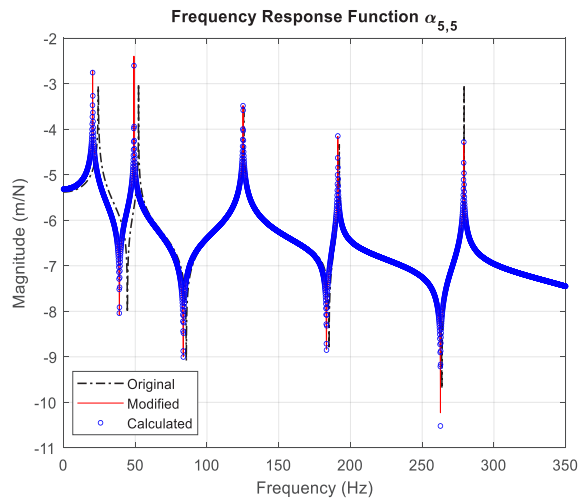


Figure 2: Mass and Stiffness modification on the rotor system

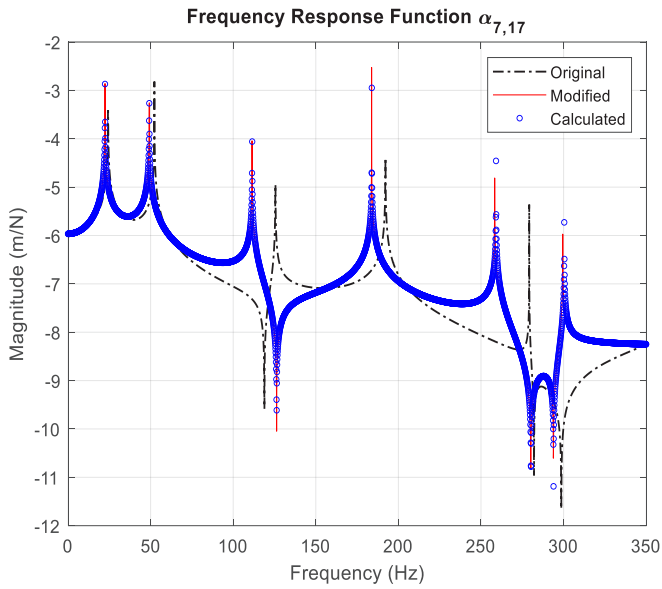


Figure 3: Mass and Disc modification on the rotor system

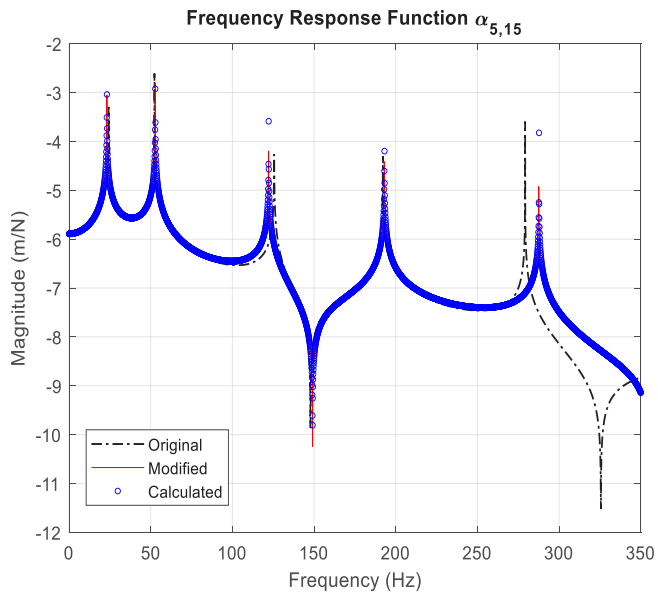


Figure 4: Stiffness and Disc modification on the rotor system

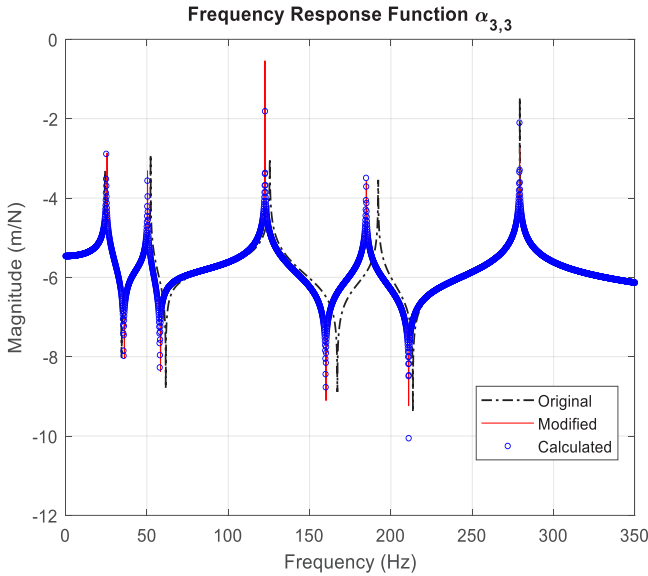


Figure 5: Mass, Stiffness and disc modification on the rotor system

RESULTS AND DISCUSSION

Considering the numerical simulation results, SMW based structural modification can be easily applied to rotor systems. This method can provide big advantage to engineers and researchers studying in structural dynamic. The resonance frequencies of a modified rotor system can be easily obtained by using the FRFs of the original rotor system and the modifications. Since the presented method directly uses the FRFs of the rotor system, it can be said that its application to engineering systems can be very practical due to FRFs can be easily measured experimentally on the rotor system. In addition, it can be said that it will provide great convenience as it can be easily calculated how the resonance frequencies of the system will change when the model update studies are carried out on the system designed during the design phase in engineering applications.

REFERANSLAR

- Bartlet F. D., Flannelly W. G., (1974). Application of antiresonance theory to helicopters, NASA Rotorcraft Dynamics Conference, Moffett Field, California.
- Birchfield N. S., (2013). Structural modification of a coupled rotordynamic system from transfer functions, MSc. Thesis, Miami University, Oxford, Ohio.
- Cakar O., Sanliturk K. Y., (2005). Elimination of transducer mass loading effects from frequency response functions, *Mechanical System and Signal Processing*, C. 19, Sayı 1, 87–104.
- Desjardins R. A., Hooper W. E., (1978). Antiresonant rotor isolation for vibration reduction, 34th Annual National Forum of the American Helicopter Society, Washington D. C.
- Hee J., (2001). Structural Modification, *Philosophical Transactions: Mathematical, Physical and Engineering Sciences*, Experimental Modal Analysis, 359(1778), 187-204.
- Hong K. L., Kim J., (1996). New analysis method for general acoustic–structural coupled systems, *Journal of Sound and Vibration*, C. 192, Sayı 2, 465–480.
- Hu Y. C., Chen Z. W., (2008). Substructure synthesis method considering dynamic behaviour of joints, *Journal of Zhejiang University*, C. 42, Sayı 8, 1404-1409.
- Hylton B., Crandall A., Koester D., Bouquillon B., Meckl P., Adams D., (2016). A Structural Dynamic Model Inversion-Based Technique to Characterize Impacts to a Full-Scale and Operational Helicopter Rotor Blade, *Journal of Applied Mechanics*, C. 83, Sayı 1, 121007.
- Imregun M., Robb D. A., Ewins D. J., (1987). Structural modification and coupling dynamic analysis using measured FRF data, *Proceeding of the 5th International Modal Analysis Conference*, 1136-1141.
- Klerk D. D., Rixen D. J., Voormeeren S. N., (2008). General framework for dynamic substructuring : history, review and clasification of techniques, *AIAA Journal*, C. 46, Sayı 5, 1169-1181.
- Kyprianou A., Mottershead J. E., Ouyang H., (2005). Structural modification. Part 2:assignment of natural frequencies and antiresonances by an added beam, *Journal of Sound and Vibration*, C. 284, 267-281.
- Liu Z., Li W., Ouyang H., (2016). Structural Modifications for Torsional Vibration Control of Shafting Systems Based on Torsional Receptances, *Shock and Vibration*, Article ID 2403426.
- Mottershead J. E., Friswell M. I., (1993). Model updating in structural dynamics: A survey. *Journal of Sound and Vibration*, C. 167, 347-375.
- Özer M. B., Royston T. J., (2005). Application of Sherman–Morrison matrix inversion formula to damped vibration absorbers attached to multi-degree of freedom systems, *Journal of Sound and Vibration*, Volume, C. 283, Sayı 3, 1235-1249.
- Özgüven H. N., (1990). Structural Modifications Using Frequency Response Functions. *Mechanical Systems and Signal Processing*, C. 4, Sayı 1, 53-63.

- Park Y. H., Park Y. S., (2000). Structure optimization to enhance its natural frequencies based on measured frequency response functions, *Journal of Sound and Vibration*, C. 229, 1235-1255.
- Pomazal R. J., (1969). The effects of local modifications on the eigenvalues and eigenvectors of damped linear systems, PhD Thesis, Michigan Technological University, Houghton, MI.
- Rayleigh J. W. S., (1945). *Theory of sound*, 2nd Edition, Dover Publications, New York.
- Rita A. D., McGarvey J. H., Jones R, (1978). Helicopter rotor isolation evaluation utilizing the dynamic antiresonant vibration isolator, *Journal of the American Helicopter Society*, C. 23, 22-29.
- Sherman, J., Morrison, W. J., (1950). Adjustment of an inverse matrix corresponding to a change in one element of a given matrix, *Annals of Mathematical Statistics*, C. 21, Sayı 1, 124–127.
- Şen M. (2022). *Shifting Resonance and Anti-resonance Frequencies of Rotors by Using Frequency Response Functions*, Firat University, Institute of Natural Sciences, PhD Thesis, Elazığ, Türkiye.
- Şen M. and Çakar O. (2023). An Efficient Method for Structural Coupling of Mechanical Systems by Using Frequency Response Functions. *Journal of Vibration and Control* First published online January 17, 2023. <https://doi.org/10.1177/10775463231152069>
- Şen M., Çakar O., and Yiğid O. (2022) *Dynamic Analysis of a Dual Rotor System*. VI-International European Conference on Interdisciplinary Scientific Research Bucharest, Romania: 1448-1456.
- Şen M., Çakar O., and Yiğid O. (2022) *Model Reduction and Dynamic Analysis of a Rotor System*. VI-International European Conference on Interdisciplinary Scientific Research Bucharest, Romania: 317-329.
- Şen M., Çakar O. (2021) *Shifting Resonance and Anti-resonance Frequencies of a Shaft-Disc-Bearing Rotor System to Desired Values by Using Frequency Response Functions*. 12th International Conference on Mathematics, Engineering, Natural and Medical Sciences, Paris, France.
- Tao L., Jimin H., (1999). Local structural modification using mass and stiffness changes. *Engineering Structures*, C 21, Sayı 11, 1028-1037.
- To W. M., (1989). *Structural modification analysis using Rayleigh quotient iteration*, Dynamics Section Report, No. 89001, Imperial College, University of London.
- Trisovic N., (2007). Eigenvalue sensitivity analysis in structural Dynamics, *FME Transactions*, C. 35, 149-156.
- Tsai S. H., Ouyang, H., Chang J. Y., (2018). Inverse structural modifications of a geared rotor-bearing system for frequency assignment using measured receptances, *Mechanical System and Signal Processing*, C. 110, 59–72.
- Wang B. P., Kitis L., Pilkey W. D., Palazzolos A., (1979). Structural modification to achieve anti-resonance in helicopters, *AIAA C. 19*, Sayı 6, 982.

- Wang M., Zheng G. T., (2012). An improved fixed interface modal synthesis method, *Journal of Astronautics*, C. 33, Sayı 3, 291-297.
- Weissenburger J. T., (1966). Effects of local modification on the eigenvalues and eigenvectors of linear systems, D. Sc. Dissetcation, Washington University, ST. Louis, MO.
- Weissenburger J. T., (1968). Effects of local modification on the vibration characteristics of linear systems, *Journal of Applied Mechanics*, C. 35, 327-332.
- Woodbury M., (1950). Inverting Modified Matrices, Memorandum Report 42, Statistical Research Group, Princeton University, Princeton, New Jersey, USA.
- Yee E. K. L., Tsuei Y. G., (1991). Method for Shifting Natural Frequencies of Damped Mechanical Systems, *AIAA Journal*, C. 29, Sayı 11, 22-32.

Chapter 15

Design of Fractional Order PD Controller Based on PSO Algorithm for Fractional Order Systems

Münevver Mine ÖZYETKİN¹

Hasan BİRDANE²

¹ Assoc. Prof. Dr; Aydın Adnan Menderes University, Department of Electrical and Electronics Engineering, Aydın, TURKEY.
m.ozyetkin@adu.edu.tr. ORCID No: 0000-0002-3819-5240.

² Res. Asst., Eskişehir Technical University, Faculty of Aviation and Space Sciences, Department of Aviation Electrics and Electronics, Eskişehir, TURKEY.
hasanbirdane@eskisehir.edu.tr, ORCID:0000-0001-5432-2839

ABSTRACT

Controllers are used to achieve the desired performance at the outputs of the systems. The best performance of the systems depends on the parameter values of the controllers. In the literature, various methods have been developed for obtaining controller parameters. Nowadays, studies on controller parameter uncertainty remain popular. In this study, a method was proposed to select the most suitable controller parameters to control a given system with FOPD (Fractional Order PD) controller. In this method, system responses were obtained by common stability boundary locus method with the PSO algorithm. The parameter equations used to obtain the stability boundary locus were obtained by the D-partition method. A fractional controller structure has three parameters: k_p , k_d and μ . In this study, a stability boundary curve was obtained for each μ value in the range of 0.1 to 1.5, at intervals of 0.1. As a result, a common region bounded by k_d of all stability boundary locus was obtained. In this region, optimal parameter values were tried to be obtained by using the PSO algorithm. The results were compared with the different methods in the literature.

Keywords: Fractional order systems, Control systems, Fractional Order PD, Stability boundary locus, Particle swarm optimization (PSO)

INTRODUCTION

The structures that ensure the proper and controlled operation of systems or devices are referred to as control systems. In other words, they are structures that maintain the output of systems in a specific form or at a certain level. There are studies conducted in the field of control systems in the literature. In these studies, the most commonly used controller types are PI (Proportional Integral), PD (Proportional Derivative), PID (Proportional Integral Derivative), and PI-PD controllers (Lee et al., 2014:5038; Onat et al., 2012:102; Tan, 2009:175; Yue, 2020:366). The controllers have a wide range of applications in both academic studies and industrial applications due to their simple structure and ease of integration into various systems. Various methods have been developed to obtain the parameter values within the structure of these controllers. Some of these methods are Internal Model Control (IMC) (Rivera et al., 1986:252), Wang – Juang – Chan (Wang et al., 1995:15), Cohen – Coon (Cohen and Coon, 1953:827), Chien – Hrones - Reswick (Chien et al., 1952:175), Ziegler-Nichols (Ziegler and Nichols, 1942:759) etc. The controller parameters obtained through these methods can make systems stable. However, the obtained controller parameter values may not always yield the best results. Therefore, determining controller parameters remains an active area of research in today's literature. In addition to these methods used to obtain controller parameters, the Stability Boundary Locus (SBL) method is also available (Hamamci and Tan, 2006:529; Tan et al., 2006:3045). By means of this method, controller parameter values that are suitable for the desired system performance can be easily selected from the region enclosed within the stability boundary locus. (Tan et al., 2006:3045). This method can be used in controllers such as PI, PD, PID and PI-PD. Apart from these controllers, there are also control systems with different structures. In the literature, the most popular controller types are fractional order controllers (FOC). The most used types of fractional-order controllers are PI^λ (Fractional Proportional Integral), PD^μ (Fractional Proportional Derivative), $PI^\lambda D^\mu$ (Fractional Proportional Integral Derivative), and $PI^\lambda - PD^\mu$ controllers. There are various studies in the literature related to these types of controllers (Hamamci, 2008:329; Hamamci and Işık, 2014:150; Ozyetkin, 2018:77; Ozyetkin et al., 2012; Ozyetkin and Tan, 2017:9230; Podlubny, 1994; Saxena et al., 2015:182). FOC have more parameters compared to integer-order controllers in terms of their structure. FOC have degrees for integral and derivative terms. The parameters of FOC can be easily obtained using the stability boundary locus method (Saxena et al., 2015:182). However, the controller parameter values obtained using the stability boundary locus may not always yield the best results. Therefore, there are developed methods to achieve the optimal system response

within the boundary region. One of these methods is the Weighted Geometrical Center (WGC) method, proposed by Onat (Onat, 2013:1539). When examining the system responses obtained using this method, it has been observed that they yield significantly better results compared to the system response received with randomly selected controller parameter values (Ozyetkin et al., 2018:274). Another method is the Centroid of the Convex Stability Region (CCSR) method (Onat, 2019:69). This method forms a triangular region within the area under the stability boundary locus. Subsequently, the centroid of the convex stability region is calculated. The values obtained at this point are used as the controller parameter values. For detailed information on this topic, please refer to (Onat, 2019:69; Ozyetkin and Birdane, 2023:81; Ozyetkin et al., 2020:1811). In this study, the control of the output of a fractional-order system with first-order time delay is investigated. The research is conducted on obtaining the parameters of a fractional-order PD (FOPD) controller by combining the convex stability region and Particle Swarm Optimization (PSO) methods. The FOPD controller has three different parameters. These parameters are k_d , k_p and μ . The stability boundary locus changes according to the μ values. For this reason, values are given at certain intervals for the μ value. D-partition method is used to obtain the stability boundary locus (Hamamci, 2008:329; 2012:1189). A separate stability boundary locus is obtained for each μ value. A triangular area is created within the common region of all curves. The apex of this triangular area differs according to the systems under consideration. The base of the triangular region is the points where the k_d axis intersects. In the proposed method in this study, the parameter values of the FOPD controllers are determined with the PSO algorithm within the obtained triangular region. In order to obtain the optimum controller parameters for the system, the PSO algorithm searches within this region for a certain number of iterations. In this study, performance indices that have been suggested for supervisory optimization algorithms in some studies in the literature are used as a fitness function (Campo, 2012). In this search process, controller performance indexes are used as a fitness function. These are the integral of squared error (ISE), the integral of absolute error (IAE), the integral of time multiply squared error (ITSE), and the integral of time multiply absolute error (ITAE). The PSO algorithm updates the velocity and position according to the values obtained from the fitness function and outputs the optimum parameter values after the iteration is complete. The proposed method and some studies in the literature are compared and it is seen that the results obtained are better.

MATERIAL AND METOD

Fractional Order PD Controllers

The closed-loop control system given in Figure 1 consists of the FOPD controller given by $C(s)$ and the fractional-order system transfer function given by $G(s)$.

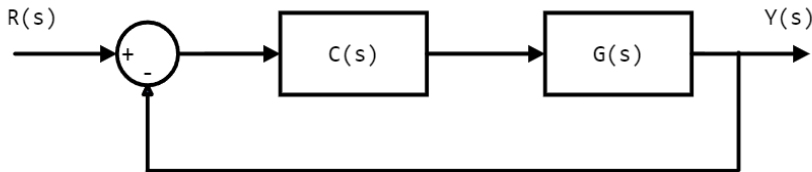


Figure 1: The Closed-Loop Control System

Equation 1 represents the transfer function of the FOPD controller. As can be seen from this equation, the controller parameters are k_p , k_d and μ . These parameters need to be appropriately tuned to achieve the desired performance at the output of the system.

$$C(s) = k_p + k_d s^\mu \quad (1)$$

Equation 2 represents the system transfer function. This transfer function can have fractional-order terms or integer-order terms. Additionally, the system includes a time delay term.

$$G(s) = \frac{N(s)}{D(s)} e^{-\tau s} = \frac{\sum_{r=0}^n x_r s^r}{\sum_{r=0}^n y_r s^r} e^{-\tau s} \quad (2)$$

Stability Boundary Locus

The stability boundary locus is a graphical representation that shows the controller parameter values that make the systems stable. The transfer function of the closed-loop control diagram given in Figure 1 can be expressed as shown in Equation 3.

$$\frac{Y(s)}{R(s)} = \frac{C(s)G(s)}{1 + C(s)G(s)} \quad (3)$$

To provide a general solution, the system transfer function represented by $G(s)$ can be expressed as shown in Equation 4.

$$G(s) = \frac{(x_n s^n + x_{n-1} s^{n-1} + \dots + x_1 s^1 + x_0 s^0)}{(y_n s^n + y_{n-1} s^{n-1} + \dots + y_1 s^1 + y_0 s^0)} e^{-\tau s} \quad (4)$$

$$= \frac{\sum_{r=0}^n x_r s^r}{\sum_{r=0}^n y_r s^r} e^{-\tau s}$$

To obtain the parameter values of the fractional-order PD controller in the system given in Figure 1, the stability boundary locus needs to be obtained. For this purpose, the D-partition method is used (Hamamci, 2008:329; 2012:1189). The characteristic equation of the closed-loop transfer function given in Equation 3 can be expressed as shown in Equation 5.

$$Q(s; k_p, k_d, \mu) = D(s) + (k_p + k_d s^\mu) N(s) e^{-\tau s} \quad (5)$$

Equation 6 is obtained when the expressions in Equation 4 are written instead of the expressions $N(s)$ and $D(s)$ in the characteristic equation.

$$Q(s; k_p, k_d, \mu) = D(s) + k_p N(s) e^{-\tau s} + k_d s^\mu N(s) e^{-\tau s}$$

$$Q(s; k_p, k_d, \mu) = \left(\sum_{r=0}^n y_r s^r \right) + k_p e^{-\tau s} \left(\sum_{r=0}^n x_r s^r \right) \quad (6)$$

$$+ k_d s^\mu e^{-\tau s} \left(\sum_{r=0}^n x_r s^r \right)$$

When the expression in Equation 6 is transformed using the substitution $s = j\omega$, Equation 7 is obtained.

$$Q(j\omega; k_p, k_d, \mu)$$

$$= \left(\sum_{r=0}^n y_r (j\omega)^r \right) + k_p e^{-j\omega\tau} \left(\sum_{r=0}^n x_r (j\omega)^r \right)$$

$$+ k_d (j\omega)^\mu e^{-j\omega\tau} \left(\sum_{r=0}^n x_r (j\omega)^r \right) \quad (7)$$

$$= \left(\sum_{r=0}^n y_r (j\omega)^r \right) + k_p e^{-j\omega\tau} \left(\sum_{r=0}^n x_r (j\omega)^r \right)$$

$$+ k_d e^{-j\omega\tau} \left(\sum_{r=0}^n x_r (j\omega)^{r+\mu} \right)$$

The terms $(j\omega)^r$, $(j\omega)^{r+\mu}$ and $e^{-j\omega\tau}$ in Equation 7 can be expressed as shown in Equation 8.

$$\begin{aligned}(j\omega)^\beta &= \omega^\beta \cos\left(\beta \frac{\pi}{2}\right) + j\omega^\beta \sin\left(\beta \frac{\pi}{2}\right) \\ e^{-j\omega\tau} &= \cos(\omega\tau) - j \sin(\omega\tau)\end{aligned}\tag{8}$$

When the expressions in Equation 8 are substituted into Equation 7, Equation 9 is obtained.

$$\begin{aligned}Q(j\omega; k_p, k_d, \mu) &= \left(\sum_{r=0}^n y_r \left(\omega^r \cos\left(r \frac{\pi}{2}\right) + j\omega^r \sin\left(r \frac{\pi}{2}\right) \right) \right. \\ &\quad + k_p \left(\sum_{r=0}^n x_r \left(\omega^r \cos\left(r \frac{\pi}{2}\right) \right. \right. \\ &\quad \left. \left. + j\omega^r \sin\left(r \frac{\pi}{2}\right) \right) \right) (\cos(\omega\tau) - j \sin(\omega\tau)) \\ &\quad + k_d \left(\sum_{r=0}^n x_r \left(\omega^{r+\mu} \cos\left((r+\mu) \frac{\pi}{2}\right) \right. \right. \\ &\quad \left. \left. + j\omega^{r+\mu} \sin\left((r+\mu) \frac{\pi}{2}\right) \right) \right) (\cos(\omega\tau) - j \sin(\omega\tau))\end{aligned}\tag{9}$$

If Equation 9 is rearranged, Equation 10 is obtained.

$$\begin{aligned}
Q(j\omega; k_p, k_d, \mu) &= \left[\sum_{r=0}^n y_r \omega^r \cos\left(r \frac{\pi}{2}\right) + j \sum_{r=0}^n y_r \omega^r \sin\left(r \frac{\pi}{2}\right) \right] \\
&+ k_p \left[\cos(\omega\tau) \sum_{r=0}^n x_r \omega^r \cos\left(r \frac{\pi}{2}\right) \right. \\
&+ \sin(\omega\tau) \sum_{r=0}^n x_r \omega^r \sin\left(r \frac{\pi}{2}\right) \\
&+ j \cos(\omega\tau) \sum_{r=0}^n x_r \omega^r \sin\left(r \frac{\pi}{2}\right) \\
&\left. - j \sin(\omega\tau) \sum_{r=0}^n x_r \omega^r \cos\left(r \frac{\pi}{2}\right) \right] \quad (10) \\
&+ k_d \left[\cos(\omega\tau) \sum_{r=0}^n x_r \omega^{r+\mu} \cos\left([r+\mu] \frac{\pi}{2}\right) \right. \\
&+ \sin(\omega\tau) \sum_{r=0}^n x_r \omega^{r+\mu} \sin\left([r+\mu] \frac{\pi}{2}\right) \\
&+ j \cos(\omega\tau) \sum_{r=0}^n x_r \omega^{r+\mu} \sin\left([r+\mu] \frac{\pi}{2}\right) \\
&\left. - j \sin(\omega\tau) \sum_{r=0}^n x_r \omega^{r+\mu} \cos\left([r+\mu] \frac{\pi}{2}\right) \right] \\
&= \Re\{Q(j\omega; k_p, k_d, \mu)\} + j\Im\{Q(j\omega; k_p, k_d, \mu)\}
\end{aligned}$$

If Equation 10 is set to zero, the real and imaginary parts are separated. Thus, Equations 11 and 12 are obtained.

$$\begin{aligned}
 Re_Q(\omega) = & \sum_{r=0}^n y_r \omega^r \cos\left(r \frac{\pi}{2}\right) \\
 & + k_p \left[\cos(\omega\tau) \sum_{r=0}^n x_r \omega^r \cos\left(r \frac{\pi}{2}\right) \right. \\
 & \left. + \sin(\omega\tau) \sum_{r=0}^n x_r \omega^r \sin\left(r \frac{\pi}{2}\right) \right] \\
 & + k_d \left[\cos(\omega\tau) \sum_{r=0}^n x_r \omega^{r+\mu} \cos\left([r+\mu] \frac{\pi}{2}\right) \right. \\
 & \left. + \sin(\omega\tau) \sum_{r=0}^n x_r \omega^{r+\mu} \sin\left([r+\mu] \frac{\pi}{2}\right) \right] = 0
 \end{aligned} \tag{11}$$

$$\begin{aligned}
 Im_Q(\omega) = & \sum_{r=0}^n y_r \omega^r \sin\left(r \frac{\pi}{2}\right) \\
 & + k_p \left[\cos(\omega\tau) \sum_{r=0}^n x_r \omega^r \sin\left(r \frac{\pi}{2}\right) \right. \\
 & \left. - \sin(\omega\tau) \sum_{r=0}^n x_r \omega^r \cos\left(r \frac{\pi}{2}\right) \right] \\
 & + k_d \left[\cos(\omega\tau) \sum_{r=0}^n x_r \omega^{r+\mu} \sin\left([r+\mu] \frac{\pi}{2}\right) \right. \\
 & \left. - \sin(\omega\tau) \sum_{r=0}^n x_r \omega^{r+\mu} \cos\left([r+\mu] \frac{\pi}{2}\right) \right] = 0
 \end{aligned} \tag{12}$$

When Equations 11 and 12 are examined, it is seen that they are similar expressions. To avoid reciprocity in transactions, the variable replacement has been made.

$$C1(\omega) = \sum_{r=0}^n x_r \omega^r \sin\left(r \frac{\pi}{2}\right) \tag{13}$$

$$C2(\omega) = \sum_{r=0}^n x_r \omega^r \cos\left(r \frac{\pi}{2}\right) \tag{14}$$

$$D1(\omega) = \sum_{r=0}^n x_r \omega^{r+\mu} \sin\left([r+\mu] \frac{\pi}{2}\right) \tag{15}$$

$$D2(\omega) = \sum_{r=0}^n x_r \omega^{r+\mu} \cos\left([r + \mu] \frac{\pi}{2}\right) \quad (16)$$

Equations 17 and 18 are obtained if the expressions given in Equations 13-16 are substituted in Equations 11 and 12.

$$\begin{aligned} Re_Q(\omega) = \sum_{r=0}^n y_r \omega^r \cos\left(r \frac{\pi}{2}\right) \\ + k_p [\cos(\omega\tau) C2(\omega) + \sin(\omega\tau) C1(\omega)] \\ + k_d [\cos(\omega\tau) D2(\omega) + \sin(\omega\tau) D1(\omega)] = 0 \end{aligned} \quad (17)$$

$$\begin{aligned} Im_Q(\omega) = \sum_{r=0}^n y_r \omega^r \sin\left(r \frac{\pi}{2}\right) \\ + k_p [\cos(\omega\tau) C1(\omega) - \sin(\omega\tau) C2(\omega)] \\ + k_d [\cos(\omega\tau) D1(\omega) - \sin(\omega\tau) D2(\omega)] = 0 \end{aligned} \quad (18)$$

Equations 17 and 18 are converted to the form in Equations 19 and 20 to obtain the variables k_p and k_d .

$$k_p A_1(\omega) + k_d A_2(\omega) = A_3(\omega) \quad (19)$$

$$k_p B_1(\omega) + k_d B_2(\omega) = B_3(\omega) \quad (20)$$

The variables in Equations 19 and 20 are given in Equations 21-26.

$$A_1(\omega) = \cos(\omega\tau) C2(\omega) + \sin(\omega\tau) C1(\omega) \quad (21)$$

$$A_2(\omega) = \cos(\omega\tau) D2(\omega) + \sin(\omega\tau) D1(\omega) \quad (22)$$

$$A_3(\omega) = - \sum_{r=0}^n y_r \omega^r \cos\left(r \frac{\pi}{2}\right) \quad (23)$$

$$B_1(\omega) = \cos(\omega\tau) C1(\omega) - \sin(\omega\tau) C2(\omega) \quad (24)$$

$$B_2(\omega) = \cos(\omega\tau) D1(\omega) - \sin(\omega\tau) D2(\omega) \quad (25)$$

$$B_3(\omega) = - \sum_{r=0}^n y_r \omega^r \sin\left(r \frac{\pi}{2}\right) \quad (26)$$

As a result, Equations 27 and 28 are obtained for k_p and k_d variables.

$$k_p(\omega) = \frac{A_3(\omega)B_1(\omega) - A_1(\omega)B_3(\omega)}{A_2(\omega)B_1(\omega) - A_1(\omega)B_2(\omega)} \quad (27)$$

$$k_d(\omega) = \frac{A_2(\omega)B_3(\omega) - A_3(\omega)B_2(\omega)}{A_2(\omega)B_1(\omega) - A_1(\omega)B_2(\omega)} \quad (28)$$

In this study, a fractional order system given by Equation 29 was used. For this system, which is given in Figure 1, a fractional order controller design is made. For the μ value, which is one of the controller parameters, the stability limit locus was obtained by giving a value in the range of 0.1-1.5 with 0.1 intervals. In the region under these curves, the most optimum k_p and k_d values were tried to be obtained by searching with the PSO algorithm.

$$G(s) = \frac{1}{s^{1.9} + s} e^{-s} = \frac{1}{s(s^{0.9} + 1)} e^{-s} \quad (29)$$

Using Equations 27 and 28, a stability boundary curve as in Figure 2 can be obtained. Here, the value of μ is taken as 0.9.

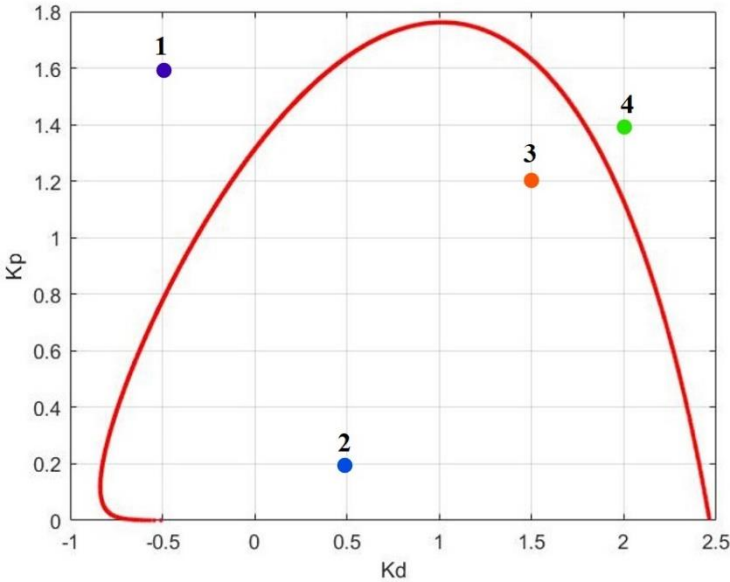


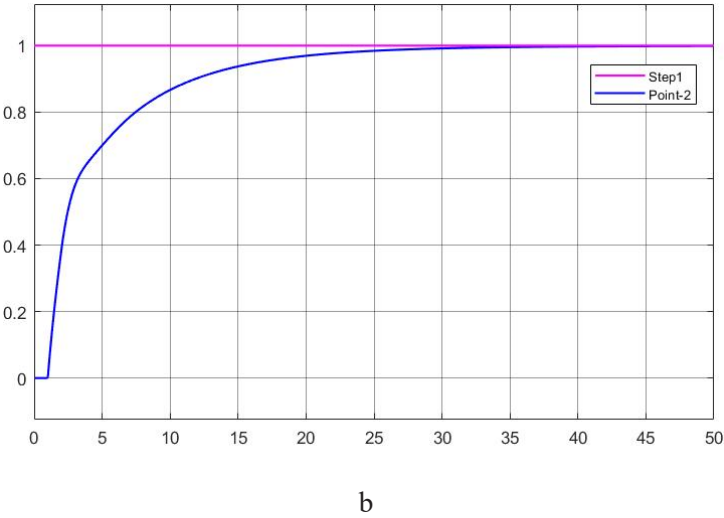
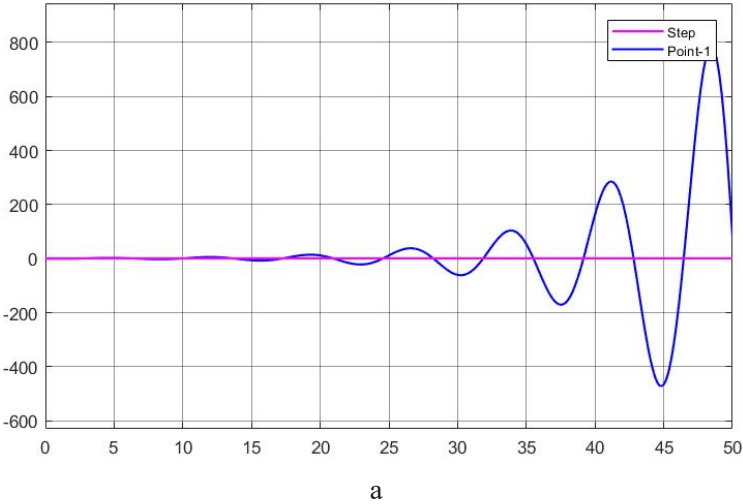
Figure 2: Stability Boundary Locus of the System for $\mu=0.9$

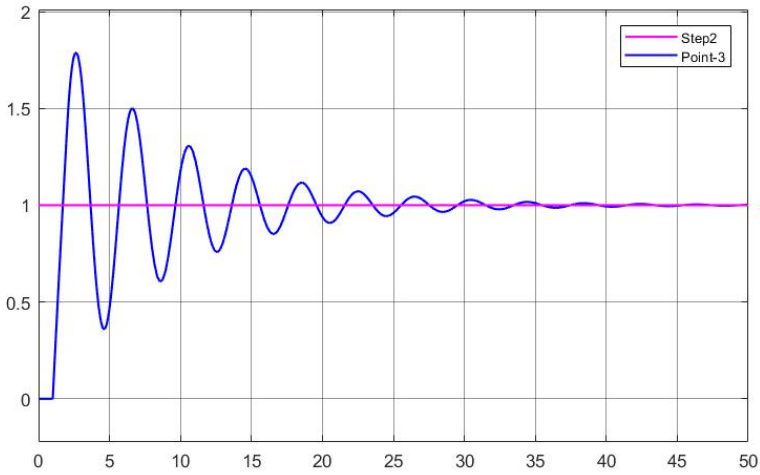
As seen in Figure 2, four different points are shown. The parameter values at these points are given in Table 1.

Table 1: k_d - k_p Values at Selected Points

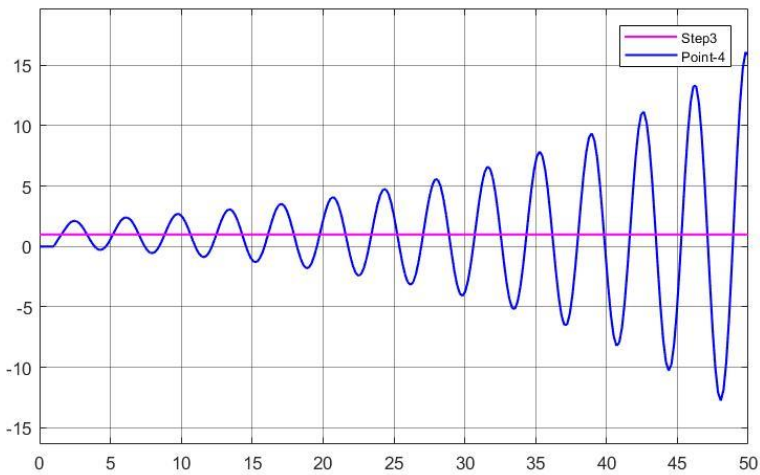
Points	k_d	k_p
1	-0.5	1.6
2	0.5	0.2
3	1.5	1.2
4	2	1.4

When we perform the stability test for the stability boundary region given in Figure 2, the k_p and k_d values at the 3rd and 4th points make the system output stable as in Figure 3b and 3c, while the k_p and k_d values at the 1st and 2nd points are as shown in Figure 3a and 3d makes the system output unstable.





c



d

Figure 3: Unit Step Responses for Different Parameter Values of $G(s)$ (a: Point 1, b: Point 2, c: Point 3, d: Point 4)

For the system given by Equation 29, when the μ value is obtained between 0.1 and 1.5, increasing with 0.1 intervals, stability regions are obtained as in Figure 4.

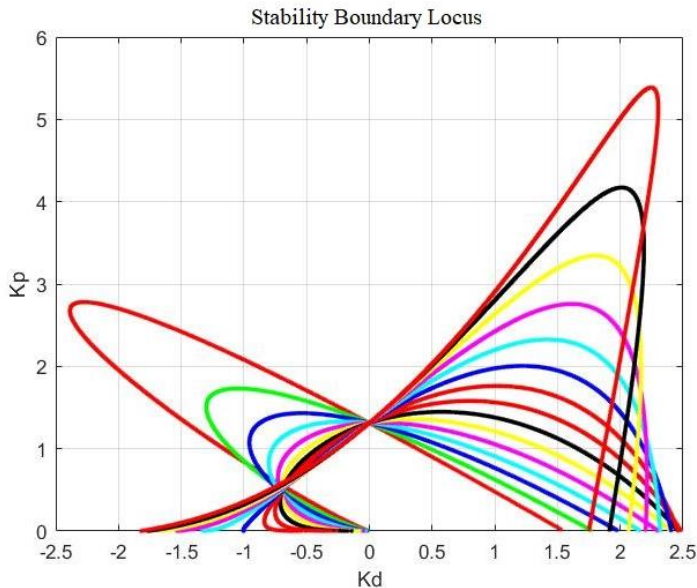


Figure 4: Stability Regions of the System for μ Values Between 0.1-1.5

When Figure 4 is examined, a common region under all curves is seen. To define this region, it is necessary to determine the corner points. For this process, points are selected on the graph. Obtained corner values are shown in Figure 5.

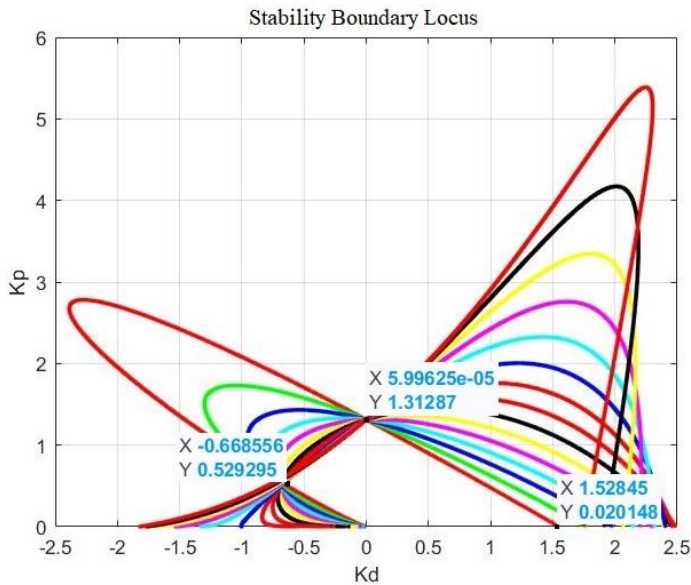


Figure 5: Boundary Points of Common Stability Region

After determining the boundary points of the common stability region, a closed area is obtained. This area is shown in black in Figure 6.

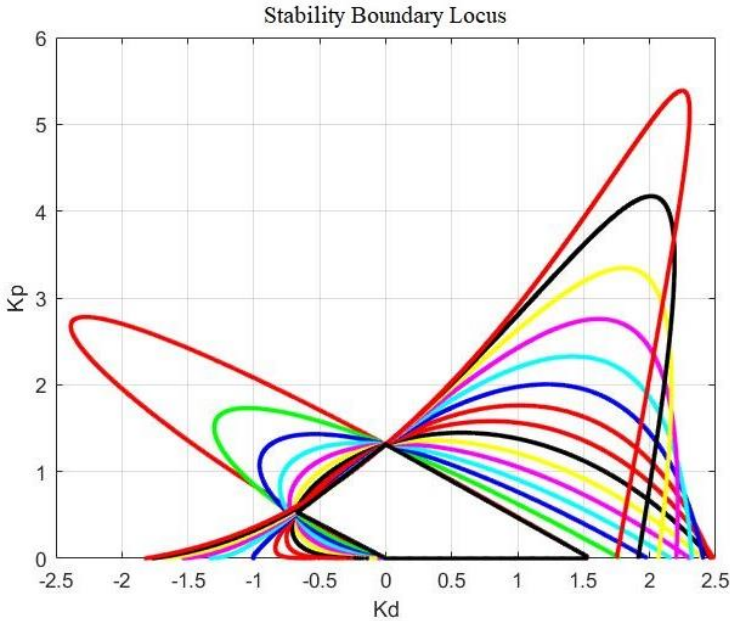


Figure 6: Common Stability Region of the System

Optimum points were tried to be found with the help of the PSO algorithm in the obtained common stability region.

Particle Swarm Optimization

One of the most well-known optimization algorithms is the PSO algorithm. The PSO algorithm was created by utilizing the lifestyles of living things in nature. This algorithm was obtained by Dr Kennedy and Dr Eberhart in 1995 by examining the behavior of animals living in swarms in nature (Kennedy and Eberhart, 1995:1942). The PSO algorithm consists of swarm and their individuals. The number of individuals in the swarm can be varies according to the type of problem. To express the swarm in the PSO algorithm, matrix notation is used as in Equation 30. Here, each line represents an individual. A swarm is formed by the gathering of individuals. The suitability of the results obtained in the PSO algorithm is tested. For this purpose, fitness functions are used. If it is desired to reach the minimum in the problem, the point where the fitness value is minimum is the optimum point. However, if the problem is to reach the maximum, the point where the fitness value is maximum is the optimum point.

In the literature, there are various studies conducted with the PSO algorithm. In these studies, it is used to obtain parameter values of integer order and fractional order PID, PI, and PD controllers (Miao et al., 2017:250; Tousi et al., 2020:22; Zennir et al., 2017:1). In the study by Kocaarslan and Tiryaki (2013: 1), the PSO algorithm was used to obtain the parameters of the PID controller. In another study, the PSO algorithm was used to obtain the parameters of the PI-PD controller for the twin rotor (Kaya et al., 2019:523). In another study, the PSO algorithm was used to control the single conical tank system with a fractional PID controller (Rajesh, 2019:758). In another study, PI-PD controller parameters were obtained with the PSO algorithm (Vastrakar and Padhy, 2013:350). The PSO algorithm has steps to create the swarm, determine the fitness function, and update the velocity and position. Some basic concepts for PSO are given below.

Creating Swarm

The most important of the basic components of the PSO algorithm is the swarm. Each individual in the swarm represents a solution set. For this reason, it is an important factor to form the swarm in order to reach the solution of the problem. In the PSO algorithm, the swarm is obtained as in Equation 30, with uniform randomness. Here, " l " represents the number of parameters within each individual, and " k " represents the number of individuals in the swarm. Each row in the swarm matrix represents an individual. Random numbers are set to be within the boundaries of the problem. Otherwise, the PSO algorithm may give incorrect results.

$$\begin{bmatrix} d_{11} & d_{12} & \dots & \dots & d_{1l} \\ \vdots & \vdots & & & \vdots \\ \vdots & \vdots & & & \vdots \\ \vdots & \vdots & & & \vdots \\ d_{k1} & d_{k2} & \dots & \dots & d_{kl} \end{bmatrix}_{k \times l} \quad (30)$$

Fitness Function

The fitness function is used to evaluate the suitability of the values obtained at the end of each iteration in the PSO algorithm. In short, it tests the fitness of individuals. In some studies, in the literature, "ISE", "IAE", "ITSE" and "ITAE" were used as fitness functions (Campo, 2012; Vastrakar and Padhy, 2013:350; Zennir et al., 2017:1). The results obtained from the fitness function are expressed in matrix form as in Equation 31.

$$\begin{bmatrix} c_{11} \\ c_{21} \\ \vdots \\ \vdots \\ c_{k1} \end{bmatrix}_{k \times 1} \quad (31)$$

Velocity and Position Update

Before starting the iteration in the PSO algorithm, it is necessary to determine the best the swarm and individuals. The fitness function values are checked to find the best value in the swarm. If the problem is to reach the highest value, the individual with the highest fitness function value is selected as the best of the swarm. However, if the problem is to reach the lowest value, the individual with the smallest fitness function value is selected as the best of the swarm. Individuals are best in their position, as individuals do not have a preliminary velocity and position before iteration begins. After the best of the flock and the best of individuals are determined, iteration for the PSO algorithm is started. Speed and position updates are made in iteration. In each iteration, individuals' speeds and positions are updated. Equation 32 is used for speed update (Kennedy and Eberhart, 1995:1942).

$$v_{ij} = \rho * v_{ij} + \alpha_1 * \sigma_1 * (\chi_{ij}^{Pb} - \chi_{ij}) + \alpha_2 * \sigma_2 * (\chi_{ij}^{Sb} - \chi_{ij}) \quad (32)$$

The parameters in the velocity update equation are as follows.

- ρ : Inertia Coefficient
- α_1 : Cognitive Coefficient
- α_2 : Social Coefficient
- σ_1 : Random Coefficient (Between 0-1)
- σ_2 : Random Coefficient (Between 0-1)
- χ_{ij} : Position of the Particle
- χ_{ij}^{Pb} : The Position of the Best of the Particle
- χ_{ij}^{Sb} : Position of the Best of the Swarm

After the speed update, the position update is made. For this, the velocity formula in Equation 33 is used.

$$\Delta\theta = \frac{\Delta\chi}{\Delta t} \Rightarrow \frac{\Delta\chi}{1} \Rightarrow \Delta\theta = \Delta\chi \quad (33)$$

In the PSO algorithm, one iteration cycle is equal to one unit of time change. The velocity change (Δv) is the ratio of the path change (Δx) to the time change (Δt). Therefore, as in Equation 33, the change in path equals the change in velocity. Therefore, Equation 34 is used when updating the position (Kennedy and Eberhart, 1995:1942).

$$\chi_{ij} = \chi_{ij} + v_{ij} \quad (34)$$

After the position update is made, the PSO algorithm tests whether the new positions of the individuals in the swarm are out of the determined search area. A correction is made so that individuals outside the search zone will re-enter the search zone. Otherwise, the algorithm may give incorrect results when it leaves the search region. When all iterations are complete or the PSO algorithm satisfies the stopping condition, the PSO algorithm outputs the best solutions.

RESULTS

A FOPD controller is designed for the system whose transfer function is given in Equation 29. The parameter values of the FOPD controller were obtained using the stability boundary locus method and the PSO algorithm. In order to obtain the stability boundary locus of the system given by Equation 29, equations depending on ω given by Equations 27 and 28 are used. FOPD controllers contain three different parameters in their structure. These are k_d , k_p and μ . But the stability boundary locus is two-dimensional. As seen in Figure 2, one of the axes shows k_d and the other shows k_p values. The stability boundary locus of the system differs according to the values given to the μ parameter. Since it cannot be predicted which μ value will have the highest performance at the system output, stability regions were drawn for different μ values in this study. In Figure 4, stability boundary curves are obtained for the system given in Equation 29, with a μ value between 0.1 and 1.5 with 0.1 step intervals. In these obtained stability boundary curves, a common region is formed for all of them. Within this common region, the value of μ can take any value between 0.1 and 1.5. Any point selected from this common stability region can transform the system into a stable structure. In the common stability region, the fractional PD controller parameters are within certain limits. In this way, the PSO algorithm can be operated easily within the common stability region. The common stability region obtained for this system is given in Figure 6. The PSO algorithm was run within the common stability region obtained in Figure 6. ISE, IAE, ITSE and ITAE were used as fitness functions in the PSO algorithm. The search region results obtained

according to these fitness functions are shown in Figure 7-10, respectively. In Figure 7, the ISE fitness function is used in the PSO algorithm. The optimum values obtained in Figure 7 are $\mu=0.9975$, $k_d=0.9267$, and $k_p=0.5185$. In Figure 8, the IAE fitness function is used in the PSO algorithm. The optimum values obtained in Figure 8 are $\mu=0.9981$, $k_d=0.8060$, and $k_p=0.6173$. In Figure 9, the ITSE fitness function is used in the PSO algorithm. The optimum values obtained in Figure 9 are $\mu=0.9930$, $k_d=0.8453$, and $k_p=0.5841$. In Figure 10, the ITAE fitness function is used in the PSO algorithm. And the optimum values are obtained as $\mu=0.9987$, $k_d=0.7442$, and $k_p=0.6083$.

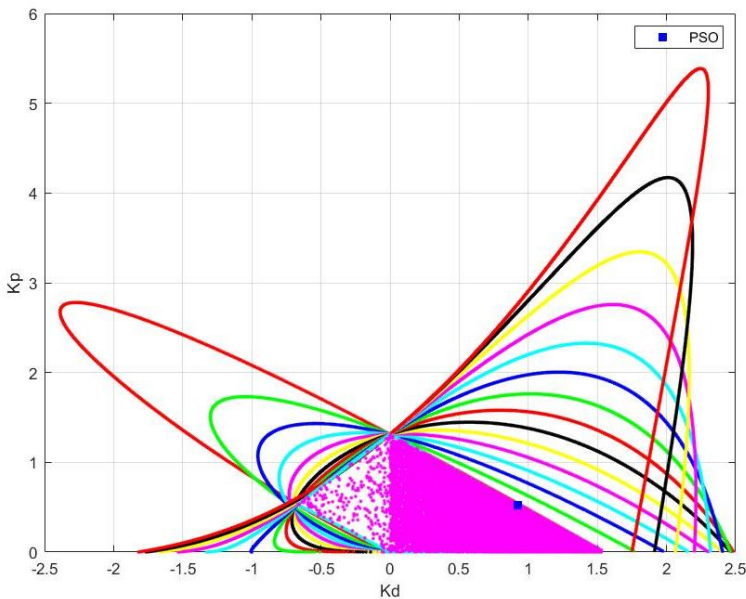


Figure 7: Searching Points Made by PSO Algorithm Using ISE Fitness Function in Common Stability Region of $G(s)$ and Optimum Value Obtained

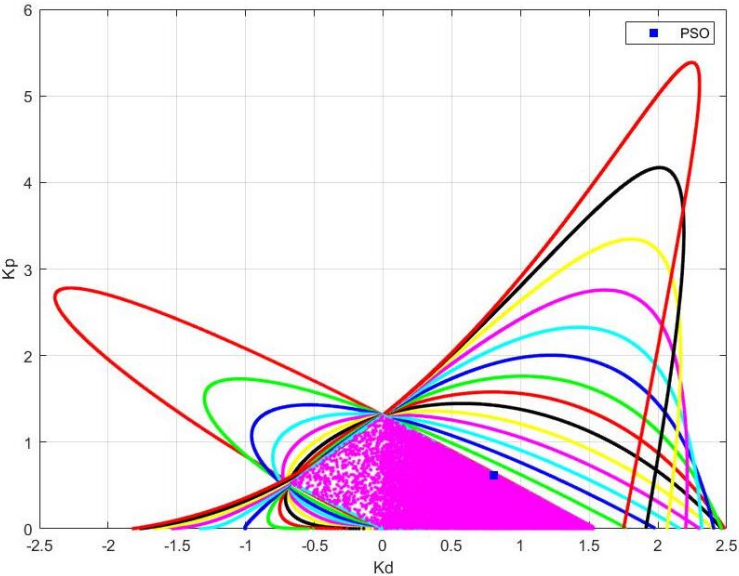


Figure 8: Searching Points Made by PSO Algorithm Using IAE Fitness Function in Common Stability Region of $G(s)$ and Optimum Value Obtained

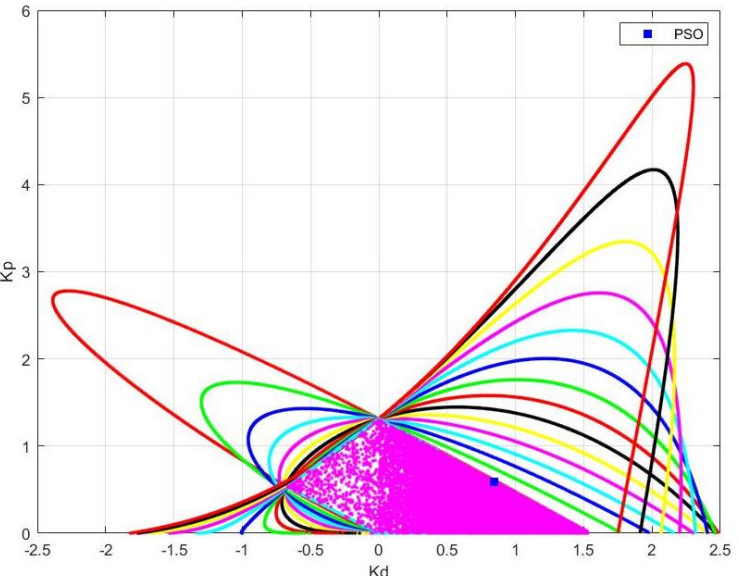


Figure 9: Searching Points Made by PSO Algorithm Using ITSE Fitness Function in Common Stability Region of $G(s)$ and Optimum Value Obtained

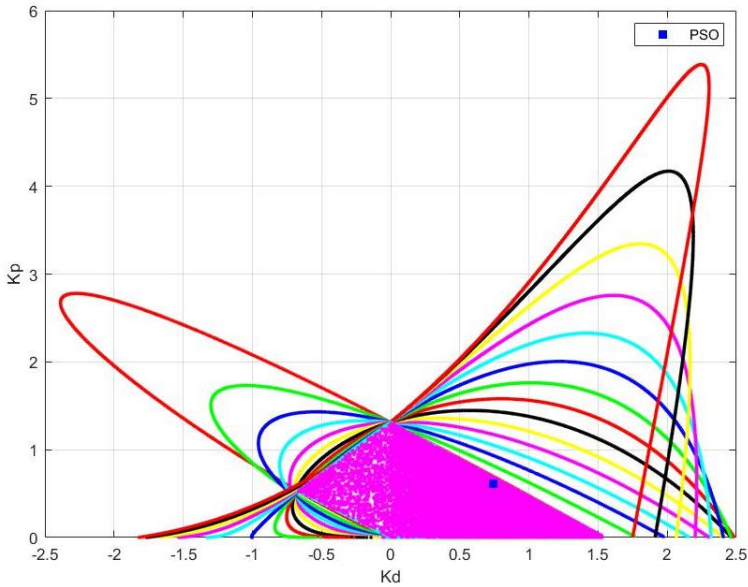
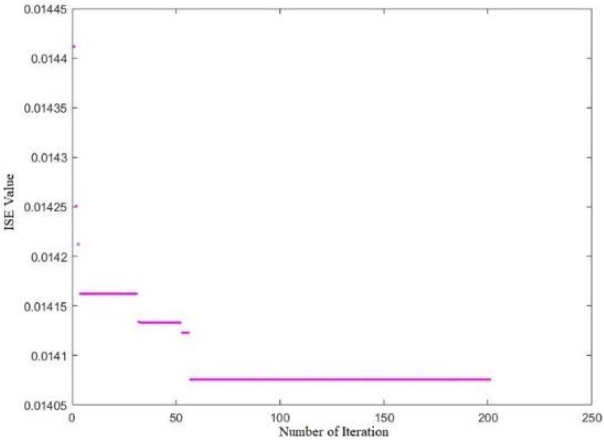
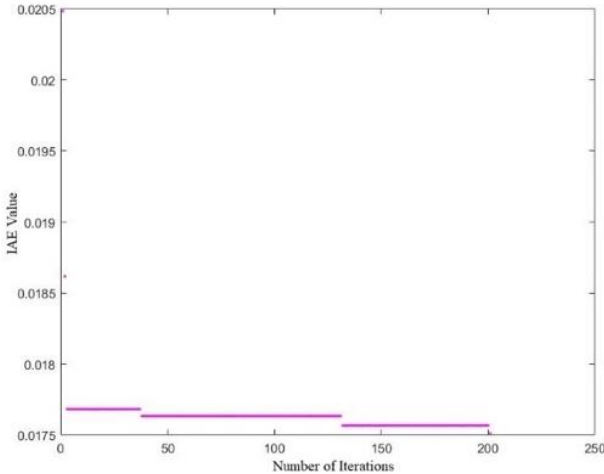


Figure 10: Searching Points Made by PSO Algorithm Using ITAE Fitness Function in Common Stability Region of $G(s)$ and Optimum Value Obtained

The PSO algorithm aims to minimize the fitness function value during the iterations. The graph of fitness function values is provided in Figure 11. It is seen that the fitness function values decrease towards the end of the iteration. The values obtained according to the number of individuals in the swarm or the number of iterations in the PSO algorithm may differ. For this reason, the number of swarm and the number of iterations were obtained by making experiments. In this study, the number of iterations for the PSO algorithm was determined as 200 and the number of individuals in the swarm was determined as 200.



a



b

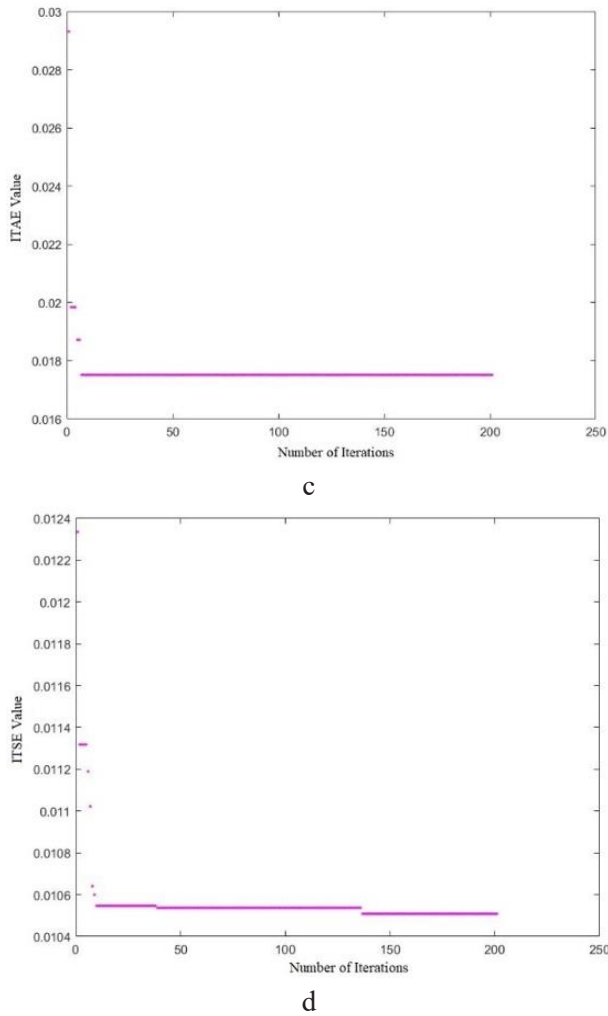


Figure 11: The Values of Fitness Functions During PSO Algorithm Iterations
(a: ISE, b: IAE, c: ITSE, d: ITAE)

The fractional order PD controller parameters obtained as a result of the PSO algorithm are given in Table 2. Obtained controller parameters were tested in Simulink environment. The results are shown in Figure 12 comparatively.

Table 2: FOPD Controller Parameters Obtained from PSO Algorithm

Fitness Function of PSO	k_p	k_d	μ
ISE	0.5185	0.9267	0.9975
IAE	0.6173	0.8060	0.9981
ITSE	0.5841	0.8453	0.9930
ITAE	0.6083	0.7442	0.9987

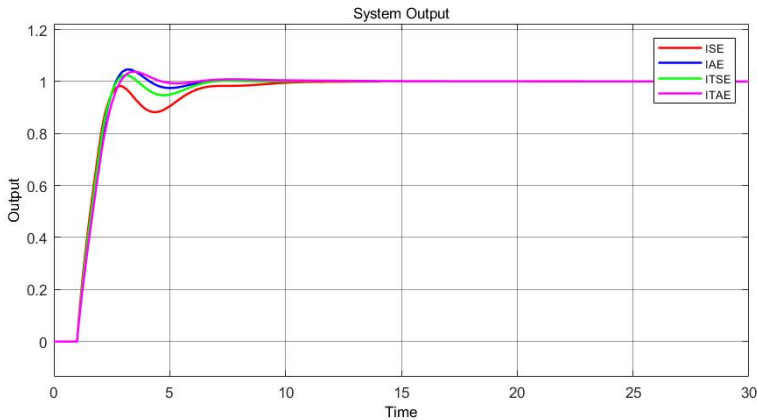


Figure 12: Unit Step Responses of the System Designed Using the Controller Parameters Obtained Because of the PSO Algorithm

In the PSO algorithm, when ITAE is used as the fitness function, the FOPD controller parameters obtained show a better performance at the system output compared to other fitness functions. When the graph in Figure 12 is examined, the controller model with the fastest settling time and the smallest oscillation is the controller model created with ITAE fitness function.

DISCUSSION AND CONCLUSIONS

The system used in this study was used in the study of Ozyetkin and Tan (2017: 9230). Using the results obtained in this study, the parameters obtained with the PSO algorithm were compared. Ozyetkin and Tan (2017: 9230) used the WGC method to obtain the parameters of the FOPD controller in their study. The results obtained in this study are given in Table 3.

Table 3: FOPD Controller Parameter Values Obtained with the WGC

k_p	k_d	μ
0.4906	0.4532	0.9
0.5462	0.5053	1
0.6183	0.5316	1.1
0.4906	0.4532	0.9

The results obtained in both studies were compared. In Figure 13, the FOPD controller coefficients obtained with the PSO algorithm using the ISE fitness function are compared with the system response.

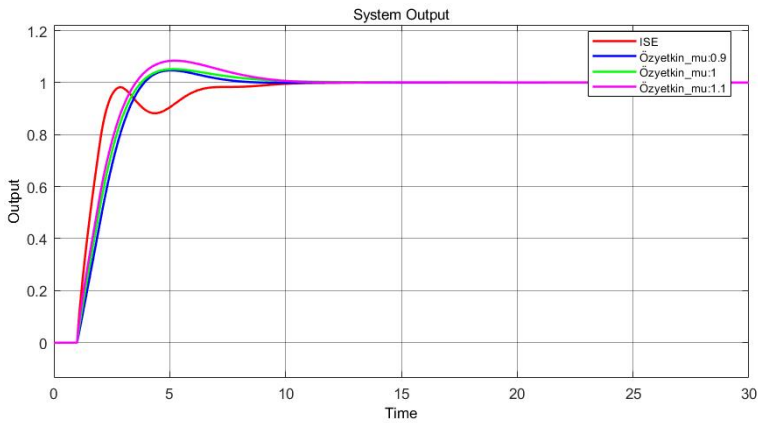


Figure 13: Comparison of System Responses of Controller Parameters Obtained with the PSO Algorithm (ISE) and the WGC Method

In Figure 14, the FOPD controller coefficients obtained with the PSO algorithm using the IAE fitness function are compared with the system response.

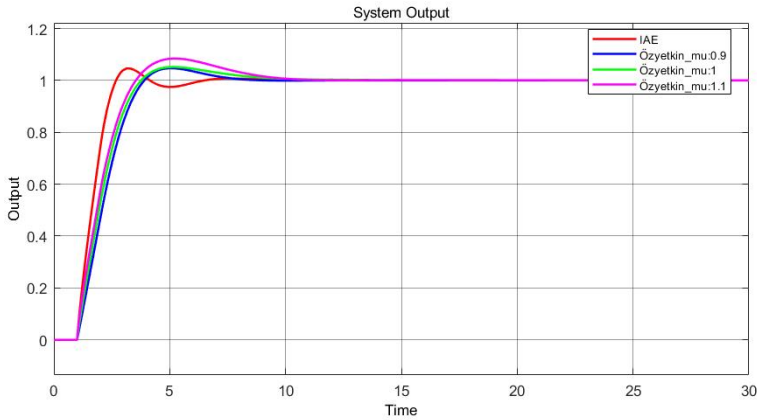


Figure 14: Comparison of System Responses of Controller Parameters Obtained with PSO Algorithm (IAE) and the WGC Method

In Figure 15, the FOPD controller coefficients obtained by the PSO algorithm using the ITSE fitness function are compared with the system response.

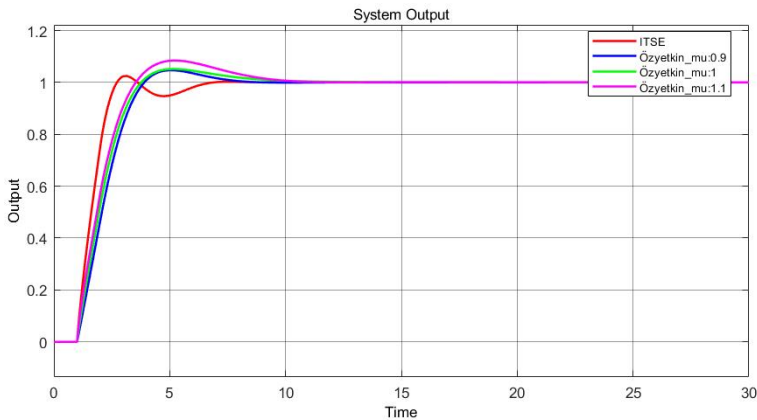


Figure 15: Comparison of System Responses of Controller Parameters Obtained by PSO Algorithm (ITSE) and WGC Method

In Figure 16, the FOPD controller coefficients obtained by the PSO algorithm using the ITAE fitness function are compared with the system response.

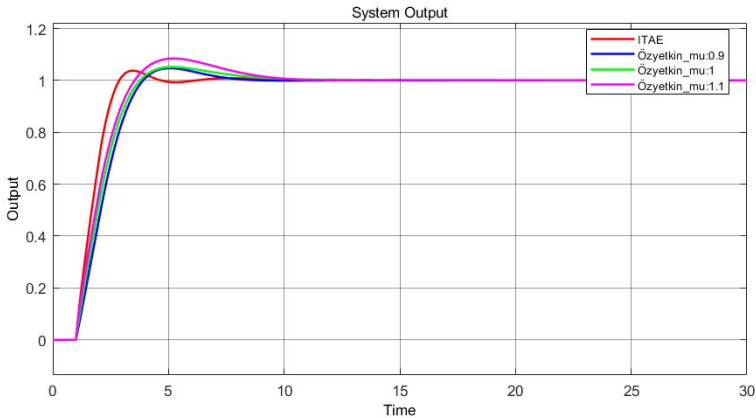


Figure 16: Comparison of System Responses of Controller Parameters Obtained by PSO Algorithm (ITAE) and WGC Method

When all the results are examined, it is seen that the controller parameters obtained with the PSO algorithm show better performances. The performance information for all system responses is given in Table 4.

Table 4: Performance of Unit Step Responses of Controller Parameters Obtained with PSO Algorithm and the WGC Method

Method	WGC (Özyetkin and Tan, 2017)			PSO			
	$\mu:0.9$	$\mu:1$	$\mu:1.1$	IAE	ISE	ITSE	ITAE
Parameters/ Fitness Functions							
Rise Time	2.3284	1.9374	1.6397	1.2341	1.2007	1.2274	1.3757
Transient Time	8.4518	7.8347	7.2612	5.4739	6.7376	5.9095	3.7114
Settling Time	8.4518	7.8347	7.2612	5.4739	6.7376	5.9095	3.7114
Settling Min	0.9015	0.9003	0.9027	0.9032	0.8806	0.9035	0.9024
Settling Max	1.0357	1.0519	1.1004	1.0429	1.0013	1.0170	1.0232
Overshoot	3.5520	5.1822	10.0320	4.2836	0.1204	1.6910	2.3091
Peak	1.0357	1.0519	1.1004	1.0429	1.0013	1.0170	1.0232
Peak Time	6.1600	5.1500	4.4500	3.2100	16.4300	3.0700	3.4700
Rise Time	2.3284	1.9374	1.6397	1.2341	1.2007	1.2274	1.3757
Transient Time	8.4518	7.8347	7.2612	5.4739	6.7376	5.9095	3.7114
Settling Time	8.4518	7.8347	7.2612	5.4739	6.7376	5.9095	3.7114

As can be seen from Table 4, it is seen that the best result is obtained by using the ITAE fitness function in the PSO algorithm. Thanks to this proposed method, while the system approaches the reference value quickly, it is observed in the results obtained that the settling time is quite short. In this study, the question

marks about determining the parameters of FOPD controllers were tried to be resolved. In this study, stability boundary locus and WGC methods, which were previously studied in the literature, were used. Depending on the μ value, more than one stability region was obtained, and their common stability region was found. A search was made to obtain the best parameter values in this common stability region with the PSO algorithm. The results obtained were compared with a previous study in the literature (Ozyetkin and Tan, 2017:9230). It has been observed that the proposed method gives superior results compared to these methods. In the future, this method is planned to be expanded and investigated for different controller types. Thanks to this study, a solution proposal has been brought to the question of how the controller parameters should be selected in the stability curve graph, which is an important problem in the literature. It is clear that new studies using the proposed method will make an important contribution to the literature.

REFERENCES

- Campo, A. B. (2012). PID Control Design. In *MATLAB - A Fundamental Tool for Scientific Computing and Engineering Applications* (Vol. 1).
- Chien, K. L., Hrones, J. A. and Reswick, J. B. (1952). On the Automatic Control of Generalized Passive Systems. *Transactions of the ASME*, 74, 175-185. doi:10.1115/1.4015724
- Cohen, G. and Coon, G. A. (1953). Theoretical Consideration of Retarded Control. *Transactions of the ASME*, 75, 827-834.
- Hamamci, S. E. (2008). Stabilization using fractional-order PI and PID controllers. *Nonlinear Dynamics*, 51, 329-343. doi:10.1007/s11071-007-9214-5
- Hamamci, S. E. (2012). PI and PID stabilization of neutral and retarded systems with time delay. *Turkish Journal of Electrical Engineering and Computer Sciences*, 20(7), 1189-1205. doi:10.3906/elk-1101-1059
- Hamamci, S. E. and Işık, İ. (2014). Stabilization of Switched Systems Using Only A Single Fractional Order PI Controller. *Balkan Journal of Electrical and Computer Engineering*, 2(3), 150-155. doi:10.17694/bajece.30482
- Hamamci, S. E. and Tan, N. (2006). Design of PI controllers for achieving time and frequency domain specifications simultaneously. *ISA Transactions*, 45(4), 529-543. doi:[https://doi.org/10.1016/S0019-0578\(07\)60230-4](https://doi.org/10.1016/S0019-0578(07)60230-4)
- Kaya, I., Takeş, C. A. and Alyoussef, F. (2019). Parçacık Sürü Optimizasyonu Tabanlı PI-PD ile Twin Rotor Denetimi. *Dicle Üniversitesi Mühendislik Fakültesi Mühendislik Dergisi*, 10(2), 523-530. doi:10.24012/dumf.548629
- Kennedy, J. and Eberhart, R. (1995). *Particle swarm optimization*. [Conference presentation] Proceedings of ICNN'95 - International Conference on Neural Networks.
- Kocaarslan, İ. and Tiryaki, H. (2013). Comparison of PSO-PID and FGPI Controllers on a Thermal Power Plant. *International Journal of Engineering Research and Development*, 5(2), 1-6.
- Lee, J., Cho, W. and Edgar, T. F. (2014). Simple Analytic PID Controller Tuning Rules Revisited. *Industrial & Engineering Chemistry Research*, 53(13), 5038-5047. doi:10.1021/ie4009919
- Miao, Z., Han, T., Dang, J. and Ju, M. (2017). *FOP/PI controller parameters optimization using PSO with different performance criteria*. [Conference presentation] 2017 IEEE 2nd Information Technology, Networking, Electronic and Automation Control Conference (ITNEC).
- Onat, C. (2013). A new concept on PI design for time delay systems: Weighted geometrical center. *International Journal of Innovative Computing, Information and Control*, 9, 1539-1556.
- Onat, C. (2019). A new design method for PI-PD control of unstable processes with dead time. *ISA Transactions*, 84, 69-81. doi:<https://doi.org/10.1016/j.isatra.2018.08.029>

- Onat, C., Hamamci, S. E. and Obuz, S. (2012). A Practical PI Tuning Approach For Time Delay Systems. *IFAC Proceedings Volumes*, 45(14), 102-107. doi:<https://doi.org/10.3182/20120622-3-US-4021.00027>
- Ozyetkin, M. and Birdane, H. (2023). The processes with fractional order delay and PI controller design using particle swarm optimization. *International Journal of Optimization and Control: Theories & Applications*, 13(1), 81-91. doi:10.11121/ijocta.2023.1223
- Ozyetkin, M. M. (2018). A simple tuning method of fractional order $PI\lambda$ - $PD\mu$ controllers for time delay systems. *ISA Transactions*, 74, 77-87. doi:<https://doi.org/10.1016/j.isatra.2018.01.021>
- Ozyetkin, M. M., Onat, C. and Tan, N. (2012). *Zaman Gecikmeli Sistemler için $PI\lambda$ Denetçi Tasarımı*. [Conference presentation] TOK 12, Niğde.
- Ozyetkin, M. M., Onat, C. and Tan, N. (2018). PID Tuning Method for Integrating Processes Having Time Delay and Inverse Response. *IFAC-PapersOnLine*, 51(4), 274-279. doi:<https://doi.org/10.1016/j.ifacol.2018.06.077>
- Ozyetkin, M. M., Onat, C. and Tan, N. (2020). PI-PD controller design for time delay systems via the weighted geometrical center method. *Asian Journal of Control*, 22, 1811-1826. doi:10.1002/asjc.2088
- Ozyetkin, M. M. and Tan, N. (2017). Practical Tuning Algorithm of $PD\mu$ Controller for Processes with Time Delay. *IFAC-PapersOnLine*, 50(1), 9230-9235. doi:<https://doi.org/10.1016/j.ifacol.2017.08.1281>
- Podlubny, I. (1994). Fractional-Order Systems and Fractional-Order Controllers. *Slovak Academy of Sciences Institute of Experimental Physics*.
- Rajesh, R. (2019). Optimal tuning of FOPID controller based on PSO algorithm with reference model for a single conical tank system. *SN Applied Sciences*, 1(7). doi:10.1007/s42452-019-0754-3
- Rivera, D. E., Morarl, M. and Skogestad, S. (1986). Internal Model Control: Pid Controller Design. *Industrial and Engineering Chemistry Process Design and Development*, 25(1), 252-265. Retrieved from <https://doi.org/10.1021/i200032a041>
- Saxena, S., Hote, Y. V. and Sondhi, S. (2015). *Fractional-order PI control of DC servo system using the stability boundary locus approach*. [Conference presentation] 2015 IEEE 10th International Conference on Industrial and Information Systems (ICIIS).
- Tan, N. (2009). Computation of stabilizing PI-PD controllers. *International Journal of Control, Automation and Systems*, 7(2), 175-184. doi:10.1007/s12555-009-0203-y
- Tan, N., Kaya, I., Yeroglu, C. and Atherton, D. P. (2006). Computation of stabilizing PI and PID controllers using the stability boundary locus. *Energy Conversion and Management*, 47(18), 3045-3058. doi:<https://doi.org/10.1016/j.enconman.2006.03.022>

- Tousi, S. M. A., Mostafanasab, A. and Teshnehlab, M. (2020). *Design of Self Tuning PID Controller Based on Competitive PSO*. [Conference presentation] 2020 4th Conference on Swarm Intelligence and Evolutionary Computation (CSIEC).
- Vastrakar, N. K. and Padhy, P. K. (2013). *Simplified PSO PI-PD Controller for Unstable Processes*. [Conference presentation] 2013 4th International Conference on Intelligent Systems, Modelling and Simulation.
- Wang, F. S., Juang, W. S. and Chan, C. T. (1995). Optimal Tuning Of PID Controllers For Single And Cascade Control Loops. *Chemical Engineering Communications*, 132(1), 15-34. doi:10.1080/00986449508936294
- Yue, W. (2020). *Study on PID Control of Aquatic Product Dryer based on Support Vector Machine Optimized by Improved Particle Swarm Algorithm*. [Conference presentation] 2020 2nd International Conference on Applied Machine Learning (ICAML).
- Zennir, Y., Mechhoud, E. A., Seboui, A. and Bendib, R. (2017). *Multi-controller approach with PSO-PI λ D μ controllers for a robotic wrist*. [Conference presentation] 2017 5th International Conference on Electrical Engineering - Boumerdes (ICEE-B).
- Ziegler, J. G. and Nichols, N. B. (1942). Optimum Settings for Automatic Controllers. *Transactions of the ASME*, 64, 759-768.

Chapter 16

Cost-Based Optimization of Raw Materials in Production of High Carbon Ferrochrome

Sinan KAPAN¹

Ünal ÇAMDALI²

Nevin ÇELİK³

Osman YİĞİD⁴

¹ Dr. Res. Asst. Firat University, Faculty of Engineerig, Department of Mechanical Engineering, Elazig, Turkey
skapan@firat.edu.tr, Orcid No: 0000-0001-5690-1041

² Prof. Dr. Ankara Yildirim Beyazit University, Faculty of Engineering and Natural Sciences, Department of Mechanical Engineering, Ankara, Turkey, ucamdali@gmail.com, Orcid No: 0000-0002-2566-9945

³ Prof. Dr. Firat University, Faculty of Engineerig, Department of Mechanical Engineering, Elazig, Turkey nevincelik23@gmail.com, Orcid No: 0000-0003-2456-5316

⁴ Res. Asst. Firat University, Faculty of Engineerig, Department of Mechanical Engineering, Elazig, Turkey oyigid@firat.edu.tr, Orcid No: 0000-0002-1798-1250

ABSTRACT

A specific facility that specializes in producing high carbon ferrochrome is investigated. Mass balance is established using data obtained from the facility. An optimization problem is formulated to determine the optimal solution that balances cost and raw material usage. The primary objective of this optimization problem is to identify the minimum-cost combination of raw materials while adhering to the constraints related to the desired high carbon ferrochrome content specified by customer orders. To achieve this goal, a model was developed using MATLAB program. The objective function, based on cost, was formulated to determine the optimal quantities of raw materials fed into the electric arc furnace. Linear programming techniques have been employed to solve the cost equation

Keywords: Raw material, carbon ferrochrome, optimization

INTRODUCTION

Over the past few decades, there has been a noticeable trend where the cost of raw materials has been on the rise, leading to increased concerns about resource scarcity. Specifically, in the context of a high carbon ferrochrome-making facility, the raw materials used include chrome ore and auxiliary materials such as coke, coal, quartz, and bauxite. The significant growth of the global stainless steel industry in the past two decades has resulted in a heightened demand for ferrochrome. Consequently, most businesses strive to identify the optimal combination of raw materials that can significantly reduce the overall cost of the final product. It is crucial to avoid a poor composition as it can result in the wastage of alloying materials and potentially compromise the quality of the output. Given their high cost, an optimization model has been developed using the most cost-effective proportions of alloying materials. Undoubtedly, employing the correct blend of raw materials enables the production of high-quality products in the most efficient manner. Ferrochrome, which typically contains 10% to 20% chromium, is a key ingredient in the production of stainless steel (Weitz & Garbers-Craig, 2016). Chromium ore finds extensive use in various industries, such as providing a protective coating for steel and other metals due to its exceptional resistance to atmospheric corrosion, chemical effects, abrasion, and hardness (Vapur et al., 2013). The increase in global energy prices naturally contributes to the escalation of raw material costs. Consequently, recent studies have focused on the efficient utilization of energy resources (Czapla et al., 2008; Czesla & Tsatsaronis, 2002; Radwan, 2012; Rangnathan et al., 2010; Singh et al., 2007). However, it has become imperative to conduct research specifically aimed at optimizing the efficient use of raw materials.

(Xiaobing et al., 2008), conducted a study for cost optimization of raw materials fed into the furnace with the help of an ant colony algorithm by considering a steel production process. The results showed that the proposed algorithm outperforms the linear problem solving techniques.

(Czapla et al., 2008) developed computer software with a genetic algorithm, taking computational models from the literature, in order to determine the optimum electrical energy in an electric arc furnace for steel production. They found that the use of artificial intelligence methods for the analysis of parameters affecting energy consumption is one of the ways to improve working indexes.

(Çamdali, 2005) determined the optimum values of the chemical components of the molten steel using linear programming method, depending on the maximum chemical reaction exergy and scrap amount for the scrap preheated electric arc furnace used in steel production. Optimum parameters and maximum exergy values for various steel types are given in tables and graphics.

(Singh et al., 2007) aimed to increase the performance of the furnace and reduce energy consumption by modeling different combinations of raw materials fed to the furnace with artificial neural networks, which is a type of optimization. They defined the effect of different combinations on the performance of the furnace as the production capacity index. A detailed statistical analysis was performed on plant data to understand the relationship between raw material and furnace performance.

(Moghadasian & Alenasser, 2011) investigated a genetic-fuzzy control system, which controls the input energy of a three-phase electric arc furnace, using a new application. Since the distance between the graphite electrodes and the metal pool in the furnace directly affects the arc formation, a fuzzy controller tuned by genetic algorithms has been developed to optimize this distance. By using the simulation results and the proposed method, they showed a significant increase in the performance of the system.

(Chen et al., 2018) examined the effect of electricity consumption and exergy efficiency with the variable states of the raw materials fed to the furnace by considering silicon production. They modeled the problem using the artificial neural network method. The results showed that the exergy efficiency and electricity consumption values of the test data were $R^2 = 0.9918$ and $R^2 = 0.9896$, respectively, with low error levels. They concluded that the developed artificial neural networks (ANN) model is useful in guiding the decision on the use of raw materials in silicon production under the condition of lower electricity consumption and higher exergy efficiency, as there is a good fit between the actual and predicted values.

(Ranganathan, 2007) developed a simulation program that can model the process under various conditions in order to increase the efficiency of the process by reducing the specific power consumption and maximizing the recovery of metals in a ferrochrome production facility. This simulation includes three main models; a) thermochemistry; b) temperature profile and c) electrical properties. They validated this simulation using data from a ferrochrome manufacturing plant.

PROBLEM DEFINITION

In this study, a facility that produces high carbon ferrochrome is considered as a case study. First of all, mass balance was established with the data obtained from this facility. Afterwards, it was handled as an optimization problem to find the best solution between cost and raw material usage.

The main purpose of this optimization problem is to determine the amount of raw material with minimum cost so as to meet the high carbon ferrochrome

content constraints determined according to the customer orders. For this, a modeling was made using the MATLAB program. The cost-based objective function of the raw materials entering the electric arc furnace is defined by equation (1). In the literature, mostly linear programming techniques have been used as a solution method for the cost optimization problems of the electric arc furnace. As can be seen from the cost equation, this problem is also considered as a linear problem.

For the mathematical modeling of the problem, the decision variables and the objective function must be defined. The decision variables are shown as follows.

$$X = (x_1, x_2, x_3, \dots x_k) \quad (1)$$

x_i represents the mass of raw material and detailed shown in Table 1.

Table 1: Notations

Mass (kg)	Notation
Coke	x_1
Coal	x_2
Soderberg	x_3
Quartzite	x_4
Bauxite	x_5
Rich Slag	x_6
Chrome Ore	x_7
H.C. Ferrochrome	x_8

The objective function to minimize the raw material costs is expressed as:

$$\min Z = c_1x_1 + c_2x_2 + \dots c_kx_k = \sum_j^k c_jx_j \quad (2)$$

where Z is the objective function and c is the price per unit mass of each raw material in dollars (\$/kg).

Constraints are divided into two groups. The first group of constraints consists of chemical composition of the product according to the customer orders and presented in Table 2. The second group of constraints are mandatory constraints such as Cr/Fe ratio, slag basicity arising from the production process.

Table 2: Constraints due to the chemical composition of high carbon ferrochrome

HC Ferrochrome	
Element	Composition (%)
Cr	%63-%64
Fe	%28,591-%26,485
C	%7,5-%8
Si	%0,9-%1,5
P	%0,009-%0,015
Cr/Fe	>2
(MgO+SiO ₂)/CaO	1

By substituting the cost values of raw materials, the objective function expressed by equation (1) turns into equation (2).

$$\begin{aligned} MinZ = & 0.2483 * x_1 + 0.13534 * x_2 + 0.52266 * x_3 + 0.01403 * x_4 \\ & + 0.02938 * x_5 + 0.00006 * x_6 + 0.1377 * x_7 \end{aligned}$$

The constraint functions for high carbon ferrochrome are defined as follows. The HC Ferrochrome given here is the useful product.

Constraints:

- The highest Cr constraint for HC Cr;

$$(x_6 * 0,0288 + x_7 * 0,2452) \leq x_8 * 0,64 \quad (3)$$

- The lowest Cr constraint for HC Cr;

$$(x_6 * 0,0288 + x_7 * 0,2452) \geq x_8 * 0,63 \quad (4)$$

- The highest S constraint for HC Cr;

$$\begin{aligned} 0.0005547 * x_1 + 0.0005505 * x_2 + 0.008 * x_4 + 0.0006419 * x_5 + \\ 0.002645 * x_6 + 0.0007325 * x_7 \leq x_8 * 0,015 \end{aligned} \quad (5)$$

- The lowest S constraint for HC Cr;

$$\begin{aligned} 0.0005547 * x_1 + 0.0005505 * x_2 + 0.008 * x_4 + 0.0006419 * x_5 + \\ 0.002645 * x_6 + 0.0007325 * x_7 \geq x_8 * 0,009 \end{aligned} \quad (6)$$

- The highest C constraint for HC Cr;

$$0.1774 * x_1 + 0.0982 * x_2 + 0.19908 * x_3 + 0.002316 * x_6 \leq x_8 * 0,08 \quad (7)$$

- The lowest C constraint for HC Cr;

$$0.1774 * x_1 + 0.0982 * x_2 + 0.19908 * x_3 + 0.002316 * x_6 \geq x_8 * 0,075 \quad (8)$$

- The highest P constraint for HC Cr;

$$0.0002 * x_1 + 0.0001 * x_2 + 0.0063 * x_3 \leq 0,00015 \quad (9)$$

- The lowest P constraint for HC Cr;

$$0.0002 * x_1 + 0.0001 * x_2 + 0.0063 * x_3 \geq 0,00009 \quad (10)$$

- The highest Fe constraint for HC Cr;

$$0.00406 * x_1 + 0.00432 * x_2 + 0.0085 * x_4 + 0.2309 * x_5 + 0.012643 * x_6 + 0.0999 * x_7 \leq 0.26485 \quad (11)$$

- The lowest Fe constraint for HC Cr;

$$0.00406 * x_1 + 0.00432 * x_2 + 0.0085 * x_4 + 0.2309 * x_5 + 0.012643 * x_6 + 0.0999 * x_7 \geq 0.28591 \quad (12)$$

- Furnace Basicity Constraint;

$$0.0242 * x_1 + 0.0118 * x_2 + 0.0052 * x_4 + 0.0166 * x_5 + 0.364 * x_6 + 0.21683 * x_7 - (1.1 * (0.0655 * x_1 + 0.065 * x_2 + 0.945 * x_4 + 0.0758 * x_5 + 0.3124 * x_6 + 0.0865 * x_7) = 0 \quad (13)$$

RESULTS AND DISCUSSION

The objective function has reached the solution to provide all the desired constraint functions. x_1 and x_2 (coke and coal) variables to meet the amount of carbon required by the system, x_3 (graphite electrode) to transfer electrical energy to the system via arc, x_4 and x_5 (quartzite, bauxite) as slag builder, x_6 and x_7 (rich slag, chrome) ore) is fed to the system in order to meet the chromium element, which is the main ingredient of ferrochrome. In the light of this information, when looking at the optimized results, it is seen that the x_1 variable is decreased and the x_2 variable is increased. It has been concluded that there is no significant change in the x_3 variable, the x_4 variable is increased and the x_5 variable is decreased, if the x_6 variable is in stock, it should be fed at higher values, and there is no big change in the x_7 variable.

The comparison of the actual raw material mass amounts obtained from the facility with the results obtained from the solution of the objective function

modeled by the MATLAB program is presented in Table 3. Also, its graphical demonstration is presented in Figure 1.

Table 3: Comparison of actual and optimized values

Input Variable	Actual Amount (kg)	Optimized Quantity (kg)	Actual Cost (\$)	Optimized Cost (\$)
x ₁	52364	44282	13002	10995,2
x ₂	14496	15000	1961,9	2030,1
x ₃	1997	1800	1043,8	940,8
x ₄	37715	38893	529,1	545,7
x ₅	8684	6000	255,1	176,3
x ₆	22750	22750	1,4	1,4
x ₇	355342	354810	48930,6	48857,3
Total			65723,9	63546,8

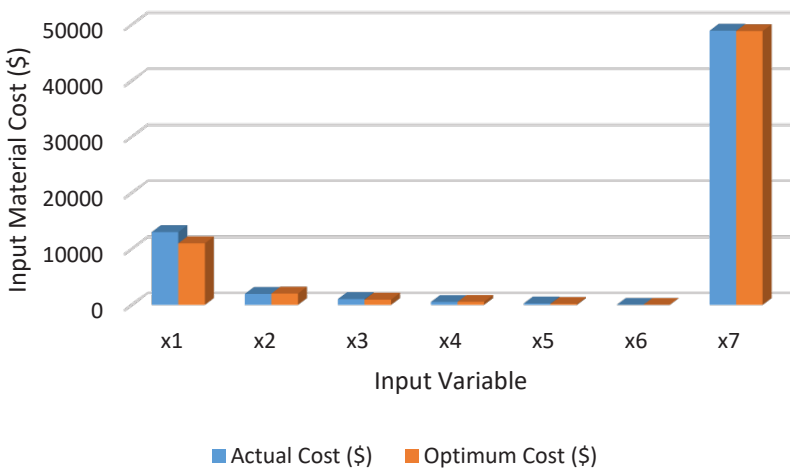


Figure 1: Comparison of actual cost values and optimum cost values

When the results are examined in terms of cost, it has been shown that there may be more suitable solutions. Considering that production continues throughout the year, except for unforeseen reasons such as maintenance and repair, it is obvious that even small improvements in the production process will lead to great savings. Since our country is dependent on foreign sources in terms of energy, it becomes clear that every work done for process improvement is valuable and needs to be supported.

REFERENCES

- Çamdali, Ü. (2005). Determination of the optimum production parameters by using linear programming in the AC electric arc furnace. *Canadian Metallurgical Quarterly*, 44(1), 103–110. <https://doi.org/10.1179/cmqr.2005.44.1.103>
- Chen, Z., Ma, W., Wu, J., Wei, K., Lv, G., & Liu, Z. (2018). Predicting the Electricity Consumption and the Exergetic Efficiency of a Submerged Arc Furnace with Raw Materials using an Artificial Neural Network. *Silicon*, 10(2), 603–608. <https://doi.org/10.1007/s12633-016-9499-4>
- Czapla, M., Karbowniczek, M., & Michaliszyn, A. (2008). The optimisation of electric energy consumption in the electric arc furnace. *Archives of Metallurgy and Materials*, 53(2), 559–565.
- Cziesla, F., & Tsatsaronis, G. (2002). Iterative exergoeconomic evaluation and improvement of thermal power plants using fuzzy inference systems. *Energy Conversion and Management*, 43(9–12), 1537–1548. [https://doi.org/10.1016/S0196-8904\(02\)00034-1](https://doi.org/10.1016/S0196-8904(02)00034-1)
- Moghadasian, M., & Alenasser, E. (2011). Modelling and Artificial Intelligence-Based Control of Electrode System for an Electric Arc Furnace. *Journal of Electromagnetic Analysis and Applications*, 03(02), 47–55. <https://doi.org/10.4236/jemaa.2011.32009>
- Radwan, A. M. (2012). Different Possible Ways for Saving Energy in the Cement Production. *Advances in Applied Science Research*, 3(2), 1162–1174.
- Ranganathan, S. (2007). Optimisation of specific power consumption in the production of ferro alloys through rationalisation of charge distribution. *Innovations In The Ferro Alloy Industry - Proceedings of the XI International Conference on Innovations in the Ferro Alloy Industry, Infacon XI, March*, 520–525.
- Rangnathan, S., Godiwalla, K. M., Satyanarayana, N. V., Kumar, P., Rao, V., Roy, A. K., & Srikant, B. (2010). Simulation of the production of ferrochromium in submerged-Arc furnace. *Proceedings of the 12th International Ferroalloys Congress: Sustainable Future*, 401–410.
- Singh, V., Tathavadkar, V., Rao, S. M., & Raju, K. S. (2007). Predicting the performance of submerged arc furnace with varied raw material combinations using artificial neural network. *Journal of Materials Processing Technology*, 183(1), 111–116. <https://doi.org/10.1016/j.jmatprotec.2006.10.004>
- Vapur, H., Top, S., Teymen, A., & Türkmenoğlu, M. (2013). Elazığ Ferrochrom Tesisi Cüruflarının Agrega Özelliklerinin Araştırılması. *Çukurova University Journal of the Faculty of Engineering and Architecture*, 28(1), 77–88.

- Weitz, H., & Garbers-Craig, A. M. (2016). Evaluation of the Furnace Method for the Production of Low Carbon Ferrochrome. *Mineral Processing and Extractive Metallurgy Review*, 37(3), 168–178. <https://doi.org/10.1080/08827508.2016.1168413>
- Xiaobing, L., Ruilin, P., Qiunan, M., & Fajing, C. (2008). Study on recipe cost optimization system based on ant colony algorithms. *2008 International Seminar on Business and Information Management, ISBIM 2008, 1*, 287–290. <https://doi.org/10.1109/ISBIM.2008.78>

Chapter 17

Rule-based Explainable Artificial Intelligence

Sinem AKYOL¹

¹ Asst. Prof.; Firat University, Engineering Faculty, Software Engineering Department.
sakyol@firat.edu.tr ORCID No: 0000-0001-9308-3500

ABSTRACT

Artificial intelligence stands out in many fields by facilitating tasks and mimicking the learning systems of humans to generate solutions. Artificial intelligence algorithms supported by deep neural networks have been increasingly utilized in various domains such as energy systems, medicine, robotics, and image processing, indicating their integration into our daily lives. However, despite these advancements, this evolving technology still lacks in establishing trust and is often regarded as an opaque "black box." Explainable Artificial Intelligence (XAI) techniques have been developed to address this issue and make models' decisions understandable, enabling individuals to comprehend and interpret them. Rule-based XAI is a method that adopts a rule-based approach to explain the results of Artificial intelligence models. In this method, interpretable rules are generated for explainability and assist users in understanding the decision-making processes of Artificial intelligence systems. Rule-based XAI methods are typically categorized as model-agnostic, relying on model optimization, or specifically designed for neural networks. These methods play a significant role in Artificial intelligence applications, particularly in finance, medicine, and law. Rule-based XAI ensures reliability and transparency by enabling users to comprehend why a particular outcome was produced by the model. Rules can represent the characteristics of input data or the outputs of the model, allowing users to interpret the results in an understandable manner. Consequently, users develop more trust in the decision-making processes of Artificial Intelligence models and gain the opportunity to question and enhance the systems' accuracy. This study provides an introduction to the widespread usage and development of Artificial intelligence and machine learning techniques in human life. Additionally, it emphasizes the significance and progression of XAI. The study defines and highlights the importance of Explainable Artificial intelligence while providing insights into its key concepts and relationships (interpretability, explanation, interpretability). By focusing on the classification of XAI methods, it introduces rule-based XAI techniques.

Keywords: Artificial Intelligence, XAI, Rule-Based XAI

1. INTRODUCTION

In particular, artificial intelligence-based algorithms powered by deep neural networks are changing the way people approach real-world tasks. In recent years, the use of machine learning algorithms to automate various aspects of scientific, business and social workflows has been increasing with the proliferation of research in the field of deep learning. The use of machine learning algorithms in the fields of energy and power systems, medicine, ophthalmology, developmental disorders, autonomous robots and vehicles, successful use classification and detection, image processing, speech and sound processing, cyber security, etc., shows that these algorithms penetrate our daily lives (Das and Rad, 2020).

Machine Learning techniques, which are a very successful method in learning complex patterns to make consistent and reliable predictions, are divided into three subgroups as supervised, unsupervised and reinforcement learning, as shown in Figure 1. Each Machine Learning method offers great solutions and opportunities to different problems in different fields from past to present. With the advancement of ensemble and deep learning models, it has become the favored method for many real-world applications such as movie recommendation, machine translation, and speech recognition. In the learning process, ML models outperform humans in terms of speed, reproducibility, and scale. These models, once implemented, can finish a task faster, generate consistent results, and can be simply and cheaply transferred to another system. Training a person to execute a task, on the other hand, takes a lengthy time and incurs additional expenditures if the individual is young. In addition, the person information cannot be reproduced by copying or transferring (Köse, 2022).

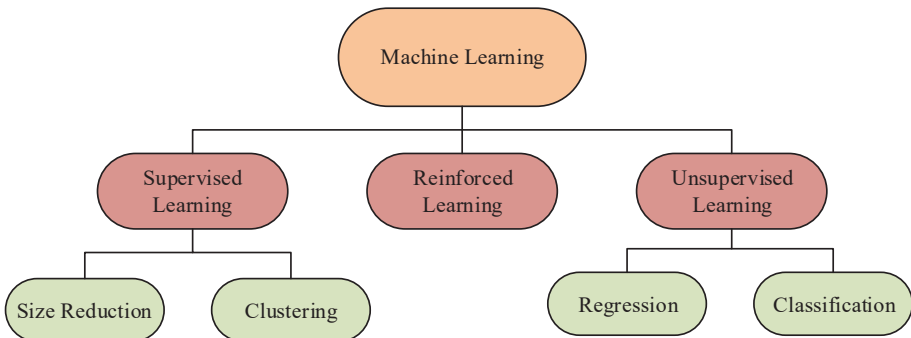


Figure 1: Classification of machine learning algorithms

A few researchers who recognized the need for explanations in artificial intelligence and machine learning-based intelligent systems started discovering

and proposing methods a long time ago. The oldest evidence of the relationship between bibliographic databases and term explanations can be found in expert systems published by Neches et al. in 1985 (Neches et al., 1985). It has been observed that there has been an increase in the studies on explainable artificial intelligence in recent years, focusing on making the results more interpretable, which have been challenging in the field of machine learning.

The article titled "DARPA's Explainable Artificial Intelligence Program: An Examination of the Importance of Explainability for the "Defense Department of Defense" investigates the importance of explainability for the Defense Department and identifies the Defense Advanced Research Projects Agency (DARPA) as an advanced study agency. This program started in 2017 and has a four-year plan. The explainable artificial intelligence project addresses three different research and development issues: the creation of more models, the design of interfaces used for explanations, and understanding the psychological needs for effective explanations. This study aims to develop explainable artificial intelligence on machine learning techniques (Gunning and Aha, 2019). In mid-2017, the Chinese government published the "Next Generation Artificial Intelligence Development Plan" to promote the high and robust scalability of artificial intelligence (Xu et al., 2019). Lastly, in mid-2018, the European Union issued the "General Data Protection Regulation" (GDPR), granting citizens "Right to Explanation" for decisions affected by algorithmic processes (Wachter et al., 2017). The search results of major bibliographic databases indicate a rapid increase in the number of publications related to Explainable AI (XAI), demonstrating a significant impact of these events among researchers. The bibliographic databases considered as the primary sources of XAI-related publications are based on research papers in the field of artificial intelligence (Islam et al., 2022).

To define XAI, Figure 2 illustrates the most frequently mentioned terminologies, showcasing the fundamental characteristics of each term and their relationships. The concept of understandability is the foundational concept in XAI, linked with other concepts (Hagras, 2018). Understandability and comprehensibility are both dependent on the ability of users to perceive the knowledge gained by a model (Páez, 2019). Understandability is strongly related to succinctness, interpretability, and explainability, for example. Succinctness refers to how brief and clear generated explanations are for humans (Abdollahi and Nasraoui, 2018), whereas explainability and interpretability refer to observers' ability to comprehend AI model outputs. Explainability and interpretability appear to be related terms that are frequently abused, causing confusion and potentially impeding the creation of standardized

terminology (Carvalho et al., 2019). Explainability in XAI refers to an AI model's active character, which includes the necessary traits and methods for clarifying or disclosing its internal workings (Adadi and Berrada, 2018). The extent to which an AI model may be passively understood by humans, on the other hand, is indicated by interpretability. Justification allows non-technical users to have an easy way to grasp the fundamental learning process of a predictive model, enabling them to justify the model's decisions. The demand for AI models to be explainable has gained traction. Generally, XAI enhances the acceptance and usability of existing AI models by allowing users to participate in debugging and model creation (Minh et al., 2022).

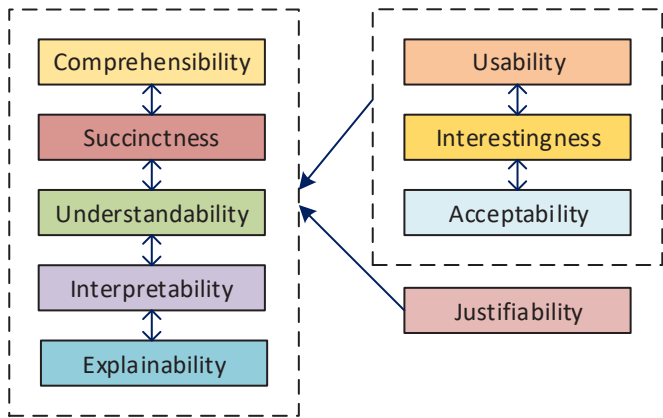


Figure 2: Connections between frequently used words in the XAI field

In this chapter, the definition of XAI is provided in the second section, along with the discussion of the need for XAI. A comparison between XAI and black box methods is presented. Subsequently, the advantages and disadvantages of XAI are addressed. In the third section, five classification methods of XAI are discussed. The fourth section focuses on rule-based XAI methods based on the output format. Finally, in the fifth section, the study is concluded.

2. EXPLAINABLE ARTIFICIAL INTELLIGENCE

In recent years, artificial intelligence has emerged as a prominent topic in almost every field of technology. AI systems greatly facilitate tasks by mimicking human learning systems and generating solutions to problems. However, this evolving AI technology has yet to fully establish trust in the results it produces for humans and is lacking in providing answers to the questions of how and why.

Machine learning models are like difficult-to-interpret black boxes. Categorical data such as gender, age, and race can often pose risks in AI models. Additionally, AI models may fall short in performance when the data used in the application stage differs from the training data. Therefore, it is crucial for AI models to be reliable, accountable, and efficient (Bilekyigit, 2022).

Due to their complicated and non-linear underlying structures, which make them opaque and difficult to understand, the majority of machine learning and deep learning models are referred to as "black boxes" by scientists and the general public. Due to this opacity, explainable artificial intelligence (XAI) architectures are now necessary. This need is primarily motivated by three factors: the need for increased model transparency, the need for human interaction with them, and the need for the accuracy of their inferences (Fox et al., 2017).

Many domain-specific and context-dependent approaches have been developed as a result to handle the interpretation of machine learning models and create explanations for humans. Given the numerous new XAI approaches that are scattered and need structure, this tendency is far from being resolved.

Artificial intelligence has become an essential field in almost every industry, leading to a rapid increase in research on Explainable Artificial Intelligence since 2019 (Arrieta et al., 2020). Explainable Artificial Intelligence techniques are methods that enable the understanding and interpretation of AI outcomes. In areas where human life is affected, such as medicine, finance, and law, the use of explainable AI techniques is particularly significant (Pehlivanlı and Deliloglu, 2021). Explainable Artificial Intelligence aims to make the decisions of models without explanations and that could create risky situations more understandable. XAI represents a set of methods that allow humans to understand, interpret, and explain the results of machine learning algorithms (Bilekyigit, 2022).

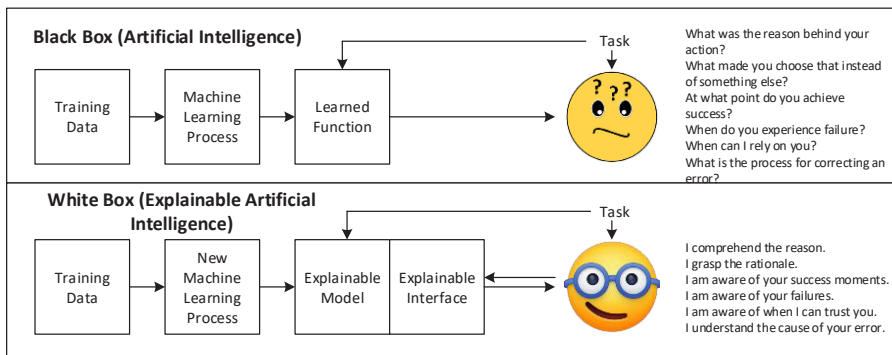


Figure 3: Comparison of artificial intelligence and XAI (URL 1)

The comparison between explainable artificial intelligence (XAI) and black box (artificial intelligence) models, also known as white box, can be seen in Figure 3. White box models are inherently interpretable, making it easier to understand their outputs, but they are less accurate. On the other hand, black box models are more accurate but less interpretable. More complex XAI techniques are required to build reliable models. In addition to white box and black box models, there are also gray box models, which provide a good balance between interpretability and accuracy (Ali et al., 2023).

XAI has many advantages. One of them is that it helps improve the model by understanding its weaknesses. Additionally, when it is difficult to trust the decisions of systems that we cannot observe and understand, explainable artificial intelligence helps establish that trust. It creates a sense of confidence in the model by minimizing the risk. It also provides the opportunity to monitor the system's performance. Along with these advantages, there are also some disadvantages. The first disadvantage is the lack of sufficient scientific research in this field. Another disadvantage is the inadequacy, accuracy, and lack of quantitative measurement of explanation maps.

3. CLASSIFICATION OF XAI METHODS

The main goal of XAI approaches is to interpret and make the entire artificial intelligence system development process transparent and understandable, from inputs to outputs. These techniques produce explanations that can be in a variety of formats, including rules, numbers, text, images, or a combination of these. The many ways in which AI-powered technologies are being used to address various issues in various industries has led to a variety of explanations (De Graaf and Malle, 2017; Vilone and Longo, 2021b). AI practitioners, system developers, and designers find practical explanations within a model that faithfully reflect the logic. For instance, rule-based explanations provide a well-defined, comprehensible set of logical guidelines. However, end-users want customizable explanations that tell a "story" by highlighting the input features that have the most influence on the model's prediction. For instance, verbal and visual explanations might intuitively convey the reasoning behind the classification of an animal image (Vilone and Longo, 2021a).

Five main criteria have been identified to distinguish XAI methods. First, an explanation's scope can be either global or limited. Globally, the objective is to make a model's complete inferential process transparent and intelligible. The goal of local scope is to explicate each model inference (Dam et al., 2018). The stage at which a method yields an explanation is referred to as the second

dimension. By taking explainability into account both at the outset and during training, ante hoc approaches seek to naturally create a model interpretable while also attaining the highest level of accuracy (Došilović et al., 2018; Lou et al., 2012). On the other hand, post hoc methods preserve a trained model and use an external explainer to replicate or explain its behavior during testing (Došilović et al., 2018; Montavon et al., 2018; Pérez, 2019). Last but not least, a model's processes for classifying images may be very different from those for classifying text-based materials. Because of this, the input data—whether numerical/categorical, visual, textual, or time series—can be extremely important to the interpretability technique. Depending on the type of problem, XAI methods can vary, such as classification or regression, depending on the underlying problem. Similarly, for the output data, different conditions may require different explanation formats: numerical, rules, textual, visual, or mixed. The classification of XAI models is shown in Figure 4.

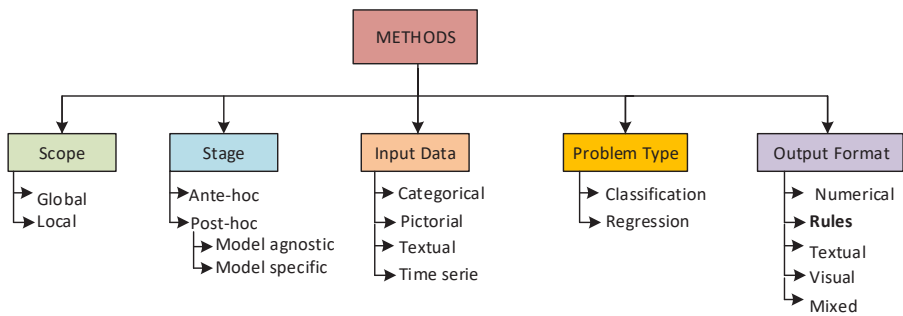


Figure 4: Classification of XAI Methods

4. RULE-BASED XAI METHODS

Understanding and explaining the decision-making processes of artificial intelligence systems is important for their reliability and acceptability. In this regard, rule-based XAI offers a strong approach to provide explanations and comprehensibility. Rule-based XAI is based on a structure consisting of explicit and understandable rules that enable the understanding of the decision-making process. This approach enhances users' trust in artificial intelligence systems by providing an explanation mechanism that elucidates how decisions are made, thereby corroborating the decisions in an interpretable manner.

4.1. Rule-Based XAI Methods with Decision Tree

Using decision trees, rule-based explanations can be generated. These rules exhibit higher interpretability while resembling a black-box model. For instance, utilizing logical conjunctions to combine divided loads along the routes from

inputs to predictions, Bride et al.'s method extracts logical formulas as decision trees. These rules provide information about the decision-making process by being analyzed with logical reasoning techniques (Bride et al., 2018). Split-Sensitive Local Model (Krishnan and Wu, 2017) and Model Extraction (Bastani and Bastani, 2017) utilize decision trees for approximating complex models, aiming to reflect the interpretability of statistical features in complex models. Mimic Rule Explanation returns symbolic rule sets that behave similarly to an underlying black-box model. This method determines the maximum region of a specific class using prototype examples and constructs the rule set that bounds this region (Asano and Chun, 2021; Vilone and Longo, 2021a).

In order to effectively combine several decision trees that were independently trained on distributed data into one tree, Andrzejak et al. suggest a three-step technique. First, each decision tree is turned into a rule set that specifies a region in the output space and duplicates a path from the root to a leaf. The full feature space is covered by each region, which is disconnected. The regions are then combined using a line sweep method, which sorts the borders of each zone and unifies nearby ones. Finally, using a C5.0-inspired technique, a decision tree is extracted from the regions (Andrzejak et al., 2013).

Another approach is referred to as Regularized Decision Rules (RDR), proposed by D'Alterio et al. RDR generates decision trees determined by experts. These trees possess a unique structure with the ability to prefer one attribute over others. The rules are explained using regular expressions and are optimized based on criteria of interpretability along with accuracy and coverage. Regularized Decision Rules have been successfully applied in various domains, particularly in medical diagnosis, financial analysis, and law (D'Alterio et al., 2020). An example image illustrating rules extracted with decision trees can be seen in Figure 5.

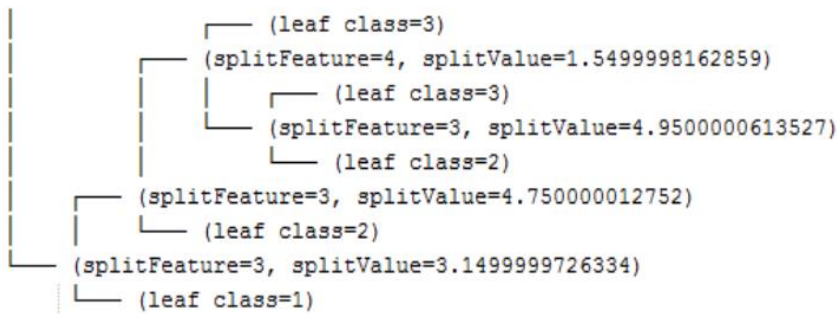


Figure 5: An example image for the rules derived from the decision tree (Bondarenko et al., 2017)

4.2. Rule-Based XAI Methods with Neural Networks

In the literature, rule-based XAI models developed using Neural Networks have been proposed. Anchor utilized LSTM (Long Short-Term Memory) to extract IF-THEN rules known as "anchors." These anchors specifically identify the features of an input example that provide sufficient information for a classifier to make accurate predictions (Ribeiro et al., 2018).

Researchers have classified XAI techniques that use IF-THEN rules to explain the inferential function of neural networks. According to the classifications made by Bologna and Hayashi (2018) and Hailesilassie (2016), these techniques can be divided into three groups: I) decompositional techniques, which draw out rules from hidden and output neurons by examining the weights attached to them; (II) pedagogical methods, which treat a basic neural network as a black box and replicate its function using the extracted rules, without considering the weights; and (III) eclectic methods, which combine elements from both decompositional and pedagogical approaches. This section categorizes XAI methods using the above three classes instead of neural network architectures (Vilone and Longo, 2021a).

Decomposition techniques: Fractionating Hidden Neuron Activation Values through Clustering (Setiono and Liu, 1995) groups the activation values of hidden neurons and substitutes them with the average of the cluster to construct IF-THEN rules. By looking at potential combinations in the fractional outputs of the fractionated network, the rules are developed. The Neural Network Knowledge Extractor (NNKX) (Bondarenko et al., 2017) creates binary decision trees from multi-layer feedforward sigmoidal neural networks in a manner similar to this. To generate the clusters, it groups and propagates backwards the activation values from the previous layer.

A better method for obtaining fractional and uncertain rules is termed Validity Interval Analysis (VIA), which is based on Interval Spread (Palade et al., 2001). The activation values of every unit (or group of units) in a DNN are found by VIA to lie within a variety of validity intervals. Each extracted rule has a single target class as its output and a set of validity intervals as its precondition. Palade et al. claim that VIA occasionally makes mistakes while determining whether a rule is appropriate for the network. The intervals are not always the best, too. By modifying the intervals for the input or output and propagating the network either forward or backward, interval spread gets around these restrictions. To attain comparable performance in terms of prediction accuracy, certain neural networks, however, need a number of fractional rules. In such cases, it has been suggested to convert these fractional

rules into fuzzy rules by introducing OR operators between the rules using a fuzzy interactive operator (Palade et al., 2001; Vilone and Longo, 2021a).

Interpretable Multi-Layer Perceptrons (IMLPs) return symbolic rules to Differentiable Interpretable Multi-Layer Perceptrons (DIMLPs) (Bologna and Hayashi, 2017; Bologna and Hayashi, 2018; Bologna, 2018). In IMLPs, each first hidden layer neuron has a single input neuron and a step activation function, but the following hidden layers are completely coupled and have a sigmoid activation function. The step activation function transforms into a staircase function in DIMLPs, which resembles the sigmoid function. After a max pooling layer, rule inference is carried out by locating the locations of pertinent discriminating hyperplanes that serve as borders between output classes.

Reverse engineering techniques are the foundation of Rule Extraction via Reverse Engineering (RxREN), which uses them to identify the data ranges of each significant neuron in the pertinent classes while removing the irrelevant input neurons that don't contribute to the outcome. The recursive method produces hierarchical rules for circumstances that distinguish between discrete characteristics and continuous attributes. A variation of RxREN is called Rule Extraction from Neural Network with Classified and Misclassified Data (RxNCM) (Biswas et al., 2017). It uses properly classified input examples in the range determination procedure, just like RxREN. The performance of the original LSTM is imitated through the use of inputs to a rule-based classifier, and the rules produced in this manner come close to matching that performance (Vilone and Longo, 2021a).

Numerous rule-based XAI techniques are monotonic, which means they produce an increasing collection of rules. A result obtained by applying new criteria, however, can occasionally render an earlier result invalid. Garcez et al. have described a technique for capturing non-monotonic symbolic rules that are encoded in networks. The algorithm begins by partially arranging the vectors according to the training dataset's activation values. Then, based on the feature values of the chosen instance, it establishes the minimal input point necessary to activate an output neuron and develops a rule (Garcez et al., 2001).

Finally, two algorithms have been proposed to extract decision trees (DTs) from weights of DNN. The first method trains a soft DT using stochastic gradient descent to partition the data and make hierarchical decisions on how to construct paths from the root to the leaves, using the predictions of the DNN and its learned filters. The second approach was created expressly for picture classification tasks and seeks to semantically explain the CNN at its core, where the network's filters should stand in for various object elements. By changing a

particular loss function, the network's filters are made to represent object pieces in order to build such DTs. The DT is then built iteratively for each filter/part pair for each image. The C4.5 rule induction approach is used in the C4.5Rule-PANE method (Zhou and Jiang, 2003) to extract IF-THEN rules from the training dataset, where the original labels are substituted with the predicted labels by the ensemble because the training set has been updated. To mimic the inference process of the ensemble, C4.5Rule-PANE extracts a rule set from the modified training dataset, where the original labels are replaced with the predicted labels by the ensemble. DecText method (Boz, 2002) extracts high-fidelity DTs from a DNN. It applies a known method to find the best split based on the values of each feature and then creates a rule set based on the sample count in each branch to predict the class that achieves the highest accuracy in each branch. The rule set is transformed into a tree structure for outputs called a lightning decision tree (Vilone and Longo, 2021a).

4.3. Rule-Based XAI Methods with Metaheuristics

Metaheuristic algorithms have been utilized to develop rule-based explainable artificial intelligence (XAI) models. Genetic algorithms are used in Genetic Rule Extraction (G-REX) (Johansson et al., 2004) to produce IF-THEN rules with AND/OR operators. The genetic algorithm is used by GLocalX (Guidotti et al., 2019; Setzu et al., 2021) to generate local rules that clarify the predictions provided by a classifier on a particular instance. These extracted rules present a set of counterfactuals that would result in different results if the instance's attributes were altered, as well as the causal explanations for the classifier's predictions.

Ant Colony Optimization (ACO), also known as the explore-exploit method, follows a sequential covering strategy. With this method, sets of unordered IF-THEN classification rules are generated, and they can be individually examined and interpreted independently from each other. ACO builds a fresh set of unordered rules at each stage and contrasts them with the ones from earlier iterations. The prior set is replaced if the new set has fewer rules or better prediction accuracy (Otero and Freitas, 2016). AntMinter+, using an iterative maximum-minimum ant system, starts with an empty set and creates a monotonic set of rules while allowing the inclusion of domain knowledge through an undirected cyclic graph representation of the solution space. The graph's edges show which subsequent variable values can be reached from a node, and nodes at the same depth in the graph represent partitions related to input variables. A rule depicts a route connecting the starting and terminating nodes. When a predefined percentage of the training points have been covered,

or when additional rules are unable to raise the classifier's accuracy, the algorithm terminates. The active learning-based method (ALBA), which uses AntMinter+ in conjunction with a nonlinear SVM, can produce rule-based models that are comprehensible and precise (Verbeke et al., 2011).

To provide interpretable rule sets that show the dependencies between inputs and outputs, four fuzzy logic-based techniques have been presented (Vilone and Longo, 2021a). The Generalized Fuzzy Genetic-Based Machine Learning (GBML) algorithm, which combines elements of the Michigan and Pittsburgh approaches, is used inside the evolutionary multi-objective optimization (EMO) framework. Each fuzzy rule is represented as a fixed-length integer string encoding the antecedent fuzzy sets, and the fuzzy rule-based classifier is represented as a variable-length unified integer string encoding the fuzzy rule set (Ishibuchi and Nojima, 2007). The fuzzy rule-based MOEAIF (Multi-Objective Evolutionary Algorithm-based Interpretable Fuzzy) model is used to categorize gene expression data. GBML and MOEAIF quantify the complexity of rule sets in terms of the number of fuzzy rules and/or the total number of antecedent conditions of the fuzzy rules in order to maximize the accuracy of rule sets based on correctly classified training patterns (Wang and Palade, 2011). The Jin (2000) approach is based on a five-step algorithm. First, it uses the data to produce fuzzy rules that are suitable for the extremes. It also eliminates superfluous and contradictory rules by comparing how similar the rules are. Thirdly, based on a local performance requirement, it uses genetic algorithms to optimize the rule structure. Fourth, it eliminates ineffective rules after performing additional training of the rule parameters using a gradient-based learning technique. Finally, it uses regularization techniques to improve interpretability (Jin, 2000).

Using a collection of relationships and features from an expert-selected input dataset, the Pierrard et al. technique constructs fuzzy rules. A frequent itemset clustering approach is then used to extract the most pertinent ones. The authors suggested employing metrics like the quantity of relationships or features in a proposition's antecedent or their support value, even though they did not provide a precise metric to assess the importance of a link (Pierrard et al., 2018).

IF-THEN classification rules are made comprehensible through the three-step evolutionary programming approach known as Interpretable Classification Rule Mining (ICRM). The number of rules and restrictions should be kept to a minimum to make things more understandable. In the beginning, it creates a rule pool with only single attribute-value comparisons. The Pittsburgh technique, based on the Iterative Rule Learning (IRL) genetic algorithm, uses

evolutionary processes to enhance the accuracy of rules using only pertinent attributes. With the exception of a class set as the default, IRL returns a rule for an output class. By maximizing the product of precision and recall, the third step maximizes the classifier's accuracy (Cano et al., 2013).

Kızıloluk and Alatas employed the Parliamentary Optimization Algorithm for rule-based disease prediction in health data (Kızıloluk and Alatas, 2015). Similarly, Akyol and Alatas utilized the Cat Swarm Optimization algorithm for automatic discovery of classification rules in databases comprising numerical or mixed-type data. No preprocessing was performed for determining the appropriate ranges of relevant attributes in the rules; instead, the optimization algorithm provided them automatically along with the rules. Moreover, they used an objective function that can easily accommodate various and flexible objectives. In their study, they obtained accurate and interpretable rules using four health datasets obtained from the UCI repository (Akyol and Alatas, 2016). A snippet of rules obtained from this study is shown in Figure 6. The first column displays the rules obtained from the decision variables in the dataset, while the second column indicates the class for which the rule operates. TP represents the number of correctly classified data, and FP represents the number of incorrectly classified data.

Rules	Class	TP	FP
4.239<Thyroidstimulating<41.033	3	23	0
3.287<Triiodothyronine<7.822	2	20	0
17.161<Thyroxin<23.019	2	7	0
87.643<T3resin<99.24 and 10.56<Thyroxin<15.188	2	5	0
Data that does not comply with the above rules	1	150	10

Figure 6: Example of rule-based XAI with metaheuristic algorithms

5. CONCLUSIONS

This study emphasized the importance of explainability in the field of artificial intelligence and focused on explainable artificial intelligence (XAI) methods. XAI aims to provide the ability to explain and interpret the results of artificial intelligence models in an understandable manner, with the goal of building trust. Among the advantages of XAI are assisting in model improvement, providing reliability, and reducing risks. In the comparison between XAI and artificial intelligence models, XAI models tend to be more interpretable but may produce less accurate results, while artificial intelligence

models achieve higher accuracy but are less interpretable. Gray box models offer a balance between interpretability and accuracy. Additionally, five main criteria have been identified for the classification of XAI methods: scope of explanation, explanation generation stage, input and output data types, problem type, and data format used. These criteria allow for the use of different forms of explanation and the development of applicable methods for various classification and regression problems.

Finally, rule-based XAI methods have been examined. Rule-based explainable artificial intelligence is an effective approach to understand and explain the decisions of artificial intelligence systems. This approach not only fosters user trust in the system but also ensures that decisions are explainable and verifiable. Rule-based explainable artificial intelligence systems hold significant importance in fields such as medicine, finance, and security, where understanding and acceptance of decisions are crucial. It is expected that further research will be conducted and new methods will be developed in this field in the future.

REFERENCES

- Abdollahi, B., & Nasraoui, O. (2018). Transparency in fair machine learning: the case of explainable recommender systems. *Human and machine learning: visible, explainable, trustworthy and transparent*, 21-35.
- Adadi A, Berrada M (2018) Peeking inside the black-box: a survey on explainable artificial intelligence (XAI). *IEEE Access* 6:52138?52160
- Akyol, S., & Alataş, B. (2016). Automatic mining of accurate and comprehensible numerical classification rules with cat swarm optimization algorithm. *Journal of the Faculty of Engineering and Architecture of Gazi University*, 31(4), 839-857.
- Ali, S., Abuhmed, T., El-Sappagh, S., Muhammad, K., Alonso-Moral, J. M., Confalonieri, R., ... & Herrera, F. (2023). Explainable Artificial Intelligence (XAI): What we know and what is left to attain Trustworthy Artificial Intelligence. *Information Fusion*, 101805.
- Andrzejak, A., Langner, F., & Zabala, S. (2013, April). Interpretable models from distributed data via merging of decision trees. In *2013 IEEE Symposium on Computational Intelligence and Data Mining (CIDM)* (pp. 1-9). IEEE.
- Arrieta, A. B., Díaz-Rodríguez, N., Del Ser, J., Bennetot, A., Tabik, S., Barbado, A., García, S., Gil-López, S., Molina, D., ve Benjamins, R. (Eds.). (2020). *Explainable Artificial Intelligence (XAI): Concepts, taxonomies, opportunities and challenges toward responsible AI* (Vol. 58). Derio (Bizkaia), Spain.
- Asano, K., & Chun, J. (2021). Post-hoc explanation using a mimic rule for numerical data. In *13th International Conference on Agents and Artificial Intelligence, ICAART 2021* (pp. 768-774). SciTePress.
- Augasta, M. G., & Kathirvalavakumar, T. (2012). Reverse engineering the neural networks for rule extraction in classification problems. *Neural processing letters*, 35, 131-150.
- Bastani, O., Kim, C., & Bastani, H. (2017). Interpretability via model extraction. *arXiv preprint arXiv:1706.09773*.
- Bilekyigit, S. (2022) Analysis of heart failure risk with machine learning methods, Karamanoğlu Mehmetbey Üniversitesi / Fen Bilimleri Enstitüsü / Mühendislik Bilimleri Ana Bilim Dalı / Bilgisayar Mühendisliği Bilim Dalı
- Biswas, S. K., Chakraborty, M., Purkayastha, B., Roy, P., & Thounaojam, D. M. (2017). Rule extraction from training data using neural network. *International Journal on Artificial Intelligence Tools*, 26(03), 1750006.

- Bologna, G. (2018). A rule extraction study based on a convolutional neural network. In *Machine Learning and Knowledge Extraction: Second IFIP TC 5, TC 8/WG 8.4, 8.9, TC 12/WG 12.9 International Cross-Domain Conference, CD-MAKE 2018, Hamburg, Germany, August 27–30, 2018, Proceedings 2* (pp. 304-313). Springer International Publishing.
- Bologna, G., & Hayashi, Y. (2017). Characterization of symbolic rules embedded in deep DIMLP networks: a challenge to transparency of deep learning. *Journal of Artificial Intelligence and Soft Computing Research*, 7(4), 265-286.
- Bologna, G., & Hayashi, Y. (2018). A comparison study on rule extraction from neural network ensembles, boosted shallow trees, and SVMs. *Applied computational intelligence and soft computing*, 2018, 1-20.
- Bondarenko, A., Aleksejeva, L., Jumutc, V., & Borisov, A. (2017). Classification tree extraction from trained artificial neural networks. *Procedia Computer Science*, 104, 556-563.
- Boz, O. (2002, July). Extracting decision trees from trained neural networks. In *Proceedings of the eighth ACM SIGKDD international conference on Knowledge discovery and data mining* (pp. 456-461).
- Bride, H., Dong, J., Dong, J. S., & Hóu, Z. (2018). Towards dependable and explainable machine learning using automated reasoning. In *Formal Methods and Software Engineering: 20th International Conference on Formal Engineering Methods, ICFEM 2018, Gold Coast, QLD, Australia, November 12-16, 2018, Proceedings 20* (pp. 412-416). Springer International Publishing.
- Cano, A., Zafra, A., & Ventura, S. (2013). An interpretable classification rule mining algorithm. *Information Sciences*, 240, 1-20.
- Carvalho, D. V., Pereira, E. M., & Cardoso, J. S. (2019). Machine learning interpretability: A survey on methods and metrics. *Electronics*, 8(8), 832.
- D'Alterio, P., Garibaldi, J. M., & John, R. I. (2020, July). Constrained interval type-2 fuzzy classification systems for explainable AI (XAI). In *2020 IEEE International Conference on Fuzzy Systems (FUZZ-IEEE)* (pp. 1-8). IEEE.
- Dam, H. K., Tran, T., & Ghose, A. (2018, May). Explainable software analytics. In *Proceedings of the 40th International Conference on Software Engineering: New Ideas and Emerging Results* (pp. 53-56).
- Das, A., & Rad, P. (2020). Opportunities and challenges in explainable artificial intelligence (xai): A survey. *arXiv preprint arXiv:2006.11371*.

- De Graaf, M. M., & Malle, B. F. (2017, October). How people explain action (and autonomous intelligent systems should too). In 2017 AAAI Fall Symposium Series.
- Došilović, F. K., Brčić, M., & Hlupić, N. (2018, May). Explainable artificial intelligence: A survey. In 2018 41st International convention on information and communication technology, electronics and microelectronics (MIPRO) (pp. 0210-0215). IEEE.
- Fox, M., Long, D., & Magazzeni, D. (2017). Explainable planning. arXiv preprint arXiv:1709.10256.
- Garcez, A. D. A., Broda, K., & Gabbay, D. M. (2001). Symbolic knowledge extraction from trained neural networks: A sound approach. *Artificial Intelligence*, 125(1-2), 155-207.
- Guidotti, R., Monreale, A., Giannotti, F., Pedreschi, D., Ruggieri, S., & Turini, F. (2019). Factual and counterfactual explanations for black box decision making. *IEEE Intelligent Systems*, 34(6), 14-23.
- Gunning, D., & Aha, D. (2019). DARPA's explainable artificial intelligence (XAI) program. *AI magazine*, 40(2), 44-58.
- Hagras, H. (2018). Toward human-understandable, explainable AI. *Computer*, 51(9), 28-36.
- Hailesilassie, T. (2016). Rule extraction algorithm for deep neural networks: A review. arXiv preprint arXiv:1610.05267.
- Ishibuchi, H., & Nojima, Y. (2007). Analysis of interpretability-accuracy tradeoff of fuzzy systems by multiobjective fuzzy genetics-based machine learning. *International Journal of Approximate Reasoning*, 44(1), 4-31.
- Islam, M. R., Ahmed, M. U., Barua, S., & Begum, S. (2022). A systematic review of explainable artificial intelligence in terms of different application domains and tasks. *Applied Sciences*, 12(3), 1353.
- Jin, Y. (2000). Fuzzy modeling of high-dimensional systems: complexity reduction and interpretability improvement. *IEEE Transactions on Fuzzy Systems*, 8(2), 212-221.
- Johansson, U., Niklasson, L., & König, R. (2004, June). Accuracy vs. comprehensibility in data mining models. In *Proceedings of the seventh international conference on information fusion* (Vol. 1, pp. 295-300). Stockholm, Sweden: Elsevier.
- Kiziloluk, S., & Alatas, B. (2015). Automatic Mining of Numerical Classification Rules with Parliamentary Optimization Algorithm. *Advances in Electrical and Computer Engineering*, 15(4), 17+.

<https://link.gale.com/apps/doc/A585717957/AONE?u=anon~2d19ecd6&sid=googleScholar&xid=3186dc12>

- Köse, U. (2022). Açıklanabilir Yapay Zekâ Metodolojileri ve Uygulamaları. Editor Ş. Sağıroğlu and M. U. Demirezen, Yorumlanabilir ve Açıklanabilir Yapay Zeka ve Güncel Konular, Vol. 4. Nobel.
- Krishnan, S., & Wu, E. (2017, May). Palm: Machine learning explanations for iterative debugging. In Proceedings of the 2Nd workshop on human-in-the-loop data analytics (pp. 1-6).
- Lou, Y., Caruana, R., & Gehrke, J. (2012, August). Intelligible models for classification and regression. In Proceedings of the 18th ACM SIGKDD international conference on Knowledge discovery and data mining (pp. 150-158).
- Minh, D., Wang, H. X., Li, Y. F., & Nguyen, T. N. (2022). Explainable artificial intelligence: a comprehensive review. *Artificial Intelligence Review*, 1-66.
- Montavon, G., Samek, W., & Müller, K. R. (2018). Methods for interpreting and understanding deep neural networks. *Digital signal processing*, 73, 1-15.
- Neches, R., Swartout, W. R., & Moore, J. D. (1985). Enhanced maintenance and explanation of expert systems through explicit models of their development. *IEEE Transactions on Software Engineering*, (11), 1337-1351.
- Otero, F. E., & Freitas, A. A. (2016). Improving the interpretability of classification rules discovered by an ant colony algorithm: extended results. *Evolutionary computation*, 24(3), 385-409.
- Páez, A. (2019). The pragmatic turn in explainable artificial intelligence (XAI). *Minds and Machines*, 29(3), 441-459.
- Páez, A. (2019). The pragmatic turn in explainable artificial intelligence (XAI). *Minds and Machines*, 29(3), 441-459.
- Palade, V., Neagu, D. C., & Patton, R. J. (2001). Interpretation of trained neural networks by rule extraction. In *Computational Intelligence. Theory and Applications: International Conference, 7th Fuzzy Days Dortmund, Germany, October 1-3, 2001 Proceedings 7* (pp. 152-161). Springer Berlin Heidelberg.
- Pehlivanlı, A. Ç., ve Deliloğlu, R. A. S. (2021). Hibrit Açıklanabilir Yapay Zeka Tasarımı ve LIME Uygulaması. *Avrupa Bilim ve Teknoloji Dergisi*(27), 228- 236
- Pierrard, R., Poli, J. P., & Hudelot, C. (2018, July). Learning fuzzy relations and properties for explainable artificial intelligence. In *2018 IEEE*

- International Conference on Fuzzy Systems (FUZZ-IEEE) (pp. 1-8). IEEE.
- Ribeiro, M. T., Singh, S., & Guestrin, C. (2018, April). Anchors: High-precision model-agnostic explanations. In *Proceedings of the AAAI conference on artificial intelligence* (Vol. 32, No. 1).
- Setiono, R., & Liu, H. (1995, August). Understanding neural networks via rule extraction. In *IJCAI* (Vol. 1, pp. 480-485).
- Setzu, M., Guidotti, R., Monreale, A., Turini, F., Pedreschi, D., & Giannotti, F. (2021). Glocalx-from local to global explanations of black box ai models. *Artificial Intelligence*, 294, 103457.
- URL 1: <https://boosted.ai/blog/asset-managers-need-explainable-ai-but-what-is-it-and-how-can-i-incorporate-it-into-my-process>
- Verbeke, W., Martens, D., Mues, C., & Baesens, B. (2011). Building comprehensible customer churn prediction models with advanced rule induction techniques. *Expert systems with applications*, 38(3), 2354-2364.
- Vilone, G., & Longo, L. (2021a). Classification of explainable artificial intelligence methods through their output formats. *Machine Learning and Knowledge Extraction*, 3(3), 615-661.
- Vilone, G., & Longo, L. (2021b). Notions of explainability and evaluation approaches for explainable artificial intelligence. *Information Fusion*, 76, 89-106.
- Wachter, S., Mittelstadt, B., & Russell, C. (2017). Counterfactual explanations without opening the black box: Automated decisions and the GDPR. *Harv. JL & Tech.*, 31, 841.
- Wang, Z., & Palade, V. (2011, December). Building interpretable fuzzy models for high dimensional data analysis in cancer diagnosis. In *BMC genomics* (Vol. 12, No. 2, pp. 1-11). BioMed Central.
- Xu, F., Uszkoreit, H., Du, Y., Fan, W., Zhao, D., & Zhu, J. (2019). Explainable AI: A brief survey on history, research areas, approaches and challenges. In *Natural Language Processing and Chinese Computing: 8th CCF International Conference, NLPCC 2019, Dunhuang, China, October 9–14, 2019, Proceedings, Part II* 8 (pp. 563-574). Springer International Publishing.
- Zhou, Z. H., & Jiang, Y. (2003). Medical diagnosis with C4. 5 rule preceded by artificial neural network ensemble. *IEEE Transactions on information Technology in Biomedicine*, 7(1), 37-42.

Chapter 18

A Study on Meta-Heuristic Algorithms Used for Problem Solving in Recent Years

Ahmet AKKAYA¹

Cemil KÖZKURT²

Rafet DURGUT³

¹ Bandırma Onyedi Eylül Üniversitesi, Mühendislik ve Doğa Bilimleri Fakültesi, Mekatronik Mühendisliği, aakkaya@bandirma.edu.tr, ORCID No: 0000-0003-4836-2310

² Dr. Öğr. Üyesi; Bandırma Onyedi Eylül Üniversitesi, Mühendislik ve Doğa Bilimleri Fakültesi, Mekatronik Mühendisliği, ckozurt@bandirma.edu.tr, ORCID No: 0000-0003-1407-9867

³ Doç. Dr.; Bandırma Onyedi Eylül Üniversitesi, Mühendislik ve Doğa Bilimleri Fakültesi, Bilgisayar Mühendisliği, rdurgut@bandirma.edu.tr, ORCID No: 0000-0002-1576-9977

Abstract

Optimization problems are encountered in different industrial spheres that contribute to the technological development of humanity. Various state-of-the-art, unique or hybrid metaheuristic algorithms have been created, developed or improved to solve optimization problems. In this study, metaheuristic algorithms used for problem solving in the last five years were examined. The scope of the study consists of 947 publications obtained by excluding conference proceedings, book chapters, graduate theses and those without Digital Object Identifier (DOI) numbers in the 1995 accessible scientific publications. The accessed publications were analyzed according to the criteria of the words in the names of the algorithms, the distribution of the publications by years, the distribution of the publications according to the number of authors, the algorithms used in the publications and the algorithms used according to the application areas of the publications. As a result of the analyzes, it was determined that 287 studies were carried out in 2020 at most. In addition, it was determined that a total of 241 studies were conducted, with the most 3 authors. Particle Swarm Optimization (PSO) was found to be the most preferred algorithm with 158. With a total of 153 studies, it has been determined that the most applied field is Computer Engineering and the most used algorithm on the basis of application is the PSO (26) algorithm in Computer Engineering.

Keywords: metaheuristic, meta-heuristic, many objective, multi objective, algorithm, algorithms, optimization.

1. Introduction

Optimization is defined as a research area that provides the most efficient use of resources such as workforce, time, capital, processes, raw materials, capacity, equipment, available in a system, to reduce costs, increase profits, increase capacity use and productivity (Türkay, 2011). In the optimization field, optimization algorithms are developed to find the best combination of decision variables in one or more objective functions. Optimization algorithms are needed to solve problems in major disciplines such as economics, health, data science and engineering in industry (Atalan, 2018; Nowozin and Wright, 2012; Marler and Arora, 2004). In the literature, it is seen that researchers apply multiobjective optimization algorithms to many optimization problems. Today, some optimization algorithms have been developed to solve various problems. Particle Swarm Optimization, Whale Optimization Algorithm, Genetic Algorithm, Gray Wolf Optimization Algorithm, Simulated Annealing Algorithm, Artificial Bee Colony Algorithm, Ant Colony Optimization Algorithm, Firefly Optimization Algorithm, Moth-Flame Optimization Algorithm, differential Evolution Optimization Algorithm, Harrison Flame Optimization Algorithm, Teaching Learning Based Optimization Algorithm, Grasshopper Swarm Optimization Algorithm, Salp Swarm Algorithm are examples of such algorithms.

Optimization algorithms can be classified as deterministic (precise) and stochastic (heuristic) according to their search methods. The most important feature of the deterministic or predictable method is that the whole search space is looked at instead of an approximate solution in the algorithm used. In this method, the same result is reached when starting with the same starting point. Although the deterministic method provides the optimum solution, it causes the working time of the algorithm to increase more than desired, especially with the increase in the problem size. Heuristic algorithms can provide near-optimal solutions for many-dimensional and multi-dimensional optimization problems in reasonable time (Akyol and Alataş, 2012). Some operators of the approximate algorithms in the domain of the optimization problem are modified and developed, and it is tried to find near-optimal or optimal solutions in a short time. Thanks to this advantage, researchers have preferred approximate algorithms to solve complex optimization problems that cannot be solved effectively with precise algorithms.

Deterministic algorithms are not suitable for solving optimization problems in a multi and many dimensional search space. In these problems, a comprehensive search cannot be made in practice, as the search area grows exponentially with the growth of the problem (Beheshti & Shamsuddin, 2013). For this reason, the use of deterministic techniques takes a lot of time. Deterministic algorithms do

not provide a suitable solution for solving optimization problems with a high-dimensional search space. Heuristic methods have been used to solve this problem. Today, metaheuristic methods have been developed by combining heuristics and using them effectively.

Approximate algorithms are divided into two groups as heuristics and metaheuristics. Heuristic algorithms are developed for a specific optimization problem and mostly depend on the nature of the problem being studied. Metaheuristic algorithms can be applied to any optimization problem regardless of the type of optimization problem (Baykasoğlu, 2001). Therefore, while heuristic algorithms have the capacity to solve a particular problem, metaheuristic algorithms can be adapted to any optimization problem. However, it is seen that metaheuristic algorithms produce more effective solutions than heuristic algorithms by using their problem-free structures.

It is very important to use the most suitable metaheuristic algorithm to solve multi or many dimensional optimization problems. In the literature, it is seen that the researchers deal with different metaheuristic algorithms by combining them as hyper-heuristic. In this manner, it is seen that they aim to provide better performance by utilizing the superior features of different metaheuristic algorithms (Burke et al., 2013) (Ting et al., 2015). In other words, researchers can solve optimization problems by combining different metaheuristic algorithms with some criteria (Baykasoğlu et al., 2019). In the related literature, researchers have found Particle Swarm Optimization (PSO) (Ang et al., 2020) for constrained design optimization problems, Simulated Annealing (SA) for scheduling problem (Leite et al., 2019), Vehicle orientation problem. Ant Colony Optimization (ACO) (Li et al., 2019), experimental studies, practical industrial applications and classification systems, Genetic Algorithm (GA) (Lin et al., 2016), Iterative Local Search Algorithm (ILS) for portfolio optimization problem (Kizys et al., 2019), Gray Wolf Optimization Algorithm (GWO) (Lu et al., 2019), Tabu Search Algorithm (TS) for assembly line balancing problem (Yılmaz and Yılmaz, 2020). In the next section, popularly used metaheuristic algorithms are given.

1.2 Metaheuristic Algorithms

Particle Swarm Optimization is one of the algorithms that can be given as an example to be inspired by nature. Briefly speaking, it was developed from swarm intelligence and inspired by the study of bird and fish swarm movement behaviors. While foraging or hunting, birds either disperse or move together before finding a place to find food (Gopal et al., 2020). Based on this behavior, a swarm of randomly located particles is created in the algorithm, and they iterate

to look for the best possible global iteration. Each particle also informs the other and they compare the data with other particle data such as birds and flocks of fish.

Whale Optimization Algorithm is another example of nature inspired algorithms. This algorithm, as the name suggests, was inspired by the hunting behavior of a whale. Whales force a pack of prey into a sphere by using a wall of bubbles they create and circling their prey. They then attack their prey by shrinking their bubble walls in a spiral. Based on the whale's behavior, a three-dimensional space is first created for the working situation to be examined. In three-dimensional space, a random location is considered the best location. Also, this position represents a whale. Then, the spherical best is determined by applying the circle reduction method or the spiral reduction method (Mirjalili and Lewis, 2016).

Genetic Algorithms is a search and optimization technique based on natural selection principles. The basic principles of this technique were introduced by John Holland. These algorithms are generally used in areas such as function optimization, scheduling, mechanical learning, design, cellular manufacturing. The most important difference from traditional optimization methods is that they use coded formats instead of parameter sets. Genetic algorithms operating according to probability rules only need objective function. They scan a specific part of the solution space, not the whole. Thus, they find a solution in a much shorter time by making an effective search (Goldberg, 1990).

Gray Wolf Optimization Algorithm is an artificial intelligence algorithm created by minimizing the use of control parameters. The population size and the number of iterations are used as control parameters in the GWO algorithm. The GWO algorithm was developed by being inspired by the foraging behavior and leadership hierarchy of gray wolves in nature. There are four types of wolves in GWO to simulate the leadership hierarchy. These are (α) alpha, (β) beta, (δ) delta and (ω) omega. In GWO, the best solution is called α . The second and third best solutions are called β and delta δ , respectively. The remaining candidate solutions are called ω . Hunting (optimization) is guided by α , β and δ (Mirjalili et al., 2014).

The Simulated Annealing Algorithm is an intuitive optimization technique designed to approach the global optimum of a given cost function, inspired by the annealing process of metals (Moriguchi, 2020). BTA is based on heating solids and then cooling them slowly. When the temperature of the heated solids drops, the internal particles of the solid reach an equilibrium state at any temperature. As the temperature rises, the BTA will travel to the neighboring area to find the best local optima. As it slowly cools down, it will try to stay at its best local optima.

Artificial Bee Colony is based on imitating the foraging behavior of bee swarms to solve multidimensional and multi-model optimization problems. The ABC algorithm was proposed by Karaboğa in 2005 (Karaboğa 2005). The sources that the bees go to in search of food represent the possible solutions of the problem to be solved in the algorithm, and the amount of nectar in the sources expresses the quality of the solution (objective function). In the ABC algorithm, there are three types of bees in a colony: employed bees, onlooker bees and scout bees (Karaboğa and Akay 2011). There is a bee in charge for each source. ABC algorithm tries to find the maximum or minimum point of the problem among the possible solutions by finding the source with the most nectar (Akay 2009).

Ant Colony Optimization Algorithm is very suitable to be run in parallel in structure. In the colony structure, there are more than one asynchronous or parallel working ant. If it is thought that there are more than one node in the parallel ant colony (parallel system) system and it is assumed that each ant is working on a node at a certain time, ants can be qualified as intelligent intermediaries in parallel systems. Ants visit all cities starting from a randomly chosen city and leave pheromones on the roads they pass. These pheromones are effective in determining the path of the next ants, so the communication between the intermediaries leads to a common result. The factor to be considered when sending each of the ants to a node is to prevent race conditions from occurring. Ants working at the same time, which is to be emphasized, should not be able to change the global data structure that holds the pheromone and selected path data at the same time. Since the main purpose in this application is to find the most suitable parametric alpha (α), beta (β), ro (ρ) values used in probability calculation in the ACO algorithm, increasing the number of ants in the colony will increase the probability of finding the most suitable values of these values.

Firefly Optimization Algorithm, fireflies are an insect that lives in hot and tropical regions, where there are about two thousand species in nature. Fireflies perform actions such as reproduction, hunting and protection from their enemies by influencing the opposite sex, thanks to their ability to create chemically cold light. The firefly optimization algorithm is one of the swarm-intelligent approaches that optimize (Pouyan et al., 2014). This algorithm works based on the principle that fireflies in nature move towards each other or in a random direction, depending on their attraction. In order to create the firefly algorithm easier and more understandable, three assumption rules are accepted (Pekdemir, 2012). All fireflies are considered asexual. So all fireflies can affect other remaining fireflies. Attractiveness has to do with the glow of the firefly. In this way, it moves from the two light-emitting fireflies towards the bright one with the dimmer light. The brightness changes depending on the distance in between.

If the brightness level is equal, random motion occurs. The brightness is determined by the fitness (objective) function. There is a fitness function that considers the brightest as the best.

Moth-Flame Optimization Algorithm was proposed by Mirjalili (Mirjalili, 2015). The MFA algorithm is inspired by the night flight strategy of moths. Moths have a flight mechanism that uses moonlight at a fixed angle. The flight mechanism strategy they use for direction determination is called transverse orientation. This strategy provides efficient and comfortable travel over long straight distances. On the other hand, moths are affected by artificial light just as they are by moonlight, and they try to act similarly by angling with this artificial light. Moths fly at a fixed angle with the light, causing a spiral movement.

Differential Evolution (DE) Optimization Technique is an evolutionary-based heuristic optimization technique first developed by Storn and Price (Storn and Price, 1997). Although it has great similarities with GA in terms of general operation and computational logic, the biggest difference of DE from GA is that the related problem can be solved by coding with decimal number sequences instead of binary number sequences. Although the mutation, crossover and selection operators used in GA are also used in DE, all individuals (chromosomes) in the population are processed by these operators, unlike GA (Keskindürk, 2006). For this purpose, each individual is compared with the new individual obtained by applying the mutation and crossover operators to three randomly selected individuals, respectively, and is transferred to the next generation by using the individual selection operator that is better in terms of objective function values. By applying this process until the given stopping condition is met, effective results can be obtained in terms of global optimum. Compared to other heuristic optimization techniques, the biggest advantages of DE are that it is less likely to find local optimum solutions and is easy to program.

Harris Falcon Optimization Algorithm imitates the hunting strategy of the Harris Falcon, one of the intelligent birds in nature. Harris hawks act as a flock, especially in the process of hunting rabbits. The herd has a leader. The leader and other members of the pack primarily make reconnaissance flights. After detecting the prey, the hunting process begins. These features of Harris hawks were modeled mathematically by Heidari in 2019 (Heidari et al., 2019). PSO is a population-based, gradientless optimization technique and can be applied to many engineering problems with an appropriate formulation.

Teach-Learning Based Optimization Algorithm is a population-based optimization technique. A group or class of learners is considered as the population and a teacher with the highest level of knowledge is determined. The teacher tries to bring the students in the class closer to their level of knowledge.

The performance of the teacher is determined by the average of the results obtained by the learners in the class. The TBLO algorithm is divided into two parts, the teacher and the learner phase. In the teacher phase, the person with the highest level of knowledge in the population is selected as the teacher and tries to bring the knowledge level of the class closer to his own level. The Student Phase, on the other hand, is when learners increase their level of knowledge by benefiting from the interaction among themselves, regardless of the teacher (Rao et al., 2011).

Grasshopper Swarm Optimization Algorithm is another nature inspired algorithm. Grasshoppers are creatures in the insect family. They are generally considered pests because of the damage they cause to agricultural crops. Grasshoppers can be seen individually in nature as well as in large flocks. Swarms of grasshoppers move like jumping and rolling cylinders. Grasshopper optimization algorithm is an algorithm that has just emerged and has a wide range of use in optimization problems. This algorithm is a swarm-based nature-inspired optimization algorithm that mimics the behavior of the locust swarm and models it mathematically (Saremi et al., 2017).

Salp Swarm Algorithm is inspired by salps belonging to the Salpidae family, which are sea creatures and whose bodies are very similar to jelly fish. They also act very similarly to jellyfish. Water is pumped into the body to push the body forward. One of the most interesting behaviors of salps is that they often behave as a swarm in the depths of the ocean as a chain of rafts. With the search method proposed by Seydali Mirjalili, real world problems are effectively found optimally in a given time. The population is first divided into two groups as leaders and followers. The leader is the salp creature at the front of the chain. Followers are the rest of the chain that follows the leader. Similar to other swarm-based techniques, the position of the salps is defined in the n-dimensional search space. n is the number of variables of the given problem. It is assumed that there is a food source called F in the target search space of the flock (Mirjalili et al., 2017).

In the next section, the method of the research is mentioned.

2. Method

With the literature review conducted within the scope of the research, the point of metaheuristic optimization algorithms was determined and the studies carried out between 2018 and 2022 were examined. In the study, firstly, a literature search was conducted using the keywords presented in Figure 1 in Google Scholar.

- | | | |
|------------------|-------------------|--------------|
| ✓ metaheuristic | ✓ many objective | ✓ algorithm |
| ✓ meta-heuristic | ✓ multi objective | ✓ algorithms |
| ✓ optimization | | |

Figure 1: Keywords used in publication search

As a result of the searches made using the keywords presented in Figure 1, 1995 scientific studies were found. From these studies, conference proceedings, book chapters, graduate theses and studies that do not have a Digital Object Identifier (DOI) number were excluded.



Figure 2: Working Process

3. Findings and Conclusions

947 studies that emerged as a result of the analyzes were examined by considering the criteria of publication name, publication year, author/authors, metaheuristic algorithms used in the study and algorithms preferred according to the application area. The results obtained in line with these examinations are presented in this part of the study.

3.1. Words Found in Algorithm Names

When the publications within the scope of the research are examined, 462 different words emerge. Among these words, it is seen that the words with a

frequency of more than 100 include algorithm, optimization, swarm, particle, search, algorithm and genetics. Descriptive statistics about the words in the names of the algorithms are given in Table 1.

Table 1: Words Found in Algorithm Names

Words	Frequency
Algorithm	1249
Optimization	922
Swarm	200
Particle	160
Search	147
Genetics	113
Whale	99
Gray	76
Wolf	75
Colony	70
Based	64
Artificial	51
Bee	40
Added, Annealing	38
Simulated, Ant	37
Firefly	36
Differential, Learning	35
Evolution, Evrim	32
moth	30
Flame	29
Teaching	28
Harris, Hawks	27
Grasshopper	23
Salp	20
Cuckoo, Butterfly	19
Flower, Pollination	17
Sine	16
bat	15
gravity	14
Cosine, Harmony	13
Wild, Spotted, Hyena, Jaya, Symbiosis, Dragonfly, Multiple, Universe	12
Balance, Weed	10
Arithmetic, Biogeography, Levy, Flight, Chimpanzee, Local	9
Game, Gradient, Coyote, Frog, Leap, Taboo, Penguin	8
Social, Fly, Water, Archimedes, Emperor, Seagull,	7
Tree, Field, Manta, Insect, Sunflower, And, Development, Swirl, Henry, Gas, Resolution, Lion	6
Cluster, Elephant, Sea, Antenna, Imperial, Invader, May, Cycle	5
Creation, Gold, Back, Snapper, Plasma, Vibrating, Horse, Seed, Antlion, Herding, Black, Widow, Food	4

Variable, Network, Group, Theory, Collector, Tracking, Mountain, Cultural, Student, Psychology, Migratory, Random, Lightning, Path, Hungry, Eyed, Aquila, Supply, Demand, Colliding, Objects, Shepherd, Mother, World, Cup, Valuable, Player, Ruler, Immune, Bald, Runge, Kutta, Ecosystem, Dice	3
Border, Smell, Mating, Plant, Interactive, School, Scarlet, Intelligence, Fish, Map, Change, Newton, Climbing, 2-Opt, Forensic, Investigation, Africa, Vultures, Alternative, Tour, Charts, Set, Rescue, Prey, Predator, Bacterial, Honey Badger, Fireworks, Transient, Giza, Pyramids, Construction, Cooperation, Chaos, Blackhole, Contrast, Dipper, Throated, Corona, Virus, Mine, Reef, Blast, Coral, Fruit, Start, Solution, Wind, Guided, Mimic, Spider, Wave, Saving, Tunica, Charged, Algae, Sail, Finder, Branch, Averages, Descent	2
Reach, Matter, Growth, Fluid, Flow, Direction, Fallen Ratio, Bottom, Left, Fill, Antelope, Spacing, Sequencing, Discretization, Atomic, Orbit, Honeybee, Pattern, Barnacles, Owl, Bigbang, Bigcrunch, Bipolar, Pairing, Tendency, Competition, Bonobo, Evaporation, Rate, Heuristic, Big, Magnified, Class, Topper, Capuchin, Slime, Mushroom, Clarke, Wright, Dwarf, Pharaoh, Rat, Meadow, Core, Cheetah, Snipe, Scattered, Wavelet, Pinear, Dbscan, Dijkstra, Dynamic, Linear, Population, Size, Reduction, Electromagnetism, Similar, Electrostatic, Discharge, Adolescent, Identity, Donkey, Smuggler, Threshold, Accepted, Carnivorous, Autodidactic, Mouse, Gaussian, Mutation, Propagation, Retrospective, Hunt, Nomadic, People, Prediction, Pigeon, Heraldic, Animal, Migration, Fast, Upgrade, Inner, Non, Multi, Level, Method, First, Appropriate, Descending, Human, Sooty, Tern, Jpeg, Caledonia, Hump, Mixed, Encryption, Rock, Earnings, Winning, Sharing, Knowledge, Coal, Quarry, Kestel, Kho, Fox, Laughter, Brother, Coordinated, Robot, Discovery, Battle, Head, Hatching, Reclining, Pole, Tail, Raven, Roost, Power, Mass, Center, League, Championship, Logistics, Gathering, Magnetic, Mendel, Compassion, Cornak, Father, Walrus, Opponent, Hermit, Crab, Shell, Ink, Musical, Seat, Metaintuitive, Raphson, Quantitative, Probabilistic, Optical, Death, Petri, Generation, Potential, Programming, Rao, Remora, Color, Open, Fire, Satin, Arbor, War, Sparrow, Squirrel, Impact, Engineering, Socio, Sperm, Spiral, Paint, Healing, Strategy, Slug, Supernova, Reptile, Driving, Training, Team, Chasing, Eden, Tangent, Chicken, Thermal, Rain, Jellyfish, Electric, Flora, Gorilla, Troops , Rabbit, Innovative, Gunner, Stack, Attachment, Procedure, Dolphin, Nest	1



Figure 3 : Words found in algorithm names

3.2. Distribution of Publications by Years

The distribution of the publications reached within the scope of the study by years is presented in Table 2.

Table 2: Distribution of Publications by Years

Years	2018	2019	2020	2021	2022	Total
Number	120	199	287	219	122	947

It is seen that the highest number of publications were written in 2020 with 287, and the least number of publications was written in 2018 with 120 in Table 2.

3.3. Distribution of Publications by Number of Authors

The distribution of the publications reached within the scope of the study according to the number of authors is presented in Figure 4.

With examining Figure 4, it is seen that the most common studies in terms of number of authors consist of 240 and 241 with 2 and 3 authors, respectively, and at least 2 and 1 with 10 and 15 authors, respectively.

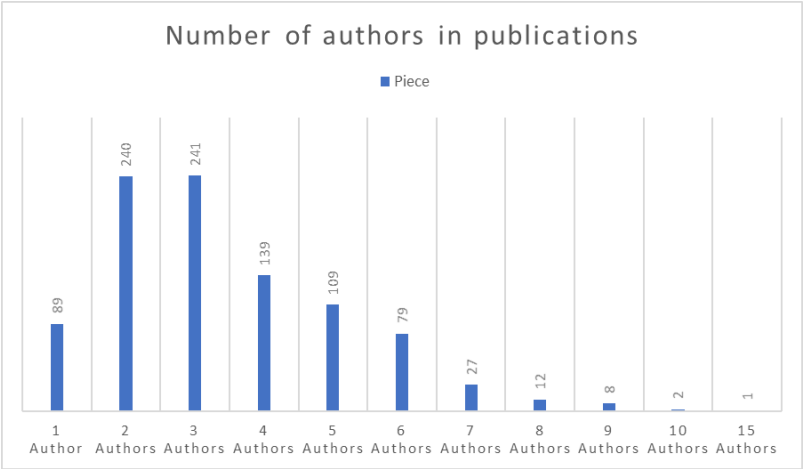


Figure 4: Distribution of publications by number of authors

3.4. Algorithms used in publications over 20

Algorithms used for 20 or more in the reviewed studies are presented in Figure 5.

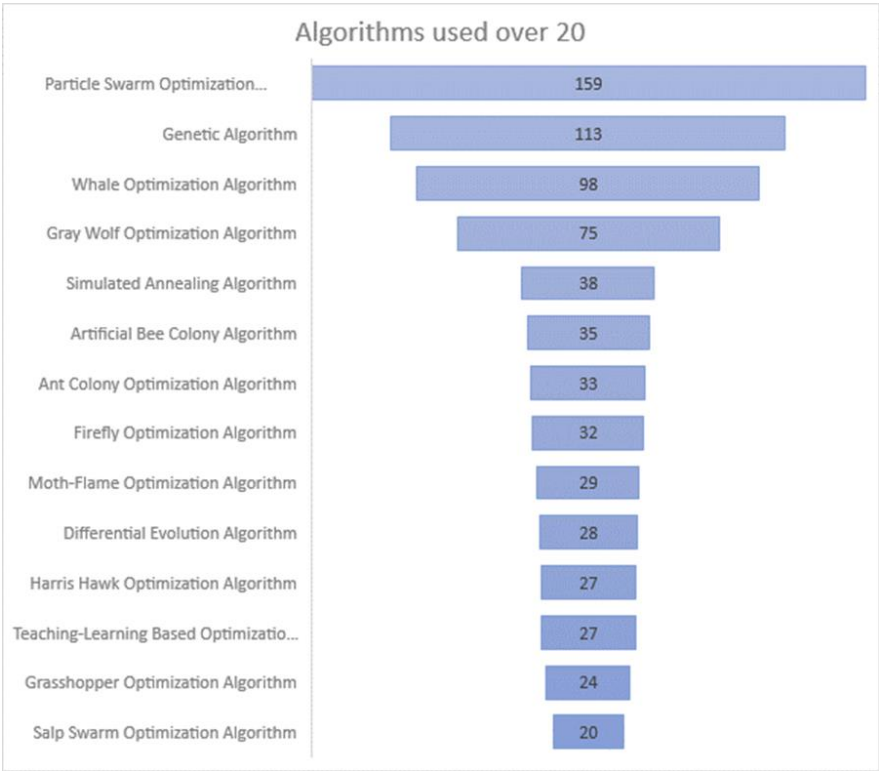


Figure 5: Algorithms used over 20

Examining Figure 5, it is seen that 159 of the Particle Swarm Optimization Algorithm, 113 of the Genetic Algorithm, 98 of the Whale Optimization Algorithm, 75 of the Gray Wolf Optimization Algorithm and 38 of the Simulated Annealing Algorithm are used as the most used algorithms.

3.5. Algorithms used in the range of 10-19 in publications

Algorithms used in the range of 10-19 in publications are presented in Figure 6.

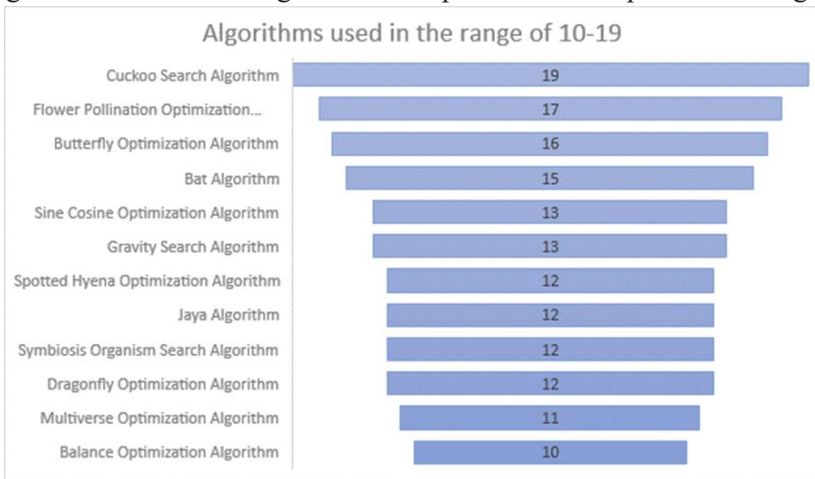


Figure 6: Algorithms used in the range 10-19

3.6. Algorithms used in the range of 7-9 in publications

Algorithms used in the range of 7-9 in publications are presented in Table 3.

Table 3: Algorithms used in the 7-9 range

Algorithm Name	Piece
Arithmetic Optimization Algorithm (AOA)	9
Biogeography - Based Optimization (BBO)	9
Levy Flight (LF)	9
Chimpanzee Optimization Algorithm (COA)	9
Coyote Optimization Algorithm (COA)	8
Frog Leaping (SFLA)	8
Harmony Search (HS) Algorithm	8
Taboo Search (TS)	8
Local Search Algorithm (LSA)	8
Archimedes OptimizationAlgorithm (AOA)	7
Atom Search Optimization (ASO)	7
Emperor Penguin Optimizer (EPO)	7
Crow Search Algorithm (CSA)	7
Seagull Optimization Algorithm (SOA)	7

3.7. Algorithms used 6 times and less in publications

Algorithms used 6 times in publications are presented in Table 4.

Table 4: Algorithms used 6 times

Algorithm Name
Sunflower Optimization Algorithm (SFO)
Vortex Search Algorithm (VSA)
Henry Gas Solubility Optimization (HGSO)
Ant Lion Optimizer (ALO)
Bees Algorithm (BA)

Algorithms used 5 times in publications are presented in Table 5.

Table 5: Algorithms used 5 times

Algorithm Name
Beetle Antennae Search (BAS) Algorithm
Marine Predator Algorithm (MPA)
Imperialist Competitive Algorithm (ICA)
Gradient - Based Optimizer (GBO) Algorithm
Invasive Weed Optimization (IWO) Algorithm
Mayfly Algorithm (MA)
Water Cycle Algorithm (WCA)
Invasive Weed Optimization (IWO)

Algorithms used 4 times in publications are presented in Table 6.

Table 6: Algorithms used 4 times

Algorithm Name
Tree-Seed Algorithm (TSA)
Antlion Optimization Algorithm (ALO)
Glowworm Swarm Optimization (GSO)
Slime Mold Algorithm (SMA)
Electromagnetic Field Optimization (EFO)
K - Nearest Neighbor Algorithm (kNN)
Elephant Herding Optimization (EHO)
Black Widow Optimization (BWO)
Manta Ray Foraging Optimization (MRFO)

Algorithms used 3 times in publications are presented in Table 7.

Table 7: Algorithms used 3 times

Algorithm Name
Greedy Search Algorithm (GSA)
Aquila Optimizer (AO)
Supply - Demand-Based Optimization (SDO)
Colliding Bodies Optimization (CBO)
Shepherd Optimization Algorithm (SOA)
Variable Neighborhood Descent (VND) Algorithm
Jellyfish Search Optimizer (JSO)
World Cup Optimization Algorithm (WCO)
Most Valuable Player Algorithm (MVPA)
Monarch Butterfly Optimization (MBO) Algorithm
Immune Plasma (IP) Algorithm
Cat Swarm Optimization (CSO) Algorithm
Bald Eagle Search Optimization Algorithm (BES)
Runge Kutta Optimization (RUN) Algorithm
Neural Network Algorithm (NN)
Vibrating Particles System (VPS) Algorithm
Artificial Ecosystem Optimization (AEO) Algorithm
Dice Gaming Optimizer (DGO) Algorithm

The algorithms used twice in publications are as follows; 2-opt algorithm, Forensic-Based Investigation (FBI) algorithm, African Vulture Optimization (MAVO) algorithm, Golden Sine Algorithm (Gold-SA), Search and Rescue optimization algorithm (SAR), Bee Colony Optimization (BCO), Horse herd Optimization Algorithm (HOA), Prey Predator Algorithm (PPA), Bacterial Foraging Optimization (BFO), Honey Badger Algorithm (HBA), Fuzzy C-means (FCM) Algorithms, Variable Neighbourhood Search (VNS), Fireworks Algorithm (FWA), Transient Search Optimization (TSO), Backtracking Search (BS), Giza Pyramids Construction (GPC) Algorithm, Cooperation Search Algorithm (CSA), Chaos Game Optimization (CGO), Black Hole Optimization (BHO) Algorithm, Comprehensive Opposition-Based Learning (COBL), Dipper Throated Optimization Algorithms (DTO), Corona virus optimization (CVO), Cultural Algorithm (CA), Mine Blast Algorithm (MBA), Coral Reefs Optimization Metaheuristic (CRO), Fruit Fly Optimization Algorithm (FOA), Wind-Driven Optimization (WDO), Satin Bowerbird Optimization (SBO), Social Mimic Optimization (SMO) Algorithm, Social Spider Optimization (SSO), Water Wave Optimization (WWO), savings algorithm (SA), Tunicate Swarm

Algorithm (TSA), Charged System Search (CSS), Wild Horse Optimizer (WHO), Artificial Algae Algorithm (AAA), Sailfish Optimizer (SFO), Lightning Search Algorithms (LSA) and Pathfinder Algorithm (PFA).

The algorithms used once in publications are as follows; Tree Growth Algorithm (TGA), Fluid Search Optimization (FSO) Algorithms, Fluid Search Optimization Algorithm (IFSO), Flow Direction Algorithm (FDA), Red Deer Algorithm (RDA), Golden Eagle Optimizer (GEO), Golden Ratio Optimization Method (GROM), Bottom – Left And Bottom-Left Fill Placement Method, Wildebeest Herd Optimization (WHO), Interval Branch and Bound Global Optimization Algorithm, Hybrid Successive Discretization Algorithm (HSDA), Fire Hawk Optimizer (FHO), Atomic Orbital Search (AOS), Bear Smell Search Algorithm (BSSA), Honeybee Mating Optimization (HBMO) Algorithm, Slime Mould Algorithm (SMA), Barnacles Mating Optimizer (BMO), Support Vector Regression Bayesian Optimization (SVR-BO), Owl Optimization Algorithm (OOA), Big Bang–Big Crunch (BB-BC) Optimization Algorithm, Bipolar Matching Tendency (BMT), Plant Competition Optimization (PCO), Bonobo Optimization (BO) Algorithm, Beetle Swarm Optimization (BSO) Algorithm, Evaporation Rate WCA (ER-WCA), Aggrandized Class Topper Optimization (CTO), Capuchin Search Algorithm (CapSA), Slime Mould Algorithm (SMA), Clarke-Wright Algorithm (CW), Dwarf Mongoose Optimization Algorithm (DMO), Prairie Dog Optimization Algorithm (PDO), Kernel Search Optimization (KSO), Cheetah Optimizer Algorithm (CO), Sandpiper Optimization Algorithm (SOA), Hybrid Scatter Search Method (HSSM), Algorithm for Generating Alternative Tour Schedules Set (Tk), Algorithm for Generating Random Initial Solution, Branch and Bound (BB), Density-Based Spatial Clustering of Application with Noise (DBSCAN) Algorithm, Dynamic Differential Annealed Optimization (DDAO), Dijkstra's Algorithm (DA), Dynamic Group-Based Optimization Algorithm (DGCO), Linear Population Size Reduction (LSHADE) Algorithm, Electromagnetism-Like (EML) Algorithm, Electrostatic Discharge Algorithm (ESDA), Adolescent Identity Search Algorithm (AISA), Donkey and Smuggler Optimization Algorithm (DSO), Threshold Acceptance (TA) Algorithm, Carnivorous Plant Algorithm (CPA), Interactive Seracı Algorithm (ISA), Interactive Autodidactic School (IAS), Elephant Herding Optimization (EHO), Back Propagation (BP) Algorithm, Backtracking Search Optimization Algorithm (BSA), Deer Hunting Optimization Algorithm (DHOA), Nomadic People Optimizer (NPO) Algorithm, Gradient Evolution (GE) Algorithm, Gradient Descent (GD) Algorithm, Multivariable Grey Prediction Evolution Algorithm (MGPEA), Group Teaching Optimization

Algorithm (GTOA), Pigeon-Inspired Optimization (PIO), Dynastic Optimization Algorithm (DOA), Animal Migration Optimization (AMO), Rapidly Random Tree (RRT), Light Gradient Boosting algorithm (LGBA), Interior-Point Optimizer (IPOPT), First Fit Decreasing (FFD) Algorithm, Human learning Optimization (HLO), Sooty Tern Optimization Algorithm (STOA), JPEG Algorithm, Caledonian Crow Learning Algorithm (NCCLA), Vocalization of Humpback Whale Optimization Algorithm (VWOA), Savings Algorithm (SA), Gaining-Sharing Knowledge-Based Optimization Algorithm (GSK), chaotic Kbest Gravity Search Algorithm (cKGSA), Border Collie Optimization (BCO), Keshtel Algorithm (KA), Kho-Kho Optimization Algorithm (KKO), Red Fox Optimization Algorithm (RFO), Ludo Game-Based Swarm Intelligence (LGSI) Algorithm, Coordinated Multi-Robot Exploration (CME), Shark Smell Optimization (SSO) Algorithm, Battle Royale Optimization (BRO) Algorithm, Krill Algorithm (KA), Chaotic Krill Head Algorithm (CKHA), Krill Herd Algorithm (KHA), Mouth-Brooding Fish (MBF), Polar Bear Optimization (PBO) Algorithm, Queuing Search (QS) Algorithm, Raven Roosting Optimization (RRO) Algorithm, Cultural Evolution Algorithm (CEA), Cluster Based Global Optimization (KTGO), Global Power Point Tracking (GMPPT) Algorithm, Political Optimizer (PO) Algorithm, Center of Mass Optimization (CMO) Algorithm, . League Championship Algorithm (LCA), Logistic-Sine Chaotic Optimization Algorithm (LS-COA), Magnetic Optimization Algorithm (MOA), Monkey Search (MS) Algorithm, Mendelian evolutionary theory optimization (METO), Pity Beetle Algorithm (PBA), Egyptian Vulture Optimization Algorithm (EVOA), Walrus Optimization Algorithm (WaOA), Hermit Crab Shell Exchange (HCSE) Algorithm, Cuttlefish Algorithm (CFA), Musical Chairs Algorithm (MCA), School-Based Optimization (SBO) Algorithm, Probabilistic Road Map (PRM), Optics-Inspired Optimization (OIO) Algorithms, Battle Royale Optimization (BRO) Algorithm, Penguins Search Optimization Algorithm (PeSOA), Petri Net(PN) Algorithm, Plasma Generation Optimization (PGO) Algorithm, Potential Field (PF) Algorithm, Q-learning Algorithm, Rao_1 Optimization Algorithm, Competitive Swarm Optimizer (CSO), Remora Optimization Algorithm (ROA), Color Harmony Algorithm (CHA), Battle Royale Optimization (BRO) Algorithm, Adaptive Sparrow Search Algorithm (ASSA), Squirrel Search Algorithm (SSA), Social Impact Theory-based Optimization (SITO), Social Group Optimization (SGO), Social Engineering Optimization (SEO), Socio Evolution & Learning Optimization Algorithm (SELO), Adaptive Sperm Swarm Optimization Algorithm (ASSO), Spiral Optimization Algorithm (SOA), Stochastic Paint Optimizer (SPO), Stochastic Hill-Climbing (SHC), Multiple-Strategy Learning (MSL), Slime Mold Algorithm

(SMA), Supernova Optimizer (SO), Reptile Search Algorithm (RSA), Hybrid Swarm Optimization Algorithm (HSO), Driving Training-Based Optimization (DTBO), Interactive Search Algorithm (ISA), Falcon Optimization Algorithm (FOA), Improved Team Game Optimization Algorithm (ITGA), Following Optimization Algorithm (FOA), Tangent Search Algorithm (TAA), Chicken Swarm Optimization (CSO), Thermal Exchange Optimization (TEO), Rain Optimization Algorithm (ROA), Artificial Atom Algorithm (A3), Artificial Fish Swarm Optimization (AFSA), Artificial Mountain Ape Optimization (A2MO), Jellyfish Search Optimizer (JSO), Artificial Electric Field Algorithm (AEFA), Artificial Flora Optimization Algorithm (AF), Artificial Gorilla Troops Optimizer (GTO), Artificial Rabbits Optimization (ARO), Algorithm of the Innovative Gunner (AIG), Heap-Based Optimizer (HBO), Lightning Attachment Procedure Optimization (LAPO) Algorithm, Dolphin Swarm Algorithm (DSA), Enhanced Nest Cuckoo Optimization Algorithm (ENCOA) and β -Hill Climbing (β -hc).

3. 8. Algorithms used according to application areas

Algorithms used 20 times or more in publications examined within the scope of the study are grouped according to their application areas. The data obtained in this direction are presented in Table 9.

Table 9: Algorithms used according to application areas

	P S O	G A	W O A	G W O	SA A	A B C	A C O	F A	M F O	D E	H H O	T L B O	G W O	S SA	T O T A L
Computer Science	26	16	28	23	6	7	5	3	10	5	9	3	8	4	153
Biomedical Eng.	3	3	0	3	2	0	1	1	0	0	1	0	0	1	15
Environment Eng	2	4	0	0	1	0	0	1	0	0	0	1	0	0	9
Electrics & Electronics Eng.	35	19	12	9	3	4	7	8	3	8	1	7	3	3	122
Industrial Eng.	14	22	19	5	15	6	8	5	7	2	4	0	2	2	111
Energy	1	1	8	5	1	1	1	1	1	1	4	2	1	2	30
Finance	3	3	1	1	0	1	1	0	0	0	0	0	2	0	12
Physical	0	1	0	0	0	0	0	0	0	0	0	0	0	0	1
Food	2	1	0	0	0	0	1	0	0	0	0	0	0	0	4
Civil Eng.	13	9	2	2	0	3	1	2	0	2	1	3	1	0	39
Geology	12	8	2	7	4	0	3	2	0	5	1	0	1	2	47
Chemical	2	1	1	0	0	0	0	0	0	0	1	0	0	0	5
Control	3	2	1	0	0	0	0	0	0	0	0	1	0	0	7
Logistics	0	1	0	0	0	0	0	0	0	0	0	0	0	0	1
Mining	0	0	0	1	0	0	0	0	0	0	0	0	0	0	1
Mechanical Eng.	11	2	4	2	1	4	2	3	3	1	1	5	1	1	41
Material Science	3	5	0	1	0	0	1	1	0	1	0	0	0	1	13
Maths	11	1	11	5	1	2	1	4	3	0	2	2	0	2	45
Mechatronics Eng.	10	4	6	7	1	3	0	1	0	1	0	2	2	0	37
Forestry	0	0	0	1	0	0	0	0	0	0	0	0	0	0	1
Automotive	0	0	0	0	0	0	1	0	1	0	1	1	1	1	6
Oil	1	1	0	0	0	1	0	0	0	0	0	0	0	0	3
Insurance	0	0	0	0	0	0	0	0	0	0	1	0	0	0	1
Tourism Business	0	1	0	0	0	0	0	0	0	0	0	0	0	0	1
Aeroplane	2	0	0	0	0	0	0	0	0	0	0	0	0	0	2
Transportation	5	7	3	2	3	2	0	0	1	1	0	0	0	0	24
Agriculture	0	1	0	1	0	1	0	1	0	1	0	0	2	1	7

As can be seen in Table 9, 153, 122 and 111 studies were carried out in the application fields of Computer Engineering, Electrics & Electronics Engineering and Industrial Engineering, respectively. It is seen that the least amount of studies are done in the fields of Physics, Logistics, Mining, Forestry and Tourism Management, one time used each. It is seen that the most used algorithm in Computer Engineering is PSO (26) and the least used algorithm is FA (3). It is seen that the most used algorithm in Electrical and Electronics Engineering is PSO (35) and the least used algorithm is HHO (1). It is seen that the most used algorithm in Industrial Engineering is GA (22) and the least used algorithm is TLBO.

4. Conclusion

In this study, a research was conducted on metaheuristic algorithms used for problem solving in 2018-2022. 947 studies that emerged as a result of the research were examined by considering the criteria of article title, article year, author/authors, meta-heuristic algorithms used in the study and determination of the algorithms used according to their application areas. As a result of the study, it was determined that metaheuristic algorithms were made with 287 at most in 2020 and at least 120 in 2018. It was seen that the studies with 2 and 3 authors at most were made 240 and 241, respectively, while the studies with at least 10 and 15 authors were made 2 and 1, respectively. 20 and more preferred algorithms are PSO (158), GA (113), WOA (98), GWO (75), SAA (38), ABC (35), ACO (33), FA (32), MFO (29), DE (28), HHO (27), TLBO (27), GWO (24) and SSA (20). Finally, when the use of 20 or more preferred algorithms according to application areas is examined, it has been determined that 153 applications are made in the field of Computer Engineering and PSO (26) algorithm is used the most in the field of Computer Engineering. Within the scope of this study, metaheuristic algorithms used for problem solving in the last five years were examined. In future studies, the frequency of preference of popular algorithms with 20 or more uses can be examined by increasing the year interval. In addition, the number of uses of hybrid models created by popular algorithms with each other can be determined, and the success rates of these hybrid models can be examined.

REFERENCES

- Akay, B. (2009). Nümerik optimizasyon problemlerinde yapay arı kolonisi (artificial bee colony) algoritmasının performans analizi.
- Akyol, S., Alataş, B. (2012). Güncel sürü zekâsı optimizasyon algoritmaları.
- Ang, K. M., Lim, W. H., Isa, N. A. M., Tiang, S. S., & Wong, C. H. (2020). A constrained multi-swarm particle swarm optimization without velocity for constrained optimization problems. *Expert Systems with Applications*, 140, 112882.
- Atalan, A. (2018). TÜRKİYE SAĞLIK EKONOMİSİ İÇİN İSTATİSTİKSEL ÇOK AMAÇLI OPTİMİZASYON MODELİNİN UYGULANMASI. *İşletme Ekonomi ve Yönetim Araştırmaları Dergisi*, 1(1), 34-51.
- Baykasoglu, A. D. İ. L. (2001). MOAPPS 1.0: aggregate production planning using the multiple-objective tabu search. *International Journal of Production Research*, 39(16), 3685-3702.
- Baykasoglu, A., Hamzadayi, A., & Akpınar, S. (2019). Single Seekers Society (SSS): Bringing together heuristic optimization algorithms for solving complex problems. *Knowledge-Based Systems*, 165, 53-76.
- Beheshti, Z., Shamsuddin, S. M. H. (2013). A review of population-based meta-heuristic algorithms. *Int. J. Adv. Soft Comput. Appl*, 5(1), 1-35.
- Burke, E. K., Gendreau, M., Hyde, M., Kendall, G., Ochoa, G., Özcan, E., & Qu, R. (2013). Hyper-heuristics: A survey of the state of the art. *Journal of the Operational Research Society*, 64, 1695-1724.
- Goldberg, D. E. (1990). *Real-coded genetic algorithms, virtual alphabets and blocking*. Champaign: University of Illinois at Urbana Champaign.
- Gopal, A., Sultani, M. M., & Bansal, J. C. (2020). On stability analysis of particle swarm optimization algorithm. *Arabian Journal for Science and Engineering*, 45, 2385-2394.
- Heidari, A.A., Mirjalili, S., Faris, H., Aljarah, I., Mafarja, M., Chen, H., 2019. Harris Hawks optimization: Algorithm and applications: Future Generation Computer Systems, Cilt. 97, s. 849-872. DOI: 10.1016/j.future.2019.02.028.
- Karaboga D., (2005), "An idea based on honey bees farm for numerical optimization", Technical Report TR06. Computer Engineering Department, Engineering Faculty, Erciyes University
- Karaboga D., Akay B., (2011), "A modified Artificial Bee Colony (ABC) algorithm for constrained optimization problems", Applied Soft Computing, Volume 11, Issue 3, April, Pages 3021-3031

- Keskindürk, T., Diferansiyel Gelişim Algoritması. İstanbul Ticaret Üniversitesi Fen Bilimleri Dergisi, 5-9, 85-99. 2006.
- Kizys, R., Juan, A. A., Sawik, B., & Calvet, L. (2019). A biased-randomized iterated local search algorithm for rich portfolio optimization. *Applied Sciences*, 9(17), 3509.
- Leite, N., Melicio, F., & Rosa, A. C. (2019). A fast simulated annealing algorithm for the examination timetabling problem. *Expert Systems with Applications*, 122, 137-151.
- Li, Y., Soleimani, H., & Zohal, M. (2019). An improved ant colony optimization algorithm for the multi-depot green vehicle routing problem with multiple objectives. *Journal of cleaner production*, 227, 1161-1172.
- Lin, F., Liu, S., Yang, Z., Zhao, Y., Yang, Z., & Sun, H. (2016). Multi-train energy saving for maximum usage of regenerative energy by dwell time optimization in urban rail transit using genetic algorithm. *Energies*, 9(3), 208.
- Lu, C., Gao, L., Pan, Q., Li, X., & Zheng, J. (2019). A multi-objective cellular grey wolf optimizer for hybrid flowshop scheduling problem considering noise pollution. *Applied Soft Computing*, 75, 728-749.
- Marler, R. T., & Arora, J. S. (2004). Survey of multi-objective optimization methods for engineering. *Structural and multidisciplinary optimization*, 26, 369-395.
- Mirjalili, S., Mirjalili, S. M., & Lewis, A. (2014). Grey wolf optimizer. *Advances in engineering software*, 69, 46-61.
- Mirjalili S., Moth-flame optimization algorithm: A novel nature-inspired heuristic paradigm, *KnowledgeBased Systems*. 89 (2015) 228-249. doi:10.1016/j.knosys.2015.07.006.
- Mirjalili, S., & Lewis, A. (2016). The whale optimization algorithm. *Advances in engineering software*, 95, 51-67.
- Mirjalili, S., Gandomi, A. H., Mirjalili, S. Z., Saremi, S., Faris, H., & Mirjalili, S. M. (2017). Salp Swarm Algorithm: A bio-inspired optimizer for engineering design problems. *Advances in engineering software*, 114, 163-191.
- Moriguchi, K. (2020). Acceleration and enhancement of reliability of simulated annealing for optimizing thinning schedule of a forest stand. *Computers and Electronics in Agriculture*, 177, 105691.
- Sra, S., Nowozin, S., & Wright, S. J. (Eds.). (2012). *Optimization for machine learning*. Mit Press.

- Pekdemir G., Çoklu İmge Eşikleme Problemlerinde Metasezgisel Algoritmaların Performans Analizi, Selçuk Üniversitesi, Fen Bilimleri Enstitüsü, Bilgisayar Mühendisliği Anabilim Dalı Yüksek Lisans Tezi, 2012.
- Pouyan B.M., Yousefi R., Ostadabbas S., Nourani M., A Hybrid Fuzzy-Firefly Approach for Rule-Based Classification, In: The Twenty-Seventh International Flairs Conference, 2014.
- Rao, R. V., Savsani, V. J., & Vakharia, D. P. (2011). Teaching-learning-based optimization: a novel method for constrained mechanical design optimization problems. *Computer-Aided Design*, 43(3), 303-315.
- Saremi, S., Mirjalili, S., & Lewis, A. (2017). Grasshopper optimisation algorithm: Theory and application. *Advances in Engineering Software*, 105, 30-47. doi:10.1016/j.advengsoft.2017.01.004
- Storn, R., & Price, K. (1997). Differential evolution-a simple and efficient heuristic for global optimization over continuous spaces. *Journal of global optimization*, 11(4), 341.
- Ting, T. O., Yang, X. S., Cheng, S., & Huang, K. (2015). Hybrid metaheuristic algorithms: past, present, and future. *Recent advances in swarm intelligence and evolutionary computation*, 71-83.
- Türkay, M. (2011). Optimizasyon Modelleri ve Çözüm Metodlari. URL: <http://home.ku.edu.tr/~mturkay/indr501/Optimizasyon.pdf>.
- Yilmaz, H., & Yilmaz, M. (2020). A mathematical model and tabu search algorithm for multi-manned assembly line balancing problems with assignment restrictions. *Engineering Optimization*, 52(5), 856-874.

Chapter 19

Treatment of Textile Industry Wastewater Containing Reactive Black 5 and Reactive Orange 16 Dyes By UV/H₂O₂ Oxidation

Ayşe Elif ATEŞ¹

Sinan ATEŞ²

¹ Res. Asst.. Gör.; İstanbul Üniversitesi-Cerrahpaşa Mühendislik Fakültesi Çevre Mühendisliği Bölümü, ayseelif.ates@iuc.edu.tr ORCID No: 0000-0001-5391-7478

² İstanbul Üniversitesi-Cerrahpaşa Mühendislik Fakültesi Çevre Mühendisliği Bölümü, sinanates89@gamil.com ORCID No: 0000-0003-0967-2367

ABSTRACT

The textile industry produces large amounts of wastewater, and direct discharge of this wastewater into the environment can cause environmental problems. Therefore, the treatment of textile industry wastewater is of great environmental importance. Wastewater contains chemicals, dye residues, organic compounds, heavy metals and other pollutants used in the textile production process. These pollutants can harm the environment when discharged directly into water sources or soil. For example, colored paint residues and chemicals can reduce the oxygen content of water in aquatic ecosystems, inhibit photosynthetic activity and threaten the life of aquatic organisms. The treatment of textile industry wastewater provides positive environmental effects. Well-designed and effective treatment systems remove pollutants from wastewater and improve water quality. This helps conserve water resources and maintain the balance of aquatic ecosystems. In addition, wastewater treatment processes are also important for the sustainability of water resources. Treated wastewater can be recovered as reusable water resources and contribute to reducing water use in water-intensive industries such as the textile industry. This ensures a more efficient and sustainable use of water resources. The treatment of textile industry wastewater also ensures compliance with environmental standards. Environmental legislation requires wastewater to comply with certain quality standards and to be discharged directly without harming the environment. Treatment processes help the industry comply with these regulatory requirements and operate in an environmentally sound manner. As a result, the treatment of textile industry wastewater is of great environmental importance. Treatment processes provide environmental benefits such as removal of pollutants, protection of water resources, sustainable water use and compliance with legal requirements. In this way, the textile industry can operate in a way that has less impact on the environment and supports sustainability goals.

Keywords: Textile industry, Wastewater, H_2O_2 , UV, Reactive Black 5, Reactive Orange 16

INTRODUCTION

The textile industry is known for its massive use of water, energy and chemicals and is a major source of its wastewater. Dyes and printing materials, processing aids, solvents and other chemicals used in the textile production process cause various organic and inorganic pollutants to be released into wastewater. These pollutants can harm the environment and water resources, affect aquatic ecosystems and threaten human health (Pattnaik, 2018). The important reasons for the treatment of textile industry wastewater should be evaluated in terms of environmental, human health and sustainability.

Environmental Impacts: When wastewater is discharged into natural water resources, it can damage aquatic ecosystems due to the organic pollutants and toxic substances it contains. These pollutants can affect aquatic life, reduce water quality and cause imbalances in aquatic ecosystems. Untreated wastewater can cause pollution of water resources and environmental disasters.

Human Health: Some chemicals in textile wastewater can be dangerous for human health. In particular, substances with carcinogenic, mutagenic or hormone-disrupting effects may cause harm to humans and other organisms by passing from wastewater to water sources. Therefore, wastewater treatment is important to protect health by reducing the exposure of toxic substances to humans and the environment.

Sustainability: Sustainable use and protection of water resources are part of global environmental goals and sustainability principles (Kumar, 2017). Effective treatment of textile industry wastewater prevents contamination of water resources, promotes water conservation and contributes to the water cycle. Thus, it contributes to the sustainable management of water resources (Khan, 2014).

The textile industry produces large volumes of wastewater, which can potentially cause environmental impacts. Therefore, the treatment of textile industry wastewater is of great importance. First of all, pollutants in textile industry wastewater can directly harm the environment and water resources. These pollutants can include organic compounds, colored substances, heavy metals, chemicals and toxic compounds. These pollutants can disrupt aquatic ecosystems, cause contamination of water resources and affect aquatic life. Untreated wastewater can also lead to increased oxygen deficiency and toxic effects in aquatic habitats. Secondly, textile industry wastewater can have adverse effects on the availability and sustainability of water resources. Direct discharge of wastewater without treatment can reduce the quality of water resources and damage drinking water supplies. Improving the quality of wastewater through treatment processes contributes to the protection of water resources and a sustainable water supply for future generations. In addition, the treatment of

textile industry wastewater is also important for public health. Untreated wastewater may cause the spread of harmful microorganisms and disease agents. Pollution of water sources and water treatment systems can adversely affect the quality of water consumed from water sources and put human health at risk. Finally, the treatment of textile industry wastewater is also important for the industry itself. Wastewater treatment processes can increase water use efficiency, utilize reusable water resources and reduce costs (Paul, 2012). It also ensures compliance with industrial standards in terms of waste management practices and environmental compliance. For these reasons, the treatment of textile industry wastewater is of great importance. Efficient implementation of wastewater treatment processes is required in terms of sustainable water resources management, environmental protection, public health and industrial ethics. In this way, the textile industry can operate in a more environmentally friendly and sustainable way.

There are many different methods and technologies for the treatment of textile industry wastewater. These methods are physical treatment, biological treatment, chemical treatment and advanced oxidation methods (Christian, 2023). Pre-Treatment: It provides removal of large solid particles, oils and other coarse contaminants contained in the wastewater. Physical filters can be used as part of pretreatment. Sedimentation: By resting the wastewater for a certain period of time, the solid particles that are denser by weight settle on the bottom. Flotation: It is a process in which light solid particles accumulate on the surface and can be easily removed by air injection or chemical additives. Activated Sludge Process: It is a process in which biologically active microorganisms are used and organic materials are broken down. This method removes most organic pollutants and is mostly performed in aerobic (oxygenated) environments. Advanced Biological Treatment: With the addition of additional biological stages (nitrification, denitrification, phosphorus removal, etc.), it provides the removal of more complex and specific pollutants. Coagulation-Flocculation: By using metal salts (eg aluminum sulfate, ferric chloride, etc.), contaminants are precipitated. This process allows the particles to come together and become more easily removed. Adsorption: Organic pollutants are retained by using activated carbon or similar adsorbents. This method is effective in removing some toxic substances and colored compounds. Ozonation: Oxidation of organic pollutants is provided by applying ozone gas to wastewater. Ozone has a strong oxidizing effect and is effective in removing tough pollutants. Advanced Oxidation Processes (AOPs): Advanced oxidation processes such as Fenton reaction, photocatalytic oxidation (using UV light) break down tough organic pollutants (Paul, 2012). These methods can be used alone or in combination and are selected depending on the

characteristics of the wastewater, the targeted level of removal and economic factors. The optimal combination of methods for the treatment of textile industry wastewater is determined depending on the specific situation and is continuously optimized (Radha, 2009). Treatment of textile industry wastewater by advanced oxidation methods has many advantages. These advantages are explained below.

- **Effective Organic Pollutant Removal:** Advanced oxidation methods ensure effective degradation and removal of organic pollutants in wastewater. These methods involve chemical or physical processes with high oxidation potential. In this way, it may be possible for organic pollutants to turn into more complex and difficult compounds or to be completely mineralized (Pang, 2013).
- **Wide Applicability:** Advanced oxidation methods are effective for removing various organic compounds. These methods can be used in the treatment of various pollutants such as colored compounds, organic pollutants that are difficult to biodegrade, harsh chemicals and toxic compounds. Therefore, they can provide an effective treatment even when textile industry wastewater has a variety of pollutants (Holkar, 2016).
- **Removal of Difficult Contaminants:** Advanced oxidation methods are particularly effective in removing tough pollutants for which some other treatment methods are ineffective or insufficient. For example, toxic and chemical resistant compounds can be broken down more easily and effectively using advanced oxidation processes. This ensures that the wastewater has higher quality and lower toxicity (Samsami, 2020)
- **High Oxidation Power:** Advanced oxidation methods use strong oxidation agents or energy sources. This ensures rapid breakdown of organic pollutants present in wastewater. For example, ozonation or advanced photocatalysis methods have high oxidation power and can effectively oxidize organic pollutants with fast reaction rates (Paździor, 2019).
- **Reducing Environmental Impacts:** Advanced oxidation methods convert organic pollutants in wastewater into various simple and harmless compounds. This ensures that the environmental impacts are reduced when wastewater is discharged into the environment. By-products from the oxidation of organic pollutants are generally less toxic or more readily biodegradable compounds.

These advantages are just a few of the reasons why advanced oxidation methods are preferred for the effective treatment of textile industry wastewater. However, it is important to consider the characteristics of the wastewater and the

type of pollutants to determine the most appropriate treatment methods in each case (Adane, 2021).

There are several types of dyes used in the textile industry. Commonly used dye types are Reactive Dyes, Disperse Dyes, Acid Dyes, Sulfur Dyes, Direct Dyes. These are just some examples and the types of dyes used in the textile industry are quite diverse. Textile dyeing processes and dye types used are selected depending on many factors such as material properties, demands, costs and environmental factors. The most used dye type in the textile industry is reactive dyes. Examples of these dyes are Reactive Orange 16, Reactive Blue 13, Reactive Green 6, Reactive Pink 31, Reactive Black 5. There are several reasons why reactive dyes are widely used in the textile industry (Chinta, 2013). (1) High Color Fastness: Reactive dyes provide high color fastness by forming a chemical bond with textile fibers. This ensures that the dyed fabric is resistant to environmental influences such as washing, abrasion, friction and sunlight. As a result, colors do not fade or fade and provide long-term durability (Kritikos, 2007). (2) Wide Color Range: Reactive dyes have a wide color gamut and provide a variety of colors. This offers a variety of design and color options in the textile industry so it is used to meet customer demands (Jager, 2018). (3) Compatible with Natural Fibers: Reactive dyes are compatible with natural fibers such as cotton, linen, viscose. It interacts well with such fibers and penetrates into the fibers, forming a permanent bond. This makes textile products feel natural and comfortable. (4) Economical and Efficient: Reactive dyes can be used cost-effectively and efficiently. The application process is generally simple and fast, which improves production efficiency. In addition, low concentrations of reactive dyes can be used, resulting in less dye consumption and less waste generation (Yang, 2020). (5) Environmental and Health Friendly: Reactive dyes are generally considered more environmentally and health friendly. They are mostly water-based, have non-toxic properties and are more easily removed in wastewater treatment systems. This supports compliance with environmental sustainability goals and health and safety requirements in textile production. All these factors are the reasons that support the widespread use of reactive dyes in the textile industry. Reactive dyes are a type of dye preferred by textile manufacturers with their advantages such as high color fastness, wide color range, compatibility, economy and environmental friendliness.

Within the scope of the study, treatment of dyeing process wastewater in the textile industry with UV, H_2O_2 and UV/ H_2O_2 was studied. The dyes used in the dyeing process are Reactive Black 5 and Reactive Orange 16. The chemical structure of these dyes is given in Figure 1.

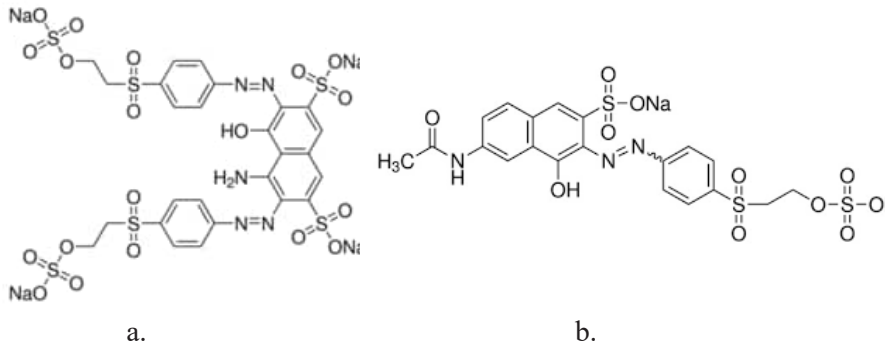


Figure 1. Chemical structure of the dye types used in the study a.) Reactive Black 5, b.) Reactive Orange 16 (Sigma aldrich)

MATERIAL AND METHOD

UV, H₂O₂ and UV/ H₂O₂ advanced oxidation processes have been used for color removal efficiency from textile industry wastewater. The hydrogen peroxide used in the study is Merck brand and it is 30%. The UV intensity in the study is 250 mj/cm². Since the pH value of the wastewater is around 5.7 as a collar, the pH has not been adjusted again. The time-dependent (30 min, 1 hour, 1.5-hour, 2-hour, 2.5-hour, 3-hour) color removal efficiencies of the processes were investigated. In addition, different concentrations (1,3,5 g/L) of H₂O₂ were added to determine the optimum H₂O₂ concentration. The image of the working setup is given in Figure 2. The UV-A lamp used has a power of 100 W.

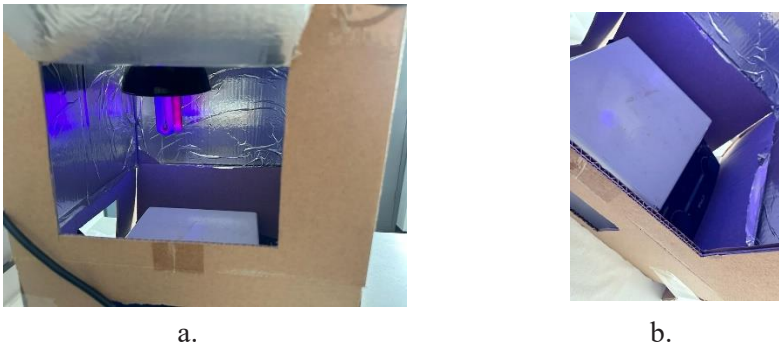


Figure 2. The experimental setup a.) UV lamp, b.) magnetic stirrer

The process wastewater characterization using reactive orange 16 and reactive black 5 dyes in the textile industry production process is given in Table 1.

Table 1. Textile Industry Wastewater Characterization

Parameter	Unit	Value
COD	mg/L	1750
BOD	mg/L	186
TSS	mg/L	550
VSS	mg/L	330
Color	Pt-Co	2250
pH	-	5,7

RESULTS AND DISCUSSION

In the case of production with reactive black 5 and reactive orange 16 dyes, the graphs of the COD and color removal efficiencies of the wastewater released in the textile industry after only H_2O_2 (Figure 3), only UV /Figure 4) and UV/ H_2O_2 (Figure 5,6,7) were given in this section.

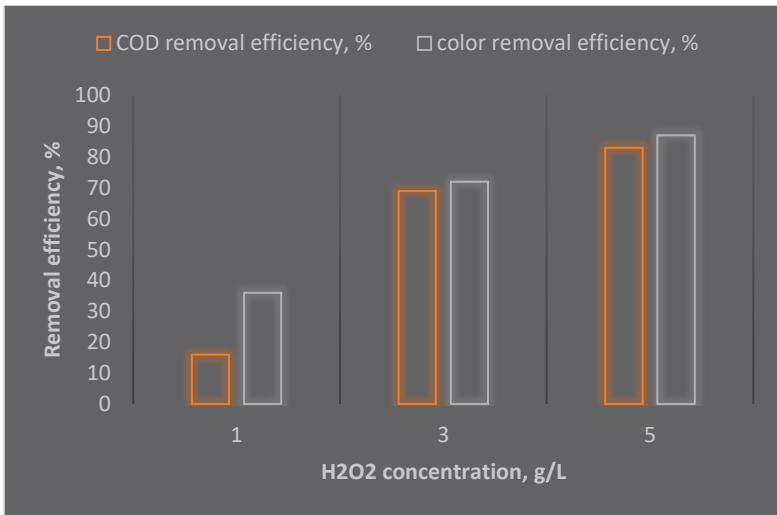


Figure 3. COD and color removal efficiencies from textile industry wastewater after oxidation by adding only H_2O_2

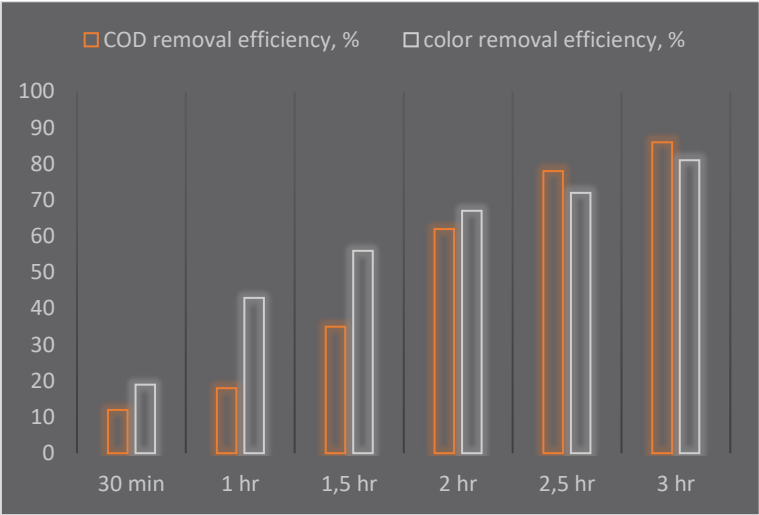


Figure 4. COD and color removal efficiencies from textile industry wastewater after oxidation by adding only UV

The main purpose of applying only H_2O_2 and UV oxidations is to compare the yields of both processes when combined as a hybrid. UV times were applied separately for each of the H_2O_2 concentrations. The yields of UV applications for 30 minutes, 1 hour, 1.5 hours, 2 hours, 2.5 hours and 3 hours at 1, 3,5 g/L H_2O_2 concentrations are given in Figures 5, 6, 7.

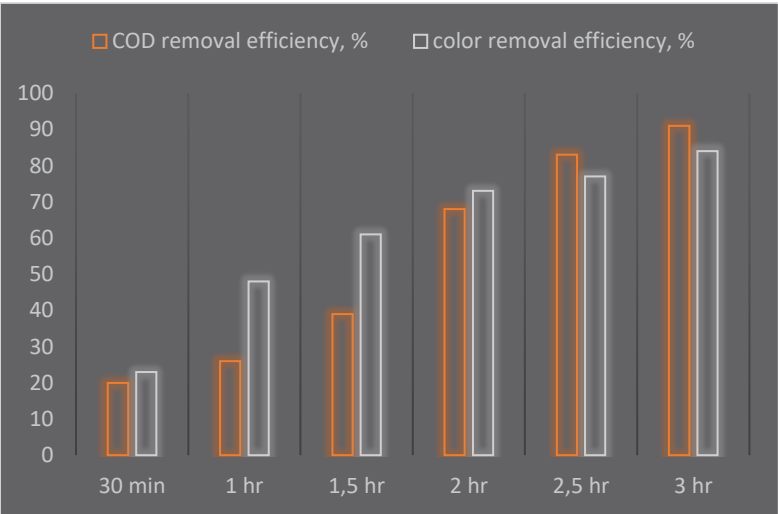


Figure 5. COD and color removal efficiencies in time-dependent UV application at 1 g/L H_2O_2 concentration

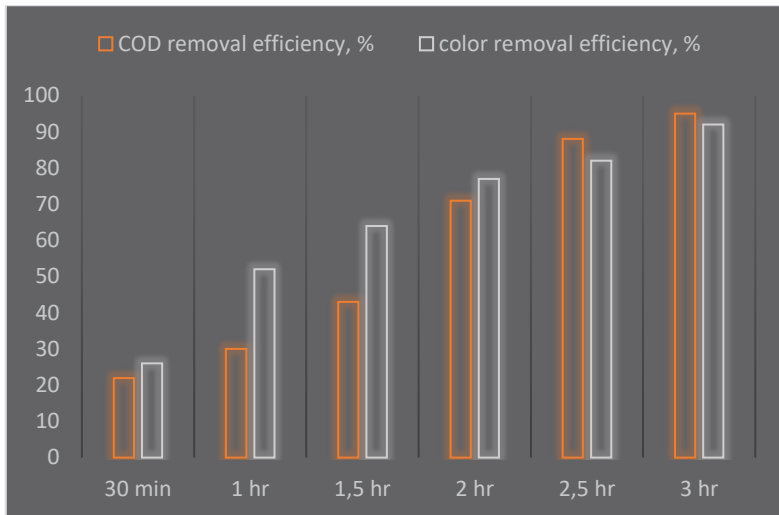


Figure 6. COD and color removal efficiencies in time-dependent UV application at 3 g/L H₂O₂ concentration

Since H₂O₂ is an oxidant, the color removal efficiency increased with increasing concentration. However, when the COD removal efficiency was examined, the increase in the H₂O₂ concentration was not as effective as the color removal. The reason for this is thought to be that the pollutant that causes COD is not only caused by the paint, but also because other chemicals used in the facility increase the concentration of resistant organic matter.

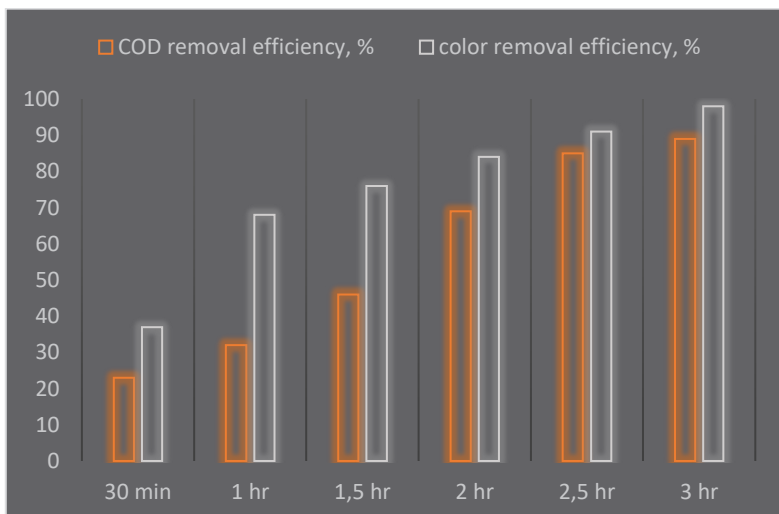


Figure 7. COD and color removal efficiencies in time-dependent UV application at 5 g/L H₂O₂ concentration

The color removal efficiency reached the highest value in hourly UV application at 5 g/L H_2O_2 concentration. The reason for this is that the effectiveness of UV in the degradation of reactive dyes increases with the inclusion of H_2O_2 as an oxidant in the process. It is 87% at 5 g/L concentration only in H_2O_2 application. In the UV application only, the color removal efficiency was found to be 81% at the end of 3 hours. In the hybrid H_2O_2 /UV process created by combining both processes, the color removal efficiency increased to 98%. However, considering the cost, it will be sufficient to use one of the two processes without the need for a hybrid process for color removal efficiency. However, in order to meet the COD discharge standards, the hybrid process must be used.

This laboratory-scale study should be set up at the facility on a pilot scale and work should be carried out for all of the wastewater released during production. In addition to treatment efficiencies, cost analysis should be made and processes should be evaluated.

REFERENCE

- Adane, T., Adugna, A. T., & Alemayehu, E. (2021). Textile industry effluent treatment techniques. *Journal of Chemistry*, 2021, 1-14.
- Chinta, S. K., & VijayKumar, S. (2013). Technical facts & figures of reactive dyes used in textiles. *Int J Eng Manag Sci*, 4(3), 308-12.
- Christian, D., Gaekwad, A., Dani, H., Shabiimam, M. A., & Kandya, A. (2023). Recent techniques of textile industrial wastewater treatment: A review. *Materials Today: Proceedings*, 77, 277-285.
- Holkar, C. R., Jadhav, A. J., Pinjari, D. V., Mahamuni, N. M., & Pandit, A. B. (2016). A critical review on textile wastewater treatments: possible approaches. *Journal of environmental management*, 182, 351-366.
- Jager, D., Kupka, D., Vaclavikova, M., Ivanicova, L., & Gallios, G. (2018). Degradation of Reactive Black 5 by electrochemical oxidation. *Chemosphere*, 190, 405-416.
- Khan, S., & Malik, A. (2014). Environmental and health effects of textile industry wastewater. *Environmental deterioration and human health: natural and anthropogenic determinants*, 55-71.
- Kritikos, D. E., Xekoukoulotakis, N. P., Psillakis, E., & Mantzavinos, D. (2007). Photocatalytic degradation of reactive black 5 in aqueous solutions: Effect of operating conditions and coupling with ultrasound irradiation. *Water research*, 41(10), 2236-2246.
- Kumar, P. S., & Saravanan, A. (2017). Sustainable wastewater treatments in textile sector. In *Sustainable fibres and textiles* (pp. 323-346). Woodhead Publishing.
- Pang, Y. L., & Abdullah, A. Z. (2013). Current status of textile industry wastewater management and research progress in Malaysia: a review. *Clean–Soil, Air, Water*, 41(8), 751-764.
- Pattnaik, P., Dangayach, G. S., & Bhardwaj, A. K. (2018). A review on the sustainability of textile industries wastewater with and without treatment methodologies. *Reviews on Environmental Health*, 33(2), 163-203.
- Paul, S. A., Chavan, S. K., & Khambe, S. D. (2012). Studies on characterization of textile industrial waste water in Solapur city. *International Journal of Chemical Sciences*, 10(2), 635-642.
- Paul, S. A., Chavan, S. K., & Khambe, S. D. (2012). Studies on characterization of textile industrial waste water in Solapur city. *International Journal of Chemical Sciences*, 10(2), 635-642.
- Paździor, K., Bilińska, L., & Ledakowicz, S. (2019). A review of the existing and emerging technologies in the combination of AOPs and biological

processes in industrial textile wastewater treatment. *Chemical Engineering Journal*, 376, 120597.

Radha, K. V., Sridevi, V., & Kalaivani, K. (2009). Electrochemical oxidation for the treatment of textile industry wastewater. *Bioresource Technology*, 100(2), 987-990.

Samsami, S., Mohamadizani, M., Sarrafzadeh, M. H., Rene, E. R., & Firoozbahr, M. (2020). Recent advances in the treatment of dye-containing wastewater from textile industries: Overview and perspectives. *Process safety and environmental protection*, 143, 138-163.

Yang, X., López-Grimau, V., Vilaseca, M., & Crespi, M. (2020). Treatment of textile wastewater by CAS, MBR, and MBBR: a comparative study from technical, economic, and environmental perspectives. *Water*, 12(5), 1306.

<https://www.sigmaaldrich.com/TR/en/product/sial/306452>

<https://www.sigmaaldrich.com/TR/en/product/sial/306509>

Chapter 20

Valorisation of Tropical Fruit Waste for Sustainable Biofuel Production through the Biorefinery Approach

Mukaddes KILIÇ BAYRAKTAR¹

Ernestine Fabiola DJOUCHE²

¹ Assistant Professor Dr.; Karabük Üniversitesi Sağlık Bilimler Fakültesi Beslenme ve Diyetetik Bölümü.
mukaddesbayraktar@karabuk.edu.tr ORCID No: 0000-0002-8871-8820

² Master Student.; Karabük Üniversitesi Sağlık Bilimler Fakültesi Gıda Toksikolojisi Bölümü.
2228310501@ogrenci.karabuk.edu.tr

ABSTRACT

Tropical fruits play an important role in the human diet and has great benefits for human health. The consumption and processing of tropical fruits such as pineapple, mango, papaya, banana to cite just that leads to the generation of large quantities of waste. The waste produced from these fruits is dangerous to the environment but can be used for sustainable biofuel production. With today's increasing global energy demand, due to economic and population growth the consumption of fossil fuels and their negative effects is of great concern. In recent years, tropical fruit waste has been observed as a renewable resource for bioenergy production and other high-value products such as fertilizers. Therefore, this study is an endeavour to highlight the main tropical fruit waste, their valorisation, and different applications. Moreover, this chapter focusses on the several biofuel production techniques including fermentation, combustion, pyrolysis, anaerobic digestion, gasification, transesterification, microwave assisted process, supercritical process, enzymatic hydrolysis, ultrasound assisted process and liquefaction have been developed in this study. All these techniques subdivided into conventional and novel biofuel production techniques and have pretreatment and hydrolysis steps in common. Biofuel production from tropical fruit waste can be effectively enhanced and sustainable through biorefinery approach. However, some challenges are associated with tropical fruit waste valorisation for biofuel production. The insights suggested in this study is of great importance for tropical fruit waste valorisation for biofuel sustainable production.

Keywords: tropical fruit waste, valorisation, sustainable biofuel production, extraction techniques, biorefinery approach

INTRODUCTION

Tropical fruits are cultivated in tropical and subtropical climates and are known for their rich nutritional content and health-promoting compounds. They also serve as a production source of income for millions of people worldwide. However, the production, consumption, and processing of tropical fruits generate substantial waste, including seeds, peels, and other by-products (Ding et al., 2023). This waste poses a significant environmental and health concern. Nonetheless, these waste materials are rich in organic substances and nutrients that can be effectively utilized. Proper waste management presents an opportunity to reduce environmental pollution, create economic prospects, and harness potential health benefits (Anaya-Esparza et al., 2021).

Furthermore, these waste products contain a multitude of bioactive compounds such as polyphenols, fibres, carotenoids, antioxidants, and other essential nutrients (Coman et al., 2020). In recent years, there has been increasing interest in the valorisation of these waste products, given the recognition of their high nutritional value, often overlooked, and discarded as part of tropical fruits (Coman et al., 2020). Additionally, the rising global energy demand and the adverse effects of fossil fuels have stimulated exploration into alternative energy sources. Biofuels offer a promising solution as they are renewable and environmentally friendly. Tropical fruit waste, including by-products, can be utilized in the production of biofuels (Zahid and Khedkar, 2021). Various methods can be employed for biofuel production from tropical fruit waste.

The biorefinery approach, consisting of biological, mechanical, and chemical processes, is employed in a bio-refinery facility to efficiently convert biomass into valuable products, including biofuels. The utilization of tropical fruit waste in biofuel production through the biorefinery approach offers several advantages over conventional methods, such as increased efficiency, reduced waste generation, and improved sustainability (Liu et al., 2012). Bio-refinery-based conversion technologies involve a combination of pre-treatment, extraction, and conversion processes, designed to optimize the utilization of tropical fruit waste for biofuels and other valuable products. By integrating multiple processes within a single bio-refinery, it becomes possible to maximize the efficiency and sustainability of the biofuel production process. This article aims to confirm the usefulness and significant importance of tropical fruit waste in sustainable biofuel production through the biorefinery approach.

TYPES AND APPLICATIONS OF TROPICAL FRUIT WASTE

Tropical fruits are not only a valuable source of nutrition but also generate a substantial amount of waste during production, transportation, and processing. Approximately 50% of tropical fruits are wasted due to spoilage, transportation issues, and other factors. However, this waste can be effectively utilized to produce biofuels such as ethanol, biodiesel, and biogas.

The table below (Table 1) presents several types of tropical fruit waste products with potential for biofuel production. These waste products include fruits, peels, crowns, seeds, leaves, and other by-products that are unsuitable for human consumption. Typically, these waste materials end up in landfills, causing environmental and health issues, such as greenhouse gas emissions, soil and water pollution, and the spread of diseases. Therefore, understanding the diverse types of tropical fruit waste that can serve as substrates for biofuel production is crucial (Ding et al., 2023).

These by-products have the potential to be converted into value-added products such as bioplastics, biofuels, food ingredients, and more. To fully benefit from these possibilities, their potential must be explored. Additionally, appropriate extraction techniques specific to each type of tropical fruit waste may be required.

Table 1: Several types of tropical fruits waste useful to produce biofuels.

Types of tropical fruit wastes	Discarded parts	References
Mango	Peels, stems, and by-products from the production of juice in other processed products.	(Haq et al., 2022)
Pineapple	Peels, crowns, and other by-products from the production of some processed products like juice.	(Hamzah et al., 2021)
Papaya	peels, seeds, and other by-products from the production of processed products.	(Kristianto et al., 2018)
Guava	Seeds, peels, and other by-products from production of processed products	(De Carvalho and Maintinguer, 2022)
Passion fruit	Seeds, skin shells and other by-products	(de Paula Ramos et al., 2022)
Longan	Seeds, peels, and other by-products	(Nguyen et al., 2022)
Lychee	Seeds and peels and other by-products	(Zhang et al., 2022)
Coconut	Hard skin shells and other by-products	(Borel et al., 2021)
banana	Peels and other by-products from processing	(Sawarkar et al., 2022)
Orange	Peels, and by-products from industrial processes	(Negro et al., 2018)
Sugarcane	Bagasse	(Katakojwala et al., 2019)

Applications of tropical fruit waste

In addition to biofuel production, tropical fruit waste can be utilized as animal feed. Livestock, such as cows, pigs, and poultry, can be fed with this waste, providing them with essential nutrients and helping to reduce feed costs, thus improving the efficiency of farming operations (Mohd et al., 2022).

Another application of tropical fruit waste is in fertilizer production. When added to the soil, tropical fruit waste can enhance soil quality by increasing nutrient availability, improving soil structure, and promoting beneficial microorganisms. By using fruit trees as a natural fertilizer, farmers can reduce their reliance on chemical fertilizers and promote sustainable agriculture.

Composting is another method for utilizing tropical fruit waste. Composting involves the breakdown of organic waste, including fruit peels and seeds, into nutrient-rich soil amendments. By composting food waste, individuals can reduce the amount of waste that ends up in landfills and contribute to sustainability (Ghinea and Leahu, 2020).

Some tropical fruits can also find applications in various industries. For example, the seeds of certain fruits can be used to produce natural dyes for food colouring and cosmetics, offering a more sustainable alternative to synthetic chemicals (Kristianto et al., 2018). By utilizing these fruits in industrial applications, companies can reduce their reliance on synthetic chemicals and promote sustainability.

Moreover, certain tropical fruits such as papaya and pineapple contain enzymes with medicinal properties. These enzymes can be extracted from fruit waste and used to treat various health issues, including digestive disorders. By incorporating fruit waste into medicinal applications, individuals can reduce their reliance on synthetic drugs and promote natural healing (Hamzah et al., 2021).

Tropical fruit waste has versatile applications ranging from biofuel production to animal feed and medicinal uses. By exploiting the potential of these waste materials, individuals and companies can reduce waste, promote sustainability, and generate economic benefits. One of the most promising applications of tropical fruit waste is in biofuel production. The simple sugars present in tropical fruits can be extracted and fermented to produce biofuels such as ethanol, biodiesel, and biogas (Nguyen et al., 2022). These biofuels serve as renewable energy sources, reducing dependence on fossil fuels and supporting sustainability.

The applications of tropical fruit waste can only be achieved by extracting beneficial materials such as sugars, oils, and polyphenols from them (Ilyas et al., 2021). Prior to biofuel production, pre-treatment of tropical fruit waste is necessary to reduce biomass size and facilitate subsequent conversion techniques.

BIOFUEL PRODUCTION TECHNIQUES

Due to the growing energy demand and the need to reduce reliance on fossil fuels, renewable alternative sources of energy, such as biofuels, have gained significant interest (Özçimen and Yücel, 2011). Biofuel production has been ongoing for several years, utilizing traditional methods such as fermentation, anaerobic digestion, pyrolysis, carbonization, transesterification, and gasification (Mahapatra et al., 2021). This article will discuss these different methods. The selection of effective biofuel production techniques has become crucial due to economic considerations and the increasing demand for biofuels. Prior to the implementation of biofuel production techniques, certain important steps, such as biomass pre-treatment, are required.

Pretreatment techniques of tropical fruit waste

Biomass pre-treatment plays a vital role in biofuel production from tropical fruit waste, primarily due to the high lignocellulosic content present in these wastes. The choice of pre-treatment processes depends on the specific type of tropical fruit waste and the desired applications. Certain pre-treatment methods may be highly effective for producing a particular bioproduct but may be unsuitable for others (Ebrahimian et al., 2022).

Physical pre-treatment involves the application of mechanical actions on the biomass, such as milling, grinding, and chipping. These processes are widely used in various biofuel production methods and serve to reduce the size of lignocellulosic materials, thereby increasing the accessible surface area (Ebrahimian et al., 2022). Physical pre-treatment is typically performed as a preliminary step before other pre-treatment methods.

Chemical pre-treatment involves the use of chemicals, such as acids, alkalis, alcohols, and organic solvents, to break down lignocellulosic compounds in the biomass. This technique is commonly employed in biofuel production processes (Özçimen and Yücel, 2011).

Physicochemical pre-treatment techniques combine both chemical and physical processes (Arpit Singh et al., 2022). These techniques utilize steam, heat, and pressure, and hot water can be employed to solubilize hemicellulose in the biomass under high pressure.

By employing appropriate pre-treatment techniques, the lignocellulosic structure of tropical fruit waste can be effectively modified, facilitating subsequent biofuel production processes.

Conventional techniques for biofuel production

Biofuel production has been practiced for a long time to meet the increasing demand for energy and reduce reliance on fossil fuels. Various methods have been employed, and in this section, we will discuss some conventional techniques that have been used to produce biofuels, including charcoal and other biofuel products.

Pyrolysis is a technique in which biomass is subjected to elevated temperatures in the absence of oxygen, causing the large organic matter to break down into smaller volatile molecules (Zhang et al., 2022). It is commonly used in biofuel production to produce solid biofuels such as biochar and bio-oil. Gaseous products, such as methane gas, carbon monoxide, and hydrogen, can also be obtained and further processed into biofuels.

Combustion involves directly burning biomass, such as wood or tropical fruit waste, to generate heat, electricity, and biochar (Liu et al., 2013). Biomass is

burned in a boiler to produce steam, which is collected in turbines to generate electricity. Combustion can also be used in the production of liquid biofuels such as ethanol and biodiesel.

Gasification is a widely used technique for biofuel production (Nanda et al., 2016b). This process involves high-temperature reactions in a gasifier, typically ranging from 700 to 900 degrees Celsius. Biomass is heated in the absence of oxygen and breaks down into its constituent components, which react with a small amount of oxygen or steam to produce syngas. Syngas can be processed and utilized for transportation and electrical purposes.

Carbonization is another technique employed in biofuel production (Liu et al., 2013). It is a slow pyrolysis process where tropical fruit waste is converted into solid char with high carbon content, commonly known as charcoal. This process offers several advantages, including low greenhouse gas emissions, and the resulting product is easily storable and transportable.

Trans-esterification is a commonly used conventional technique for biofuel production (Özçimen and Yücel, 2011). It involves the reaction of extracted vegetable oil or fatty acid from tropical fruit waste with alcohol to produce biodiesel. This process typically requires a catalyst and can be conducted at relatively low temperatures.

Fermentation is a conventional technique that has been used for centuries to produce bioethanol. It utilizes microorganisms such as yeast or bacteria to convert extracted sugars from fruit waste into biofuels, particularly ethanol (Valentino et al., 2019). Large-scale fermentation is typically conducted in fermenters, and the resulting bioethanol can be used as a fuel additive or blended with gasoline.

Anaerobic digestion is a process that involves the use of microorganisms to break down organic matter in biomass in the absence of oxygen, producing biogas, primarily methane and carbon dioxide (Valentino et al., 2019). Biogas can be used as a fuel for heat and electricity generation. The process of biofuel production through anaerobic digestion starts with hydrolysis, followed by pre-treatment using acids before passing the biomass into a digester. In the digester, the biomass is converted into methane gas, which can be used as a renewable energy source. A by-product called digestate is also produced, which can be used as a biofertilizer (Figure 1).

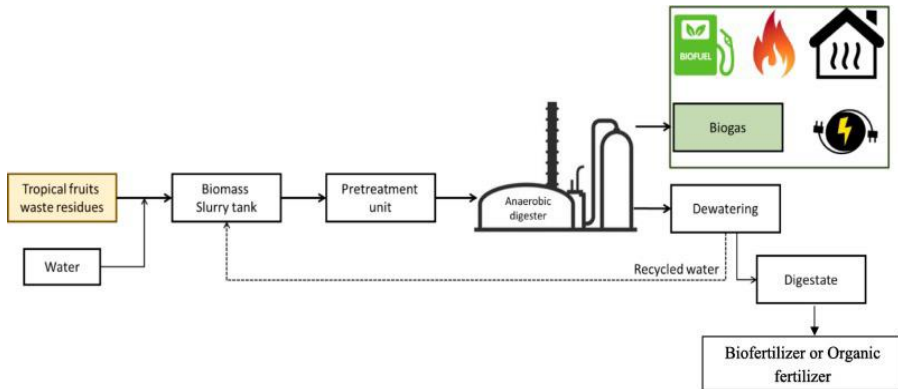


Figure 1: Biofuel production through anaerobic digestion (Zheli et al., 2023)

The figure (Figure 1) demonstrates the biofuel production process through anaerobic digestion, specifically focusing on tropical fruit waste. Anaerobic digestion is a process used to convert tropical fruit waste into biogas in the absence of oxygen. It takes place in an anaerobic digester, where the biomass undergoes hydrolysis and pre-treatment before being converted into methane gas. This methane gas serves as a renewable energy source. The process also produces a by-product called digestate, which can be used as a biofertilizer to enhance soil quality. Anaerobic digestion of tropical fruit waste offers a sustainable solution for biofuel production and nutrient recycling.

Novel techniques for biofuel production

In recent years, several other techniques have been developed as alternatives to the conventional techniques mentioned above to maximize the production of different biofuel products (Dinn, 2017). These methods include the supercritical process, microwave-assisted process, and ultrasound-assisted process. These processes require specific technologies but emit fewer greenhouse gases compared to conventional techniques.

The supercritical process is a novel technique used for biofuel production, such as biodiesel and bio-oil. It can utilize a wide range of biomass materials and convert them into biofuel using supercritical fluids like supercritical water and supercritical carbon dioxide. This method serves as a modern alternative to transesterification and pyrolysis.

The microwave-assisted process is another innovative technique employed to produce liquid biofuels like biodiesel (Jawad et al., 2022). This method involves the use of microwave radiation in the presence of a catalyst. The microwaves generate elevated temperatures that help activate the catalyst, facilitating a uniform and efficient conversion of biomass into biofuel.

The ultrasound-assisted process utilizes an ultrasound reactor to enhance the conversion of biomass into biofuels in the presence of a catalyst (Sharma et al., 2021). High-frequency sound waves are employed to accelerate the reaction between the biomass and catalyst, leading to a more efficient conversion process. This technique results in the production of liquid biofuels, such as biodiesel.

Figure 2 illustrates the various biofuel production techniques specifically from tropical fruit waste and highlights the corresponding biofuel products that can be obtained. The figure provides a visual representation of the different methods discussed in the text, including conventional techniques (such as pyrolysis, combustion, gasification, carbonization, trans-esterification, fermentation, and anaerobic digestion) and novel techniques (such as the supercritical process, microwave-assisted process, and ultrasound-assisted process). It serves as a concise summary of the diverse approaches available for converting tropical fruit waste into valuable biofuels.

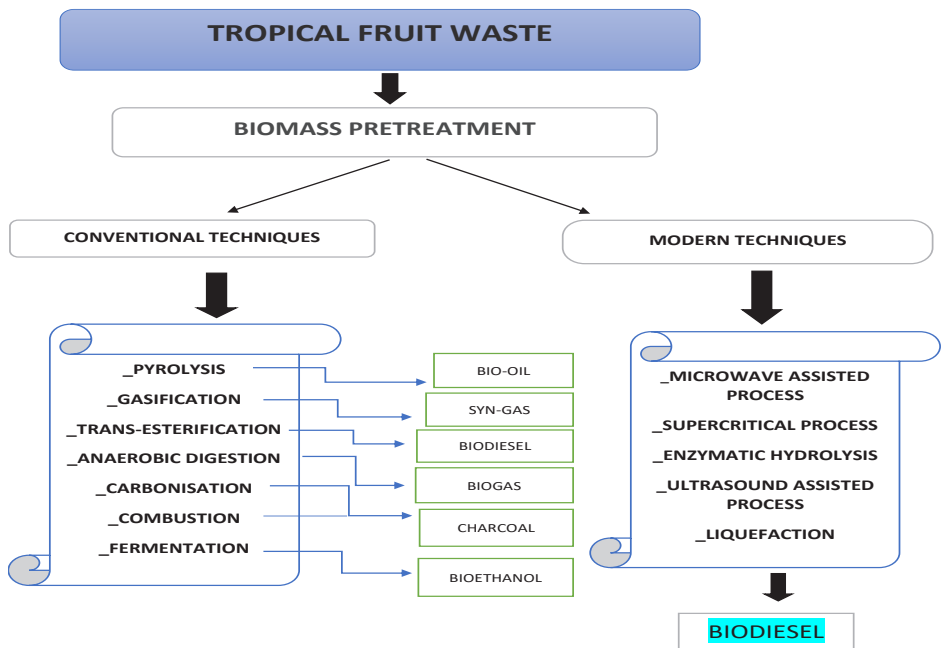


Figure 2: Different biofuel production techniques from tropical fruit waste and their respective products.

BIOREFINERY A SUSTAINABLE APPROACH FOR BIOFUEL PRODUCTION

Biorefinery is a sustainable approach to biofuel production that combines various biomass conversion processes and equipment to synthesize valuable products like biofuels, bioplastics, biochemicals, and materials (Cherubini, 2010). This review focuses on the production of biofuel from tropical fruit waste using the biorefinery approach (Ebrahimian et al., 2022). The approach involves several steps to obtain the desired product.

The biorefinery approach begins with biomass preparation, which includes collecting different tropical fruit waste products and conducting processes like drying and removing non-profitable waste such as paper and sand (Arpit Singh et al., 2022). Pre-treatment is another crucial step in the biorefinery approach as it breaks down biomass molecules into smaller ones. Physical pre-treatment techniques like grinding, milling, and chipping are used to make the biomass more accessible, followed by chemical pre-treatments like hydrolysis using water and enzymes to break down cellulose and hemicellulose compounds (Nguyen et al., 2022). Acids such as sulfuric acid and hydrochloric acid may also be used. This facilitates the liberation of simple sugars for the fermentation step.

Fermentation follows the pre-treatment process and utilizes the simple sugars obtained from biomass to produce biofuels like ethanol or renewable diesel. Microorganisms like bacteria or yeast are employed in the fermentation process (Ebrahimian et al., 2022). After fermentation, ethanol is distilled to purify it and remove impurities, resulting in high-quality biofuel suitable as a gasoline substitute (Valentino et al., 2019).

To further valorise the tropical fruit waste, a solid-liquid separation step is necessary, allowing for the use of different techniques to obtain valuable products. The liquid part undergoes pyrolysis for bio-oil production, while the solid part can be converted using anaerobic digestion to produce biogas, carbonization to produce biochar, or liquefaction for biodiesel production (Ebrahimian et al., 2022; Valentino et al., 2019).

Overall, the biorefinery approach offers an opportunity to reduce waste and generate renewable energy from tropical fruit waste. It enables the production of various biofuels depending on the technology and methods employed. Optimizing biofuel production is crucial for improving efficiency and minimizing environmental impact, which involves selecting appropriate feedstocks, catalysts, microorganisms, and enzymes (Li et al., 2019; S. Liu et al., 2012b). The ongoing research focuses on enhancing the efficiency and economic viability of these processes.

FUTURE PERSPECTIVE AND CHALLENGES

Biofuel production from tropical fruit waste brings significant benefits, including waste reduction and renewable energy generation. However, there are challenges that need to be addressed for future perspectives. One major challenge is the availability of tropical fruit waste. These fruits are produced seasonally and vary in availability across different countries. Ensuring a constant supply of fruit waste is crucial for sustainable biofuel production. One way to tackle this issue is by utilizing a wide variety of tropical fruit waste to compensate for different seasonal availability. By addressing these challenges, the valorisation of tropical fruit waste for biofuel production can be achieved in a sustainable manner.

CONCLUSION

In conclusion, tropical fruit waste offers various advantages that can be utilized in diverse applications. The waste contains valuable bioactive compounds such as dietary fibres, antioxidants, and phytochemicals, which can be extracted and used in food formulations, nutraceuticals, and pharmaceuticals. Conventional techniques like fermentation and anaerobic digestion have demonstrated the importance of tropical fruit waste in different applications. Additionally, novel techniques have been developed to enhance production efficiency. The biorefinery approach enables not only biofuel production but also the extraction of animal feed, cosmeceuticals, functional food, and nutraceuticals. This entire process promotes a circular economy and a healthier environment. By exploiting the potential of tropical fruit waste for biofuel production, we can reduce our dependence on non-renewable energy sources and contribute to a cleaner and more sustainable environment.

REFERENCES

- Anaya-Esparza, L. M., de la Mora, Z. V., Vázquez-Paulino, O., Ascencio, F., and Villarruel-López, A. (2021). Bell peppers (*Capsicum annum* L.) losses and wastes: Source for food and pharmaceutical applications. *Molecules*, 26, 17.
- Arpit Singh, T., Sharma, M., Sharma, M., Dutt Sharma, G., Kumar Passari, A., and Bhasin, S. (2022). Valorization of agro-industrial residues for production of commercial biorefinery products. *Fuel*, 322.
- Borel, L. D. M. S., de Lira, T. S., Ataíde, C. H., and de Souza Barrozo, M. A. (2021). Thermochemical conversion of coconut waste: material characterization and identification of pyrolysis products. *Journal of Thermal Analysis and Calorimetry*, 143(1).
- Cádiz-Gurrea, M. de la L., Villegas-Aguilar, M. del C., Leyva-Jiménez, F. J., Pimentel-Moral, S., Fernández-Ochoa, Á., Alañón, M. E., and Segura-Carretero, A. (2020). Revalorization of bioactive compounds from tropical fruit by-products and industrial applications by means of sustainable approaches. *Food Research International*, 138.
- Cherubini, F. (2010). The biorefinery concept: Using biomass instead of oil for producing energy and chemicals. *Energy Conversion and Management*, 51(7).
- Coman, V., Teleky, B. E., Mitrea, L., Martău, G. A., Szabo, K., Călinoiu, L. F., and Vodnar, D. C. (2020). Bioactive potential of fruit and vegetable wastes. In *Advances in Food and Nutrition Research*, 91.
- Dang, B. T., Ramaraj, R., Huynh, K. P. H., Le, M. V., Tomoaki, I., Pham, T. T., Hoang Luan, V., Thi Le Na, P., and Tran, D. P. H. (2023). Current application of seaweed waste for composting and biochar: A review. In *Bioresource Technology*, 375.
- De Carvalho, R. P., and Maintinguer, S. I. (2022). Application of a Two-Stage Anaerobic System from Guava Processing Waste to Bioenergy. *Industrial Biotechnology*, 18(4).
- de Paula Ramos, B., Perez, I. D., Paiano, M. S., Vieira, M. G. A., and Boina, R. F. (2022). Activated carbons from passion fruit shells in adsorption of multimetal wastewater. *Environmental Science and Pollution Research*, 29(1).
- Ding, Z., Ge, Y., Sar, T., Kumar, V., Harirchi, S., Binod, P., Sirohi, R., Sindhu, R., Wu, P., Lin, F., Zhang, Z., Taherzadeh, M. J., and Awasthi, M. K. (2023). Valorization of tropical fruits waste for production of commercial biorefinery products – A review. *Bioresource Technology*, 374.
- Dinn, J. P. (2017). Biofuels, A Sustainable Alternative to Fossil Fuels? Mapping Politics, 8(2).

- Ebrahimian, F., Denayer, J. F. M., and Karimi, K. (2022). Potato peel waste biorefinery for the sustainable production of biofuels, bioplastics, and biosorbents. *Bioresource Technology*, 360.
- Hamzah, A. F. A., Hamzah, M. H., Man, H. C., Jamali, N. S., Siajam, S. I., and Ismail, M. H. (2021). Recent updates on the conversion of pineapple waste (*Ananas comosus*) to value-added products, future perspectives and challenges. *Agronomy*, 11, 11.
- Haq, A., Khan, A., Haji, K., Khan, S., Shah, A. A., Hasan, F., Ahmed, S., de los Reyes, F. L., and Badshah, M. (2022). Enhancement of biogas yield during anaerobic digestion of *Jatropha curcas* seed by pretreatment and co-digestion with mango peels. *Biomass Conversion and Biorefinery*, 12(5).
- Ilyas, T., Chowdhary, P., Chaurasia, D., Gnansounou, E., Pandey, A., and Chaturvedi, P. (2021). Sustainable green processing of grape pomace for the production of value-added products: An overview. *Environmental Technology and Innovation*, Vol. 23.
- Jawad, A. H., Saber, S. E. M., Abdulhameed, A. S., Reghioua, A., AlOthman, Z. A., and Wilson, L. D. (2022). Mesoporous activated carbon from mangosteen (*Garcinia mangostana*) peels by H₃PO₄ assisted microwave: Optimization, characterization, and adsorption mechanism for methylene blue dye removal. *Diamond and Related Materials*, 129.
- Katakojwala, R., Naresh Kumar, A., Chakraborty, D., and Mohan, S. V. (2019). Valorization of sugarcane waste: Prospects of a biorefinery. *Industrial and Municipal Sludge: Emerging Concerns and Scope for Resource Recovery*.
- Kristianto, H., Kurniawan, M. A., and Soetedjo, J. N. M. (2018). Utilization of Papaya Seeds as natural coagulant for synthetic textile coloring agent wastewater treatment. *International Journal on Advanced Science, Engineering and Information Technology*, 8(5).
- Li, P., Sakuragi, K., and Makino, H. (2019). Extraction techniques in sustainable biofuel production: A concise review. *Fuel Processing Technology*, 193.
- Liu, S., Abrahamson, L. P., and Scott, G. M. (2012a). Biorefinery: Ensuring biomass as a sustainable renewable source of chemicals, materials, and energy. *Biomass and Bioenergy*, 39.
- Liu, S., Abrahamson, L. P., and Scott, G. M. (2012b). Biorefinery: Ensuring biomass as a sustainable renewable source of chemicals, materials, and energy. *Biomass and Bioenergy*, 39, 1–4.
- Liu, Z., Quek, A., Kent Hoekman, S., and Balasubramanian, R. (2013). Production of solid biochar fuel from waste biomass by hydrothermal carbonization. *Fuel*, 103.

- Mahapatra, S., Kumar, D., Singh, B., and Sachan, P. K. (2021). Biofuels and their sources of production: A review on cleaner sustainable alternative against conventional fuel, in the framework of the food and energy nexus. *Energy Nexus*, 4.
- Mohd Zaini, H., Roslan, J., Saallah, S., Munsu, E., Sulaiman, N. S., and Pindi, W. (2022). Banana peels as a bioactive ingredient and its potential application in the food industry. *Journal of Functional Foods*, 92.
- Nanda, S., Isen, J., Dalai, A. K., and Kozinski, J. A. (2016a). Gasification of fruit wastes and agro-food residues in supercritical water. *Energy Conversion and Management*, 110.
- Nanda, S., Isen, J., Dalai, A. K., and Kozinski, J. A. (2016b). Gasification of fruit wastes and agro-food residues in supercritical water. *Energy Conversion and Management*, 110, 296–306.
- Negro, V., Ruggeri, B., and Fino, D. (2018). Recovery of Energy from Orange Peels Through Anaerobic Digestion and Pyrolysis Processes after d-Limonene Extraction. *Waste and Biomass Valorization*, 9(8).
- Nguyen, T. V. T., Unpaprom, Y., Manmai, N., Whangchai, K., and Ramaraj, R. (2022). Impact and significance of pretreatment on the fermentable sugar production from low-grade longan fruit wastes for bioethanol production. *Biomass Conversion and Biorefinery*, 12(5).
- Özçimen, D., and Yücel, S. (2011). Novel Methods in Biodiesel Production. *Biofuel's Engineering Process Technology*.
- Sharma, P., Gaur, V. K., Sirohi, R., Varjani, S., Hyoun Kim, S., and Wong, J. W. C. (2021). Sustainable processing of food waste for production of bio-based products for circular bioeconomy. *Bioresource Technology*, 325.
- Valentino, F., Lorini, L., Pavan, P., and Majone, M. (2021). Development of a biorefinery platform for urban waste valorisation into biogas and added-value products. *Chemical Engineering Transactions*, 86, 13–18.
- Valentino, F., Moretto, G., Gottardo, M., Pavan, P., Bolzonella, D., and Majone, M. (2019). Novel routes for urban bio-waste management: A combined acidic fermentation and anaerobic digestion process for platform chemicals and biogas production. *Journal of Cleaner Production*, 220.
- Zahid, A., and Khedkar, R. (2021). Valorisation of Fruit and Vegetable Wastes: A Review. *Current Nutrition and Food Science*, 18(3).
- Zhang, Y., Ahmad, M. S., Shen, B., Yuan, P., Shah, I. A., Zhu, Q., Ibrahim, M., Bokhari, A., Klemeš, J. J., and Elkamel, A. (2022). Co-pyrolysis of lychee and plastic waste as a source of bioenergy through kinetic study and thermodynamic analysis. *Energy*, 256.

Chapter 21

Mathematical Modelings for the Thin-Layer Drying of Red Pepper Slices

Murat ERDEM¹

Muhammet AYDIN²

Filiz ÖZGEN³

¹ Assistant Professor; Firat University, Vocational School of Technical Sciences, Elazig, Turkey.
muraterdem@firat.edu.tr ORCID No:0000-0003-0287-1881

² Assistant Professor; Firat University, Engineering Faculty, Mechatronics Engineering, Elazig, Turkey.
muhammeta@firat.edu.tr ORCID No:0000-0003-2746-9477

³ Associate Professor; Firat University, Technology Faculty, Mechanical Engineering, Elazig, Turkey.
fozgen@firat.edu.tr ORCID No:0000-0003-2278-2093

ABSTRACT

In this study, the effects of drying air velocity and drying temperature on red pepper have been experimentally investigated in a convective type dryer. To examine the effect of drying air velocity and temperature on drying, experiments were carried out on red pepper samples for drying air velocities of 1 and 1.5 m/s at 25, 35, 45 °C, and 10% relative humidity of the drying air. The experimental results showed that the drying air velocity and air temperature have played an important role in the total drying time. The lowest drying time (5 hours 30 minutes) was obtained at 45 °C and 1.5 m/s, the highest drying time (12 hours) was at 25 °C and 1 m/s. Freshly harvested products were successfully dried in a convective dryer at different air velocities. Studies at varied velocities in a convective dryer are advantageous in terms of maintaining color quality and brightness. Besides, mathematical models were developed for this experimental study. Modelings have been achieved by comparing fifteen different thin-layer drying models. A great similarity was found between the obtained experimental data and the created model. As a result, the best models are modified-2 Wang-Singh for 25 °C, modified-1 Wang-Singh model for 35 °C, and Midilli-Kucuk model for 45 °C at 1.0 m/s velocity. In the same way, the best models for 1.5 m/s velocities are Wangh-Singh model for 25 °C, Midilli-Kucuk model for 35 °C and 45 °C.

Keywords: Drying behavior, mathematical modeling, red pepper, energy requirement.

INTRODUCTION

When large amounts of agricultural products are not consumed immediately, their durability is very short. It is possible to keep these products freshly as a consequence of some particular processes. Drying processing is one of these operations, which are aimed at extending the economic life of agricultural products while maintaining their nutritional features till they are consumed. The drying process is defined as an industrial-scale preservation method with heated air (with forced or natural convection) to reduce the water quantity of fruits and vegetables, reduce their water activity, and thus minimize biochemical, chemical, and microbiological deterioration (Cerci and Akpınar, 2016). Drying is the process of lowering the water content of fruits and vegetables from 80-95 percent to 10-20 percent and extending their shelf life. However, qualitative characteristics like as taste, look, color, and nutritional value should be preserved as much as possible, and when water is added to be cooked, it should be able to receive water in amounts similar to those present when they are fresh (Zhang et al., 2019). The drying process is a heat and mass transfer event, and one of the oldest food preservation methods is drying agricultural products with solar radiation. But this method, the quality of the food is seriously reduced due to the contact of various creatures such as rain, wind-induced dust, dirt, insects, and flies during sun drying. It is possible to overcome these problems by performing the drying process in planned near systems. In drying applications in a natural environment, the long drying time, the product's being exposed to environmental effects and the diminution in nutritional values adversely affect the quality and economic value of the products. According to this case, the drying phenomenon with special-purpose unnatural dryers both shortens the drying time and provides better quality and cleaner products with a long shelf life (Kumar et al., 2016).

Artificial dryers are used to dry a wide range of fruits and vegetables such as cornelian cherry (Ozgen, 2015), pepper (Krzykowski et al., 2018), apple (Sacilik and Elicin, 2006), kiwi (Dalvand et al., 2012), onion (Arslan and Özcan, 2010), and potato (Joykumar Singh and Pandey, 2012) are some of the dried fruits and vegetables in convective type dryers. In the literature, some studies are addressing the drying characteristics of fruits and vegetables as a mathematical model as well as studies (Agbede et al., 2020; Doymaz, 2013; Evin, 2012; Guo et al., 2021; Hao et al., 2021; Zielinska and Markowski, 2010).

In the literature, there are some studies investigating deal with the effects of parameters such as air temperature, humidity, flow rate during drying of fruits, vegetables, and the properties of the dried material on drying characteristics. Junka and Rattanamechaikul (Junka and Rattanamechaikul, 2021), made mathematical modeling by examining the drying characteristics of mushrooms at 70-150 °C

temperatures. They saw that the drying rate increase, as the drying velocity increased. Pham et al. (Pham et al., 2020), studied the drying characteristics of foods by developing a new model. Results obtained by mathematical modeling were compared with experimental results, humidity and temperature distributions were estimated. Tunckal and Doymaz (Tunckal and Doymaz, 2020) performed a mathematical modeling and performance analysis of banana slices using a heat pump drying system. Banana slices were dried at different temperatures, it was observed that the drying time increased as the temperature and slice thickness increased. Also, different drying models were applied to explain the drying kinetics of banana slices and the best was determined. EL Khadraoui et al. (EL khadraoui et al., 2019), experimentally examined the drying of red pepper slices in the greenhouse and under the open sun and made mathematical modeling. 8 different mathematical models were used by using a newly developed dryer in drying experiments. Although all drying models discussed in this study adequately represent the drying behavior of pepper, the Henderson and Pabis model was determined to be better than other models. Wang et al. (Wang et al., 2017), determined the most appropriate time by examining the drying properties, surface color, red pigment content, microstructure, and texture of red peppers at different times (30, 60, 90, 120, 150, 180, 210, and 240 s) under high humidity hot weather conditions. Ozgen and Celik (Ozgen and Celik, 2018), experimentally investigated the drying characteristics of kiwi fruit in a convective type dryer at 45 °C drying air temperature and 0.5, 1.0, and 1.5 m/s drying air velocities, for kiwi samples of 4 mm and 8 mm thickness. It has been observed that the drying air velocity plays an important role in the total drying time. Prithani and Dash (Prithani and Dash, 2020), examined the drying behavior of kiwi fruit at different temperatures in an ultrasonic drying system. By analyzing the effects of ultrasound application, water loss, sugar gain, and moisture diffusion of the samples, they showed that mass transfer can be increased with low energy and cost. Akpinar et al. (Akpinar et al., 2003), investigated the thin layer drying behavior of red pepper slices in a convective dryer experimentally and mathematically modeled with the help of different drying models. Drying experiments were carried out at an inlet temperature of 10 °C with a drying air of 55, 60, and 70 °C and drying air of 1.5 m/s. Eleven different thin layer mathematical drying models were compared to estimate drying curves and the most suitable model was determined. Bechlin et al. (Bechlin et al., 2020), examined the effects of ozone treatment and hot air drying on an orange peel. Their work contributed to a better understanding of how ozone behaves physically on the chemical and biological parameters of citrus products. Red pepper is very rich in terms of vitamins A and C, it is a very important antioxidant and strengthens the immune system. It can be consumed as raw and cooked vegetables, as well as

widely used in making pickles and sauces. Dried and powdered red ground pepper is used in the food industry as a spice and flavoring. However, it has an important role in the health sector (Arslan and Özcan, 2011).

As a result of global warming and forest fires, there is a great food shortage due to the destruction of agricultural areas and the decrease in water resources all over the world. As a result, serious increases in food prices occurred due to the shortage of products. Due to such situations, drying and storage of products under appropriate conditions is of vital importance for consumers. For this purpose, the drying of products should be encouraged all over the world. Also, today, due to the Covid-19 pandemic, there has been a food shortage in some countries, and many people have been affected much more by this pandemic because they have low immune systems. Therefore, foods with a long shelf life and rich in vitamins that can be consumed at all times should be dried and stored. For this purpose, in the present study, the drying characteristics of red pepper grown in different regions in Turkey were examined by drying in a convective type dryer.

MATERIALS AND METHOD

Experimental set-up and measurement procedure

For this experimental study, a convective-type dryer set-up was constructed and tested in Technology Faculty of Fırat University, Elazığ, Turkey. The schematic diagram of the dryer used in the experimental work is shown in Figure 1.

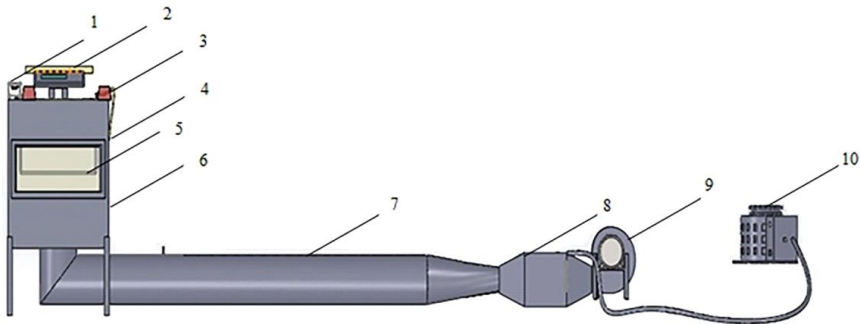










Fig. 1. Schematic assembly of the convective dryer (1. Humidity measurement, 2. Digital balance, 3. Thermometer-Anemometer, 4. Drying air outlet, 5. Drying tray, 6. Drying chamber, 7. Airflow channel, 8. Heating system, 9. Fan, 10. Variac)

As shown in Figure 1, the experimental setup consists of a fan, heater, drying cabinet, airflow duct, air inlet and outlet channels, a humidity meter, a digital scale with a range of measurement of 0-6100 g with a precision of 0.1g to evaluate the product's mass loss. The digital scale is 30 cm long, 19 cm wide. In conjunction with the scale, a drying tray measuring 27 cm in length and 21 cm in width was created, and the products to be dried were placed on the tray, and the mass loss of the product was read from the scale at regular intervals. The drying chamber is 60 mm long, 40 mm wide, 60 mm high in the form of a rectangular prism, and is made of 3 mm thick sheet metal. At the bottom of the cabinet, a hole with a diameter of 120 mm is opened and connected to the airflow channel. The hot air from the flow channel comes into contact with the product from the bottom, and a 100 mm diameter channel on the cabinet's side surface is opened to release the heated air. The airflow duct, which connects to the drying chamber from the bottom, is 2.5m long, 120 mm wide, and 3 mm thick sheet metal. This channel is insulated with 30 mm thick glass wool and has an aluminum tape covering on the top. With the help of temperature measuring instruments on the cabin, product temperature and chamber outlet temperature are determined by using T type thermocouple. The airflow rate is controlled with the help of a 0.537 kW radial fan. The radial fan has a power of 50 Hz, 220 volts, and 2.5 amperes. The system's fan has a constant velocity of 2800 1/min. The heating system is made up of 2000 W wires, and the drying air temperature is stabilized via a variac. The chamber outlet temperature and the product's internal temperature were measured using a thermometer with a measuring range of $-20 + 80^{\circ}\text{C}$. The drying air velocity is measured using an anemometer with a measurement range of 0.15-3 m/s. The dried red pepper samples were placed on the tray connected to the scale, and the mass loss was recorded at 15-minute intervals.

Table 1 lists the measurement devices used in this study (Ozgen, 2015). This table includes experimental photos as well as technical specifications.

Table 1. The experimental photos of the convective dryer (Ozgen, 2015)

<i>Unit</i>	<i>Technical specification</i>	<i>Photos</i>
Drying chamber	Rectangular chamber length (60 mm) Width (40 mm), Covering Material: Sheet iron (3 mm), Height (60 mm)	
Airflow channel	Galvanized sheet: Channel pipe diameter (120 mm), Channel length: (2.5 m), Insulation thickness (30 mm)	
Digital balance	Measurement range 0-6100g and $\pm 0,1$ g accuracy, Sample tray length (27 cm)-width (21 cm), Digital balance length (30 cm)-width (19 cm)	
Fan	The radial fan: maximum power (0.537 kW), 220 Volt, 50 Hertz; 2.5 Amperes, 2800 reverse/min	
Heating system	An electric heater (2000 W) was installed inside the duct	

Thermometer- Anemometer	Temperature measuring ranges: -20 to +80°C, Air velocity measuring ranges: 0.15 m/s to 3 m/s, Sizes: 50-34.9 mm, Measuring elements Thermocouple K, J or T.	
Variac	Volt measuring ranges: 0 to +260 Volt, 2.5 Amperes, 50 Hz.	
Humidity and temperature measurement	Measurement ranges: 0 to + 45°C (±5°C), from 10 to 90% RH (±5 %RH).	

Drying kinetics, thermal performance analysis

The moisture content of a product is a measure of its relative humidity. Moisture content is measured in two ways: wet base and dry base (Ozgen, 2015).

Moisture content according to the wet base:

$$M_{wb} = \frac{M_w}{M_T} \quad (1)$$

Moisture content to dry base, while expressed by the equation:

$$M_{db} = \frac{M_w}{M_k} \quad (2)$$

It is given in the form. Where M_w denotes the product's water weight, M_T denotes the product's total weight, and M_k denotes the product's dry weight.

The moisture content is defined as the ratio of the product's moisture content at any time to the moisture content at the beginning. Humidity:

$$M = \frac{M_t - M_e}{M_0 - M_e} \quad (3)$$

determined by the equation. M_t is the product's weight at time t , M_e is the equilibrium moisture weight, and M_0 is the product's beginning weight.

The drying air velocity is the change in the moisture content of the dried product per unit time.

The drying air velocity is computed using the equation below.

$$\frac{dW}{dt} = \frac{M_t - M_{t+\Delta t}}{\Delta t} \quad (4)$$

Where $M_{t+\Delta t}$ is the weight of the product at time $t+\Delta t$.

Common drying kinetics model fitting

Previously, available thin-layer drying models in the literature were studied to fit the red pepper curve. The thin-layer drying models studied are shown in Table 2. Curve fitting was performed separately for three different temperatures (25 °C, 35 °C, 45 °C) and two different airflow velocities ($u = 1$ m/s and $u = 1.5$ m/s).

Table 2. Mathematical Models for Drying Kinetics (Chandra and Singh, 1995; Handerson, S.M., Pabis, 1961; Henderson, 1974; Lewis, 1921; Midilli et al., 2002; Page, 1949; Wang, C.Y., Singh, 1978; White, G.M., Bridges, T.C., Loewer, O.J., Ross, 1978)

Number	Model Name	Model Equation
1	Newton (Lewis)	$MR=e^{(-k.t)}$ [1]
2	Handerson and Pabis	$MR=a.e^{(-k.t)}$ [2]
3	Logaritmic	$MR=a.e^{(-k.t)} + b$ [3]
4	Midilli-Kucuk	$MR=a.e^{(-k.t^n)} + bt$ [4]
5	Wangh-Singh	$MR=1 + a.t + b.t^2$ [5]
6	Modified-1 Wangh-Singh	$MR=a + b.t + c.t^2$
7	Modified-2 Wangh-Singh	$MR=a + b.t + c.t^2 + d.t^3$
8	Modified-3 Wangh-Singh	$MR=a + b.t + c.t^2 + d.t^3 + e.t^4$
9	Page	$MR=e^{(-k.t^n)}$ [6]
10	Modified Page	$MR=(e^{(-k.t)})^n$ [7]
11	Two Term	$MR=a.e^{(-k_1t)} + b.e^{(-k_2t)}$ [8]
12	Aghashlo et al.	$MR=e^{(-\frac{a.t}{1+b.t})}$
13	Present 1	$MR=a + b.t^n$
14	Present 2	$MR=a + b.t^{n_1} + c.t^{n_2}$
15	Present 3	$MR=a.t^{n_1} + b.t^{n_2} + c.t^{n_3} + d$

A nonlinear regression model was used to match experimental findings of moisture ratio (MR) against drying time to thin-layer drying models, and the Statistical Package for the Social Sciences was used to provide it (SPSS). The fifteen structures studied are listed in Table 2. The correlation coefficient (R^2), the sum of square error (SSE), root mean square error (RMSE), and Chi-square (χ^2) were statistical variables used to select the option that best fits the moisture ratio–time data. While making the selection, attention was paid to the criteria of high R^2 value, low results of SSE, RMSE, and χ^2 values. SSE, RMSE, and χ^2 results were obtained via Microsoft Excel from Eqs. (1)–(3), while R^2 values were reported by SPSS.

$$SSE = \frac{1}{N} \sum_{i=1}^N \left(M_{R_{exp,i}} - M_{R_{pred,i}} \right)^2 \quad (5)$$

$$RMSE = \left[\frac{1}{N} \sum_{i=1}^N \left(M_{R_{exp,i}} - M_{R_{pred,i}} \right)^2 \right]^{\frac{1}{2}} \quad (6)$$

$$\chi^2 = \frac{\sum_{i=1}^N (M_{R_{exp,i}} - M_{R_{pred,i}})^2}{N-z} \quad (7)$$

In these expressions, $M_{R_{exp}}$, $M_{R_{pred}}$, N , and z denote the experimental moisture ratio, the predicted moisture ratio, the number of samples, and the number of parameters used in the fitting curve, respectively.

Colour of products

The experiments containing the effect of drying air velocity and temperature on drying of red peppers were carried out for 1.0 and 1.5 m/s velocities of air at 25, 35, 45 °C, respectively, and 10% relative humidity. To the dryer to stabilize, before 1 hour starting the drying process, the set-up device was operated. Freshly picked red peppers were used in the experiment. The samples were cleaned with tap water and sliced with a knife after 3 hours at room temperature. Then, on the drying tray, 142 g of fresh red pepper was placed. Every 15 minutes, the mass loss during drying was measured from the balance. It has been determined that operating at different velocities in a convective dryer has the advantage of keeping the brightness and color quality and it is compatible with the literature (Di Scala and Crapiste, 2008; Soysal et al., 2009) Different views of the red peppers used during the experiment are given in Figure 2.



Fig. 2. View of red pepper used in the experiment.

RESULTS AND DISCUSSION

In this experimental study, the drying behavior of red pepper at different air temperatures and its velocities has been investigated. Within the scope of the study, the compatibility of the results with the mathematical models available in the literature was investigated, and at the same time, new mathematical models were developed. It is thought that the results and mathematical models will be useful due to the irrigation problems of agricultural lands that have emerged with global warming and the food shortages that occur all over the world with Covid-19. Obtained results are presented in graphics and tables.

Figures 3 and 4 show the variation of moisture content with drying time on a wet basis (w.b.) for air inlet velocities of 1 and 1.5 m/s, respectively. The moisture content was determined as 0.82 on a wet basis. In the literature review, it is seen in the graphs that the moisture content is mostly made on the wet basis. The reason for this is the large numbers appearing in the calculation made on the dry basis and the difficulties in the reader's understanding of the subject. Moisture content according to wet basis has decreased as a function of drying time as expected in the analysis performed for both 1 and 1.5 m/s. This study shows that the boundary conditions are appropriate. For these two air inlet velocities, the drying process accelerates as the temperature inlet increases. In other words, when the air inlet temperatures increase at constant air velocities, the drying time decreases. Likewise, when the drying speed increases, the drying process is also faster. As seen in Figures 3 and 4, drying times for 25, 35, and 45°C at air velocities of 1 and 1.5 m/s are 720, 585, 510 and 645, 555, 390 minutes, respectively. This shows that both the air inlet velocity and the air inlet temperature affect the drying behavior. It is very important to choose the boundary conditions correctly so that the product doesn't deteriorate and crust during the drying process. If the drying process takes too long, especially meat, fish, etc. such products may deteriorate, and at very high velocities, since the outer surface of the product dries quickly (scabbing), it will be difficult for the water in the product to come out, and in this case, the drying process will result in failure. The reason why the curves in Figures 3 and 4 are slightly wavy may be parameters such as temperature and velocity changes due to sudden voltage fluctuations and measuring mistakes. In addition, it should be taken into account that this situation may be caused by the internal structure of the product itself.

Dimensionless moisture content plots (Scala, 1-0) on a wet basis are obtained in Figures 5 and 6 for air inlet velocities of 1 m/s and 1.5 m/s. These curves give healthier results than dimensional parameters. The drying velocity profiles of the pepper drying curves used in this study are expressed in Figures 7 and 8. At the beginning of the drying process, the amount of moisture in the product is high, so, evaporation is also high. After, as the amount of moisture in the product decreases, the drying rate decreases at the same rate. Peaks in the drying rate are due to the exposure of different parts of the product to different temperatures and air velocities in some cases. It has been understood that these results are generally by the literature.

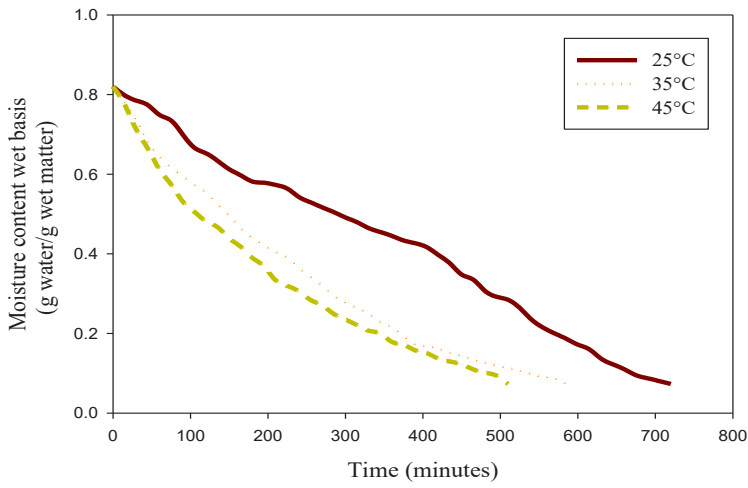


Fig. 3. Variation of wet basis moisture content with drying time for $V=1$ m/s.

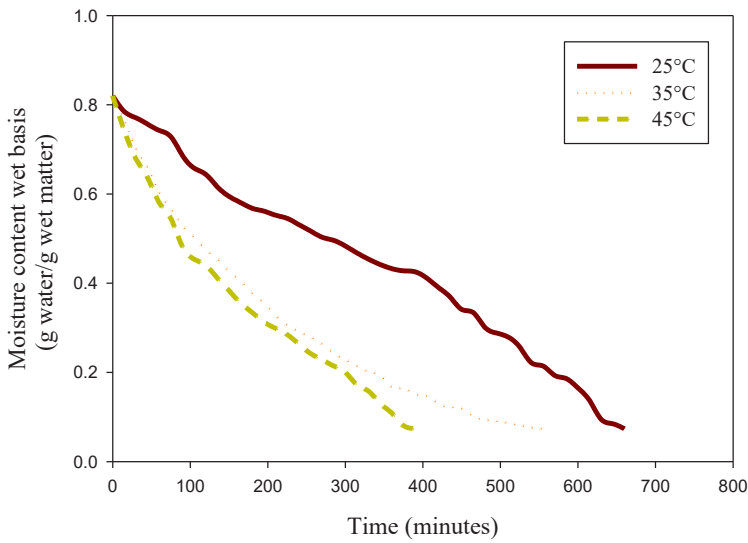


Fig. 4. Variation of wet basis moisture content with drying time for $V=1.5$ m/s.

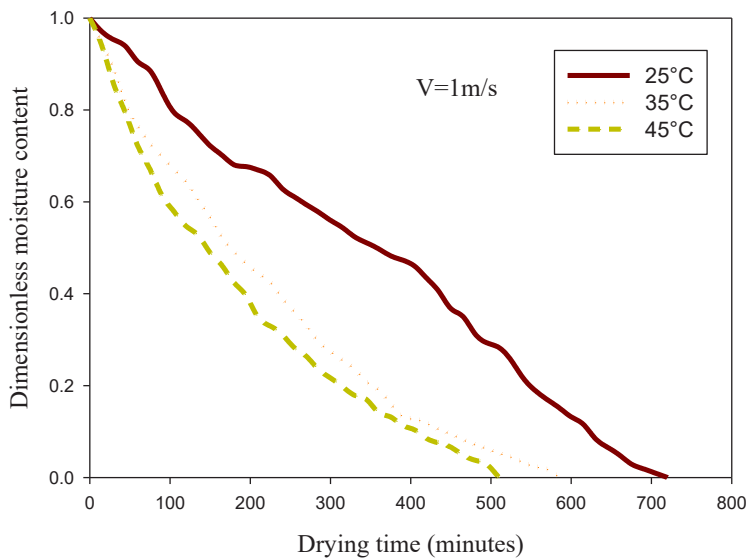


Fig. 5. Variation of drying rate with drying time for $V=1\text{ m/s}$.

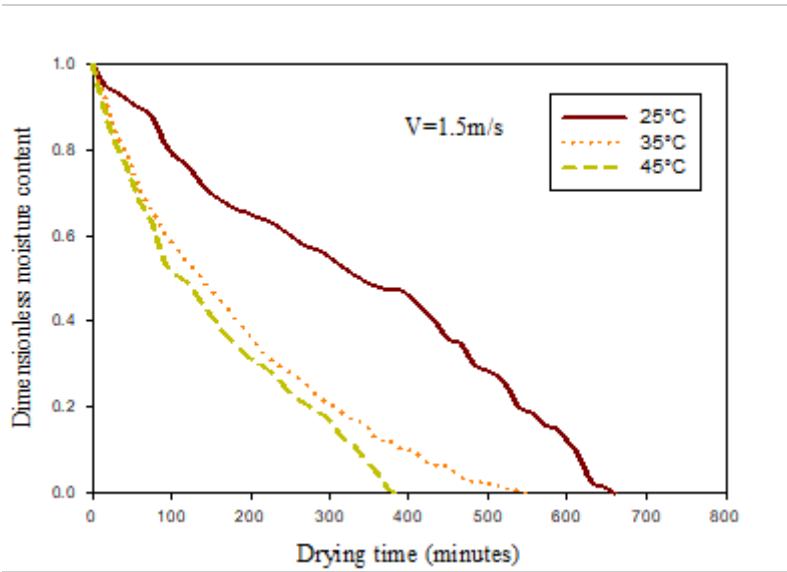


Fig. 6. Variation of drying rate with drying time for $V=1.5\text{ m/s}$.

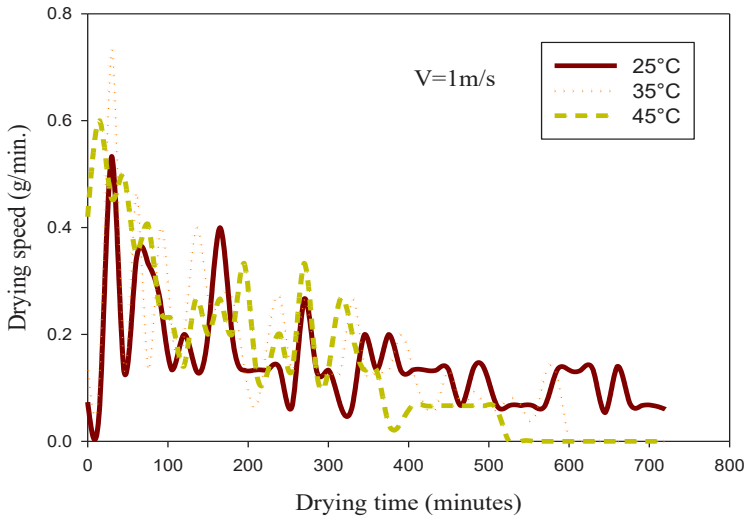


Fig. 7. Variation of drying speed with drying time for $V=1$ m/s.

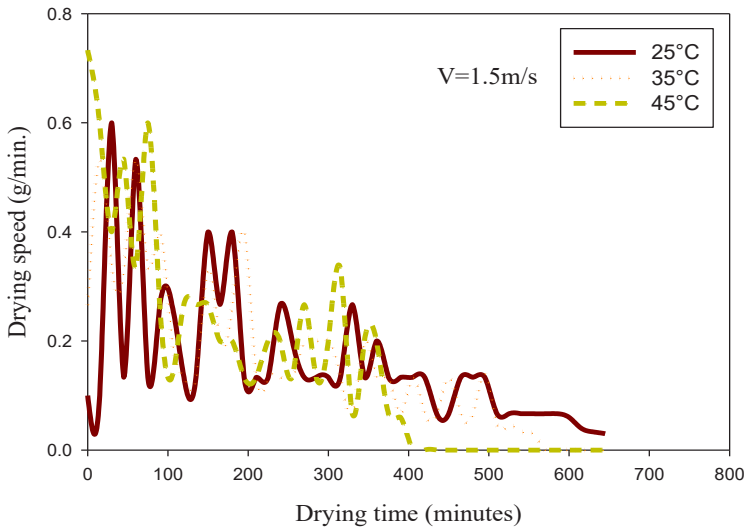


Fig. 8. Variation of drying rate with drying time for $V=1.5$ m/s.

Energy requirement

The total energy requirement of the drying system during drying at the working speeds and temperatures is shown in Figure 9. The energy requirement values calculated for 1.5 m/s and 25, 35, 45 °C are 18.34 kWh, 15.42 kWh, and 10.83 kWh, respectively. Likewise, the energy requirement values calculated

for 1 m/s and 25, 35, 45 °C are 13.34 kWh, 10.84 kWh, and 9.45 kWh. For the experimental set used in this study, the best and worst operating conditions in terms of energy requirement are 1 m/s - 45 °C (9.45 kWh) and 1.5 m/s - 25 °C (18.34 kWh), respectively. The ratio between these two values is 1.941 times.

The overall energy need for a convective type dryer is also calculated (Eq. (8) and (Koyuncu et al., 2007).

$$E_t = A v \rho c \Delta T D t \tag{8}$$

A is the drying airflow surface area, v is the drying air velocity, ρ is the air density, c is the specific heat of air, T is the temperature difference between the dryer's inlet and exit, and Dt is the total drying time in this equation. A brief notification for a reading facility is made before presenting the testing data. The cases that are being tested are coded, and the codes are shown in Figure 9.

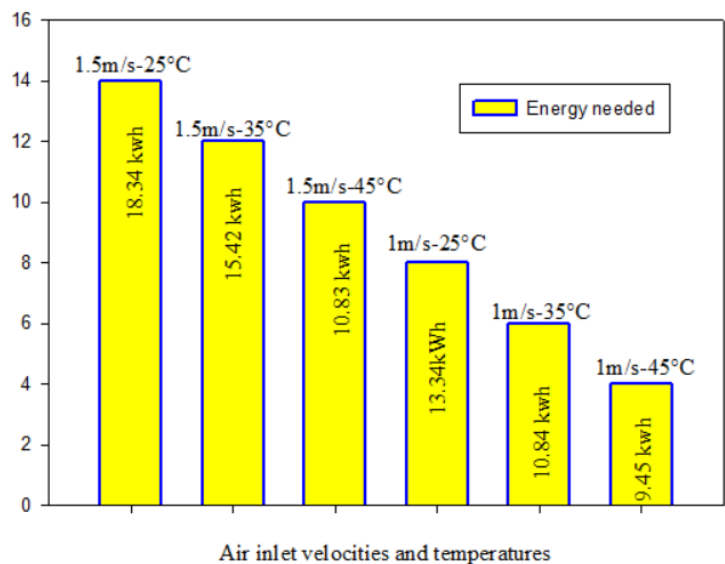


Fig. 9. The total energy requirement of the system under operating conditions

Evaluation of the drying process model

Experimental data obtained by drying red peppers have been translated to moisture ratio. In Table 2, curve fitting was performed using 15 thin-layer drying models to find the mathematical model that would approximately correspond to the MR values. Since three different drying temperatures and two different drying velocities were used, the processes were repeated for 6 different

situations. The results are given in Tables 3 and 4, which were created according to the drying velocities. Table 3 and Table 4 show the best five results of thin-layer drying models mentioned in Table 2.

Table 3. Results of Best Mathematical Models for Drying Kinetics (u=1 m/s)

Model	T °C	Model Coefficients	R ²	SSE	RMSE	χ^2
<i>Logaritmi c</i>	25	a=2,992158, k=0,000393,	0,9924	0,000360	0,018978	0,000384
	35	b=-2,177297	0,9981	0,000088	0,009354	0,000095
	45	a=0,901462, k=0,002948, b=-0,091300 a=0,817664, k=0,004010, b=-0,014049	0,9979	0,000090	0,009485	0,000098
<i>Midilli- Kucuk</i>	25	a=0,828223, b=-0,000300,	0,9872	0,000609	0,024684	0,000663
	35	k=0,001007, n=1,044271	0,9981	0,000088	0,009358	0,000097
	45	a=0,904220, b=-0,093446, k=0,002992, n=0,996757 a=0,958302, b=-0,129223, k=0,007746, n=0,845406	0,9990	0,000044	0,006592	0,000049
<i>Modified 1 Wang- Singh</i>	25	a=0,795657, b=-0,001006,	0,9942	0,000278	0,016668	0,000296
	35	c=-0,00000003	0,9982	0,000084	0,009142	0,000090
	45	a=0,794498, b=-0,002256, c=-0,00001788 a=0,755668, b=-0,002416, c= 0,00000224	0,9921	0,000336	0,018341	0,000368
<i>Modified 2 Wang- Singh</i>	25	a=0,812492, b=-0,001302,	0,9953	0,000226	0,015037	0,000246
	35	c=0,000001, d=-9,6*10e-10	0,8122	0,008711	0,093331	0,009679
	45	a=0,474670, b= 0,002448, c=-0,000015, d=-17*10e-9 a=0,838085, b=-0,003795, c=0,000008, d=-67*10e-10	0,9963	0,000156	0,012494	0,000176
<i>Two Term</i>	25	a=0,351035, b=0,523738,	0,9490	0,002431	0,049303	0,002647
	35	k1=0,002268, k2=0,002269	0,9962	0,000174	0,013206	0,000194
	45	a=0,864578, b=-0,056338, k1=0,003824, k2=0,015519 a=0,682014, b=0,125521, k1=0,004178, k2=0,004148	0,9978	0,000095	0,009747	0,000107

Table 3 shows the results of the mathematical models obtained at different temperatures (25 °C, 35 °C, and 45 °C) when the drying velocity was 1 m/s. It is understood that the best model for 25 °C is modified-2 Wang-Singh since the R² value is high and the other values (SSE, RMSE, and X²) are little. Similarly,

modified1 Wang-Singh model for 35 °C is seen as a suitable model. In addition to that, it is clear that the Midilli-Kucuk model can be used for the 45 °C by taking the same criteria into account.

Table 4. Results of Best Mathematical Models for Drying Kinetics (u=1.5 m/s)

Model	T °C	Model Coefficients	R ²	SSE	RMSE	χ^2
<i>Logaritmik</i>	25	a=3,446958, k=0,000334,	0,9855	0,000598	0,024458	0,000641
	35	b=-2,645846	0,9985	0,000064	0,007999	0,000007
	45	a=0,804103, k=0,004200, b=-0,004629 a=0,837924, k=0,004333, b=-0,051097	0,9923	0,000315	0,017760	0,000355
<i>Midilli-Kucuk</i>	25	a=2,150038, b=-1,355774,	0,9844	0,000643	0,025361	0,000706
	35	k=0,003728, n=1,064919	0,9994	0,000028	0,005272	0,000031
	45	a=0,899143, b=-0,075797, k=0,007682, n=0,867661 a=1,559465, b=-0,730109, k=0,010054, n=0,697512	0,9966	0,000140	0,011839	0,000165
<i>Modified1 Wang-Singh</i>	25	a=0,777298, b=-0,000927,	0,9885	0,000472	0,021733	0,000506
	35	c=-0,00000016	0,9937	0,000272	0,016500	0,000296
	45	a=0,766115, b=-0,002538, c=0,00000239 a=0,826458, b=-0,003711, c= 0,00000491	0,9719	0,001148	0,033886	0,001292
<i>Modified2 Wang-Singh</i>	25	a=0,792691, b=-0,000995,	0,9868	0,000542	0,023283	0,000595
	35	c=3*10e-8, d=-2,9*10e-10	0,9982	0,000080	0,008925	0,000089
	45	a=0,797462, b=-0,003264, c=0,000006, d=-40*10e-10 a=0,815239, b=-0,003789, c=0,000007, d=-45*10e-10	0,9863	0,000560	0,023670	0,000658
<i>Modified3 Wang-Singh</i>	25	a=0,833433, b=-0,002180, c=0,000006, d=-9,2*10e-10	0,9971	0,000121	0,011006	0,000136
	35	e=44*10e-13 a=1,091952, b=-0,010655, c=0,000055, d=-13*10e-8	0,8958	0,004524	0,067260	0,005209
	45	e=10*10e-11 a=0,940075, b=-0,012242, c=0,000102, d=-36*10e-8 e=4,3*10e-10	0,9335	0,002719	0,052143	0,003337

Table 4 shows the results of the curves fitted for the drying values of different temperatures (25 ° C, 35 ° C and 45 ° C) when the drying velocity is used as 1.5 m / s. When the results are examined, it is clear that the best model for 25 ° C is the modified 3 Wangh-Singh because the R² value is the highest,

and the SSE, RMSE, and X^2 values are the smallest. In the same way, the Midilli-Kucuk model is seen as a suitable model for 35 ° C and 45 ° C.

Graphs of experimental and predicted MR values are given for two different velocities to verify the selected mathematical models. Figure 10 shows the results for a flow rate of 1 m/s. When this graph is examined, it can be said that the experimental MR information and the estimated MR values have good harmony. Curves largely overlap. The obtained R^2 values and other criteria already indicated that such a result would be reached. In Figure 11, the results are repeated for 1.5 m/s flow velocity. From here, it can be seen that the mathematical models capture the experimental MR values very well. These mathematical models can be used to calculate MR values for red pepper in future studies.

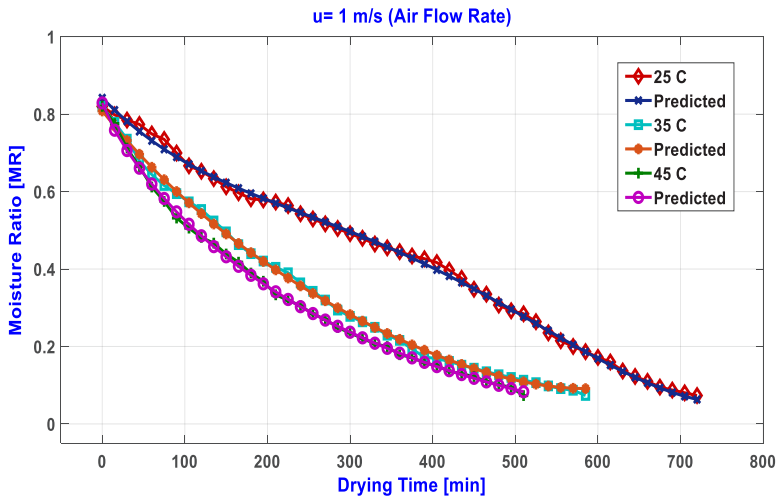


Fig. 10. The results of a flow rate of 1 m/s in mathematical modeling.

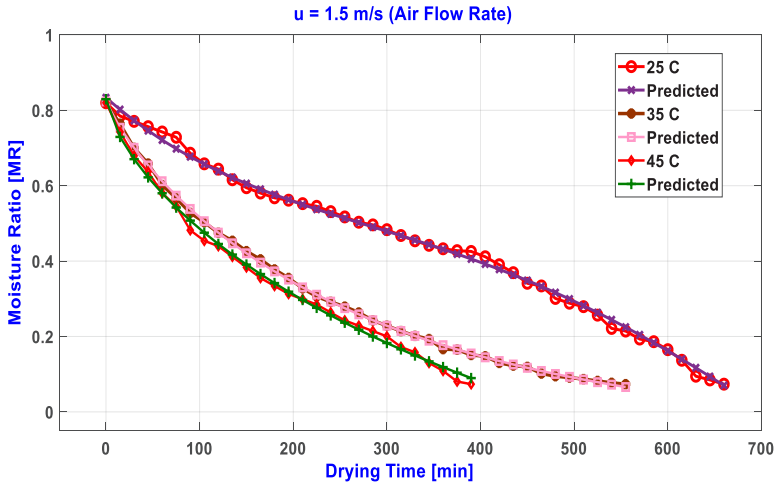


Fig. 11. The results of a flow u rate of 1.5 m/s in mathematical modeling.

CONCLUSIONS

In this study, red pepper pieces were experimentally investigated in a convection drying set at different speeds and temperatures. In this study, humidity curves, drying rate graphs, total energy requirements were examined. The main goal of the study is to work on mathematical modeling. For this purpose, firstly, the compatibility of many models in the literature with our experimental results was investigated, and then three new mathematical models were developed by our study results.

To express the drying kinetics of red pepper, MR values were calculated with drying data obtained at two different velocities (1 m/s, 1.5 m/s) and 3 different temperatures (25 °C, 35 °C, 45 °C) were applied to 15 different thin-layer drying models. As a result of the statistical analysis, modified 2 Wang-Singh model for 25 °C, modified 1 Wang-Singh model for 35 °C and Midilli-Kucuk model for 45 °C at 1 m/s velocity; modified 3 Wangh-Singh model for 25 °C, Midilli-Kucuk model for 35 °C and 45 °C at 1.5 m/s velocities provided the best fit. Also, three different mathematical models were developed for three different air inlet temperatures (25, 35, and 45 °C). It is suggested that the three new mathematical models developed and which we think will contribute a lot to the literature, should be applied to other products as well.

REFERENCES

- Agbede, O. O., Oke, E. O., Akinfenwa, S. I., Wahab, K. T., Ogundipe, S., Aworanti, O. A. and Babatunde, K. A. (2020). Thin layer drying of green microalgae (*Chlorella* sp.) paste biomass: drying characteristics, energy requirement and mathematical modeling. *Bioresource Technology Reports*, 11, 100467.
- Arslan, D. and Özcan, M. M. (2010). Study the effect of sun, oven and microwave drying on quality of onion slices. *LWT-Food Science and Technology*, 43(7), 1121-1127.
- Arslan, D. and Özcan, M. M. (2011). Dehydration of red bell-pepper (*Capsicum annuum* L.): Change in drying behavior, colour and antioxidant content. *Food and bioproducts processing*, 89(4), 504-513.
- Aymen, E. L., Hamdi, I., Kooli, S. and Guizani, A. (2019). Drying of red pepper slices in a solar greenhouse dryer and under open sun: Experimental and mathematical investigations. *Innovative Food Science and Emerging Technologies*, 52, 262-270.
- Bechlin, T. R., Granella, S. J., Christ, D., Coelho, S. R. M. and Paz, C. H. D. O. (2020). Effects of ozone application and hot-air drying on orange peel: moisture diffusion, oil yield, and antioxidant activity. *Food and Bioproducts Processing*, 123, 80-89.
- Cerci, K. N. and Kavak Akpınar, E. (2016). Experimental determination of convective heat transfer coefficient during open sun and green-house drying of apple slices.
- Dalvand, M. J., Mohtasebi, S. S. and Rafiee, S. (2012). Study on effective structural parameters on drying rate of kiwi fruits in a solar ehd dryer. *International Journal of Multidisciplinary Sciences and Engineering*, 3(5), 66-70.
- Doymaz, İ. (2013). Hot-air drying of purslane (*Portulaca oleracea* L.). *Heat and Mass Transfer*, 49, 835-841.
- Di Scala, K. and Crapiste, G. (2008). Drying kinetics and quality changes during drying of red pepper. *LWT-Food Science and Technology*, 41(5), 789-795.
- Evin, D. (2012). Thin layer drying kinetics of *Gundelia tournefortii* L. *Food and bioproducts processing*, 90(2), 323-332.
- Guo, J., Zheng, L. and Li, Z. (2021). Microwave drying behavior, energy consumption, and mathematical modeling of sewage sludge in a novel pilot-scale microwave drying system. *Science of the Total Environment*, 777, 146109.

- Hao, W., Zhang, H., Liu, S., Mi, B. and Lai, Y. (2021). Mathematical modeling and performance analysis of direct expansion heat pump assisted solar drying system. *Renewable Energy*, 165, 77-87.
- Junka, N. and Rattanamechaikul, C. (2021). Mathematical modelling to control fungal growth in paddy dried using fluidisation. *Biosystems Engineering*, 204, 312-325.
- Akpinar, E. K., Bicer, Y. and Yildiz, C. (2003). Thin layer drying of red pepper. *Journal of food engineering*, 59(1), 99-104.
- Krzykowski, A., Dziki, D., Rudy, S., Gawlik-Dziki, U., Polak, R. and Biernacka, B. (2018). Effect of pre-treatment conditions and freeze-drying temperature on the process kinetics and physicochemical properties of pepper. *Lwt*, 98, 25-30.
- Kumar, M., Sansaniwal, S. K. and Khatak, P. (2016). Progress in solar dryers for drying various commodities. *Renewable and Sustainable Energy Reviews*, 55, 346-360.
- Ozgen, F. (2015). Experimental investigation of drying characteristics of cornelian cherry fruits (*Cornus mas* L.). *Heat and Mass Transfer*, 51, 343-352.
- Ozgen, F. and Celik, N. (2018). Evaluation of design parameters on drying of kiwi fruit. *Applied Sciences*, 9(1), 10.
- Pham, N. D., Khan, M. I. H. and Karim, M. A. (2020). A mathematical model for predicting the transport process and quality changes during intermittent microwave convective drying. *Food chemistry*, 325, 126932.
- Prithani, R. and Dash, K. K. (2020). Mass transfer modelling in ultrasound assisted osmotic dehydration of kiwi fruit. *Innovative Food Science and Emerging Technologies*, 64, 102407.
- Sacilik, K. and Elicin, A. K. (2006). The thin layer drying characteristics of organic apple slices. *Journal of food engineering*, 73(3), 281-289.
- Singh, N. J. and Pandey, R. K. (2012). Convective air drying characteristics of sweet potato cube (*Ipomoea batatas* L.). *Food and Bioproducts Processing*, 90(2), 317-322.
- Soysal, Y., Ayhan, Z., Eştürk, O. and Arkan, M. F. (2009). Intermittent microwave-convective drying of red pepper: Drying kinetics, physical (colour and texture) and sensory quality. *Biosystems engineering*, 103(4), 455-463.
- Tuncal, C. and Doymaz, İ. (2020). Performance analysis and mathematical modelling of banana slices in a heat pump drying system. *Renewable Energy*, 150, 918-923.

- Wang, J., Fang, X. M., Mujumdar, A. S., Qian, J. Y., Zhang, Q., Yang, X. H. and Xiao, H. W. (2017). Effect of high-humidity hot air impingement blanching (HHAIB) on drying and quality of red pepper (*Capsicum annuum* L.). *Food chemistry*, 220, 145-152.
- Zhang, X. L., Zhong, C. S., Mujumdar, A. S., Yang, X. H., Deng, L. Z., Wang, J. and Xiao, H. W. (2019). Cold plasma pretreatment enhances drying kinetics and quality attributes of chili pepper (*Capsicum annuum* L.). *Journal of Food Engineering*, 241, 51-57.
- Zielinska, M. and Markowski, M. (2010). Air drying characteristics and moisture diffusivity of carrots. *Chemical Engineering and Processing: Process Intensification*, 49(2), 212-218.

Chapter 22

An Overview of the Empirical Investigations into the Classification of Power Quality Disturbances

SİTKİ AKKAYA¹

¹ Asst. Prof. Dr.; Sivas University of Science and Technology, Department of Electrical and Electronics Engineering, sakkaya@sivas.edu.tr ORCID No: 0000-0002-3257-7838

ABSTRACT

Stable fundamental frequency and amplitude on electrical power systems are supposed to be. However, different types of disturbances affect negatively these parameters in these systems. These disturbances, collectively known as power quality disturbances (PQDs), encompass a range of phenomena such as sag, interruption, swell, harmonics, flicker, interharmonics, spike, notch, and transient effects. These disturbances may emerge singular or in double or triple combinations in the power system. There are unpredictable and variable different effects on the system components which can lead to destructive results. Real dataset acquisition related to these disturbances is so tough through the randomness and sophisticated structure of the power systems. For that reason, the importance of performing experimental studies to investigate and analyze these disturbances has increased significantly. This study has been gleaned to ensure an important resource to the researchers for the investigation of PQDs. Additionally, the study assures comprehensive guidance, offering researchers insights into the different types of PQDs and their characteristics. With the presentation of the knowledge on these disturbances and their impacts, the study has a purpose to support researchers in their performance to understand and address the challenges led by PQDs. Defining the significance of experimental studies, this compilation consists of some methodologies, experimental setups, and tools employed for PQDs. It acknowledges the requirement for experimental dataset to improve research in this field and highlights the importance of investigations for the PQDs.

Keywords: Power Systems, Power Quality Disturbances, PQD, Experimental Setup, Fundamental Frequency, Harmonics, Interharmonics, Sag, Swell, Interruption, Flicker, Spike, Notch, Transient, IEEE 1159, IEEE 1459, IEC 61000-4-7, IEC 61000-4-15, IEC 61000-4-30

1. INTRODUCTION

Ensuring the stability of fundamental frequency and amplitude parameters, specifically set at 50 Hz and 220 V_{rms} in Turkey, is remarkably important for power systems. Any instability in these parameters can have detrimental effects, including the improper functioning of electrical devices, efficiency losses, and even severe damage. For instance, voltage swell can lead to high voltage faults, while voltage sags can cause sensitive electronic devices to malfunction. Furthermore, voltage interruptions can result in energy losses and disrupt business continuity.

Several standards exist that define power quality disturbances and provide guidelines for their analysis. For instance, IEEE 1159 defines power quality parameters and measurement methods, while IEEE 1459 focuses on interpreting power system measurements in a meaningful way. Standards such as IEC 61000-4-7, IEC 61000-4-15, and IEC 61000-4-30 offer guidelines for testing and evaluating power system disturbances. EN 50160 also establishes limits similar to other standards [1]–[5].

In order to effectively analyze power quality (PQ) issues, it is crucial to understand the definitions of various disturbances, their causes, and their impact on power systems. Additionally, real-time implementation or acquiring problem-specific data is essential for later analysis of Power Quality Disturbances (PQDs). However, on account of the time-varying nature of power systems and the associated risks to human safety, obtaining direct and relevant data can be challenging. Consequently, the use of experimental setups becomes necessary to conduct investigations and gather data for the Detection and Classification (D&C) of PQDs. This study aims to fulfill this need by presenting the most prevalent power quality phenomena along with their corresponding experimental setups.

The primary objective of this study is to serve as a partial guide for researchers in the field of PQDs. By providing a comprehensive overview of experimental setups used in the analysis of PQDs, this study seeks to facilitate and support further research in this area. The compilation of relevant information and setups will aid researchers in conducting their investigations, thereby advancing the understanding and management of PQDs.

The structure of this paper is organized as the following: In section 2, PQDs in power systems are given with single and multiple PQDs and illustrated images. Subsequently, literature for experimental studies on the classification of PQDs. Then, related experimental setups for the classification of PQDs mentioned previously are presented in detail in 4th section. The final section presents the summary and discussion of this study.

2. TYPES OF POWER QUALITY DISTURBANCES

In power systems, the most important parameters are fundamental frequency and amplitude. A pure sinusoidal signal which is modeled with a fundamental sinusoidal signal with 50 Hz frequency and a normalized amplitude while called Class C1 is desired in power systems. Fundamental frequency and amplitude symbolized with and must be at 50 Hz and 220 in Turkey. However, these parameters are changed by some power quality disturbances like flicker, harmonics, sag, swell, interruption, notch, spike, transient, etc. which are the most common disturbances. As defined in IEEE 1159, power quality disturbances have typical mathematical models with amplitude, frequency, and time characteristics at different ranges. These can emerge singular or multiple as flicker, harmonics, sag, swell, interruption, notch, spike, transient, et c. Some of them are defined with models and time-series images as the following in Table 1 and but the pure signal is ignored.

Table 1: Examples of PQD classes

Class	Type	Class	Type
C2	Sag	C10	Sag+Harmonics
C3	Swell	C11	Swell+Harmonics
C4	Interruption	C12	Interruption+Harmonics
C5	Flicker	C13	Flicker+Harmonics
C6	Transient	C14	Sag+Transient
C7	Harmonics	C15	Swell+Transient
C8	Notch	C16	Spike+Transient
C9	Spike	C17	Notch+Transient

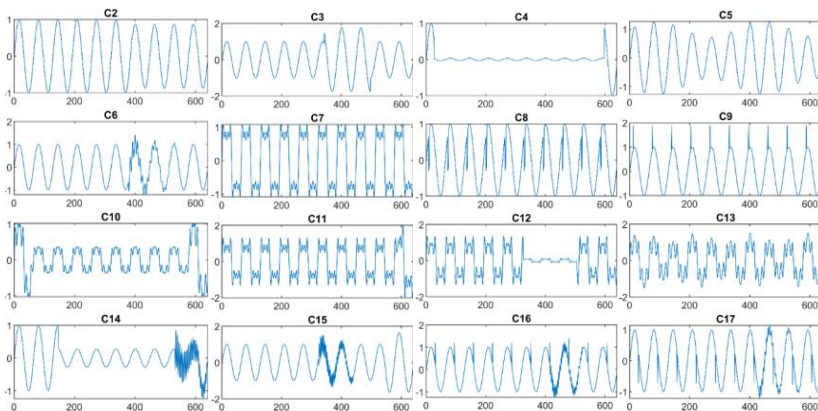


Figure 1: Images of PQD classes in Table 1

For the precious analysis of PQDs, the right identification and classification are required. But, real-time implementation or acquiring problem-specific data is

essential for the analysis of PQDs. Because of the time-varying nature of power systems and the entity of the risks for human safety, direct and relevant PQD data are being enforced. As a result, the utilization of experimental setups is necessary to perform investigations and collect data for the D&C of PQDs. Therefore, some studies and the experimental setup will be given in the following sections.

3. LITERATURE FOR EXPERIMENTAL STUDIES ON THE CLASSIFICATION OF POWER QUALITY DISTURBANCES

Some experimental studies on the classification of PQDs are available in the literature as the following.

The study in [6] proposes a smart sensor system using the Hilbert Transform to detect, classify, and quantify PQDs. It addresses the need for accurate monitoring in electrical grids, analyzing voltage and current waveforms. The sensor's design, implementation, and experimental results are discussed, showcasing its real-time monitoring, accurate detection, and classification capabilities. The sensor provides valuable information for preventive maintenance and enhancing grid reliability.

A method using the least mean square (LMS) algorithm and ADALINE is proposed for the measurement of amplitudes and phases of harmonics / interharmonics / subharmonics parameters faster and more accurately [7].

A project on the diagnosis of PQDs intends to create advanced FFT (Fast Fourier Transform), DWT (Discrete Wavelet Transform), and EMD (Empirical Mode Decomposition) -based hybrid signal processing algorithms with Machine Learning Algorithms (MLAs) for the detection and categorization of different kinds of PQDs in smart grids [8]. The goal of the project is to test and demonstrate the effectiveness of these techniques by performing simulations and conducting experiments to diagnose PQ issues in smart grids. The successful implementation of these techniques can ultimately enhance the efficiency and dependability of power systems.

A signal processing-based method for the classification of PQDs called as Mystery Curve is introduced in [9]. The focus of the study is on accurately identifying and characterizing PQDs. This method can separate normal and disturbed PQ conditions by analyzing related features and signal characteristics. That study highlights the accurate D&C of PQDs of the method. It also discusses the performance and implementation of the method. The Mystery Curve method offers an innovative solution for improving PQ monitoring and analysis according to the results.

A cross-correlation analysis-based method is proposed for real-time D&C of PQDs [10]. It aims to accurately identify and classify different types of PQDs in

real time. The method can detect and classify disturbances such as voltage sags, swells, and harmonics by comparing measured power quality signals with reference waveforms. It offers the advantages of swift and correct identification of power quality events and discusses implementation sights and performance evaluation. Hereby, the method provides a promising solution for enhancing power system monitoring and analysis by effectively detecting and classifying PQDs in real-time.

The work in [11] puts forward a new technique for the classification of PQDs. This approach consists of three sequential steps and focuses on examining time-dependent spectral characteristics. The objective is to enhance the precision of PQD classification by considering the dynamic behavior of the disturbances over time. That study accentuates the methodology and experimental outcomes, with the efficiency of the suggested approach in precisely detecting and classifying different kinds of PQDs.

A method for accurately recognizing PQDs when there is prominent background noise is presented in [12]. This method consubstantiates the FastICA (Fast Independent Component Analysis) and Random Forest (RF) algorithms to achieve a high level of accuracy for detecting PQDs with significant noise. It presents a detailed explanation of the methodology and experimental results that prove the effectiveness of the stated method in accurately identifying PQDs even in the presence of considerable noise.

A Detrended Fluctuation Analysis (DFA) -based method is proposed for diagnosing PQDs [13]. DFA is used for the analysis of the fluctuations in power signals and extraction of relevant features for PQD identification and classification. DFA can accurately distinguish various types of disturbances with the help of long-range correlations. The study highlights the benefits of DFA in PQ diagnosis, including its ability to detect short-time variations and its practical implementation considerations. Shortly, this study presents DFA as a promising tool for accurately characterizing and classifying of PQDs, thereby enhancing power quality management in electrical systems.

A novel method using a time-frequency analysis technique enhances the efficiency and adaptability of the S-transform for feature extraction [14]. This method can adjust the S-transform parameters based on the specific characteristic of different disturbances. That enables accurate feature extraction from complex disturbances like harmonics, interharmonics, and transients. Also, it improves the management and monitoring of PQDs in electrical systems, contributing to their performance and reliability. This method offers a valuable tool for analyzing complex PQDs and extracting meaningful features, by providing a fast and adaptive solution.

An Integrated Deep Learning (I-DL) -based multi-label PQD classification method is performed in [15]. This study has a purpose for accurate identification and classification of different types of PQDs. It combines convolutional neural networks (CNNs), RNNs, and detection algorithms to detect related features and parameter limitations in PQ signals. The I-DL model is effective in dealing with complex and overlapping disturbances. The study underlines the advantages of the method and negotiates the training process, model architecture, and evaluation metrics.

An innovative single-shot-based algorithm is introduced in [16] with the aim of efficient detection of PQDs. When PQDs disrupt the reliable operation of electrical systems, the algorithm can get rid of this challenge. By using advanced signal processing techniques, the algorithm analyzes voltage and current waveforms to identify various types of disturbances, including sags, swells, and harmonics. Requiring multiple samples or extended observation periods, this algorithm captures and analyzes the waveform in a single shot, violently reducing detection time. Experimental results approve its effectiveness in accurately detecting disturbances with high precision and low false alarm rates. This innovative algorithm offers several benefits, including rapid detection, improved accuracy, and reduced false alarms. Hence, it can significantly enhance power quality monitoring, increasing the reliability and efficiency of electrical systems.

A hybrid method using the Multi-objective Grey Wolf Optimizer (MOGWO), 2D-Riesz Transform (RT), and MLAs is introduced in [17] for classifying PQDs. This method involves extracting features from power signals using the 2D-RT, optimizing feature selection with MOGWO, and employing MLAs like SVM and RF for classification. The method demonstrates accurate classification of PQDs and effective feature selection through MOGWO. This hybrid method gives enhancement for power system monitoring and analysis by accurately identifying and categorizing PQDs.

A PQD D&C technique combining the Deep Learning (DL) and Stockwell Transform (ST) algorithms is studied in [18]. PQDs can have a significant impact on electrical systems. Thus, effective detection and classification methods are required. This technique utilizes the ST, a time-frequency analysis technique, to extract relevant features from PQDs. DL algorithms then use these features to recognize patterns and classify various types of PQDs, such as voltage sags, swells, harmonics, and flickers. The implementation process, including preprocessing steps, feature extraction using the ST, and the training of DL models for classification is given. The robustness and high accuracy of the technique are shown by the results. This technique presents a powerful solution

for PQ analysis, enhancing power system monitoring and management, by combining the ST and DL.

A Wasserstein Adversarial (WA) learning technique is existing in [19] to accurately identify PQDs even in situations with incomplete data. Data may be missing or incomplete in practical scenarios. There are some challenges to the accurate identification of disturbances. This method addresses the issue by training a generator and discriminator network using WA learning. The generator network completed the missing information, while the discriminator network distinguishes the real and completed data. This method effectively accomplishes incomplete data and achieves D&C of PQDs accurately, by leveraging WA learning. The high effectiveness and potential of the method for power system monitoring are indicated by the experimental results.

4. EXPERIMENTAL SETUPS FOR CLASSIFICATION OF PQDS

Some experimental setups for the studies mentioned above are available in the following.

Experimental setup for [6] consists of a PQD generator, a load induction motor, a smart sensor including voltage clamps, a PC with MATLAB, a voltage signal sampling and conditioning board, DAS (Data Acquisition System) board, an FPGA-based board, and a touch screen, can be seen in Figure 2. Overall, it presents a promising solution for power quality analysis, improving the efficient operation of electrical grids.

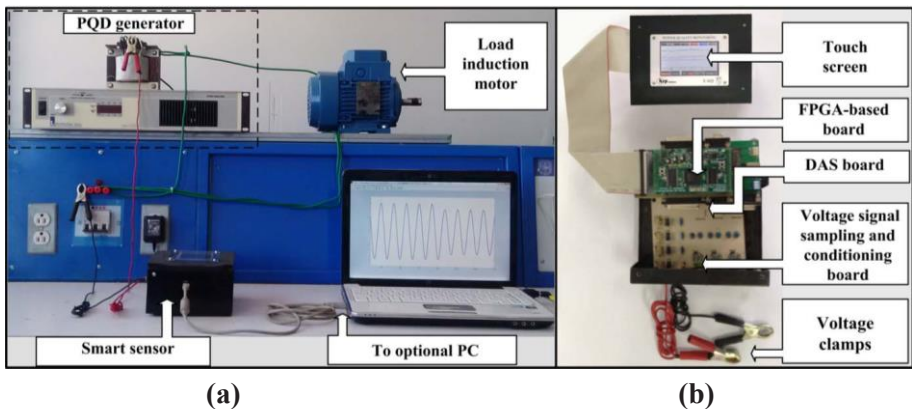
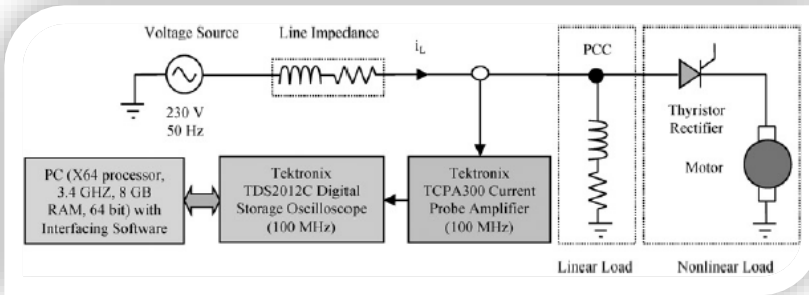


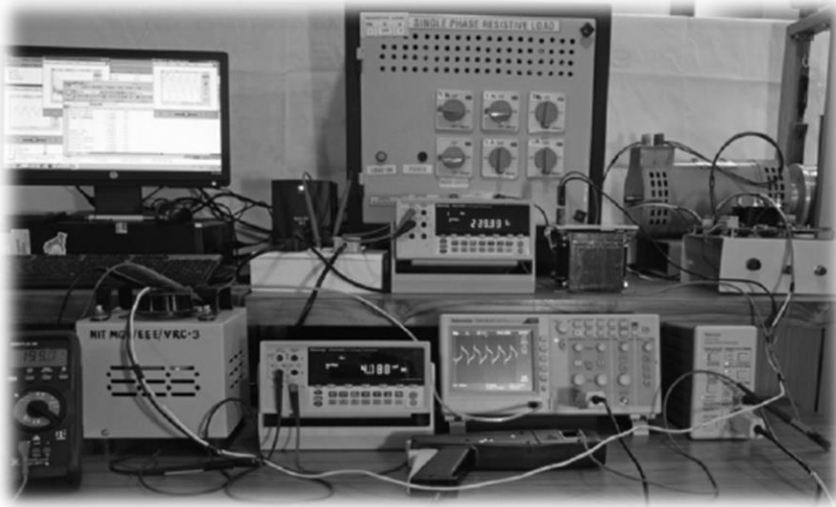
Figure 2: Smart Sensor Experimental Setup for PQDs [6]

A study in [7] was performed on a setup consisting of (virtually) line impedance, a linear load, a thyristor, and a motor as a nonlinear load because of harmonic generation property. Tektronix TDS2012C Digital Storage

Oscilloscope (DSO) (100 MHz) measures the current from the point of common coupling (PCC) by Tektronix TCPA300 Current Probe Amplifier (100 Mhz) and then the acquired data is assessed in a PC (X64 processor, 3.4 GHz, 8 GB RAM, 64 Bit) with MATLAB and related software of the DSO. As a result, a faster and more accurate method for harmonic parameters has been improved. Figure 3 shows a diagram of the test system for the real-time estimation of the signal parameter and a photograph of the experimental setup.



(a)

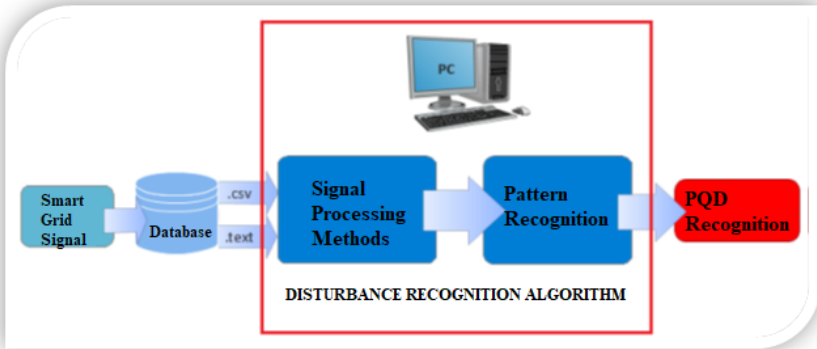


(b)

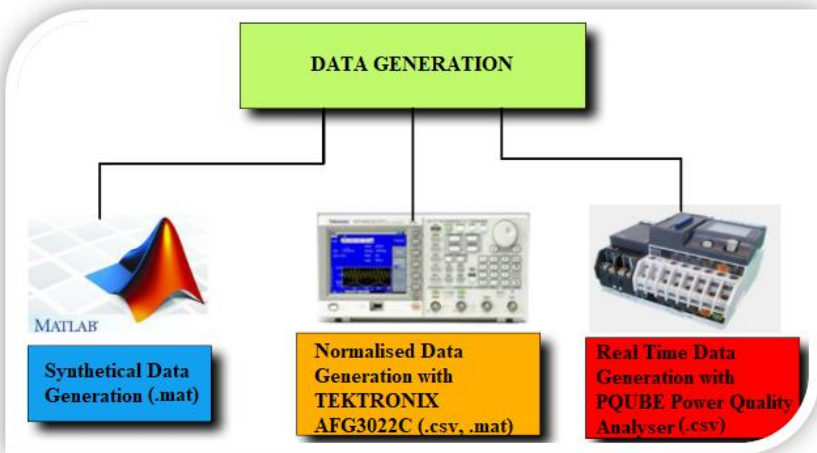
Figure 3: Images for the measurement of harmonic parameters [7] (a) Diagram of the real-time estimation of the signal parameter (b) Photograph of the experimental setup

The algorithm of the proposed system and the data acquisition methods of the Project study in [8] are illustrated in Figure 4. a and b respectively. In that project,

MATLAB software was for synthetical dataset and method improvement, Tektronix AFG 3022C for the experimental dataset, and PQUBE Power Quality Analyser for the real-time dataset for PQD D&C.



(a)



(b)

Figure 4: Diagnosis of PQDs with Signal Processing Techniques [8]

(a) Flowchart of the Algorithm (b) Data acquisition methods

Another study in [9] uses an experimental setup consisting of a PC with MATLAB/Simulink, a DSO, a multimeter, an autotransformer, a prototype model transformer, a current sensor, and a 10:1 passive probe in Figure 5.

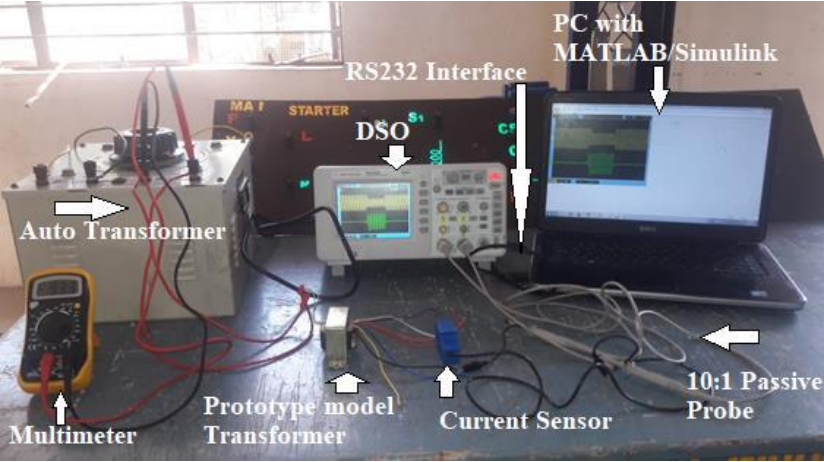


Figure 5: Experimental Setup of The Mystery Curve [9]

A PC, a motor, a rheostat, incandescent lamps as the load, a dimmer stat, a DAS, a DSO a multimeter, a signal condition circuit, a board, and instrument transformers are used in the study of [10] as the experimental setup in Figure 6.

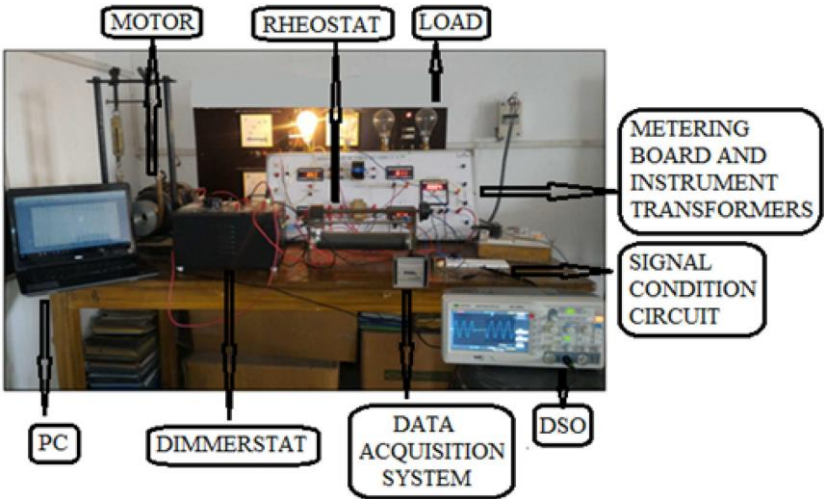


Figure 6: Experimental setup of real-time PQDs [10]

In a study [11], an experimental setup consisting of four layers which are a Neutral Point Clamped (NPC) Inverter grid- on/off an experimental platform, a Signal Conditioning Block including a CHV-25P/500 card, and a Low-pass filter, an NI PCI-6229 Signal Acquisition Block, a PC for Signal Processing Block like in Figure 7.

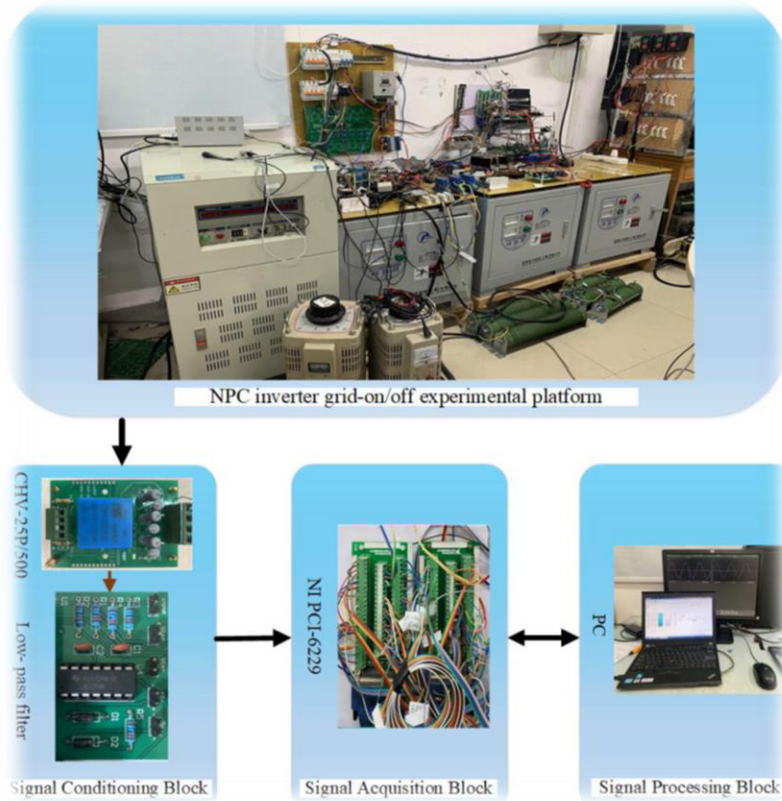


Figure 7: 4-layer experimental setup in [11]

A PC and a power quality analyzer with probes as field measurement equipment create the experimental setup for [12] which is shown in Figure 8.

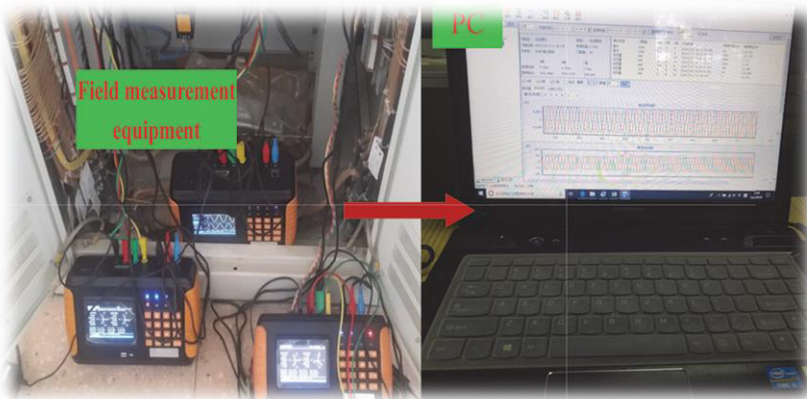
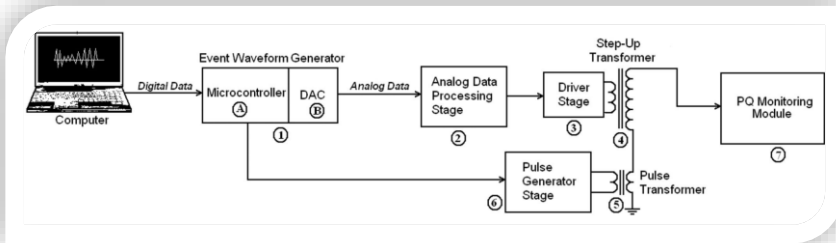
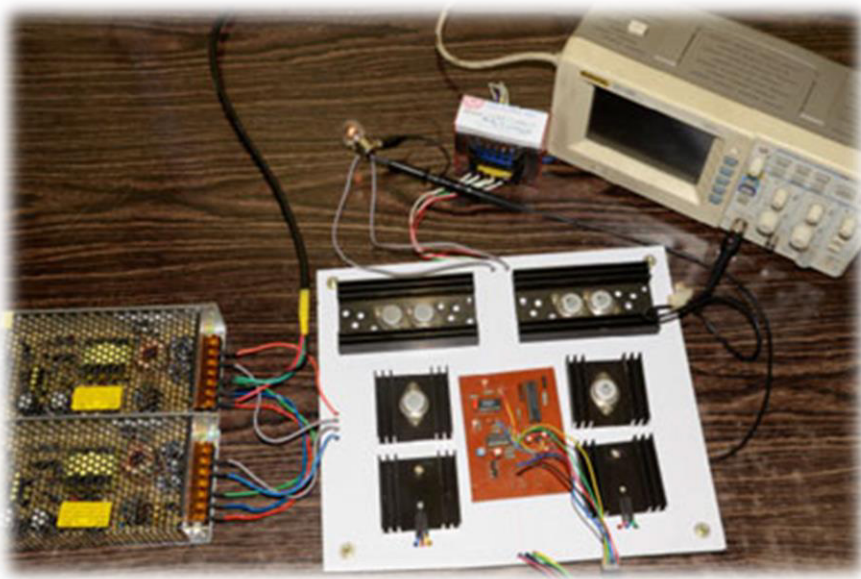


Figure 8: Two-component PQD experimental setup used in [12]

A PC, an event waveform generator consisting of a microcontroller and a Digital/Analog Converter (DAC), an analog data processing stage, a driver stage and a step-up transformer, a pulse generator, a pulse transformer, and a PQ monitoring module are used for event generation and PQD monitoring of the study in [13] as in Figure 9.



(a)



(b)

Figure 9: PQD Event Generation and Monitoring in [13] a) Flowchart (b) Experimental Setup

The study in [14] has utilized an experimental setup consisting of a PC, a DPO 3012 oscilloscope, an MR1200M portable multichannel waveform monitoring recorder, a Chroma 61511 Programmable AC source, and a control computer as in Figure 10.

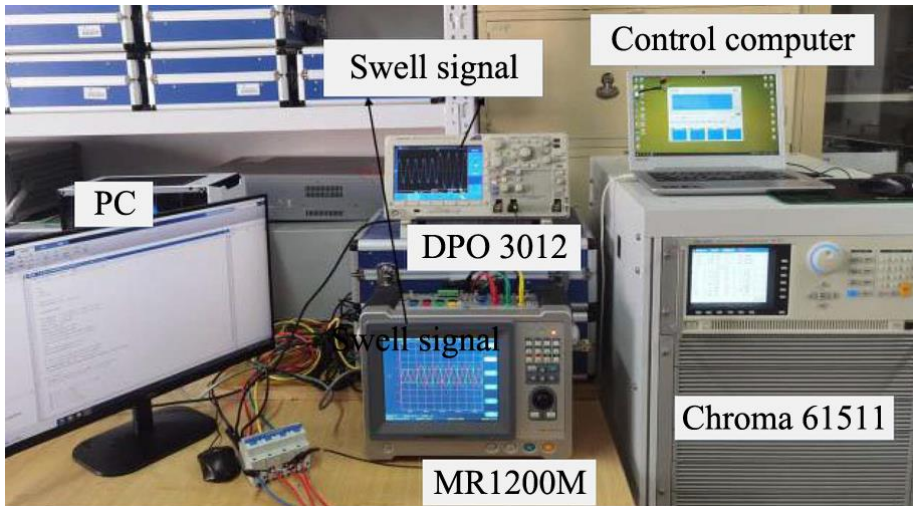


Figure 10: An Experimental setup for Feature Extraction of Complex Quality Disturbance [14]

Another study in [15] utilized a basic experimental configuration consisting of a FLUKE 6105A event power generator and a DSO like in Figure 11.

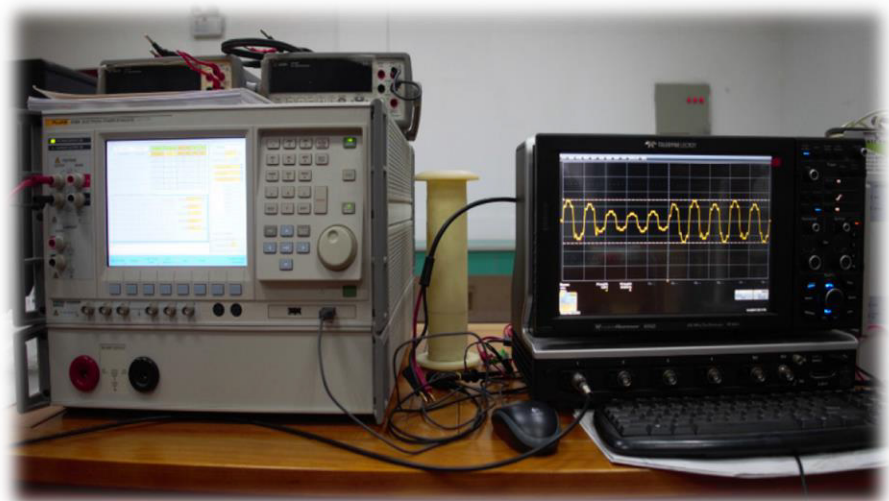


Figure 11: Basic Experimental Configuration in [15]

An experimental setup of study [16] including a laptop, a residual current circuit breaker, a DAS, an AC programmable power source, and a Raspberry PI3 is illustrated in Figure 12.

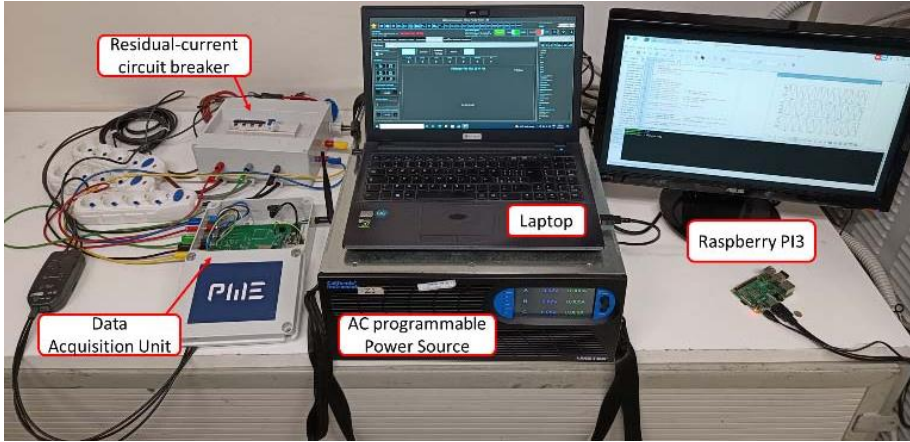


Figure 12: Single Shot PQD Detector Experimental Setup [16]

The setup for [17] in Figure 13 composes of a laptop, a PC based Oscilloscope, an electric panel, 4x1 kVar capacitors, a switchboard, a 7.5 kW Asynchronous Motor (ASM), a 5.00 kW Permanent Magnet Synchronous Generator (PMSG), a 7.50 kW inverter, Voltage/Current Sensor Boards, a Motor Control Panel, a 3.00 kW, a 1.50 kW, a 0.75 kW ASM, and a 0.37 kW ASM.

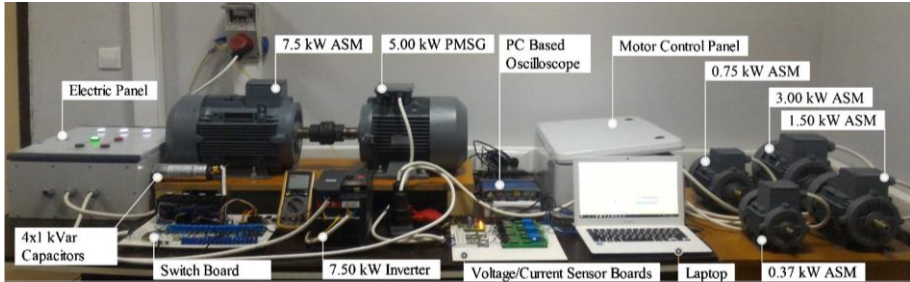


Figure 13: Experimental Setup Used for Classification of PQDs in [17]

For the implementation of the method in [18], an experimental setup in Figure 14 including a PC, a load resistor, a current transformer, a sensing resistor, NI PXIe-1017 Touch Screen Monitor, TB-4300C terminal block, a Tektronix TDS2012 Digital Oscilloscope, and an HL- 610S programmable AC power supply has been used.

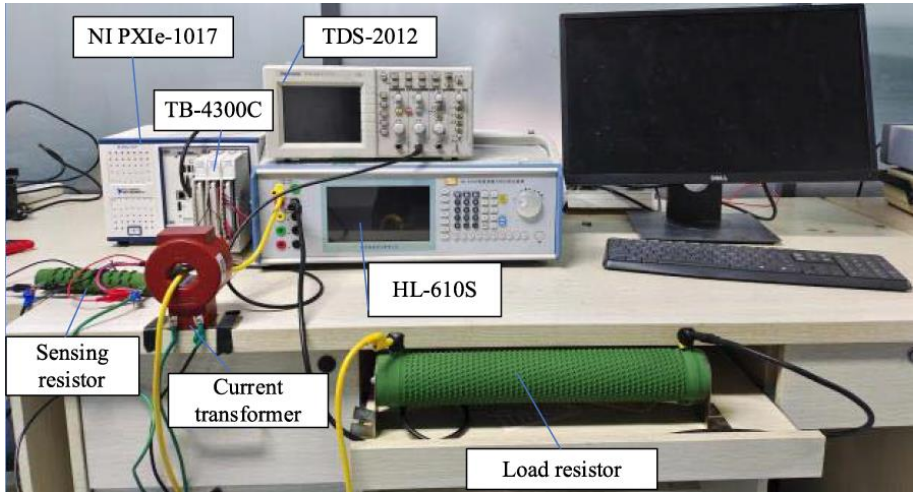
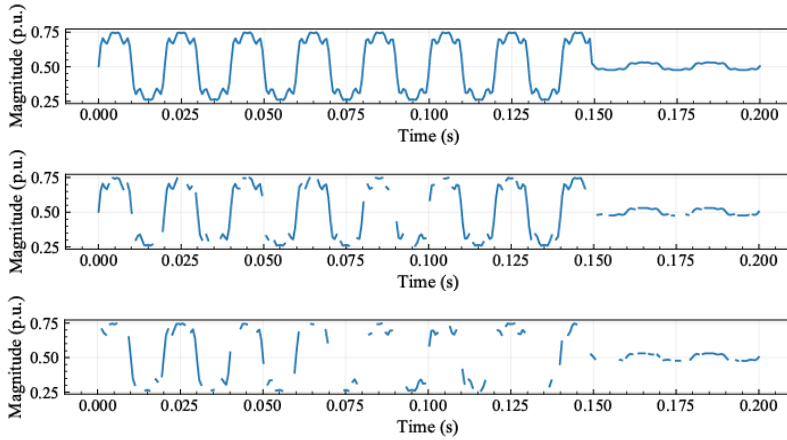
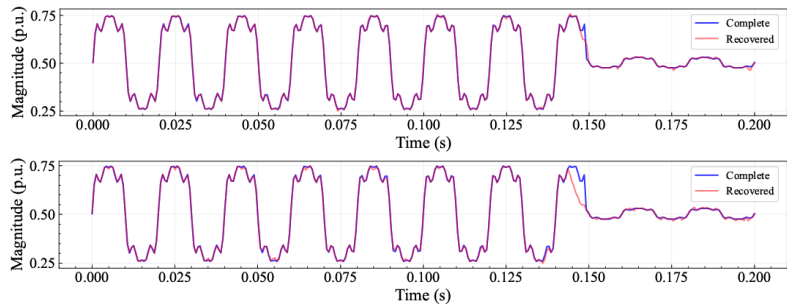


Figure 14: An experimental setup used for ST and DL[18]

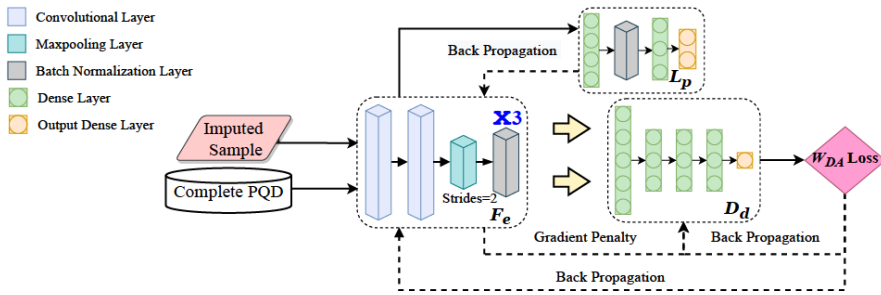
The experiments for [19] are implemented using Python, and Tensorflow in DELL-Precision-7920 Tower with Quadro P6000 GPU. Waveforms for under-missing rates, recovery of these waveforms, and the Structure of WA domain adaption are yielded in Figure 15.



(a)



(b)



(c)

Figure 15: Incomplete Data on PQD [19] a) Waveforms for under missing rates are 0, 0.2, and 0.4 respectively. b) Recovered waveforms for these c) Structure of Wasserstein Adversarial domain adaption for PQDs

5. SUMMARY AND DISCUSSION

As a summary, Table 2 presents an overview of the different setups used for the classifications of PQDs. This study provides a valuable resource for researchers, ensuring light on the significance of detecting and classification of PQDs, and providing insights into the experimental setups employed. These setups encompass a large range of instruments, data acquisition systems, and analysis tools that enable the measurement, monitoring, and analysis of PQDs. Furtherly, software applications compatible with these devices are given. The methods, algorithms, and techniques investigated in these setups contribute to the development of innovative solutions at enhancing the efficiency, reliability, and performance of power systems. By utilizing these experimental setups, researchers can have valuable knowledge about PQDs and can advance the detection and classification of PQDs. It is worth noting that the setups presented in Table 2 not only for stated PQDs in the related studies but also for combinations of disturbances that may arise together. Moreover, this study can provide to facilitate making up optimized experimental setups, allowing researchers to design and implement more effective methodologies for PQDs.

Table 2: Table of Experimental Setups on PQDs

Ref.	Devices / Components / Software	No of PQDs	Ref.	Devices / Components / Software	No of PQDs
[6]	<ul style="list-style-type: none"> • A PC, • A PQD generator, • A smart sensor ➤ Voltage clamps, ➤ A voltage signal sampling board ➤ A conditioning board, • DAS board, • An FPGA-based board, • A touch screen, • MATLAB • A line impedance, • A linear load, • A thyristor, • A motor as a nonlinear load, 	9	[13]	<ul style="list-style-type: none"> • A PC, • An event waveform generator, ➤ A Microcontroller, ➤ A DAC, • An analog data processing stage, ➤ A driver stage, ➤ A step-up transformer, • A pulse generator, • A pulse transformer, • A PQ monitoring module. 	19
[7]	<ul style="list-style-type: none"> • Tektronix TDS2012C DSO (100 MHz). • Tektronix TCPA300 Current Probe Amplifier (100 Mhz). 	8	[14]	<ul style="list-style-type: none"> • A PC, • A DPO 3012 oscilloscope, • An MR1200M portable multichannel waveform monitoring recorder, • A Chroma 61511 Programmable AC source, • A control computer. 	20

[8]	<ul style="list-style-type: none">• A PC (X64 processor, 3.4 GHz, 8 GB RAM, 64 Bit),• MATLAB.• Tektronix AFG 3022C,• PQUBE Power Quality Analyser,• MATLAB.	6	[15]	<ul style="list-style-type: none">• A FLUKE 6105A event power generator,• A DSO,• MATLAB.	14
[9]	<ul style="list-style-type: none">• A PC• A DSO,• A multimeter,• An autotransformer,• A prototype model transformer,• A current sensor,• A 10:1 passive probe,• MATLAB / Simulink.	10	[16]	<ul style="list-style-type: none">• A laptop,• A residual current circuit breaker,• A DAS,• An AC programmable power source,• A raspberry PI 3.	7
[10]	<ul style="list-style-type: none">• A PC,• A motor,• A rheostat,• Incandescent lamps,• A dimmer stat,• A DAS,• A DSO,• A multimeter,• A signal condition circuit,• A board,• Instrument transformers.	11	[17]	<ul style="list-style-type: none">• A laptop,• A PC based Oscilloscope,• An electric panel,• 4x1 kVar capacitors,• A switchboard,• A 7.5 kw ASM,• A 5.00 kw PMSG,• A 7.50 kw inverter,• Voltage/Current Sensor Boards,• A Motor Control Panel,• A 3.00 kw, a 1.50 kw,• A 0.75 kw ASM,• A 0.37 kw ASM.	18
[11]	<ul style="list-style-type: none">• A PC,• A Neutral Point Clamped Inverter (NPC) inverter grid- on/off,• An experimental platform,• A Signal Conditioning Block➤ CHV-25P/500 card,➤ A Low-pass filter,• An NI PCI-6229 Signal Acquisition Block,	10	[18]	<ul style="list-style-type: none">• A PC,• A load resistor,• A current transformer,• A sensing resistor,• NI PXIe-1017 Touch Screen Monitor,• A TB-4300C terminal block,• A Tektronix TDS2012DSO,• An HL-610S programmable AC power supply.	9
[12]	<ul style="list-style-type: none">• A PC,• A 3-Phase Power Analyser with probes.	10	[19]	<ul style="list-style-type: none">• A PC,• Tensorflow in DELL-Precision-7920 Tower with Quadro P6000 GPU,• Python.	10

REFERENCES

- [1] IEEE Power and Energy Society, *IEEE Recommended Practice for Monitoring Electric Power Quality*, vol. 1995, no. 1. 2009.
- [2] IEEE Power & Energy Society, *2010-1459-IEEE Standard Definitions for the Measurement of Electric Power Quantities Under Sinusoidal, Nonsinusoidal, Balanced, or Unbalanced Conditions*. 2010.
- [3] I. Standard and N. Internationale, “IEC Standard 61000-4-7: General guide on harmonics and interharmonics measurements and measuring instruments for power supply networks and attached devices used for the measurements,” 2008.
- [4] I. Power and E. Society, *IEEE Recommended Practice — Adoption of IEC 61000-4-15 : 2010 , Electromagnetic compatibility (EMC)— Testing and measurement techniques — Flickermeter — Functional and design specifications*, no. October. 2011.
- [5] International Electrotechnical Commission, “IEC Standard 61000-4-30: Testing and measurement techniques - Power quality measurement methods,” vol. 2003, p. 90, 2003.
- [6] D. Granados-Lieberman, M. Valtierra-Rodriguez, L. A. Morales-Hernandez, R. J. Romero-Troncoso, and R. A. Osornio-Rios, “A Hilbert transform-based smart sensor for detection, classification, and quantification of power quality disturbances,” *Sensors (Switzerland)*, vol. 13, no. 5, pp. 5507–5527, 2013.
- [7] U. Singh and S. N. Singh, “Application of fractional Fourier transform for classification of power quality disturbances,” *IET Sci. Meas. Technol.*, vol. 11, no. 1, pp. 67–76, 2017.
- [8] T. Yalçın, “Akıllı Şebekelerde Güç Kalitesi Bozukluklarının İşaret İşleme Yöntemleriyle Tanısı Program Kodu : 1002 Proje No : 114E919 Proje Yürütücüsü : Turgay Yalçın Danışman :,” 2016.
- [9] R. Narayanaswami, D. Sundaresan, and V. Ranjan Prema, “The Mystery Curve: A Signal Processing Based Power Quality Disturbance Detection,” *IEEE Trans. Ind. Electron.*, vol. 68, no. 10, pp. 10078–10086, 2021.
- [10] S. De and S. Debnath, “Real-time cross-correlation-based technique for detection and classification of power quality disturbances,” *IET Gener. Transm. Distrib.*, vol. 12, no. 3, pp. 688–695, 2017.
- [11] Y. Liu, T. Jin, M. A. Mohamed, and Q. Wang, “A Novel Three-Step Classification Approach Based on Time-Dependent Spectral Features for Complex Power Quality Disturbances,” *IEEE Trans. Instrum. Meas.*, vol. 70, 2021.
- [12] J. Liu, H. Song, H. Sun, and H. Zhao, “High-Precision Identification of

- Power Quality Disturbances under Strong Noise Environment Based on FastICA and Random Forest,” *IEEE Trans. Ind. Informatics*, vol. 17, no. 1, pp. 377–387, 2021.
- [13] S. Das, A. K. Pradhan, A. Kedia, S. Dalai, B. Chatterjee, and S. Chakravorti, “Diagnosis of Power Quality Events Based on Detrended Fluctuation Analysis,” *IEEE Trans. Ind. Electron.*, vol. 65, no. 9, pp. 7322–7331, 2018.
- [14] L. Pan, Z. Han, X. Wenxu, and J. Qingquan, “A Fast Adaptive S-Transform for Complex Quality Disturbance Feature Extraction,” *IEEE Trans. Ind. Electron.*, vol. 70, no. 5, pp. 5266–5276, 2022.
- [15] X. Xiao and K. Li, “Multi-Label Classification for Power Quality Disturbances by Integrated Deep Learning,” *IEEE Access*, vol. 9, no. Vmd, pp. 152250–152260, 2021.
- [16] C. Iturrino-garcía *et al.*, “An Innovative Single Shot Power Quality Disturbance Detector Algorithm,” vol. 71, 2022.
- [17] S. Karasu and Z. Saraç, “Classification of power quality disturbances by 2D-Riesz Transform, multi-objective grey wolf optimizer and machine learning methods,” *Digit. Signal Process. A Rev. J.*, vol. 101, p. 102711, 2020.
- [18] C. Cui, Y. Duan, H. Hu, L. Wang, and Q. Liu, “Detection and Classification of Multiple Power Quality Disturbances Using Stockwell Transform and Deep Learning,” *IEEE Trans. Instrum. Meas.*, vol. 71, pp. 1–12, 2022.
- [19] G. Feng and K. W. Lao, “Wasserstein Adversarial Learning for Identification of Power Quality Disturbances with Incomplete Data,” *IEEE Trans. Ind. Informatics*, vol. PP, no. Xx, pp. 1–10, 2023.

Chapter 23

A Novel Method for the Analysis of Multiscale Fracture Problems with Energy Density Concepts

Murat SARIBAY ¹

¹ Department of Mechanical Engineering, Istanbul Bilgi University, Eyupsultan, Istanbul, Turkey, 34060, murat.saribay@bilgi.edu.tr, ORCID: 0000-0002-4265-0488

ABSTRACT

Multiscale modeling has recently been a matter of interest for the reliability of engineering structures. These problems might become more interesting if flaws exist in the model. Investigation of multiscale fracture problems necessitates using a suitable parameter for the analysis of examples with cracked structures. One of the well-known parameters for the solution of fracture problems, i.e., energy release rate, is mono scale. However, a pseudo transitional energy release rate was defined to address the cross-scaling properties of this parameter. On the other hand, relying on the determination of energy release rates for multiscale fracture analysis might come up with a potential drawback. In a numerical fracture solution in which energy release rates are sought, there is the possibility of obtaining negative values which is not a real physical situation. Hence, a positive definite parameter, called energy density function, can be a better alternative for the crack output. In addition, energy release rates can also be given as a function of energy density functions.

Energy densities may be in the form of local or global quantities which were described in SED (strain energy density) theory in detail. Furthermore, these functions may be applied to both dissipative and non-dissipative systems. Therefore, details related to local and global energy densities must be well understood for conservative and non-conservative problems. In that way, an accurate transition between energy density and energy release rate concepts can be accomplished. It should also be noted that one of the major challenges in multiscale analysis is concerned with bridging fine and coarse scale behaviors. Well known classical fracture theories were mostly derived with the consideration of only macroscale levels. In addition, various developments that have been demonstrated in the literature for the analysis of macroscopic cracks have not been implemented in multiscale problems yet. This study intends to make a valuable contribution to the current topic by introducing a new approach that enables the investigation of multiscale fracture problems.

Keywords: Local and global energy densities, Pseudo energy release rate, Multiscale fracture

1. Introduction

Strain energy density (SED) approach [1] for the solution of fracture mechanics problems has been an effective tool since 1970s. The advantages of this theory over classical approaches are apparent. For instance, SED theory can deal with crack propagation phenomenon without using any additional theorems. Besides, a challenging problem in fracture mechanics, i.e., the analysis of cracks under mixed-mode loading conditions [2], can easily be handled with this theory. As an addition to that, notable studies [3, 4] showed that it can be applied to the solution of multiscale problems with some limitations. Recently, this has been a popular subject for researchers working in this field.

A series of multiscale problems were solved and given in [5, 6]. They analytically derived the necessary equations for the analysis of multiscale problems by using representational volume elements (RVEs). The name of this procedure was ‘computational homogenization’. Being a good start-up example for the solution of these types of problems, the methodologies lacked a couple of significant additions. First, they were only derived for micro-macro scales transition. Besides that, only stress and strain fields were defined, with no apparent derivations included for any type of fracture parameters. Application of computational homogenization for multiscale cracked structures was successfully performed in [7, 8] with detailed theoretical explanations. Another computational procedure was given in [9], which presented a modified polynomial dimensional decomposition method for stochastic multiscale fracture analysis of functionally graded materials. In [10], numerical and experimental methods were used to demonstrate microscale and mesoscale investigation of a two-dimensional cracked three-point bending asphalt mixture beam. As an outstanding development, the computational development required for the analysis of multiscale fracture problems with the inclusion of time-dependent loading was explained in [11]. Moreover, a recent general summary for various multiscale solution techniques of fracture related problems was given in [12]. Other notable studies in multiscale fracture can be found in [13-18]. The number of significant works performed in this field has substantially increased in the last decade but there is still much more to contribute.

Positive definite local and global energy density functions in SED theory were defined in [19, 20] and it was shown that proximity of these functions in space is the decisive factor for the determination of fracture stability. However, the interactions between these two functions could further be explored and shown in detail for developing a new methodology regarding the solution of multiscale problems. A unique feature of this investigation may be related to the conservative and non-conservative energy densities. It should also be noted that

the energy density approach used in the literature for the solution of fracture mechanics problems has mostly been associated with non-dissipative systems. Besides, there are also a few studies which concentrate on dissipative mechanisms by using SED theory. For the case of a conservative or non-dissipative system, the values of available local and global energy densities are expected not to suffer from any loss. On the other hand, if the system is a dissipative one, then the local and global energy densities cannot be treated as reversible parameters anymore. As a result, available energy densities will be less than their corresponding values for the initial state. Non-dissipative systems are analyzed with the aid of energy density functions in [21, 22] and details for dissipative energy densities are given in [1, 23].

In contrast to the positive definiteness of the energy density function, calculation of energy release rates might involve a specific risk for numerical analysis. This risk is associated with possible negative values for energy release rate values as the outcome of the computation for fracture output. Physically speaking, negative energy release rates represent a ‘closed crack’ form, which indicates a partial or full contact between crack surfaces. For example, if the problem includes a crack growth phenomenon, this situation can be misleading for the sake of the analysis. Therefore, energy density factor solutions may be more reliable in such cases. A common example that gives negative energy release rate results is the models with piezoelectric materials. Some fracture studies involving piezoelectricity are given in [24-30], mostly comparing energy density and energy release rate solutions. They emphasized the differences between the results of these two parameters under various conditions for poling direction, permeability, and BCs.

Fracture parameters can be computed with the aid of modern computational procedures that are available to the users. A Fortran 90 software, called FRAC3D, was initially developed [31] at Lehigh University ME&M Department and has been a remarkable finite element program for the solution of fracture mechanics problems with high complexity (in terms of analysis type, loading, material behavior or geometry). Following that, this program was further extended to analyze transient fracture problems [32]. FRAC3D benefits from special enriched elements that account for the singularities at the crack tip. A newer version of this finite element (FE) code has recently been developed [33], and it includes the computation of SED theory parameters in addition to the determination of classical fracture output such as the energy release rate and J-integral.

In this study, fundamentals of energy density functions will be given initially. Following that, conservative and non-conservative cases will be described in detail for local and global energy densities. Definition of pseudo energy release

rate in multiscale approach will also be presented. Verification of conservative energy densities will be demonstrated with the aid of a computational FE program. As the final task, an overall plan for the proposed approach will be stated in the conclusion part.

2. Definitions of local and global energy densities

For an isotropic material that behaves linear elastically, the volume energy density dW/dV can be given as

$$\frac{dW}{dV} = \int_0^\epsilon \sigma_{ij} d\epsilon_{ij} \quad (1)$$

where σ_{ij} and ϵ_{ij} are the components of stress and strain tensors. The right-hand side of Eq. (1) specifies the area under the true stress – true strain curve.

Significance of the energy density function given in Eq. (1) can be better understood with the aid of two theorems that were originally postulated by Sih [1]:

Failure site: Locations of yielding and fracture coincide with the maximum of the relative maximums of dW/dV (dW/dV_{\max}^{\max}) and maximum of the relative minimums of dW/dV (dW/dV_{\min}^{\max}), respectively.

Threshold condition: When dW/dV_{\max}^{\max} reaches its critical value, failure initiation by yielding occurs. Similarly, there is a critical value for dW/dV_{\min}^{\max} which controls failure by fracture.

As these two theorems dictate, the strain energy density function determines the location of the failure (yielding or fracture), and the intensity of their corresponding values specifies whether the failure will be seen or not. Besides these theorems, there should be a criterion that governs the stability of a fractured part. Unstable fracture is a phenomenon that is not desired for the structural integrity of the components. For this purpose, Sih [1] defined two distinctive notions for dW/dV values in a medium, i.e., global and local. In Fig.1, coordinate systems for the extraction of local (r_j, θ_j) and global (R, θ) values of dW/dV are given. Global energy densities possess single values for every location in a structure, which are calculated based on the global coordinate system. However, local dW/dV values are determined by referring to the coordinate systems that are defined at multiple points in a medium. There is one significant matter that should be emphasized regarding the definitions of local and global energy densities; at each location in a system, there is only one global value for the energy density function. In addition, local dW/dVs simply correspond to the values of energy densities in specific regions of the structure. These regions may

even be in the form of infinitesimal volumes (or surfaces for plane strain problems) compared to the overall dimensions of the global system.

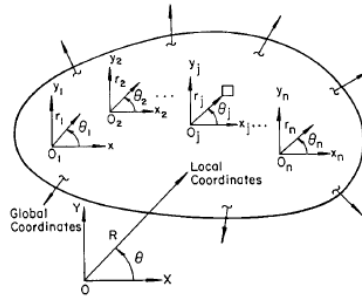


Figure 1. Local and global energy densities [1].

The energy densities were presented in global and local variations considering the following argument: A global instability should always be preceded by a local failure, and the distance between the maximum of minimum values for global and local energy densities gives a clear insight about the overall stability of the system. Besides, this distance can also give an idea about fracture behavior of the entire structure. This may be particularly important for multi-component structures whose stability may be heavily influenced by the local failure of individual parts. For a more detailed explanation of the current subject, [19] and [20] are highly referenced. Examples given in those studies are very helpful to understand this phenomenon.

The concept of energy density theory can further be explored by restating the energy density function given in Eq. (1). To calculate the energy density for any point in a system, the stress components for a unit volume material at that specific location should be known. This can be better shown as

$$\frac{dW}{dV} = \frac{1}{2E} (\sigma_{xx}^2 + \sigma_{yy}^2 + \sigma_{zz}^2) - \frac{\nu}{E} (\sigma_{xx}\sigma_{yy} + \sigma_{yy}\sigma_{zz} + \sigma_{zz}\sigma_{xx}) + \frac{1+\nu}{E} (\tau_{xy}^2 + \tau_{yz}^2 + \tau_{zx}^2) \quad (2)$$

Apparently, the energy density function can directly be computed once the material properties of the structure and stress components at a point in the system are available.

3. Conservative energy densities for non-dissipative systems

The energy criterion dictates that a crack will start to propagate once the energy required for a crack to grow is sufficient to overcome the resistance of the material. During crack growth, an amount of elastic strain energy is dissipated

due to the creation of a new surface. This process is quantified with the energy release rate, or the change in potential energy within crack surface area for a linear elastic material. Energy release rate can simply be interpreted with a central through crack length of $2a$ under remote tension. For the right end crack tip, energy release rate can be expressed as the difference of energy density states (for a propagated crack) by [3]

$$G = \frac{1}{2} \lim_{\Delta a \rightarrow 0} \frac{W(a+\Delta a) - W(a)}{\Delta a} = \frac{1}{2} \frac{\Delta W}{\Delta a} \quad (3)$$

Note that Eq. (3) is evaluated assuming constant plate thickness (h), since the original form of this equation has the term $\Delta W/\Delta A$, and surface area is determined from $\Delta A = \Delta a \cdot h$.

The determination of the energy release rate in Eq. (3) requires the assumption of a unit crack extension. To relate this phenomenon with a non-dissipative system where energy densities are conserved, the following comment is to be understood in an accurate manner: 'a conservative medium should recover to its original state as being a non-dissipative system'. To apply this notion to the energy densities given in Eq. (3), consider the initial state of a crack with the length of a_1 , and propagate the crack to a subsequent length as a_2 , i.e.,

$$G_{a_1 \rightarrow a_2} = \frac{1}{2} \frac{W_{a_2} - W_{a_1}}{a_2 - a_1} \quad (4)$$

For a conservative system, if state 2 is brought back to initial state (geometrically) with the aid of any crack closure methods, then the following relation can be expressed in a discrete form by denoting the final state with a_1^* :

$$W_{a_1} = W_{a_1^*} \quad (5)$$

Eq. (5) is a significant checkpoint to see whether the medium is a non-dissipative system or not for a crack propagation problem.

To demonstrate the relation between the global energy density function per unit volume $(dW/dV)^g$ and the total energy density W_T , the following equation can be given:

$$W_T = \int \left(\frac{dW}{dV} \right)^g dV \quad (6)$$

which may be determined using the stress components at each point (Eq. (2)) and the result being for the total volume of the entire structure. Note that these stress components are taken w.r.t. the global coordinates (R, θ) shown in Fig. 1. Combination of Eqs. (5) and (6) yields to the final form for a conservative system with global energy densities:

$$\left(\int \left(\frac{dW}{dV} \right)^g dV \right)_{a1} = \left(\int \left(\frac{dW}{dV} \right)^g dV \right)_{a1}^* \quad (7)$$

A similar approach may be useful to depict the conservation of total energy density obtained by the superposition of local energy densities. Local coordinate systems are shown in Fig. 1, i.e., r_j and θ_j . An important reminder is inevitable at this point; determination of the local energy density functions at each local coordinate system requires splitting up the entire structure to smaller regions or elements. Besides that, the borders between these regions should not contain any point of interest. This is critical since the energy density function dW/dV should be unique and calculated only once for each point in a system. Under these circumstances, total energy density for a given region that depends on the local energy density functions $((dW/dV)^l)$ becomes

$$W_j = \int \left(\frac{dW}{dV_j} \right)^l dV_j \quad (8)$$

In Eq. (8), $(dW/dV_j)^l$ values are evaluated w.r.t. the local coordinates (r_j , θ_j) as shown in Fig.1. For the next step, total energy density for the entire structure may be defined as the summation of the local regions' total energy densities as

$$W_T = \sum_{j=1}^n W_j \quad (9)$$

where the entire system is composed of 'n' sub-regions.

As it was done with the global energy densities for the demonstration of conservative systems and taking Eqs. (8-9) into account, the basic relation (including local energy densities) for a non-dissipative system which assumes a unit crack extension followed by closure can be stated as

$$\left(\sum_{j=1}^n \int \left(\frac{dW}{dV_j} \right)^l dV_j \right)_{a1} = \left(\sum_{j=1}^n \int \left(\frac{dW}{dV_j} \right)^l dV_j \right)_{a1}^* \quad (10)$$

Eq. (10) should be satisfactory to ensure a non-dissipative system.

Finally, the following equations can be given considering the relations between global and local energy densities:

$$\left(\int \left(\frac{dW}{dV} \right)^g dV \right)_{al} = \left(\sum_{j=1}^n \int \left(\frac{dW}{dV_j} \right)^l dV_j \right)_{al} \quad (11)$$

$$\left(\int \left(\frac{dW}{dV} \right)^g dV \right)_{al}^* = \left(\sum_{j=1}^n \int \left(\frac{dW}{dV_j} \right)^l dV_j \right)_{al}^* \quad (12)$$

4. Non-conservative energy densities for dissipative systems

For a non-conservative system, the energy density function can be updated with the following relation [20]:

$$\left(\frac{dW}{dV} \right)^* = \left(\frac{dW}{dV} \right) - \left(\frac{dW}{dV} \right)_p \quad (13)$$

The term $(dW/dV)^*$ in Eq. (13) refers to the available energy density and $(dW/dV)_p$ is the dissipated energy density which is a measure of irreversibility. Dissipated energy density is zero for conservative systems, and for non-conservative ones it could be given as

$$\left(\frac{dW}{dV} \right)_p > 0 \quad (14)$$

The meaning of dissipated energy density can be better understood with the aid of the true stress – true strain graph shown in Fig. 2.

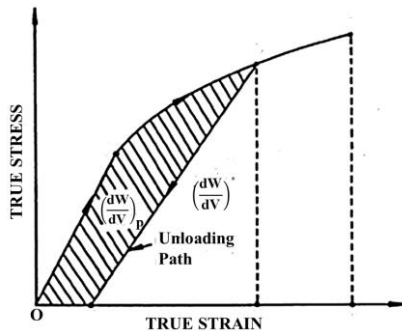


Figure 2. True stress – true strain graph for a dissipative system [20].

In Fig. 2, shaded area corresponds to the dissipated energy density, and the available energy density is also shown.

Application of the concept demonstrated in previous section, in other words, reinstating the crack to its initial length after crack extension, could be modified for dissipative systems. So, Eq. (5) should be expressed in a different form to demonstrate the change in total energy density between the initial and final states of a non-conservative system as

$$W_{a1} = W_{a1}^* + (W_p)_{a1 \rightarrow a1}^* \quad (15)$$

in which $(W_p)_{a1 \rightarrow a1}^*$ takes the irreversibility during crack extension-recovery stages into account. Furthermore, if Eq. (15) is restated in terms of the global energy densities within a system, then it should take the following form:

$$\left(\int \left(\frac{dW}{dV} \right)^g dV \right)_{a1} = \left(\int \left(\frac{dW}{dV} \right)^g dV \right)_{a1}^* + \left(\int \left(\frac{dW}{dV} \right)^g dV \right)_p_{a1 \rightarrow a1}^* \quad (16)$$

where the second term on the right-hand side will take all dissipative effects into account for the entire system during state changes in crack geometry, i.e., from $a1 \rightarrow a2$ and $a2 \rightarrow a1^*$. In other words, the following relation will hold for the entire system:

$$\left(\int \left(\frac{dW}{dV} \right)^g dV \right)_p_{a1 \rightarrow a1}^* > 0 \quad (17)$$

Considering 'n' independent local regions, a representation demonstrating the irreversibility during crack extension-recovery stages can be given with the local energy densities as

$$\left(\sum_{j=1}^n \int \left(\frac{dW}{dV_j} \right)^l dV_j \right)_{a1} = \left(\sum_{j=1}^n \int \left(\frac{dW}{dV_j} \right)^l dV_j \right)_{a1}^* + \left(\sum_{j=1}^n \int \left(\frac{dW}{dV_j} \right)^l dV_j \right)_p_{a1 \rightarrow a1}^* \quad (18)$$

and the additional term for the local case will also be positive and can be shown by

$$\left(\sum_{j=1}^n \int \left(\frac{dW}{dV_j} \right)^l dV_j \right)_p_{a1 \rightarrow a1}^* > 0 \quad (19)$$

A significant remark should be made at this point. While relating the local and global energy densities for conservative systems (Eqs. (11-12)), superpositions of the local contributions from each sub-region were sufficient to determine the total energy density. On the other hand, in a dissipative system, even though the total energy density loss can be found by adding losses that are associated with each sub-region, the analyst should be careful while considering losses for different sub-regions. It may be anticipated that corresponding losses for sub-regions may vary depending on the location under interest.

Calculation of the energy release rate shown in Eq. (4) for conservative systems can also be updated in the presence of irreversibility. In such a case, if the available energy density for state 2 is denoted as W_{a2}^{nc} , then the energy release rate under the influence of non-conservative effects can be shown as

$$(G_{a1 \rightarrow a2})^{nc} = \frac{1}{2} \frac{W_{a2}^{nc} - W_{a1}}{a_2 - a_1} \quad (20)$$

and the relation between the energy release rates for conservative and non-conservative cases of a specific problem can be given by

$$G_{a1 \rightarrow a2} = (G_{a1 \rightarrow a2})^{nc} + (G_{a1 \rightarrow a2})_I, \quad W_{a2}^{nc} < W_{a2} \quad (21)$$

where $G_{a1 \rightarrow a2}$ is the energy release rate for the conservative case, $(G_{a1 \rightarrow a2})_I$ is the difference in energy release rate due to irreversibility and W_{a2} is the energy density level for crack state 2 of the conservative model.

5. Pseudo energy release rate in multiscale approach

The energy release rate formula presented in Eq. (3) involves the ratio of energy density differences over a presumed crack extension. In previous sections, the concentration was mostly related to the energy density concepts. On the other hand, cross-scaling of energy release rates can be achieved through the crack extension parameter Δa . In Eq. (3), the limit $\Delta a \rightarrow 0$ is approachable but can not be attained. The matter for choosing a suitable size of Δa becomes a practical issue in a numerical analysis. Furthermore, all quantities in Eq. (3) are determined at mono scale, the only exception being the interpretation of the limit $\Delta a \rightarrow 0$.

Definition of a pseudo energy release rate should be useful at this point to provide transition between different scale levels [3]:

$$G^* = \frac{1}{2} \lim_{\Delta a_{ma} < \Delta a_{ma}} \frac{\Delta W_{ma}}{\Delta a_{ma}} = \frac{1}{2} \frac{\Delta W_{ma}}{\Delta a_{ma}} \quad (22)$$

Note that $\Delta a \rightarrow 0$ is replaced by $>\Delta a_{ma} <$ that restricts the extension near the crack tip level at a macro increment level. In addition, Eq. (22) can be considered as the rate change of global macro energy ΔW_{ma} with reference to a local macro crack segment Δa_{ma} . The intention of relating the pseudo energy release rate to a lower scale, such as micro, leads to an update in Eq. (22) by rewriting it as

$$G^* = \frac{1}{2} \frac{\Delta W_{ma}}{\Delta a_{mi}} \left(\frac{\Delta a_{mi}}{\Delta a_{ma}} \right) = G^{mi/ma} \left(\frac{\Delta a_{mi}}{\Delta a_{ma}} \right) \quad (23)$$

In this form given by Eq. (23), pseudo energy release rate can now be used for the transition from macro to micro scale.

In a fatigue problem for which the life span of the system is given as a function of years, cross-scaling could be realized by using a transitional crack length. Letting $a^{mi/ma}(t)$ be a transitional crack length function of time t with an initial value of $a^{mi/ma}(0)$, the following relation can be given:

$$a^{mi/ma}(t) = \left(\frac{\Delta a_{mi}}{\Delta a_{ma}} \right) a^{mi/ma}(0) \quad (24)$$

Combination of Eqs. (23-24) leads to the final relation for macro-micro translation involving pseudo energy release rate as

$$G^*/G^{mi/ma} = a^{mi/ma}(t)/a^{mi/ma}(0) \quad (25)$$

Application of the procedure explained by Eqs. (22) through (25) to the transition between other scales, such as micro-nano and nano-pico, yields to the expressions stated below:

$$G^*/G^{na/mi} = a^{na/mi}(t)/a^{na/mi}(0) \quad (26)$$

$$G^*/G^{pi/na} = a^{pi/na}(t)/a^{pi/na}(0) \quad (27)$$

Transitional functions $(a^{mi/ma}(t), a^{na/mi}(t), a^{pi/na}(t))$ shown in Eqs. (25) through (27) have significant roles concerning the reliability of pseudo energy release rate. As an example, following transitional crack length functions were given for 2024-T3 material with initial crack sizes of $a^{mi/ma}(0) = 2.4 \text{ mm}$, $a^{na/mi}(0) = 3e - 4 \text{ mm}$, and $a^{pi/na}(0) = 1e - 8 \text{ mm}$ [3]:

$$a^{mi/ma}(t) = 2.4 - 1678.57t + 1057.86t^2 - 282.254t^3 + 41.346t^4 - 3.59221t^5 + 0.185164t^6 - 52.4493e^{-4}t^7 + 63.0051e^{-6}t^8 \quad (28)$$

$$a^{na/mi}(t) = 3e^{-4} + 11277.3t - 12939.1t^2 + 6339.19t^3 - 1719.02t^4 + 278.651t^5 - 26.9996t^6 + 1.44788t^7 - 0.0331488t^8 \quad (29)$$

$$a^{pi/na}(t) = 1e^{-8} - 31.104e^{-4}t + 89.36e^{-3}t^2 - 1.0533t^3 + 6.8872t^4 - 28.3t^5 + 78.03t^6 - 149.927t^7 + 204.7t^8 - 199.79t^9 + 138.35t^{10} - 66.349t^{11} + 20.94t^{12} - 3.91t^{13} + 0.327t^{14} \quad (30)$$

More details on this subject can be found in [3, 4, 34], including the investigations that demonstrate scale effects on the reliability of the method.

6. A computational fracture analysis tool: FRAC3D program

Theoretical expressions given in previous sections for the current topic could be implemented to an existing computational tool. In that way, arguments given in previous sections can be verified. It should also be noted that computational analysis of fracture related problems involves the complexity associated with the singularities present at the crack tip. FRAC3D finite element software that was introduced in [31] was shown to be an effective tool for the solution of fracture problems. The main advantage of FRAC3D program over other software is its ability to obtain accurate results with a smaller number of elements around the crack region. Hence, computational times are greatly reduced by using this program. Most of the commercial software available in the literature benefits from having a lot of elements along the crack front. FRAC3D removes this necessity with its enriched element formulation.

The theory used in enriched element formulation is based on the incorporation of asymptotic displacement behavior directly into the crack tip elements. Enriched elements include additional degrees of freedom to account for the stress intensity factors along the crack front. Fig. 3 illustrates the detailed formulation for the displacements of local enriched elements. Here, in addition to the isoparametric FEM notation for the regular elements, three more terms are used to determine stress intensity factors. F, G and H are the asymptotic functions that are computed at a location (ξ, η, ρ) in an element. In FRAC3D's enriched methodology, there are also transition elements which are located between enriched and regular elements. Z_0 in Fig. 3 is a 'zeroing' function which has a value of '0' for regular elements and '1' for enriched elements. For transition elements, Z_0 varies between '0' and '1'. More information on this subject can be found in [31] and [32].

$$\begin{aligned}
 u(\xi, \eta, \rho) &= \sum_{j=1}^r N_j(\xi, \eta, \rho) u_j + Z_0(\xi, \eta, \rho) \{ \mathbf{K}_I(\Gamma) F_1(\xi, \eta, \rho) + \mathbf{K}_{II}(\Gamma) G_1(\xi, \eta, \rho) + \mathbf{K}_{III}(\Gamma) H_1(\xi, \eta, \rho) \} \\
 v(\xi, \eta, \rho) &= \sum_{j=1}^r N_j(\xi, \eta, \rho) v_j + Z_0(\xi, \eta, \rho) \{ \mathbf{K}_I(\Gamma) F_2(\xi, \eta, \rho) + \mathbf{K}_{II}(\Gamma) G_2(\xi, \eta, \rho) + \mathbf{K}_{III}(\Gamma) H_2(\xi, \eta, \rho) \} \\
 w(\xi, \eta, \rho) &= \sum_{j=1}^r N_j(\xi, \eta, \rho) w_j + Z_0(\xi, \eta, \rho) \{ \mathbf{K}_I(\Gamma) F_3(\xi, \eta, \rho) + \mathbf{K}_{II}(\Gamma) G_3(\xi, \eta, \rho) + \mathbf{K}_{III}(\Gamma) H_3(\xi, \eta, \rho) \}
 \end{aligned}$$

Regular elements
Enriched elements

Figure 3. Enriched displacements at a location in an element [33].

FRAC3D program's crack related output involves parameters such as stress intensity factors, energy release rates and energy density functions. As the next step, having the capability for the analysis of multiscale fracture problems with macro-micro, micro-nano and nano-pico transitions is necessary.

7. Numerical Example: Verification of conservative energy densities

To illustrate the concept given by Eq. (5) for conservative systems, a simple example will be demonstrated in this section. Computations were performed by using FRAC3D finite element program.

Fig. 4 shows an edge cracked plate subjected to uniform static loading. Global coordinate system (R, θ) is shown with its origin at the crack tip. Plane strain conditions are enforced. It should also be emphasized that LEFM rules are valid, in other words, plastic zone is relatively small compared to the crack dimensions. The origin of the coordinate system is placed at the initial crack tip (state 1, crack length a_1). Following values are used for the loading and material properties: $\sigma = 83$ MPa, $E = 200$ GPa and $\nu = 0.3$. Plate thickness is 10 mm. Crack lengths a_1 (50 mm) and a_2 (55 mm) correspond to the initial and extended crack states, respectively. Final crack length is a_1^* (**50 mm**) after reinstating initial crack geometry. The crack is simply expected to grow in $\theta = 0$ direction for this geometry under current loading conditions.

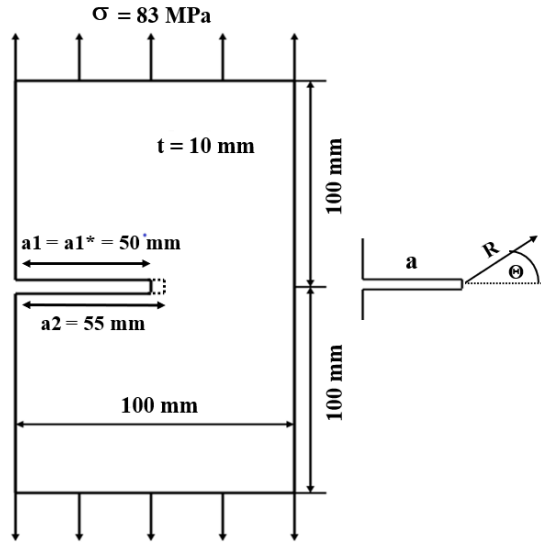


Figure 4. An edge cracked plate under remote loading.

FE model for the current example is depicted in Fig. 5. A mesh with 1536 quadratic hexahedron elements along with 8997 nodes is used for the model with initial crack length. For the case of propagated crack, entire FE mesh is kept the same, however, crack is extended for another element (on 2D plane) at $\theta = 0$, resulting in a slight increase in total number of nodes. To reinstate the system back to the initial state ($a1^*$), crack surface for one element that corresponds to $(a2 - a1)$ is closed. This could be realized by tying the DOFs for the nodes that are located on that specific surface defined by two elements: one at the top of the crack surface and the other one at the bottom. By using this methodology, the nodes on the corresponding surface move together and hence they cannot be treated as a free crack surface. In other words, the crack is partially closed, and the initial state is reached. Geometrical illustrations for three different states of crack surface can be seen in Fig. 5.

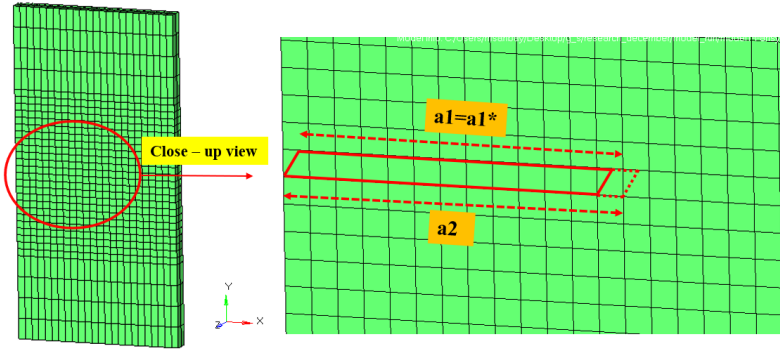


Figure 5. FE mesh and geometrical states for the crack surfaces of the edge cracked plate.

Fig. 6 and Fig. 7 depict the global energy densities of the edge cracked plate for $\theta = 0$ and 45 degrees, respectively. Results for two different crack states are given for demonstration, i.e., $a1$ and $a1^*$. Note that the coordinate system shown in Fig. 4 is used. Apparently, energy densities for the final state of the crack geometry, $a1^*$, are in good agreement with the same values for the initial crack state ($a1$). This is an anticipated outcome for a non-dissipative system as explained in Section 4. In addition, global energy densities have a minimum at $\theta = 0$, whereas the same comment cannot be made for the results at $\theta = \pi/4$. These minimums have special meanings in SED theory as discussed in Section 3.

If corresponding energy densities for the other θ values of both crack states are to be checked, similar outcome (as in Fig. 6 and Fig. 7) is anticipated. Hence, all the points in this system should have identical energy densities when the crack geometry is brought back to its initial state. That means the total energy density will remain the same, which is an indication of a conservative system. Besides that, all results given below for the energy densities can be treated as ‘global’, since they are obtained with reference to a single coordinate system. If local coordinate systems were considered and the energy densities for multiple regions were superposed, then the resulting value is expected to be a good approximation to the total energy density determined from the global analysis.

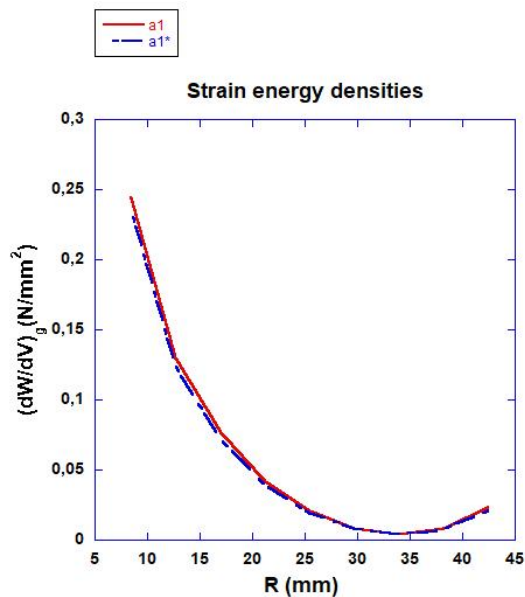


Figure 6. Global energy densities wr.t. the distance (R) from the origin at $\theta = 0$ for the edge cracked plate. Results correspond to the crack states $a1$ and $a1^*$.

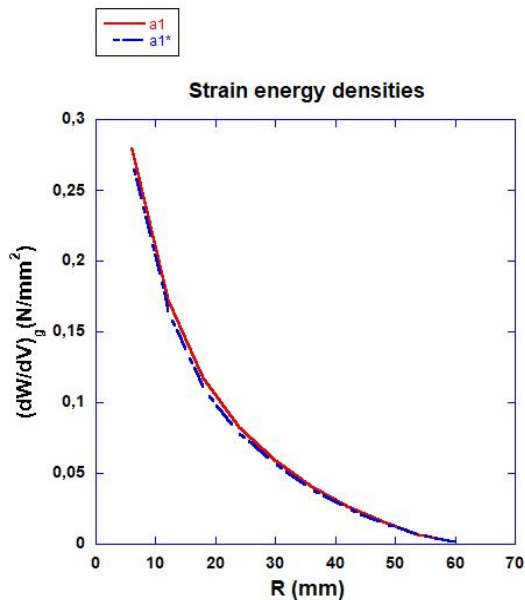


Figure 7. Global energy densities wr.t. the distance (R) from the origin at $\theta = \pi/4$ for the edge cracked plate. Results correspond to the crack states $a1$ and $a1^*$.

8. Concluding Remarks

Taking the discussions stated in previous sections into account, a novel method for the analysis of multiscale fracture problems can be proposed. Following arguments can be given to describe the methodology to investigate the problem at hand:

- Multiscale modeling and analysis of crack problems require a special technique which differs from traditional macroscale approaches. For instance, well-known energy release rate formulations cannot be directly used. Furthermore, possible negative energy release rate values that might be seen during fracture computations introduce additional complexity to the solution procedure. In such cases, energy density function could be a better alternative due to its positive definiteness.
- Pseudo transitional energy release rate (Eq. (22)) provides cross-scaling in a multiscale problem. Energy release rates can be linked between different scale levels once energy densities and transitional crack lengths are determined (Eqs. (23-24)). Moreover, calculations for energy density parameters are not expected to be scale sensitive. Understanding energy density concepts and accurate computation of this parameter are both crucial for the current objective.
- Fundamentals of strain energy density (SED) approach are given in detail. Global and local energy densities and the interaction between these two distinct parameters are significant to address fracture failure. Besides, it is also essential to comprehend conservative and non-conservative energy densities along with global and local definitions. A simple example of an edge cracked plate is given to demonstrate conservative behavior of energy densities.
- Features of FRAC3D finite element program are summarized along with its basics and advantages. From FE modeling point of view, special elements like representational volume elements (RVEs) can be developed for multiscale analysis. Corresponding implementations to this software can be done to accomplish the current task.
- Computation of energy density functions can already be performed by using FRAC3D program. An overall methodology can be established to investigate multiscale fracture problems. Following the computation of global and local energy densities for conservative or non-conservative systems, pseudo transitional energy release rates can be calculated. It should be noted that this type of analysis also requires the determination of transitional crack lengths.

References

- [1] Sih, G.C., *Mechanics of fracture initiation and propagation: Surface and volume energy density applied as failure criterion*, First ed., Kluwer Academic Publishers, Boston, US, 1991.
- [2] Sih, G.C., Strain-energy-density factor applied to mixed mode crack problems, *Int J Frac.*, 10 (3):305-321, 1974.
- [3] Sih, G.C., Pseudo global energy released locally by crack extension involving multiscale reliability, *Theor Appl Frac Mech*, 55:52-59, 2011.
- [4] Sih, G.C., Crack tip mechanics based on progressive damage of arrow: Hierarchy of singularities and multiscale segments, *Theor Appl Frac Mech*, 51:11-32, 2009.
- [5] Pippan, R., Gumbsch, P., *Multiscale modeling of plasticity and fracture by means of dislocation mechanics*, Springer Wien, New York, pp. 336-403, 2010.
- [6] Guo, X., *Multiscale materials modeling: Fundamentals and applications*, Woodhead publishing, Cambridge, pp. 134-160, 2007.
- [7] Oliver, J., Caicedo, M., Roubin, E., Huespe, A.E., Hernandez, J.A., Continuum approach to computational multiscale modeling of propagating fracture, *Comp Meth Appl Mech Eng*, 294:384-427, 2015.
- [8] Oliver, J., Caicedo, M., Huespe, A.E., Hernandez, J.A., Roubin, E., Reduced order modeling strategies for computational multiscale fracture, *Comp Meth Appl Mech Eng*, 313:560-595, 2017.
- [9] Rahman, S., Chakraborty, A., Stochastic multiscale fracture analysis of three-dimensional functionally graded composites, *Eng Frac Mech*, 78:27-46, 2011.
- [10] Yin, A., Yang, X., Yang, S., Jiang, W., Multiscale fracture simulation of three-point bending asphalt mixture beam considering material heterogeneity, *Eng Frac Mech*, 78:2414-2428, 2011.
- [11] Hewitt, S., Margetts, L., Shterenlikht, A., Revell, A., A massively parallel multiscale CAFÉ framework for the modelling of fracture in heterogenous materials under dynamic loading, *Adv Eng Soft*, 139:102737, 2020.
- [12] Budarapu, P.R., Rabczuk, T., Multiscale methods for fracture: A review, *J Ind Inst Sci*, 97 (3):339-376, 2017.
- [13] Gonzalez, C., Llorca, J., Multiscale modeling of fracture in fiber-reinforced composites, *Acta Mater*, 54:4171-4181, 2006.
- [14] Patil, R.U., Mishra, B.K., Singh, I.V., A multiscale framework based on phase field method and XFEM to simulate fracture in highly heterogeneous materials, *Theor Appl Frac Mech*, 100:390-415, 2019.
- [15] Friderikos O., Baranger, E., Ladeveze, P., Multiscale GFEM with

- superposition of crack enrichment functions driven by finite fracture mechanics: Theory, first computation and open problems, *Comp Struct*, 164:145-157, 2017.
- [16] Nguyen, V.P., Valls, O.L., Stroeve, M., Sluys, L.J., Computational homogenization for multiscale crack modeling. Implementational and computational aspects, *Int J Num Meth Eng*, 89 (2):192-226, 2012.
- [17] Talebi, H., Silani, M., Bordas, S., Kerfriden, P., Rabczuk, T., A computational library for multiscale modeling of material failure, *Comp Mech*, 53:1047-1071, 2014.
- [18] Rahimabadi, A.A., Kerfriden, P., Bordas, S., Scale selection in nonlinear fracture mechanics of heterogenous materials, *Phil Mag*, 95 (28-30):3328-3347, 2015.
- [19] Sih, G.C., Stability and integrity of mechanical joints in flight vehicles: local and global energy density, *Theor Appl Frac Mech*, 10:135-149, 1988.
- [20] Sih, G.C., Mechanics and physics of energy density theory, *Theor Appl Frac Mech*, 4:157-173, 1985.
- [21] Boulenuar, A., Benseddiq, N., Merzoug, M., A strain energy density theory for mixed mode crack propagation in rubber-like materials, *J Theor Appl Mech.*, 54 (4):1417-1431, 2016.
- [22] Fajdiga, G., Zafosnik, B., Determining a kink angle of a crack in mixed mode fracture using maximum energy release rate, SED and MTS criteria, *J Mult Eng Sci Tech (JMEST)*, 2 (1):356-362, 2015.
- [23] Sih, G.C., Energy absorption and dissipation associated with mass activation and deactivation for open systems, *Theor Appl Frac Mech*, 52:63-71, 2009.
- [24] Boldrini, C., Viola, E., Crack energy density of a piezoelectric material under general electromechanical loading, *J Theor Appl Frac Mech.*, 49:321-333, 2008.
- [25] Spyropoulos, C.P., Energy release rate and path independent integral study for piezoelectric material with crack, *Int J Sol Struct*, 41:907-921, 2004.
- [26] Lin, S., Narita, F., Shindo, Y., Comparison of energy release rate and energy density criteria for a piezoelectric layered composite with a crack normal to interface, *Theor Appl Frac Mech*, 39:229-243, 2003.
- [27] Zhang, P.W., Wu, H.P., Wang, B., Time-harmonic P-waves engulfing a rectangular limited-permeable crack in piezoelectric medium: Energy density and energy release, *Theor Appl Frac Mech*, 55:169-184, 2011.
- [28] Fang, Q.H., Feng, H., Liu, Y.W., Jiang, C.P., Energy density and release rate study of an elliptic-arc interface crack in piezoelectric solid under anti-plane shear, *Theor Appl Frac Mech*, 55:20-30, 2011.

- [29] Yu, M., Fang, Q.H., Liu, Y.W., Zeng, X., Screw dislocation and elliptic inhomogeneity of a confocal crack in magnoelectroelastic medium: Comparison of energy release rate and strain energy density, *Theor Appl Frac Mech*, 59:34-40, 2012.
- [30] Shindo, Y., Narita, F., Matsuda, T., Electric field dependence of the mode I energy release rate in single-edge cracked piezoelectric ceramics: effect due to polarization switching/dielectric breakdown, *Acta Mech*, 219:129-143, 2011.
- [31] Ayhan, A.O., Nied, H.F., Stress intensity factors for three-dimensional surface cracks using enriched finite elements, *Int J Num Meth Eng*, 54:899-921, 2002.
- [32] Saribay, M., Nied, H.F., Dynamic stress intensity factors for suddenly loaded structures using enriched finite elements, *Theor Appl Frac Mech*, 70:59-67, 2014.
- [33] Saribay, M., Local and global energy densities associated with welding residual stresses of cracked structures, *Theor Appl Frac Mech*, 108:102671, 2020.
- [34] Sih, G.C., Ideomechanics of transitory and dissipative systems associated with length, velocity, mass and energy, *Theor Appl Frac Mech*, 51 (3):149-160, 2009.

Chapter 24

A Review of the Experimental Studies on Analysis of Power Quality Disturbances

SİTKİ AKKAYA¹

¹ Asst. Prof. Dr.; Sivas University of Science and Technology, Department of Electrical and Electronics Engineering, sakkaya@sivas.edu.tr ORCID No: 0000-0002-3257-7838

ABSTRACT

A stable voltage with consistent frequency and amplitude is the most important thing for power systems. Some standards on power quality disturbances (PQDs) like IEEE 1159, IEEE 1459, IEC 61000 - 4 - 7, 61000 - 4 - 15, and 61000 - 4 - 30, and more are available. These standards set rules for the different parameters value of voltages while an arrangement of the PQDs with some limitations for the stability of the power systems. However, electrical power systems are sensitive to some disturbances that can lead to fluctuations in fundamental frequency and amplitude of voltage. These disturbances can emerge such as sag, swell, interruption, harmonics, flicker, interharmonics, and more. They can occur independently or in combination, and their effects on system components are both unpredictable and variable. That is, it is crucial to carry out a comprehensive analysis and examination of these disturbances. One of the main challenges in studying PQDs is the difficulty in obtaining real datasets due to the inherent nature of power systems and the random occurrence of events. Consequently, there is a growing demand for experimental studies to explore the subtleties of these disturbances. The objective of this particular study is to support and enhance research on PQDs by presenting a comprehensive compilation of suitable information alongside experimental setups for researchers specializing in this field. By providing access to this valuable resource, the study aims to facilitate further investigation and exploration of power quality disturbances, enabling researchers to gain deeper insights and develop effective strategies for addressing these issues.

Keywords: Power Systems, Power Quality Analysis, Power Quality Disturbances, PQA, PQD, Experimental Setup, Fundamental Frequency Variation, Fundamental Voltage Amplitude, Harmonics, Interharmonics, Sag, Swell, Interruption, Flicker, IEEE 1159, IEEE 1459, IEC 61000-4-7, IEC 61000-4-15, IEC 61000-4-30

1. INTRODUCTION

Maintaining a stable fundamental frequency and amplitude which are set at 50 Hz and 220 V_{rms} in Turkey is crucial for power systems. Instability in these parameters can lead to improper functioning of electrical devices, efficiency losses, and even serious damages. For instance, voltage swell can cause high voltage faults, voltage sags can result in the malfunctioning of sensitive electronic devices. Additionally, voltage interruptions can lead to energy losses and business continuity issues.

Some standards on power quality disturbances and analysis are available. One, IEEE 1159 defines power quality parameters and measurement methods, while IEEE 1459 focuses on meaningful interpretation of power system measurements. IEC 61000-4-7, IEC 61000-4-15, and IEC 61000-4-30 provide guidelines for testing and evaluating disturbances in power systems. EN 50160 also set some limits similar to other standards [1]–[5].

To effectively analyze power quality issues, it is important to definitions of various power quality disturbances, their causes, and their effects on power systems. The other important thing is real-time implementation or problem acquisitions to use for power quality analysis later. However, since the power systems are time-varying and the associated risks to human safety, obtaining such data directly can be challenging. Therefore, the utilization of an experimental setup becomes necessary for conducting investigations and acquiring data for power quality analysis. This study aims to address this need by presenting the most prevalent power quality phenomena and their corresponding experimental setups. The primary purpose of this study is to ensure a partial guide for researchers in the field of Power Quality Analysis (PQA). By providing a comprehensive overview of experimental setups on PQAs, this study aims to facilitate and support further research in this field.

This paper is organized as the following: In the second section, power quality phenomenons in power systems are given with definitions, causes, impacts, and illustrated images. Subsequently, experimental setups for power quality analysis utilized in the works of literature are presented in detail in 3rd section. In the final section, the summary and discussion of this study are yielded.

2. POWER QUALITY PHENOMENONS IN POWER SYSTEMS

In power systems, the most important phenomenons are fundamental frequency and amplitude. A pure sinusoidal signal which is modeled with Eq. 1 is desired in these systems. Fundamental frequency and amplitude symbolized with f_0 and A must be at 50 Hz and 220 V_{rms} in Turkey. However, these phenomenons are changed by some power quality disturbances like harmonics,

interharmonics, sag, swell, interruption, etc which are the most common disturbances. As defined in IEEE 1159, power quality disturbances have typical mathematical models with amplitude, frequency, and time characteristics at different ranges. These can emerge singular or multiple as flicker, harmonics, sag, swell, interruption, etc. Some of them are defined with models and time-series images as follows.

Fundamental Frequency Deviation & Voltage Amplitude Variation

Fundamental frequency and Voltage amplitude are symbolized with f_0 , and A in Eq. (1) as mentioned above. Variations of these are out of favor and can be led to destructive results. But the desired model of the power system Voltage must be like this equation.

$$v(t) = A \sin(2\pi f_0 t), \quad f_0 = 50 \text{ Hz}, A = 220 \text{ V}_{rms} \quad (1)$$

Harmonics

Harmonics are the most common disturbances and are available permanently in power systems. They must be degraded as well as possible. The highest level harmonics, 3^{rd} , 5^{th} , and 7^{th} are active and must be tracked continuously. According to these harmonics and the limitations based on the standards, a signal with harmonics is given in Eq. (2). $\alpha_3, \alpha_5, \alpha_7$ are the coefficients of the related harmonics. $v_1(t)$ is a time-series signal shown in Figure 1. In this figure and the rest of the study, the time scale is set to 0.2 sec.

$$v_1(t) = \sin(2\pi f_0 t) + \alpha_3 \sin(2\pi 3 f_0 t) + \alpha_5 \sin(2\pi 5 f_0 t) + \alpha_7 \sin(2\pi 7 f_0 t), \quad 0,05 \leq \alpha_3, \alpha_5, \alpha_7 \leq 0,5 \quad (2)$$

Interharmonics

Interharmonics are the most common disturbances and are available permanently in power systems like harmonics. They must be degraded as well as possible, too. The visible form of interharmonics is light flicker. Therefore, these are called together. According to the limitations based on IEC 61000-4-15, a signal with flicker is given as $v_2(t)$ with Eq. (3). $\alpha_{flicker}$ and $f_{flicker}$ are the amplitude and the frequency of flicker which is caused by 2 different interharmonics with the frequencies of $(f_0 - f_{flicker}, f_0 + f_{flicker})$ and the half amplitude of the flicker. $v_2(t)$ displays the flickered signal shown in Figure 2. It is clearly shown that there is a voltage fluctuation and also this led to fundamental frequency fluctuation in the field, too.

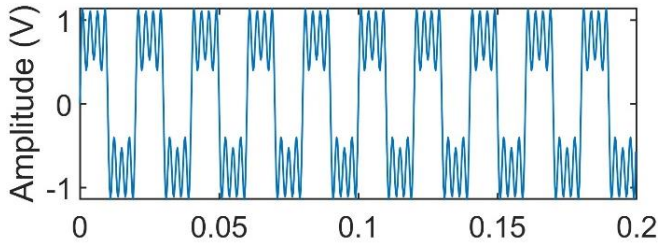


Figure 1: Harmonics

$$v_2(t) = [1 + \alpha_{flicker} \sin(2\pi f_{flicker} t)] \sin(2\pi f_0 t), \quad \begin{matrix} 0,05 \leq \alpha_{flicker} \leq 0,2794 \\ 1 \text{ Hz} \leq f_{flicker} \leq 25 \text{ Hz} \end{matrix} \quad (3)$$

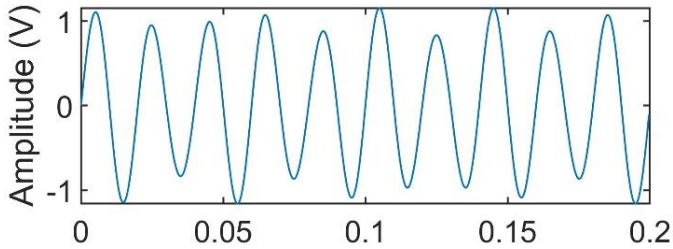


Figure 2: Flicker based on Interharmonics

Sag, Swell, and Interruption

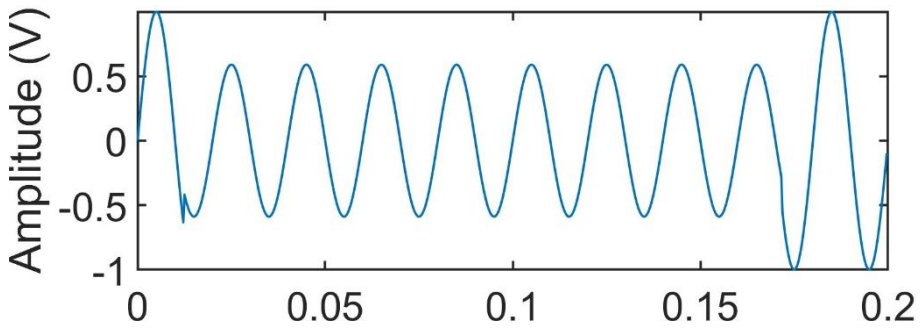
The other most common disturbances are sag, swell, and interruption which can be terminative for the power systems. These have mathematical models as Eq. 4, 5, and 6, respectively. These can change with given intervals according to the IEEE 1459 standard. Figure 3 indicates these PQDs.

$$v_3(t) = [1 - \alpha_{sag}(u(t - t_1) - u(t - t_2))] \sin(2\pi f_0 t), \quad \begin{matrix} T_0 = 1/f_0 \\ 0,1 \leq \alpha_{sag} \leq 0,9 \end{matrix} \quad (4)$$

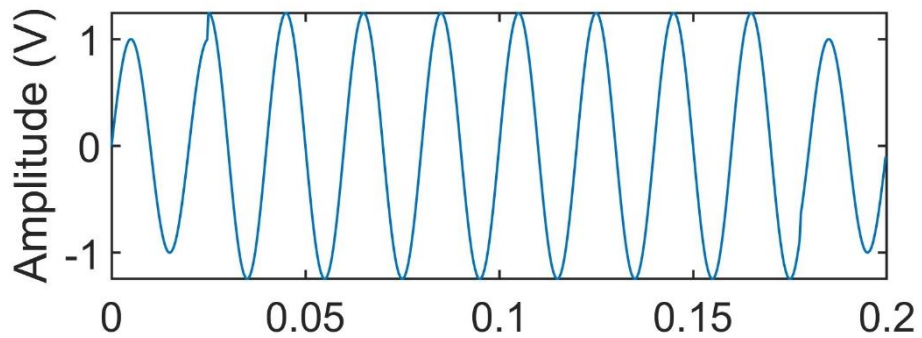
u : unit step function

$$v_4(t) = [1 + \alpha_{swell}(u(t - t_1) - u(t - t_2))] \sin(2\pi f_0 t), \quad 0,1 \leq \alpha_{swell} \leq 0,8 \quad (5)$$

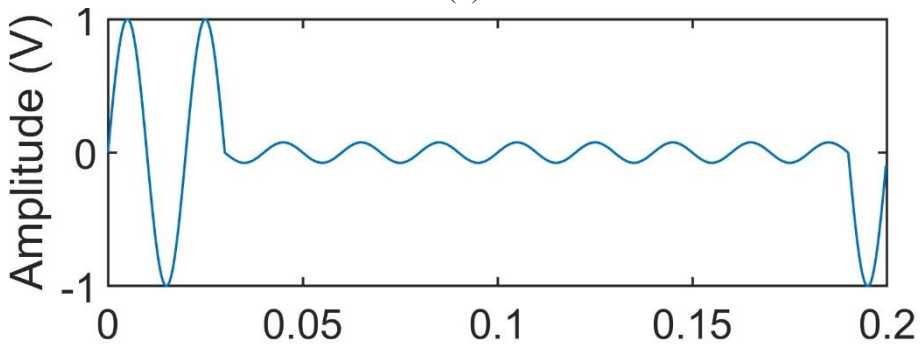
$$v_5(t) = [1 - \alpha_{interruption}(u(t - t_1) - u(t - t_2))] \sin(2\pi f_0 t), \quad \begin{matrix} 0,9 \leq \alpha_{interruption} \leq 1 \\ T_0 \leq t_2 - t_1 \leq 9T_0 \end{matrix} \quad (6)$$



(a)



(b)



(c)

Figure 3: Sag, Swell, and Interruption (a) Sag (b) Swell (c) Interruption

These disturbances are triggered by different devices or components. The impacts of these disturbances are due to the type of disturbances. Table 1 categorizes these disturbances with causes and impacts as the following.

Table 1: The Most Common Power Quality Phenomenons

CATEGORY	CAUSES	IMPACTS
Fundamental frequency variation	<ul style="list-style-type: none">• Arc furnaces• Extreme conditions of loading• Generation loss	<ul style="list-style-type: none">• Harmonic filters detuning• Motors run slower• Trivial most of the time
Voltage fluctuation	<ul style="list-style-type: none">• AC motor drives• Arc furnaces• Interharmonic current components• Motor starting• Welding furnaces	<ul style="list-style-type: none">• Flicker in different types of lamps• Light flicker
Harmonics	<ul style="list-style-type: none">• Industrial furnaces• Nonlinear loads• Transformers• Generators• Rectifier equipment• Converter sections of uninterruptible power supply (UPS),• Variable Frequency Drivers (VFDs)• Battery chargers• Welding furnaces• Arc furnaces	<ul style="list-style-type: none">• Maloperation of sensitive equipment and relays• Capacitor fuse or capacitor failures• Interruption of 3-phase operation• Generators overheating• Motors overheating• Telephone interference
Sag	<ul style="list-style-type: none">• Generation loss• Network overloading• Inductive loading• Local and remote faults• Poor power factor• Lack of var support• Switch on large loads	<ul style="list-style-type: none">• All equipment without backup supply facilities• Resetting of control system• Motor stalling/tripping• Sensitive equipment tripping
Interruption	<ul style="list-style-type: none">• Control malfunctions• CB tripping• Equipment failures• Power system faults	<ul style="list-style-type: none">• Computer shutdowns• Loss of supply to customer equipment• Motor tripping
Swell	<ul style="list-style-type: none">• Capacitor switching• Load switching• System voltage regulation	<ul style="list-style-type: none">• Unsteady-state voltage

3. EXPERIMENTAL SETUPS FOR PQA

For the measurement of harmonics and interharmonics in a variable fundamental frequency, a two-stage ADALINE (Adaptive Linear Neural Network) model is proposed [6]. The utilized experimental setup consisting of a PC (Personel Computer), an AWG (Arbitrary Waveform Generator), a Multifunction DAQ (Data Acquisition) PCI-6036E card, and the other connection components is shown in Figure 4. Acquired data is processed and analyzed with MATLAB. Then using the data, a new method is proposed.

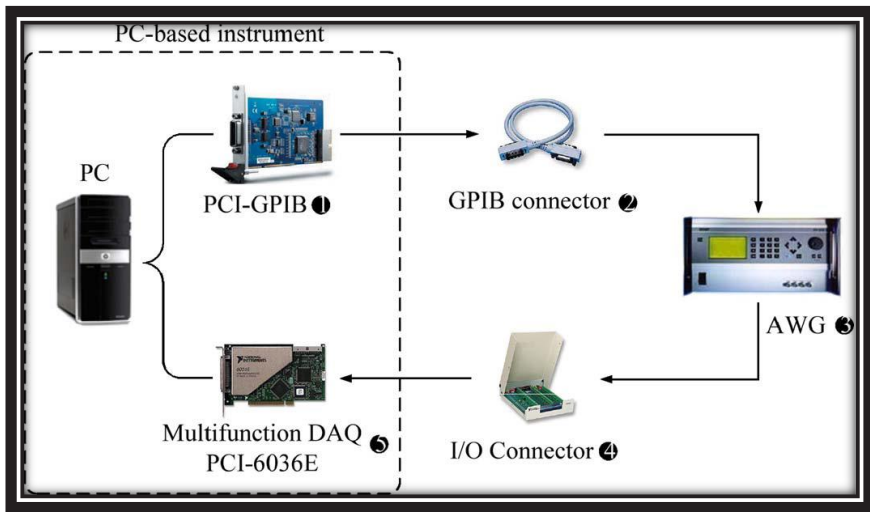


Figure 4: Experimental Setup for Harmonics and Interharmonics Measurement [6]

In another study, an estimation method for time-varying harmonics with the Extended Real Model of the Kalman Filter (ERMKF) was proposed [7]. For the implementation of this study, an AWG, a Digital Phosphor Oscilloscope (DPO), two PCs (for controlling AWG and implementations of the algorithms), and the components for connections as in Figure 5. The data acquisition is made with LabVIEW and then this data is used for the improvement of an estimation method based on ERMKF for time-varying harmonics.

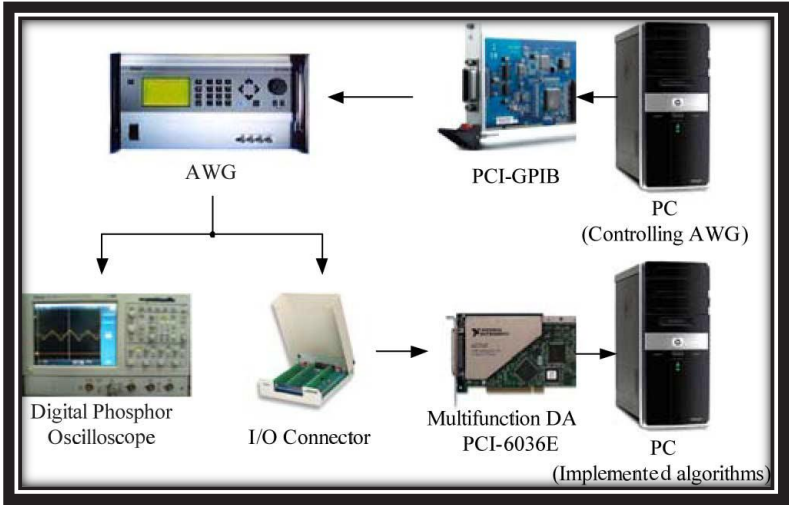


Figure 5: Experimental Setup for Time-Varying Harmonics Estimation [7]

A similar study for time-varying harmonics and interharmonics using variable harmonic and interharmonic sources as well as AWG displayed in Figure 6 has been performed to be used as virtual instrumentation and an educational platform [8]. This setup provides virtual and educational usability to the users.

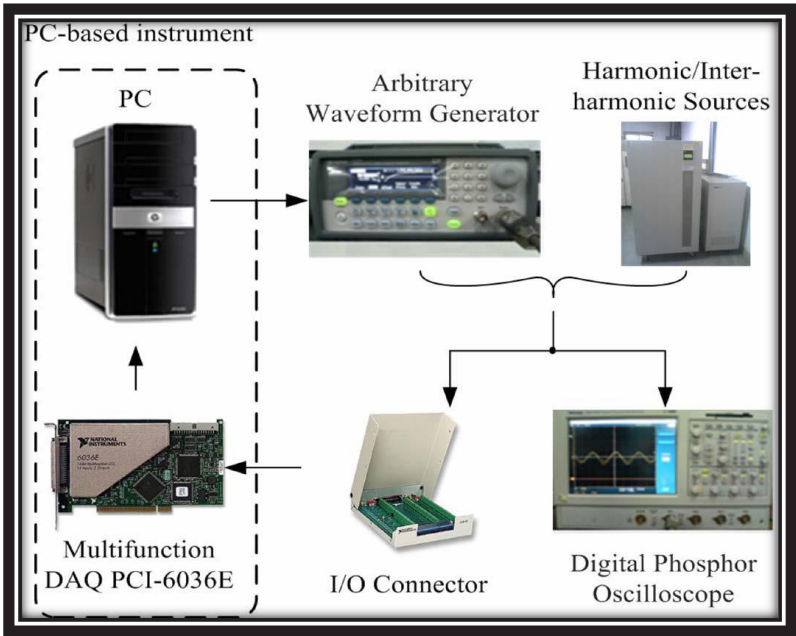


Figure 6: Experimental Setup for Virtual Instrumentation and Educational Platform [8]

Another important phenomenon is voltage variations and tracking is also critical for power systems. For this goal, a prony based solution procedure was produced in [9]. This study was performed on the setup in Figure 7 comprising only an AWG, a DAQ with connector, and a PC with the help of LabVIEW to implement the virtual analyzer.

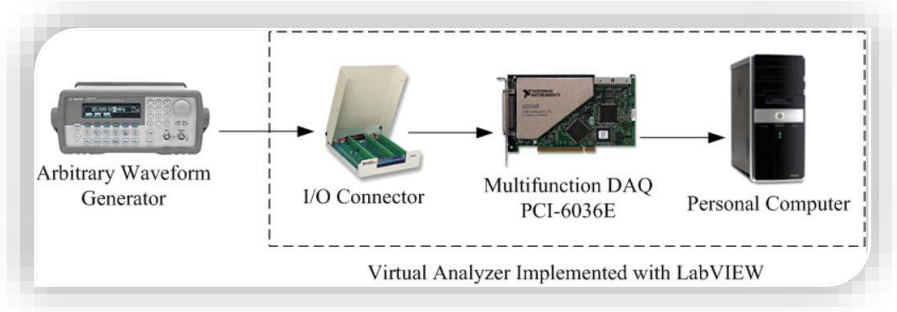


Figure 7: A Setup for Voltage Variations [9]

Additionally, another method based on FFT (Fast Fourier Transform) and ADALINE for the fast estimation of harmonics using MATLAB was proposed in [10]. This study was made out with a laptop, a Chroma 6590 programmable AC Source, a Ni USB 6009, and a Gw Instek differential probe GDP-025 as shown in Figure 8. As mentioned before, acquired data was performed in MATLAB and the method has been created.



Figure 8: Experimental Setup for Fast Estimation of Harmonics [10]

Power quality monitoring is also important for an electrical machine. So, a MATLAB application will track its operation and power quality statement by using an experimental setup. This setup consists of a DC powered 3 Phase

Synchronous Generator with a load and a 3 Phase induction motor driver with a PowerFlex 525 AC drive. Moreover, Picoscope USB with High Voltage differential probe with a clamp, and a 3 Phase Power Analyser are available. These collect data from the 3 Phase induction motor and the 3 Phase Synchronous Generator. Figure 9 illustrates the detailed configuration of this setup [11].

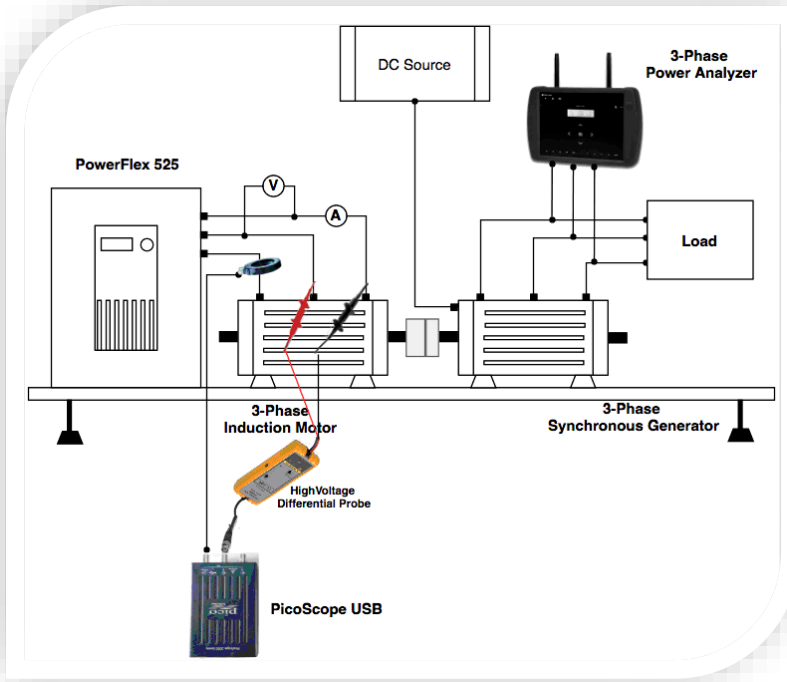
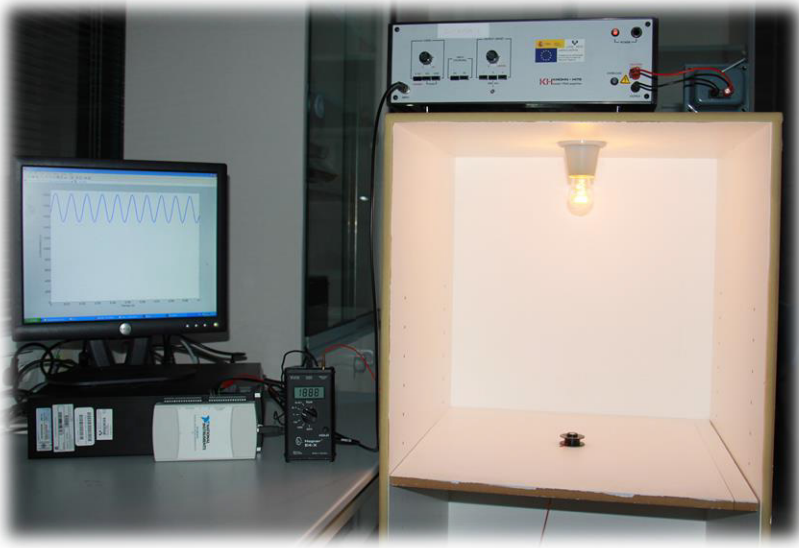
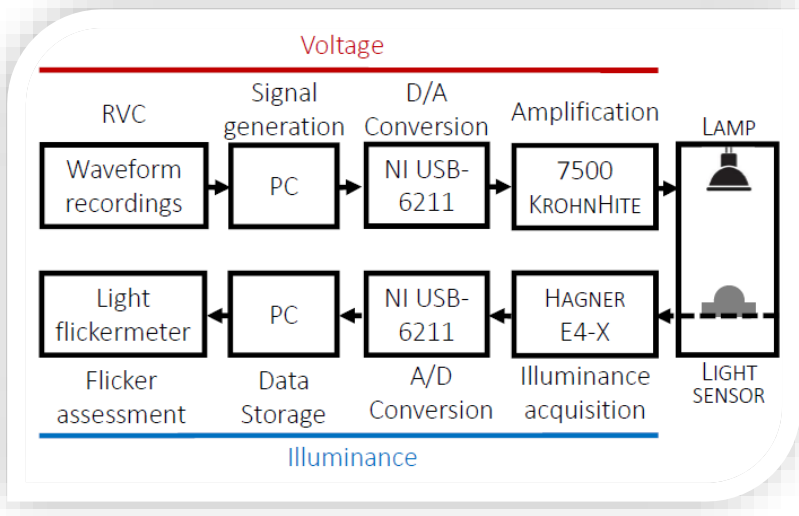


Figure 9: Power Quality Monitoring of Electrical Machines [11]

Another power quality disturbance, the light flicker effect is led by interharmonics. High-frequency interharmonic components also generate this effect as well as low-frequency ones. IEC 61000-4-15 proposed a flickermeter according to the incandescent lamps. This flickermeter detects the effects of low-frequency interharmonics. However, it cannot detect high-frequency interharmonics effects caused by modern lamps having rectifiers. So, recent studies have focused on the flicker effect of modern lamps in case of different voltages. A similar study performs with Raspberry Pi and MATLAB on an experimental setup. This setup has a signal generator with PC, a NI-USB 6211 D/A convertor, a 7500 Khronhite amplification, a lamp and a detector in a box, a Hagner E4-X illuminance acqusitor, NI-USB 6211 D/A convertor, and flickermeter assessment on PC as in Figure 10 [12].



(a)

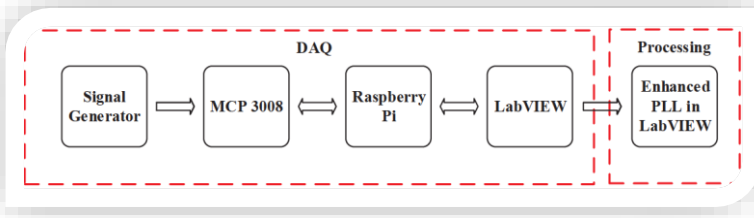


(b)

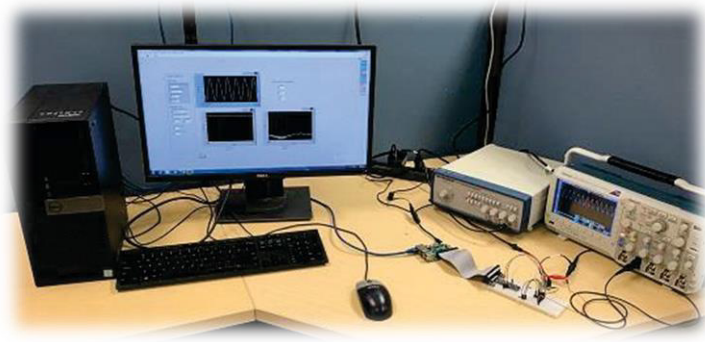
Figure 10: Experimental Setup for Flicker Effect (a) An Image (b) Flowchart [12]

An implementation of an improved phase-locked loop (PLL) using Raspberry Pi is proposed in [13] using the experimental setup in Figure 11. By utilizing the computational power of Raspberry Pi, the enhanced PLL achieves accurate frequency tracking and reduced phase error. It covers the design, components, and algorithms involved in the implementation, presenting experimental results

that validate its effectiveness. This realization advances PLL technology and increases the control system capabilities of Raspberry Pi. The enhanced PLL offers benefits such as improved frequency stability, faster lock-in time, and enhanced tracking performance compared to traditional designs. The use of affordable and accessible computing platforms like Raspberry Pi demonstrates the potential for achieving precise and efficient frequency synchronization in various applications. In that study, There is a two-step- experimental setup. The first is the DAQ step including Signal Generator, MCP 3008 card, and Raspberry Pi. The other one is signal processing with enhanced PLL in LabVIEW.



(a)

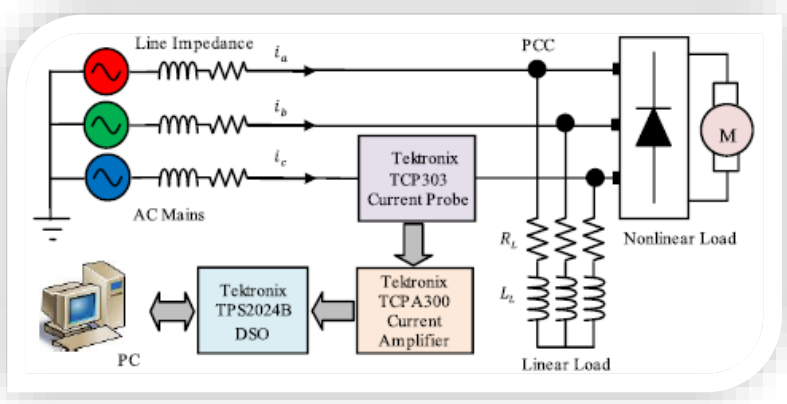


(b)

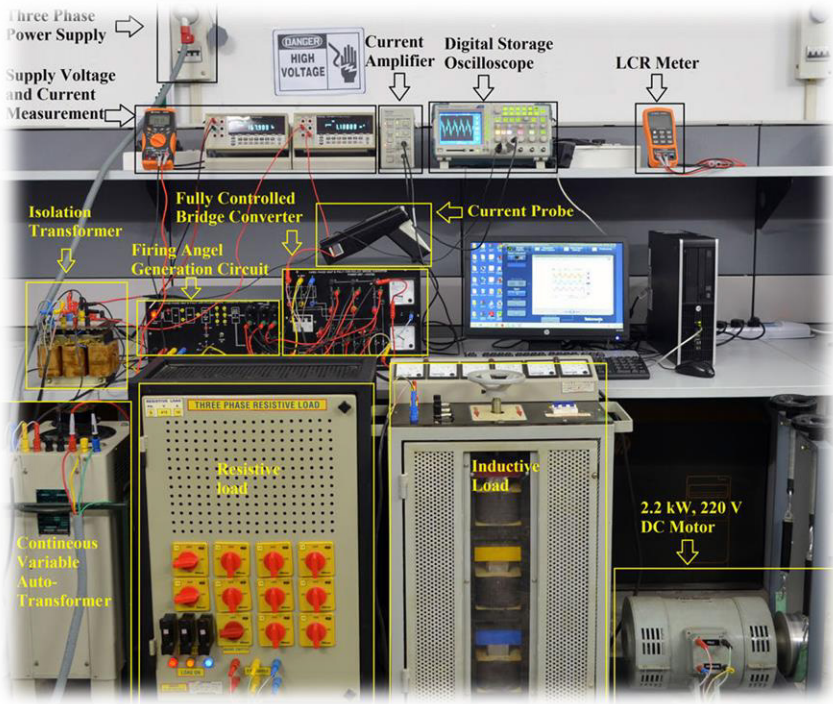
Figure 11: Experimental Setup using Raspberry PI and LabVIEW
(a) Flowchart (b) Setup [13]

A novel technique for estimating harmonic and interharmonic components in power systems is presented in [14]. The proposed method employs a multi-stage adaptive linear neuron (MS ADALINE) and a high-speed digital signal processor (DSP) for real-time processing. According to simulation results, this method surpasses other conventional approaches in terms of precision and speed, indicating its applicability in power system monitoring and control. Consequently, the article concludes that adopting the MS ADALINE-based technique has the potential to significantly enhance the efficiency and reliability

of power systems. This study has used an experimental setup in Figure 12.a. consisting of a Tektronix TCP303 current probe, a Tektronix A300 current amplifier, and Tektronix TPS2024B DSO (Digital Storage Oscilloscope), and a PC for the acquisition of real data from the PCC (point of common coupling) of the electrical system with nonlinear loads, linear loads and linear impedances. This study also used MATLAB as software. 3 phase supplied hardware platform consists of a variable source, a multimeter, a current amplifier, a DSO, an isolation transformer, a fully controlled bridge converter, a firing angle generation circuit, a resistive load, an induction load, and a 2.2 kW 220 VAC motor, a continuously variable autotransformer like in Figure 12. b. The proposed method's performance is evaluated under various conditions, including changing the frequency and amplitude of the input signal and the presence of noise and disturbances in this setup. The experimental and simulation results are compared. It is seen that this method has more accuracy, speed, and resistance to noise and disturbances than the other methods. Whence, it is a promising method to optimize the performance of power system monitoring and control applications.



(a)



(b)

Figure 12: Experimental Setup for Power System Harmonics and Interharmonics [14] a) Scheme of the setup b) Photograph of the setup

A method for the estimation of the fundamental frequency new of three-phase power systems is presented in [15]. This study is performed in simulative and experimental implementations for the assessment of the effectiveness of the

proposed method. For the tracking of input signal frequency, the method exploits a digital signal processing algorithm combining a three-phase resonant filter and a phase-locked loop (PLL). The performance of the proposed method is evaluated by both simulation and experimental setup. The proposed method is conducted on the experimental setup which is made up of a dSPACE controller card with the help of a CLP 1104 board, a DL-750 scope coder, and a PC as in Figure 13.

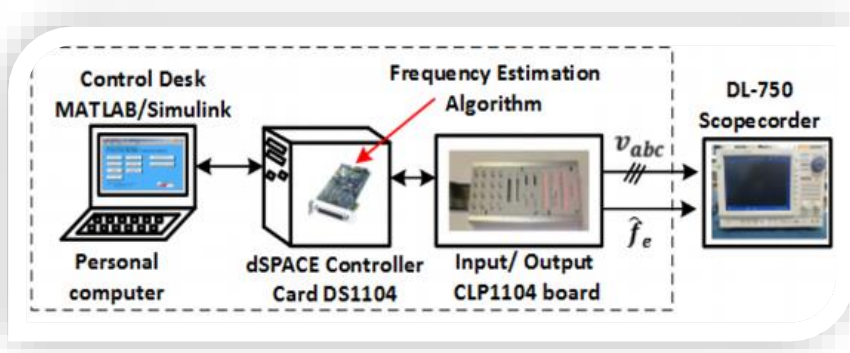
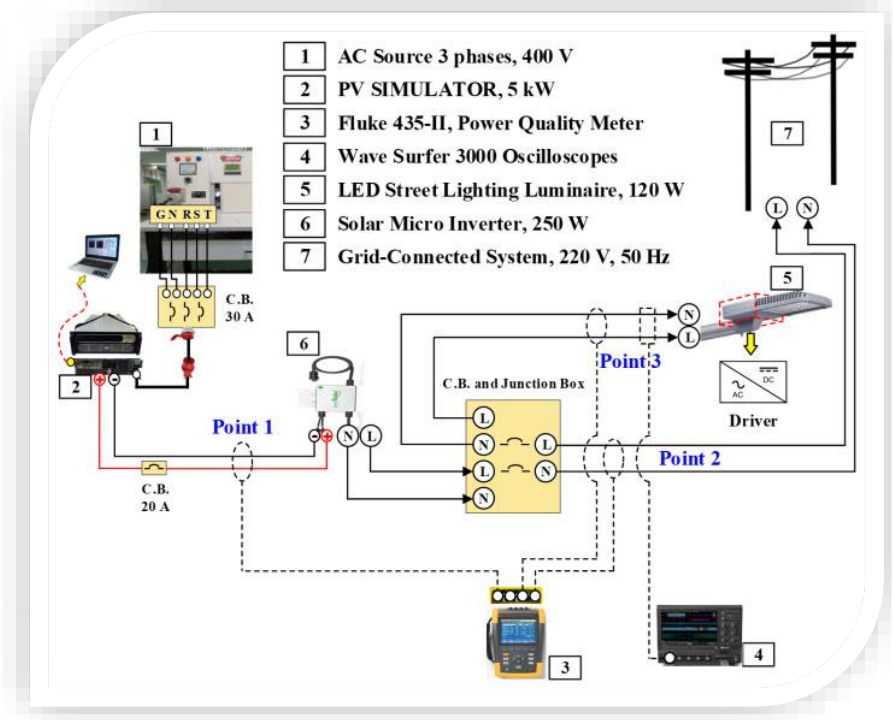
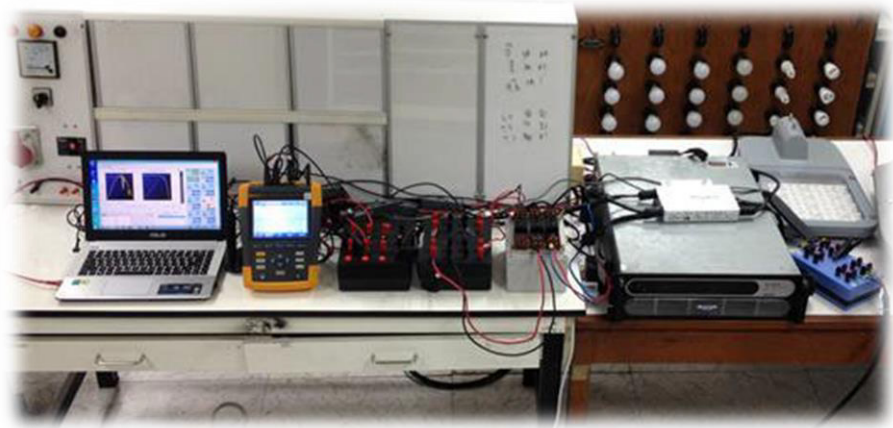


Figure 13: Experimental Setup for Improved Fundamental Frequency Estimator Study in [15]

The study in [16] discusses the details of the experimental setup used to evaluate the proposed nano-grid technology integrated into a road lighting system. The experimental setup included the installation of an AC source 3 phases, a PV simulator, a Fluke 435-II power quality meter, a wave surfer 3000 oscilloscope, a LED Street lighting luminaire, a solar micro-inverter, and a grid-connected system like in Figure 14. That study provides information on the reasons for conducting the study, the methods used to evaluate the viability of the proposed solution, and the outcomes of experiments conducted on the nano-grid technology in an actual setting. This study ensures a practical technique based on nano grid technology for road lighting systems and some important advantages. These advantages are the minimization of energy consumption and carbon emissions while enhancing the dependability and resilience of the lighting system.



(a)



(b)

Figure 14: The Road Lighting Integrated Nanogrid System (a) Schematic Diagram (b) Experimental Setup [16]

The study in [17] presents a detection method for harmonic components in power system signals. Since this method is effective in terms of computation, it

is suitable for real-time applications in the power system signals. It uses a discrete Fourier transform and a windowing function for the precise detection and harmonics extraction by the input signal. It has high performance in both simulation and actual power grid implementation. Also, it has precious harmonic component extraction and low computational time. For that, it can be a beneficial tool for monitoring and controlling the power quality of power systems.



Figure 15: Experimental Setup in [17] used for Harmonic Extraction

A study in [18] presents a new method to compress power-quality waveforms compression, with the purpose of continuous recording and reduced storage requirements. This method using spectral variation analysis identifies and removes redundant information from the waveform while conserving important spectral components. This method provides efficient data compression without losing accuracy and feasibility. The study highlights the advantages, such as covering primarily waveform features and adaptability to some PQDs. Additionally, the implementation and computational complexity of the method

are discussed. The experimental setup uses A PC, a power generator, a signal conditioner circuit, an Analog/Digital Converter (ADC) board, an FPGA, and an oscilloscope illustrated in Figure 16.

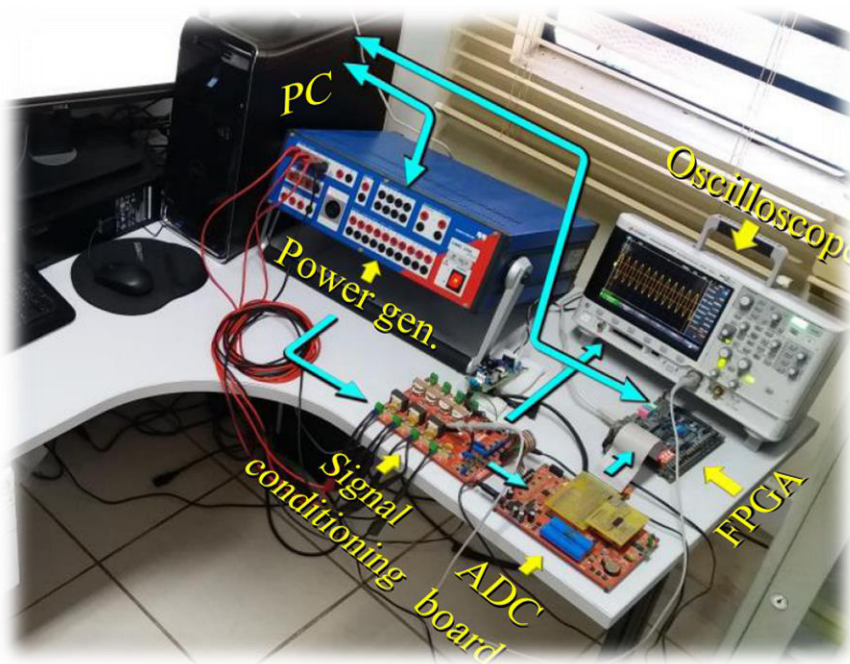


Figure 16: Experimental Setup in [18] used for Spectral Variation-Based Signal Compression

A Recurrent Wavelet Petri Fuzzy Neural Network (RWPFNN) -based voltage restoration control method has been proposed for microgrids [19]. The focus has been on enhancing voltage stability and reliability in microgrids. The RWPFNN combines Recurrent Neural Networks (RNN), wavelet analysis, Petri nets, and fuzzy logic to effectively control the voltage restoration process. It considers the dynamic behavior of the microgrid and utilizes wavelet analysis for information processing. That study highlights the benefits of the RWPFNN-based control, including improved voltage stability, minimized system losses, and enhanced microgrid performance. Implementation aspects and practical considerations are also applied in an experimental setup consisting of a PC as a host, a TMS320F28335 (DSP1) and a TMS320F28335 (DSP2) for signal processing, a Serial Peripheral Interface (SPI), Peripheral Circuits, an OP4510, and an oscilloscope like in Figure 17. Results of the study show the method offers a promising solution for voltage control in microgrids.

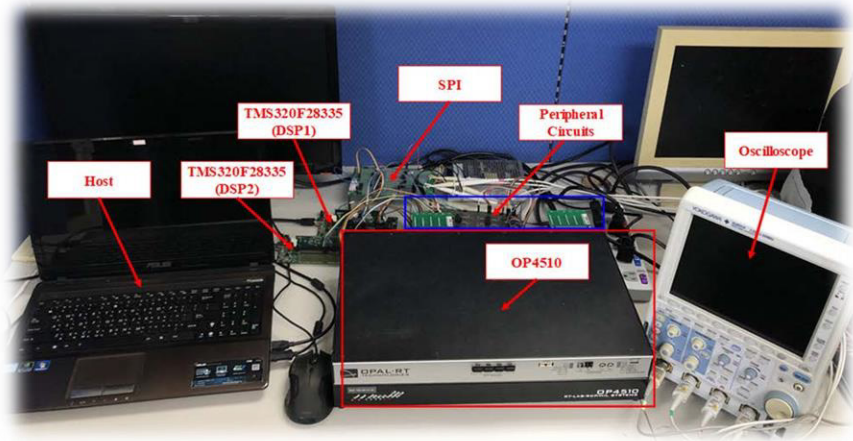


Figure 17: Experimental Setup in [19] used for RWPFNN

4. SUMMARY AND DISCUSSION

In summary, all these setups with researched parameters are shown in

.This study gives a hint to researchers about the experimental setups and the importance of analyzing and addressing various power quality challenges. These setups include a range of instruments, data acquisition systems, and analysis tools to measure, monitor, and analyze different power quality parameters. Not only devices but also some software are operated in these setups. The investigated methods, algorithms, and technologies contribute to the development of innovative solutions for improving the efficiency, reliability, and performance of power systems. Through these experimental setups, researchers can gain valuable insights into power quality issues and work towards the advancement of power system technologies. These setups are not only for the stated PQ parameters but also for other parameters mentioned before. Also, some optimized setups can be arranged by means of this table, too.

Table 2: Table of Experimental Setups on Analysis of PQDs

Ref.	Devices / Components / Software	Researched PQ parameters
[6], [7]	<ul style="list-style-type: none"> • A PC, • An AWG, • A Multifunction DAQ PCI-6036E card, • Connection components <ul style="list-style-type: none"> ➤ GPIB connector, ➤ PCI-GPIB converter, ➤ I/O connector, • MATLAB. 	<ul style="list-style-type: none"> ○ <i>Harmonics</i> ○ <i>Interharmonics</i>
[8]	<ul style="list-style-type: none"> • An AWG, • A DPO, • Two PCs, <ul style="list-style-type: none"> ➤ GPIB connectors, ➤ A PCI-GPIB converter, • LabVIEW. 	<ul style="list-style-type: none"> ○ <i>Harmonics,</i> ○ <i>Interharmonics</i> ○ <i>Fundamental Frequency Tracking</i>
[9]	<ul style="list-style-type: none"> • An AWG, • A DAQ, • An I/O connector, • A PC, • LabVIEW. 	<ul style="list-style-type: none"> ○ <i>Voltage Variations</i> ○ <i>Fundamental Frequency Tracking</i>
[10]	<ul style="list-style-type: none"> • A Chroma 6590 Programmable AC Source, • A NI USB 6009 DAQ card, • A GW Instek differential probe GDP-025, • MATLAB • Laptop 	<ul style="list-style-type: none"> ○ <i>Harmonics</i>
[11]	<ul style="list-style-type: none"> • A DC power generator, • A Picoscope USB, • 3 Phase Synchronous Generator with <ul style="list-style-type: none"> ➤ A load, • A 3 Phase induction motor driver with <ul style="list-style-type: none"> ➤ A Powerflex 525 AC drive, • A High Voltage differential probe with <ul style="list-style-type: none"> ➤ A clamp, • A 3-Phase Power Analyser, • MATLAB. 	<ul style="list-style-type: none"> ○ <i>Power Quality Monitoring</i>
[12]	<ul style="list-style-type: none"> • A Raspberry Pi, • A PC, • A NI-USB 6211 D/A convertor, • A 7500 Khronhite amplification, • A lamp, • A detector in a box, • A Hagner E4-X illuminance acquisitor, • LabVIEW, • MATLAB. 	<ul style="list-style-type: none"> ○ <i>Interharmonics</i> ○ <i>Flicker</i> ○ <i>Fundamental Frequency Tracking</i>

[13]	<ul style="list-style-type: none"> • A Signal Generator, • A MCP 3008 card, • A Raspberry Pi, • LabVIEW. 	<ul style="list-style-type: none"> ○ Frequency Tracking ○ Phase Error Reduction
[14]	<ul style="list-style-type: none"> • Tektronix, • A TCP303 current probe, • An A300 current amplifier, • A TPS2024B DSO, • An electrical system with <ul style="list-style-type: none"> ➤ Nonlinear loads, ➤ Linear loads ➤ Linear impedances, • A PC, • MATLAB. 	<ul style="list-style-type: none"> ○ Harmonics ○ Interharmonics
[15]	<ul style="list-style-type: none"> • A DSpace controller card, • A CLP 1104 board, • A DL-750 scope card, • A PC 	<ul style="list-style-type: none"> ○ Fundamental Frequency Estimation ○ 3-Phase Systems
[16]	<ul style="list-style-type: none"> • An AC source 3 phases, • A PV simulator, • A Fluke 435-II PQ meter, • A wave surfer 3000 oscilloscope, • A LED Street lighting luminaire, • A solar micro-inverter, • A grid-connected system 	<ul style="list-style-type: none"> ○ Energy Consumption Minimization ○ Lighting System Resilience Enhancement ○ Lighting System Dependability Enhancement
[17]	<ul style="list-style-type: none"> • A load resistor, • A load inductor, • A filter inductor, • A rectifier module, • A current sensor, • A microcontroller PCB, • An oscilloscope. 	<ul style="list-style-type: none"> ○ Harmonics, ○ Power Grid Monitoring ○ Power Grid Control
[18]	<ul style="list-style-type: none"> • A PC, • A power generator, • A signal conditioner circuit, • An ADC board, • An FPGA, • An oscilloscope. 	<ul style="list-style-type: none"> ○ PQ Compression ○ Waveforms Spectral Variation Analysis ○ Power Disturbances Variations
[19]	<ul style="list-style-type: none"> • A laptop, • A residual current circuit breaker, • A DAS, • An AC programmable power source, • A Raspberry PI3. 	<ul style="list-style-type: none"> ○ Sags ○ Swells ○ Harmonics ○ PQ Monitoring ○ Electrical Systems Reliability ○ Electrical Systems Efficiency

REFERENCE

- [1] IEEE Power & Energy Society, *2010-1459-IEEE Standard Definitions for the Measurement of Electric Power Quantities Under Sinusoidal, Nonsinusoidal, Balanced, or Unbalanced Conditions*. 2010.
- [2] IEEE Power and Energy Society, *IEEE Recommended Practice for Monitoring Electric Power Quality*, vol. 1995, no. 1. 2009.
- [3] I. Standard and N. Internationale, “IEC Standard 61000-4-7: General guide on harmonics and interharmonics measurements and measuring instruments for power supply networks and attached devices used for the measurements,” 2008.
- [4] I. Power and E. Society, *IEEE Recommended Practice — Adoption of IEC 61000-4-15: 2010 , Electromagnetic compatibility (EMC)— Testing and measurement techniques — Flickermeter — Functional and design specifications*, no. October. 2011.
- [5] International Electrotechnical Commission, “IEC Standard 61000-4-30: Testing and measurement techniques - Power quality measurement methods,” vol. 2003, p. 90, 2003.
- [6] C. I. Chen and G. W. Chang, “A two-stage ADALINE for harmonics and interharmonics measurement,” *Proc. 2010 5th IEEE Conf. Ind. Electron. Appl. ICIEA 2010*, vol. 56, no. 6, pp. 340–345, 2010.
- [7] C. I. Chen and Y. C. Chin, “Extended real model of kalman filter for power system harmonic measurements,” *Asia-Pacific Power Energy Eng. Conf. APPEEC*, vol. 25, no. 1, pp. 17–26, 2010.
- [8] C. I. Chen and G. W. Chang, “Virtual instrumentation and educational platform for time-varying harmonic and interharmonic detection,” *IEEE Trans. Ind. Electron.*, vol. 57, no. 10, pp. 3334–3342, 2010.
- [9] C. I. Chen and G. W. Chang, “An efficient prony-based solution procedure for tracking of power system voltage variations,” *IEEE Trans. Ind. Electron.*, vol. 60, no. 7, pp. 2681–2688, 2013.
- [10] Z. P. Goh, M. A. M. Radzi, Y. Von Thien, H. Hizam, and N. I. A. Wahab, “Hybrid FFT-ADALINE algorithm with fast estimation of harmonics in power system,” *IET Signal Process.*, vol. 10, no. 8, pp. 855–864, 2016.
- [11] F. M. Arrabal-Campos, A. Alcayde, F. G. Montoya, J. Martinez-Lao, and R. Banos, “A MATLAB application for monitoring the operation and power quality of electrical machines,” *Proc. Int. Conf. Harmon. Qual. Power, ICHQP*, vol. 2018-May, pp. 1–5, 2018.
- [12] S. Lodetti *et al.*, “Flicker of modern lighting technologies due to rapid voltage changes,” *Energies*, vol. 12, no. 5, pp. 1–16, 2019.
- [13] R. Kolla, Z. Wang, Z. Miao, and L. Fan, “Realization of Enhanced Phase

- Locked Loop using Raspberry Pi and LabVIEW,” *51st North Am. Power Symp. NAPS 2019*, pp. 1–6, 2019.
- [14] P. Garanayak, R. T. Naayagi, and G. Panda, “A High-Speed Master-Slave ADALINE for Accurate Power System Harmonic and Inter-Harmonic Estimation,” *IEEE Access*, vol. 8, pp. 51918–51932, 2020.
- [15] A. K. Verma, R. K. Jarial, P. Roncero-Sanchez, and M. R. Ungarala, “Improved Fundamental Frequency Estimator for Three-Phase Application,” *IEEE Trans. Ind. Electron.*, vol. 68, no. 9, pp. 8992–8998, 2021.
- [16] S. Yoomak and A. Ngaopitakkul, “Investigation and Feasibility Evaluation of Using Nanogrid Technology Integrated into Road Lighting System,” *IEEE Access*, vol. 8, pp. 56739–56754, 2020.
- [17] S. K. Jana and S. S., “A Computationally Efficient Harmonic Extraction Algorithm For Grid Applications,” *IEEE Trans. Power Deliv.*, vol. 8977, no. c, 2021.
- [18] E. B. Kapisch, V. V. De Morais, L. R. M. Silva, L. M. A. Filho, and C. A. Duque, “Spectral Variation-Based Signal Compression Technique for Gapless Power Quality Waveform Recording in Smart Grids,” *IEEE Trans. Ind. Informatics*, vol. 18, no. 7, pp. 4488–4498, 2022.
- [19] F. J. Lin, J. C. Liao, C. I. Chen, P. R. Chen, and Y. M. Zhang, “Voltage Restoration Control for Microgrid with Recurrent Wavelet Petri Fuzzy Neural Network,” *IEEE Access*, vol. 10, pp. 12510–12529, 2022.

Chapter 25

Current Approach in Sourdough Fermentation

Çisem BULUT ALBAYRAK¹

Lütfiye ÇETİN²

Eren GÜVENDİ³

¹ Asst. Prof. Dr. Aydın Adnan Menderes University, Engineering Faculty, Food Engineering, Aydın, TURKIYE, cisembulut@gmail.com , <https://orcid.org/0000-0002-7993-5372>

² Food Engineer, Aydın Adnan Menderes University, Engineering Faculty, Food Engineering, Aydın, TURKIYE, <https://orcid.org/0009-0008-2156-504X>

³ Food Engineer, Aydın Adnan Menderes University, Engineering Faculty, Food Engineering, Aydın, TURKIYE, erenguendi28@gmail.com, <https://orcid.org/0009-0005-8517-0168>

ABSTRACT

Sourdough fermentation is one of the oldest biotechnological practice and commonly used in bread production. Various lactic acid bacteria (LAB) and yeast species are responsible. The leading LAB species are *Lactobacillus plantarum* (*Lactiplantibacillus plantarum*), *Lactobacillus brevis* (*Levilactobacillus brevis*), *Lactobacillus sanfranciscensis* and *Lactobacillus fermentum* (*Limosylactobacillus fermentum*). Moreover, yeast genera as *Saccharomyces*, *Candida*, *Kazachstania*, *Torulopsis*, *Yarrowia* and *Pichia* provide important contributions. Number and kind of microorganisms can be affected by several parameters such flour and water amounts, fermentation temperature and time duration.

Although bakery yeasts have great impact in the commercial area, there existed increasing interest for sourdough culture due to some health and functional properties. Sourdough fermentation provides improved mineral bioavailability and enhanced dietary fibers. In addition, the glycemic index can be reduced. Improved protein digestibility and reduction of content of anti-nutrient factors are other beneficial sides. The aim of this chapter is to examine the recent literature on sourdough fermentation and the applications comprehensively and make projections. In particular, improvements of sensory properties, volatile compounds, extending shelf life have been focused for sourdough fermentation and applications. Although the use of sourdough is increasing worldwide, it creates difficulties in the industry due to the maintenance of microbial culture and cost. In the future, the attempts for its wider commercialization and application within different formulations can be expected.

Keywords: Sourdough, fermentation, lactic acid bacteria, yeast.

INTRODUCTION

Sourdough is defined as a dough of flour and water fermented by yeasts and lactic acid bacteria (LAB). It is mainly used as a leavening agent to produce bakery products. Currently, sourdough fermentation has been taken attention to obtain cereal-based foods due to functional and health promoting properties (Albagli et al., 2021).

Fermentation and bread have always been popular elements as they represent civilization and spirituality throughout history. Sourdough bread is originated in Egypt. Aish, which is an Arabic term and means life, coincides with the pronunciation of yeast and bread in the Egyptian dialect. It has become the main element of many religious reproductions because of its nutritional meaning, according to Tacuina Sanitatis (Arora et al., 2021).

The first milestone for sourdough cultures was description of *Lactobacillus sanfranciscensis* (*Fructilactobacillus sanfranciscensis*) (Sugihara et al., 1971). Due to superiority of bakery yeast in industrial area, investigations for sourdough fermentation has been delayed until late 1900s. In the recent years, sourdough fermentation has gained more scientific interest for the last 30 years due to the popularity of fermented products (Arora et al., 2021).

Sourdoughs contribute to the sensory, rheological and shelf life of bakery products due to their special microbial content and functionality. Main attractive properties are listed below;

- Increased mineral bioavailability
- Enriched dietary fibers
- Reduced glycemic index
- Enhanced protein digestibility
- Elimination of the anti-nutritional factors

When the sourdoughs are compared with commercial yeasts, the final product quality seems having good advantage in some bakery and bread productions. For instance, In the some breads produced, sourdough stands out in terms of sensory score, digestibility and nutritional properties (Siepmann et al., 2018).

Besides, sourdough fermentation also improves the properties of gluten-free products (mixtures of rice, corn and several pseudo-cereals). Sourdough fermentation is also a good way to recycle lots of food by-products, milling by-products, and agricultural waste. Sourdough fermentation is a method used to steadily increase bran content in various baked goods (Pontonio et al., 2020). Nevertheless, sourdough fermentation prevents the lipase activity of the grain

seed, allowing the products to have a long shelf life and a variety of nutrient content (Rizzello et al., 2010).

Although several superiorities of bakery yeast in terms of standard production, commercialization, low price and wide range of using area, sourdough has also taken attention due to some desirable and multifunctional properties.

Table 1: Comparison of bakery yeast and sourdough.

Bakery Yeast	Sourdough
Only one type of yeast (<i>Saccharomyces cerevisiae</i>)	It is a mixture of LAB and yeast species
Low cost for its production	High cost for defined sourdough cultures
Worldwide commercialized	It is not completely commercialized
Standard production	Some difficulties for standardization
Limited health benefits	Enhanced healthy properties
Wide usage area	Limited usage area
Contribute defined aroma	Various volatile and aroma compounds

HEALTH PROMOTING PROPERTIES

Mineral bioavailability

Phytic acid can be found naturally in plant based foods such as grains and legumes. It supports formation of insoluble complexes with minerals and other substances therefore dietary bioavailability is reduced (Arora et al., 2021). Phytases are hydrolyzing enzymes accountable for the digestion of phytic acid.

Sourdough fermentation and acidification activates flour endogenous phytases and microbial enzymes, a significant increase in mineral bioavailability (calcium, sodium, magnesium, iron and zinc) can be observed. The pH level is in the range of 4.3–4.6 for optimal acidification. This acidification can cause reduction of phytic acid and minerals become bioavailable (Arora et al., 2021). LAB and yeast species of sourdough fermentation can also harbor phytase enzyme activity. Therefore, sourdough fermentation is an excellent way to increase the mineral bioavailability of floury foods produced by cereals, pseudo-cereals and legumes.

Dietary fibers

Dietary fibres are composed of plant polysaccharides and lignin. In most cases, they can not be digested by human enzymes. High consumption of dietary fibre have various health promoting properties such as preventing the diabetes, hypertension, obesity, cardiovascular and gastrointestinal disorders. The World Health Organization reports that it is necessary to take 25

g of dietary fiber (DF) daily, but active consumption is noticeably lower. Therefore, it is desirable to carry out dietary interventions to increase DF intake.

Although pseudo-cereals and cereals (hemicellulose, resistant starch, β -glucans, arabinoxylans) are common sources of DF, the common goal is to increase the DF content of bakery products, including gluten-free products, with enriching by various percentages of bran (5-20%), wheat germ (4-7.5%), spent cereals for beer (5-20%) or legume flours (Arora et al., 2021). Fortification of bakery products with those DF has some limitations and in some cases sensory and rheology properties are affected negatively. However, the fortification with bran up to 20% by sourdough fermentation was studied by several researchers (Gobbetti et al., 2014 ; Arora et al., 2021).

Glycemic index

High content of fast digestible carbohydrates in the diet leads the rapid increasing of the blood glucose levels. The glycemic index (GI) is numerical value of foods that indicates the potential to increase the blood sugar after consumption. Recent clinical studies show that GI responses after eating bread also depend on gut microbiome functionality in humans. Therefore, personalized dietary recommendations become more important (Korem et al., 2017). Additionally, the effects of sourdough baked goods on the gut microbiome can also play role for GI responses.

There existed various researches to examine the sourdough fermentation on GI and glycemic load. In one of the recent study, the control breads had higher GI values than the sourdough breads (Demirkesen-Bicak et al., 2021). In particular, sourdough fermentation with high acid levels combined with soluble fibres can be effective way to decrease GI (Gobbetti et al., 2014).

Protein digestibility

Many scientific evidences show that fermentation is related to an improved digestibility, primarily in relation to proteins. The stability of protein hydrolysates and the in vitro ingestibility of protein are increased by sourdough fermentation. Longer fermentation times can improve protein digestibility properties. In recent years, developing of gluten free products has gained attention for people with celiac disorders. Several strains of LAB were combined with fungal proteases and they were used to decrease the residual gluten content. Many of the research articles aimed to explore the role of sourdough fermentation in gluten reduction (Graça et al., 2021; Fraberger et al., 2020; Fu et al., 2023; Tovar and Gänzle, 2020).

Degradation of anti-nutritional factors

Although cereals, pseudo-cereals and legumes are very rich in nutrients, they sometimes contain anti-nutritional factors that restrict their consumption or can cause important health problems. Phytic acid, raffinose, condensed tannins, vicine and convict, saponins and trypsin inhibitors are main ones and they can be present present in various vegetable environments. For example, raffinose can not be digested by pancreatic enzymes, but it can be fermented by gas-producing bacteria in the colon and cause intestine problems. Again, condensed tannins and trypsin inhibitors prevent digestive enzymes, and some difficulties can exist for digestion of proteins and other nutrients. Biologically active glycosides, such as saponins, vicine and convicine, lead the destruction of red blood cells and can block their absorption by forming complexes with nutrients. Vicine and convicine are important precursors of the aglycones divisin and isouramil, the main causative agent of favism which is genetic based disorders.

Sourdough fermentation can be effective tool and cost effective way to eliminate those factors. For instance, in one of the recent study, several grains and legumes were fermented, and decreased concentrations of raffinose (62–80%), condensed tannins (23%), trypsin inhibitors (23–44%) and saponins (68%) were reported (Montemurro et al., 2019).

CEREALS USED IN SOURDOUGH FERMENTATION

Cereal flours produced from the *Poaceae* family of cereals are widely used in sourdough production. Flours obtained from soft and hard wheat are common ones. Dry grinding of wheat grains and gluten network formation during the dough preparation are important for baking quality.

The main component of wheat flour is carbohydrates, consisting of starch (70–75%), free saccharides (1–2%) and crude fiber (2–3%) (De Vuyst et al., 2021). Starch is the main nutritional source for yeasts and it absorbs water in dough, contributes to viscosity and is included in the gluten network that keep the gas and structure. Fructans and arabinoxylans are major components of dietary fibers. Fructans are nutritionally important components that support yeast activity. Arabinoxylans allow the dough to hold gas better by absorbing water, thus increasing viscoelasticity that contributes to the physical structure. The benefit to the dough texture is very important against the damage that LAB activity will cause to the gluten network during fermentation.

The proteins in wheat flour consist of gliadin and glutenin. Those proteins have role for the real viscoelasticity and gas holding capacity of the dough. They do this by forming disulfide bridges in the glutenin macropolymer of the gluten network through water binding and thiol/disulfide exchange reactions as the dough is mixed

and kneaded. When LAB acidify the dough, gluten dissolves more due to the positive net charge of proteins. However, starch retrogradation by further swelling of starch granules delays staling, resulting in increased loaf volume and crumb softness. Another component that affects the baking quality of flour is enzymes such as α -amylase, β -amylase, proteases and oxidizing enzymes.

Lipids, which have a positive effect on the baking quality of the flour, are found in 1-2% of wheat flour. Glycolipids, which are independent of starch, increase the dough's kneading ability and gas holding capacity, extend the oven spring and delay the return of starch by increasing the bread volume and crumb resistance.

Phenolics, minerals and vitamins are other important compounds found in wheat flour and they help the sensory and/or nutritional quality of bread.

Rye flour is also widely used in sourdough fermentation. Starch is lower than wheat flour, especially in terms of arabinoxylan pentosans. The fiber content is higher than wheat flour and protein amounts are similar. However, the gluten proteins which are important for dough texture are less suitable. Additionally, α -amylase is higher, and β -amylase is lower in rye flour. Furthermore, it needs proper acidification by fermentation therefore too much starch hydrolysis can be prevented (Deleu et al., 2020). Another point is fermentation of rye flour and water allows better dissolution of pentosans. Although arabinoxylans are sensitive to oxidative gelatinization in an acidic conditions, they give rye dough its real texture (De Vuyst et al., 2021). Many other grain flours can be used in the production of sourdough, such as: barley, millet, oat, sorghum, einkorn. Although cereal flours are often used in sourdough production, flours produced from pseudo cereals, legumes and alternative seeds can also be preferred (Bartkiene et al., 2013; Carbó et al., 2020; Hoehnel et al., 2020; Jagelaviciute and Cizeikiene, 2021; Maidana et al., 2021; Perri et al., 2021; Shiri et al., 2021).

Although the mentioned flours have different compositions, they also contain specific compounds. For example, β -glucan is higher in barley and oat flours, and the concentrations of phenolic compounds are higher in sorghum and millet flours (De Vuyst et al., 2021; Gänzle and Zheng, 2019). Additionally, oat and buckwheat flours contain some compounds that show antimicrobial activity, such as phenolics, tannins and some enzymes (De Vuyst, et al., 2017). Surprisingly, it is also possible to produce cereal gruels, porridge and beverage with artisanal and industrial fermentation processes by using different grain flours such as barley, maize, millet, and etc.. In those fermentations, technological aims are different from sourdough fermentations. For example, in the boza fermentation, main aim is aroma development. However, in bread production main aim is to improve dough quality and bread texture (Gänzle and Zheng, 2019).

MICROORGANISMS IN SOURDOUGH FERMENTATION

Sourdough fermentation is one of the oldest methods of dough fermentation, which takes place by self-fermentation of lactic acid bacteria (LAB) and yeast. The number, presence and interaction between microorganisms (LAB and yeast) depends on many internal and external factors (Demirkesen-Bıçak et al., 2021). While LAB contribute to the acidification process, yeasts help to increase volume of the dough by carbon dioxide production (Roby et al., 2020). Besides, acetic acid bacteria, which are rarely used, are responsible for the formation of acidic aroma, texture and crust color of the dough (De Vuyst et al., 2021). In 30 years, literature, types and species of identified microorganisms in sourdough fermentation were shown Table 2.

Lactic Acid Bacteria

Lactic acid bacteria (LAB) are anaerobic (aerotolerant) bacteria, members of the Firmicutes families, and also Gram-positive, catalase-negative and non-spore forming (De Vuyst et al., 2021). They can be found in various environments. For instance, they can occur in fermented food products, human body, plant materials, and the bodies of insects. Homofermenters use flour saccharides and they produce lactic acid from pyruvate by EMP pathway to generate ATP. However, in heterofermenters ATP is obtained by phosphogluconate pathway and they produce lactic acid and ethanol or acetic acid and CO₂. They can be found in many diverse foods and beverages, for example, fermented cereals, vegetable products, meat and dairy products. In particular, heterofermentative LAB species which are the members of the *Lactobacillaceae* play an important role in sourdough production. These species show good adaptation to the sourdough environment (De Vuyst and Neysens, 2005).

Lactic acid (homo- and heterofermentative LAB) and acetic acid (heterofermentative LAB) contribute to the acidic taste in final product.. The acidic taste of sourdoughs is affected by the ratio of lactic acid to acetic acid. Both lactic acid (fresh and mild acidity) and acetic acid (sharp and strong vinegar-like acidity) are effective in lowering the pH level. On the other hand, only acetic acid contributes to the aroma because it is volatile (De Vuyst et al., 2021).

Table 2: Identified LAB and yeasts in the last 30 years (Arora et. al.,2021)

LAB	Identifying Frequency	Yeasts	Identifying Frequency
<i>L. plantarum</i>	142	<i>Saccharomyces cerevisiae</i>	87
<i>L. brevis</i>	93	<i>Kazachstania humilis</i>	49
<i>L. sanfranciscensis</i>	90	<i>Yarrowia keelungensis</i>	18
<i>L. fermentum</i>	56	<i>Torulaspora delbrueckii</i>	17
<i>L. curvatus</i>	51	<i>Kazachstania unispora</i>	13
<i>L. sakei</i>	42	<i>Kazachstania exigua</i>	13
<i>L. paralimentarius</i>	36	<i>Pichia kudriavzevkii</i>	10
<i>L. pentosus</i>	32	<i>Kazachstania barnetti</i>	10
<i>L. casei</i>	31	<i>Kluyveromyces marxianus</i>	7
<i>L. rossiae</i>	30	<i>Candida krusei</i>	7
<i>L. paracasei</i>	24	<i>Rhoadotorula nucionalaginoso</i>	6
<i>L. pontis</i>	23	<i>Kazachstania servazzi</i>	6
<i>L. reuteri</i>	20	<i>Saccharomyces bayanus</i>	5
<i>L. paraplantarum</i>	18	<i>Meyerozyma guilliermondii</i>	5
<i>L. panis</i>	16	<i>Pichia membranaefaciens</i>	4
<i>L. spicheri</i>	15	<i>Kazachstania bulderi</i>	4
<i>L. helveticus</i>	14	<i>Meyerozyma carpophila</i>	3
<i>L. hammesii</i>	14	<i>Kluyveromyces lactis</i>	3
<i>L. rhamnosus</i>	12	<i>Hyphopichia pseudoburtoni</i>	3
<i>L. farciminis</i>	11	<i>Candida glabrata</i>	3
<i>L. alimentarius</i>	11	<i>Candida pelliculosa</i>	3
<i>L. delbrueckii</i>	10	<i>Torulopsis holmii</i>	2
<i>L. namurensis</i>	10	<i>Saccharomycopsis fibuligera</i>	2
<i>L.frumenti</i>	9	<i>Millerozyma farinosa</i>	2
<i>L. mindensis</i>	9	<i>Metschnikowia pulcherrima</i>	2
<i>L. coryniformis</i>	8	<i>Candida tropicalis</i>	2
<i>L. nantensis</i>	8	<i>Candida parapsilosis</i>	2
<i>L.fructvorans</i>	7		
<i>L. buchneri</i>	7		
<i>L.parabuchneri</i>	7		

Acetic Acid Bacteria

Although LAB are dominant in sourdough, Acetic Acid bacteria (AAB) can also present and provide some contributions. They are aerobic bacteria belonging to the family of α -proteobacteria, and they also Gram-negative, catalase-negative, oxidase-positive and non-spore forming bacteria (De Vuyst et al., 2021). They can be naturally found in ethanol and carbohydrate rich environments such as flowers and fruits. The following Acetobacter and/or Gluconobacter species can be found in sourdough fermentations (De Vuyst et al., 2021)

Acetobacter cerevisiae
Acetobacter fabarum

Acetobacter indonesiensis
Acetobacter lovaniensis group species
Acetobacter malorum group species
Acetobacter orleanensis
Acetobacter oryzifermentans
Acetobacter pasteur ianus
Acetobacter senegalensis
Gluconoobacter sengalensis
Gluconobacter frateurii group
Komagataeibacter sucrofermentans
Komagataeibacter xylinus

Acetic acid is produced by partial oxidation of the substrates in the periplasm of cells. For this process, acetic acid is obtained from ethanol and/or gluconic acid by glucose. Special cofactor-dependent dehydrogenases embedded in the cytoplasmic membrane were used. The acetic acid can provide an acidic contribution to the taste of sourdough breads and foods. Additionally, eight single-strain dough fermentations were studied and the aroma potentials in sourdough productions were examined. Among bacteria, *A. cerevisiae* was also tested (Ripari et al., 2016). Acetic fermentation also results in a simple volatiles profile, mainly characterised by acetic acid, butanoic acid, and acetaldehyde. 2-Pentylfuran. In addition, AAB can produce fructans that can promote to the texture of sourdough breads with starter culture-initiated sourdough productions. The use of *G. albidus*, *K. baliensis* is examined to produce fructans in the presence of sucrose or sugar cane molasses (Hermann et al., 2015; Ua-Arak et al., 2016, 2017). In all these applications, a constant agitation has been applied because oxygen is essential for AAB. Moreover, AAB have impact on color of the bread crumb, possibly by producing dihydroxy acetone (Comasio et al., 2020).

Yeasts

A total of 80 yeast species have been identified worldwide, mainly belonging to the genera *Saccharomyces*, *Candida*, *Kazachstania*, *Torulopsis*, *Yarrowia* and *Pichia*. Although LAB work well with *Kazachstania exigua* or *Kazachstania humilis*, the most frequently used species is *Saccharomyces cerevisiae* (Arora et al., 2021).

Yeasts are single-celled fungi that reproduce mainly facultatively aerobic or asexually and sexually in starvation state (Neiman, 2005). Although many species have role in the food fermentations, some of them cause spoilage

problems. Acid tolerant and fermentative yeasts belonging to Ascomycota are preferred in sourdough fermentation (De Vuyst et al., 2016). According to the frequency of use in 394 back slopped sourdoughs *S. cerevisiae* (68% of the sourdoughs), *K. humilis* (20%), *W. anomalus* (6 %), *Torulaspora delbrueckii* (6 %), *Pi. kudriavzevii* (6 %), and *C. glabrata* (4 %) are the main species (De Vuyst et al., 2017).

Sourdough yeast ferments the saccharides in flour to pyruvate via Embden-Meyerhof-Parnas (EMP), providing ATP and reducing power, and then converting pyruvate to ethanol and CO₂(alcoholic fermentation). The formation of glycerol and succinic acid plays a role in balancing redox. In dough fermentation, ethanol evaporates during cooking, glycerol facilitates the capture of carbon dioxide, and succinic acid lowers the pH. All these changes support the formation of the gluten network and contribute to the rheology of the dough (De Vuyst et al., 2021).

Moreover, yeasts have role in the crumb flavor of the bakery products by producing different aroma active metabolites (De Vuyst et al., 2021). Esters are responsible for the fruity-floral aroma of bread, while diacetyl, a product of pyruvate metabolism, plays a role in the crumb flavor. While mixing the dough in the presence of yeasts and adding oxygen will increase the yeast metabolites so therefore it is desirable situation.

Selection of Starter Cultures for Sourdough Production

In sourdough fermentation, the use of selected LAB and yeast can provide improved performance and / or target certain characteristics and are the reason for preferences.

Sourdough starter candidates can be isolated from sourdough fermentations and flours. Additionally, various cereals,pseudo-cereals, legumes and milling by-products can be other potential sources for isolation. The main selection criteria are listed below.

- Technological, biochemical and nutritional characteristics
- Acid production and growth rates
- Antifungal activity
- Exopolysaccharide (EPS) formation
- Synthesis of volatile compounds
- Proteolysis
- Flavor and aroma development

In the study by Liu et al., (2020), volatile compounds responsible for sourdough aroma were investigated in the sourdough fermentation. Ten different types of LAB obtained from Chinese sourdough dough and sourdough fermentation was evaluated by RNA sequencing. The volatiles of sourdough fermented with different species were reported using principal component analysis (PCA) method. In this study, in which aldehyde and ketone-rich homofermentatives and ester and ethanol-rich heterofermentatives were investigated by PCA, *Lactobacillus sanfranciscensis* and *Lactobacillus plantarum* species, which provide two different flavors, were dominant.

Some specific properties, such as GABA (Coda et al., 2010) synthesis and angiotensin I-converting enzyme (ACE) inhibitory and antioxidant peptides (Coda et al., 2011) degradation of phytic acid (Yıldırım and Arıcı, 2019) and digestibility (Demirkesen Bıçak et al., 2021) were the other criteria evaluated for sourdough starter selection (Arora et al., 2021).

Classification of Sourdough Production Process

Sourdough production can be categorized according to the inoculum used to initiate the fermentation, or traditional based on the process technology applied (De Vuyst et al., 2021).

In the inoculum-based classification, there are three types of sourdough production processes (Types I, II and III) that affect the microbiology of mature sourdoughs (Figure 1).

Type I sourdough production stages show fermentations of the flour-water mixture via traditional daily back slopping. It is based on taking a little bit of the previous sourdough sample and fermenting it with fresh dough. Sometimes it can be kept in the refrigerator for a few days or weeks. Type I sourdoughs are often used to produce traditional bread. For example, it can be commonly applied and in artisan bakeries and homemade breads.

Type II sourdough production process shows the prolonged fermentation of a flour-water mixture, which is initiated by the addition of a common starter culture that targets specific characteristics of the final product, such as fermentation and aroma development. Type II sourdough is a commercial product it is sold in bakeries as a semi-liquid, heat-treated, spray-dried, tumble-dried, or freeze-dried forms. They can be used for flavoring or as technological purposes. In particular, dough leavening or, bread shelf life are the most of the important technological aims. The microorganisms are usually still metabolically active only in the case of semi-liquid sourdough. In the type II sourdoughs, specific strains of the acid-fast LAB strains of the flour-water mixture were used.

Finally, Type III fermentation process shows starter culture-initiated fermentation of flour-water mixtures (as in Type II), followed by daily back slopping (as in Type I). Thus, Type III fermentation processes are a mixture of Type I and Type II fermentation processes and can be used by some artisanal and industrial bakeries.

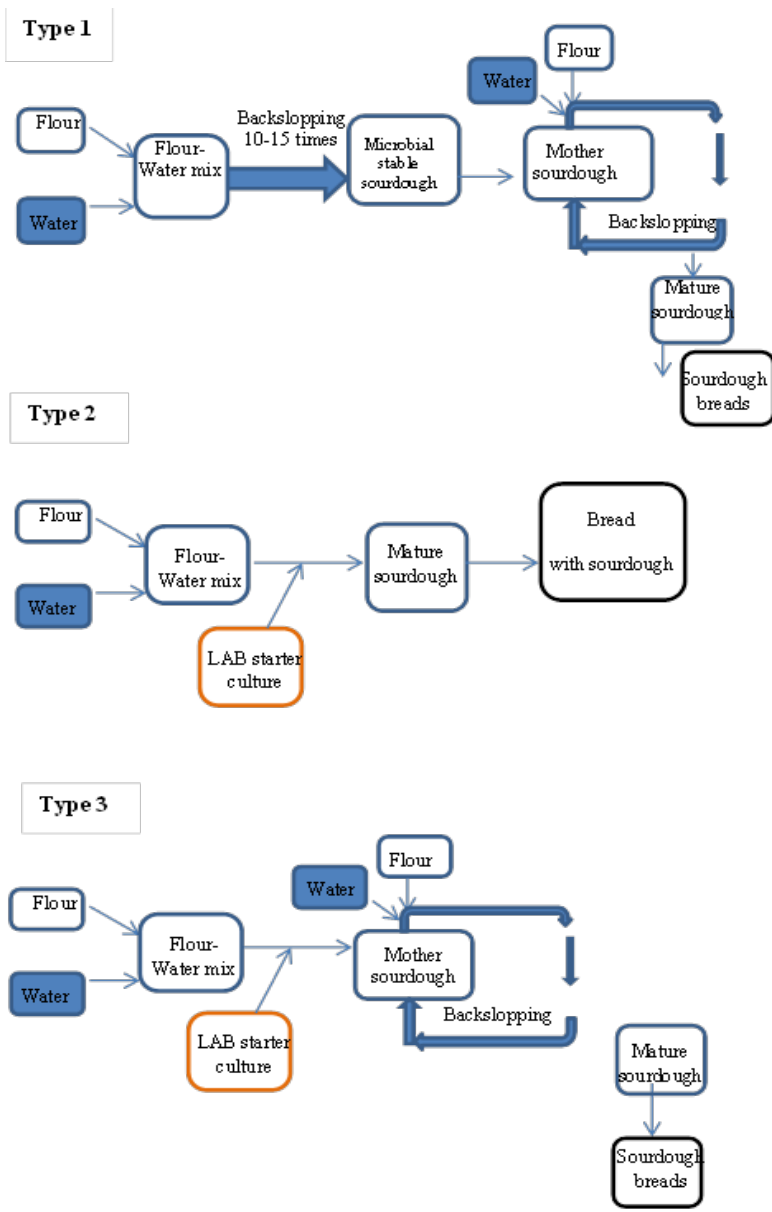
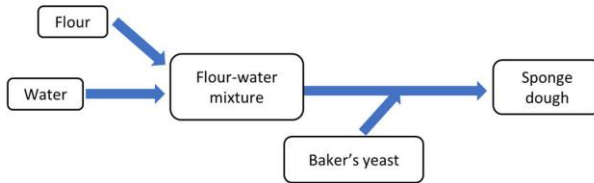


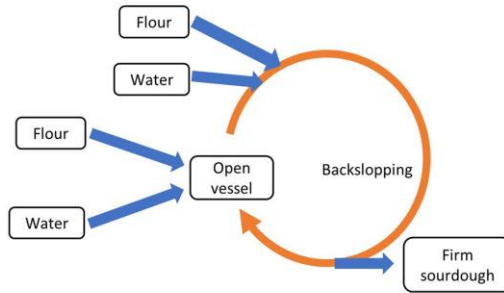
Figure 1: Inoculum based sourdough production processes (De Vuyst et al., 2021)

In the process technology-based classification, there are four types of sourdough production processes. These are Type 0, Type I, Type II, Type III and their details are presented in Figure 2.

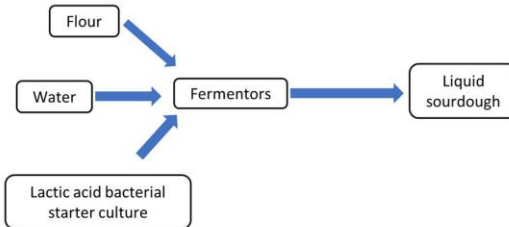
Type 0



Type I



Type II



Type III

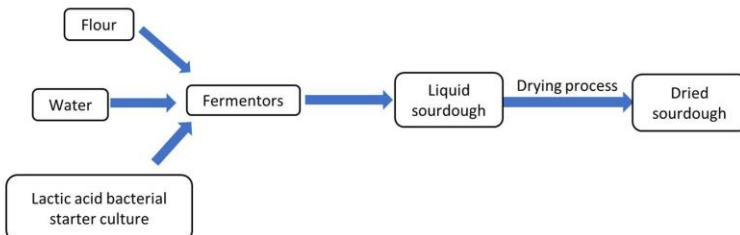


Figure 2. Process technology-based classification of sourdough De Vuyst et al., 2021)

Type 0 sourdough manufacturing processes show sponge doughs or pre-doughs in which fermentation of flour-water mixtures take place in short time and only limited LAB growth is observed. In this technique bakery yeast is also used. In most cases, yeasts grow faster than LAB. Limited acidifying and flavoring effects can be provided by the LAB species. Typical Type 0 products are French baguettes, Italian ciabattas and American crackers. They are generally not considered sourdough products.

Type I sourdough process symbolizes traditional sourdough with daily back slopping at room temperature (20–30 °C) and low dough yield (<200), short to moderate fermentation times (6–24 hours), and a pH of approximately 4.0. Years of cultivation of these original mother doughs have been kept for years and a rich collection was built up. Some of them are saved in the Puratos Fermentation library (www.puratos.com/en/innovation/Center-for-Bread-Flavor/Sourdough-library/).

Type II sourdough production processes aim to increase acidification and/or other sourdough-specific properties. They are also carried out at controlled temperatures above ambient (30–37 °C) and are known as accelerated, one-step fermentations. This is initiated by the acid-stable starter culture, and which allow a simple handling of the sourdoughs at high Dough Yield (> 200). These processes take one to three days and therefore pH values can often be below 4.0. These sourdoughs are commercialized in liquid or pasty form or as hard or crumbly products and dried powders. They frequently harbor species of *Limosilactobacillus* (previously known as *Lactobacillus*) and *Lactobacillus* (e.g., *Lb. amylovorus*, *Lb. acidophilus*, and *Lb. crispatus*) (De Vuyst et al., 2021; Gänzle and Zheng, 2019).

Finally, in the Type III sourdough production processes, sourdoughs produced as in Type II and they are dried by using spray or drum drier. They are not metabolically active. Both Type II and Type III sourdoughs are used by artisanal and industrial bakeries for acidification and flavoring purposes. Since yeasts are deactivated by those methods, addition bakery yeast can be necessary (De Vuyst et al., 2021).

Various Food Products by Sourdough Fermentations

Sourdough fermentations are commonly used in bakery products and (Table 3) and in the most cases bread was the main food product. Many researches were focused on the addition on non-flour ingredients to improve health properties. For instance, chickpea, cow pea, olives pomace and the other legumes are used in the different studies. Sourdough fermentation and those ingredients increase the functional properties and consumer acceptance. Also, it

can support product diversity in the market. Apart from usual bread other bakery products such as cake, crostini also has been studied.

In one of the latest study, Calasso et al. (2023) extended the shelf life of bakery products by using type 3 sourdough combined with probiotic mixture (*Lactobacillus acidophilus*, *L. casei*, *Bifidobacterium* spp., *Bacillus coagulans*). They used this innovative dough to produce fresh base-pizza and focaccia . Physicochemical, protein, microbiological and volatile compounds were analyzed during 10 days. A more stable and heterogeneous microbiota were observed during storage. Additionally, the abundance of *Alternaria infectoria* and *A. alternata* was negatively affected. Relatively higher concentration of volatile carboxylic acids was also observed in this study. They concluded that microbiological and chemical properties of bakery products can be improved by addition of BCs and tIII-SD without chemical preservatives.

Table 3: Various food products by sourdough fermentations.

Food Product	Aim	Main Findings	References
Chickpea protein concentrate	To produce nutrient-enhanced sustainable chickpea protein concentrate using <i>Pediococcus</i> spp. starter culture obtained from back slopping fermentation.	While fermentation increased the water holding capacity, it decreased the foaming capacity. The nutritional and functionality of chickpea concentrate has been increased.	Xing et al. (2020)
Chinese steamed bread	To survey the microbial diversity of jiaozi and type I sourdough and the effect of these starter cultures on the volatile profile of final bread products.	<i>Weissella cibaria</i> and <i>Lactobacillus sanfranciscensis</i> were dominant in jiaozi and type I sourdoughs, respectively. Higher concentrations of volatiles were determined in products fermented with jiaozi. In products Type I acids, furans, aldehydes and corresponding alcohols were predominant	Yan et al. (2019)
Microalgae-based sourdough 'crostini'	To determine the functional and nutritional effect of <i>Arthrospira platensis</i> F&M-C256 (spirulina) biomass addition on crostini	Higher protein content and a lower dry matter and protein digestibility.	Niccolai et al. (2019)
Sorghum-based sourdough	Analyses of the textural, nutritional and sensory properties of sorghum sourdough bread fermented by	Sample with chickpea showed less hardness and high protein ash content in the compressions, the specific volume was high in the sample	Olojede et al. (2020)

	<i>P.pentosaceus</i> with the addition of chickpea and cowpea.	with legumes. Chickpea supplement is a good alternative to chemical dough additives.	
Bakery product with olive pomace	Enrichment of bread and biscuit whose functional component is olive pomace by different types of flour and fermentation.	Increase in phenolic compounds in fermented with sourdough. Sourdough breads enriched with pomace reduced IL-8 intestinal cells due to the anti-inflammatory characteristics.	Di Nunzio et al. (2020)
Sourdough bread enriched with hops extract and rice bran	To examine technological, bioactive and sensory properties of hops sourdough fermented with rice bran added wheat bread.	Sourdough fermentation with rice bran flour did not affect crumb moisture and density, but increased loaves volume and consumer satisfaction. Added rice bran darkened the crumb color.	Irakli et al. (2019)
Non-traditional sourdough corn/rice bread with quinoa, chia and hemp flour	To investigate the performance of chia, hemp and quinoa flours in gluten-free bread fermented with <i>L. sanfranciscensis</i> .	<i>L. sanfranciscensis</i> W2 has adapted and worked with non-traditional substrates like quinoa chia and hemp. Flour type and fermentation time affected the characteristics of non-traditional sourdough. The unfermented chia and hemp flour increased the firmness and staling rate, while the use of non-traditional hemp and quinoa sourdough decreased the rate of bread staling and extended this period.	Jagelaviciute and Cizeikiene (2021)
Microwave steamed cake with sourdough	To examine the quality and textural properties and potential improvements of sourdough on microwave steamed cake.	Specific volume, firmness and chewing criteria were improved. The dielectric properties of dough, extractability of protein and free sulfhydryl amount increased. Increase in the quality of the sample, and it became an inspiration for sourdough-based products and the adjustment of the microwave texture.	Zhou et al. (2021)

RECENT STUDIES OF SOURDOUGH FERMENTATIONS FOR BREAD PRODUCTION

There are various studies for the production of sourdough bread. Some of the recent studies and investigations carried out are shown in Table 4 below. These researches and examinations have generally been taken into account to improve the physiological (taste, aroma and smell) properties of bread produced with sourdough and its contribution to consumer health. Examples include bio-flavored sourdough bread, rye bread with rowan powder, gluten-free bread, and

bread with starter cultures such as kefir with coconut water. In addition, potential of hybrid technology (infrared cooking with traditional method) to produce traditional sourdough bread is also examined.

In one of the recent study, encapsulated kombucha sourdough without baker's yeast was used for bread production and physical, storage and consumer acceptability characteristics were examined (Mohd Roby et al., 2020). The bioactive components of kombucha sourdough starter and kombucha-free sourdough starter were determined by multivariate analysis with the help of 1H-NMR analysis. As a result of the main component analyses for bioactive metabolites, the presence of 15 metabolites that serve to distinguish sourdough that does not contain kombucha has been determined. Some compounds that make up the difference between the two sourdoughs are: alpha-aminobutyric acid, alanine, acetic acid, riboflavin, pyridoxine, anserine, tryptophan, gluconic acid and trehalose. Compared to traditional and sourdough bread, the loaf volume made with encapsulated kombucha sourdough increased, and there was also a significant decrease in crumb firmness. Encapsulated kombucha sourdough offers to produce a functional sourdough bread, as it extends its shelf life by 5-10 days and sensually pleases the consumer.

Table 4: Recent studies of sourdough fermentation for bread production.

Food Product	Aim	Main Results	References
Sourdough bread with Coconut water kefir (CWK)	The use of fermentation starter culture containing coconut water kefir (CWK) and <i>Lactobacillus fermentum</i> and <i>Lactobacillus plantarum</i> were tested to improve the production of sourdough bread	The bread sample fermented for 24 h with a CWK, <i>L. plantarum</i> and without dry yeast, had significantly higher values for almost all amino acids and a lower protein content compared to samples using CWK with <i>L. fermentum</i> without dry yeast..	(Limbad et al., 2020)
Rye-wheat bread made by adding rowan powder	To investigate potential of a nutritional acidifying additive based on plant materials (rowan powder) for rye-wheat bread production technology.	Addition of Rowan powder, provided better taste and odor. The optimum amount of mountain ash powder in the formulation of rye-wheat bread was 3.5% Bread made with diacetate showed better compressibility and swelling capacity than control bread.	(Dubrovskaya et al., 2020)
Sourdough bread	Gelveri To produce Gelveri bread by sourdough method and to investigate the possibility of using infrared (IR) and ultraviolet-C technologies while commercializing it.	Microbiological quality and shelf life could be improved without affecting other quality parameters with IR application, but a small decrease in pH level was observed. IR furnace can be combined with stone furnaces.	(Gokmen et al., 2021)

Gluten-free sourdough bread production	To develop a new starter microbial mix that serves to improve the quality and microbiological safety of gluten-free bread. To screen 8 LAB and 5 yeast strains for sourdough bread.	<i>S.cerevisiae</i> Y205 had the highest fermentative activity and alcohols. Dough proofing time increased (1.2–1.3 times) for sourdough compared to the control.	(Parakhina et al., 2021)
Bioflavored sourdough bread	To produce a reproducible sourdough product with a better taste, texture and aroma, by selected and defined lactic acid bacteria and yeast strains.	A sourdough bread fermented using the formulated consortium gave an impression of delectable taste and texture. This could show consumers that there is a healthier, tastier and viable way to make commercial yeast and sourdough breads available.	(Marolia et al., 2022)

CONCLUSION

Although sourdough has been used ancient times, it has not become very common in industrial area. However, there has been increasing consumer interest for sourdough in recent years due to the potential health benefits.

One of the important difficulties is standard production because interaction of sourdough microorganisms during fermentation and production can be easily affected many factors.

Additionally defining and developing sourdough microorganism mixtures and their proper utilization has not been clarified yet.

In the future, specific health properties can be focused for sourdough fermentation and specific products can be developed by considering the consumers health expectations. For example, specific sourdough breads have can be developed for diabetic and celiac patients. Furthermore, specific products can be advanced for athletes. Although berad has been focused in many studies, this technology can be used to develop new and diverse cereal based products in the market in the future.

REFERENCES

- Albagli, G., do Monte Schwartz, I., Amaral, P. F., Ferreira, T. F., & Finotelli, P. V. (2021). How dried sourdough starter can enable and spread the use of sourdough bread. *LWT*, 149, 111888.
- Arora, K., Ameer, H., Polo, A., Di Cagno, R., Rizzello, C. G., & Gobbetti, M. (2021). Thirty years of knowledge on sourdough fermentation: A systematic review. *Trends in Food Science & Technology*, 108, 71-83.
- Bartkiene, E., Schleining, G., Rekstyte, T., Krungleviciute, V., Juodeikiene, G., Vaiciulyte-Funk, L., & Maknickiene, Z. (2013). Influence of the addition of lupin sourdough with different lactobacilli on dough properties and bread quality. *International journal of food science & technology*, 48(12), 2613-2620.
- Calasso, M., Marzano, M., Caponio, G. R., Celano, G., Fosso, B., Calabrese, F. M., ... & De Leo, F. (2023). Shelf-life extension of leavened bakery products by using bio-protective cultures and type-III sourdough. *LWT*, 177, 114587.
- Carbó, R., Gordún, E., Fernández, A., & Ginovart, M. (2020). Elaboration of a spontaneous gluten-free sourdough with a mixture of amaranth, buckwheat, and quinoa flours analyzing microbial load, acidity, and pH. *Food science and technology international*, 26(4), 344-352.
- Coda, R., Rizzello, C. G., & Gobbetti, M. (2010). Use of sourdough fermentation and pseudo-cereals and leguminous flours for the making of a functional bread enriched of γ -aminobutyric acid (GABA). *International Journal of Food Microbiology*, 137, 236-245.
- Coda, R., Rizzello, C. G., Pinto, D., & Gobbetti, M. (2011). Selected lactic acid bacteria synthesize antioxidant peptides during sourdough fermentation of cereal flours. *Applied and Environmental Microbiology*, 78, 1087-1096.
- Comasio, A., S. Van Kerrebroeck, H. Harth, F. Verté, and L. De Vuyst. 2020b. Potential of bacteria from alternative fermented foods as starter cultures for the production of wheat sourdoughs. *Microorganisms* 8 (10):1534.
- Deleu, L. J., Lemmens, E., Redant, L., & Delcour, J. A. (2020). The major constituents of rye (*Secale cereale* L.) flour and their role in the production of rye bread, a food product to which a multitude of health aspects are ascribed. *Cereal Chemistry*, 97(4), 739-754.
- Demirkesen-Bicak, H., Arici, M., Yaman, M., Karasu, S., & Sagdic, O. (2021). Effect of different fermentation condition on estimated glycemic index, in vitro starch digestibility, and textural and sensory properties of sourdough bread. *Foods*, 10(3), 514.

- De Vuyst, L., and P. Neysens. 2005. The sourdough microflora: Biodiversity and metabolic interactions. *Trends in Food Science & Technology* 16 (1–3):43–56.
- De Vuyst, L., Harth, H., Van Kerrebroeck, S., & Leroy, F. (2016). Yeast diversity of sourdoughs and associated metabolic properties and functionalities. *International Journal of Food Microbiology*, 239, 26-34.
- De Vuyst, L., Van Kerrebroeck, S., & Leroy, F. (2017). Microbial ecology and process technology of sourdough fermentation. *Advances in applied microbiology*, 100, 49-160.
- De Vuyst, L., Comasio, A., & Kerrebroeck, S. V. (2021). Sourdough production: fermentation strategies, microbial ecology, and use of non-flour ingredients. *Critical Reviews in Food Science and Nutrition*, 1-33.
- Di Nunzio, M., Picone, G., Pasini, F., Chiarello, E., Caboni, M. F., Capozzi, F., ... & Bordoni, A. (2020). Olive oil by-product as functional ingredient in bakery products. Influence of processing and evaluation of biological effects. *Food Research International*, 131, 108940.
- Dubrovskaya, N., Parakhina, O., Lokachuk, M., Savkina, O., & Kuznetsova, L. (2020). Rowan powder based acidifying additive acidifying additive-an alternative to sourdough in the rye-wheat bread production.
- Fraberger, V., Ladurner, M., Nemec, A., Grunwald-Gruber, C., Call, L. M., Hochegger, R., ... & D'Amico, S. (2020). Insights into the potential of sourdough-related lactic acid bacteria to degrade proteins in wheat. *Microorganisms*, 8(11), 1689.
- Fu, W., Jia, X., Liu, C., Meng, X., Zhang, K., Tao, S., & Xue, W. (2023). Sourdough yeast-bacteria interactions results in reduced immunogenicity by increasing depolymerization and hydrolysis of gluten. *Innovative Food Science & Emerging Technologies*, 103281.
- Gänzle, M. G., & Zheng, J. (2019). Lifestyles of sourdough lactobacilli—Do they matter for microbial ecology and bread quality? *International Journal of Food Microbiology*, 302, 15-23.
- Gobbetti, M., Rizzello, C. G., Di Cagno, R., & De Angelis, M. (2014). How the sourdough may affect the functional features of leavened baked goods. *Food microbiology*, 37, 30-40.
- Gokmen, S., Erdem, N., Kocabas, A., & Yetim, H. (2021). Using a hybrid technology to produce traditional sourdough Gelveri bread: infrared cooking assisted with traditional method. *Journal of Food Science and Technology*, 58, 962-967.

- Graça, C., Lima, A., Raymundo, A., & Sousa, I. (2021). Sourdough fermentation as a tool to improve the nutritional and health-promoting properties of its derived-products. *Fermentation*, 7(4), 246.
- Hermann, M., Petermeier, H., & Vogel, R. F. (2015). Development of novel sourdoughs with in situ formed exopolysaccharides from acetic acid bacteria. *European Food Research and Technology*, 241, 185-197
- Hoehnel, A., Bez, J., Sahin, A. W., Coffey, A., Arendt, E. K., & Zannini, E. (2020). *Leuconostoc citreum* TR116 as a microbial cell factory to functionalise high-protein faba bean ingredients for bakery applications. *Foods*, 9(11), 1706.
- Irakli, M., Mygdalia, A., Chatzopoulou, P., & Katsantonis, D. (2019). Impact of the combination of sourdough fermentation and hop extract addition on baking properties, antioxidant capacity and phenolics bioaccessibility of rice bran-enhanced bread. *Food chemistry*, 285, 231-239.
- Jagelaviciute, J., & Cizeikiene, D. (2021). The influence of non-traditional sourdough made with quinoa, hemp and chia flour on the characteristics of gluten-free maize/rice bread. *Lwt*, 137, 110457.
- Korem, T., Zeevi, D., Zmora, N., Weissbrod, O., Bar, N., Lotan-Pompan, M., ... & Segal, E. (2017). Bread affects clinical parameters and induces gut microbiome-associated personal glycemic responses. *Cell metabolism*, 25(6), 1243-1253.
- Limbad, M., Gutierrez Maddox, N., Hamid, N., & Kantono, K. (2020). Sensory and physicochemical characterization of sourdough bread prepared with a coconut water kefir starter. *Foods*, 9(9), 1165.
- Liu, T., Li, Y., Yang, Y., Yi, H., Zhang, L., & He, G. (2020). The influence of different lactic acid bacteria on sourdough flavor and a deep insight into sourdough fermentation through RNA sequencing. *Food chemistry*, 307, 125529.
- Maidana, S. D., Finch, S., Garro, M., Savoy, G., Gänzle, M., & Vignolo, G. (2020). Development of gluten-free breads started with chia and flaxseed sourdoughs fermented by selected lactic acid bacteria. *LWT*, 125, 109189.
- Marolia, K. Z., Khan, B. K., Raval, N., & Sharma, Y. (2022). Production of bio-flavored sourdough bread. *African Journal of Biological Sciences*, 4(1), 127-138.
- Mohd Roby, B. H., Muhialdin, B. J., Abadl, M. M. T., Mat Nor, N. A., Marlin, A. A., Lim, S. A. H., ... & Meor Hussin, A. S. (2020). Physical properties, storage stability, and consumer acceptability for sourdough

- bread produced using encapsulated kombucha sourdough starter culture. *Journal of food science*, 85(8), 2286-2295.
- Montemurro, M., Pontonio, E., Gobbetti, M., & Rizzello, C. G. (2019). Investigation of the nutritional, functional and technological effects of the sourdough fermentation of sprouted flours. *International Journal of Food Microbiology*, 302, 47-58.
- Neiman, A. M. (2005). Ascospore formation in the yeast *Saccharomyces cerevisiae*. *Microbiology and Molecular Biology Reviews*, 69(4), 565-584.
- Niccolai, A., Venturi, M., Galli, V., Pini, N., Rodolfi, L., Biondi, N., ... & Tredici, M. R. (2019). Development of new microalgae-based sourdough “crostini”: Functional effects of *Arthrospira platensis* (spirulina) addition. *Scientific Reports*, 9(1), 1-12.
- Olojede, A. O., Sanni, A. I., & Banwo, K. (2020). Effect of legume addition on the physiochemical and sensorial attributes of sorghum-based sourdough bread. *LWT*, 118, 108769.
- Parakhina, O., Lokachuk, M., Kuznetsova, L., Savkina, O., Pavlovskaya, E., & Gavriloova, T. (2021). Evaluation of selected lactic acid bacteria as starter cultures for gluten-free sourdough bread production.
- Perri, G., Coda, R., Rizzello, C. G., Celano, G., Ampollini, M., Gobbetti, M., ... & Calasso, M. (2021). Sourdough fermentation of whole and sprouted lentil flours: In situ formation of dextran and effects on the nutritional, texture and sensory characteristics of white bread. *Food Chemistry*, 355, 129638.
- Pontonio, E., Dingo, C., Di Cagno, R., Blandino, M., Gobbetti, M., & Rizzello, C. G. (2020). Brans from hull-less barley, emmer and pigmented wheat varieties: From by-products to bread nutritional improvers using selected lactic acid bacteria and xylanase. *International Journal of Food Microbiology*, 313, 108384.
- Ripari, V., Cecchi, T., & Berardi, E. (2016). Microbiological characterisation and volatiles profile of model, ex-novo, and traditional Italian white wheat sourdoughs. *Food chemistry*, 205, 297-307.
- Rizzello, C. G., Nionelli, L., Coda, R., De Angelis, M., & Gobbetti, M. (2010). Effect of sourdough fermentation on stabilisation, and chemical and nutritional characteristics of wheat germ. *Food Chemistry*, 119, 1079–1089.
- Shiri, A., Ehrampoush, M. H., Yasini Ardakani, S. A., Shamsi, F., & Mollakhalili-Meybodi, N. (2021). Technological characteristics of inulin

- enriched gluten-free bread: Effect of acorn flour replacement and fermentation type. *Food Science & Nutrition*, 9(11), 6139-6151.
- Siepmann, F. B., Ripari, V., Waszczynskyj, N., & Spier, M. R. (2018). Overview of sourdough technology: From production to marketing. *Food and Bioprocess Technology*, 11(2), 242–270.
- Sugihara, T. F., Kline, L., & Miller, M. W. (1971). Microorganisms of the San Francisco sour dough bread process. I. Yeasts responsible for the leavening action. *Applied Microbiology*, 21, 456–458.
- Tovar, L. E. R., & Gänzle, M. G. (2021). Degradation of wheat germ agglutinin during sourdough fermentation. *Foods*, 10(2), 340.
- Ua-Arak, T., Jakob, F., & Vogel, R. F. (2016). Characterization of growth and exopolysaccharide production of selected acetic acid bacteria in buckwheat sourdoughs. *International journal of food microbiology*, 239, 103-112.
- Yan, B., Sadiq, F. A., Cai, Y., Fan, D., Chen, W., Zhang, H., & Zhao, J. (2019). Microbial diversity in traditional type I sourdough and jiaozi and its influence on volatiles in Chinese steamed bread. *LWT*, 101, 764-773.
- Yildirim, R. M., & Arici, M. (2019). Effect of the fermentation temperature on the degradation of phytic acid in whole-wheat sourdough bread. *Lwt*, 112, 108224.
- Zhou, J., Yan, B., Wu, Y., Zhu, H., Lian, H., Zhao, J., ... & Fan, D. (2021). Effects of sourdough addition on the textural and physiochemical attributes of microwaved steamed-cake. *LWT*, 146, 111396.
- Xing, Q., Dekker, S., Kyriakopoulou, K., Boom, R. M., Smid, E. J., & Schutyser, M. A. (2020). Enhanced nutritional value of chickpea protein concentrate by dry separation and solid state fermentation. *Innovative Food Science & Emerging Technologies*, 59, 102269.
- (www.puratos.com/en/innovation/Center-for-Bread-Flavor/Sourdough-library/)